Sensing Systems for Active Control of Sound Transmission into Cavities

Ben S. Cazzolato

Department of Mechanical Engineering

The University of Adelaide

South Australia 5005

Printed April 6, 1999. Submitted for the degree of Doctor of Philosophy on the 24th of December, 1998; awarded 29th of March, 1999.

Abstract

Driven by the need to reduce the sound transmitted into aircraft cabins from the power plant, this thesis investigates the active control of sound transmitted through structure into coupled enclosures. In particular, it examines alternatives to conventional microphone and accelerometer error sensors.

This study establishes a design framework for the development and analysis of an active noise control system which can be applied to any complex vibro-acoustic system. The design approach has focused on using techniques presently used in industry to enable the transfer of the active noise control technology from the research stage into practical noise control systems. The structural and acoustic sub-systems are modelled using FEA to estimate the *in vacuo* structural modal response of the structure and the acoustic pressure modal response (with rigid boundary conditions) of the interior cavity. The acoustic and structural systems are then coupled using modal coupling theory.

Within this framework, two novel error sensors aimed at overcoming observability problems suffered by traditional microphone and accelerometer sensors are investigated: namely, acoustic energy density sensors and shaped radiation modal vibration sensors.

Acoustic Energy Density Sensors

The principles of the measurement of energy density are discussed and the errors arising from its measurement using two and three-microphone sensor configurations are considered for a one-dimensional reactive sound field and a plane wave sound field. The error

analysis encompasses finite separation effects, instrumentation errors (phase and sensitivity mismatches, and physical length errors), diffraction and interference effects, and other sources of error (mean flow and turbulence, temperature and humidity, statistical effects). Following the one-dimensional study, four 3-axis energy density sensor designs are proposed and error analysis is conducted over the same acoustic fields as for the one-dimensional study. The design and construction of the simplest arrangement of the 4 three-axis sensors is discussed with reference to design issues, performance and limitations.

The strategy of using energy density control is investigated numerically for a purely acoustic system and a coupled panel-cavity system. Energy density control is shown to provide greater local and global control compared to that possible using an equivalent number of microphones. The performance of the control system is shown to be relatively insensitive to the placement of the energy density sensor. For an enclosed cavity system with high modal overlap, the zone of local control achieved by minimising energy density is found to be approximately the same as the zone of local control obtained when minimising pressure and pressure gradient in a diffuse sound field. It is also shown that if there is only one control source used per energy density sensor, global control will be almost optimum. The addition of further control sources leads to an improvement in global control, however, the control is no longer optimal. The control system is found to be very tolerant of errors in the estimate of the energy density and thus the use of simpler energy density sensor designs is justified.

Finally, an experiment is presented in which the global performance achieved by controlling a three-axis energy density sensor is compared with the performance achieved by minimising the acoustic potential energy and minimising the sum of squared pressures at a finite number of microphones. The experimental results are found to reflect the numerical results.

Radiation Modal Sensors

The active minimisation of harmonic sound transmission into an arbitrarily shaped enclosure using error signals derived from structural vibration sensors is investigated numerically and experimentally. It is shown that by considering the dynamics of the coupled system, it is possible to derive a set of "structural radiation" modes which are orthogonal with respect to the global potential energy of the coupled acoustic space and which can be sensed by structural vibration sensors. Minimisation of the amplitudes of the "radiation modes" is thus guaranteed to minimise the interior acoustic potential energy. The coupled vibro-acoustic system under investigation is modelled using Finite Element Analysis which allows systems with complex geometries to be investigated rather than limiting the analysis to simple, analytically tractable systems. Issues regarding the practical implementation of sensing the orthonormal sets of structural radiation modes are discussed. Specific examples relating to the minimisation of the total acoustic potential energy within a curved rectangular panel and a coupled cavity are given, comparing the performance offered using vibration sensing of the radiation modes on the structure with the more traditional error sensing; namely, the discrete sensing of the structural kinetic energy on the structural boundary and the acoustic potential energy in the enclosed space approximated by the mean squared pressures at several locations.

Contents

Statement of Originality

To the best of my knowledge and belief, all the material presented in this thesis, except where otherwise referenced, is my own original work, and has not been published previously for the award of any other degree or diploma in any university. If accepted for the award of the degree of Doctor of Philosophy, I consent that this thesis be made available for loan and photocopying.

Ben S. Cazzolato

Acknowledgments

I would like to acknowledge the efforts of all the people who have made a contribution towards this thesis. Many thanks to my parents, Kay and Reg Cazzolato, who encouraged my mathematical and scientific interests from an early age, and to their financial support while finishing.

I would also like to thank Professor Colin H. Hansen for his supervision, inputs and freely flowing red pen, without which the thesis would most likely never have been completed. The author would also like to give thanks to Dr. Scott D. Snyder for his contributions and enlightening discussions, to Dr. Anthony Zander, Marc Simpson and Dr. Kym Burgemeister for their early inputs, and to those unfortunate enough to share an office with me, Carly-Woo Howard and Dr Xiao Jung Qiu, who tolerated my dark moods when finishing. I am also indebted to the “electronics guys”, Silvio De Ieso, George Osborne and Derek Franklin for all their help with the design and construction of the electronics and experimental apparatus.

This research has been undertaken with the support of the Australian Research Council and the Sir Ross & Keith Smith Fund which is gratefully acknowledged.

Finally, I would like to express my gratitude to Thu-Lan for her endless encouragement, support and patience during the preparation of this thesis.

Chapter 1

Introduction and Literature Review

1.1 Motivation and Contributions of this Thesis

One key area of interest of active noise and vibration control (ANVC) has been the application to the control of low frequency sound transmission in stiffened light weight vibro-acoustic systems with internal acoustic spaces such as aircraft and automobiles. Light-weight structural systems are inherently poor at reducing the sound transmission from external sources into an interior acoustic space. Conventional passive noise control techniques typically require the addition of mass elements, thereby negating the benefits offered by the use of light-weight materials. ANVC provides an alternative technique for reducing low frequency noise in enclosed spaces without the weight penalties of passive techniques. For this reason, there has been considerable interest in applying ANVC to aircraft and this partly provides the motivation for the material presented in this thesis.

Early active noise control applications aimed at minimising the sound transmission into enclosures often suffered from poor local and global control of the interior sound field. In many of the applications the poor results were mostly due to the inherent limitations of the physical control system, and in particular observability problems associated with the sensing and actuating systems.

In this thesis, two novel methods for sensing the sound transmitted from a structure into a coupled cavity for use in active noise control systems are investigated. Both methods are aimed at overcoming observability problems associated with traditional error sensors such as microphones in acoustic systems and accelerometers in structural and structural-acoustic systems. The first method is based on sensing acoustic energy density at a point. The second method is based on modal filtering of radiation modes, which when minimised, directly minimise the cost function to which their contributions are orthogonal.

In Chapter 2, the background theory for predicting the dynamic response of a fully coupled vibro-acoustic system is derived in terms of the rigid-walled acoustic modes and *in-vacuo* structural modes. The modal models of the two sub-systems are coupled using *modal coupling theory*. A technique for using Finite Element Analysis (FEA) to derive the modal models is presented with issues related to data extraction discussed. The systems of equations is validated in Appendix A and the forced response results are compared against a fully coupled FEA analysis. It is shown that the modal coupling technique adequately predicts the fully coupled response, including the shift in the natural frequencies, the magnitude of the power transmission between the sub-systems and structural-acoustic reciprocity.

Active noise control using energy density sensing has been shown to offer significant advantages compared to the use of conventional microphones. The aims of the work presented in Chapters 3 and 4 were two-fold. First to design a three-dimensional energy density sensor design suitable for use in practical active noise control systems. Second, to extend the earlier work of Sommerfeldt *et al* who have investigated lightly damped rigid-walled cavities and to apply energy density control in both lightly and moderately damped acoustic systems with compliant walls. However, prior to designing a practical energy density sensor it is necessary to investigate the limitations resulting from the physical sensing of energy density. In Chapter 3, an error analysis for sensing energy density in

one and three dimensions is presented. Two- and three-microphone arrangements for use in one-dimensional sound fields are studied, and then the approach is extended to three dimensions, covering four different 3D energy density sensor designs. Having analysed the various designs for sensing energy density in three-dimensional sound fields a suitable design is built and the limitations discussed.

With the system theory derived, the numerical procedure validated and an error analysis conducted, energy density at a point is used as a cost function in a coupled vibro-acoustic system, as discussed in Chapter 4. The performance of the 4 three-dimensional sensor designs are compared when used as an error sensor in an active control system to minimise the interior acoustic potential energy in the cavity. The influence of the source of the excitation (acoustic or structural) and damping of the system on the control system performance is investigated in detail. The shape of the controlled sound field is investigated, in particular the zone of local control around the energy density sensor. Analytical results are verified experimentally for a curved rectangular panel backed by a small rigid cavity.

Structural error sensors are often used in preference of acoustic error sensors in active noise control systems because of their physical convenience. However, control of structural vibration levels is not necessarily an effective means of controlling the acoustic potential energy within the cavity enclosed by the structure. By considering the global error criteria, such as the acoustic potential energy, it is possible to derive orthonormal groups of structural modes that contribute to the error criteria. By measuring these orthonormal sets, known as structural radiation modes, and using these as error signals, control of the acoustic space may be achieved with improved results compared to simple vibration level measurements.

A technique for using structural radiation modal sensors to measure the sound transmitted from a structure into a receiving cavity is derived in Chapter 5. The limitations are discussed and techniques for overcoming these are proposed. The procedure is demon-

strated in a numerical simulation of a simple vibro-acoustic system. Radiation modes derived from alternative formulations of cost functions are also investigated; potential energy of the cavity, sound power radiated in to the cavity, the potential energy over a subspace and the energy density at a point.

Formulation of the sensor equations for Polyvinylidene Fluoride (PVDF) shaped sensors are derived and simplified approximations are analysed. These sensor equations are then applied to the experimental verification of structural sensing of sound transmission into cavities in Chapter 6. The performance of continuous PVDF sensors is compared with the performance obtained using distributed discrete sensors.

The conclusions of the thesis are made in Chapter 7 along with recommendations for future work. Some of the work presented in this thesis has been previously published by the author in condensed form in international journals and conference proceedings. The relevant articles have been reproduced in the Appendix.

1.2 Literature Review

The following literature review divides the research into active noise control and active structural acoustic control of interior noise. Literature specific to the material covered in this thesis is presented here and addressed more thoroughly in the relevant chapters.

1.2.1 Scope

The literature review addresses the following topics:

Modal coupling theory. The coupling of structures with an enclosed contiguous fluid is considered and a variety of simplifications to the complete coupled solution are presented. Particular attention is given to techniques applicable to lightly coupled systems where analysis via uncoupled modal models is sufficiently accurate.

FEA & BEA. Discrete numerical modelling techniques such as Finite Element Analysis (FEA) and Boundary Element Analysis (BEA) have been used to model relatively simple three-dimensional systems for the purposes of investigating ANVC. A summary of the work to date in this field is presented with gaps in the applications highlighted.

Quadratic optimisation. A standard control theory optimisation technique known as quadratic optimisation and its application to control source strength is discussed.

Error criteria. When optimising the control signals to the control system, suitable error criteria or cost functions must be selected to provide a quantifiable measure of the performance of the system. Several error criteria including, sum of the squared pressures at discrete locations, global acoustic potential energy, sum of the squared velocity levels at discrete locations and global structural kinetic energy are discussed.

Radiation modes. The use of the structural radiation modes to estimate the power radiated into the free-field and the sound transmission into contiguous cavities is discussed.

Shaped sensing and modal control. The design issues for using shaped piezoelectric sensors and actuators are discussed and their application and benefits to modal control presented.

Energy density sensing and control. The performance of energy density control at a point for rigid-walled cavities is reviewed.

1.2.2 System Response Prediction and Analysis

1.2.2.1 Introduction

To examine the issues and mechanisms influencing the performance of an ANVC system, the physical response of the mechanical system to which it is applied needs to be modelled adequately. The following review concentrates on stiffened light-weight structures coupled to a contiguous lightly damped acoustic space. The stiffening may come through significant shell curvature or stiffeners attached to the shell.

1.2.2.2 Underlying Theory and Analytical Models

There exists an extensive amount of literature concerning sound transmission through lightweight structures into contiguous cavities. Where the influence of the fluid loading has a significant effect on the vibration of the enclosing structure, the problem of analysis of the vibrational behaviour of the resulting coupled system is highly complex, except in certain idealised cases. However, in many systems where the structure exhibits some degree of stiffness, the fluid medium is air, the cavity is sufficiently large that the radiation loading on the structure is small, and the damping is relatively small, then the analysis can be simplified considerably. A considerable portion of the work in vibro-acoustic coupling has dealt with these types of (weakly coupled) systems. Weak coupling allows the *in vacuo* modal response of the structure and the response of a rigidly enclosed space to be used to determine the coupled system response. The two uncoupled modal models may then be coupled via modal coupling theory (Pope 1971, Dowell, Gorman III & Smith 1977, Fahy 1985, Pan & Bies 1990, Pan 1992, Snyder & Hansen 1994*a*). Much of the early work and theory of coupled vibro-acoustic systems is covered in the comprehensive text on *sound and structural vibration : radiation, transmission and response* by Fahy (1985). And although a definitive review is beyond the scope of this thesis, it is instructive to present an overview the more relevant structural-acoustic papers in order to put the

current approach in perspective.

During the 1960's many papers were presented on the problem of modelling coupled vibro-acoustic systems. Due to the computational limits at the time the papers were written, the problem was broken down into several frequency regions in which numerous assumptions were made to simplify the analysis. Lyon (1963) and Pretlove (1966) both considered the theoretical coupling of a single flexible rectangular panel forming one face of an otherwise rigid enclosure. It was assumed in the analyses that the generalised acoustic stiffnesses (fluid loading) are small relative to the panel stiffnesses and that the fundamental *in vacuo* panel natural frequency is lower than the natural frequency of the first cavity mode. The frequency range was broken into three distinct parts: "low frequencies" below the fundamental panel resonance where both the panel and interior volume are stiffness controlled; "intermediate frequencies", where the panel is resonant and the cavity is stiffness controlled; and "high" frequencies in which the both the panel and the interior volume display resonant behaviour. The space average energy approach used by these authors does not lend itself directly to the detailed modal model required for the present analyses; however, the qualitative discussions of the underlying mechanisms are still valid.

The vibration of a rectangular flexible panel backed by an air filled rigid rectangular box was theoretically derived by Fahy (1968, 1969) using a modal model. The author quantifies the requirement for weak coupling and further qualifies that the weak coupling assumption does not necessarily hold for low-order acoustic modes and small volumes, and at super-critical frequencies with light panels. It was shown that when the modal density is high, the power transmission between structural and acoustic modes is only significant when the difference between the natural frequencies of the cavity and structure is less than the mean of the half power bandwidth of the two modes. Mode pairs satisfying this condition are referred to as having *proximate modal coupling*. The response of the system can be adequately modelled using only proximate modal pairs down to a lower limiting

frequency. Analysis lower than this limit requires use of all modal pairs to avoid significant errors. Fahy (1970) extends the analysis to include a cylinder with small openings at either ends. The procedure, like that for the rectangular panel/cavity system, is modal based with similar conclusions as reported previously; namely, that at any frequency a very small percentage of all possible structural-acoustic modal pairs (0.01%) accounted for the majority (80%) of the acoustic power flow from the structure into the cavity.

Pope (1971) and Dowell et al. (1977) both present an investigation of sound transmission into small enclosures and consider the effects of acoustically induced coupling between shell modes. Highly detailed analytical formulations of the harmonic solution to the resonant transmission of sound through a structure into a contiguous acoustic space based upon a modal interaction model are presented. The theory is experimentally verified for a closed cylinder (Pope 1971) and a rectangular parallelepiped enclosure with a single flexible panel with good agreement. Pope (1971) extends the theory to include a stationary ergodic random process as input into the system. Important conclusions of the investigations are that the normal *in vacuo* mechanical reactance levels are well above the acoustically induced joint and cross reactance levels, except near the cavity natural frequencies. Physically this means that the acoustically induced modal coupling of the structural modes is not significant, except at acoustic resonances. The effective mass loading, which is represented by the joint reactance functions, is sufficiently low so as to be ignored. It can be shown theoretically (Pope 1971, Dowell et al. 1977, Fahy 1985) that the shell modal displacements approach zero when the excitation frequency is equal to the real valued rigid walled cavity natural frequency because of the infinite fluid loading; however, the sound pressure within the cavity will nevertheless remain quite high. Fahy (1985) points out that in practice, the fluid loading is limited by dissipative mechanisms within the fluid and at its boundaries and can be modelled by applying an *ad hoc* damping term to the fluid bulk modulus which leads to a small imaginary term in the denominator of the Green function of the acoustic space.

It should be noted that the natural frequencies and modes of a coupled system are usually different from those of the individual uncoupled systems (Dowell et al. 1977, Fahy 1985). The total vibrational energy of a mode of the coupled system is divided between the structure and the fluid. In many cases a greater proportion of the energy resides either in the fluid or the structure. This allows two coupled modes to be identified, namely "cavity controlled or dominated" and "structure controlled or dominated" modes (Fahy 1985, Pan & Bies 1990). This has important implications on the control mechanisms of an ANVC system and will limit the performance of single control source type control systems.

A paper by Pan & Bies (1990) on the free and forced response of an acoustic-structural coupled system presents an extensive literature survey on the study of sound fields inside enclosures with flexible walls, with particular reference to rectangular cavity systems. The authors and Pan (1992) in a subsequent paper derive in detail the response of a coupled rectangular cavity/panel system using modal coupling theory drawing from the work of previous authors. Pan & Bies (1990) show that when the structure is thin and the damping is low, radiation to the external space is an important cause of sound energy loss from the cavity. This is particularly true if an internal cavity mode is well coupled with a panel mode.

Snyder & Hansen (1994*a*) used the modal coupling theory derived by Pope (1971) to develop a closed-form solution of the coupled response of the system with application to active noise and vibration control. Although the analysis presented was very detailed, they made the mistake of neglecting the gyrostatic coupling (cross-reactance) terms which account for the effect the impedance of the structure has on the response of the cavity. It should be noted that for some weakly coupled structural acoustic systems it is possible to neglect the structural/acoustic interaction when predicting the sound pressure field in the enclosure under operation of the acoustic sources alone. However, at the structural resonances, neglecting this interaction in realistic systems may result in some discrep-

ancy between the theoretical and experimental results (Fanzoni & Dowell 1995, Fanzoni & Bliss 1998). In addition, without this term, structural-acoustic reciprocity and hence conservation of energy would not hold.

The modal coupling method is not without its problems. Since the acoustic modes are for a rigid walled enclosure, the solution for the pressure based on the finite modal expansion, though accurate in the interior of the cavity, does not converge to the boundary normal velocity. This mathematical condition associated with finite summations is referred to as Gibb's phenomenon. Since the rigid walled acoustic modes satisfy the Neumann boundary condition, the velocity predicted at the boundary is zero. This inaccuracy in the velocity field can be substantial in the vicinity of vibrating boundaries (Jayachandran, Hirsch & Sun 1998, Fahy 1985). Therefore, this technique is inappropriate for investigating the impedance conditions, sound intensity or energy density at the vibrating boundaries of the enclosure. The error in the velocity (pressure gradient) is a function of the proximity to the boundary and the number of acoustic modes used in the expansion, or more specifically the acoustic wavelength at the largest acoustic mode. However, Jayachandran et al. (1998) have investigated the effects of the inaccuracies at the boundaries of a coupled vibro-acoustic system and have found that the inaccuracies do not affect the control prediction when minimising the acoustic potential energy.

1.2.2.3 Numerical Techniques

The vibrational behaviour of finite bounded fluid and solid systems may generally be expressed in terms of a series solution to the governing equations. If the geometry of the vibro-acoustic system and the boundary conditions are simple, then it is generally possible to derive analytical expressions for the terms in the series solution to the governing differential equations. However, with the majority of real systems it is not possible to obtain analytical solutions to the model equations because of the geometric, dynamic, and/or kinematic complexity of the system being modelled. Hence, discrete approxima-

tions such as Finite Element Analysis (FEA) and Boundary Element Analysis (BEA) are used as alternatives. The field quantities that are actually continuous throughout a region of the elastic continuum are represented by their numerical values at discrete locations in space, with assumed interpolation functions that approximate the distribution of these quantities between the points. FEA and Finite Difference Analysis formulation require discretisation (meshing) of the acoustic medium, while BEA only needs a model of the bounding surface confining the domain to be studied.

Analysis of sound fields in closed volumes is usually accomplished by using FEA, in which the fluid space is theoretically divided into contiguous elements of linear dimensions substantially smaller than the acoustic wavelength of the highest frequency of interest (Fahy 1985).

As with the analytical derivation of the coupled equations of motion, it is possible to formulate a fully coupled Finite Element Model (FEM). When using a mixed finite element formulation it is common to use displacement degrees of freedom (dofs) for the structure and pressures for the cavity dofs as this has the advantage that a direct comparison can be made with experimental results. Unfortunately, the resulting overall system matrices become unsymmetric. Subsequently the eigenvalue problem becomes difficult to solve and an iterative non-symmetric eigen solver routine such as the Lanczos algorithm is required (Rajakumar, Ali & Yanus 1992). The unsymmetric matrices may be made symmetric by reformulating the matrices in terms of the velocity potential (Everstine 1981, Fahy 1985, Taylor & Everstine 1986). The effect on the equations of motion of switching from a velocity potential as the unknown is to remove the coupling sub-matrix from the mass and stiffness matrices. When the problem has damping present, the reformulation yields symmetric matrices with no penalties but still requires a computationally intensive complex eigen-solver. However, for problems with no (structural and acoustic) damping present, the symmetric reformulation may offer no advantages over the unsymmetric set of equations (Everstine 1981). This is because the reformulation converts an

undamped, non-symmetric problem to one which is "damped" and symmetric. Both of these sets of equations require a complex eigenvalue extraction routine to solve, even though the eigenvalues turn out to be real.

There exists an extensive literature base for the solution of fully coupled vibro-acoustic systems using FEA. However, due to the extremely large computational requirements needed to solve such systems which were not available to the author, the approach is not suitable for the current study. As an alternative, the structural and acoustic systems can be analysed separately using FEA then coupled together using modal coupling theory.

For example, Craggs (1971) studied a transient coupled system using a displacement and pressure FE formulation. He acknowledged the difficulty of solving the unsymmetric eigenvalue problem and only presented solutions to models containing in the order of 10 pressure dofs. Realistic systems require at least 2 orders of magnitude greater number dofs to adequately model the higher order modes. With the computation effort of most unsymmetric eigenvalue problems being proportional to the 4th power of the number of dofs, this results in an increase in the computational difficulty of 8 orders of magnitude. The increase in computing speed over this period is approximately 5 orders of magnitude. Clearly it will be another decade before fully coupled analyses of realistic systems are practical for most computing systems. Other fully coupled analyses have generally limited the frequency range of the analysis in order to keep the modal density down (Nefske, Wolf & Howell 1982, Huang & Carlson 1993). This subsequently reduces the required number of degrees of freedom making the problem computationally tractable but often inaccurate at higher frequencies.

Several studies on post-coupled finite vibro-acoustic models exist in the current body literature. Sung & Nefske (1984) compared FEA predicted vs measured sound pressure levels for an automotive cabin. The authors used MSC-NASTRAN finite element code to perform the calculations. The forced response analysis was achieved using a modal superposition technique of the two uncoupled models and a pre-calculated structural-acoustic

coupling matrix. In obtaining the modal solution, only a selected portion of the structural and acoustic modes were retained for the synthesis procedure. This offered considerable savings in computational time and storage. Results were presented below 100 Hz and the predicted and measured SPL's were within 15 dB of each other.

Unruh & Dobosz (1988) presented the results of a detailed FE study of a fuselage structure and acoustic cabin volume. The approach taken was to use the uncoupled models of the fuselage structure in a vacuum and the cabin volume hard-wall acoustic modes and then couple them via modal coupling theory. The authors make reference to the very large system of unsymmetric matrices that are formed if a fully coupled analysis is performed. The authors make even further simplifications to the theory by assuming that the self and cross impedance associated with gyro-static coupling can be ignored thereby reducing the structural and acoustic impedance matrices from symmetric to diagonal matrices. They claim that this assumption is valid except for small general aviation aircraft wherein the fundamental acoustic mode was close to a dominant resonant structural mode. The structural system investigated consisted of a ring and stringer stiffened cylinder with an integral floor. The detailed structural model consisted of 606 nodes and required 99 hours CPU time on a VAX 11/780 to extract 98 modes. It is interesting to note that a typical entry level Unix workstation such as the Silicon Graphics Indigo 2 is approximately 200 times faster than the VAX, therefore to solve a similar model would only require approximately half an hour of CPU time. The cabin interior acoustic model was generated from a two-dimensional acoustic model of the cabin cross-section then extended analytically to three-dimensions. This was clearly a necessity because of the inadequate computing power available. The acoustic model only consisted of 126 dofs. The interior SPL to input force transfer function was accurate to within 20 dB.

Two-dimensional analysis is used extensively (Nefske et al. 1982, Unruh & Dobosz 1988) to simplify the FE model of the acoustic space. This technique is only suitable for systems with regular geometries, and therefore not appropriate for the systems currently

being investigated.

The modal coupling technique was successfully used by De Rosa, Pezzullo, Lecce & Marulo (1994) to analyse a three-dimensional modally dense irregularly shaped six-sided box. The analysis technique significantly reduced the computational loads compared to a fully-coupled dynamic response analysis.

With Finite Difference Analysis (FDA), the fluid region is divided up by a linear grid and field values are assigned to the grid intersection points. FDA requires that the grid is a rectangular Cartesian coordinate system, whereas the mesh for FE analysis can take diverse geometric forms. As FD analysis has the distinct disadvantage that it does not readily accommodate boundaries that do not conform to the grid line pattern it will not be reviewed here.

Boundary Element Analysis is another numerical technique suitable for modelling structure-fluid interaction. It is based on an exact analytical Helmholtz integral formulation. Unlike the FEA and FDA, the mesh is only required around the bounding surface of the structure. Hence, the calculation of sound intensity, sound power and sound radiation efficiency using BEA is generally far more efficient than either FEA of FDA. The sound pressure and particle velocity can also be calculated at so-called field points, i.e., points in the acoustic domain that do not lie on the surface of the body. However, to completely map the interior acoustic response using BEA would generally require more effort than an equivalent FEA or FDA model of similar mesh density. In addition, should the eigenvalues of the acoustic space be required then a forced response calculation is necessary to determine the resonance frequencies of the acoustic domain. Because of the inherent limitations of BEA, it was decided to perform all numerical modelling using FEA.

Calculation of the coupling between the structural and acoustic meshes is straightforward as long as the two meshes have coincident nodes. In some larger practical applications with very flexible bounding structures, however, the mesh requirements are very different. Since the wavelength of an acoustic mode is much longer than the typical struc-

tural mode at the same frequency, the mesh for the acoustic model can be much coarser than that for the structural model. Coyette, Dubois-Pelerin & Migeot (1994) derived a procedure to couple unequal structural and acoustic meshes.

1.2.3 Active Noise Control of Interior Spaces

Much of the early work on active control of enclosed acoustic fields was applied to enclosures with infinitely rigid wall conditions. These studies led to the application of quadratic optimisation theory to reduce the sum of the squared pressures at several points or the global acoustic potential energy using monopole acoustic sources (Bullmore, Nelson & Elliott 1986, Nelson, Curtis, Elliott & Bullmore 1987*b*, Nelson, Curtis, Elliott & Bullmore 1987*a*, Bullmore, Nelson, Curtis & Elliott 1987, Elliott, Curtis, Bullmore & Nelson 1987, Elliott & Nelson 1987). Further studies into enclosures with fixed boundary conditions investigated the minimisation of power output from internal control sources and active absorption of sound power by the control sources (Guicking, Karcher & Rollwage 1983, Curtis, Nelson & Bullmore 1987, Tohyama & Suzuki 1987, Elliott, Joseph, Nelson & Johnson 1991, Snyder & Tanaka 1993*b*).

The logical extension of these numerical studies was to apply ANVC to enclosed spaces with modally reactive walls (Pan & Bies 1990, Pan & Hansen 1991, Pan, Hansen & Bies 1991, Snyder & Hansen 1994*a*, Snyder & Hansen 1994*b*, Sas, Bao, Augusztinovicz & Desmet 1995). This allowed further development of control strategies such as sound power radiated into the cavity by the enclosure boundaries. It has been shown, both theoretically as well as experimentally, that minimisation of radiated power from the boundary structure (in the absence of interior acoustic sources) will minimise the internal potential energy, if the enclosed sound field is lightly damped (Johnson 1996, Kang & Kim 1997).

Many of the techniques used in the above papers have been applied to more compli-

cated cylindrical vibro-acoustic systems. Therefore, these will not be reviewed in detail but will be incorporated into the discussion on ANVC in cylindrical structures below.

1.2.3.1 Simplified Models

Simplified analytical models of enclosed spaces have been used extensively in gaining an understanding of the underlying mechanisms of active noise control in coupled structural/acoustic systems. Typically the analytical models of fuselage type structures have been finite, isotropic thin elastic cylindrical shells within a vacuum, while the acoustic system response has been modelled using rigid enclosure assumptions.

The first reported application of active noise control in an aircraft environment was by Zalas & Tichy (1984). This program to reduce harmonic noise in the interior of a commuter aircraft in flight was successful over a limited frequency range. The complex structure of the aircraft, however, tended to mask the underlying mechanisms of the vibro/acoustic coupling. Subsequent work by other investigators has focussed on more fundamental evaluations in laboratory models or analytical studies.

There exists two principal approaches used for actively controlling the interior noise levels in aircraft fuselages; namely, acoustic control via the use of loudspeakers operating within the aircraft interior which directly control the acoustic response, and structural acoustic control in which vibrational force inputs operate on the structural response of the fuselage in order to reduce the sound energy radiated into the cabin.

1.2.3.2 Acoustic Control Sources

The effect of driving frequency on the performance of an active control system in a thin-walled cylinder was experimentally investigated by Abler & Silcox (1987). Control was achieved using acoustic control sources in the plane of the primary sources. The system response was dominated by a single acoustic mode due to *interface modal filtering*. Significant noise level reductions were obtained in the plane of the control sources for all

excitation frequencies. When the excitation frequency was below the cut on frequency of the dominant cavity mode, the acoustic field associated with the control source decayed (longitudinally) more rapidly than the acoustic field driven by the structure. The difference in the primary and controlled sound levels resulted in poor performance away from the plane of excitation. The small value of the decay for the primary field was due to the field being a forced response driven by the structure. This was verified by the small phase change of the primary acoustic field over the cylinder length, typical of the long structural wavelength. However, when the system was excited at the cut-on frequency of the dominant acoustic mode, the level of control was maintained over a greater length along the cylinder. The implication was that the shell excitation close to the source plane dominated the overall acoustic energy input into the interior space. The acoustic energy then propagated axially as a duct mode. These findings were confirmed numerically by Lester & Fuller (1987).

Silcox, Lester & Abler (1989) extended the work by analytically evaluating the performance of an active noise control system within an infinite elastic shell. The cost function used to optimise the control source strengths was the space average squared sound pressures integrated over the source plane. The analytical predictions were verified with experimental measurements taken on a finite length cylinder with both structural and acoustic damping at the end caps to approximate the infinite cylinder analytical model. Excellent noise control was achieved in the source plane for both the analytical prediction and experimental measurements. Significant acoustic modal spill-over was observed when the number of control sources was less than twice the order of the highest order azimuthal modes to be controlled. When the Nyquist criteria was applied, effective control was demonstrated for equi-spaced control sources judiciously located.

Bullmore, Nelson & Elliott (1990) used a simple analytical theory to model the fuselage structural response of a B.Ae. 748 aircraft as a finite, isotropic thin cylindrical shell with a floor, and the cabin acoustic response as a rigid walled enclosure. It was intended

that this relatively simple model would enable an approximate determination of the spatial effectiveness of active control as a function of frequency and as a function of the number and location of the secondary sources introduced. The fuselage model was excited by two point forces, each force corresponding to one of the propeller pressure fields impinging on the fuselage surfaces. With only 16 secondary acoustic sources, the possibility of achieving global control was considered and rejected. Instead, control in an extended region along the cabin length at seated head height was attempted. Average spatial reductions of 14 dB for the fundamental BPF were achieved in this region.

1.2.3.3 Active Structural Acoustic Control (ASAC)

A second body of research into active noise control within aircraft has been concerned with the reduction of interior noise within enclosed spaces by active control of structural vibration. The application of active forces instead of acoustic sources as a means of noise control has a number of distinct disadvantages. As they are usually applied at a point, they are spatially white, leading to undesired modal spill-over and degradation in control performance. Systems which have high modal densities and strong structural-acoustic coupling are particularly affected by this phenomenon.

Fuller & Jones (1987) claim that prior to their study, active vibration control had not been used to reduce interior noise (referred to as ASAC), although the application of structural actuators to control sound radiation was first suggested by Chaplin (1983). The authors experimentally investigated the feasibility of achieving global acoustic control using vibration control within a finite unstiffened aluminium cylinder, representative of a simplified aircraft fuselage. Significant reductions (10 to 20 dB) in the interior noise levels for a resonant response were obtained with a single control force. This was only made possible because of the low structural and acoustic modal density which resulted in only one structural mode being strongly coupled to the cavity. Since a single control force was used, vibration levels were found to increase because of modal spill-over. When the

response of the system was off-resonance, the modal density of the interior sound field increased and subsequently the performance of the system suffered from spill-over of energy into uncontrolled shell modes, some of which were well coupled to the interior space. It was concluded that in order to minimise the interior noise levels, at least one shaker would be needed for each well coupled structural mode. Similar findings were reported by Jones & Fuller (1987).

Jones & Fuller (1989) extended the experimental study of sound transmission into an unstiffened cylinder for multiple control forces applied to the structure. It was concluded that direct structural control of the acoustic space generally requires fewer control sources than active acoustical control. It also became apparent that while the interior sound field could be reduced with structural sources, the structural vibration levels may actually increase. This modal spillover can be avoided by using distributed actuators (Sun, Norris, Rossetti & Highfill 1994).

Thomas, Nelson & Elliott (1988) address the issue of optimising control force locations on the skin of a thin cylindrical shell (as a model for a BAe 748 fuselage). Quadratic optimisation theory was used to calculate the optimum spatial configuration for the control forces in order to minimise the total strain energy in the shell and also to minimise the sum of the squares of the displacements at several locations. A sensitivity analysis on the number of modes required for convergence of the strain energy was performed and showed that more modes were required for convergence with point control forces than distributed forces. It was concluded that a very localised force excites a greater number of higher order modes in the shell. The authors failed to carry the sensitivity analysis further when estimating the performance of the active vibration control system, ie distributed forces vs point forces. The authors point out that the structural response of the shell does not couple efficiently with the higher order modes of the acoustic space within the cylinder. Hence the sum of the squares of the displacements at a number of positions of the shell surface is not the most suitable cost function for controlling the acoustic field.

Similar conclusions were made by Fuller, Silcox, Metcalf & Brown (1989) and Rossetti & Norris (1996) who found that minimising structural motion does not necessarily lead to a reduction in the transmitted acoustic field.

Subsequent work by Thomas, Nelson & Elliott (1993*a*) found that the large number of modes significant in the vibration of the cylinder and the very large number of modes excited by discrete secondary forces makes significant reductions in the vibration impossible to obtain by using realistic numbers of secondary forces. This phenomenon was first reported by Bullmore et al. (1987), where it was shown that active control is most successful at a structural resonance when the number of strongly excited modes is low. However, in the complementary paper Thomas, Nelson & Elliott (1993*b*), it was shown that when using the acoustic potential energy as the basis of a cost function, it is possible to achieve considerable reductions of the total acoustic potential energy within the cylinder with very few secondary forces, often resulting in an increase in the structural vibration levels. This behaviour is accounted for by the specific coupling between the structural and acoustic modes of the cylinder. The authors propose the use of a composite cost function which would incorporate both acoustic and structural error sensors to prevent an increase in structural vibration levels while still achieving reductions in the acoustic potential energy.

Active control of interior noise in model aircraft fuselages using piezo-ceramic actuators was experimentally studied by Fuller, Snyder, Hansen & Silcox (1992). The fuselage model had a removable floor enabling the study of interior noise mechanisms in simple geometries (floor removed) and more complex geometries representative of aircraft interiors (floor present). The results demonstrate that global attenuation of the order of 10-15 dB in interior noise levels can be achieved using piezo-ceramic actuators, irrespective of whether the system was responding at a structural or acoustic resonance. Like the earlier work of Fuller & Jones (1987), a reduction of the interior sound field through modal rearrangement was accompanied by an increase in the structural response when driving at an

acoustic resonance.

1.2.3.4 Mechanisms

A great deal of work has been published on the mechanisms of active control of interior noise, particularly in cylinders. Abler & Silcox (1987), Lester & Fuller (1987), Silcox et al. (1989) and Silcox, Fuller & Lester (1990) have modelled the response of an infinitely long, thin, uniform, elastic cylinder to external monopole sources representing propeller noise sources. The filtering effect of the structural acoustic coupling (*interface modal filtering*) between the shell and the acoustic cavity is observed in both the theoretical and experimental studies. It was concluded that at any given frequency, a distribution of shell azimuthal modes will generally give rise to one or two dominant interior acoustic modes according to this resonant behaviour. This has different implications for acoustic and force control inputs. The key noise suppression mechanism for acoustic sources is a reduction of the back pressure loading on the wall, and thus, the wall is essentially uncoupled from the acoustic space. Rather than absorbing the incoming acoustic energy, the acoustic control sources reduce the pressure in combination with the primary sources. The input impedance of the cavity is significantly reduced, and less energy can be transferred from the shell vibration (even with the vibration increase) to the cavity space.

Fuller, Hansen & Snyder (1991) and others (Pan, Hansen & Bies 1990, Pan & Hansen 1991, Pan et al. 1991, Snyder & Hansen 1991) identified two main mechanisms for structural control of the interior sound field for enclosed spaces. In the first called *modal suppression*, only the dominantly radiating modes in the structure are reduced. Other modes, which may be of larger amplitude but do not couple with the interior field are left untouched. In the second, called *modal restructuring* (or *modal rearrangement*), the overall modal response of the structure is modified, both in amplitude and temporal phase, to achieve a lower level of coupling with the interior acoustic field. This mechanism often leads to an increase in the vibration levels of the structure. The authors found that

modal suppression tends to occur when the system response is dominated by the structural modes and modal rearrangement occurs when the system response is dominated by acoustic modes.

Later studies on the subject of ASAC versus ANC showed that structural sources were more effective at controlling structurally dominated modes than a similar number of acoustic sources, while at the acoustic resonances, acoustic sources outperformed the structural sources (Hirsch & Sun 1998). One of the major concerns with structural control, particularly when using point forces, is that it may lead to fatigue of the structure. By combining the structural and acoustic sources, as opposed to only using structural sources, it is possible to reduce the controlled vibration levels of the structure. Hirsch & Sun (1998) also showed that if the acoustic sources were combined in such a manner to emulate the radiation patterns from the structure, then these meta-acoustic sources could lead to significant improvements in control, and would outperform structural control sources, even if the system response was dominated by structural modes.

1.2.3.5 FEA Modelling and ANC

Martin (1993) and the subsequent paper by Martin, Vignassa & Peseux (1994) reported on the use of a coupled finite element approach to predict the system response of a simplified model of a Fokker 100 and an ATR 42. The analysis strategy is overly simplified to be of any practical significance, at least for small aircraft. They make the assumption that the acoustic field is a propagation problem not an eigenvalue problem. This type of analysis is only suitable for systems of high modal density and high damping when the objective is for local control. The authors incorrectly assume that because reaction forces at the wing/fuselage are tangential to the shell surface that wing motion does not contribute to the sound field inside the shell. They have failed to consider the noise generation due to the bending modes of the cylinder and more importantly the bending moments at the wing/fuselage attachment points. The results are a little inconclusive, however, significant

noise level reductions were achieved for the numerical model. Little information about the results and the accuracy of the modelling was supplied.

Recently there has been a surge of studies using FEA and BEA to study active noise and vibration control for more irregular geometries: aircraft cabins (Alvelid 1993, Dai & Fuller 1995), earth moving machine cab (Carletti, Miccoli & Vecchi 1996). However, these studies have broken little new ground.

1.2.4 Radiation Modes

Vibration control sources have been shown to offer two distinct advantages over more conventional acoustic sources when controlling interior noise: fewer secondary sources are generally required for global control of the interior noise field (Charette, Guigou & Berry 1995); and surface mounted actuators are far less intrusive than bulky speaker/cabinet arrangements. However, the gains in system compactness are not necessarily realised in practice when microphones placed throughout the cavity are used to provide the controller error signals to achieve global control.

As an alternative, surface mounted structural vibration sensors have also been used as error sensors and although a reduction in the vibration of the structure may be achieved, a reduction in the interior sound field does not necessarily follow, particularly at low frequencies where the modal density is low (Thomas et al. 1988, Pan et al. 1990). Clearly a control system using structural error sensors to directly measure the surface vibration is unsuitable for the control of sound transmission. However, it has been shown recently that is possible to calculate a quantity (*radiation mode*) from the vibration of the structure, which is directly proportional to the sound radiated into an enclosed space (Snyder & Tanaka 1993*a*).

Structural sensing using orthogonal surface velocity patterns (radiation modes) has been applied to the measurement and control of the sound power radiated into

free field from vibrating beams (Cunefare 1991, Baumann, Saunders & Robertshaw 1991, Naghshineh & Koopmann 1993, Cunefare & Currey 1994), plates (Elliott & Johnson 1993, Currey & Cunefare 1995, Johnson & Elliott 1995, Snyder, Tanaka, Burgemeister & Hansen 1995, Johnson 1996, Burgemeister 1996, Snyder & Burgemeister 1996, Burgemeister & Snyder 1997), shells (Borgiotti 1990, Photiadis 1990, Borgiotti & Jones 1993, Borgiotti & Jones 1994, Chen & Ginsberg 1995, Chen 1997, Naghshineh, Chen & Koopmann 1998), spheres (Chen & Ginsberg 1995) and recently, double panel systems (Pan, Sutton & Elliott 1998). The approach involves decomposing the surface vibration, usually via a Singular Value Decomposition, into a number of surface velocity distributions which contribute independently to the radiated sound field. Snyder & Tanaka (1993*a*) have extended the work to include a brief study of the active control of sound transmitted into a coupled rectangular enclosure. However their work failed to address many of the practical implementation issues such as the frequency dependence of the eigenvalues and eigenvectors. Johnson (1996) also briefly investigated the interior radiation mode of a small rectangular panel radiating into a large enclosure. He showed that at high frequencies when the enclosure becomes diffuse, the radiation modes of the rectangular panel exhibit similar shape and frequency dependent characteristics as a baffled panel with the same dimensions radiating into free space.

It has been shown that for both free-field radiation and transmission problems only a very limited number of radiation modes contribute to the sound radiated from a vibrating structure and it is the number of efficiently radiating modes, rather than the modal response of the structure, which defines the system dimensionality (Borgiotti 1990) and subsequently, the control system order. Sarkissian (1991) showed that the number of efficiently radiating modes was of the order of kl where l is the major dimension of the structure, and was significantly less than the number of structural modes excited.

The information derived from the orthonormal decomposition of the power radiated from structures into the free-field has not been limited to active control applications but

also has been applied to improving the design of structures to minimise the sound power radiated into the free field under forced excitation (Naghshineh, Koopmann & Belegundu 1992, Constans, Koopmann & Belegundu 1998) and has been experimentally validated by Constans et al. (1998). The use of interior radiation modes has been applied to the design of low noise radiators in duct-like systems (Verbeek, Kuijpers & Verheij 1998, Kuijpers, Verbeek & Verheij 1998).

1.2.4.1 Shaped Sensors

Having discussed the merits of modal sensing and control of radiation modes, it is pertinent to also discuss the techniques in which the modes are sensed. The early structural modal sensors, aimed at sensing normal structural modes, were typically created from a combination of weighted discrete sensors such as accelerometers (Balas 1978, Meirovitch & Baruh 1982, Meirovitch & Baruh 1985, Meirovitch & Bennighof 1986, Morgan 1991). These discrete meta sensors suffered from spatial aliasing and observation spillover (Meirovitch & Thangjitham 1990) which results in performance degradation. By increasing the ratio of the number of discrete sensors to the number of significant modes, the spillover is reduced (Clark 1995). Techniques were introduced to help overcome these limitations such as judicious placement of the sensors (Elliott & Johnson 1993, Snyder et al. 1995) and band-pass filters were used to restrict the bandwidth of operation to that influenced most by the modes in the control system (Clark 1995).

With the aim to overcoming these problems, Lee & Moon (1990) successfully used a polyvinylidene fluoride (PVDF) thin film as a continuous distributed modal sensor on a cantilevered beam and drew heavily from the comprehensive “theory of laminated piezoelectric plates for the design of distributed sensors/actuators” published by Lee (1990). Lee (1990) showed that by varying the shape of the piezoelectric film, it is possible to weight the gain of the transducer over the surface of a plate and thus measure particular structural modes. PVDF film is sensitive to induced strain, and like all other strain sensors,

the sensitivity is proportional to the second derivative of the out-of-plane displacement for thin plates and shells. The equations for relating strain (and charge sensitivity) to out of plane displacements was covered by Lee (1990). Later developments in modal sensing using PVDF were to extend the sensor theory to include rectangular plates with arbitrary boundary conditions (Burke & Hubbard Jr. 1991) and sensors with arbitrary spatial distributions (Sullivan, Hubbard & Burke 1996).

Experimental studies on sensing normal structural modes have included beams (Miller, Collins & Peltzman 1990, Lee, Chiang & O'Sullivan 1991, Charette, Guigou, Berry & Plantier 1994, Callahan & Baruh 1995, Pines 1996), plates (Burke & Hubbard Jr. 1991, Carey & Stulen 1993, Burdisso & Fuller 1994, Callahan & Baruh 1995, Snyder et al. 1995, Tanaka, Kikushima & Fergusson 1998), pipes (Royston 1994, Royston 1995) and cylindrical shells (Tzou, Zhong & Natori 1991).

PVDF sensors have not only been limited to sensing normal structural modes but have also been applied to sensing sound radiation from structures. Several researchers have investigated simple continuous sensors in the shape of uniform strips to minimise the radiation from beams and plates (Clark, Fuller & Wicks 1991, Clark & Fuller 1992*b*, Clark & Fuller 1992*d*, Clark & Fuller 1992*a*). The sensors were designed to sense the odd-odd modes on a rectangular plate since these are the most efficient acoustic radiators and were relatively successful in reducing the sound power radiated into the far field. In concluding, the authors note that almost optimal levels of control were achieved on resonance (when a single mode dominates the response and the control mechanism is modal control). However, the control achieved off-resonance using the strip sensors was slightly less than that offered by several microphones (when several structural modes contribute to the response and the control mechanism is modal rearrangement).

It was found by Clark & Fuller (1992*b*) that the uniform strip design was not the most effective arrangement since it becomes increasingly responsive to higher order modes and biased the high wavenumber structural modes. Improvements in shape functions

followed, with Rex & Elliott (1992) in "QWSIS - A new sensor for structural radiation control", showed that if a sensor had a sensitivity which varied quadratically over the surface of a beam, then the output from the sensor was proportional to the total transverse displacement over the length of the beam (which is the same shape as the most efficient radiation mode). The theory of a Quadratically-Weighted Strain-Integrating Sensor (QWSIS) was extended to rectangular plates by Johnson & Elliott (1993) and Johnson (1996). Although successful and simple for a clamped-clamped rectangular panel, the QWSIS for a simply supported rectangular panel was a little more difficult requiring a double layer of PVDF film across the surface. To overcome this difficulty, Charette et al. (1995) and Charette, Berry & Guigou (1998) used a decomposition on experimental measurements to derive shaped PVDF strips which were proportional to the volume velocity of a clamped-clamped rectangular panel. The technique was very successful and could be applied to a panel with arbitrary boundary conditions.

There has been considerable effort by others in sensing the higher order radiation modes of simply supported panels. The theoretical study by Snyder, Hansen & Tanaka (1993) showed the importance of sensing radiation modes as opposed to normal structural modes when attempting to minimise sound radiation. Using the earlier work of Lee & Moon (1990) several approximations were made to allow strip shape sensors to be used to measure the radiation mode (Snyder & Tanaka 1995, Snyder et al. 1995, Tanaka, Snyder & Hansen 1996).

There have been other sensor shapes which have proved successful in controlling sound radiation. Sommerfeldt & Scott (1994) and Scott & Sommerfeldt (1997) used PVDF film sensor shaped from a modified $sinc$ function to provide a low-pass wavenumber filter. Since the radiated power depends only on the structural wavenumber components whose magnitudes are less than or equal to the acoustic wavenumber, minimisation of the sensor output will minimise the sound power radiated (Sommerfeldt 1993). A discrete wavenumber transform has also been used to sense the sound radiated from a simply

supported beam (Clark & Fuller 1992*c*, Wang 1998).

Clark & Fuller (1994) used PVDF sensors on an enclosed finite cylinder to minimise the sound radiated to the free field. The modal sensors were shaped to respond to 3 radial modes of the cylinder in the frequency range of interest. When the cylinder was driven at resonance, minimisation of the sensor outputs led to significant reduction in the free field sound. However, not surprisingly, free field control did not occur when the cylinder was driven off-resonance. The poor performance was attributed to a high modal density and inadequate number of strip modal sensors. It is also likely that control of the structural modes was a poor cost function and a better cost function would have been the free field radiation modes of the cylinder (Borgiotti 1990, Naghshineh, Chen & Koopmann 1995).

Although the majority of the research into continuous modal sensors has used PVDF as the transducer, other techniques such as optical fibre sensors do exist. Cox & Lindner (1991) used an optical fibre sensor to control the vibration of a flexible beam and Rex & Elliott (1992) suggested the use of optical fibres to measure the volume velocity from a beam. Because the practical implementation of optical fibres is considerably more difficult and expensive than for PVDF film sensors, they have remained more a curiosity than practical transducer.

When using continuous modal sensors in controlling acoustic radiation it is important that not only the magnitudes of the desired modes be accurately estimated but also the radiation efficiency of the modes be accounted for. In single channel control systems this is not an issue; however, in multi-channel control systems it is the radiation efficiencies which determine the relative contributions of each of the modes to the global cost function.

1.2.4.2 Modal Actuators

Distributed piezoelectric actuators have been extensively studied (Burke & Hubbard Jr. 1987, Burke & Hubbard Jr. 1988, Clark et al. 1991, Burke & Hubbard Jr. 1991, Lee et al.

1991, Kim & Jones 1991, Burke, Hubbard Jr. & Meyer 1993) and have been shown to reduce modal spillover and improve controllability. Piezoelectric actuators offer a number of additional practical benefits: they are very easily attached to the structure; they are very lightweight; are compact and require significantly less space than point forces (or sound sources); and, do not require a mass or structure to supply a back reaction force (Dimitriadis & Fuller 1991, Kim & Jones 1991).

Early control of sound radiation with distributed actuators used judiciously placed actuators. These were optimised in the sense that the boundaries of the actuators extended along the nodal lines of the modes desired to be suppressed (Dimitriadis & Fuller 1991) and were relatively successfully in reducing modal spillover. Other simple but effective approaches reflected the early distributed sensors, and were aimed at controlling the structural modes responsible for the majority of the sound radiation / transmission. Van Niekerk, Tongue & Packard (1995) used a circular piezoelectric actuator to control the sound transmission through a concentric circular plate in a duct. Since the actuator covered 60% of the plate surface area, it was very effective at controlling the first plate mode, the mode that most strongly influences the acoustic plane wave generation. Sun et al. (1994) designed a PZT modal actuator for a cylindrical shell that had control authority only for the structural modes which efficiently coupled to the acoustic modes. In doing so they were able to reduce modal spillover and reduce the interior noise levels without increasing the structural vibration.

Using the reciprocal relationship that exists for any piezoelectric transducer it is possible to create modal actuators from the same expressions as used for modal sensors. These produce the same benefits that the modal sensors exhibit, namely a reduction in modal spillover and improved controllability due to un-coupling of the modal response. PZT as a shaped modal actuator poses significant difficulties because of the brittle nature of the material. Subsequently more flexible materials have been used such as PVDF and although PVDF does not have sufficient control authority at low frequencies for most prac-

tical applications, it has been used successfully in the control of very flexible lightweight space structures (Bailey & Hubbard 1985, Choi 1995). Because of the lack of control authority, researchers have looked at alternative materials. One such material which shows great promise for modal actuators is an elastomeric piezoelectric solid commonly referred to as *piezo-rubber*. Being relatively flexible, piezo-rubber can be used to form non-planar transducers easily without the need for casting and grinding; unfortunately, the lack of material availability has kept the research interest low (Lafleur, Shields & Hendrix 1991, Shields & Lafleur 1997).

1.2.4.3 Modal Control

Control of radiation modes not only guarantees global minimisation of the orthogonal cost function but also has significant advantages over control using physical coordinates (Meirovitch & Baruh 1982, Meirovitch & Baruh 1985). Independent modal control for active noise control problems has been shown to (Morgan 1991): minimise the number of actuators, sensors, and corresponding system dimensionality of the control system, as well as minimising the control effort; provide robustness to system uncertainty; and minimise the adaptive convergence time by uncoupling the modal responses. Clark (1995) provides an excellent discussion on the advantages and disadvantages of modal coordinates versus physical coordinates for adaptive feed-forward control which is summarised in Table 1.1 (Clark 1995, Table I).

1.2.5 Energy Density Sensing and Control

1.2.5.1 Active control

It has long been known that the energy density in a one-dimensional sound field is approximately constant throughout the field and for 3-D systems with high modal densities it has been shown that the spatial variance of energy density is significantly less than the

Control in Physical Coordinates		Control in Modal Coordinates	
Advantages	Disadvantages	Advantages	Disadvantages
Ideal for local control.	Global control requires actuator and sensor optimisation as well as signal processing.	Global power control is readily achieved.	Requires *a priori* knowledge of system mode shapes.
Minimal *a priori* signal processing required.	Large adaptive filters are required for broadband control.	Controller is non interacting due to orthogonal coordinates.	Requires a coordinate transformation from physical coordinates to modal coordinates on the input and the output.
Ease of implementation with filtered-x LMS algorithm.	Convergence of MIMO controller is slow due to coupling between actuators and sensors.	A single coefficient adaptive filter is all that is required for broadband control of each mode.	Control and observation spillover can lead to performance degradation.
	Control is typically dependent upon system identification of each control to error transfer function.	A time-averaged gradient decent approach is practical, eliminating the need for control to error system identification.	
	Control to error transfer function may be non-minimum phase.	Optimal control for each mode is always minimal phase.	
		Convergence of each mode is simultaneous.	
		Control system is insensitive to drifts in the system resonant frequencies.	

Table 1.1: The advantages and disadvantages of feed-forward control in physical coordinates and modal coordinates (from Clark, 1995 - Table I)

potential energy (Cook & Schade 1974). To overcome the observability difficulties that are inherent with microphones as error sensors, such as pressure nodes, Sommerfeldt & Nashif (1991) suggested minimising the energy density at discrete locations. In a numerical simulation the authors found that minimisation of the energy density at a discrete location significantly outperformed the minimisation of squared pressures. Subsequent practical studies using the two microphone technique to estimate the particle velocity in one-dimensional fields (Sommerfeldt & Nashif 1992, Nashif & Sommerfeldt 1992, Sommerfeldt & Nashif 1994, Sommerfeldt & Parkins 1994) verified the earlier findings and showed that the location of the energy density sensor makes little difference to the controlled levels. Sommerfeldt, Parkins & Park (1995) extended their earlier work to three dimensions and built a 3 axis energy density sensor made from 6 electret microphones mounted in a wooden sphere. The preliminary results indicated that controlling energy density has the potential to achieve greater global control than controlling squared pressures. Park & Sommerfeldt (1997) successfully showed that energy density control can also be applied to enclosures excited by broadband noise. Shen & Sun (1997) showed that a 4-microphone energy density sensor is suitable for active noise control applications and that the global noise reduction offered by a single energy density sensor in a cylindrical shell was comparable to 32 microphones uniformly spaced in a ring around the shell.

The application of energy density control has also been applied to the control of a pure tone in a diffuse sound field (Elliott & Garcia-Bonito 1995, Garcia-Bonito & Elliott 1995*b*). It was found that minimising both the pressure and pressure gradient along one axis rather than simply pressure, resulted in a significant increase in the 10 dB zone of quiet, from a sphere of diameter $\lambda/10$ around the pressure sensor to $\lambda/2$, for an ellipsoid with its longest axis in the direction of the measured pressure gradient.

1.2.5.2 Sensing and Errors

There is very little published literature about the sensor systems and the errors arising from the measurement of energy density, especially with regard to its use in active control systems. However, a great deal has been written about measuring acoustic intensity (Pavic 1977, Elliott 1981, Thompson & Tree 1981, Thompson 1982*b*, Thompson 1982*a*, Kitech & Tichy 1982, Pascal & Carles 1982, Krishnappa 1983, Boden & Abom 1986, Watkinson 1986, Elko 1991*b*) , a detailed summary of which may be found in Fahy (1995). Much of this literature is directly relevant to the the measurement and error analysis of energy density sensors as will be seen in Chapter 3.

Measurements of acoustic intensity and thus acoustic energy density are subject to errors associated with the following factors: approximations are made in the assumed relations between the directly transduced quantities and the energy density (inherent errors); imperfections of the sensor transducers; imperfections of the signal processor in its function of converting the acquired analogue signals into the quantities required to compute energy density; errors of calibration; variations of transducer sensitivity from the calibration value caused by environmental conditions; 'noise' produced either by non-acoustic disturbances, such as turbulent airflow, or by the instrument itself (Fahy 1995).

The measurement of sound intensity and energy density requires estimates of both the pressure and particle velocity. A microphone is almost exclusively used to measure the pressure, however, measurement of the particle velocity is not as simple. The most common technique of estimating the particle velocity is the *two-microphone technique* which uses two separated microphones to estimate the gradient at the midpoint of the two elements, from which the particle velocity can be calculated. The mean pressure is generally used as the "sensor pressure".

There are three distinct sources of error which occur when estimating acoustic energy density using the two microphone technique; namely, finite separation (inherent) errors,

diffraction and interference effects at the microphones, and instrumentation errors. The inherent errors act to limit the upper frequency range of the sensor and the instrumentation errors such as magnitude and phase mismatches act to limit the low frequency range.

It should be noted that sensing energy density is significantly more tolerant of instrumentation errors than sensing sound intensity. This is because the calculation of sound intensity requires the product between the pressure and particle velocity to be taken, and when these are in quadrature or close to quadrature, such as in a reactive sound field, any small error in phase between the pressure and particle velocity leads to a large error in the active sound intensity. The calculation of acoustic energy density takes the sum of the squares of the pressure and particle velocity, and therefore is only susceptible to errors in magnitudes of the two components.

Chapter 2

Theoretical Models

2.1 Introduction

Prior to evaluating the effectiveness of the active noise control system, it is first necessary to predict the response of the physical system (coupled structural/acoustic) to some excitation. This requires that either an analytical, numerical or experimental model of the vibro-acoustic system be developed, which then allows the calculation of the interior sound field generated by structural or acoustic sources.

This chapter develops a generalised numerical framework for the investigation of any arbitrarily shaped structure radiating periodic sound into a contiguous cavity. The model permits the use of acoustic sources (both internal and external) and structural sources and allows for the investigation of a variety of feedforward control strategies.

As discussed in the previous chapter, there are many approaches available for solving the response of a coupled vibro-acoustic system. It was decided to use a combination of two approaches that have been successful in the past, namely *Modal Coupling Analysis* and *Finite Element Analysis*. The modal coupling approach developed by Lyon & Maidanik (1962), Fahy (1969), Pope (1971) and Dowell et al. (1977) and elegantly summarised by Fahy (1985) provides a method for expressing the vibro-acoustic system in terms of

the uncoupled modes of the fluid and the structure.

A finite element approach was chosen as the method to derive the modal models for two reasons: it does not suffer from the restriction that analytical models do, in that it allows objects of arbitrary geometry to be modelled; and suitable commercial FE code was available.

The modelling technique developed here has been numerically verified in Appendix A for the case of sound transmission from a curved panel radiating into a rectangular cavity. This system will also form the basis for a numerical and experimental study on sensing systems for active control of sound transmission into cavities.

2.2 Modal Interaction Model

Much of the work detailed in the following chapter is not new (as is indicated by the references throughout). It is presented here, with outline derivations when appropriate, in order to provide a self-contained and unified account of the coupled analysis and control theory. The analytical models of the system response were formulated by using the modal coupling theory of Pope (1971) and Fahy (1985).

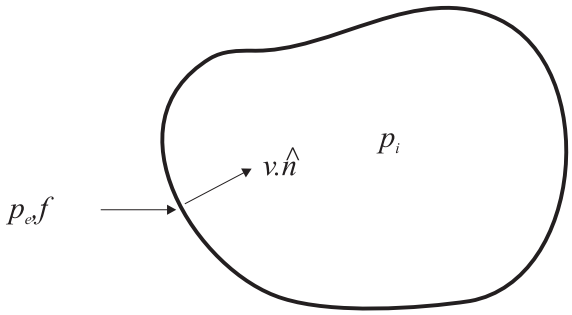

Figure 2.1: Arbitrary vibrating structure radiating into a contiguous cavity.

2.2.1 Uncoupled Response

In the following section a direct and concise derivation of the acoustic pressure of a cavity due to the motion of the bounding structure is given. The acoustic pressure is derived in terms of the normal modes of the *rigid-walled* cavity. The equations of motion of the structure are derived in terms of the *in vacuo* structural normal modes. Finally, the complete coupled fluid-structural equations of motion are obtained. Positive harmonic time dependence of the form $e^{j\omega t}$ is assumed for the analysis but has been omitted for the sake of brevity.

2.2.1.1 Rigid-Walled Acoustic Response

Referring to Figure 2.1, it can be shown that in the absence of sources in the fluid, the acoustic pressure, p, subject to rigid-walled boundary conditions $(\partial p/\partial \hat{n} = 0)$, satisfies the homogeneous wave equation (Fahy 1985)

$$\nabla^2 p - \frac{1}{c_0^2}\frac{\partial^2 p}{\partial t^2} = 0 \tag{2.1}$$

where c_0 is the speed of sound in air. The modal solution to Equation (2.1) at some point in the cavity, $\vec{\mathbf{r}}$, is given by (Humi & Miller 1992)

$$p(\vec{\mathbf{r}}) = \sum_{l=1}^{\infty} p_l \phi_l(\vec{\mathbf{r}}) \tag{2.2}$$

where p_l is the complex amplitude of the lth acoustic pressure mode defined by the mode shape function ϕ_l and natural frequency ω_l. For a monopole with volume velocity, q_c, operating in the cavity, it can be shown that the sound pressure at any point $\vec{\mathbf{r}}$ in the enclosure is (Pope 1971)

$$p(\vec{\mathbf{r}}) = j\rho_0 \omega q_c G_a(\vec{\mathbf{r}}_c \,|\, \vec{\mathbf{r}}) \tag{2.3}$$

where ρ_0 is the density of the air, ω is the frequency of interest and $G_a(\vec{\mathbf{r}}_c \mid \vec{\mathbf{r}})$ is the Green's function of the acoustic space given by

$$G_a(\vec{\mathbf{r}}_c \mid \vec{\mathbf{r}}) = \sum_{l=1}^{\infty} \frac{\phi_l(\vec{\mathbf{r}}_c)\phi_l(\vec{\mathbf{r}})}{\Lambda_l Z_l} \tag{2.4}$$

where Λ_l is the modal volume of the lth cavity mode, defined as the volume integration of the square of the mode shape function, ie

$$\Lambda_l = \int_V \phi_l^2(\vec{\mathbf{r}}) dV(\vec{\mathbf{r}}) \tag{2.5}$$

where V is the volume of the cavity. Z_l is the rigid-walled acoustic input impedance of the lth cavity mode given by

$$Z_l = (k_l^2 + j\eta_{a_l} k_l k - k^2) \tag{2.6}$$

where k is the wavenumber of the sound in the cavity, k_l is the lth eigenvalue of the cavity, η_{a_l} is the viscous modal loss factor of the lth acoustic mode which is equal to twice the critical damping ratio, ξ_{a_l}, of the lth cavity mode.

The pressure in the cavity from the operation of L_a acoustic sources is given by the linear superposition of the pressure due to each source given by Equation (2.3) (Snyder & Hansen 1994*a*)

$$p(\vec{\mathbf{r}}) = \sum_{i=1}^{L_a} j\rho_0 \omega q_{c,i} G_a(\vec{\mathbf{r}}_{c,i} \mid \vec{\mathbf{r}}) \tag{2.7}$$

where $q_{c,i}$ is the volume velocity of the ith acoustic source located at a position $\vec{\mathbf{r}}_{c,i}$ in the acoustic space.

In practice the Green's function (Equation (2.4)) is not evaluated over all modes but rather over a subset of modes, say n_a acoustic modes. This is necessary for numerical

modelling as it keeps the size of the matrices manageable. For the numerical analysis Equation (2.7) can be rewritten in matrix form in terms of the modal pressure amplitudes, $\mathbf{p}$, and the generalised volume velocity, $\mathbf{Q}$, ie

$$p(\vec{\mathbf{r}}) = \boldsymbol{\phi}^{\mathrm{T}}(\vec{\mathbf{r}})\mathbf{p} = \boldsymbol{\phi}^{\mathrm{T}}(\vec{\mathbf{r}}) \left[j\rho_0\omega\boldsymbol{\Lambda}^{-1} \cdot \mathbf{Z}_l^{-1}\mathbf{Q} \right] \tag{2.8}$$

where $\boldsymbol{\phi}(\vec{\mathbf{r}})$ is the (n_a x 1) column vector of the n_a acoustic modes evaluated at $\vec{\mathbf{r}}$, $\mathbf{p}$ is the (n_a x 1) column vector of pressure modal amplitudes, $\boldsymbol{\Lambda}$ is the (n_a x n_a) diagonal modal volume matrix, the diagonal elements of which are given by Equation (2.5), $\mathbf{Z}_l$ is the (n_a x n_a) diagonal rigid-walled acoustic input impedance matrix, the diagonal elements of which are given by Equation (2.6) and $\mathbf{Q}$ is the (n_a x 1) generalised volume velocity vector, the lth element of which is given by $Q_l = \int_V q(\vec{\mathbf{r}})\phi_l(\vec{\mathbf{r}})dV$.

The $\cdot$ in Equation (2.8) indicates the element by element product of the two arrays (Matlab 5.4 1998). For example, given two (m x n) matrices $\mathbf{A}$ and $\mathbf{B}$, then

$$\mathbf{A} \cdot \mathbf{B} = \begin{bmatrix} a_{11}b_{11} & a_{12}b_{12} & \cdots & a_{1n}b_{1n} \\ a_{21}b_{21} & a_{22}b_{22} & \cdots & a_{2n}b_{2n} \\ \vdots & \vdots & \ddots & \vdots \\ a_{m1}b_{m1} & a_{m1}b_{m1} & \cdots & a_{mn}b_{mn} \end{bmatrix} \tag{2.9}$$

It should be noted for the case of the matrix $\mathbf{A}$ is diagonal then $\mathbf{A} \cdot \mathbf{B} = \mathbf{AB}$. This approach was used to increase the speed of the simulations. For L discrete sources the total generalised volume velocity vector of the discrete modal system is,

$$\mathbf{Q} = \boldsymbol{\Phi}_l\mathbf{q}^{\mathrm{T}} \tag{2.10}$$

where $\boldsymbol{\Phi}_l$ is the (n_a x L_a) matrix of acoustic mode shape functions evaluated at the L source locations and $\mathbf{q}$ is the (1 x L_a) row vector of acoustic source strengths.

2.2.1.2 *In-vacuo* Structural Response

An expression for the structural velocity at some point on the structure, $\vec{\mathbf{x}}$, can be derived in terms of its *in vacuo* modes as given by (Snyder & Hansen 1994*a*)

$$v(\vec{\mathbf{x}}) = \sum_{i=1}^{\infty} v_i \psi_i(\vec{\mathbf{x}}) \tag{2.11}$$

where v_i is the complex amplitude of the ith structural mode defined by the mode shape function ψ_i and natural frequency ω_i.

For a point force of strength, f_c, operating normal to the structure, it can be shown that the velocity at any point $\vec{\mathbf{x}}$ on the structure is (Pope 1971)

$$v(\vec{\mathbf{x}}) = j\omega f_c \delta(\vec{\mathbf{x}} - \vec{\mathbf{x}}_c) G_s(\vec{\mathbf{x}}_c \,|\, \vec{\mathbf{x}}) \tag{2.12}$$

where $G_s(\vec{\mathbf{x}}_c \,|\, \vec{\mathbf{x}})$ is the Green's function of the structure given by

$$G_s(\vec{\mathbf{x}}_c \,|\, \vec{\mathbf{x}}) = \sum_{i=1}^{\infty} \frac{\psi_i(\vec{\mathbf{x}}_c)\psi_i(\vec{\mathbf{x}})}{M_i Z_i} \tag{2.13}$$

and where M_i and Z_i are the modal mass and the *in vacuo* structural input impedance of the ith mode respectively, given by

$$M_i = \int_S m(\vec{\mathbf{x}}) \psi_i^2(\vec{\mathbf{x}}) dA(\vec{\mathbf{x}}) \tag{2.14}$$

$$Z_i = (\omega_i^2 + j\eta_{s_i}\omega_i^2 - \omega^2) \tag{2.15}$$

in which $m(\vec{\mathbf{x}})$ is the surface density of the structure and η_{s_i} is the modal loss factor of the ith structural mode.

The velocity on the structure from the operation of L_s forces is given by the linear superposition of the velocity due to each source given by Equation (2.12) (Snyder &

Hansen 1994*a*)

$$v(\vec{\mathbf{x}}) = \sum_{i=1}^{L_s} j\omega f_{c,i}\delta(\vec{\mathbf{x}} - \vec{\mathbf{x}}_{c,i})G_s(\vec{\mathbf{x}}_{c,i} \mid \vec{\mathbf{x}}) \tag{2.16}$$

where $f_{c,i}$ is the ith force located at a position $\vec{\mathbf{x}}_{c,i}$ in the structure.

As was the case with the acoustic Green's function, the structural Green's function (Equation 2.4) is also truncated to a subset of modes, say n_s structural modes. Equation (2.16) can be rewritten in matrix form in terms of the modal velocity amplitudes, $\mathbf{v}$, and the modal generalised force, $\mathbf{F}$, as

$$v(\vec{\mathbf{x}}) = \psi^{\mathrm{T}}(\vec{\mathbf{x}})\mathbf{v} = \psi^{\mathrm{T}}(\vec{\mathbf{x}})\left[j\omega\mathbf{M}^{-1} \cdot \mathbf{Z}^{-1}\mathbf{F}\right] \tag{2.17}$$

where $\boldsymbol{\psi}(\vec{\mathbf{x}})$ is the (n_s x 1) column vector of the n_s structural modes evaluated at $\vec{\mathbf{x}}$, $\mathbf{v}$ is the (n_s x 1) column vector of velocity modal amplitudes, $\mathbf{M}$ is the (n_s x n_s) diagonal modal mass matrix, the diagonal elements of which are given by Equation (2.14), $\mathbf{Z}$ is the (n_s x n_s) diagonal *in vacuo* structural input impedance matrix, the diagonal elements of which are given by Equation (2.15) and $\mathbf{F}$ is the (n_s x 1) generalised force column vector, the ith element of which is given by $F_i = \int_s f(\vec{\mathbf{x}})\psi_i(\vec{\mathbf{x}})dS$.

For L_s discrete forces the total generalised force vector of the discrete modal system is,

$$\mathbf{F} = \boldsymbol{\Psi}_i\mathbf{f}^{\mathrm{T}} \tag{2.18}$$

where $\boldsymbol{\Psi}_i$ is the (n_s x L_s) matrix of structural mode shape functions evaluated at the L_s force locations and $\mathbf{f}$ is the (1 x L_s) row vector of discrete complex forces.

2.2.2 Coupled Response

Having derived the uncoupled modal models it is necessary to couple them using modal coupling theory. The fluid pressure on the surface of the structure is the agent by which the fluid influences structural motion, and the normal surface velocity of the structure is the agent by which the structure influences the fluid (Fahy 1985).

The governing equation for the coupled vibro-acoustic system is the inhomogeneous wave equation

$$\nabla^2\Phi - \frac{1}{c_0^2}\frac{\partial^2\Phi}{\partial t^2} = q \tag{2.19}$$

where Φ is the acoustic potential function and is related to the acoustic pressure and fluid particle velocity by the following

$$p = -\rho_0\frac{\partial\Phi}{\partial t} \tag{2.20}$$

$$v = \nabla\Phi \tag{2.21}$$

Therefore, if the boundaries of the cavity are rigid then $\partial\Phi/\partial\hat{n} = 0$, where $\hat{n}$ is the normal to the boundary surface. The boundary condition over a flexible structure is determined by continuity of the normal air particle velocity and the normal structure velocity on the surface (positive normal outwards), ie $\partial\Phi/\partial\hat{n} = \partial w/\partial t$, where w is the structural displacement normal to the surface. It can be shown that the coupled modal equations of motion for the structure and the cavity in terms of the w and Φ are given by (Fahy 1985)

$$\ddot{w}_i + \omega_i^2 w_i = -\frac{\rho_0 S}{M_i}\sum_{l=1}^{\infty}\dot{\Phi}_l B_{l,i} + \frac{F_i}{M_i} \tag{2.22}$$

$$\ddot{\Phi}_l + \omega_l^2 \Phi_l = \frac{c_0^2 S}{\Lambda_l} \sum_{i=1}^{\infty} \dot{w}_i B_{l,i} - \frac{c_0^2 Q_l}{\Lambda_l} \tag{2.23}$$

where Φ_l is the potential of the lth acoustic mode, Q_l and Λ_l are the generalised volume velocity and modal volume of the lth acoustic mode, w_i is the modal displacement of the ith structural mode (positive normal outwards), F_i and M_i are the generalised force and modal mass of the ith structural mode. $B_{l,i}$ is the non-dimensional coupling coefficient between the lth acoustic mode and the ith structural mode, defined as (Pope 1971)

$$B_{l,i} = \frac{1}{S} \int_S \phi_l(\vec{\mathbf{r}}) \psi_i(\vec{\mathbf{r}}) dA(\vec{\mathbf{r}}) \tag{2.24}$$

It is possible to rearrange Equations (2.22) and (2.23) in terms of the modal amplitudes of the structural velocity and cavity pressure. Solving Equation (2.23) for arbitrary frequency ω and using the expression $\ddot{\Phi}_l = -\omega^2 \Phi_l$ gives

$$\Phi_l = \frac{c_0^2}{\Lambda_l(\omega_l^2 - \omega^2)} \left[S \sum_{i=1} v_i B_{l,i} - Q_l \right] \tag{2.25}$$

Adding the *ad hoc* damping terms for the cavity, $j\eta_{a_p}\omega_p\omega$, to Equation (2.25) and using $p = -\rho_0 \frac{\partial \Phi}{\partial t} = -j\rho_0 \omega \Phi$ an expression for the modal pressure in the cavity resulting from both the structure and interior acoustic sources is given by

$$p_l = \frac{j\rho_0 c_0^2 \omega}{\Lambda_l(\omega_l^2 + j\eta_{a_l}\omega_l\omega - \omega^2)} \left[-S \sum_{i=1} v_i B_{l,i} + Q_l \right] \tag{2.26}$$

and rewriting in terms of the acoustic wavenumber,

$$p_l = \frac{j\rho_0 \omega}{\Lambda_l(k_l^2 + j\eta_{a_l} k_l k - k^2)} \left[-S \sum_{i=1} v_i B_{l,i} + Q_l \right] \tag{2.27}$$

Likewise, solving Equation (2.22) for arbitrary frequency ω and using the expressions

$\ddot{w}_i = -\omega^2 w_i$ and $\dot{\Phi}_l = -p_l/\rho_0$ gives

$$w_i = \frac{1}{M_i(\omega_i^2 - \omega^2)} \left[S \sum_{l=1} p_l B_{l,i} + F_i \right] \tag{2.28}$$

Adding the *ad hoc* damping terms for the structure, $j\eta_{s_i}\omega_i^2$, to Equation (2.28) and using $v_i = \dot{w}_i = j\omega w_i$ an expression for the modal velocity of the structure resulting from both interior acoustic and structural forces is given by

$$v_i = \frac{j\omega}{M_i(\omega_i^2 + j\eta_{s_i}\omega_i^2 - \omega^2)} \left[S \sum_{l=1} p_l B_{l,i} + F_i \right] \tag{2.29}$$

2.2.2.1 Structure to acoustic interior transfer function, $\mathbf{Z}_a$

The modal pressure amplitudes of the cavity as a result of the vibration of the structure can be obtained from Equation (2.27)

$$\mathbf{p} = \mathbf{Z}_a \mathbf{v} \tag{2.30}$$

where $\mathbf{Z}_a$ is the (n_a x n_s) structural to acoustic modal internal radiation transfer function matrix, the terms of which are

$$Z_a(l,i) = -\frac{j\rho_0 S\omega}{\Lambda_l(k_l^2 + j\eta_{a_l}k_l k - k^2)} B_{l,i} \tag{2.31}$$

Although derived independently through a potential formulation, Equation (2.32) is identical to that given by Snyder & Hansen (1994*a*) apart from the sign of the expression. Therefore, for a positive normal directed into the cavity, $\mathbf{Z}_a$ is given by

$$Z_a(l,i) = \frac{j\rho_0 S\omega}{\Lambda_l(k_l^2 + j\eta_{a_l}k_l k - k^2)} B_{l,i} \tag{2.32}$$

2.2.2.2 Interior acoustic to structure transfer function, $\mathbf{Z}_b$

Rewriting Equation (2.29) in matrix form the modal velocity amplitudes of the structure arising from the acoustic pressure are given by

$$\mathbf{v} = \mathbf{Z}_b \mathbf{p} \tag{2.33}$$

where $\mathbf{Z}_b$ is the (n_s x n_a) acoustic to structural modal internal radiation transfer function, the terms of which are

$$Z_b(l,i) = \frac{jS\omega}{M_i Z_i} B_{l,i} \tag{2.34}$$

For a positive normal directed inwards $\mathbf{Z}_b$ is given by

$$Z_b(l,i) = -\frac{jS\omega}{M_i Z_i} B_{l,i} \tag{2.35}$$

2.2.2.3 Solution of coupled system of equations

Acoustic sources Consider the forced response of the system due to acoustic sources only. The cavity response is given by Equation (2.27). The closed-form solution for the cavity response with a positive normal directed outwards is obtained with the substitution into Equation (2.29) of Equation (2.27) for the velocity amplitudes and neglecting the force term,

$$p_r = \frac{j\rho_0\omega}{\Lambda_r(k_r^2 + j\eta_{a_r}k_r k - k^2)} \left[-S \sum_{i=1}^{\infty} \frac{j\omega}{M_i Z_i} \left[S \sum_{l=1}^{\infty} p_l B_{l,i} \right] B_{r,i} + Q_r \right] \tag{2.36}$$

Rearranging gives,

$$\frac{-j\Lambda_r(k_r^2 + j\eta_{a_r}k_r k - k^2)}{\rho_0\omega} p_r = j\omega S^2 \sum_{i=1}^{\infty} \sum_{l=1}^{\infty} \frac{B_{l,i}B_{r,i}}{M_i Z_i} p_l + Q_r \tag{2.37}$$

For a positive normal directed inwards, the above expression becomes,

$$\frac{-j\Lambda_r(k_r^2 + j\eta_{a_r}k_r k - k^2)}{\rho_0\omega}p_r = -j\omega S^2 \sum_{i=1}^{\infty}\sum_{l=1}^{\infty}\frac{B_{l,i}B_{r,i}}{M_i Z_i}p_l + Q_r \tag{2.38}$$

If the infinite sums over l and i are truncated to n_a acoustic modes and n_s structural modes, respectively, the response of the cavity to the finite number of monopole sources can be written in matrix form as,

$$\mathbf{p} = \mathbf{Z}_q^{-1}\mathbf{Q} \tag{2.39}$$

where $\mathbf{p}$ is the (n_a x 1) vector of acoustic pressure participation factors (each element of which represents the modal pressure amplitude of a particular acoustic mode), $\mathbf{Q}$ is the total (n_a x 1) generalised volume velocity vector (each element of which represents the relative contribution of the acoustic sources to a particular mode) and $\mathbf{Z}_q$ is the (n_a x n_a) acoustic modal input impedance matrix for a positive normal directed inwards, the terms of which are,

$$\begin{aligned} Z_q(u,u) &= j\omega S^2 \sum_{i=1}^{n_s}\frac{B_{u,i}B_{u,i}}{M_i Z_i} - \frac{j\Lambda_u(k_u^2 + j\eta_{a_u}k_u k - k^2)}{\rho_0\omega}, \text{diagonal terms} \\ Z_q(u,v) &= j\omega S^2 \sum_{i=1}^{n_s}\frac{B_{u,i}B_{v,i}}{M_i Z_i}, \text{off} - \text{diagonal terms} \end{aligned} \tag{2.40}$$

where u and v refer to the u^{th} and v^{th} acoustic modes, $Z_q(u,v)$ represents the pressure response of mode v to a unit response of mode u. It should be noted that the inverse of the second term for the diagonal expression is simply the volume velocity to pressure impedance matrix for rigid walled conditions.

The term $j\omega S^2 \sum_{i=1}^{n_s}\frac{B_{u,i}B_{v,i}}{M_i Z_i}$ is known as the gyrostatic coupling term. It was neglected by Snyder & Hansen (1994*a*), although they refer to the work of Pan (1992) which provides details on how to include the effects of coupling in their set of equations.

It should be noted that for some weakly coupled structural acoustic systems it is possible to neglect the structural/acoustic interaction when predicting the sound pressure field in the enclosure under operation of the acoustic sources alone. However, at the structural resonances, neglecting this interaction in realistic systems may result in some discrepancy between the theoretical and experimental results (Fanzoni & Dowell 1995, Fanzoni & Bliss 1998) and without this term structural-acoustic reciprocity does not hold.

Structural sources Consider the forced response of the system due to structural forces only. The structural response is given by Equation (2.29). The solution for the structural response is obtained by substituting Equation (2.27) for the pressure amplitudes into Equation (2.29) and neglecting the volume velocity term,

$$v_r = \frac{j\omega}{M_r Z_r}\left[-S\sum_{l=1}^{\infty}\frac{j\rho_0\omega}{\Lambda_l(k_l^2+j\eta_{a_l}k_l k-k^2)}\left[S\sum_{i=1}^{\infty}v_i B_{l,i}\right]B_{l,r}+F_r\right] \tag{2.41}$$

Rearranging,

$$\frac{-jM_r Z_r}{\omega}v_r = -j\omega\rho_0 S^2\sum_{i=1}^{\infty}\sum_{l=1}^{\infty}\frac{B_{l,i}B_{l,r}}{\Lambda_l(k_l^2+j\eta_{a_l}k_l k-k^2)}v_i+F_r \tag{2.42}$$

If the infinite sums over l and i are truncated to n_a acoustic modes and n_s structural modes, respectively, the response of the structure to the finite number of forces can be written in matrix form,

$$\mathbf{v} = \mathbf{Z}_I^{-1}\mathbf{F} \tag{2.43}$$

where $\mathbf{v}$ is the (n_s x 1) vector of structural modal velocity participation factors, $\mathbf{F}$ is the total generalised force and $\mathbf{Z}_I$ is the (n_s x n_s) structural modal input impedance matrix,

the terms of which are,

$$Z_I(u,u) = j\omega\rho_0 S^2 \sum_{l=1}^{n_a} \frac{B_{l,u}B_{l,u}}{\Lambda_l(k_l^2 + j\eta_{a_l}k_l k - k^2)} - \frac{jM_u Z_u}{\omega}, \text{diagonal terms}$$

$$Z_I(u,v) = j\omega\rho_0 S^2 \sum_{l=1}^{n_a} \frac{B_{l,u}B_{l,v}}{\Lambda_l(k_l^2 + j\eta_{a_l}k_l k - k^2)}, \text{off} - \text{diagonal terms} \tag{2.44}$$

where u and v refer to the u^{th} and v^{th} structural modes, $Z_I(u,v)$ represents the structure response of mode v to a unit response of mode u. It should be noted that the inverse of the second term for the diagonal expression is simply the force to velocity impedance matrix for the *in vacuo* structure. This expression is identical to that derived by Snyder & Hansen (1994*a*).

2.2.2.4 Generalised expression for coupled response

Using Equations (2.39), (2.30) and (2.43) the modal pressure amplitudes arising from both monopole volume velocity sources and structural point forces are given by

$$\mathbf{p} = \mathbf{Z}_q^{-1}\mathbf{Q} + \mathbf{Z}_a\mathbf{Z}_I^{-1}\mathbf{F} \tag{2.45}$$

The pressure at a point can be obtained by substitution of Equation (2.45) into Equation (2.2). Using Equations (2.39), (2.33) and (2.43) the modal structural velocities arising from both monopole volume velocity sources and structural point forces are given by

$$\mathbf{v} = \mathbf{Z}_b\mathbf{Z}_q^{-1}\mathbf{Q} + \mathbf{Z}_I^{-1}\mathbf{F} \tag{2.46}$$

The velocity at a point on the structure can be obtained by substitution of Equation (2.46) into Equation (2.11).

2.2.3 Limitations of the Modal Coupling Approach

It should be noted that since the acoustic modes are for a rigid walled enclosure, then the solution for the pressure based on the finite modal expansion, though accurate in the interior of the cavity, does not converge to the boundary normal velocity. This mathematical condition associated with finite summations is referred to as Gibb's phenomenon. Since the rigid walled acoustic modes satisfy the Neumann boundary condition, the velocity predicted at the boundary is zero and this inaccuracy in the velocity field can be substantial in the vicinity of vibrating boundaries (Jayachandran et al. 1998, Fahy 1985). Therefore, this technique is inappropriate for investigating the impedance conditions, sound intensity or energy density at the vibrating boundaries of the enclosure.

The error in the velocity (pressure gradient) is a function of the proximity to the boundary and the number of acoustic modes used in the expansion, or more specifically the acoustic wavelength at the largest acoustic mode. Jayachandran et al. (1998) have investigated the effects of the inaccuracies at the boundaries of a coupled vibro-acoustic system and found that the inaccuracies do not affect the control prediction when minimising the acoustic potential energy.

2.3 Active Control of Sound and Vibration

Snyder & Hansen (1994*a*) developed a theoretical framework suitable for aiding in the design of feedforward active systems to control the sound transmission into coupled enclosures using the modal coupling approach previously outlined. Their work has formed the basis for the following formulation of active control of sound and vibration in a coupled vibro-acoustic system. However, in their formulation they failed to account for the gyrostatic cross-coupling when using acoustic control sources. The gyrostatic coupling has been accounted for by including the acoustic modal input impedance matrix, $\mathbf{Z}_q$, when calculating the response of the system excited by acoustic sources.

Expressions for the following have been derived (in Appendix B) with respect to the control source strengths:

- Sum of the squared acoustic pressures at discrete locations
- Total internal acoustic potential energy
- Sum of the squared structural velocities at discrete locations
- Total structural kinetic energy

The work of Snyder & Hansen (1994*a*) did not account for excitation of the structure from internal acoustic sources. The theory has been expanded here to accommodate this option.

For the following analysis it has been assumed that the primary excitation has been from a source external to the cavity, ie sound transmission into the cavity, as this accounts for the majority of cavity noise problems. It is a very simple procedure to extend the theory to have primary acoustic noise sources.

2.3.1 Determination Of Optimum Control Source Amplitudes And Phases

Since the acoustic pressure and structural velocity levels are a linear function of the control force or volume velocity, quadratic optimisation theory can be used to determine the optimum driving phase and magnitude (Nelson et al. 1987*b*, Nelson & Elliott 1992). This involves expressing the error criteria as a quadratic function of the variable of interest (namely the control source strengths), differentiating with respect to that variable and then setting the gradient of the derivative to find the optimum value of the variable. The procedure and result is summarised below.

The general *Hermitian quadratic form* is defined by Nelson & Elliott (1992) as

$$J = \mathbf{x}^{\mathrm{H}}\mathbf{A}\mathbf{x} + \mathbf{x}^{\mathrm{H}}\mathbf{b} + \mathbf{b}^{\mathrm{H}}\mathbf{x} + c \tag{2.47}$$

where $\mathbf{A}$ is a Hermitian matrix and $\mathbf{x}$ is a vector of complex magnitudes, so that $\mathbf{x}^{\mathrm{H}}\mathbf{A}\mathbf{x}$ is a real scalar. If $\mathbf{A}$ is positive definite, then J will have a unique global minimum for some set of optimum $\mathbf{x}$ given by (Nelson & Elliott 1992)

$$\mathbf{x}_0 = -\mathbf{A}^{-1}\mathbf{b} \tag{2.48}$$

Substituting the expression for $\mathbf{x}_0$ into the general expression for J, the unique minimum is found to be

$$J = c - \mathbf{b}^{\mathrm{H}}\mathbf{A}^{-1}\mathbf{b} \tag{2.49}$$

Nelson & Elliott (1992) point out that for the case of discrete error sensing, if there are more control sources than error sensors then the system of equations becomes undetermined. This means that the Hermitian matrix $\mathbf{A}$ becomes positive semi-definite ($\mathbf{x}^{\mathrm{H}}\mathbf{A}\mathbf{x} = 0$ for some $\mathbf{x} \neq 0$) and also singular. Therefore, the optimum defined by Equation (2.48) is no longer valid. Under these circumstances the cost function J can be driven to zero by an infinite number of combinations of secondary sources, and an additional constraint is necessary to obtain a unique solution. The authors suggest that minimising the control effort, ie $\mathbf{x}^{\mathrm{H}}\mathbf{x}$, is a suitable constraint.

Given the Hermitian quadratic form

$$J = \mathbf{e}^{\mathrm{H}}\mathbf{e} \quad \text{where} \quad \mathbf{e} = \mathbf{d} + \mathbf{C}\mathbf{x} = 0 \tag{2.50}$$

with the additional constraint of minimising $\mathbf{x}^{\mathrm{H}}\mathbf{x}$, the optimum set of control variables is

given by (Nelson & Elliott 1992)

$$\mathbf{x}_0 = -\mathbf{C}^{\mathrm{H}}(\mathbf{C}\mathbf{C}^{\mathrm{H}})^{-1}\mathbf{d} \tag{2.51}$$

2.3.2 Acoustic Pressure at Discrete Locations

The sum of squared pressures at l error sensing locations is given by the following quadratic matrix expression

$$\sum_{i=1}^{l} |p(\vec{\mathbf{r}}_i)|^2 = \mathbf{p}_e^{\mathrm{H}}\mathbf{p}_e \tag{2.52}$$

where $\mathbf{p}_e$ is the (l x 1) column vector of complex pressures at the l error sensing locations. Rewriting the above expression in terms of the acoustic and structural control sources (Appendix B) gives,

$$\sum_{i=1}^{l} |p(\vec{\mathbf{r}}_i)|^2 = \begin{bmatrix} \mathbf{f}_c \\ \mathbf{q}_c \end{bmatrix}^{\mathrm{H}} \mathbf{A} \begin{bmatrix} \mathbf{f}_c \\ \mathbf{q}_c \end{bmatrix} + \begin{bmatrix} \mathbf{f}_c \\ \mathbf{q}_c \end{bmatrix}^{\mathrm{H}} \mathbf{b} + \mathbf{b}^{\mathrm{H}} \begin{bmatrix} \mathbf{f}_c \\ \mathbf{q}_c \end{bmatrix} + c \tag{2.53}$$

where $\mathbf{f}_c$ and $\mathbf{q}_c$ are the source strength vectors of the L_s structural control forces and L_a acoustic control sources and

$$\mathbf{A} = \begin{bmatrix} \mathbf{A}_v & \mathbf{A}_{vq}^{\mathrm{H}} \\ \mathbf{A}_{vq} & \mathbf{A}_q \end{bmatrix} \tag{2.54}$$

$$\mathbf{b} = \begin{bmatrix} \mathbf{Z}_a\mathbf{Z}_I^{-1}\Psi_c & \mathbf{Z}_q^{-1}\mathbf{\Phi}_c \end{bmatrix}^{\mathrm{H}} \mathbf{Z}_w\mathbf{Z}_a\mathbf{v}_p \tag{2.55}$$

$$c = \mathbf{v}_p^{\mathrm{H}}\mathbf{Z}_a^{\mathrm{H}}\mathbf{Z}_w\mathbf{Z}_a\mathbf{v}_p \tag{2.56}$$

where $\mathbf{\Phi}_c$ is the (n_a x L_a) matrix of (n_a x 1) acoustic mode shape function vectors $\phi(\vec{\mathbf{r}})$ evaluated at the L_a acoustic control source locations. Likewise $\mathbf{\Psi}_c$ is the (n_s x L_s) matrix of (n_s x 1) structural mode shape function vectors $\psi(\vec{\mathbf{x}})$ evaluated at the L_s control force

locations. The uncontrolled sum of the mean square pressures is given by the scalar term c. The Hermitian weighting matrix $\mathbf{Z}_w$ is given by

$$\mathbf{Z}_w = \mathbf{\Phi}_e^* \mathbf{\Phi}_e^{\mathrm{T}} \tag{2.57}$$

in which $\mathbf{\Phi}_e$ is the (n_a x l) matrix of (n_a x 1) acoustic mode shape function vectors $\phi(\vec{\mathbf{r}})$ evaluated at the l error sensing locations.

Here $\mathbf{A}_v$ is the matrix $\mathbf{A}$ for vibration control sources operating alone and is given by

$$\mathbf{A}_v = \mathbf{\Psi}_c^{\mathrm{H}} (\mathbf{Z}_I^{-1})^{\mathrm{H}} \mathbf{Z}_a^{\mathrm{H}} \mathbf{Z}_w \mathbf{Z}_a \mathbf{Z}_I^{-1} \mathbf{\Psi}_c \tag{2.58}$$

$\mathbf{A}_q$ is the matrix $\mathbf{A}$ for the acoustic control source operating alone, with elements given by

$$\mathbf{A}_q = \mathbf{\Phi}_c^{\mathrm{H}} (\mathbf{Z}_q^{-1})^{\mathrm{H}} \mathbf{Z}_w \mathbf{Z}_q^{-1} \mathbf{\Phi}_c \tag{2.59}$$

and the cross-coupling matrix $\mathbf{A}_{vq}$ is given by,

$$\mathbf{A}_{vq} = \mathbf{\Phi}_c^{\mathrm{H}} (\mathbf{Z}_q^{-1})^{\mathrm{H}} \mathbf{Z}_a^{\mathrm{H}} \mathbf{Z}_w \mathbf{Z}_a \mathbf{Z}_I^{-1} \mathbf{\Psi}_c \tag{2.60}$$

The optimum set of control forces and volume velocities which produce the unique global minimum value of the quadratic function in Equation (2.53) are defined by the relationship (Nelson et al. 1987*b*)

$$\begin{bmatrix} \mathbf{f}_c \\ \mathbf{q}_c \end{bmatrix}_{opt} = -\mathbf{A}^{-1}\mathbf{b} \tag{2.61}$$

producing the minimum of the squared pressure levels at the error locations

$$\sum_{i=1}^{l} |p(\vec{\mathbf{r}}_i)|^2 = c - \mathbf{b}^{\mathrm{H}}\mathbf{A}^{-1}\mathbf{b} \tag{2.62}$$

It should be noted that for Equation (2.61) to define a unique global minimum, the matrix $\mathbf{A}$ must be positive definite. In terms of the physical control system this means that there must be as many error sensor locations as control sources (assuming that there are many more modes than control source locations). If not, then it is necessary to apply the additional constraint of minimising the control effort by using the optimum control strengths given by Equation (2.51), ie

$$\begin{bmatrix} \mathbf{f}_c \\ \mathbf{q}_c \end{bmatrix}_{opt} = -\mathbf{C}^{\mathrm{H}} \left(\mathbf{C}\mathbf{C}^{\mathrm{H}}\right)^{-1} \mathbf{d} \tag{2.63}$$

where

$$\mathbf{C}^{\mathrm{H}} = \left[\mathbf{Z}_a \mathbf{Z}_I^{-1} \Psi_c \;\; \mathbf{Z}_q^{-1} \mathbf{\Phi}_c\right]^{\mathrm{H}} \mathbf{\Phi}_e^* \tag{2.64}$$

and

$$\mathbf{d} = \mathbf{\Phi}_e^{\mathrm{T}} \mathbf{Z}_a \mathbf{v}_p \tag{2.65}$$

2.3.3 Minimisation of the Internal Acoustic Potential Energy

The procedure for calculating the control source volume velocities and forces which minimise the acoustic potential energy are much the same as that outlined for minimising the sound pressure at discrete locations. The derivation of the potential energy equation is included in Appendix B since the formulation in Snyder & Hansen (1994*a*) has several errors and does not account for the gyrostatic cross-coupling when using acoustic con-

trol sources. The gyrostatic coupling has been accounted for by including the acoustic modal input impedance matrix, $\mathbf{Z}_q$, when calculating the response of the system excited by acoustic sources. The results are summarised below.

The time averaged acoustic potential energy within an enclosure is given by (Snyder & Hansen 1994*a*)

$$E_p = \frac{1}{4\rho_0 c_0^2} \int_V |p(\vec{\mathbf{r}})|^2 dr \tag{2.66}$$

In Appendix B it is shown that by integrating and expanding Equation (2.66) the potential energy of the cavity in terms of the modal pressure amplitudes is given by

$$E_p = \frac{1}{4\rho_0 c_0^2} \sum_{i=1}^{\infty} \Lambda_i |p_i|^2 = \mathbf{p}^{\mathrm{H}} \mathbf{\Lambda} \mathbf{p}^{\mathrm{H}} \tag{2.67}$$

where $\mathbf{\Lambda}$ is a (n_a x n_a) diagonal matrix, the diagonal terms of which are

$$\Lambda(i,i) = \frac{\Lambda_i}{4\rho_0 c_0^2} \tag{2.68}$$

where Λ_i is the modal volume of the ith cavity mode.

Expressing the acoustic potential energy in terms of the primary and secondary sources,

$$E_p = \begin{bmatrix} \mathbf{f}_c \\ \mathbf{q}_c \end{bmatrix}^{\mathrm{H}} \mathbf{A} \begin{bmatrix} \mathbf{f}_c \\ \mathbf{q}_c \end{bmatrix} + \begin{bmatrix} \mathbf{f}_c \\ \mathbf{q}_c \end{bmatrix}^{\mathrm{H}} \mathbf{b} + \mathbf{b}^{\mathrm{H}} \begin{bmatrix} \mathbf{f}_c \\ \mathbf{q}_c \end{bmatrix} + c \tag{2.69}$$

where $\mathbf{A}$, $\mathbf{b}$ and c are given by Equations (2.54), (2.55) and (2.56) respectively, with the matrix $\mathbf{Z}_w$ given by

$$\mathbf{Z}_w = \mathbf{\Lambda} \tag{2.70}$$

The optimum set of control forces and volume velocities which produce the unique global minimum value of the quadratic function in Equation (2.69) are given by Equation (2.61) resulting in a minimum given by Equation (2.62). In any realistic acoustic model, the control system equations should not be undetermined as there will generally be many more acoustic modes than control sources. Subsequently it is unnecessary to derive the under constrained optimum control strengths for control of acoustic potential energy.

2.3.4 Minimisation of Structural Velocity Levels at Discrete Points

The surface normal structural velocity level at any point $\vec{\mathbf{x}}$ is given by

$$v(\vec{\mathbf{x}}) = v_p(\vec{\mathbf{x}}) + v_c(\vec{\mathbf{x}}) \tag{2.71}$$

In terms of the matrices previously defined, the primary and control velocity levels at any point on the structure can be expressed as

$$v_p(\vec{\mathbf{x}}) = \psi^T(\vec{\mathbf{x}})\mathbf{v}_p \tag{2.72}$$

$$v_c(\vec{\mathbf{x}}) = \psi^T(\vec{\mathbf{x}})\left[\mathbf{Z}_I^{-1}\mathbf{\Psi}_c\mathbf{f}_c + \mathbf{Z}_b\mathbf{Z}_q^{-1}\mathbf{\Phi}_c\mathbf{q}_c\right] \tag{2.73}$$

where $\psi(\vec{\mathbf{x}})$ is the (n_s x 1) vector of structural mode shape functions evaluated at a location $\vec{\mathbf{x}}$.

It is shown in Appendix B that the sum of the squared velocity levels at a set of error sensing points can be expressed as

$$\sum_{i=1}^{l} |v(\vec{\mathbf{x}}_i)|^2 = \begin{bmatrix} \mathbf{f}_c \\ \mathbf{q}_c \end{bmatrix}^{\mathrm{H}} \mathbf{A} \begin{bmatrix} \mathbf{f}_c \\ \mathbf{q}_c \end{bmatrix} + \begin{bmatrix} \mathbf{f}_c \\ \mathbf{q}_c \end{bmatrix}^{\mathrm{H}} \mathbf{b} + \mathbf{b}^{\mathrm{H}} \begin{bmatrix} \mathbf{f}_c \\ \mathbf{q}_c \end{bmatrix} + c \tag{2.74}$$

where,

$$\mathbf{A} = \begin{bmatrix} \mathbf{A}_v & \mathbf{A}_{vq}^{\mathrm{H}} \\ \mathbf{A}_{vq} & \mathbf{A}_q \end{bmatrix} \tag{2.75}$$

$$\mathbf{b} = \left[\mathbf{Z}_I^{-1}\boldsymbol{\Psi}_c \;\; \mathbf{Z}_b\mathbf{Z}_q^{-1}\boldsymbol{\Phi}_c\right]^{\mathrm{H}} \mathbf{Z}_w\mathbf{v}_p \tag{2.76}$$

$$c = \mathbf{v}_p^{\mathrm{H}}\mathbf{Z}_w\mathbf{v}_p \tag{2.77}$$

and

$$\mathbf{Z}_w = \boldsymbol{\Psi}_e^{*}\boldsymbol{\Psi}_e^{\mathrm{T}} \tag{2.78}$$

where $\boldsymbol{\Psi}_e$ is the (n_s x l) matrix of (n_s x 1) structural mode shape function vectors $\psi(\vec{\mathbf{x}})$ evaluated at the l error sensing locations.

Here $\mathbf{A}_v$ is the matrix $\mathbf{A}$ for vibration control sources operating alone and is given by

$$\mathbf{A}_v = \boldsymbol{\Psi}_c^{\mathrm{H}}(\mathbf{Z}_I^{-1})^{\mathrm{H}}\mathbf{Z}_w\mathbf{Z}_I^{-1}\boldsymbol{\Psi}_c \tag{2.79}$$

$\mathbf{A}_q$ is the matrix $\mathbf{A}$ for the acoustic control source operating alone, with elements given by

$$\mathbf{A}_q = \boldsymbol{\Phi}_c^{\mathrm{H}}(\mathbf{Z}_q^{-1})^{\mathrm{H}}\mathbf{Z}_b^{\mathrm{H}}\mathbf{Z}_w\mathbf{Z}_b\mathbf{Z}_q^{-1}\boldsymbol{\Phi}_c \tag{2.80}$$

and $\mathbf{A}_{vq}$ is given by,

$$\mathbf{A}_{vq} = \boldsymbol{\Phi}_c^{\mathrm{H}}(\mathbf{Z}_q^{-1})^{\mathrm{H}}\mathbf{Z}_b^{\mathrm{H}}\mathbf{Z}_w\mathbf{Z}_I^{-1}\boldsymbol{\Psi}_c \tag{2.81}$$

The optimum control source strengths to minimise Equation (2.74) are given by Equation (2.61) resulting in a minimum given by Equation (2.62). For the case when the set

of equations is undetermined ($\mathbf{A}$ is singular) then it is necessary to apply the additional constraint of minimising the control effort by using the optimum control strengths given by Equation (2.63) with

$$\mathbf{C}^{\mathrm{H}} = \left[\mathbf{Z}_I^{-1}\boldsymbol{\Psi}_c \;\; \mathbf{Z}_b\mathbf{Z}_q^{-1}\boldsymbol{\Phi}_c\right]^{\mathrm{H}} \boldsymbol{\Psi}_e^* \tag{2.82}$$

and

$$\mathbf{d} = \boldsymbol{\Psi}_e^{\mathrm{T}}\mathbf{v}_p \tag{2.83}$$

2.3.5 Minimisation of the Structural Kinetic Energy

The instantaneous kinetic energy of the structure is given by (Snyder & Hansen 1994*a*)

$$E_k = \frac{1}{2}\int_S \rho_s(\vec{\mathbf{x}})h(\vec{\mathbf{x}})|v(\vec{\mathbf{x}})|^2 dA \tag{2.84}$$

where $h(\vec{\mathbf{x}})$ is the thickness of the structure in the direction normal to the velocity. Evaluating the integral and using modal orthogonality it is shown in Appendix B that the time averaged structural kinetic energy can be expressed as

$$E_k = \begin{bmatrix} \mathbf{f}_c \\ \mathbf{q}_c \end{bmatrix}^{\mathrm{H}} \mathbf{A} \begin{bmatrix} \mathbf{f}_c \\ \mathbf{q}_c \end{bmatrix} + \begin{bmatrix} \mathbf{f}_c \\ \mathbf{q}_c \end{bmatrix}^{\mathrm{H}} \mathbf{b} + \mathbf{b}^{\mathrm{H}} \begin{bmatrix} \mathbf{f}_c \\ \mathbf{q}_c \end{bmatrix} + c \tag{2.85}$$

where $\mathbf{A}$, $\mathbf{b}$ and c are given by Equations (2.75), (2.76) and (2.77) respectively, with the matrix $\mathbf{Z}_w$ given by

$$\mathbf{Z}_w = \frac{\mathbf{M}}{4} \tag{2.86}$$

where $\mathbf{M}$ is the diagonal matrix of modal masses, where the ith element is given by

$$M_i = \int_S \rho_s(\vec{\mathbf{x}}) h(\vec{\mathbf{x}}) \psi_i(\vec{\mathbf{x}})^2 dA \tag{2.87}$$

The optimum control source strengths to minimise Equation (2.85) are given by Equation (2.61) resulting in a minimum given by Equation (2.62). As was the case for the minimisation of internal acoustic potential energy, the minimisation of the total structural kinetic energy should not lead to an undetermined set of equations.

2.4 Finite Element Analysis

A Finite Element Analysis (FEA) of both the structure and the acoustic space was performed using ANSYS. ANSYS provides the capability of modelling the interaction of an acoustic fluid with a structure; however, the coupled set of equations which are formed when modelling a coupled system are characterised by unsymmetric mass and stiffness matrices. The solution of the coupled set of equations requires much greater computational resources than the symmetric equivalent obtained with uncoupled systems, also, the physical mechanisms involving coupling of various structural mode types with particular cavity mode types can be elucidated with the uncoupled analysis but remain a mystery if fully coupled analysis is used. In addition, it was found that there were not the computational resources available to perform a fully coupled FE analysis on the systems likely to be investigated. As a result, the modal coupling approach detailed above was used instead of the fully coupled analysis.

2.4.1 Acoustic Model

The sound pressure, p, inside a cavity with rigid wall conditions is described by the homogeneous wave equation

$$\nabla^2 p - \frac{1}{c_0^2}\frac{\partial^2 p}{\partial t^2} = 0 \tag{2.88}$$

where c_0 is the speed of sound in air. The air particle velocity, v, in the cavity is related to the sound pressure by

$$\nabla p = -\rho_0 \frac{\partial v}{\partial t} \tag{2.89}$$

where ρ_0 is the density of air. The formulation for the pressure based fluid elements within ANSYS expresses the unknown acoustic pressure within an element in terms of the pressure values at the nodes as follows

$$p = \sum_{i=1}^{m} N_i p_i \tag{2.90}$$

where, N_i are a set of linear shape functions, p_i are the nodal pressures and m is the number of nodes.

Substituting the pressure expression into the acoustic wave equation and applying Galerkin's weighted residual finite element procedure leads to the following finite element matrix equation for the fluid mesh (ANSYS Theory Manual 1998, Chapter 8.2)

$$[\mathbf{K}_f]\Phi_i - \omega_i^2[\mathbf{M}_f]\Phi_i = 0 \tag{2.91}$$

where $[\mathbf{K}_f]$ is the fluid equivalent stiffness matrix, $[\mathbf{M}_f]$ is the fluid equivalent mass matrix, and Φ_i and ω_i are the mode shape vector (eigenvector) and the natural angular frequency respectively of mode *i*. The eigenvectors and eigenvalues are extracted using the

Block Lanczos method fully described in the ANSYS Structural Analysis Guide (1998). Damping is neglected at this stage since the undamped solvers in ANSYS are significantly faster than the solvers for damped systems. Damping was added during the solution stage much like the *ad hoc* damping terms used in the modal solution section above. For systems with low modal damping this procedure is perfectly reasonable, however, systems with heavy damping may need to be solved using the damped solvers to fully account for the cross coupling which occurs between damped modes.

The *Fluid-30* acoustic elements were used for the modal analysis of the acoustic space. The elements are available in three configurations, two of which are available during the automatic mesh generation procedure and are shown below in Figure 2.2. The cubic element (8 noded brick) is only suitable for meshing cavities with 8 sides. All other geometries require the use of the tetrahedral configuration of the element. The tetrahedral shaped element is less accurate than the equivalent cubic element; hence, a greater mesh density when using tetrahedral elements is required to achieve the same accuracy as would be obtained from cubic elements.

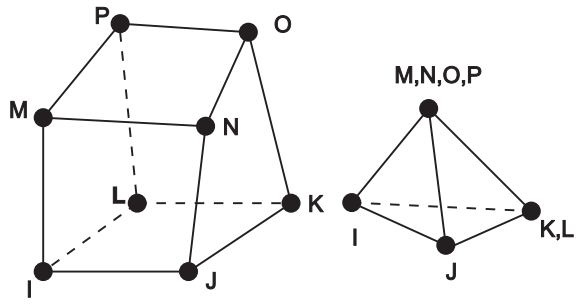

Figure 2.2: *Fluid-30* 3D acoustic fluid element.

The cavity mode shape vectors returned by ANSYS can be normalised to either unity or the mass matrix. By normalising the mode shapes to the mass matrix, the modal volume of the cavity can be obtained directly; that is (ANSYS Theory Manual 1998, Chapter

17.3)

$$\Phi_i^{\mathrm{T}}[\mathbf{M}_{f_e}]\Phi_i = 1 \tag{2.92}$$

where Φ_i is the mode shape function vector for the ith mode and $[\mathbf{M}_{f_e}]$ is the fluid element mass matrix defined as (ANSYS Theory Manual 1998, Chapter 8.2)

$$[\mathbf{M}_{f_e}] = \frac{1}{c_0^2}\int_{V_e}[\mathrm{N}][\mathrm{N}]^{\mathrm{T}}dV \tag{2.93}$$

where $[\mathrm{N}]$ is the vector of linear shape functions for the fluid element. If the mode shape vectors are normalised to unity (ie the maximum element is 1) then by definition

$$\hat{\Phi}_i^{\mathrm{T}}[\mathbf{M}_{f_e}]\hat{\Phi}_i = \frac{\Lambda_i}{c_0^2} \tag{2.94}$$

where $\hat{\Phi}_i$ is the mode shape vector normalised to unity and Λ_i is the modal volume of the ith cavity mode defined by Equation (2.5). From Ewins (1995) it can be shown the relationship between the mass normalised mode shape function Φ_i and the more general form $\hat{\Phi}_i$ with the largest element normalised to unity is simply (Ewins 1995)

$$\Phi_i = \frac{c_0}{\sqrt{\Lambda_i}}\hat{\Phi}_i \tag{2.95}$$

Hence, given that $\max(\hat{\Phi}_i) = 1$ the maximum element of the ANSYS mass-normalised mode shape function vector is equal to the ratio of the speed of sound in air to the square root of the modal volume, ie

$$\Lambda_i = \frac{c_0^2}{\max(\Phi_i^2)} \tag{2.96}$$

The above equation holds true because each node has only one degree of freedom.

For structural elements with 6 degrees of freedom, this technique is not always valid (see below).

The modal volume used in the response analysis performed on MATLAB was extracted from the mode shape data and then the acoustic mode shapes were normalised to unity for subsequent analysis.

2.4.2 Structural Model

Two structural elements have been used in the FE modelling of the structure. The *Shell-63* element is a 3D solid thin shell elastic element and is available in a four noded (quadrilateral) and three noded (triangular) configuration as shown in Figure 2.3. The quadrilaterals can only be used when the area to be meshed has four sides. All other geometries require meshing with triangular elements. To have coincident nodes for the structural and acoustic models it was necessary to use triangular elements in conjunction with tetrahedral elements and quadrilateral elements with brick fluid elements.

Therefore, for systems with 6 sided geometries such as boxes it was possible to mesh the system with quadrilateral & brick elements. However, in order to use the automatic mesh generator within ANSYS for systems with more complicated geometries, it was necessary to mesh the systems using triangular and tetrahedral elements.

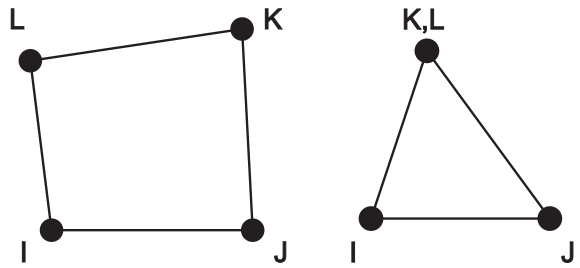

Figure 2.3: *Shell-63* elastic shell element.

Stiffeners fixed to the structure have been modelled using beam elements. Beam elements provide additional stiffening to the FE model without increasing the number of

dofs and are therefore preferable to using an equivalent shell element to achieve the stiffening. The use of beam elements does have drawbacks as an increase in the size of the FE wavefront in the solution process often occurs when beam elements are added to the model. This has the potential of increasing the computation requirements but the increase is significantly less than would result from using shell elements for stiffeners. The *Beam-24* element used in the ANSYS FE model is a thin-walled 3D elastic beam element. The cross-section of the element is user defined and allows stiffeners of arbitrary cross-section to be modelled.

The mode shape vectors of the structure returned by ANSYS can be normalised to either unity or the mass matrix. By normalising the mode shapes to the mass matrix, the modal mass of the structure can be obtained directly, ie (ANSYS Theory Manual 1998, Chapter 17.3)

$$\mathbf{\Psi}_i^{\mathrm{T}}[\mathbf{M}_{s_e}]\mathbf{\Psi}_i = 1 \tag{2.97}$$

where $\mathbf{\Psi}_i$ is the mode shape function vector for the ith mode and $[\mathbf{M}_{s_e}]$ is the mass matrix of the structural element, defined as (ANSYS Theory Manual 1998, Chapter 2.2)

$$[\mathbf{M}_{s_e}] = \rho \int_{V_e} [\mathrm{N}][\mathrm{N}]^{\mathrm{T}} dV \tag{2.98}$$

where $[\mathrm{N}]$ is the vector of linear shape functions for the structural element. By default, when the mass matrices for the Shell63 element are formulated within ANSYS they are a *consistent mass matrix*, the exact formulation depending on the specific element shape function. In physical terms this means that the mass matrix is fully or semi-populated and is not necessarily diagonal. To extract the modal mass from the mode shape data as was done for the modal volume of the acoustic model (see Equation 2.96) it is necessary for

the rotational inertia of the element to be negligible. This requirement holds true for thin shells just as in the classical Bernoulli-Euler beam theory. Within ANSYS it is possible to delete the rotational terms from the mass matrix for the *Shell-63* element and for thin shells this *reduced mass matrix* often provides more accurate solutions compared to the consistent mass matrix. All the simulations used in this thesis have used a reduced mass matrix for the shell elements (ie, KEYOPT(7)=1). In addition to the removal of the rotary inertias, a *lumped mass* technique (LUMPM,ON) was used for the modal solution, where the total element mass in each direction is distributed equally to the nodes of the element. In other words, concentrated masses (located at the nodes of the element) replace the distributed element mass, ie. the off-diagonal terms are zero. Both the reduced mass and lumped mass approximations have the added advantage of shortening solution times.

With these two approximations in place and letting the mode shape vector correspond to the out of plane displacements (see Equation 2.105 below), the relationship between the mass normalised mode shape function Ψ_i and the more general form $\hat{\Psi}_i$ with the maximum element normalised to unity is simply (Ewins 1995)

$$\Psi_i = \frac{\hat{\Psi}_i}{\sqrt{M_i}} \tag{2.99}$$

Hence, given that $\max(\hat{\Psi}) = 1$ it can be shown that the maximum element of the ANSYS mode shape function vector is equal to the inverse of the square root of the modal mass, ie

$$M_i = \frac{1}{\max(\Psi_i^2)} \tag{2.100}$$

where M_i is the modal mass of the ith structural mode given by Equation (2.14). The modal mass for each mode was extracted from the mode shape file using Equation (2.100). The structural mode shapes were then normalised to unity to remain consistent with the

theory of Snyder & Hansen (1994*a*).

2.4.3 Extraction of Miscellaneous FE Data

In order to evaluate the boundary integral equation when coupling the structural and acoustic models (Equation 2.24), the effective surface area of each node was required. It was originally intended to take the effective mass of each node (without the beam elements) and divide by the surface density to obtain the surface area. Attempts were made to use the ANSYS binary file containing the mass matrix data. However, extraction of data from the binary files within ANSYS proved extremely difficult because of insufficient literature regarding the format of the binary file. The software agents were contacted and a request for additional information was made, however, little help was forthcoming.

Instead, an alternative approach was used, where a unit pressure was applied to the surface of the structure with all the n_s nodal degrees of freedom fixed. An (n_s x 3) reaction force matrix, $\mathbf{f}$ is then obtained. The magnitude of the reaction force at each node is approximately equal to the effective nodal area. Therefore, the (n_s x 1) effective nodal area vector is

$$\mathbf{s} = |\mathbf{f}| \tag{2.101}$$

where the elements of $\mathbf{s}$ are the effective area of each node. The unit vector to the normal to the surface is obtained by normalising the reaction force matrix,

$$\hat{\mathbf{n}} = \frac{\mathbf{f}}{|\mathbf{f}|} \tag{2.102}$$

where $\hat{\mathbf{n}}$ is the (n_s x 3) normal vector matrix, the rows of which define the normal to the surface at each node.

Due to the discrete nature of the model the non-dimensional coupling coefficient given

by Equation (2.24) was calculated using a finite summation rather than a continuous surface integral, ie

$$B_{l,i} \approx \frac{1}{S} \sum_{n=1}^{n_s} s_n \phi_l(\vec{\mathbf{x}}_n) \psi_i(\vec{\mathbf{x}}_n) \tag{2.103}$$

where S is the surface area given by the sum of all the nodal areas,

$$S \approx \sum_{n=1}^{N} s_n \tag{2.104}$$

This first order discrete approximation to the surface integral was also used by De Rosa et al. (1994) when post-coupling two FE models during the ASANCA studies.

The direction of the resultant force was the inward normal to the surface at that node. By calculating the inner (dot) product of the unit normal nodal vector and the structural mode shape matrices, the mode shape normal to the surface was obtained, ie

$$\Psi_i = \hat{\mathbf{n}} \bullet [\Psi_{x,i}, \Psi_{y,i}, \Psi_{z,i}] \tag{2.105}$$

Like any discrete approximation, the accuracy of this estimation technique can suffer in regions of high curvature and low element density. However, this error has a negligible effect on the boundary integral estimation of the coupled power flow. This is because the areas of high curvature have relatively high local impedances and hence these regions exhibit low local sound transmission between the cavity and the structure.

2.5 Experimental Techniques

2.5.1 Measurement of Acoustic Transfer Impedance and Volume Velocity

The acoustic transfer impedance describes the relationship between the complex pressure at a point within the acoustic domain arising from an acoustic source and the volume velocity of the source. For a monopole source, by virtue of reciprocity, the transposition of source position and measurement position will yield the same impedance. In order to measure to acoustic transfer impedance of the cavity it is necessary to measure the volume velocity of the acoustic source. Anthony & Elliott (1991) review three techniques for the measurement of the volume velocity; laser velocimetry, measurement of the internal source pressure, and using a moving-coil loudspeaker as an output transducer (Salava's method). The key findings of the study have been presented below.

Laser velocimetry is a technique that enables the velocity at a point, normal to the beam, to be determined. This is achieved by measuring the resulting Doppler shift in the reflected beam. When the acoustic source behaves as a rigid piston in a baffle, then the volume velocity is given by the product of the velocity on the "piston" surface and the surface area. In practice, a non-uniform surface, such as a loudspeaker, is commonly used as a radiator. At low frequencies a loud speaker diaphragm can be considered "piston like" although a small velocity gradient will exist across the diaphragm. However, at high frequencies, the motion of different parts of the diaphragm will be out of phase as various diaphragm modes are excited. In such situations, to determine the total volume velocity over a non-uniform surface it is necessary to integrate the velocity of the diaphragm over the surface. This may be approximated by a finite summation.

The volume velocity of a source may be measured using an ordinary loudspeaker as a volume velocity sensor (Salava 1988). The sensor loudspeaker is connected face-to-face

to the driving loudspeaker such that the volume between the two diaphragms is smaller than the backing enclosure. The sensor diaphragm is driven by that of the driving loudspeaker, and assuming that the enclosure is rigid, is the only source of acoustic radiation. The output voltage from the sensor is directly related to the velocity at the centre of the diaphragm. This approach loads the driving loudspeaker which can act to reduce output power.

The third and most commonly employed technique (Snyder & Hansen 1989, Snyder & Hansen 1994*b*) is to measure the internal pressure of a loudspeaker mounted within an acoustically sealed enclosure. The volume velocity radiated by the source is directly proportional to the internal pressure. This technique does not account for wave motion in the enclosure which will arise when the wavelength of the driving frequency is comparable with the internal dimensions.

Anthony & Elliott (1991) concluded that the laser velocimetry method was accurate but impractical as a measurement tool. The other two techniques performed extremely well, giving measurements of volume velocity within 1dB of the reference measurement up to 500Hz (for a 110mm diameter driver), although Salava's method was found to provide a slightly more accurate measurement of the volume velocity.

Using Anthony & Elliott (1991) conclusions it was decided to use the simplest of the three techniques, namely measuring the backing enclosure sound pressure with a microphone. This technique has the additional advantage that any sensitivity and phase errors in the microphone measurements are cancelled when the transfer function is calculated.

The volume velocity of the loudspeaker with a backing enclosure is given by (Beranek 1988)

$$q = \frac{p_i}{Z_v} = -j\frac{p_i \omega V}{\rho_0 c_o^2} \tag{2.106}$$

where Z_v is the acoustic impedance of the backing cavity, V is the volume of the backing

cavity, ω is the angular frequency of the excitation, ρ_0 and c_0 are density and speed of sound in the fluid respectively.

2.5.2 Prediction of Control using Measured Transfer Functions

The technique for predicting the level of control offered to a causal system from actuators described in Section 2.3 can also be applied to measure transfer function data. This is a very common experimental technique used to predict the maximum level of control that can be achieved by the physical system (Dorling, Eatwell, Hutchins, Ross & Sutcliffe 1989, Rossetti, Norris, Southward & Sun 1993). The control prediction from measured transfer function data has three distinct advantages over using a real-time controller to measure the amount of control that can be achieved:

- Prediction gives an estimate of the maximum possible control level that can be achieved and removes the uncertainty in the controller from the measurements.
- The real time control experiments take considerably longer to perform since it is necessary to ensure that the system has converged to a stable and optimum state (which is never certain).
- It is simple to get a complete spectrum of the control system performance when using measured transfer function data, whereas, with real time control, this is almost impossible. In practice, if the controller is to achieve an optimal solution, the system needs to be feed-forward excited by a single tone. This results in a spectrum composed of discrete frequencies, as opposed to the (almost) continuous spectra from the measured transfer function data.

The mathematical formulation of the technique is identical to that using predicted transfer functions presented in section 2.3 with the exception that measured transfer functions are

used in place of predicted transfer functions.

Chapter 3

Energy Density Sensing

3.1 Introduction

Global noise reduction is the objective of many active noise control applications in small enclosures such as aircraft cabins and automobiles, and it is widely accepted that the most appropriate quantity to minimise in these cases is the potential energy within the cavity, which provides a measure of the mean square pressure integrated throughout the space. In practice it is not possible to spatially integrate the pressure field so it is approximated with a number of discrete microphones. For small regular systems with low modal densities excited at low frequencies it is often easy to achieve global control with one or two judiciously located microphones. However in most systems where the spatial variation of the pressure field can be difficult to predict, many more microphones may be needed, particularly when the wavelength is small. Acoustic energy density at a point, which is formed by the sum of the acoustic potential and kinetic energies, can be used as an alternative to measuring the pressure at a point.

The purpose of the study described here was to investigate various physical configurations of energy density sensors for use in active noise control systems. Selection of error sensors for ANC are typically driven by cost, simplicity and size and this study was no

exception. It will be shown that an effective energy density sensor can be implemented using only 4 microphones rather than 6 microphones as used in previous sensors and although there is a significant reduction in accuracy, it has been shown that active energy density control is extremely robust and insensitive to the various errors that occur (Sommerfeldt & Parkins 1994). Subsequently, the degradation in accuracy experienced with the 4 microphone sensor is acceptable for active noise control applications.

The errors arising in the measurement of acoustic energy density will now be derived for measurement in one-dimensional sound fields. It will then be extended to three dimensions where 4 three-dimensional energy density sensors will be analysed. Having investigated the sensitivity to errors a three-axis energy density sensor is built and its performance assessed.

3.2 Principles of Acoustic Energy Density Measurement

The instantaneous acoustic energy density $E_D(t, \vec{\mathbf{x}})$ at some point $\vec{\mathbf{x}}$, is given by the equation (Nashif & Sommerfeldt 1992),

$$E_D(t, \vec{\mathbf{x}}) = \frac{p(t, \vec{\mathbf{x}})^2}{2\rho c^2} + \frac{\rho v(t, \vec{\mathbf{x}})^2}{2} \tag{3.1}$$

where $p(t, \vec{\mathbf{x}})$ and $v(t, \vec{\mathbf{x}})$are the instantaneous pressure and particle velocity at $\vec{\mathbf{x}}$ respectively, c is the speed of sound and ρ is the density of the fluid. The instantaneous particle velocity in a one dimensional sound field is given by Euler's equation

$$v(t, \vec{\mathbf{x}}) = -\frac{1}{\rho} \int \frac{\partial p(t, \vec{\mathbf{x}})}{\partial x} dt \tag{3.2}$$

In practice, it is very difficult to directly measure the particle velocity and is generally

estimated using a two-microphone finite difference approximation of the pressure gradient (Fahy 1995) as shown in Figure 3.1.

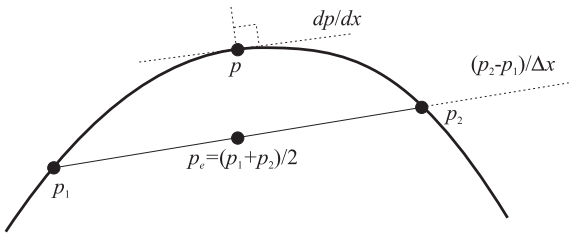

Figure 3.1: Illustration of the estimation of the particle velocity and pressure from two-microphone technique. Typically the sound pressure estimate shows greater error than the particle velocity estimate.

The finite difference approximation for the pressure gradient between two points $\vec{\mathbf{x}}_1$ and $\vec{\mathbf{x}}_2$ is

$$\nabla_{xx} p(t, \vec{\mathbf{x}}) \approx \frac{p(t, \vec{\mathbf{x}}_2) - p(t, \vec{\mathbf{x}}_1)}{\Delta x} \tag{3.3}$$

Using the finite difference approximation, Equation (3.2) can be re-written as

$$v(t, \vec{\mathbf{x}}) \approx -\frac{1}{2h\rho} \int [p(t, \vec{\mathbf{x}}_2) - p(t, \vec{\mathbf{x}}_1)] dt \tag{3.4}$$

where $2h$ is the distance separating the acoustic centres of the microphones, commonly referred to as the *separation distance*. The pressure at the point midway between the microphones is approximated by the finite sum

$$p(t, \vec{\mathbf{x}}) \approx \frac{p(t, \vec{\mathbf{x}}_1) + p(t, \vec{\mathbf{x}}_2)}{2} \tag{3.5}$$

Hence the instantaneous acoustic energy density using two microphones is approximated by

$$E_D(t, \vec{\mathbf{x}}) \approx \frac{[p(t, \vec{\mathbf{x}}_1) + p(t, \vec{\mathbf{x}}_2)]^2}{8\rho c^2} + \frac{\left[\int [p(t, \vec{\mathbf{x}}_2) - p(t, \vec{\mathbf{x}}_1)] dt\right]^2}{8\rho h^2} \tag{3.6}$$

From Equation (3.1) the time averaged acoustic energy density at $\vec{\mathbf{x}}$ is therefore given by

$$\bar{E}_D(\vec{\mathbf{x}}) = \frac{\bar{p}^2(\vec{\mathbf{x}})}{2\rho c^2} + \frac{\rho \bar{v}^2(\vec{\mathbf{x}})}{2} = \frac{1}{2\rho c^2}\left[\bar{p}^2(\vec{\mathbf{x}}) + (\rho c \bar{v})^2(\vec{\mathbf{x}})\right] \tag{3.7}$$

where $\bar{p}$ and $\bar{v}$ are the time averaged acoustic pressure and particle velocity at $\vec{\mathbf{x}}$ respectively.

3.3 Errors in the Measurement of Acoustic Energy Density in 1-D

The following error analysis for acoustic energy density has drawn heavily from the work of Fahy (1995) and others (Pavic 1977, Elliott 1981, Thompson & Tree 1981, Thompson 1982*b*, Thompson 1982*a*, Kitech & Tichy 1982, Pascal & Carles 1982, Krishnappa 1983, Boden & Abom 1986, Watkinson 1986, Elko 1991*b*) regarding errors in sound intensity measurements.

As was discussed in Chapter 1, there are three distinct sources of error which occur when estimating acoustic energy density using the two microphone technique, namely; finite separation (inherent) errors, diffraction and interference effects at the microphones and instrumentation errors.

The purpose of the following error analysis is to gain some primary understanding of the errors that may arise during the measurement of energy density using the two-microphone technique. It will be shown that the errors in both the pressure and particle velocity components of the energy density will act to bias the overall energy density estimate. Therefore the error analysis will initially investigate the effects of errors on the pressure, particle velocity and energy density for one dimensional sound fields. The study is then extended to a statistical study of the errors arising in three-dimensional fields.

Drawing direct comparisons between the errors when estimating the energy density and the effects that errors in the energy density estimate have on the control system is very difficult. However, it will be shown in the following chapter, where the effects of these errors on the control of sound transmission into a cavity is used as a case study, that as the error in the energy density estimate increases the control is reduced.

For active noise control systems using a LMS algorithm, the phase errors between the channels (pressure and particle velocity estimates) are relatively inconsequential, providing the arising group delay does not affect the causality of the system. This result is in contrast to the effect of phase errors between pressure and velocity when estimating acoustic intensity which can result in significant magnitude errors when the pressure and velocity are in quadrature. Therefore, for active control using energy density it is important to look at the relative error in magnitude between the pressure and particle velocity estimates, especially when there is only a single energy density sensor.

For control systems with multiple energy density sensors it is very difficult to compare the relative error between the pressure and velocity estimates for all channels. In addition, the usefulness of the results is questionable since it is not only the relative error between the pressure and velocity estimates which affect the control effort but also the relative (bias) error between energy density sensors. Therefore, for multiple sensors it is more prudent to look at the overall error in the energy density measurement which also simplifies the interpretation of the results.

One may argue that if the sensors are to be used as sensors for control systems, then maybe the absolute error in the energy density estimate is not the parameter that should be investigated but rather that the effects the errors have on the level of control should be analysed. This is true, but the level of complexity increases another order of magnitude when the dynamic response of the control system is introduced into the equation and it becomes very difficult to draw general conclusions.

The following errors will now be analysed for a one-dimensional sound field:

Inherent Errors arise due to finite sum and finite difference approximations used to estimate the pressure and particle velocity respectively,

Phase Error is an instrumentation error and is due to phase mismatches between microphone pairs which occur commonly in practice,

Sensitivity Error is also an instrumentation error and arises from sensitivity mismatches between microphone pairs,

Length Error is another form of instrumentation error, but unlike the phase and sensitivity error which arise from transduction and electrical sources, the length error is due to errors in the physical construction,

Diffraction and Interference Effects arise from the finite size of the body housing the microphones, and,

Other Errors including the effect of mean flow and turbulence, environmental effects such as humidity and temperature and statistical or random errors.

3.3.1 Finite Separation (Inherent) Errors

The two microphone technique used for the transduction of sound pressure and particle velocity is subject to systematic errors which arise from the fact that they involve approximations, namely Equations (3.4) and (3.5). The inherent errors are functions of the type of field under investigation and the orientation and position of the sensor within the field. The implication of this fact is that the magnitude of the inherent error can never be precisely estimated in an arbitrary sound field. Therefore examples of errors in a range of idealised sound fields are presented to provide an indication of their sensitivity to the parameters of the field and of the sensor (Fahy 1995).

The following analysis applies to a one dimensional sound field with spatial variation in the direction of the sensor, which for convenience will be denoted x. According to the

Taylor series expansion (Fahy 1995), the pressure at a point is given by

$$\begin{aligned} p(x+h,t) &= p(x,t) + hp^{i}(x,t) + (h^2/2)p^{ii}(x,t) + (h^3/6)p^{iii}(x,t) + ... \\ &+ (h^n/n!)p^{n}(x,t) + ... \end{aligned} \tag{3.8}$$

where $p^n(x,t)$ denotes the n^{th} derivative of p with respect to x at any time t.

Consider a pair of microphones of which the acoustic centres are separated by a distance $2h$. Equation (3.5) gives the estimated pressure at the point midway between the transducer centres as

$$\begin{aligned} p_e(t) &= \frac{p(x+h)+p(x-h)}{2} \\ &= p(t) + (h^2/2)p^{ii}(t) + (h^4/24)p^{iv}(t) + ... + (h^{2n}/2n!)p^{2n}(t) + ... \end{aligned} \tag{3.9}$$

in which explicit indication of spatial position has been dropped. From Equation (3.4), the estimated axial particle velocity component at the centre of the sensor is given by

$$\begin{aligned} v_e(t) &= -\frac{1}{2\rho h}\int [p(x-h) - p(x+h)]dt \\ &= -\frac{1}{\rho}\int_{-\infty}^{t} \left[p^{i}(\tau) + (h^2/6)p^{iii}(\tau) + (h^4/120)p^{v}(\tau) + ...\right] d\tau \end{aligned} \tag{3.10}$$

The normalised errors in the estimates of p and v, are obtained by dividing the estimate (be it pressure or velocity) by the exact measurement and subtracting 1, ie

$$e(p) = (p_e - p)/p \tag{3.11}$$

and

$$e(v) = (v_e - v)/v \tag{3.12}$$

Substituting the Taylor series expansions for the pressure and particle velocity, given by Equations (3.9) and (3.10), into the expressions for the normalised errors, given by Equations (3.11) and (3.12), results in

$$e(p) = [(h^2/2)p^{ii}(t) + (h^4/24)p^{iv}(t) + ...]/p(t) \tag{3.13}$$

and

$$e(v) = \frac{\int_{-\infty}^{t}[(h^2/6)p^{iii}(\tau) + (h^4/120)p^{v}(\tau) + ...]d\tau}{\int_{-\infty}^{t} p^{i}(\tau)d\tau} \tag{3.14}$$

These expressions can only be evaluated if the time history of p and of its spatial derivatives are known which is the case with harmonic fields. Consider a harmonic field defined by, $p(x,t) = \Re\{P(x)e^{j\omega t}\}$ and $v(x,t) = \Re\{V(x)e^{j\omega t}\}$; the explicit indication of x-dependence has been omitted. Now, the complex velocity magnitude is

$$V = (j/\omega\rho)P^{i} \tag{3.15}$$

and the magnitude of the velocity estimate is

$$V_e = -(j/2\omega\rho h)(P_1 - P_2) \tag{3.16}$$

and the normalised error in the velocity estimate is given by

$$e(v) = \frac{[(h^2/6)P^{iii} + (h^4/120)P^{v} + ...]}{P^{i}} \tag{3.17}$$

From Equation (3.7) the estimated time averaged acoustic energy density is approxi-

mated by

$$\bar{E}_{D_e} \approx \frac{[P_1 + P_2]\,[P_1 + P_2]^*}{16\rho c^2} + \frac{[P_2 - P_1]\,[P_2 - P_1]^*}{16\rho\omega^2 h^2} \tag{3.18}$$

The Taylor series expansion of the time averaged energy density estimate is (derived in Appendix B)

$$\begin{aligned}\bar{E}_{D_e} = {} & \frac{1}{4\rho c^2}\left[PP^* + \frac{h^2}{2}\left(P^*P^{ii} + PP^{ii*}\right) + \frac{h^4}{4}\left(P^{ii*}P^{ii} + \frac{PP^{iv*}}{6} + \frac{P^*P^{iv}}{6}\right)\right] \\ & + \frac{1}{4\rho\omega^2}\left[P^iP^{i*} + \frac{h^2}{6}\left(P^{i*}P^{iii} + P^iP^{iii*}\right) + \frac{h^4}{12}\left(\frac{P^{iii*}P^{iii}}{3} + \frac{P^iP^{v*}}{10} + \frac{P^{i*}P^v}{10}\right)\right]\end{aligned} \tag{3.19}$$

The exact time averaged energy density is given by

$$\bar{E}_D = \frac{PP^*}{4\rho c^2} + \frac{\rho VV^*}{4} \tag{3.20}$$

Substituting Equation (3.15) into the above equation

$$\bar{E}_D = \frac{PP^*}{4\rho c^2} + \frac{P^iP^{i*}}{4\rho\omega^2} = \frac{1}{4\rho c^2}\left(PP^* + \frac{P^iP^{i*}}{k^2}\right) \tag{3.21}$$

The normalised error in the energy density is given by

$$e(\bar{E}_D) = (\bar{E}_{D_e} - \bar{E}_D)/\bar{E}_D \tag{3.22}$$

Therefore the Taylor series expansion of the normalised time averaged energy density

error is

$$e(\bar{E}_D) \quad + \quad \left[\frac{h^2}{2}\left(P^*P^{ii} + PP^{ii*}\right) + \frac{h^4}{4}\left(P^{ii*}P^{ii} + \frac{PP^{iv*}}{6} + \frac{P^*P^{iv}}{6}\right)\right] / \left(PP^* + \frac{P^iP^{i*}}{k^2}\right)$$
$$+ \quad \frac{1}{k^2\left(PP^* + \frac{P^iP^{i*}}{k^2}\right)}$$
$$\times \left[\frac{h^2}{6}\left(P^{i*}P^{iii} + P^iP^{iii*}\right) + \frac{h^4}{12}\left(\frac{P^{iii*}P^{iii}}{3} + \frac{P^iP^{v*}}{10} + \frac{P^{i*}P^v}{10}\right)\right] \tag{3.23}$$

In the future, when referring to the normalised energy density error the reference to time averaged will be omitted for brevity.

Although not immediately obvious from the above expression it will be shown that in general the majority of the inherent error comes from the finite sum approximation of the pressure rather than the finite difference approximation used for the particle velocity. It is therefore interesting to consider the case of a three-microphone energy density sensor where the centre microphone measures the pressure at the centre of the sensor as seen in Figure 3.2. The additional microphone does not increase the accuracy of the finite difference approximation. Consequently, all the inherent error is due to the velocity approximation and although the error is still in the order of $(kh)^2$ the error is substantially reduced. Use of this arrangement will be made in the investigation of three-dimensional energy density sensors in the later sections.

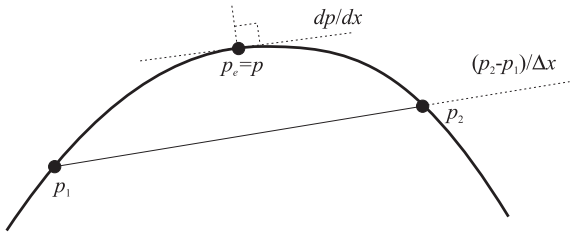

Figure 3.2: Particle velocity from two-microphone technique with an additional centre microphone.

The inherent energy density error for a three-microphone sensor in a reactive one-

dimensional sound field is given by the second term in Equation (3.23), ie

$$e(E_{D_3}) \approx \frac{1}{k^2\left(PP^* + \frac{P^iP^{i*}}{k^2}\right)} \times \left[\frac{h^2}{6}\left(P^{i*}P^{iii} + P^iP^{iii*}\right) + \frac{h^4}{12}\left(\frac{P^{iii*}P^{iii}}{3} + \frac{P^iP^{v*}}{10} + \frac{P^{i*}P^v}{10}\right)\right] \quad (3.24)$$

The errors associated with two common idealised models of sound fields are now analysed, namely; a one-dimensional reactive sound field and a plane progressive wave.

3.3.1.1 One-Dimensional Reactive Sound Field

The sound field which exhibits greatest variation in the acoustic potential energy is a cavity with a single mode excited. This situation is commonly encountered in low modal density cavities and poses significant problems when using microphones as error sensors.

For a harmonic sound field of frequency, ω, in which $p(x,t) = \Re\{P(x)e^{j\omega t}\}$ and $v(x,t) = \Re\{V(x)e^{j\omega t}\}$, consider a stationary reactive sound field defined by the following

$$p(x,t) = P_0\cos(k_l x)\Re\{e^{j\omega t}\} = P_0\cos(k_l x)\cos(\omega t) \quad (3.25)$$

where ω is the driving frequency of the sound and k_l is the eigenvalue of the mode given by $k_l = \frac{n\pi}{L}$, where n is an integer and L is the length of the cavity. The velocity corresponding to a point x_0 is given by

$$v(x_0,t) = -\frac{1}{\rho}\int \frac{\partial p(x_0)}{\partial x}dt = \frac{P_0k_l}{\rho\omega}\sin(k_lx_0)\sin(\omega t) \quad (3.26)$$

For the sound field given by Equation (3.25) the exact energy density throughout the acoustic space is

$$E_D = \frac{P_0^2}{4\rho c^2} \quad (3.27)$$

The pressure and pressure gradients are given by

$$P = P_0 \cos(k_l x) \tag{3.28}$$

$$P^i = -k_l P_0 \sin(k_l x) \tag{3.29}$$

$$P^{ii} = -k_l^2 P_0 \cos(k_l x) = -k_l^2 P \tag{3.30}$$

$$P^{iii} = k_l^3 P_0 \sin(k_l x) = -k_l^2 P^i \tag{3.31}$$

To investigate the effect that wavelength has on the accuracy of the estimates it is prudent to let the length of the cavity increase with frequency such that $L = \frac{n\lambda}{2}$, ie $k_l = k$. This then allows a direct comparison with the case of a free propagating wave. The normalised errors for the pressure, velocity and energy density are given by Equations (3.11) , (3.12) and (3.22). For a reactive sound field the errors are given by (Fahy 1995, Section 5.6.1 and Appendix B) as

$$e(p) = \cos(kh) - 1 \approx -\frac{(kh)^2}{2} + \frac{(kh)^4}{24} - \frac{(kh)^6}{720} + ... \tag{3.32}$$

$$e(v) = \frac{\sin(kh)}{kh} - 1 \approx -\frac{(kh)^2}{6} + \frac{(kh)^4}{120} - \frac{(kh)^6}{5040} + ... \tag{3.33}$$

$$e(E_D) = -(kh)^2 \left[\frac{2\cos^2(kx)+1}{3}\right] + (kh)^4 \left[\frac{13\cos^2(kx)+2}{45}\right] - ... \tag{3.34}$$

Note that the normalised error in the estimate of the pressure is approximately three times that of the normalised error in the velocity. By differentiating the above expression for the energy density with respect to x and setting the derivative to zero, the maximum and minimum error can be found. It can be shown that the zero gradient occurs at $\sin(2kx) = 0$, ie $kx = \frac{n\pi}{2}$. Therefore the maximum and minimum are given respectively

by

$$\begin{aligned} e(E_D) = & \quad -(kh)^2 + \tfrac{(kh)^4}{3} - \ldots \quad , kx = n\pi \\ = & \quad -\tfrac{(kh)^2}{3} + \tfrac{2(kh)^4}{45} - \ldots \quad , kx = (2n+1)\pi/2 \end{aligned} \tag{3.35}$$

The first term is the error when the acoustic pressure is at a maximum and the particle velocity is zero. Therefore the error is all due to the error in the pressure measurement and so the above expression can be arrived by

$$e(E_{D_{kx=n\pi}}) = (1 + e(p))^2 - 1 = 2e(p) + e^2(p) \tag{3.36}$$

Likewise, the smallest error in the energy density occurs when the particle velocity is at a maximum and is given by

$$e(E_{D_{kx=(2n+1)\pi/2}}) = (1 + e(v))^2 - 1 = 2e(v) + e^2(v) \tag{3.37}$$

For the three-microphone sensor the normalised inherent error is

$$e(E_{D_3}) \approx \sin^2(kx) \left[-\frac{(kh)^2}{3} + \frac{2(kh)^4}{45} - \ldots \right] \tag{3.38}$$

For the three-microphone sensor, the energy density error is obviously zero when at a pressure maximum, ie $kx = 0$, and has a maximum when at a velocity maximum, ie $kx = (2n+1)\pi/2$, given by the second term in Equation (3.35). Therefore, the additional microphone has reduced the energy density error by a factor of three.

The inherent error for both the two-microphone sensor and the three-microphone sensor are plotted against the non-dimensional separation, $2kh$, for a single mode reactive sound field and a position to cavity length ratio of $x/L = 1/4$ in Figure 3.3. Obviously the error for the pressure, velocity and energy density vary with position so it is necessary

to select some position which typifies the error as a function of non-dimensional separation. $x/L = 1/4$ was chosen as the magnitude of the pressure and velocity are equal at this location. To verify the Taylor series approximations for the errors previously derived, these have been compared against the exact errors calculated in MATLAB using the expression for the sound field, Equation (3.25), and the two-microphone estimates of the pressure and velocity from Equations (3.5) and (3.4) respectively.

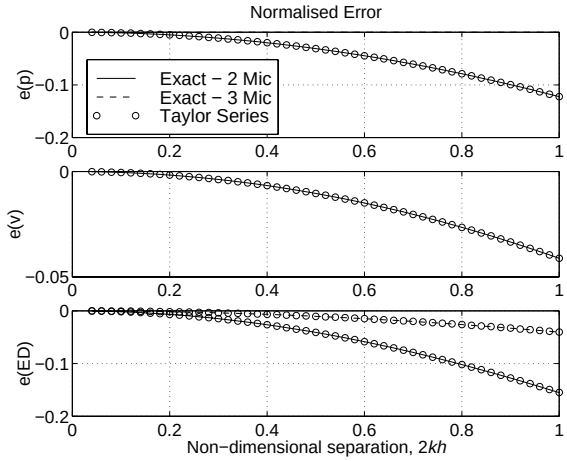

Figure 3.3: Inherent p-p errors as a function of the non-dimensional separation distance ($2kh$) for a reactive one-dimensional sound field with $x/L = 1/4$: (a) pressure error, $e(p)$; (b) particle velocity error, $e(v)$; (c) energy density error, $e(ED)$.

3.3.1.2 Plane Progressive Wave

Consider a plane wave defined by the following

$$p(x,t) = \Re\{P_0 e^{j\omega t - jkx}\} \tag{3.39}$$

The pressure and gradients are given by

$$P = P_0 e^{-jkx} \tag{3.40}$$

$$P^i = -jkP \tag{3.41}$$

$$P^{ii} = -k^2 P \tag{3.42}$$

$$P^{iii} = jk^3 P = -k^2 P^i \tag{3.43}$$

It can be shown that the energy density in a plane progressive sound field is given by

$$E_D = \frac{P_0^2}{2\rho c^2} \tag{3.44}$$

It is interesting to note that the energy density in a plane progressive sound field is twice that in a one-dimensional reactive sound field. The normalised errors for the pressure, velocity (Fahy 1995) and energy density (Appendix B) are given by

$$e(p) = \cos(k_l h) - 1 \approx -\frac{(k_l h)^2}{2} + \frac{(k_l h)^4}{24} - \frac{(k_l h)^6}{720} + ... \tag{3.45}$$

$$e(v) = \frac{\sin(kh)}{kh} - 1 \approx -\frac{(kh)^2}{6} + \frac{(kh)^4}{120} - \frac{(kh)^6}{5040} + ... \tag{3.46}$$

$$e(E_D) = -\frac{2}{3}(kh)^2 + \frac{17}{90}(kh)^4 - ... \tag{3.47}$$

Therefore the error in the energy density measurement for a progressive sound field is independent of position as one would expect. It is interesting to note that the first term in the error is the same as that for the error in intensity for the two-microphone technique.

For the three-microphone sensor the normalised inherent error for a plane progressive

wave is

$$e(E_{D_3}) \approx -\frac{1}{6}(kh)^2 + \frac{1}{45}(kh)^4 - ... \tag{3.48}$$

The use of the additional microphone has therefore reduced the normalised error by a factor of 4.

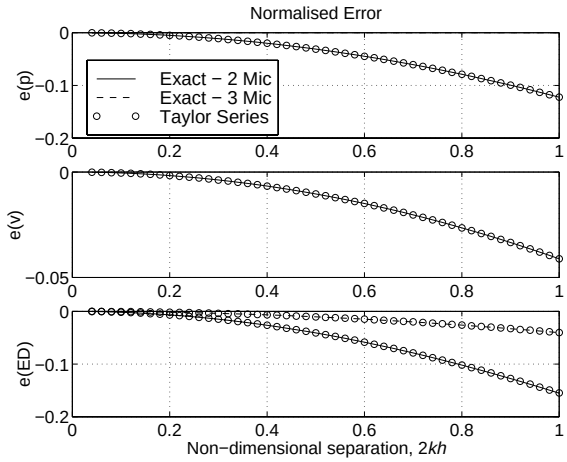

Figure 3.4: Inherent p-p errors as a function of the non-dimensional separation distance ($2kh$) for a plane progressive wave: (a) pressure error, $e(p)$; (b) particle velocity error, $e(v)$; (c) energy density error, $e(ED)$.

3.3.2 Instrumentation Errors

The two most common instrumentation errors are differences in the transducer transfer functions, commonly referred to as *linear distortion*. Matching the transfer functions (both amplitude and phase responses) of the microphones is of vital importance, particularly at low frequencies where the actual phase difference of the sound pressures is small.

3.3.2.1 Phase Mismatch Errors

The effect of phase response mismatch upon the accuracy of any particular measurement depends on the relative magnitudes of the phase mismatch of the microphone channels

and the actual phase difference of the sound pressures at the sensing points; the latter depends on the nature of the sound field, and the location and orientation of the sensor within the sound field (Fahy 1995). For example, in a reactive sound field, the actual phase difference between the sensing points varies between kd to 0 as the sensor axis is rotated through 90° from an initial orientation parallel to the direction of energy flux. Therefore, the normalised phase error varies from a finite value to infinity and so does the normalised velocity error.

Figure 3.5 illustrates the effect of a phase error of $\pm\phi_s$ on the estimates of p and Δp. It can be clearly seen that not only is there an error in the magnitude of the two estimates but a phase error is also is introduced. Unlike the significant detrimental effects phase errors have on the measurement of acoustic intensity, phase errors during the measurement of energy density are relatively benign.

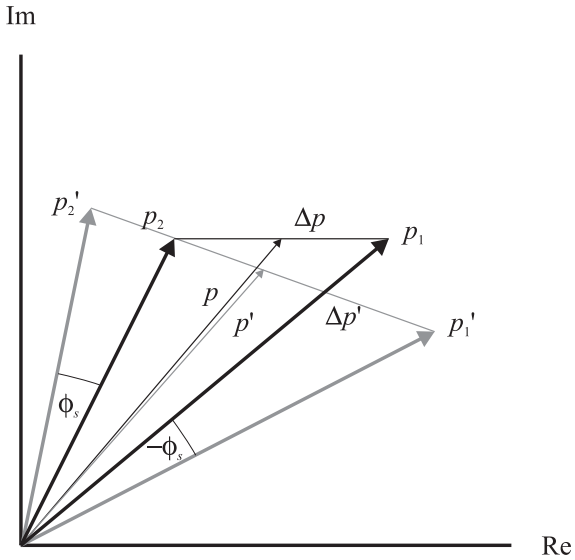

Figure 3.5: Phasor diagram showing the effect of transducer phase mismatch. Adapted from Fahy (1995).

Therefore, in the case of simple harmonic fields the pressure responses of the two microphones with a phase mismatch $\pm\phi_s$ are given by the products of the true pressures

by $e^{j\phi_s}$, ie

$$\hat{p}_1(x,t) = p_1(x,t)e^{j\phi_s} \tag{3.49}$$

$$\hat{p}_2(x,t) = p_2(x,t)e^{-j\phi_s} \tag{3.50}$$

The actual phase difference between the transducers (for both a plane wave and a single mode reactive sound field) is $\phi_0 = 2kh$ where $2h$ is the sensor separation distance. It will be shown that the pressure, velocity and energy density errors are a function of the ratio of the phase mismatch error to the actual phase difference, $2\phi_s/\phi_0$.

The effects of phase mismatch will now be analysed for two types of idealised sound fields.

One-dimensional reactive sound field Using the expression for a stationary reactive sound field, Equation (3.25), the mean of the two pressures with a total microphone phase mismatch of $2\phi_s$ is now

$$\hat{p}_{e=}\frac{\hat{p}_1 + \hat{p}_2}{2} = \frac{P_0}{2}[\cos(kx+kh)\cos(\omega t+\phi_s) + \cos(kx-kh)\cos(\omega t-\phi_s)] \tag{3.51}$$

where the $\hat{}$ represents the pressure response with the phase mismatch. It can be shown (see Appendix B) that the pressure estimate with the phase error is equal to the pressure estimate without the phase error plus an additional term due to the phase error, ie

$$\hat{p}_e = p_e + \alpha_p \tag{3.52}$$

where α_p is the additional error due to the phase mismatch, given by

$$\alpha_p = P_0 \phi_s \sin(kx) \sin(kh) \sin(\omega t) \tag{3.53}$$

Using Equation (3.11) the normalised error for the pressure estimate is (derived in Appendix B and) given by

$$e(\hat{p}) = e(p) + j\phi_s \tan(kx) \sin(kh) \tag{3.54}$$

where $e(p)$ is the normalised pressure error without the phase mismatch arising from wholly the finite sum and is given by Equation (3.32).

As with the pressure estimate, the velocity estimate is equal to the velocity estimate without the phase error plus an additional term due to the phase error (see Appendix B), ie

$$\hat{v}_e = v_e + \alpha_v \tag{3.55}$$

where α_v is the additional error due to the phase mismatch, given by

$$\alpha_v = \frac{P_0}{\rho\omega} \frac{\phi_s}{h} \cos(kx) \cos(kh) \cos(\omega t) \tag{3.56}$$

Using Equation (3.12) the normalised error for the velocity estimate is (derived in Appendix B and) given by,

$$e(\hat{v}) = e(v) - j \frac{\phi_s}{kh} \cot(kx) \cos(kh) \tag{3.57}$$

where $e(v)$ is the normalised particle velocity error without the phase mismatch arising from wholly the finite difference and is given by Equation (3.33).

The normalised error of the energy density for small kh is derived in Appendix B and is given by

$$e(\hat{E}_D) \approx e(E_D) + \cos^2(kx)\left(\frac{2\phi_s}{2kh}\right)^2 \tag{3.58}$$

where $e(E_D)$ is the normalised error in the energy density without the phase mismatch arising from wholly the finite separation and is given by Equation (3.34).

Therefore, the normalised error in the energy density arising from the phase mismatch is proportional to the square of the ratio of the phase error to the actual phase difference. In the case of $kx = 0$

$$e(\hat{E}_D) = e(E_D) + \frac{(2\phi_s)^2}{(2kh)^2} \tag{3.59}$$

It is quite clear that the second term in the normalised error dominates the expression as $2kh$ approaches $2\phi_s$, which acts to limit the lowest frequency at which the energy density sensor can be used successfully. It should be noted that the error in the energy density given by Equation (3.58) is independent of the sign of the phase error. The Taylor series expansions for the normalised error in pressure, velocity and energy density as given by Equations (3.54), (3.57) and (3.58) using a phase difference of $2\phi_s = 1^\circ$ are plotted against the non-dimensional separation distance in Figure 3.6 below where they are compared against the exact errors with a non-dimensional position of $x/L = 1/4$. The normalised error is also plotted against the non-dimensional separation distance in Figure 3.7 for a variety of phase errors.

For a 3-microphone sensor the normalised error for the pressure is obviously zero, the error for the velocity is the same as given by Equation (3.57) and the normalised error in the energy density is given by Equation (3.58), where $e(E_D) = e(E_{D_3})$ is given by Equation (3.38). Therefore, it can be concluded that although the use of the additional

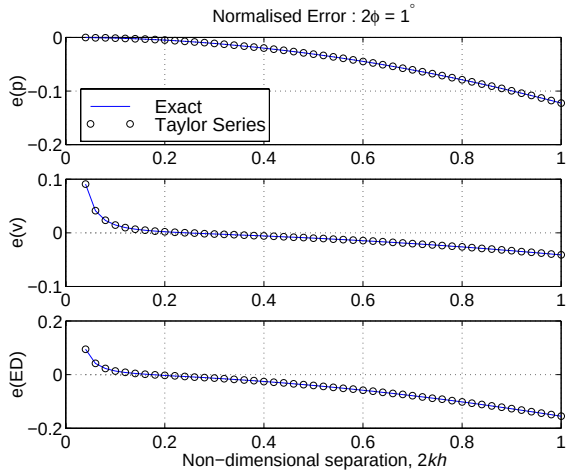

Figure 3.6: Normalised error in energy density in a reactive one-dimensional sound field as a function of the non-dimensional separation distance ($2kh$) with $x/L = 1/4$: (a) pressure error, $e(p)$; (b) particle velocity error, $e(v)$; (c) energy density error, $e(ED)$.

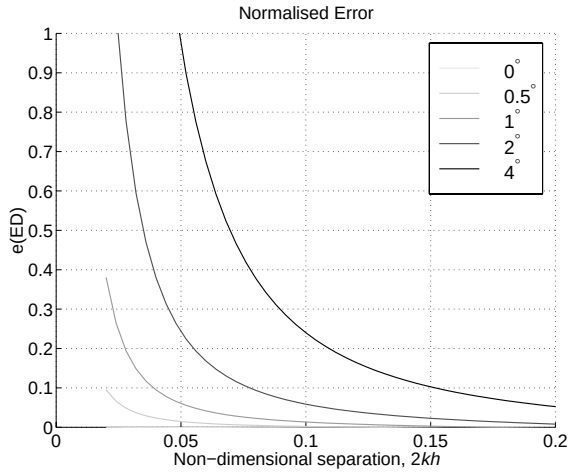

Figure 3.7: Normalised error in energy density as a function of the non-dimensional separation distance ($2kh$) in a reactive one-dimensional sound field for a variety of transducer phase mismatches with $x/L = 1/4$. For the case of no phase error ($0°$) there is no significant error in energy density.

microphone does extend the upper bound at which the sensor can be used, it does not assist in reducing the lower frequency limit.

Plane progressive wave In the case of a plane wave the effect of a phase mismatch is equivalent to modifying the sensor separation distance, ie for a phase mismatch of $2\phi_s$ the sensor separation distance is $k\hat{h} = kh - \phi_s$ or $\frac{\hat{h}}{h} = 1 - \frac{\phi_s}{kh}$. The normalised errors for the pressure, velocity and energy density are given by (see Appendix B)

$$e(p) = \cos(k\hat{h}) - 1 \approx -\frac{(k\hat{h})^2}{2} + \frac{(k\hat{h})^4}{24} - \frac{(k\hat{h})^6}{720} + ... \tag{3.60}$$

$$e(v) = \frac{\sin(k\hat{h})}{kh} - 1 \approx \left(1 - \frac{\phi_s}{kh}\right)\left(1 - \frac{(k\hat{h})^2}{6} + \frac{(k\hat{h})^4}{120} - \frac{(k\hat{h})^6}{5040} + ...\right) - 1 \tag{3.61}$$

$$e(\hat{E}_D) \approx \frac{1}{2}\left[1 - \left(k\hat{h}\right)^2 + \frac{1}{3}\left(k\hat{h}\right)^4\right] + \frac{\left(1 - \frac{\phi_s}{kh}\right)^2}{2}\left[1 - \frac{1}{3}\left(k\hat{h}\right)^2 + \frac{2}{45}\left(k\hat{h}\right)^4\right] - 1 \tag{3.62}$$

As kh approaches zero, the normalised error in the energy density approaches,

$$e(\hat{E}_D) \approx -\frac{\phi_s}{kh} + \frac{\left(\frac{\phi_s}{kh}\right)^2}{2} \tag{3.63}$$

The Taylor series expansions for the normalised error in pressure, velocity and energy density as given by Equations (3.60), (3.61) and (3.62) using a phase difference of $2\phi_s = 1^\circ$ are plotted against the non-dimensional separation distance in Figure 3.8 below where they are compared against the exact errors. Figure 3.8 shows that the normalised error in the pressure still approaches zero, despite the phase mismatch; however, when the phase error approaches the free field phase difference the normalised error in both the velocity and energy density initially increase at 6 dB per octave reduction then eventually increase

at 12 dB per octave reduction. This is also shown graphically in Figure 3.9 where the error in energy density is plotted against non-dimensional separation distance for a variety of phase errors.

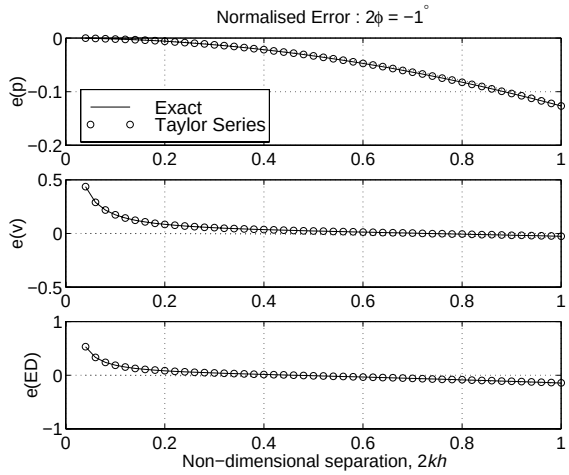

Figure 3.8: Normalised errors as a function of the non-dimensional separation distance ($2kh$) in plane wave conditions for a transducer phase mismatch of $-1°$: (a) pressure error; (b) particle velocity error; (c) energy density error.

In the case of the three-microphone sensor the statement regarding the reactive sound field holds, namely that the error in pressure is zero, the velocity error is the same as for the two-microphone sensor given by Equation (3.61) and the energy density is given by the second term in Equation (3.62), ie

$$e(\hat{E}_{D_3}) \approx \frac{\left(1-\frac{\phi_s}{k\hat{h}}\right)^2}{2}\left[1-\frac{1}{3}\left(k\hat{h}\right)^2+\frac{2}{45}\left(k\hat{h}\right)^4\right]-\frac{1}{2} \tag{3.64}$$

3.3.2.2 Sensitivity Errors

In addition to phase mismatch, the two microphone sensitivities may differ. The pressure sum and difference are altered in both magnitude and phase by the sensitivity mismatch (Fahy 1995). The effect is illustrated in Figure 3.10.

If the sensitivity difference between the transducers is $\pm T$ such that the ratio of the

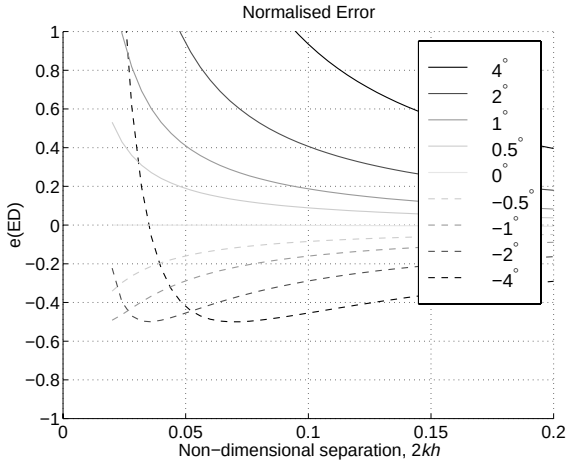

Figure 3.9: Normalised error in energy density as a function of the non-dimensional separation distance ($2kh$) in plane wave conditions for a variety of transducer phase mismatches.

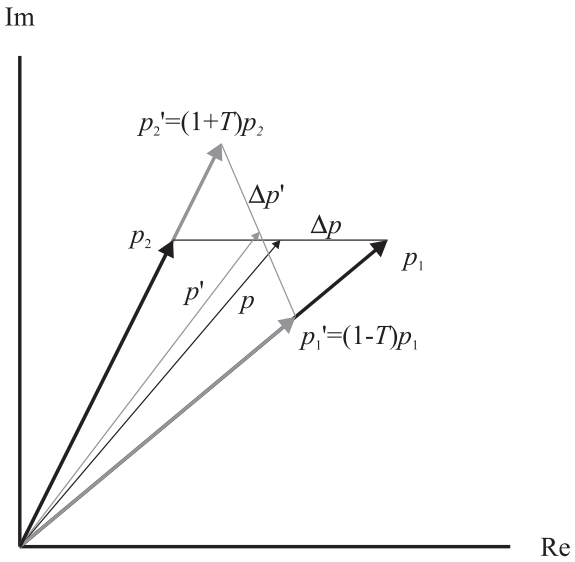

Figure 3.10: Phasor diagram showing the effect of transducer sensitivity mismatch. Adapted from Fahy (1995).

sensitivities is given by $(1+T)/(1-T) \approx 1+2T$ for small T, ie

$$\hat{p}_1(x,t) = p_1(x,t)(1-T) \tag{3.65}$$

$$\hat{p}_2(x,t) = p_2(x,t)(1+T) \tag{3.66}$$

The sharing of the error over the two microphones was done in order to simplify the analytical derivation of the errors arising from the sensitivity mismatch. The effects of sensitivity mismatch will now be analysed for two types of idealised sound fields.

One-dimensional reactive sound field Given a stationary reactive sound field defined by the following

$$p(x,t) = P_0 \cos(kx)\Re\{e^{i\omega t}\} = P_0 \cos(kx)\cos(\omega t) \tag{3.67}$$

where ω and k are the frequency and wavenumber of the sound respectively, the velocity at a point x_0 is given by

$$v(x_0,t) = -\frac{1}{\rho}\int \frac{\partial p(x_0)}{\partial x} dt = \frac{P_0 k}{\rho\omega}\sin(kx_0)\sin(\omega t) \tag{3.68}$$

The mean of the two pressures is estimated by two microphones spaced $2h$ apart,

$$\hat{p}_e = \frac{\hat{p}_1 + \hat{p}_2}{2} = \frac{P_0}{2}[(1-T)\cos(kx+kh)\cos(\omega t) + (1+T)\cos(kx-kh)\cos(\omega t)] \tag{3.69}$$

where the $\hat{}$ represents the pressure response due to the sensitivity mismatch. It can be shown (see Appendix B) that the pressure estimate with the sensitivity error is equal to the pressure estimate without the sensitivity error, p_e, plus an additional term due to the

sensitivity error, ie

$$\hat{p}_e = \frac{\hat{p}_1 + \hat{p}_2}{2} = p_e + \beta_p \tag{3.70}$$

where β_p is the additional error due to the magnitude mismatch, given by

$$\beta_p = P_0 T \sin(kx) \sin(kh) \cos(\omega t) \tag{3.71}$$

Therefore, the normalised error of the pressure estimate is (derived in Appendix B)

$$e(\hat{p}) = e(p) + T \tan(kx) \sin(kh) \tag{3.72}$$

where $e(p)$ is the normalised pressure error without the sensitivity mismatch arising from wholly the finite sum approximation and is given by Equation (3.32).

It can be seen that the normalised error in the pressure becomes infinite for $kx = \pi/2$. This is because the exact pressure is zero at this location and as a result, any error in the pressure produces an infinite error in the normalised error.

As with the pressure estimate, the velocity estimate is equal to the velocity estimate without the sensitivity error plus an additional term due to the sensitivity error (see Appendix B), ie

$$\hat{v}_e = v_e + \beta_v \tag{3.73}$$

where β_v is the additional error due to the magnitude mismatch, given by

$$\beta_v = -\frac{P_0 T}{h\rho\omega} \cos(kx) \cos(kh) \sin(\omega t) \tag{3.74}$$

The normalised error of the velocity estimate is (derived in Appendix B)

$$e(\hat{v}) = e(v) + T\frac{\cos(kh)}{kh\tan(kx)} = \left[\frac{\sin(kh)}{kh} - 1\right] + T\frac{\cos(kh)}{kh\tan(kx)} \tag{3.75}$$

where $e(v)$ is the normalised particle velocity error without the sensitivity mismatch arising from wholly the finite difference approximation and is given by Equation (3.33).

The normalised error in the time averaged energy density estimate is given by (see Appendix B),

$$e(\hat{E}_D) = e(E_D) + \frac{2T}{4}\sin(2kx)\sin(2kh)\left(1 - \frac{1}{(kh)^2}\right) + \left(\frac{2T}{2kh}\right)^2\cos^2(kx)\cos^2(kh) \tag{3.76}$$

where $e(E_D)$ is the normalised error in the energy density without the sensitivity mismatch arising from wholly the finite separation and is given by Equation (3.34).

The first term in the expression is negligible for small sensitivity mismatches and can be ignored. However, the second term is significant and becomes very large as kh decreases. The above equation for small kh can be rewritten as

$$e(\hat{E}_D) \approx e(E_D) - \left(\frac{2T}{2kh}\right)\sin(2kx) + \left(\frac{2T}{2kh}\right)^2\cos^2(kx) \tag{3.77}$$

Therefore, in order to keep the error in the energy density small, the non-dimensional error in sensitivity $2T$ should be significantly less than the non-dimensional microphone separation $2kh$.

The Taylor series expansions for the normalised error in pressure, velocity and energy density as given by Equations (3.72), (3.75) and (3.76) using a sensitivity difference of $2T = 1\%$ are plotted against the non-dimensional separation distance in Figure 3.11 below where they are compared against the exact errors with a non-dimensional position of $x/L = 1/4$.

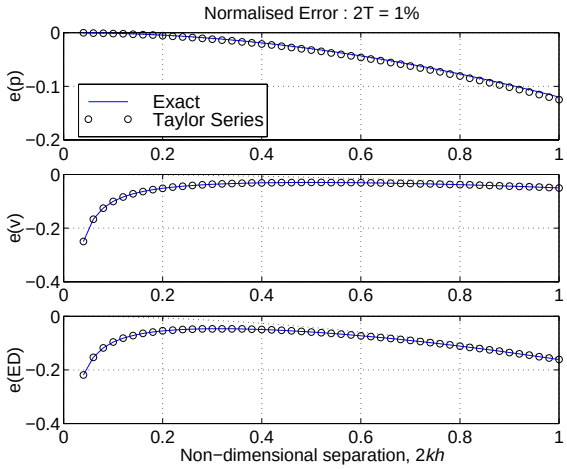

Figure 3.11: Normalised errors as a function of the non-dimensional separation distance ($2kh$) in a reactive one-dimensional sound field for a transducer sensitivity mismatch ($2T$) of 1% and $x/L = 1/4$: (a) pressure error $e(p)$; (b) particle velocity error $e(v)$; (c) energy density error $e(ED)$.

The normalised error in the pressure still approaches zero, despite the sensitivity mismatch. However, when the wavenumber becomes small, both the velocity and energy density errors increase at 12 dB per halving in frequency (octave). This is shown graphically in Figure 3.12 where the error in energy density is plotted against wavenumber for a variety of sensitivity errors.

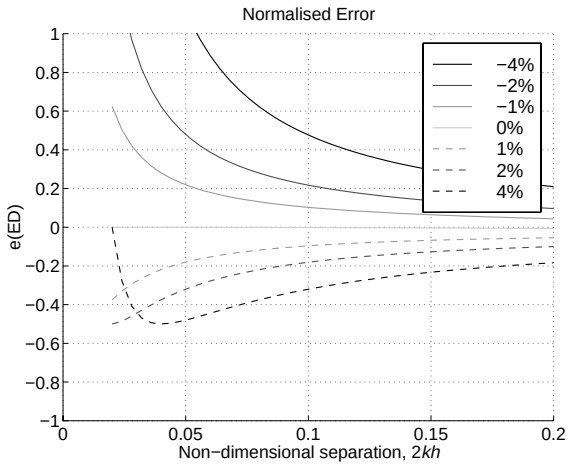

Figure 3.12: Normalised error in energy density as a function of the non-dimensional separation distance ($2kh$) in a reactive one-dimensional sound field for several transducer sensitivity mismatches ($2T$) with $x/L = 1/4$.

For a three-microphone sensor, the pressure error is zero, the velocity error is the same as the two-microphone sensor given by Equation (3.75) and the normalised error in the energy density estimate for small kh is given by Equation (3.76), where $e(E_D) = e(E_{D_3})$ and $e(E_{D_3})$ is given by Equation (3.38).

Plane progressive wave It can be shown that for a plane progressive sound field, the pressure estimate for a sensitivity mismatch is given by (see Appendix B)

$$\hat{p}_e = p_e + \beta_p \tag{3.78}$$

where β_p is the additional error due to the magnitude mismatch, given by

$$\beta_p = jPT\sin(kh) \approx jhkPT\left[1 - \frac{(kh)^2}{6} + \frac{(kh)^4}{120} - ...\right] \tag{3.79}$$

The normalised pressure error is therefore

$$e(\hat{p}) = e(p) + jT\sin(kh) = [\cos(kh) - 1] + jT\sin(kh) \tag{3.80}$$

Therefore, the sensitivity error introduces both a magnitude and phase error into the pressure estimate. The velocity estimate is given by

$$\hat{v}_e = v_e + \beta_v \tag{3.81}$$

where β_v is the additional error due to the magnitude mismatch, given by

$$\beta_v = -\frac{T}{jh\rho\omega}P\cos(kh) \approx -\frac{T}{jh\rho\omega}P\left[1 - \frac{(kh)^2}{2} + \frac{(kh)^4}{24} - ...\right] \tag{3.82}$$

The normalised velocity error is

$$e(\hat{v}) = e(v) + jT\frac{\cos(kh)}{kh} = \left[\frac{\sin(kh)}{kh} - 1\right] + jT\frac{\cos(kh)}{kh} \tag{3.83}$$

As with the normalised pressure error, the sensitivity error introduces both a magnitude and phase error which becomes very large as kh approaches zero.

The energy density estimate is given by

$$\hat{E}_{D_e} = E_{D_e} + \frac{P^2T^2\sin^2(kh)}{4\rho c^2} + \frac{T^2P^2\cos^2(kh)}{4\rho c^2(kh)^2} \tag{3.84}$$

The normalised error is thus,

$$e(\hat{E}_D) = e(E_D) + \frac{T^2}{2}\left(\sin^2(kh) + \frac{\cos^2(kh)}{(kh)^2}\right) \tag{3.85}$$

where $e(E_D)$ is the normalised error in the energy density without the phase mismatch arising from wholly the finite separation and is given by Equation (3.47).

For small kh Equation (3.85) is approximately given by

$$e(\hat{E}_D) = e(E_D) + \frac{T^2}{2(kh)^2} \tag{3.86}$$

The normalised error in the pressure, velocity and energy density is plotted against the non-dimensional separation distance in Figure 3.13 for a sensitivity mismatch of $2T = 1\%$. The effect of the sensitivity error is shown graphically in Figure 3.14 where the error in energy density is plotted against non-dimensional separation distance for a variety of sensitivity errors.

Clearly it is essential that the sensitivity of the two microphones are well matched and in practice, $2T < 1\%$ is certainly achievable.

For a three-microphone sensor, the pressure error is zero, the velocity error is the same

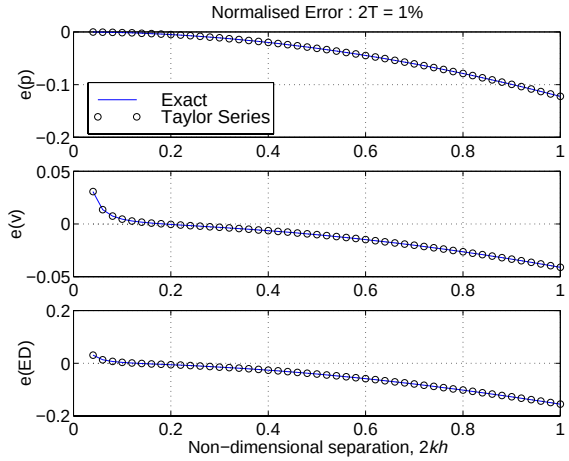

Figure 3.13: Normalised errors as a function of the non-dimensional separation distance ($2kh$) in a plane progressive sound field for a transducer sensitivity mismatch ($2T$) of 1%: (a) pressure error $e(p)$; (b) particle velocity error $e(v)$; (c) energy density error $e(ED)$.

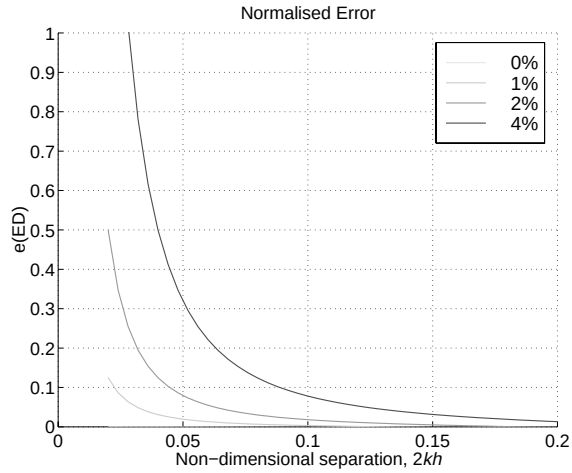

Figure 3.14: Normalised error in energy density as a function of the non-dimensional separation distance ($2kh$) in a plane progressive sound field for several transducer sensitivity mismatches ($2T$).

as the two-microphone sensor given by Equation (3.83) and the normalised error in the energy density estimate is given by the first and third term Equation (3.85), ie

$$e(\hat{E}_D) = e(E_{D_3}) + \frac{T^2}{2}\left(\frac{\cos^2(kh)}{(kh)^2}\right) \tag{3.87}$$

where $e(E_{D_3})$ is the inherent error for the three-microphone sensor given by Equation (3.38).

3.3.2.3 Length Errors

Because of manufacturing tolerances, the distance between acoustic centres of the microphones can vary. Typically, the accuracy may be in the order of ± 1mm. It has been shown that length errors can lead to significant errors in intensity measurements (Boden & Abom 1986, Fahy 1995). In the case of one-dimension sound fields, it is only the length error component in the direction of energy flux that will cause errors in the estimates as shown in Figure 3.15. For example, if there is no spatial variation of pressure in the y-direction, ie $\frac{\partial p}{\partial y} = 0$, then an error in the y-position, $\hat{y} = y + \epsilon$, will not affect the pressure estimate, ie $p(\hat{y}) = p(y)$, however, an error in the x-position will.

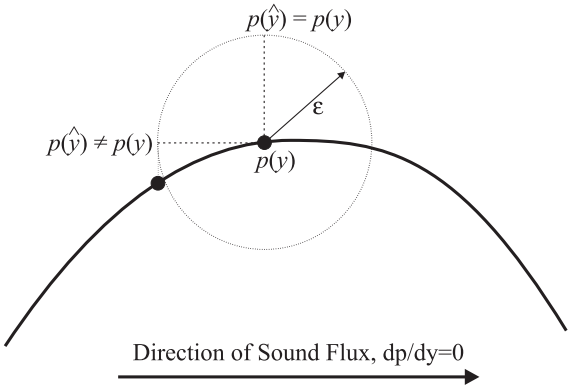

Figure 3.15: Effects of a length error in the measurement of pressure at a point.

If the error in position is given by $\pm\epsilon$, then the non-dimensional spacing is given by $k\hat{h} = kh + k\epsilon$ or $\frac{\hat{h}}{h} = 1 + \frac{k\epsilon}{kh}$. The effects of length errors will now be analysed for two

types of idealised sound fields.

One-dimensional reactive sound field The normalised error for the pressure, velocity and energy density estimate is given by (see Appendix B)

$$e(\hat{p}) = \cos(k\hat{h}) - 1 \approx -\frac{(k\hat{h})^2}{2} + \frac{(k\hat{h})^4}{24} - \frac{(k\hat{h})^6}{720} + ... \tag{3.88}$$

$$e(\hat{v}) = \frac{\sin(k\hat{h})}{kh} - 1 \approx \left(1 + \frac{k\epsilon}{kh}\right)\left(1 - \frac{(k\hat{h})^2}{6} + \frac{(k\hat{h})^4}{120} - \frac{(k\hat{h})^6}{5040} + ...\right) - 1 \tag{3.89}$$

$$e(\hat{E}_D) \approx \cos^2(kx)\left[1 - \left(k\hat{h}\right)^2 + \frac{(k\hat{h})^4}{3}\right] + \sin^2(kx)\left(\frac{k\hat{h}}{kh}\right)^2\left[1 - \frac{(k\hat{h})^2}{3} + \frac{2(k\hat{h})^4}{45}\right] - 1 \tag{3.90}$$

Using $\frac{\hat{h}}{h} = 1 + \frac{k\epsilon}{kh}$, the normalised error for the energy density estimate is

$$\begin{aligned} e(\hat{E}_D) \quad \approx \quad & \cos^2(kx)\left[1 - \left(k\hat{h}\right)^2 + \frac{(k\hat{h})^4}{3}\right] \\ & + \sin^2(kx)\left(1 + \frac{k\epsilon}{kh}\right)^2\left[1 - \frac{(k\hat{h})^2}{3} + \frac{2(k\hat{h})^4}{45}\right] - 1 \end{aligned} \tag{3.91}$$

The error in transducer position produces almost no change in the error for the pressure estimate. However, the velocity estimate is biased by $\frac{\epsilon}{h}$ and the energy density error is biased by approximately $2\frac{\epsilon}{h}\sin^2(kx)$.

The Taylor series expansions for the normalised error in pressure, velocity and energy density as given by Equations (3.88), (3.89) and (3.90) using a 4% error in the transducer location are plotted against the non-dimensional separation distance in Figure 3.16, where

they are compared against the exact errors with a non-dimensional position of $x/L = 1/4$.

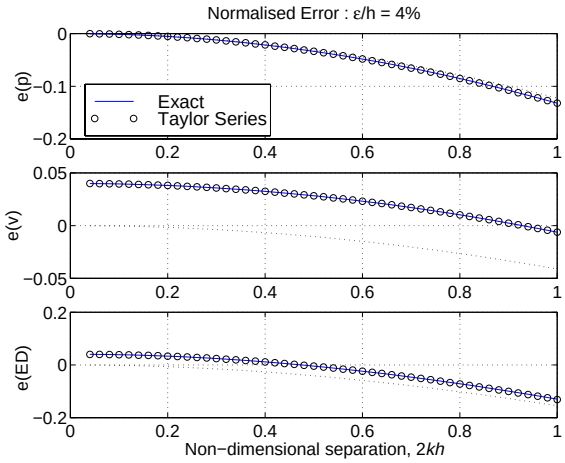

Figure 3.16: Normalised errors as a function of the non-dimensional separation distance ($2kh$) in a reactive one-dimensional sound field for a $\frac{\epsilon}{h} = 4\%$ error in the transducer position with $x/L = 1/4$: (a) pressure error $e(p)$; (b) particle velocity error $e(v)$; (c) energy density error $e(ED)$.

The normalised error in the energy density is shown graphically in Figure 3.17 where the error is plotted against non-dimensional separation distance for a variety of length errors.

For a three-microphone sensor, for small kh the error in energy density is given by,

$$e(\hat{E}_D) \approx \cos^2(kx) + \sin^2(kx)\left(1 + \frac{k\epsilon}{kh}\right)^2 \left[1 - \frac{(k\hat{h})^2}{3} + \frac{2(k\hat{h})^4}{45}\right] - 1 \qquad (3.92)$$

Therefore, the additional microphone does not greatly assist in reducing the low frequency error resulting from length effects in a reactive sound field.

Plane progressive wave In the case of a plane wave the effect of an error in the length is the same as a phase mismatch. For a length error of 2ϵ then $k\hat{h} = kh + k\epsilon$ or $\frac{\hat{h}}{h} = 1 + \frac{k\epsilon}{kh}$. The normalised errors for the pressure, velocity and energy density are given

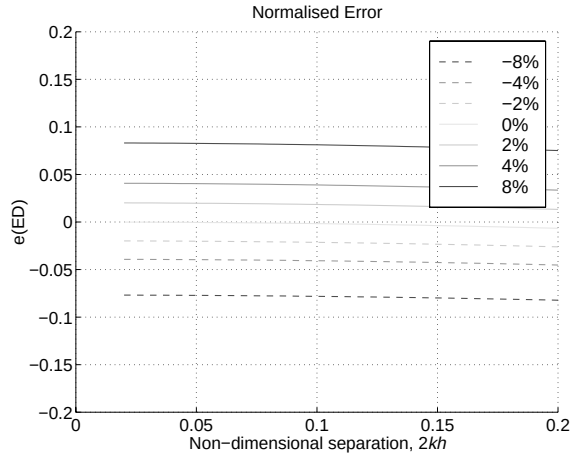

Figure 3.17: Normalised error in the energy density estimate as a function of the non-dimensional separation distance ($2kh$) in a reactive one-dimensional sound field for a several transducer position errors with $x/L = 1/4$.

by (see Appendix B)

$$e(p) = \cos(k\hat{h}) - 1 \approx -\frac{(k\hat{h})^2}{2} + \frac{(k\hat{h})^4}{24} - \frac{(k\hat{h})^6}{720} + ... \tag{3.93}$$

$$e(v) = \frac{\sin(k\hat{h})}{kh} - 1 \approx \left(1 + \frac{k\epsilon}{kh}\right)\left(1 - \frac{(k\hat{h})^2}{6} + \frac{(k\hat{h})^4}{120} - \frac{(k\hat{h})^6}{5040} + ...\right) - 1 \tag{3.94}$$

$$e(\hat{E}_D) \approx \frac{1}{2}\left[1 - \left(\hat{h}k\right)^2 + \frac{1}{3}\left(\hat{h}k\right)^4\right] + \frac{\left(1 + \frac{k\epsilon}{kh}\right)^2}{2}\left[1 - \frac{1}{3}\left(\hat{h}k\right)^2 + \frac{2}{45}\left(\hat{h}k\right)^4\right] - 1 \tag{3.95}$$

As was the case for the reactive sound field, the pressure estimate changes very little, the velocity is biased by $\frac{\epsilon}{h}$ and the energy density error is also biased by $\frac{\epsilon}{h}$ for small ϵ/h as $(1+\epsilon/h)^n \approx 1+n\epsilon/h$. Therefore the effect of the spacing error is to increase the finite difference error by a factor of approximately $\frac{\epsilon}{h}$ which can be seen in Figure 3.18 for an error of 4%.

The normalised error in the energy density is shown graphically in Figure 3.19 where

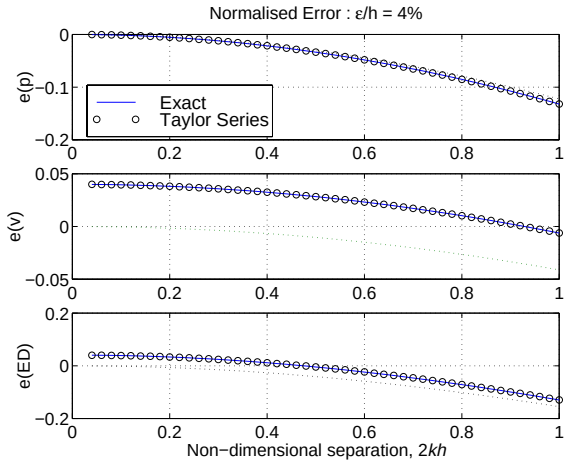

Figure 3.18: Normalised errors as a function of the non-dimensional separation distance ($2kh$) in a free progressive sound field for a $\frac{\epsilon}{h} = 4\%$ error in the transducer position : (a) pressure error $e(p)$; (b) particle velocity error $e(v)$; (c) energy density error $e(ED)$.

the error is plotted against non-dimensional separation distance for a variety of length errors.

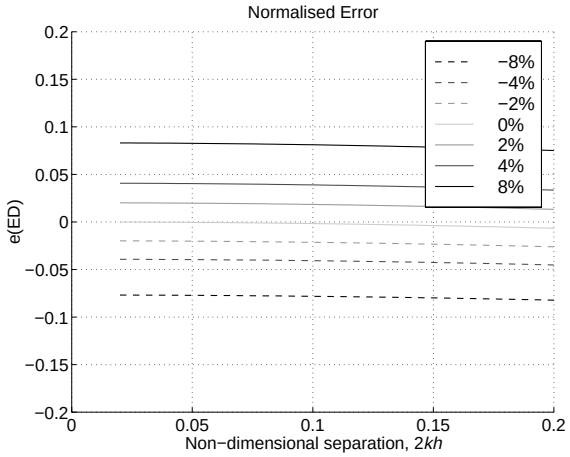

Figure 3.19: Normalised error in energy density estimate as a function of the non-dimensional separation distance ($2kh$) in a free progressive sound field for several transducer position errors $\frac{\epsilon}{h}$.

For a three-microphone sensor the normalised errors are given by the errors arising from a phase mismatch with $\phi_s = k\epsilon$. The normalised error in the pressure is clearly zero, the error for the velocity is the same as for the two-microphone sensor given by Equation (3.94) and the normalised error in the energy density is given by the second

term in Equation (3.95), ie

$$e(\hat{E}_{D_3}) \approx \frac{\left(1+\frac{k\epsilon}{k\hat{h}}\right)^2}{2}\left[1-\frac{1}{3}\left(\hat{h}k\right)^2+\frac{2}{45}\left(\hat{h}k\right)^4\right]-\frac{1}{2} \tag{3.96}$$

Therefore, since it is the $\frac{\epsilon}{h}$ bias error arising from the $\left(1+\frac{k\epsilon}{kh}\right)^2$ term that dominates the error in the energy density estimate at low frequencies, it can be concluded that the use of the additional microphone does not reduce the bias error in the energy density resulting from length errors in a progressive plane wave.

3.3.3 Other Error Sources

3.3.3.1 Diffraction and Interference Effects at the Microphones

Diffraction and interference effects arising from the finite size of the closely spaced microphones are extremely difficult to estimate. This effect becomes more important at very high frequencies where it results in large phase deviations. Fortunately, at the same time, the phase deviations at high frequencies have less influence over the accuracy (see section on phase and sensitivity errors).

Based on previous research on the obstacle effects on the measurement of sound intensity (Elliott 1981, Kitech & Tichy 1982, Krishnappa 1983), the errors are thought to be negligible within the frequency range of most active noise control applications (60-600Hz) and will not be considered here. Naturally, the more solid material used the greater the effects of diffraction and therefore the design should aim to minimise the solid bulk.

3.3.3.2 Mean Flow and Turbulence

According to Fahy (1995), strictly speaking, the two-microphone technique used for the sensing of particle velocity is invalid in the presence of mean flow, however small, because

it is based on the zero mean flow momentum equation. It can be shown that in the presence of mean flow with Mach number, M, the momentum equation becomes (Fahy 1995)

$$\frac{\partial p}{\partial x} = -i\omega\rho_0 u(1 - M) \tag{3.97}$$

where u is the particle velocity due to the acoustic field. Therefore, the error in the energy density will be small if $M \ll 1$. It should be noted that the mean flow may arise from exposure of the sensor to vibrations and hence should be avoided.

In any measurements in the presence of mean flow there will always be unsteady components which act on the microphones which can lead to errors. Therefore, the sensor must be protected from the effects of turbulence which is commonly achieved with the use of foam windshields.

3.3.3.3 Environmental Effects

For the two-microphone technique to work effectively in a range of environments it is essential that the microphones used are stable over a range of temperatures and humidities. Obviously, sensors used in stable environments such as laboratories can tolerate temperature and humidity sensitivities, whereas sensors used on site require highly stable microphones. These issues will be discussed in the following chapter on the three-dimensional energy density sensor.

3.3.3.4 Statistical or Random Errors

Random errors are not influenced by the specific measurement situation and may arise from electrically generated random noise, turbulent flow and local vibrations on the instrument (Boden & Abom 1986, Fahy 1995). The random error in the transfer function

estimate between two microphones is given by (Boden & Abom 1986)

$$\epsilon_r(|H_{12}|) \approx \sqrt{\frac{1-\gamma_{12}^2}{2n\gamma_{12}^2}} \tag{3.98}$$

$$\sigma(\Phi_{12}) \approx \epsilon_r(|H_{12}|) \tag{3.99}$$

where ϵ_r is the normalised random error in the transfer function, γ_{12}^2 equals the coherence between the signals from the two microphones, n is the number of averages and σ is the standard deviation of the transfer function in radians. It is evident from the above equations that in order to keep the random errors small, the coherence must be kept high. In practice, the coherence between microphones with small spacings is always high ($\gamma^2 > 0.9$) and subsequently, the error in the transfer function between the microphones is low.

While random errors may be an issue for the measurement of time averaged sound intensity it is not a significant issue for the use of energy density as an error signal. This is particularly true in this study since the energy density sensor was being used in a feed-forward control system, where the effects of uncorrelated random noise are negligible on the calculation of the optimum phase and magnitude of the control sources. However, the noise does reduce the dynamic range of the system and if the noise signal becomes large compared to the signals due to the primary field then this may limit the reduction that can be achieved. If care is taken, then the effect of these random errors are inconsequential and subsequently, these effects were not thoroughly investigated here. Even for feedback systems which will attempt to control the uncorrelated noise, it is not expected that this type of error will significantly reduce the level of control provided that good signal to noise ratios are maintained.

3.3.4 Comments

It should be noted that in practice a variety of errors will occur in the measurement of the energy density and the resulting normalised errors are not simply additive but rather the errors become compounded in a very complicated fashion and are heavily dependent on the sound field characteristics. It can be said however, that the above analysis does provide an indication of the magnitude of the errors to be expected from a typical sensor operating in two idealised sound fields. Table 3.1 presents a summary of the typical errors experienced during the measurement of energy density.

Error Type	Low Frequency Limit		High Frequency Limit	
	Reactive Field	Plane Wave	Reactive Field	Plane Wave
Inherent	0	0	$-(kh)^2\left[\frac{2\cos^2(kx)+1}{3}\right]+\ldots$	$-\frac{2}{3}(kh)^2+\ldots$
Phase	$\cos^2(kx)\left(\frac{2\phi_s}{2kh}\right)^2$	$-\frac{2\phi_s}{2kh}+\frac{1}{2}\left(\frac{2\phi_s}{2kh}\right)^2$	$-(kh)^2\left[\frac{2\cos^2(kx)+1}{3}\right]+\ldots$	$-\frac{2}{3}(kh)^2+\ldots$
Sensitivity	$-\left(\frac{2T}{2kh}\right)\sin(2kx)+\left(\frac{2T}{2kh}\right)^2\cos^2(kx)$	$\frac{1}{2}\left(\frac{2T}{2kh}\right)^2$	$-(kh)^2\left[\frac{2\cos^2(kx)+1}{3}\right]+\ldots$	$-\frac{2}{3}(kh)^2+\ldots$
Position	$\cos^2(kx)+\sin^2(kx)\left(1+2\frac{2\epsilon}{2h}\right)-1$	$\frac{2\epsilon}{2h}$	$-(kh)^2\left[\frac{2\cos^2(kx)+1}{3}\right]+\ldots$	$\frac{2\epsilon}{2h}-\frac{2}{3}(kh)^2+\ldots$

Table 3.1: Summary of approximated normalised errors in energy density, $e(E_D)$, where $2kh$ is the non-dimensional spacing between microphones, kx is the position in the reactive sound field, $2\phi_s$ is the phase error, $2T$ is the error in the sensitivity and 2ϵ is the error in the location of the microphones.

Table 3.1 can be used to define the frequency bounds for a sensor. For example, let the permissible normalised error in the energy density be 10% and the operating range be the decade 60-600 Hz. For a reactive sound field, the location of the sensor in the field determines the size of the error, so it important to use the the largest error in the field. The upper frequency limit defines the largest the sensor may be, ie $2h < 57$mm. All other instrumentation errors determine the smallest the sensor may be. For a phase error of $2\phi_s = 1^\circ$, then $2h > 50$mm. For a sensitivity error of $2T = 0.5\%$, then $2h > 45$mm. For a position error of $2\epsilon = 2$mm, then $2h > 40$mm. A suitable compromise for such a design may be $2h = 50$mm. This in fact has formed the basis of the design of the 3D

sensor configurations studied in the following sections.

3.4 3-D Energy Density Sensor Configurations

In the following chapter, various configurations of 3-axis energy density sensors have been considered for use as error sensors in active noise control systems. An expression for the measured error in energy density from a 4, 6 and 7 microphone sensor arising from the finite-difference and finite-sum approximations is derived. It will be shown that for active control applications the energy density in three dimensions can be adequately measured with 4 microphones rather than the conventional 6 used in previous sensors. It is also argued that if an extremely accurate measure of energy density is required a 7-microphone sensor should be used. This has less than half the error of a 6-microphone sensor of the same dimensions with the addition of a single microphone.

Four sensor configurations were considered for this numerical study. The first and most common sensor is a 6-microphone sensor used by Sommerfeldt et al. (1995). This consists of 3 pairs of microphones separated by a distance $2h$, on 3 orthogonal axes and is shown in Figure 3.20. It should be noted that Sommerfeldt et al. (1995) mounted the microphones within a sphere (rather than as shown in Figure 3.20) in an attempt to use the effects of diffraction caused by the sensor (Elko 1991*a*) to produce more favourable bias conditions, and in doing so reduce the inherent errors. The pressure sensed by the sensor is the mean of that sensed by each of the 6 microphones. The velocity for each axis was calculated using Equation (3.4). The “acoustic centre” or “measurement point” is given by the geometric centre of the sensor.

The second sensor, a 7-microphone configuration, was a variation of the first. The additional microphone was located at the geometric centre of the 6-microphone sensor to measure the pressure for the sensor (see Figure 3.20). By measuring the pressure directly rather than interpolating, the error in pressure associated with the finite-sum was avoided.

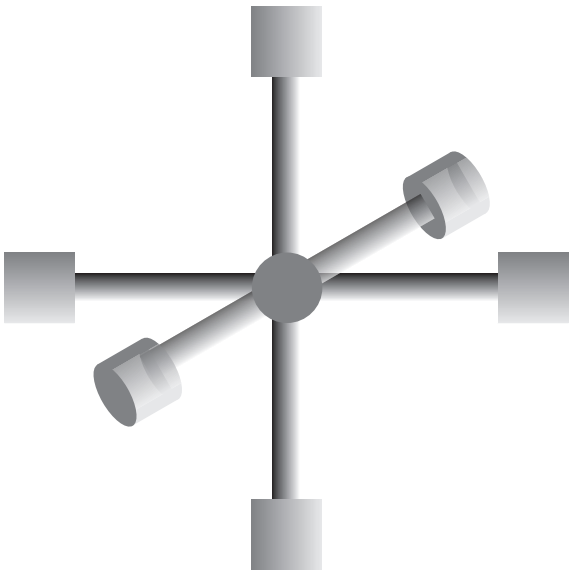

Figure 3.20: Energy density sensor using 6 or 7 microphones.

The third was a 4-microphone sensor as seen in Figure 3.21. Three microphones (marked x, y and z), each forming one of the ends of the 3 orthogonal axis (marked *x*, *y* and *z*), were located on a circle 120 degrees apart. The origin of the sensor was located on the normal to the plane of the circle and passing through the centre of the circle. The distance from the centre microphone (microphone o) to the other microphones was $2h$. The pressure sensed by the centre microphone was used as the pressure for the sensor. The velocities were calculated using Equation (3.4). The advantage of this design is that less signal conditioning channels are required compared to the 6 and 7 microphone sensors. The current design was arrived at independently, however, the idea of a four-microphone sensor to measure the acoustic energy density is not new. Schumacher & Hixson (1983) presented a paper on a four-microphone orthogonal array used to measure the energy density in reverberant and semi-reverberant sound fields. The author also found in Fahy (1995) a similar configuration used for the measurement of acoustic intensity. The application of such a design for the measurement of acoustic intensity is highly questionable due to the significant errors arising from the finite separation of the microphones; however, for the measurement of energy density in an active noise control system it will be

shown that the design is adequate.

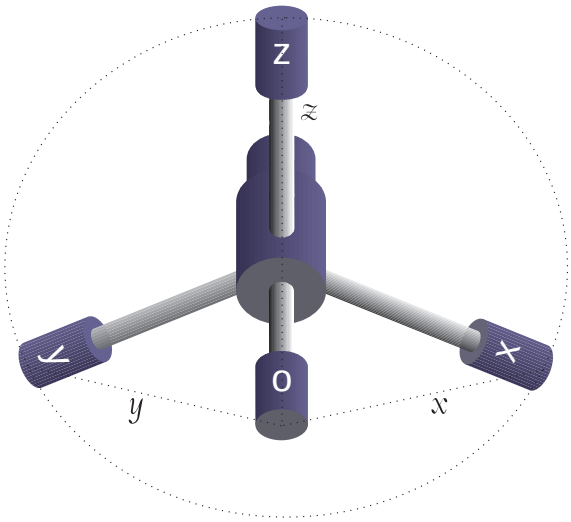

Figure 3.21: 4 Microphone 3-axis energy density sensor.

For the 4-microphone sensor, it can be shown that the positions of the microphones relative to the centre of the circle formed by the three planar microphones, with the z-axis of the Cartesian coordinate system in the direction of the out of plane microphone, is given by the following matrix,

$$\hat{\mathbf{X}} = \begin{bmatrix} 0 & \frac{-h2\sqrt{2}}{\sqrt{3}} & \frac{h\sqrt{2}}{\sqrt{3}} & \frac{h\sqrt{2}}{\sqrt{3}} \\ 0 & 0 & h\sqrt{2} & -h\sqrt{2} \\ \frac{h2}{\sqrt{3}} & 0 & 0 & 0 \end{bmatrix} \tag{3.100}$$

The geometric centre is defined as the mean of all four positions, ie

$$\begin{aligned}\mathbf{X}_0 &= \begin{bmatrix} 0 & \frac{-h2\sqrt{2}}{\sqrt{3}} & \frac{h\sqrt{2}}{\sqrt{3}} & \frac{h\sqrt{2}}{\sqrt{3}} \\ 0 & 0 & h\sqrt{2} & -h\sqrt{2} \\ \frac{h2}{\sqrt{3}} & 0 & 0 & 0 \end{bmatrix} \begin{bmatrix} \frac{1}{4} \\ \frac{1}{4} \\ \frac{1}{4} \\ \frac{1}{4} \end{bmatrix} \\ &= \begin{bmatrix} 0 \\ 0 \\ \frac{h}{2\sqrt{3}} \end{bmatrix} \end{aligned} \tag{3.101}$$

Therefore, the position vector for the 4-microphone sensor from the geometric centre of the sensor is given by $\mathbf{X} = \hat{\mathbf{X}} - \mathbf{X}_0$, ie

$$\mathbf{X} = \begin{bmatrix} 0 & \frac{-h2\sqrt{2}}{\sqrt{3}} & \frac{h\sqrt{2}}{\sqrt{3}} & \frac{h\sqrt{2}}{\sqrt{3}} \\ 0 & 0 & h\sqrt{2} & -h\sqrt{2} \\ \frac{h\sqrt{3}}{2} & -\frac{h}{2\sqrt{3}} & -\frac{h}{2\sqrt{3}} & -\frac{h}{2\sqrt{3}} \end{bmatrix} \tag{3.102}$$

It is worth noting that this design has two advantages over the former two designs. The most obvious advantage is less signal conditioning and channels are required reducing thus the cost and complexity of the unit and making calibration easier. The other advantage is associated with installation. The plane formed by the 3 circumferentially located microphones of the 4 microphone sensor sits flush against surfaces whereas it is not so neat with the 6/7 microphone sensor.

The fourth configuration of energy density sensor investigated was an adaptation of the previous four microphone sensor. Rather than using the pressure at the “origin microphone”, the mean pressure sensed by the four microphones was used as the pressure for the sensor. The particle velocities were calculated as before.

For all the following calculations it has been assumed the microphones were omni-

directional. Other effects such as diffraction have also been neglected. This assumption is valid for the frequency range of interest for active noise control applications of such sensors.

3.5 Errors in the Measurement of Acoustic Energy Density with 3-D Sensors

For single axis energy density sensors the error analysis is relatively simple and analytical expressions can be easily derived. Deriving expressions of the energy density for the three axis sensors is not so straightforward, since it is not only the position within the field which influences the accuracy but also the orientation of the sensor within the field. Therefore, numerical integration has been used to calculate the accuracy of each sensor as follows:

1. Define the pressure field.
2. Define the original positions of the microphones.
    (a) Apply a spatial error if required.
3. Select the position of the sensor within the field.
4. Apply a coordinate transformation (rotation and translation).
5. Calculate the pressure at each microphone.
6. Apply the following instrumentation corrections if required
    (a) Phase mismatch
    (b) Sensitivity error

7. Calculate the pressure and velocity vectors for the sensor.

8. Using the results from step 7 calculate the ED measured by the sensor for the particular orientation.

9. Repeat from steps 2(a) to 8 for all possible angles and positions.

10. Sum (integrate) the results and calculate the “average” error.

3.5.1 Error Analysis

It will be shown that the errors arising from the measurement of the energy density in three-dimensions are similar to those arising in one-dimension. At the high frequency limit, the errors associated with the three-dimensional sensors are of similar magnitude but typically less than those of the one-dimensional sensor arrangements. However, the errors associated with the three-dimensional sensor arrangements at the low frequency limit are typically three times larger the the one dimensional sensors.

3.5.1.1 Original Position Matrices

The position of each element of the sensor can be defined by a position matrix, where $\mathbf{X}_4$, $\mathbf{X}_6$ and $\mathbf{X}_7$ correspond to the 4 element, the 6 element and 7 element sensor respectively,

$$\mathbf{X}_4 = \begin{bmatrix} 0 & \frac{-h2\sqrt{2}}{\sqrt{3}} & \frac{h\sqrt{2}}{\sqrt{3}} & \frac{h\sqrt{2}}{\sqrt{3}} \\ 0 & 0 & h\sqrt{2} & -h\sqrt{2} \\ \frac{h\sqrt{3}}{2} & -\frac{h}{2\sqrt{3}} & -\frac{h}{2\sqrt{3}} & -\frac{h}{2\sqrt{3}} \end{bmatrix} \tag{3.103}$$

$$\mathbf{X}_6 = \begin{bmatrix} -h & h & 0 & 0 & 0 & 0 \\ 0 & 0 & -h & h & 0 & 0 \\ 0 & 0 & 0 & 0 & -h & h \end{bmatrix} \tag{3.104}$$

$$\mathbf{X}_7 = \begin{bmatrix} -h & -h & 0 & 0 & 0 & 0 & 0 \\ 0 & 0 & -h & -h & 0 & 0 & 0 \\ 0 & 0 & 0 & 0 & -h & -h & 0 \end{bmatrix} \tag{3.105}$$

3.5.1.2 Coordinate Transforms

The original position of each sensor was rotated, first by an amount α about the z-axis, followed by a rotation β about the y-axis and finally a rotation γ about the x-axis. Combining the three basic rotation matrices into a single rotation matrix by performing successive matrix multiplications leads to

$$\mathbf{R} = \begin{bmatrix} C_\alpha C_\beta & -S_\alpha C_\beta & S_\beta \\ S_\alpha C_\gamma + C_\alpha S_\beta S_\gamma & C_\alpha C_\gamma + S_\alpha S_\beta S_\gamma & -C_\beta S_\gamma \\ S_\alpha S_\gamma - C_\alpha S_\beta C_\gamma & C_\alpha S_\gamma + S_\alpha S_\beta C_\gamma & C_\beta C_\gamma \end{bmatrix} \tag{3.106}$$

where C and S represent the cosine and sine respectively. Each sensor was then displaced by a displacement column vector

$$\Delta \mathbf{x}_i = \begin{bmatrix} x \\ y \\ z \end{bmatrix} \tag{3.107}$$

Therefore the final expression for the orientation and position of the sensor elements is given by the following transform

$$\hat{\mathbf{X}}_i = \mathbf{R}\mathbf{X}_i + \Delta \mathbf{X}_i \tag{3.108}$$

where the subscript i refers to the number of elements in the sensor and $\Delta \mathbf{X}_i$ is the displacement matrix with i columns given by Equation (3.107).

3.5.1.3 Spatial Errors

Spatial errors result in a shift in the position of the elements of the sensor with each element of the sensor shifted by the following

$$\mathbf{s} = \begin{bmatrix} s_x \\ s_y \\ s_z \end{bmatrix} \tag{3.109}$$

Therefore, rewriting Equation (3.108) to include the spatial error leads to

$$\hat{\mathbf{V}}_i = \mathbf{R}\left[\mathbf{X}_i + \mathbf{S}_i\right] + \Delta\mathbf{X}_i \tag{3.110}$$

where $\mathbf{S}_i$ is the displacement matrix with i columns given by Equation (3.109).

3.5.1.4 Pressure Response

If P is the pressure operator, then the pressure at each microphone position is given by the pressure row vector

$$\mathbf{p}_i = P(\hat{\mathbf{V}}_i) \tag{3.111}$$

The pressure operator is a function which defines the acoustic field. In the case of a one-dimension reactive sound field or a progressive plane wave the pressure operator, P, is given by Equations (3.25) and (3.39) respectively.

3.5.1.5 Phase Mismatch Errors

The phase mismatch can be modelled as a temporal rotation in the elements of the sensor, ie for the 4-microphone sensor Equation (3.111) becomes

$$\mathbf{p}_i = \mathbf{\Phi} P(\hat{\mathbf{V}}_i) \tag{3.112}$$

where $\mathbf{\Phi}$ is the phase mismatch matrix (for the 4-microphone sensor) defined by

$$\mathbf{\Phi} = \begin{bmatrix} e^{j\phi_1} & 0 & 0 & 0 \\ 0 & e^{j\phi_2} & 0 & 0 \\ 0 & 0 & e^{j\phi_3} & 0 \\ 0 & 0 & 0 & e^{j\phi_4} \end{bmatrix} \tag{3.113}$$

where ϕ_i is the phase error about some arbitrary reference.

3.5.1.6 Sensitivity Errors

The individual microphones may differ in sensitivity which alters both the pressure sum and difference and subsequently the estimated sensors pressure and particle velocity. The pressure estimate can be altered by pre-multiplying the "true" pressure vector by the diagonal sensitivity matrix, $\mathbf{T}_i$ with the diagonal elements of the matrix corresponding to the microphone sensitivities,

$$\hat{\mathbf{p}}_i = \mathbf{T}_i \mathbf{p}_i \tag{3.114}$$

3.5.1.7 Sensor Pressure & Velocity

The pressure and velocity (weighted by ρc as per Equation 3.7) of the sensor, given by a 4 element vector $\mathbf{d}$, can be calculated using a linear combination of the individual micro-

phones, ie

$$\mathbf{d} = \mathbf{D}\hat{\mathbf{p}}^{\mathrm{T}} \tag{3.115}$$

where $\mathbf{D}$ is the sensor dependent (4 x n_d) pressure to energy density transfer matrix, n_d is the number of microphones per sensor and $\mathbf{d}$ is the (4 x 1) energy density column vector given by,

$$\mathbf{d} = \begin{bmatrix} p \\ \rho c v_x \\ \rho c v_y \\ \rho c v_z \end{bmatrix} \tag{3.116}$$

4-Microphone sensor without summer The energy density column vector for the 4-microphone sensor without a pressure summer (, ie the pressure estimate used by the sensor is simply the pressure measured by the origin microphone,) is given by

$$\mathbf{d}_4 = \mathbf{D}_4\hat{\mathbf{p}}_4^{\mathrm{T}} \tag{3.117}$$

where the (4 x 4) pressure to energy density transfer matrix is

$$\mathbf{D}_4 = \begin{bmatrix} 1 & 0 & 0 & 0 \\ -\frac{j}{2kh} & \frac{j}{2kh} & 0 & 0 \\ -\frac{j}{2kh} & 0 & \frac{j}{2kh} & 0 \\ -\frac{j}{2kh} & 0 & 0 & \frac{j}{2kh} \end{bmatrix} \tag{3.118}$$

4-Microphone sensor with summer The energy density column vector for the 4-microphone sensor with a pressure summer, ie the pressure estimate used by the sensor is

the mean of the pressures measured by the 4 microphones, is given by

$$\mathbf{d}_{4_s} = \mathbf{D}_{4_s}\hat{\mathbf{p}}_4^{\mathrm{T}} \tag{3.119}$$

where the $(4 \text{ x } 4)$ pressure to energy density transfer matrix is

$$\mathbf{D}_{4_s} = \begin{bmatrix} \frac{1}{4} & \frac{1}{4} & \frac{1}{4} & \frac{1}{4} \\ -\frac{j}{2kh} & \frac{j}{2kh} & 0 & 0 \\ -\frac{j}{2kh} & 0 & \frac{j}{2kh} & 0 \\ -\frac{j}{2kh} & 0 & 0 & \frac{j}{2kh} \end{bmatrix} \tag{3.120}$$

6-Microphone sensor The energy density column vector for the 6-microphone sensor (with a pressure estimate equal to the mean of the six microphones) is given by

$$\mathbf{d}_6 = \mathbf{D}_6\hat{\mathbf{p}}_6^{\mathrm{T}} \tag{3.121}$$

where the $(4 \text{ x } 6)$ pressure to energy density transfer matrix is

$$\mathbf{D}_6 = \begin{bmatrix} \frac{1}{6} & \frac{1}{6} & \frac{1}{6} & \frac{1}{6} & \frac{1}{6} & \frac{1}{6} \\ -\frac{j}{2kh} & \frac{j}{2kh} & 0 & 0 & 0 & 0 \\ 0 & 0 & -\frac{j}{2kh} & \frac{j}{2kh} & 0 & 0 \\ 0 & 0 & 0 & 0 & -\frac{j}{2kh} & \frac{j}{2kh} \end{bmatrix} \tag{3.122}$$

7-Microphone sensor The energy density column vector for the 7-microphone sensor (with the pressure of the sensor equal to the centre microphone) is given by

$$\mathbf{d}_7 = \mathbf{D}_7\hat{\mathbf{p}}_7^{\mathrm{T}} \tag{3.123}$$

where the (4 x 7) pressure to energy density transfer matrix is

$$\mathbf{D}_7 = \begin{bmatrix} 0 & 0 & 0 & 0 & 0 & 0 & 1 \\ -\frac{j}{2kh} & \frac{j}{2kh} & 0 & 0 & 0 & 0 & 0 \\ 0 & 0 & -\frac{j}{2kh} & \frac{j}{2kh} & 0 & 0 & 0 \\ 0 & 0 & 0 & 0 & -\frac{j}{2kh} & \frac{j}{2kh} & 0 \end{bmatrix} \tag{3.124}$$

3.5.1.8 Energy Density

The time averaged energy density measured by each sensor is given by the following expression

$$\bar{E}_D = \frac{1}{4\rho c^2}\mathbf{d}^{\mathrm{H}}\mathbf{d} \tag{3.125}$$

3.5.2 Simulation Results

A simulation using the procedure outlined above was run to calculate the accuracy of the three-dimensional energy density sensor configurations. The energy density for the 4 sensor configurations was calculated for a one-dimensional reactive sound field and a progressive plane wave. Each of the 3 orthogonal angles were stepped from 0 to π in steps of $\pi/8$ so as to get a measure of the effect orientation has on the energy density estimate. The position in the reactive sound field was varied from 0 to $\lambda/2$ in steps of $\lambda/16$. This was unnecessary with the plane wave simulation since the energy density estimate is independent of position. These intervals were found to be sufficient for the error to have converged to 3 significant figures. The following results have been calculated from the simulation;

- Normalised mean energy density estimate given by

$$\frac{\bar{E}_D}{E_D} = \frac{1}{nE_D}\sum_{i=1}^{n} E_{D_i} \tag{3.126}$$

  where $\bar{E}_D$ is the mean energy density, E_D is the true energy density, E_{D_i} is the ith estimate of the energy density and n is the number of estimates.

- Normalised rms error about exact ED given by

$$e(E_D)_{rms} = \frac{1}{E_D}\sqrt{\frac{1}{n}\sum_{i=1}^{n}\left(E_{D_i} - E_D\right)^2} \tag{3.127}$$

- Normalised standard deviation or square root of the variance which is equal to the expected value of the squared differences of the estimates from the mean ED given by

$$e(\bar{E}_D)_{rms} = \frac{1}{E_D}\sqrt{\frac{1}{n}\sum_{i=1}^{n}\left(E_{D_i} - \bar{E}_D\right)^2} \tag{3.128}$$

- Normalised maximum and minimum ED given by

$$\frac{E_{D_{max}}}{E_D} = \max(E_{D_i})/E_D \tag{3.129}$$

  and

$$\frac{E_{D_{min}}}{E_D} = \min(E_{D_i})/E_D \tag{3.130}$$

  respectively.

The mean energy density estimate, Equation (3.126), gives a measure of the average bias error in the energy density from each of the sensors. The difference between the estimate

and the true value is known as the *bias* of the estimate. The normalised bias is simply the bias divided by the true energy density, ie $b(E_D) = (\bar{E}_D - E_D)/E_D$. The rms error, Equation (3.127), is a measure of the deviation of the estimated energy density from the exact value. This is important when one is using different types of sensors, for example, a combination of microphones and energy density sensors. The normalised standard deviation or square root of the variance, Equation (3.128), is the portion of the error that is not systematic (Bendat & Piersol 1986, Section 1.4.3) and gives a measure of the deviation of the estimated energy density experienced during the measurement in a field. This is important when using sensors of the same type as the control effort weighting will be the same for all sensors. It can be shown that the rms error is equal to the square root of the variance plus the square of the bias (Bendat & Piersol 1986)

$$e(E_D)_{rms} = \sqrt{e(\bar{E}_D)^2_{rms} + \left(\frac{\bar{E}_D}{E_D} - 1\right)^2} \tag{3.131}$$

Therefore, if the normalised bias is zero or negligible, then the rms error and root of the square variance are equal. The maximum and minimum, Equations (3.129) and (3.130), give an indication of the range of expected values.

3.5.2.1 Finite Separation Errors (Inherent)

Using the procedure outlined in Section 3.5.1, the ratios of the exact energy density to the approximation for each sensor are as follows.

One dimensional reactive field The five measures of the accuracy of the energy density estimate for the four sensor configurations, as given by Equations (3.126) to (3.130), are plotted in Figure 3.22. It is quite apparent that the 6 and 7 microphone configurations outperform the 4 microphone configurations with the exception of the error in the mean (the bias) seen in Figure 3.22(a), where the 4 microphone sensor without the

summer is similar to the 7 microphone configuration. This is because both arrangements do not use a finite sum to approximate the pressure. It can be seen that the rms error of the 7 microphone sensor is half that of the 6 microphone sensor and a quarter that of the 4 microphone sensor with the pressure summer.

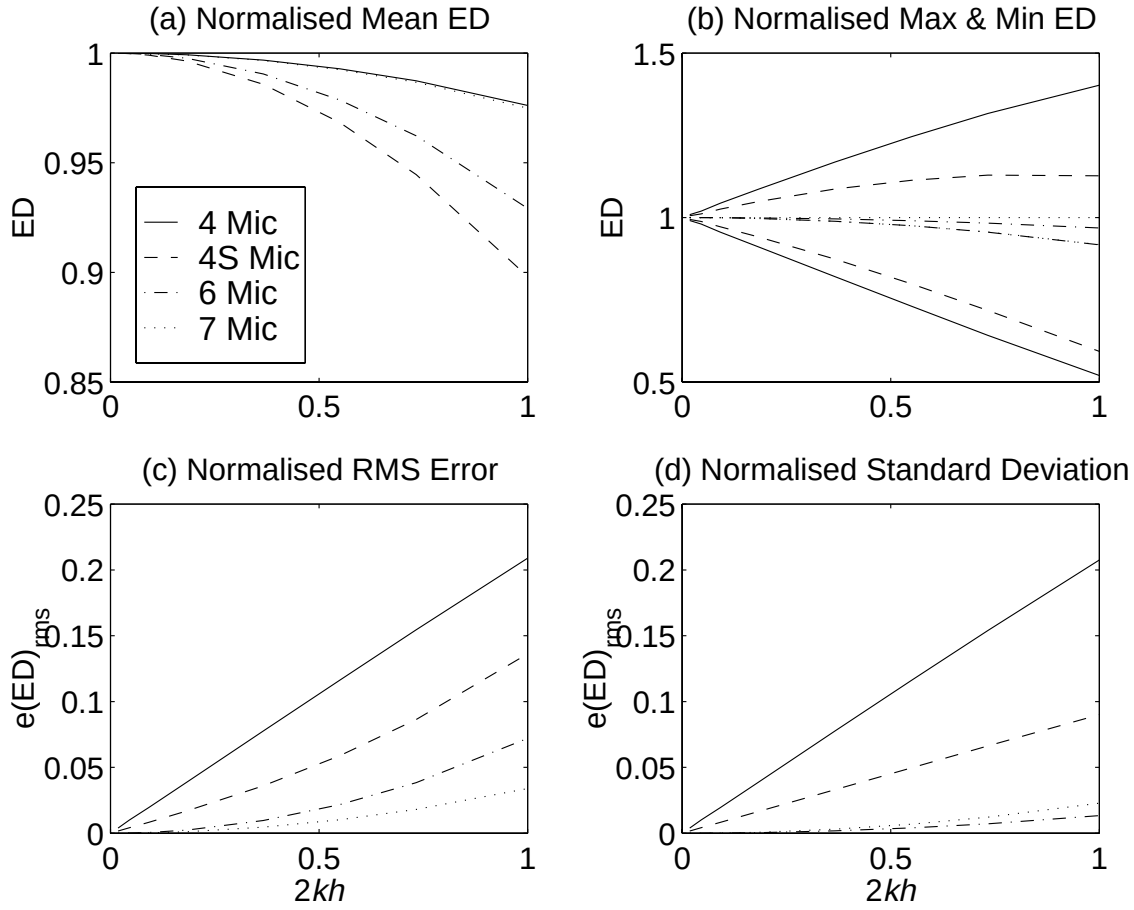

Figure 3.22: Normalised energy density errors as a function of the non-dimensionalised separation distance $2kh$ in a reactive sound field. (a) Normalised mean energy density, (b) normalised maximum and minimum, (c) normalised rms error and (d) normalised standard deviation.

A linear regression was performed on the results shown above, where a fifth order polynomial with respect to $2kh$ was fitted to each of the 5 curves. The polynomials listed below are accurate to 3 significant figures (for $2kh < 1$), and where possible, the coefficients have been expressed as rational number, otherwise the coefficients have been recorded as 3 digit decimal. It was found that the normalised mean energy density for the

4 microphone sensor configurations converged to the following for large kh,

$$\frac{\bar{E}_D}{E_D} = \begin{array}{ll} 1 - 0.024\,(2kh)^2 & , \text{4 Microphone Probe without summer} \\ 1 - 0.108\,(2kh)^2 & , \text{4 Microphone Probe with summer} \\ 1 - 0.072\,(2kh)^2 & , \text{6 Microphone Probe} \\ 1 - 0.025\,(2kh)^2 & , \text{7 Microphone Probe} \end{array} \tag{3.132}$$

The normalised mean energy density for the one-dimensional case is either $1 - 0.167\,(2kh)^2$ or $1 - 0.042\,(2kh)^2$ for the two and three-microphone sensor respectively. The six-microphone three-dimensional sensor is equivalent to the two-microphone sensor in one-dimension since the pressure in the centre of the sensor must be estimated, whereas, the seven-microphone three-dimensional sensor is equivalent to the three-microphone sensor in one-dimension since the centre pressure is measured directly. It is interesting to note that on average, both the six and seven-microphone sensors perform better in one-dimensional reactive sound fields than their equivalent one-dimensional arrangements. The reason for the six-microphone 3-D sensor performing better than the two-microphone sensor is simply that the additional four microphones allows a better estimate of the mean sensor pressure. For example, if the six-microphone sensor has one if its principle axes aligned with the sound field, then the centre pressure is given by $\hat{p}_0 = \frac{1}{6}\Sigma_{i=1}^{6} p_i = (p_1 + p_2)/6 + \frac{2}{3}p_0$ whereas the centre pressure of the two-microphone sensor is given by $\hat{p}_0 = (p_1 + p_2)/2$. Therefore the inherent error of the two-microphone sensor in a reactive sound field is approximately 3 times that of the six-microphone sensor.

The normalised rms error is given by,

$$e(E_D)_{rms} = \begin{cases} 0.213\,(2kh) & \text{, 4 Microphone Probe without summer} \\ 0.089(2kh) + 0.068\,(2kh)^3 - 0.026\,(2kh)^4 & \text{, 4 Mic. Probe with summer} \\ 0.073\,(2kh)^2 & \text{, 6 Microphone Probe} \\ 0.034\,(2kh)^2 & \text{, 7 Microphone Probe} \end{cases} \quad (3.133)$$

The normalised standard deviation is given by,

$$e(\bar{E}_D)_{rms} = \begin{cases} 0.213\,(2kh) & \text{, 4 Microphone Probe without summer} \\ 0.090(2kh) & \text{, 4 Microphone Probe with summer} \\ 0.014\,(2kh)^2 & \text{, 6 Microphone Probe} \\ 0.023\,(2kh)^2 & \text{, 7 Microphone Probe} \end{cases} \quad (3.134)$$

The maximum normalised energy density estimate is

$$\frac{E_{D_{max}}}{E_D} = \begin{cases} 1 + 0.480\,(2kh) & \text{, 4 Microphone Probe without summer} \\ 1 + 0.295(2kh) - 0.150(2kh)^2 & \text{, 4 Microphone Probe with summer} \\ 1 - 0.031\,(2kh)^2 & \text{, 6 Microphone Probe} \\ 1 & \text{, 7 Microphone Probe} \end{cases} \quad (3.135)$$

The maximum normalised energy density for the one-dimensional case is given by either $1 - 0.083\,(2kh)^2$ or 1 for the two and three-microphone sensor respectively. The

minimum normalised energy density estimate is

$$\frac{E_{D_{min}}}{E_D} = \begin{cases} 1 - 0.480\,(2kh) & , \text{4 Microphone Probe without summer} \\ 1 - 0.295(2kh) - 0.150(2kh)^2 & , \text{4 Microphone Probe with summer} \\ 1 - 0.084\,(2kh)^2 & , \text{6 Microphone Probe} \\ 1 - 0.084\,(2kh)^2 & , \text{7 Microphone Probe} \end{cases} \tag{3.136}$$

The minimum normalised energy density for the one-dimensional case is given by either $1 - 0.250\,(2kh)^2$ or $1 - 0.083\,(2kh)^2$ for the two and three-microphone sensor respectively. As expected, the maximum and minimum values of the normalised energy density of the three-microphone sensor in one-dimension are equal (within the accuracy of the simulation) to the maximum and minimum values for the 7-microphone sensor in three-dimensions.

Plane progressive wave The five measures of the accuracy of the energy density estimate for the four sensor configurations, as given by Equations (3.126) to (3.130), are plotted in Figure 3.23. For the plane progressive wave it is quite apparent that the two models without the finite sum approximation, namely the 4-microphone sensor without the pressure summer and the 7-microphone sensor without the pressure summer (Equations (3.118) and (3.124) respectively), out perform the two configurations which rely on the finite sum approximation. One may conclude that for free field conditions the 4 microphone sensor without the summer will have a smaller error than the 6 microphone sensor with the pressure summer. For real cavities the sound field lies somewhere between a reactive sound field and a plane wave depending on the level of damping. Therefore, for acoustic systems which are heavily damped it is possible that the 4 microphone sensor without a pressure summer will have a smaller error than the 6 microphone arrangement at high frequencies.

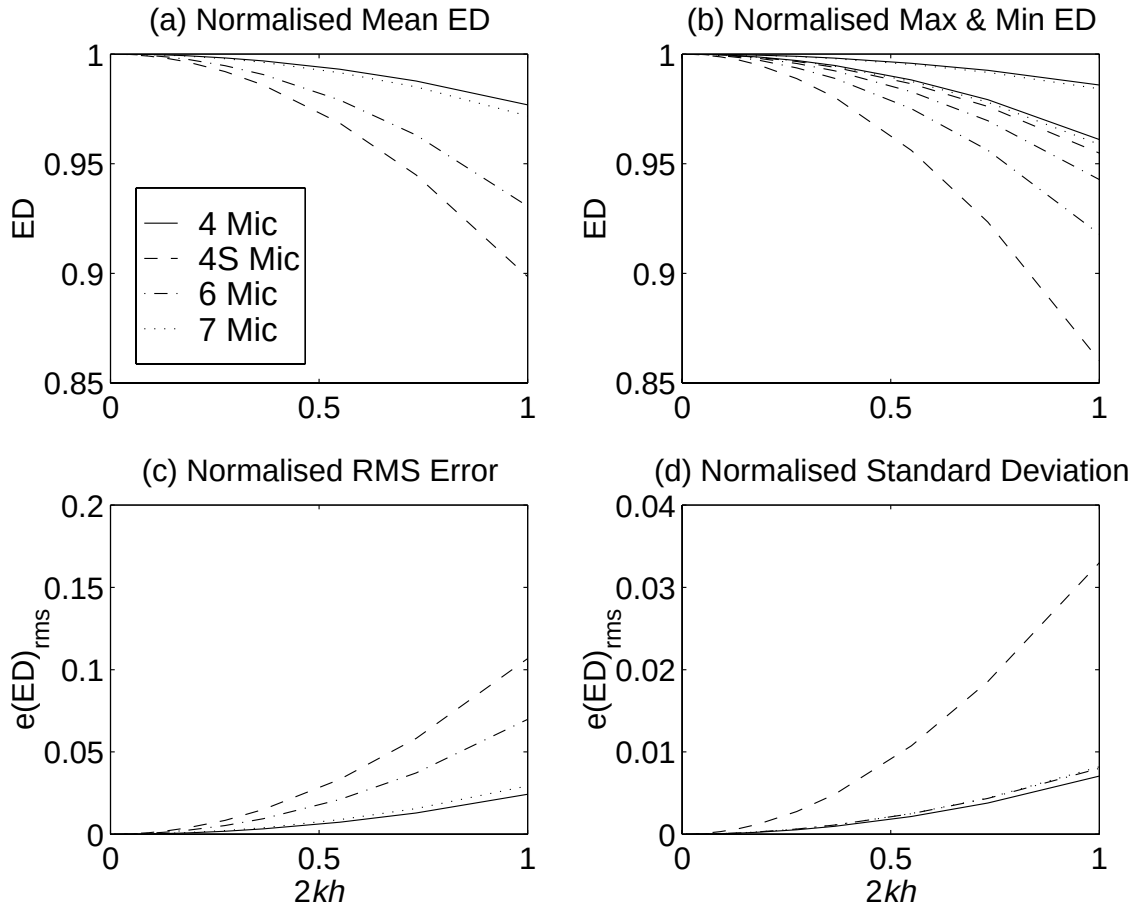

Figure 3.23: Normalised energy density errors as a function of the non-dimensionalised separation distance $2kh$ for a plane progressive wave. (a) Normalised mean energy density, (b) normalised maximum and minimum, (c) normalised rms error and (d) normalised standard deviation.

It was found that the normalised mean energy density for the 4 microphone sensor configurations converged to the following for large kh,

$$\frac{\bar{E}_D}{E_D} = \begin{cases} 1 - 0.023\,(2kh)^2 & , \text{4 Microphone Probe without summer} \\ 1 - 0.107\,(2kh)^2 & , \text{4 Microphone Probe with summer} \\ 1 - 0.070\,(2kh)^2 & , \text{6 Microphone Probe} \\ 1 - 0.028\,(2kh)^2 & , \text{7 Microphone Probe} \end{cases} \tag{3.137}$$

The normalised mean energy density for the one-dimensional case is either $1 - 0.167\,(2kh)^2$ or $1 - 0.042\,(2kh)^2$ for the two and three-microphone sensor respectively. It can be seen that the normalised rms error is given by,

$$e(E_D)_{rms} = \begin{cases} 0.024\,(2kh)^2 & , \text{4 Microphone Probe without summer} \\ 0.114\,(2kh)^2 & , \text{4 Microphone Probe with summer} \\ 0.071\,(2kh)^2 & , \text{6 Microphone Probe} \\ 0.030\,(2kh)^2 & , \text{7 Microphone Probe} \end{cases} \tag{3.138}$$

The normalised standard deviation is given by,

$$e(\bar{E}_D)_{rms} = \begin{cases} 0.007\,(2kh)^2 & , \text{4 Microphone Probe without summer} \\ 0.038(2kh)^2 & , \text{4 Microphone Probe with summer} \\ 0.009\,(2kh)^2 & , \text{6 \& 7 Microphone Probes} \end{cases} \tag{3.139}$$

The maximum normalised energy density estimate is

$$\frac{E_{D_{max}}}{E_D} = \begin{cases} 1 - 0.014\,(2kh)^2 & , \text{4 Microphone Probe without summer} \\ 1 - 0.045(2kh)^2 & , \text{4 Microphone Probe with summer} \\ 1 - 0.057\,(2kh)^2 & , \text{6 Microphone Probe} \\ 1 - 0.016\,(2kh)^2 & , \text{7 Microphone Probe} \end{cases} \quad (3.140)$$

The minimum normalised energy density estimate is

$$\frac{E_{D_{min}}}{E_D} = \begin{cases} 1 - 0.039\,(2kh)^2 & , \text{4 Microphone Probe without summer} \\ 1 - 0.150(2kh)^2 & , \text{4 Microphone Probe with summer} \\ 1 - 0.084\,(2kh)^2 & , \text{6 Microphone Probe} \\ 1 - 0.042\,(2kh)^2 & , \text{7 Microphone Probe} \end{cases} \quad (3.141)$$

Because the error in the energy density estimate for the one-dimensional cases in a plane wave are independent of position, the maximum and minimum is given by the mean energy density estimate.

3.5.2.2 Phase Mismatch

The same two fields were analysed with a phase shift imposed between the microphones. As the phase mismatch affects the calculation of the velocity much more than the calculation of the pressure, the phase shift was applied between matched microphone pairs. A phase difference of 1° has been used for the simulation and was chosen since it was found that most high quality electret microphones will have phase errors of less than 1°. In the case of the 6 and 7 microphone sensors this meant a $\pm\frac{1}{2}^\circ$shift with each pair. For the 4 microphone sensor, the "origin microphone" sensor was given a 1° phase shift. This was believed to be an acceptable approach to an error that would arise randomly.

One dimensional reactive field The five measures of the accuracy of the energy density estimate for the four sensor configurations, as given by Equations (3.126) to (3.130), arising from a 1° phase mismatch in a reactive sound field (for the four sensor configurations) are plotted in Figure 3.24.

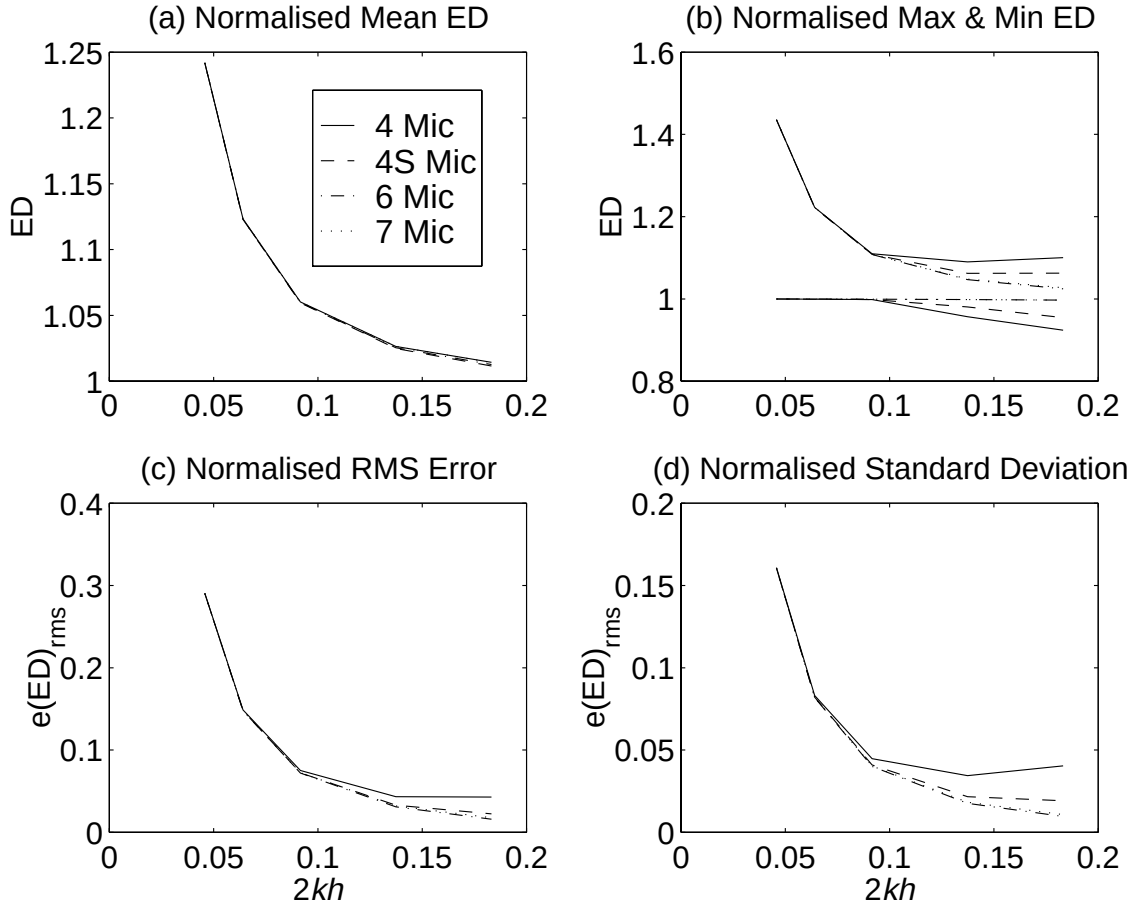

Figure 3.24: Normalised energy density errors as a function of the non-dimensionalised separation distance $2kh$ for a phase mismatch of 1° between microphone pairs in a reactive sound field. (a) Normalised mean energy density, (b) normalised maximum and minimum, (c) normalised rms error and (d) normalised standard deviation.

It was found that the normalised mean energy density for all sensor configurations converged to the following for small wavenumbers ($kh \leq \phi_s$),

$$\frac{\bar{E}_D}{E_D} = 1 + \frac{5}{3}\left(\frac{2\phi_s}{2kh}\right)^2 \tag{3.142}$$

where ϕ_s is in radians. It can be shown that the normalised mean energy density for both the one dimensional cases is $1 + \frac{1}{2}\left(\frac{2\phi_s}{2kh}\right)^2$. Therefore, the bias error for the three-dimensional case is $\frac{10}{3}$ times larger. The normalised rms error is given by,

$$e(E_D)_{rms} = 2\left(\frac{2\phi_s}{2kh}\right)^2 \tag{3.143}$$

the normalised standard deviation, which gives a measure of the deviation about the mean, is given by,

$$e(\bar{E}_D)_{rms} = \frac{\sqrt{11}}{3}\left(\frac{2\phi_s}{2kh}\right)^2 \tag{3.144}$$

and the maximum and minimum energy density are respectively given by

$$\frac{E_{D_{max}}}{E_D} = 1 + 3\left(\frac{2\phi_s}{2kh}\right)^2 \tag{3.145}$$

and

$$\frac{E_{D_{min}}}{E_D} = 1 \tag{3.146}$$

The maximum energy density estimate for both the one-dimensional cases is $1 + \left(\frac{2\phi_s}{2kh}\right)^2$ which is three times less than the maximum error for the three-dimensional case. The error in the minimum energy density estimate for the one-dimensional cases is also zero.

Plane progressive wave The five measures of the accuracy of the energy density estimate for the four sensor configurations, as given by Equations (3.126) to (3.130), arising from a 1° phase mismatch in a progressive plane wave for the four sensor configurations are plotted in Figure 3.25.

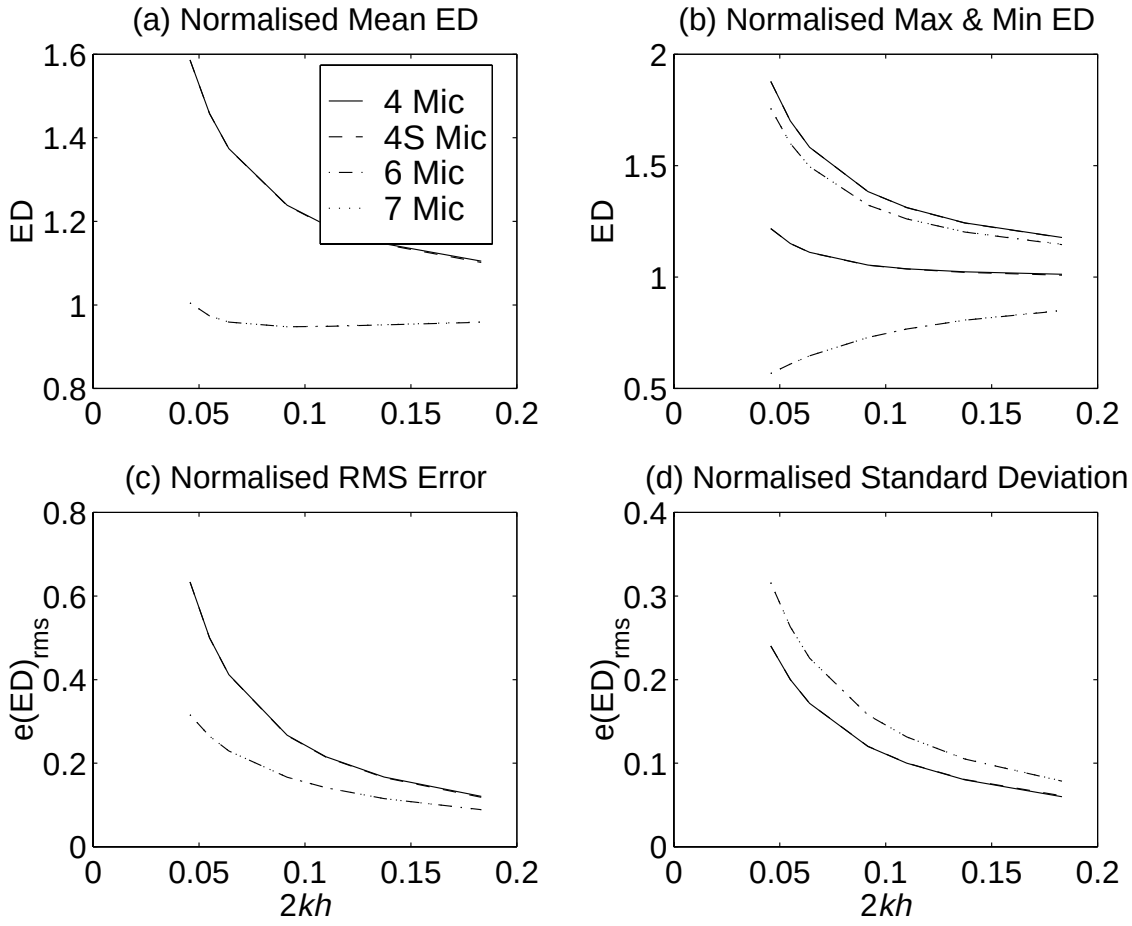

Figure 3.25: Normalised energy density errors as a function of the non-dimensionalised separation distance $2kh$ for a phase mismatch of 1° between microphone pairs in a plane progressive wave. (a) Normalised mean energy density, (b) normalised maximum and minimum, (c) normalised rms error and (d) normalised standard deviation.

It was found that the normalised mean energy density for the microphone sensor configurations converged to the following for small kh,

$$\begin{aligned}\frac{\bar{E}_D}{E_D} &= 1+\left(\frac{2\phi_s}{2kh}\right)+\frac{3}{2}\left(\frac{2\phi_s}{2kh}\right)^2 \quad , 4\,\text{Microphone Probes} \\ & \quad 1-0.56\left(\frac{2\phi_s}{2kh}\right)+\frac{3}{2}\left(\frac{2\phi_s}{2kh}\right)^2 \quad , 6\,\&\,7\,\text{Microphone Probes}\end{aligned} \tag{3.147}$$

The normalised mean energy density for the one-dimensional cases is $1-\left(\frac{2\phi_s}{2kh}\right)+\frac{1}{2}\left(\frac{2\phi_s}{2kh}\right)^2$. When $\phi_s < kh$ the mean energy density is given by the first two terms in the above expression and therefore the error in the regime for the 4 microphone sensors is approximately the same as the error arising for the one-dimensional case. The error for the 6 and 7 microphone sensor configurations is approximately half that of the one-dimensional case. However, as kh becomes very small, ie $\phi_s > kh$, the last term dominates and therefore, the error in the mean energy density estimate for the three-dimensional case is approximately 3 times larger than the one-dimensional case. The normalised rms error is given by,

$$\begin{aligned}e(E_D)_{rms} &= 1.08\left(\frac{2\phi_s}{2kh}\right)+1.47\left(\frac{2\phi_s}{2kh}\right)^2 \quad , 4\,\text{Microphone Probes} \\ & \quad -0.04\left(\frac{2\phi_s}{2kh}\right)+1.30\left(\frac{2\phi_s}{2kh}\right)^2 \quad , 6\,\&\,7\,\text{Microphone Probes}\end{aligned} \tag{3.148}$$

The normalised standard deviation is given by,

$$\begin{aligned}e(\bar{E}_D)_{rms} &= 0.63\left(\frac{2\phi_s}{2kh}\right) \quad , 4\,\text{Microphone Probes} \\ & \quad 0.83\left(\frac{2\phi_s}{2kh}\right) \quad , 6\,\&\,7\,\text{Microphone Probes}\end{aligned} \tag{3.149}$$

The maximum normalised energy density estimate is

$$\frac{E_{D_{max}}}{E_D} = \begin{array}{l} 1+\sqrt{3}\left(\frac{2\phi_s}{2kh}\right)+\frac{3}{2}\left(\frac{2\phi_s}{2kh}\right)^2 \quad , 4\,\text{Microphone Probes} \\ 1+\sqrt{2}\left(\frac{2\phi_s}{2kh}\right)+\frac{3}{2}\left(\frac{2\phi_s}{2kh}\right)^2 \quad , 6\ \&\ 7\,\text{Microphone Probes} \end{array} \tag{3.150}$$

The minimum normalised energy density estimate is

$$\frac{E_{D_{min}}}{E_D} = \begin{array}{l} 1+\frac{3}{2}\left(\frac{2\phi_s}{2kh}\right)^2 \quad , 4\,\text{Microphone Probes} \\ 1-(1+\frac{1}{\sqrt{2}})\left(\frac{2\phi_s}{2kh}\right)+\frac{3}{2}\left(\frac{2\phi_s}{2kh}\right)^2 \quad , 6\ \&\ 7\,\text{Microphone Probes} \end{array} \tag{3.151}$$

For large kh, the energy density error due to any phase mismatch approaches zero and therefore the total error in the energy density is due wholly to the inherent errors.

3.5.2.3 Sensitivity Mismatch

For the following analysis it has been assumed that the amplitudes of the individual microphone channels were calibrated to an accuracy of 1% between microphone pairs and that the cross sensitivity was independent of frequency.

One dimensional reactive field The five measures of the accuracy of the energy density estimate for the four sensor configurations, as given by Equations (3.126) to (3.130), arising from a 1% sensitivity mismatch for the four sensor configurations are plotted in Figure 3.26.

It was found that the normalised mean energy density for all the sensor configurations converged to the following for small kh,

$$\frac{\bar{E}_D}{E_D} = 1+\tfrac{5}{3}\left(\tfrac{2T}{2kh}\right)^2 \tag{3.152}$$

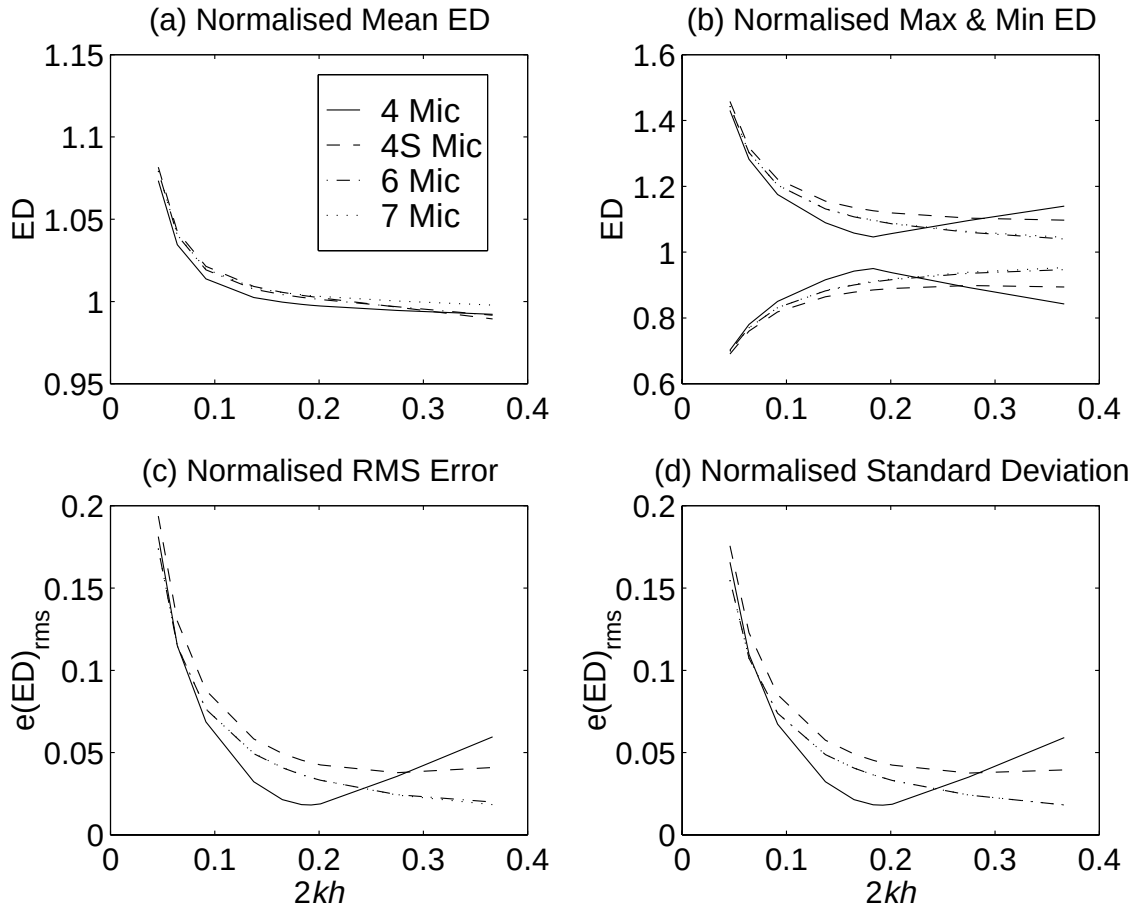

Figure 3.26: Normalised energy density errors as a function of the non-dimensionalised separation distance $2kh$ for a 1% sensitivity mismatch between microphone pairs in a reactive sound field. (a) Normalised mean energy density, (b) normalised maximum and minimum, (c) normalised rms error and (d) normalised standard deviation.

The normalised rms error is given by,

$$e(E_D)_{rms} = \begin{cases} 0.33\left(\frac{2T}{2kh}\right) + 1.81\left(\frac{2T}{2kh}\right)^2 & , \text{4 Microphone Probe w/o Summer} \\ 0.36\left(\frac{2T}{2kh}\right) + 1.79\left(\frac{2T}{2kh}\right)^2 & , \text{4 Microphone Probe with Summer} \\ 0.28\left(\frac{2T}{2kh}\right) + 1.84\left(\frac{2T}{2kh}\right)^2 & , \text{6 \& 7 Microphone Probes} \end{cases} \quad (3.153)$$

The normalised standard deviation is given by,

$$e(E_D)_{rms} = \begin{cases} 0.50\left(\frac{2T}{2kh}\right) + 0.84\left(\frac{2T}{2kh}\right)^2 & , \text{4 Microphone Probe w/o Summer} \\ 0.52\left(\frac{2T}{2kh}\right) + 0.83\left(\frac{2T}{2kh}\right)^2 & , \text{4 Microphone Probe with Summer} \\ 0.42\left(\frac{2T}{2kh}\right) + 0.88\left(\frac{2T}{2kh}\right)^2 & , \text{6 \& 7 Microphone Probes} \end{cases} \quad (3.154)$$

The maximum normalised energy density estimate is

$$\frac{E_{D_{max}}}{E_D} = \begin{cases} 1 + 1.70\left(\frac{2T}{2kh}\right) + 1.52\left(\frac{2T}{2kh}\right)^2 & , \text{4 Microphone Probe w/o Summer} \\ 1 + 1.74\left(\frac{2T}{2kh}\right) + 1.49\left(\frac{2T}{2kh}\right)^2 & , \text{4 Microphone Probe with Summer} \\ 1 + 1.71\left(\frac{2T}{2kh}\right) + 1.50\left(\frac{2T}{2kh}\right)^2 & , \text{6 \& 7 Microphone Probes} \end{cases} \quad (3.155)$$

The minimum normalised energy density estimate is

$$\frac{E_{D_{min}}}{E_D} = \begin{cases} 1 - 1.72\left(\frac{2T}{2kh}\right) + 1.50\left(\frac{2T}{2kh}\right)^2 & , \text{4 Microphone Probe w/o Summer} \\ 1 - 1.73\left(\frac{2T}{2kh}\right) + 1.50\left(\frac{2T}{2kh}\right)^2 & , \text{4 Microphone Probe with Summer} \\ 1 - 1.71\left(\frac{2T}{2kh}\right) + 1.50\left(\frac{2T}{2kh}\right)^2 & , \text{6 \& 7 Microphone Probes} \end{cases} \quad (3.156)$$

Plane progressive wave The five measures of the accuracy of the energy density estimate for the four sensor configurations, as given by Equations (3.126) to (3.130), arising from a 1% sensitivity mismatch for the four sensor configurations are plotted in Figure 3.27 below.

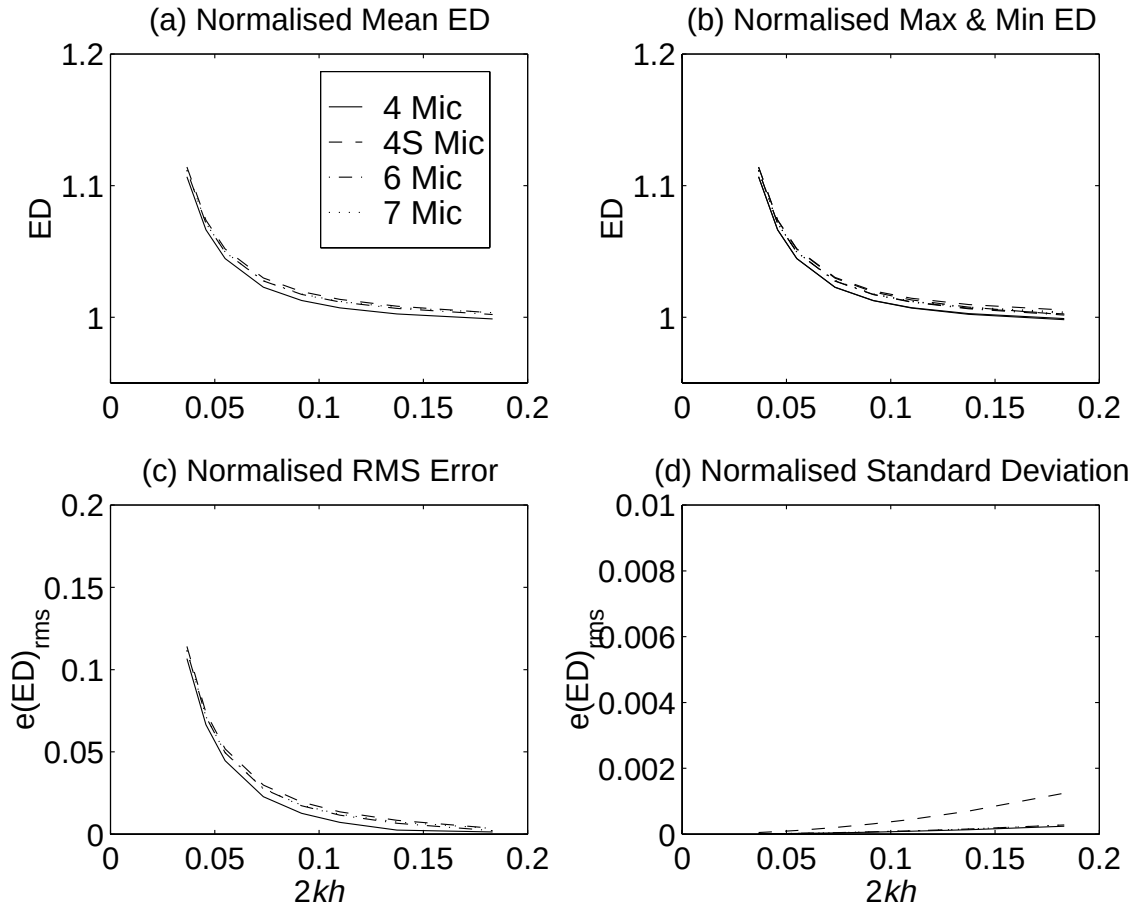

Figure 3.27: Normalised energy density errors as a function of the non-dimensionalised separation distance $2kh$ for a 1% sensitivity mismatch between microphone pairs in a plane progressive wave. (a) Normalised mean energy density, (b) normalised maximum and minimum, (c) normalised rms error and (d) normalised standard deviation.

It was found that the mean normalised energy density for all sensor configurations converged to the following for small kh,

$$\frac{\bar{E}_D}{E_D} = 1 + \frac{3}{2}\left(\frac{2T}{2kh}\right)^2 \tag{3.157}$$

which is 3 times larger than for the one-dimensional case. The normalised rms error is given by,

$$e(E_D)_{rms} = \frac{3}{2}\left(\frac{2T}{2kh}\right)^2 \tag{3.158}$$

the normalised standard deviation is given by,

$$e(\bar{E}_D)_{rms} = 0 \tag{3.159}$$

and the maximum and minimum energy density are respectively given by

$$\frac{E_{D_{max}}}{E_D} = 1 + \frac{3}{2}\left(\frac{2T}{2kh}\right)^2 \tag{3.160}$$

and

$$\frac{E_{D_{min}}}{E_D} = 1 + \frac{3}{2}\left(\frac{2T}{2kh}\right)^2 \tag{3.161}$$

For large kh, the energy density error due to any sensitivity mismatch approaches zero and therefore the total error in the energy density is due wholly to the inherent errors.

3.5.2.4 Spatial Error

The affect of spatial errors on the energy density estimate has been investigated. A 2mm error between microphone pairs was used since it was typical of the spatial tolerances achievable. This was achieved by multiplying the original position matrices, defined by Equations (3.103) to (3.105), by the following ratio $\frac{2+2h}{2h}$, where h is in mm. This had the effect of stretching the physical positions of the microphones but was unaccounted for when calculating the pressure average and gradient.

One dimensional reactive field The five measures of the accuracy of the energy density estimate for the four sensor configurations, as given by Equations (3.126) to (3.130), arising from a 2mm error between microphone pairs for the four sensor configurations are plotted in Figure 3.28 below. Since the bias errors arising from the spatial error at small kh are only a function of the non-dimensional spatial error $\frac{\epsilon}{h}$ (see below), it was necessary to keep $\frac{\epsilon}{h}$ constant. Figure 3.28 is therefore only valid for a non-dimensional spatial error of $\frac{\epsilon}{h} = 4\%$.

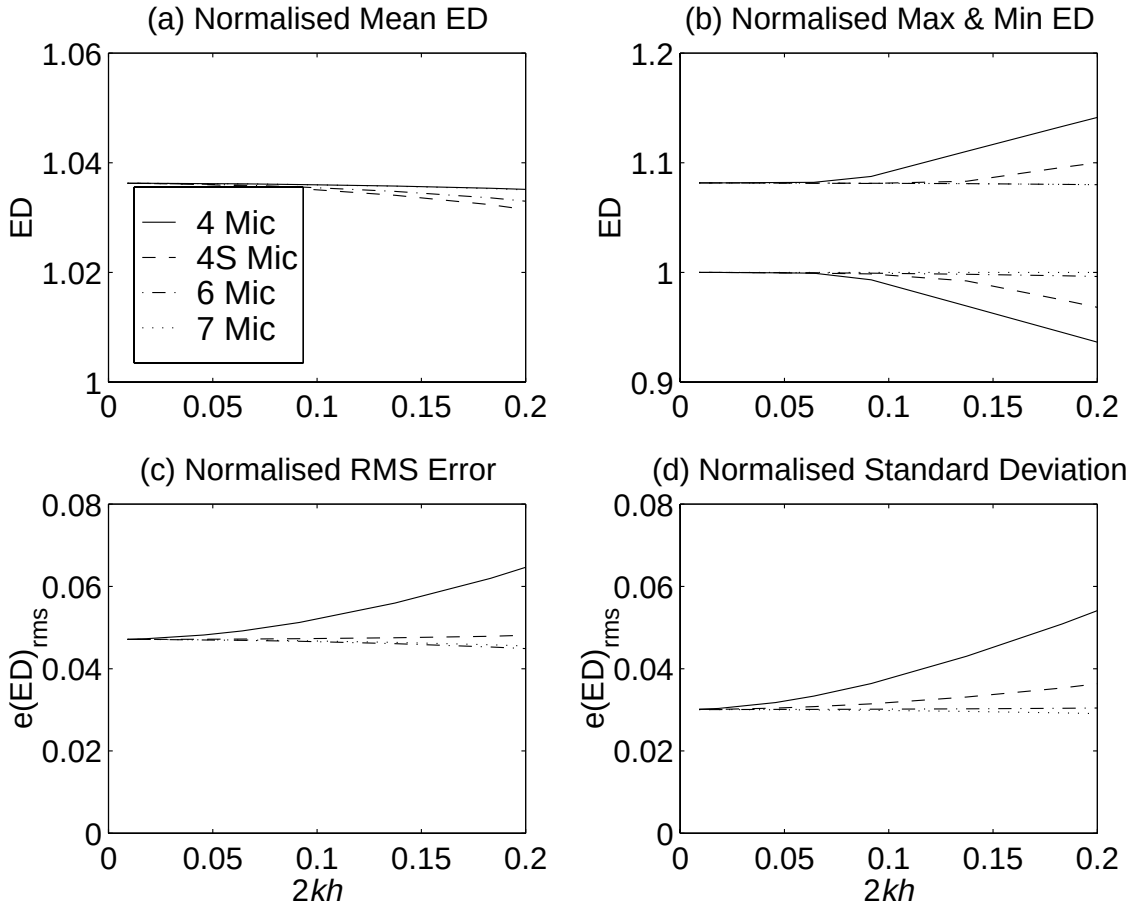

Figure 3.28: Normalised energy density errors as a function of the non-dimensionalised separation distance $2kh$ for a 2mm spatial error between microphone pairs in a reactive sound field, ie $\frac{\epsilon}{h} = 4\%$. (a) Normalised mean energy density, (b) normalised maximum and minimum, (c) normalised rms error and (d) normalised standard deviation.

The variance of the errors with respect to kh at high wavenumbers is associated with the inherent errors. At small kh it was found that the mean normalised energy density for

all sensor configurations was independent of wavenumber and is given by the following ,

$$\frac{\bar{E}_D}{E_D} = 1 + 0.91\left(\frac{\epsilon}{h}\right) \tag{3.162}$$

the normalised rms error is given by,

$$e(E_D)_{rms} = 1.18\left(\frac{\epsilon}{h}\right) \tag{3.163}$$

the normalised standard deviation is given by,

$$e(\bar{E}_D)_{rms} = 0.75\left(\frac{\epsilon}{h}\right) \tag{3.164}$$

and the maximum and minimum energy density are respectively given by

$$\frac{E_{D_{max}}}{E_D} = 1 + 2.04\left(\frac{\epsilon}{h}\right) \tag{3.165}$$

and

$$\frac{E_{D_{min}}}{E_D} = 1 \tag{3.166}$$

All for plots in Figure 3.28 show finite separation effects as the non-dimensional separation ($2kh$) increases.

Plane progressive wave The five measures of the accuracy of the energy density estimate for the four sensor configurations, as given by Equations (3.126) to (3.130), arising from a 2mm error between microphone pairs for the four sensor configurations are plotted in Figure 3.29 below. As was the case with the reactive sound field, the bias errors arising from the spatial error are only a function of $\frac{\epsilon}{h}$ for small kh. Figure 3.29 is therefore only valid for $\frac{\epsilon}{h} = 4\%$.

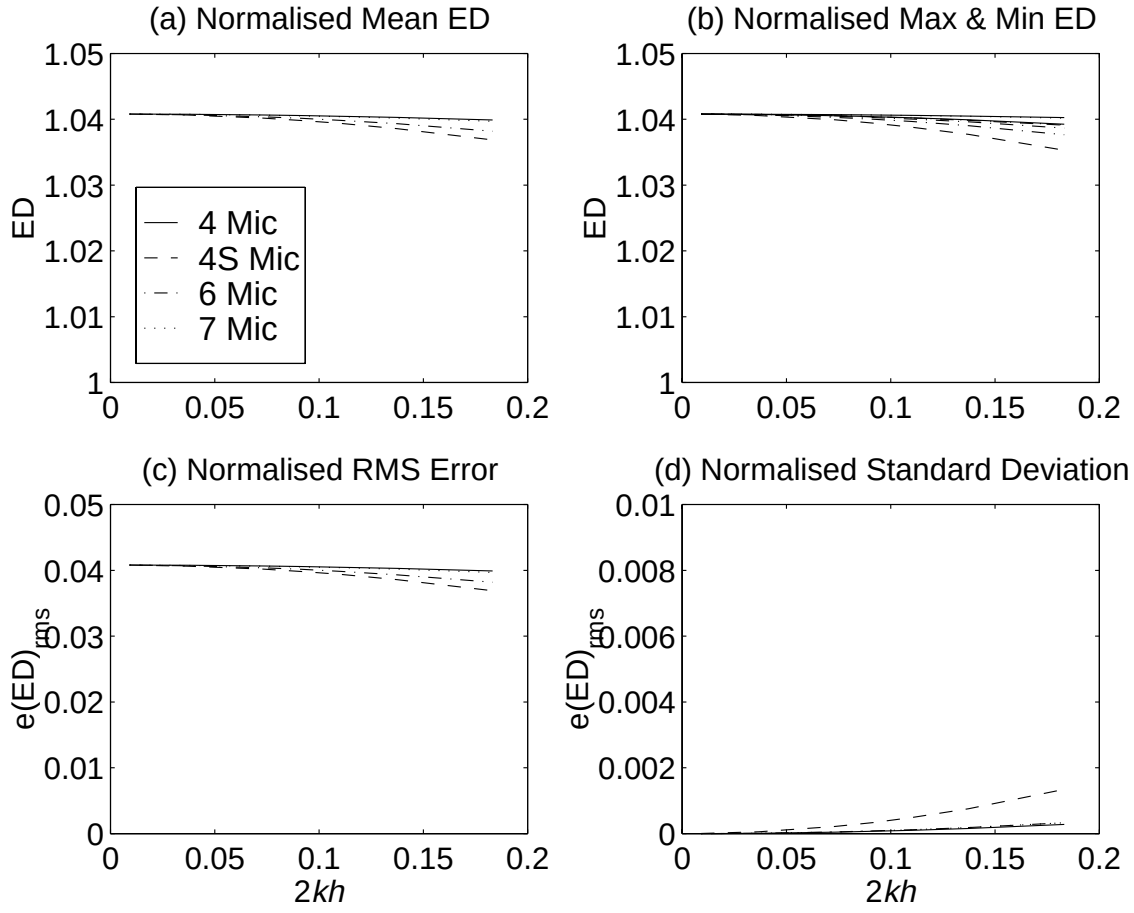

Figure 3.29: Normalised energy density errors as a function of the non-dimensionalised separation distance $2kh$ for a 2mm spatial error between microphone pairs in a plane progressive wave, ie $\frac{\epsilon}{h} = 4\%$. (a) Normalised mean energy density, (b) normalised maximum and minimum, (c) normalised rms error and (d) normalised standard deviation.

It was found that for small kh the mean normalised energy density for all probe configurations was given by the following ,

$$\frac{\bar{E}_D}{E_D} = 1 + \left(\frac{\epsilon}{h}\right) \tag{3.167}$$

the normalised rms error is given by,

$$e(E_D)_{rms} = \left(\frac{\epsilon}{h}\right) \tag{3.168}$$

the normalised standard deviation is given by,

$$e(\bar{E}_D)_{rms} = 0 \tag{3.169}$$

and the maximum and minimum energy density are respectively given by

$$\frac{E_{D_{max}}}{E_D} = \left(\frac{\epsilon}{h}\right) \tag{3.170}$$

and

$$\frac{E_{D_{min}}}{E_D} = \left(\frac{\epsilon}{h}\right) \tag{3.171}$$

This shows that the effect of a spatial error on the energy density estimate in a progressive plane wave is simply to bias the estimate by $\frac{\epsilon}{h}$.

3.5.3 Comments

It has been shown that the energy density in both a reactive sound field and a plane wave can be adequately measured for active noise control applications using only four microphones rather than the 6 used conventionally.

The normalised errors in the energy density for all the 3D sensors converge to approximately the same value for the low frequency limit in the idealised one dimensional fields investigated here. This is to be expected since it was shown in the previous section that the errors at the low frequency limit are due to the finite difference approximation of the velocity. The slight differences quoted are due to the coarse step size used to integrate over all possible orientations.

It was found that for the low frequency limit, the errors for the three-dimensional sensors were typically 3 times larger than were recorded for the one-dimensional case. This is due to the errors arising from each axis adding to the total error. For the high frequency limit on the other hand it was found that for both the reactive sound field and a plane wave, the errors for the three dimensional sensors were less than the equivalent one-dimensional sensors. This is simply due to the three-dimensional sensors providing a better estimate of both the pressure and velocities, but particularly the pressure, through better geometry.

When investigating the inherent errors in plane wave conditions, it was shown that at the high frequency limit the 4-microphone sensor without the summer performed significantly better than either the 4-microphone sensor with the summer or the 6-microphone sensor. This was because of the large errors associated with the finite sum used by the latter two sensor arrangements. The gain in performance was slightly offset by the reduction in performance at the low frequency limit. Therefore, it may be concluded that the bandwidth of the 4-microphone sensor without a summer and the 6-microphone sensor in free field conditions is approximately equal. The bandwidth of the 4-microphone sensor with the summer is actually less than the 4-microphone sensor without the summer. One may argue that since the 4-microphone sensor without the summer is the simplest of the three sensor designs, it is the better arrangement for free field control. The opposite holds in reactive conditions and since the experiments were conducted in a reactive sound field, the 4-microphone energy density sensor with a pressure summer was used.

3.6 3 Axis Energy Density Sensor

A physical energy density sensor was built in order to compare energy density control against conventional microphone control under real conditions. As shown in the previous sections, it is essential that instrumentation errors be kept to a minimum in order for the energy density sensor to work over a broad bandwidth. For active noise control systems it is desirable that the sensing elements be inexpensive which tends to compromise the accuracy of the error sensors. Therefore it is necessary to find some balance between these two competing interests.

The following section addresses the design criteria and issues regarding errors to arrive at a suitable design. The system has been tested for error sensitivity and issues regarding its use are discussed.

3.6.1 Microphone Selection

It was found that a small 6 mm electret microphone element (REALISTIC - Cat. No. 33-1063) provided the necessary phase and magnitude accuracy between elements. Because the sensor was only to be used within controlled environments, the effects of temperature and humidity were not of concern. However, in order to determine the permissible operating environments the microphone sensitivity to temperature was measured and is shown in Figure 3.30. As can be seen, the microphone chosen suffers from the effects of temperature and is only suitable for measurements where the temperature and humidity are constant. As a comparison, it was compared against 2 another inexpensive electret microphone (from China), a sub-miniature condenser microphone made by LECTRET (Model 1207) and a B&K Type 4177 microphone. As expected, the B&K microphone performed very well as did the LECTRET microphone. The latter is currently being used to develop a more robust sensor suitable for harsher environments. The phase sensitivity to temperature for the LECTRET was also measured to ensure stability over a wide temperature

range and is plotted in Figure 3.31. The two graphs show that the LECTRET condenser microphone is suitable for operation over a wide range of temperatures.

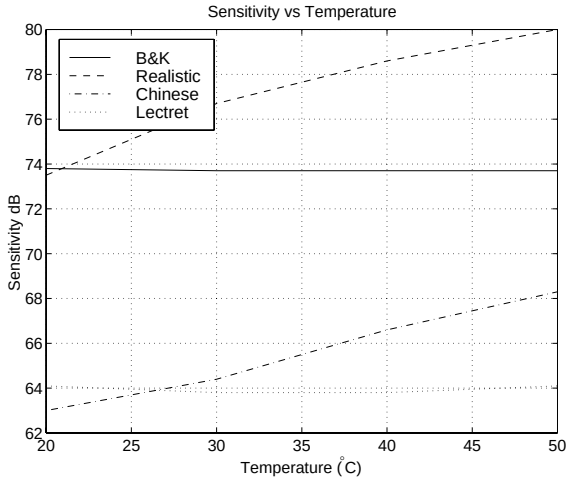

Figure 3.30: Effect of temperature on the microphone sensitivity for two electret microphones (Realistic and Chinese), an inexpensive condenser microphone (Lectret) and a B&K Type 4177 microphone. Courtesy of Dr Xiaojun Qiu.

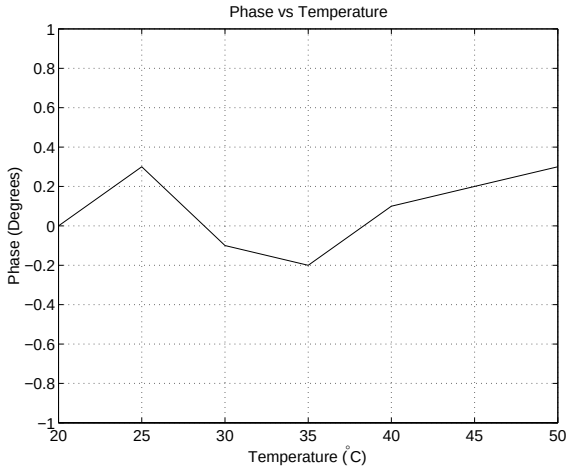

Figure 3.31: Effect of temperature on the microphone phase for the Lectret microphone. Courtesy of Dr Xiaojun Qiu.

A typical transfer function between two Realistic elements housed in a small enclosure is shown in Figure 3.32. As can be seen, the elements have a very similar response, with the magnitude error in the order of 0.1 dB and the phase error typically less than $\pm 1^{\circ}$. This is similar to the phase response reported by Sommerfeldt et al. (1995). The measurement

of the transfer function suffered from poor coherence below 50 Hz as a result of the inherent roll-off of the element sensitivity below 50 Hz.

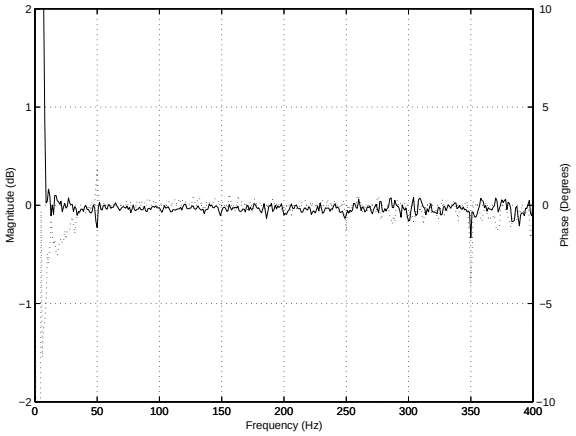

Figure 3.32: Back to back transfer function between two electret elements. Magnitude and phase are the solid and dotted line respectively.

In selecting suitable microphones it is necessary for them to be omni-directional (in both phase and magnitude). The electret element used for the energy density sensor described here had a polar phase variation of less than 1° and a polar sensitivity variation of less than 0.1 dB over the design bandwidth.

3.6.2 Optimal Microphone Spacing

In selecting a separation distance between the microphones it is important to achieve a balance between the errors arising from the linear distortion (phase, sensitivity and spatial errors) of the microphone channels and the errors associated with the finite separation errors. The lower frequency limit is constrained by magnitude of the linear distortion and the upper frequency limit constrained by the finite separation effects.

Based on the measured phase and magnitude errors for the electret microphones and the one-dimensional error analysis it was concluded that for the decade 60-600 Hz a microphone spacing of 50 mm would be optimal. However, it will be shown in Section 3.6.4 that this was somewhat optimistic since the signal conditioning required to calculate the

finite difference between elements introduced significant additional phase and sensitivity mismatch errors which were initially believed to be negligible. These errors arose from the poor components used in the electronic circuitry. In addition, the three-dimensional error analysis has shown that the error in the energy density estimate increases with increasing number of axes measured which also contributed to reducing the operational bandwidth effectively to half a decade.

3.6.3 3D Energy Density Sensor Design

Since the errors associated with the various energy density sensor designs do not significantly influence the level of noise reduction that can be achieved with control systems (see Chapter 4), the simplest arrangement was built, namely the 4-microphone energy density sensor shown as a third angle projection in Figure 3.33. Figures 3.34 and 3.35 show the 4-microphone sensor and the signal conditioning unit (SCU) which provides the necessary amplification and differentiation to output both pressure and particle velocity. The design and performance analysis of the SCU was originally done using SIMULINK within MATLAB. A SIMULINK schematic showing the basic operations of the SCU is shown in Figure 3.36. It should be noted that the second order Butterworth filters were not implemented in the current design but are intended to be used in a future SCU. The purpose of the RMS meter will be discussed later. A more detailed electronic circuit diagram of the signal conditioning unit is shown in Appendix C.

The energy density sensor signal conditioning unit provided the necessary amplification for the microphones, gain control on the microphone input channels and gain control over the velocity outputs. This allows microphones of different sensitivities to be used together. And more importantly, by adjusting the sensitivity to avoid clipping the sensor can be used over a very large dynamic range (˜150 dB) with an operating dynamic range exceeding 100 dB.

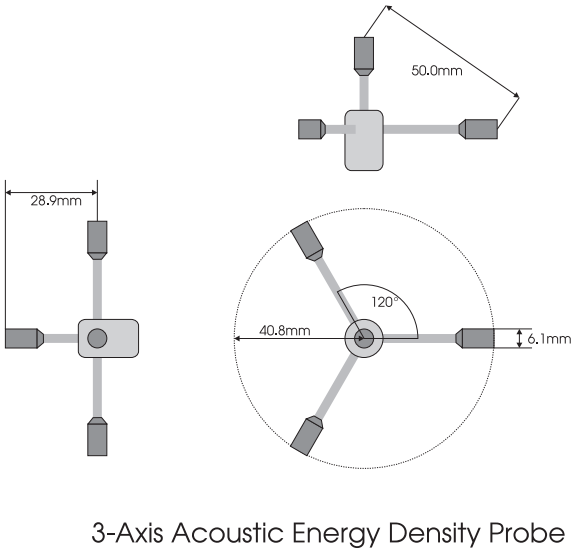

Figure 3.33: 4-Microphone 3-axis energy density sensor with 50 mm spacing.

Figure 3.34: 4-Microphone energy density sensor used for the experiments.

Figure 3.35: The signal conditioning unit housing the microphone amplifiers and differential amplifiers used to calculate mean pressure and particle velocity for three axes.

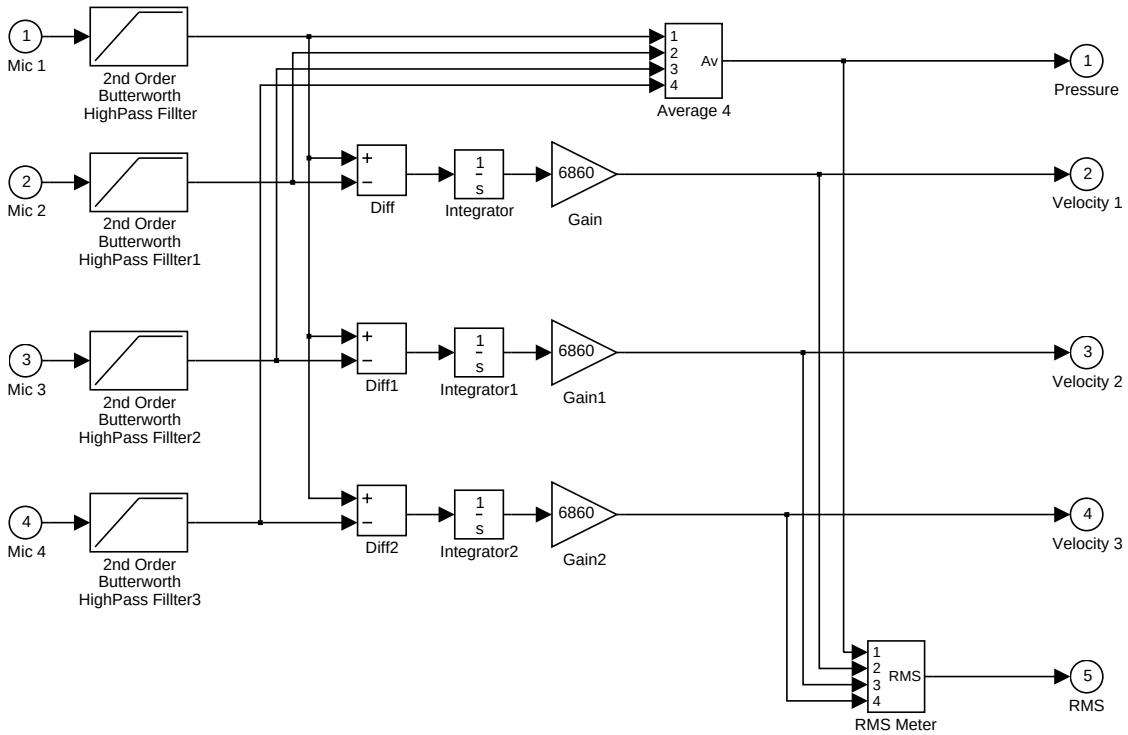

Figure 3.36: Simulink schematic of the signal conditioning unit.

The velocity outputs from the signal conditioning unit are multiplied by ρc so that when the sum of the squared outputs (pressure and the three orthogonal velocities) from the signal conditioning unit are minimised then the energy density is minimised. It should be noted that as the pressure and velocity signals are primarily used as error signals they could have been normalised to any value. However, since the energy density sensor was to be used in conjunction with other microphones it was decided that the pressure channels were to be normalised to unity (ie no gain) so that sensor and any additional microphone signals were weighted equally. This was equivalent to multiplying the absolute energy density by $2\rho c^2$ and consequently, should the calibrated energy density be required, then it was necessary to divide the sum of the squared outputs by $2\rho c^2$. Normalising Equation (3.7) by $2\rho c^2$ gives

$$\hat{E}_D(t) = p^2(t) + [\rho c v(t)]^2 \tag{3.172}$$

3.6.4 Performance

The microphones were calibrated using a specially adapted pistonphone. The gain pots on the signal conditioning unit were adjusted until the signals from all microphone channels were equal.

When building the sensor it was found that the electret microphones were very susceptible to damage during the soldering process. Although the sensitivity was not affected the phase was, which acted to degrade the performance of the sensor. Therefore, great care was taken to avoid overheating the elements during soldering.

It is inevitable that with analog electronic systems the response of the individual channels are not identical. This will therefore act to reduce the operating bandwidth of the sensor as shown in the previous sections. Figure 3.37 shows the pressure-pressure transfer function between the two electret elements previously shown in Figure 3.32 after pass-

ing through the signal conditioning unit. To compare the transfer functions between the sensor microphones a very small cavity and loudspeaker system was built to house the sensor. The first acoustic mode of the cavity was of the order of 1kHz so effectively the pressure was uniform throughout the cavity (although the velocity was not).

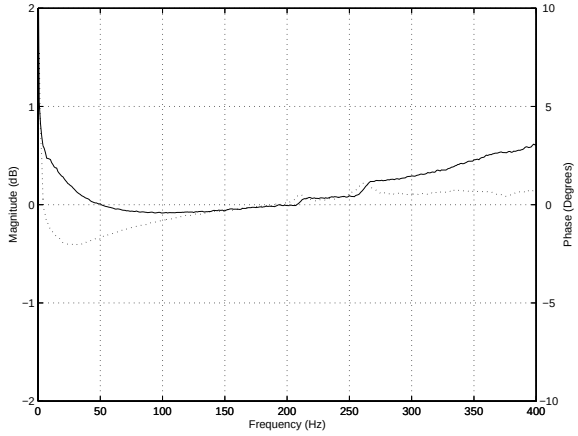

Figure 3.37: Back to back transfer function between two electret elements after the signal conditioning unit. Magnitude and phase are the solid and dotted line respectively.

Comparing Figures 3.37 and 3.32 it can be seen that the signal conditioning unit has indeed disturbed the phase and magnitude response of the channels. The magnitude error is less than 1dB and has a negligible effect on the energy density error within the design bandwidth. However, the phase error below 100 Hz is significant and below 50 Hz too large for accurate energy density measurements.

Looking at Figure 3.35 it can be seen that there are gain pots for the velocity channels. These allow sensors of different dimensions to be used with the signal conditioning box. The velocity channels were calibrated by the following procedure;

- The reference (origin) microphone input channel was grounded. This effectively sets one of the pressure channels to zero.

- A sound source (the calibrator) of known pressure amplitude was placed over the 3 other microphones on the sensor.

- The scaled velocity to pressure transfer function was measured.
- The gain pots were adjusted until the velocity to pressure transfer function was equal to $\frac{1}{k\Delta x}$ (10.92 for 100Hz with 50mm spacing).
- A double check was performed by switching the grounded and microphone channel and confirming that the velocity to pressure transfer function was equal to $\frac{1}{k\Delta x}$. Figure 3.38 shows the velocity spectrums created by grounding either the common microphone or the x-axis microphone. It can be seen that the two spectra are consistent in the design bandwidth.

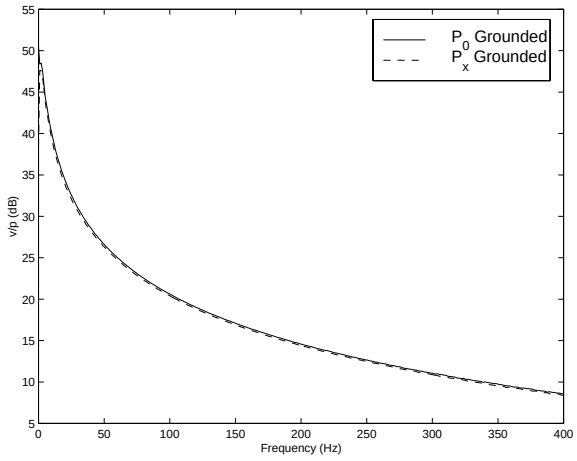

Figure 3.38: Velocity spectrum when grounding either one of the two microphones.

The velocity outputs from the signal conditioning unit were checked against a theoretical transfer function by placing the sensor in a small reactive broadband sound field. The velocity to pressure transfer function is plotted in Figure 3.39.

From 200 Hz to 400 Hz the particle velocity to pressure transfer function is the same as the predicted transfer function. Between 100 Hz and 200 Hz the transfer function has hit the noise floor of the velocity channel. Below 100 Hz the phase error seen in Figure 3.37 becomes significant, and below 50 Hz erroneous. For LMS control, the error in velocity does not significantly affect the energy density estimate provided that the velocity

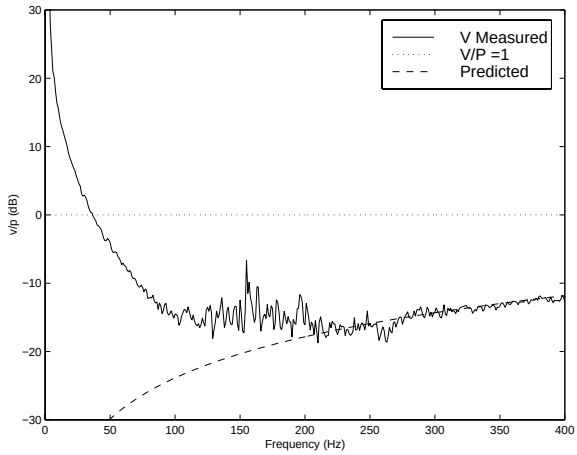

Figure 3.39: Velocity to pressure transfer function in a small reactive enclosure.

is significantly smaller than the pressure. Experience has shown that a "cross channel sensitivity" of 10 dB is quite acceptable, particularly for active control systems with a much greater number of error sensors than control sources. This would limit the use of the sensor to frequencies above 70 Hz and indeed it has been found that the sensor is effective down to approximately 70 Hz.

In active noise control applications it is essential that the error sensors have a large dynamic range (at least 100 dB) in order to continue to provide quality error signals once the control system is activated. Figure 3.40 shows the noise floor, the maximum broadband pressure (0 - 20 kHz) the velocity channels could tolerate before clipping and the equivalent maximum pressure level based on the op. amp rail voltage (3V). The dynamic range of the sensor for a single tone is approximately 110 dB. For broadband applications the energy is shared across a finite bandwidth so it is more appropriate to refer to the dynamic range as a power spectral density. To estimate the dynamic range for broadband applications it is necessary to divide the single tone dynamic range by the operating bandwidth, Δf in Hz, ie

$$10\log_{10}(PSD) = 110 - 10\log_{10}(\Delta f) \tag{3.173}$$

For a bandwidth of 20 kHz this gives a dynamic range of approximately 67 dB which is close to what was measured in Figure 3.40.

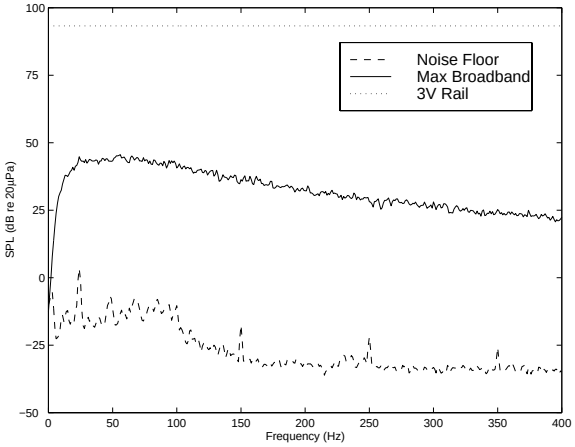

Figure 3.40: Power spectral density of noise floor and maximum levels of pressure and velocity.

Some thought went into the most appropriate form of output from the signal conditioning unit. For feedforward noise problems with a single dominant tone it is possible to have only a single output channel which is equal to the instantaneous energy density. This has the advantage of reducing the number of error signals in the control system. The process for obtaining the “DC” energy density would have been achieved by summing the squared time averaged level of the pressure channel and each of the three velocity channels (ignoring phase differences) and taking the square root as shown in the SIMULINK schematic in Figure 3.41. This DC level could then have been displayed on a liquid crystal display to indicate the approximate time averaged energy density as shown in Figure 3.36. Although not shown here, by multiplying the time averaged energy density level by the reference signal, a single time dependent error channel could be achieved. Howard & Hansen (1996) investigated the use of such a technique for the measurement and control of sound power with some success. However, this idea was discarded for the current design since it limited the sensors use to feedforward single tone applications - a small subset of ANC applications.

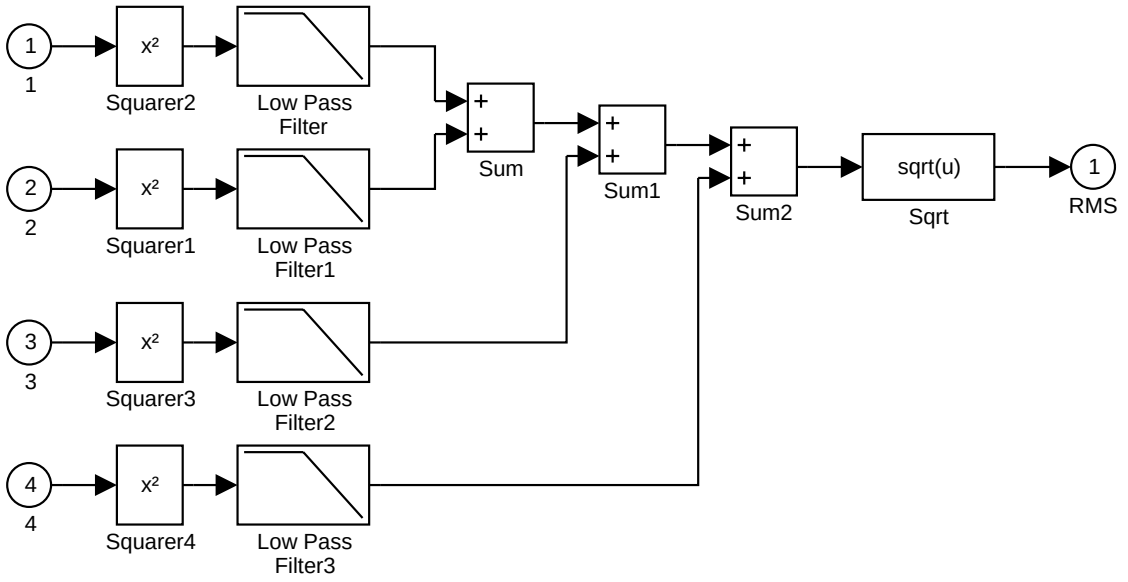

Figure 3.41: SIMULINK schematic of the "RMS meter" used to calculate the time averaged "DC" rms energy density.

Windshields were placed over the microphones to help remove the effects of any mean flow and turbulence on the velocity estimates. The effects of the wind socks on the microphone response were negligible over the design bandwidth.

3.6.5 Comments and Future Designs

Although the electronics associated with the current design proved to suffer from phase and magnitude errors, it has paved the way for future designs. Analog circuits have several advantages over digital systems, namely; they are significantly cheaper, tend to occupy less space and generally have smaller delays in processing. Therefore, a new analog signal conditioning unit is currently being built from higher grade surface mount components. This should help to remove the unwanted errors between channels and extend the low frequency limit at which the sensor can be used.

It was originally believed that the inherent low frequency roll-off of the microphones would be adequate in providing low frequency (<50 Hz) attenuation. This is necessary because of the way the velocity is calculated (see Equation (3.2)). Any error between

the two microphones at low frequencies results in extremely large errors in the velocity estimates because of the $1/\omega$ term. It was found in practice that the sensor was extremely sensitive to very low frequency noise such as doors closing and motion of the sensor itself and would cause overloading of the circuits. It is planned to add multi-pole high pass filters to future signal conditioning units to remove these adverse effects.

It has been shown that there is an optimum frequency range of operation for the energy density sensor and outside this bound the errors become significant and may interfere with the performance as an error sensor for active control applications. In the following chapter, the use of the energy density sensor as an error sensor will be investigated for a coupled enclosure. This will be compared against more traditional error criteria such as minimisation of squared pressures and acoustic potential energy.

Chapter 4

Active Control of Sound using Energy Density

In the previous chapter the issues surrounding the sensing of energy density were investigated, in particular the sensitivity of the energy density sensors to errors. This chapter will explore the effectiveness of using energy density as a cost function for active noise control as compared to acoustic potential energy and the sum of the squared pressures at discrete locations.

Energy density control has been numerically and experimentally investigated for the curved panel/cavity system detailed in Appendix A. For the numerical simulations, an uncoupled acoustic system and coupled structural-acoustic system have been studied with experiments on the coupled enclosure-panel system used to verify the results from the simulations.

It will be shown that the energy density sensors, in general, provide better results than an equivalent number of discrete microphones. For low modal density systems the sensors offer better global control (provided that there are sufficient sensors) and in high modal density situations the sensors offer much larger zones of local control. Despite the energy density sensor offering better local and global control, it will be seen that they still suffer

from the same limitations that microphones have, namely: as the modal density increases, the number of sensors needed to achieve global control increases; acoustically excited sound fields require fewer sensors to achieve global control than structurally excited sound fields; and as the damping increases control becomes more local.

4.1 Minimisation of Energy Density at Discrete Points

In order to conduct the numerical experiments on the vibro-acoustic model it necessary to develop a mathematical approach to solving the system of equations for the minimisation of the energy density at discrete points. The derivation in the following section is similar to that presented in Chapter 2 for minimisation of the sum of squared pressures at discrete locations.

It was shown that the time averaged energy density estimate at a point provided by a single energy density sensor is given by Equation (3.125) in Chapter 3, ie

$$E_D = \frac{1}{4\rho c^2}\mathbf{d}^{\mathrm{H}}\mathbf{d} \tag{4.1}$$

where $\mathbf{d}$ is the energy density column vector given by

$$\mathbf{d} = \begin{bmatrix} p \\ \rho c v_x \\ \rho c v_y \\ \rho c v_z \end{bmatrix} \tag{4.2}$$

For the finite element model, as with the physical measurement of energy density, the 3 orthogonal velocity vectors need to be derived from the pressure gradient and hence at least 4 closely spaced pressure estimates are needed. For the FE model this can be done

in two ways:

1. The first is to use the energy density sensor geometries discussed in Chapter 3 to estimate the energy density at a point. This requires that the positions of the sensor elements be co-located with the nodes of the acoustic elements. By doing so, the effectiveness of the various sensors in a control situation can be investigated. This approach also has the advantage that the magnitude of the error in the estimate can be determined approximately using the error analysis of Chapter 3. However, the technique requires modification of the FE model every time a sensor is added or moved, which requires some considerable effort.

2. The second technique is to use the closest 4 nodes to a point to determine the energy density at that point. This technique is adequate provided that the separation distances between the nodes are small relative to the wavelength. This technique has the advantage that the FE model does not need to be meshed every time the sensor configuration is changed. However, for models with coarse meshes the estimates may suffer from large errors and it does not allow the performance of particular sensor configurations to be investigated.

Both techniques have distinct advantages and disadvantages. The co-located technique has been used to look at the effectiveness of the various sensor configurations at high frequencies. The second technique has been used to compare energy density control with pressure squared control for several sensors.

4.1.1 Co-located Nodes

In terms of the measured quantities, ie acoustic pressures at the sensing locations, the energy density is given by

$$E_D = \frac{1}{4\rho c^2}\mathbf{p}_e^{\mathrm{H}}\mathbf{D}_i^{\mathrm{H}}\mathbf{D}_i\mathbf{p}_e \tag{4.3}$$

where $\mathbf{D}_i$ is given by Equations (3.118), (3.120), (3.122) or (3.124) and $\mathbf{p}_e$ is the column vector whose elements are the pressures at the locations of the sensor elements

$$\mathbf{p}_e = \Phi_e^{\mathrm{T}}\mathbf{p} \tag{4.4}$$

in which $\mathbf{\Phi}_e$ is the (n_a x n_d) column vector of (n_a x 1) acoustic mode shape function vectors $\phi(\vec{\mathbf{r}})$ evaluated at the n_d sensor microphone positions.

For control systems with l energy density sensors, the cost function is given by

$$\sum_{i=1}^{l}\frac{1}{4\rho c^2}\left[|p(\vec{\mathbf{r}}_i)|^2 + |\rho c v(\vec{\mathbf{r}}_i)|^2\right] \approx \sum_{i=1}^{l}\left[\frac{1}{4\rho c^2}\mathbf{p}_{e,i}^{\mathrm{H}}\mathbf{D}_i^{\mathrm{H}}\mathbf{D}_i\mathbf{p}_{e,i}\right] \tag{4.5}$$

where the left hand term in Equation (4.5) is the true sum of energy densities at the sensors, while the right hand term is the finite-separation estimate. The velocity term includes all three orthogonal velocity components, ie , $v(\vec{\mathbf{r}}_i) = v_x(\vec{\mathbf{r}}_i) + v_y(\vec{\mathbf{r}}_i) + v_z(\vec{\mathbf{r}}_i)$. Equation (4.5) can be written using matrix terms as

$$E_D = \frac{1}{4\rho c^2}\mathbf{p}_e^{\mathrm{H}}\mathbf{D}^{\mathrm{H}}\mathbf{D}\mathbf{p}_e \tag{4.6}$$

where $\mathbf{D}$ is the ($4l$ x $n_d l$) band diagonal energy density transfer function matrix, composed

of l (4 x n_d) sub-matrices, and may be written as,

$$\mathbf{D} = \begin{bmatrix} \mathbf{D}_1 & 0 & .. & 0 \\ 0 & \mathbf{D}_2 & .. & 0 \\ : & : & \ddots & : \\ 0 & 0 & .. & \mathbf{D}_l \end{bmatrix} \tag{4.7}$$

and $\mathbf{p}_e$ is the ($n_d l$ x 1) column vector of sensor microphone positions, composed of l sub-vectors of n_d microphone positions, where each sub-vector corresponds to the microphone positions for a single sensor.

Writing the energy density as a quadratic function with respect to the control sources gives

$$\sum_{i=1}^{l} \frac{1}{4\rho c^2} \left[|p(\vec{\mathbf{r}}_i)|^2 + |\rho c v(\vec{\mathbf{r}}_i)|^2 \right] = \begin{bmatrix} \mathbf{f}_c \\ \mathbf{q}_c \end{bmatrix}^{\mathrm{H}} \mathbf{A} \begin{bmatrix} \mathbf{f}_c \\ \mathbf{q}_c \end{bmatrix} + \begin{bmatrix} \mathbf{f}_c \\ \mathbf{q}_c \end{bmatrix}^{\mathrm{H}} \mathbf{b} + \mathbf{b}^{\mathrm{H}} \begin{bmatrix} \mathbf{f}_c \\ \mathbf{q}_c \end{bmatrix} + c \tag{4.8}$$

where $\mathbf{f}_c$ and $\mathbf{q}_c$ are the source strength vectors of the L_s control forces and L_a acoustic sources and

$$\mathbf{A} = \begin{bmatrix} \mathbf{A}_v & \mathbf{A}_{vq}^{\mathrm{H}} \\ \mathbf{A}_{vq} & \mathbf{A}_q \end{bmatrix} \tag{4.9}$$

$$\mathbf{b} = \left[\mathbf{Z}_a \mathbf{Z}_I^{-1} \Psi_c \;\; \mathbf{Z}_q^{-1} \mathbf{\Phi}_c \right]^{\mathrm{H}} \mathbf{Z}_w \mathbf{Z}_a \mathbf{v}_p \tag{4.10}$$

$$c = \mathbf{v}_p^{\mathrm{H}} \mathbf{Z}_a^{\mathrm{H}} \mathbf{Z}_w \mathbf{Z}_a \mathbf{v}_p \tag{4.11}$$

where $\mathbf{\Phi}_c$ is the (n_a x L_a) column vector of (n_a x 1) acoustic mode shape function vectors $\phi(\vec{\mathbf{r}})$ evaluated at the L_a control acoustic source locations. Likewise $\mathbf{\Psi}_c$ is the (n_s x L_s) column vector of (n_s x 1) structural mode shape function vectors $\psi(\vec{\mathbf{x}})$ evaluated at the

L_s control force locations. The uncontrolled sum of the mean square pressures is given by the scalar term c. The Hermitian weighting matrix $\mathbf{Z}_w$ is given by

$$\mathbf{Z}_w = \frac{1}{4\rho c^2}\mathbf{\Phi}_e^* \mathbf{D}^{\mathrm{H}} \mathbf{D} \mathbf{\Phi}_e^{\mathrm{T}} \tag{4.12}$$

The sub-matrices of the matrix $\mathbf{A}$ are the same as those used when controlling the sum of squared pressures at discrete locations, ie $\mathbf{A}_v$ is the matrix $\mathbf{A}$ for vibration control sources operating alone and is given by

$$\mathbf{A}_v = \mathbf{\Psi}_c^{\mathrm{H}} (\mathbf{Z}_I^{-1})^{\mathrm{H}} \mathbf{Z}_a^{\mathrm{H}} \mathbf{Z}_w \mathbf{Z}_a \mathbf{Z}_I^{-1} \mathbf{\Psi}_c \tag{4.13}$$

$\mathbf{A}_q$ is the matrix $\mathbf{A}$ for the acoustic control source operating alone, with elements given by

$$\mathbf{A}_q = \mathbf{\Phi}_c^{\mathrm{H}} (\mathbf{Z}_q^{-1})^{\mathrm{H}} \mathbf{Z}_w \mathbf{Z}_q^{-1} \mathbf{\Phi}_c \tag{4.14}$$

and the cross-coupling matrix $\mathbf{A}_{vq}$ is given by,

$$\mathbf{A}_{vq} = \mathbf{\Phi}_c^{\mathrm{H}} (\mathbf{Z}_q^{-1})^{\mathrm{H}} \mathbf{Z}_a^{\mathrm{H}} \mathbf{Z}_w \mathbf{Z}_a \mathbf{Z}_I^{-1} \mathbf{\Psi}_c \tag{4.15}$$

The optimum set of control forces and volume velocities which produce the unique global minimum value of the quadratic function in Equation (4.8) are given by Equation (2.61).

It should be noted that when the number of control sources is greater than or equal to the number of error sensors, ie an under constrained system of equations, the reduction in the total acoustic potential energy achieved using energy density control is the same as achieved by minimising the sum of the squared pressures at the microphone locations. This is because the energy density column vector, given by Equation (4.2), is simply

a linear combination of the pressure vector of the error sensors making up the sensor, and since the control matrix is semi-definite, any linear combination of the outputs from the error sensors will be driven to zero. When this is the case, the further constraint of minimising the control effort can be added to achieve a unique solution.

4.1.2 Arbitrary Nodes

The previous technique of using co-located nodes suffers from the difficulty that every time the sensor is moved to a new location, the FE modal needs to be re-meshed. A simpler approach is to estimate the pressure and pressure gradient at a particular location using four closely located existing points within the FE mesh. The following approach is only suitable when the non-dimensional microphone spacing is small, ie when $2kh < 1$ or $2h < \lambda/2\pi$. This is approximately the same constraint for modal analysis of FE models, namely that there be at least 6 elements per wavelength. Therefore, the following approach is suitable within the frequency bandwidth defined by the modal model.

Consider a point $\vec{\mathbf{r}}_0 = [\mathbf{x}_0, \mathbf{y}_0, \mathbf{z}_0]$ in the acoustic space where energy density control is wanted. The 4 closest nodes to this point are given by $\vec{\mathbf{r}}_1$, $\vec{\mathbf{r}}_2$, $\vec{\mathbf{r}}_3$ and $\vec{\mathbf{r}}_4$ respectively. A first order approximation to the pressure at each of the nodes using the pressure and pressure gradient at $\vec{\mathbf{r}}_0$ is given by

$$\begin{bmatrix} \hat{p}(\vec{\mathbf{r}}_1) \\ \hat{p}(\vec{\mathbf{r}}_2) \\ \hat{p}(\vec{\mathbf{r}}_3) \\ \hat{p}(\vec{\mathbf{r}}_4) \end{bmatrix} = \begin{bmatrix} 1 & \Delta x_1 & \Delta y_1 & \Delta z_1 \\ 1 & \Delta x_2 & \Delta y_2 & \Delta z_2 \\ 1 & \Delta x_3 & \Delta y_3 & \Delta z_3 \\ 1 & \Delta x_4 & \Delta y_4 & \Delta z_4 \end{bmatrix} \begin{bmatrix} p(\vec{\mathbf{r}}_0) \\ \frac{\partial p(\vec{\mathbf{r}}_0)}{\partial x} \\ \frac{\partial p(\vec{\mathbf{r}}_0)}{\partial y} \\ \frac{\partial p(\vec{\mathbf{r}}_0)}{\partial z} \end{bmatrix} \tag{4.16}$$

where, $\Delta x_i = x_i - x_0$, $\Delta y_i = y_i - y_0$, $\Delta z_i = z_i - z_0$ and $\hat{}$ represents the pressure estimate.

This can be rewritten in terms of the energy density column vector $\mathbf{d}$, ie

$$\begin{bmatrix} \hat{p}(\vec{\mathbf{r}}_1) \\ \hat{p}(\vec{\mathbf{r}}_2) \\ \hat{p}(\vec{\mathbf{r}}_3) \\ \hat{p}(\vec{\mathbf{r}}_4) \end{bmatrix} = \begin{bmatrix} 1 & -jk\Delta x_1 & -jk\Delta y_1 & -jk\Delta z_1 \\ 1 & -jk\Delta x_2 & -jk\Delta y_2 & -jk\Delta z_2 \\ 1 & -jk\Delta x_3 & -jk\Delta y_3 & -jk\Delta z_3 \\ 1 & -jk\Delta x_4 & -jk\Delta y_4 & -jk\Delta z_4 \end{bmatrix} \begin{bmatrix} p(\vec{\mathbf{r}}_0) \\ \rho c v_x(\vec{\mathbf{r}}_0) \\ \rho c v_y(\vec{\mathbf{r}}_0) \\ \rho c v_z(\vec{\mathbf{r}}_0) \end{bmatrix} \tag{4.17}$$

The right hand vector may be calculated by inverting the square matrix, ie the estimate of the energy density column vector using the four closest nodes is given by

$$\hat{\mathbf{d}}_a = \begin{bmatrix} \hat{p}(\vec{\mathbf{r}}_0) \\ \rho c \hat{v}_x(\vec{\mathbf{r}}_0) \\ \rho c \hat{v}_y(\vec{\mathbf{r}}_0) \\ \rho c \hat{v}_z(\vec{\mathbf{r}}_0) \end{bmatrix} = \mathbf{D}_a \begin{bmatrix} p(\vec{\mathbf{r}}_1) \\ p(\vec{\mathbf{r}}_2) \\ p(\vec{\mathbf{r}}_3) \\ p(\vec{\mathbf{r}}_4) \end{bmatrix} \tag{4.18}$$

where

$$\mathbf{D}_a = \begin{bmatrix} 1 & -jk\Delta x_1 & -jk\Delta y_1 & -jk\Delta z_1 \\ 1 & -jk\Delta x_2 & -jk\Delta y_2 & -jk\Delta z_2 \\ 1 & -jk\Delta x_3 & -jk\Delta y_3 & -jk\Delta z_3 \\ 1 & -jk\Delta x_4 & -jk\Delta y_4 & -jk\Delta z_4 \end{bmatrix}^{-1} \tag{4.19}$$

With the energy density column vector now available the energy density control simulations can proceed as per the co-located nodes. It is possible to improve the estimate of $\hat{\mathbf{d}}_a$ by increasing the number of nodes used in the estimate (provided the additional nodes also fit the necessary proximity constraint). If this is the case, the $\mathbf{D}_a$ matrix is non-square and requires the use of a pseudo (least squares) inverse to invert the matrix.

4.2 Numerical Simulation

For cavities with rigid walls, the particle velocity normal to the bounding surfaces is zero. Therefore, the rank of the control system matrix is reduced by one for each displacement degree of freedom that is zero and subsequently these control channels become redundant. For example, were a microphone placed in the corner of a rigid rectangular box, then the particle velocities in the 3 orthogonal directions are zero, so if the pressure is minimised, then all dof's at this point are zero, ie the energy density is minimised. Therefore if energy density control was used in such locations, then three out of the four control channels would be redundant. This property of rigid walls has certain advantages and has been used to extend the zones of quiet with pressure control in diffuse sound fields (Garcia-Bonito & Elliott 1995*a*, Garcia-Bonito, Elliott & Boucher 1997).

Consequently the benefit of energy density control is not fully realised at the boundaries of rigid cavities and therefore such cases have not been considered in the simulations. Rather, situations where it is not possible to place the microphones at zero velocity positions will be investigated.

Unfortunately, due to the constraints of the modelling approach used here (the specifics of which are detailed in Section 2.2.3), it is not possible to estimate the velocity from the pressure gradient at the boundaries. Hence energy density control at the boundaries of either compliant or absorptive walls (as the velocity at these boundaries will not be zero) cannot be modelled accurately.

Since the controller complexity is determined by the number of control channels, to draw comparisons between microphone error sensors and energy density error sensing, one must compare one ED sensor against 4 microphones. In some cases, 4 well placed microphones will provide better control than a single energy density sensor, particularly at very low frequencies. This is because the condition number of the control matrix ($\mathbf{A}$) for the 4 channel system using energy density moves from ∞ to unity as the modal density

increases. Therefore at low frequencies when the modal density is low, the number of truly independent channels goes from 1 to 4 so the real advantage of ED control is only realised in medium to high modal density systems.

As has been shown previously with primary acoustic excitation, very few acoustic modes tend to be excited, whereas structural excitation tends to drive many acoustic modes. These two cases provide a broad range of conditions for testing the sensor. At very high frequencies the cavity response begins to approach that of a diffuse field, particularly when the cavity is excited via the bounding structure and the modal damping is high.

It will be shown that the source of the primary excitation (acoustic or structural) will have a very significant effect on the level of global control that can be achieved, which is not only a control source issue but also a sensing issue. The global sensing of structurally excited sound fields is extremely difficult, particularly in close proximity to the vibrating boundary and therefore more sensors are required to achieve significant control.

4.2.1 Finite Element Model

The system used for the numerical study here was identical to the system in Appendix A which was used to verify the theory and software code. The finite element models of the shell and the cavity are shown in Figure 4.1 along with the locations of the structural and acoustic sources used during the simulations. The shell and the contiguous acoustic space were modelled separately using the FEA package ANSYS, then coupled using modal coupling theory (Fahy 1985) within MATLAB. The structural FE model consisted of 400 rectangular shell elements and 2646 degrees of freedom. The acoustic model consisted of 2000 acoustic brick elements and (coincidentally) 2646 degrees of freedom. The curved panel, with a curvature radius of 2.4 m, was made of 1.6 mm thick aluminium with simply supported end conditions. The other 5 walls of the cavity, measuring 0.985m x 0.420m x

0.250m, were made from 19mm medium density fibre-board (MDF) and were considered to be rigid. Damping of the system was light with the modal loss factor for both the structure and the cavity set to 2% unless otherwise stated. The material properties used for the simulation are shown in Table 4.1.

Medium	Material Property	Value
Air	Density	1.21 $\mathrm{kg/m^3}$
	Speed of Sound	343 $\mathrm{m/s}$
Aluminium	Thickness	1.6 mm
	Young's Modulus	70.3 GPa
	Density	2700 $\mathrm{kg/m^3}$
	Poisson's Ratio	0.35

Table 4.1: Material properties used for the finite element models.

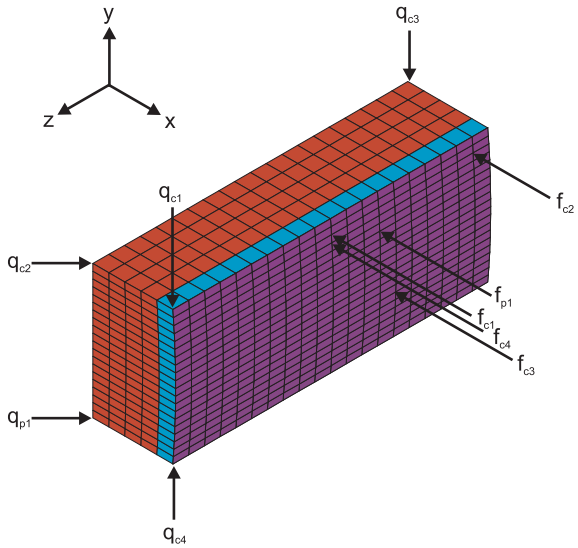

Figure 4.1: Curved panel - cavity system used for the numerical simulations. Purple - Structural shell elements, Cyan - Acoustic brick elements with structural dofs and Red - Acoustic brick elements without structural dofs. Nomenclature : q = volume velocity sources, f = structural forces, p = primary source and c = control source.

The first 30 acoustic modes and the first 100 normal structural modes were extracted using the finite element model described previously. The natural frequencies of the first

15 modes of the two un-coupled systems and coupled system are shown in Table 4.2.

Mode [y,z]	Coupled Frequency (Hz)	Un-Coupled Frequency (Hz)
$[1,1]_s$	73	58
$[2,1]_s$	94	95
$[2,2]_s$	117	118
$[1,2]_s$	135	145
$[2,3]_s$	158	159
$[0,1,0]_a$	185	175
$[3,1]_s$	205	206
$[2,4]_s$	207	209
$[1,3]_s$	212	215
$[3,2]_s$	219	219
$[3,3]_s$	241	243
$[2,5]_s$	256	258
$[1,4]_s$	259	261
$[3,4]_s$	276	277
$[1,5]_s$	290	293

(s = structural, a = acoustic)

Table 4.2: Natural frequencies of the coupled vibro-acoustic system.

4.2.2 Comparison of Energy Density Control for Different Sensor Configurations

The four types of sensors analysed in Chapter 3 were used for the following simulations. This allowed the effectiveness of the different sensors to be evaluated. To obtain the nodal pressures at the microphone locations it was necessary to define additional key-points in the FE model at these locations. This resulted in an additional 2 meshes, quite different from that shown in Figure 3.21; one for the 4 microphone sensors (as shown in Figure 4.2) and another for the 6/7 microphone energy density sensors. The mesh for the arbitrarily

selected nodes simulations was completely constructed from brick elements, whereas the other two had brick elements adjacent to the panel (so as to enable FE model of the panel to be used for all three acoustic FE models) with the rest meshed with tetrahedral elements. Tetrahedral elements are considerably stiffer than similar sized brick elements so some differences in the models are expected at the higher frequencies. Therefore, care should be taken when comparing the results between the three models. It was originally intended to use a single FE model for all the simulations but all attempts to get ANSYS to mesh the volumes in the solid model were unsuccessful. The FE model completely comprised of brick elements has been used in all subsequent sections because of the greater accuracy compared to the models containing the tetrahedral elements. The origin of the FE model is at the rear right-hand end of the model, mid way between the top and bottom sides. The centre of the model is therefore at $\begin{bmatrix} 0.125 & 0.000 & 0.493 \end{bmatrix}$.

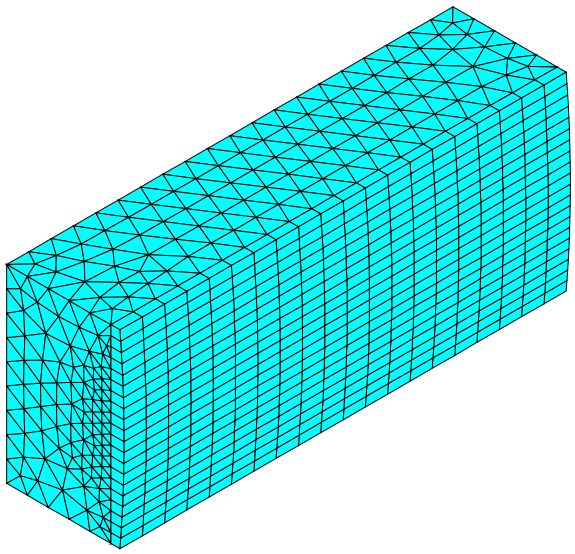

Figure 4.2: Curved panel - cavity system used for the numerical simulations of the 4-microphone energy density sensor.

The energy density sensors were located in the centre of the cavity (or as close as possible, in the arbitrary node case). This location was chosen since it is a very poor choice of sensor location when using microphones because it lies on the pressure nodal surfaces of many acoustic modes. The locations of the sensor microphones including the

acoustic centre of the sensor (a/c) were as follows:

Arbitrary nodes:
$$\begin{bmatrix} 0.104 & -0.021 & 0.493 \\ 0.155 & -0.021 & 0.493 \\ 0.104 & 0.000 & 0.493 \\ 0.104 & 0.000 & 0.443 \end{bmatrix} \text{ - a/c } \begin{bmatrix} 0.117 & -0.011 & 0.480 \end{bmatrix}$$

4 Microphone sensor:
$$\begin{bmatrix} 0.125 & 0.000 & 0.514 \\ 0.084 & 0.000 & 0.485 \\ 0.145 & 0.035 & 0.485 \\ 0.145 & -0.035 & 0.485 \end{bmatrix} \text{ - a/c } \begin{bmatrix} 0.125 & 0.000 & 0.493 \end{bmatrix}$$

4 Mic. w/o summer:
$$\begin{bmatrix} 0.125 & 0.000 & 0.514 \\ 0.084 & 0.000 & 0.485 \\ 0.145 & 0.035 & 0.485 \\ 0.145 & -0.035 & 0.485 \end{bmatrix} \text{ - a/c } \begin{bmatrix} 0.125 & 0.000 & 0.493 \end{bmatrix}$$

6 Microphone sensor:
$$\begin{bmatrix} 0.100 & 0.000 & 0.493 \\ 0.150 & 0.000 & 0.493 \\ 0.125 & -0.025 & 0.493 \\ 0.125 & 0.025 & 0.493 \\ 0.125 & 0.000 & 0.468 \\ 0.125 & 0.000 & 0.518 \end{bmatrix} \text{ - a/c } \begin{bmatrix} 0.125 & 0.000 & 0.493 \end{bmatrix}$$

7 Microphone sensor:

$$\begin{bmatrix} 0.100 & 0.000 & 0.493 \\ 0.150 & 0.000 & 0.493 \\ 0.125 & -0.025 & 0.493 \\ 0.125 & 0.025 & 0.493 \\ 0.125 & 0.000 & 0.468 \\ 0.125 & 0.000 & 0.518 \\ 0.125 & 0.000 & 0.493 \end{bmatrix} \text{ - a/c } \begin{bmatrix} 0.125 & 0.000 & 0.493 \end{bmatrix}$$

The reason for the difference in acoustic centres between the arbitrary node sensor and the other four configurations is that, when selecting arbitrary nodes, it is not possible to guarantee the geometric centre to be at the desired location. The reduction in acoustic potential energy when minimising potential energy and energy density at a point for the 3 FE models (5 configurations) are plotted in Figures 4.3, 4.4 and 4.5.

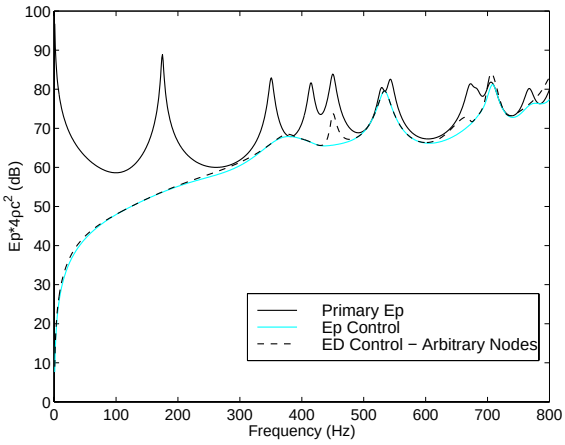

Figure 4.3: Energy density control for the energy density sensor with arbitrarily selected nodes. Acoustic primary source and a single acoustic control source.

There is very little difference in the primary and controlled acoustic potential energy levels between the 5 control configurations. To highlight the negligible differences between results obtained using the different control strategies, the performance offered by the four different sensor configurations (coincident nodes) is compared against that achieved using the four closest nodes (arbitrary nodes) to the desired location in Figure

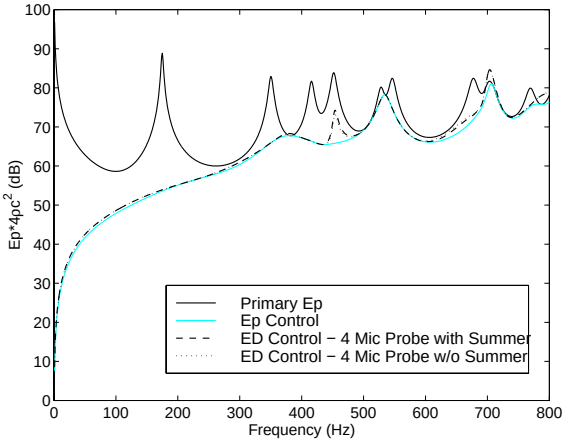

Figure 4.4: Energy density control for the 4 microphone sensor configurations. Acoustic primary source and a single acoustic control source.

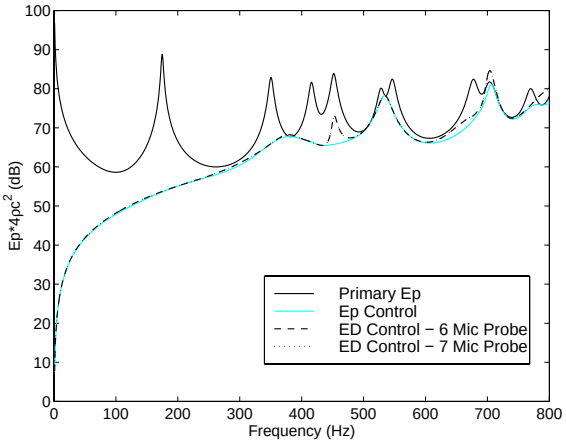

Figure 4.5: Energy density control for the 6 and 7 microphone sensor configurations. Acoustic primary source and a single acoustic control source.

4.6. The few small differences seen, for example form 780 to 800 Hz, can be quite easily attributed to the differences in the FE models rather than the control strategy.

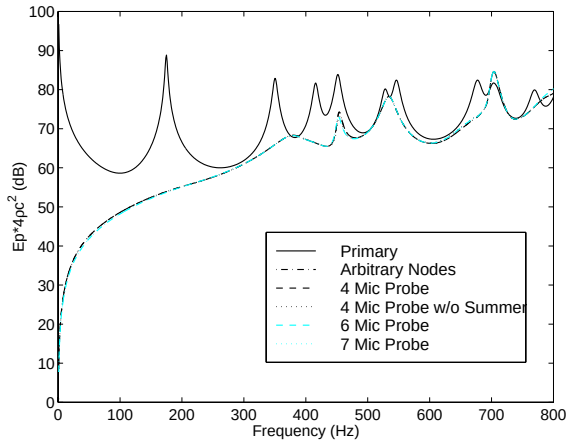

Figure 4.6: Energy density control for various sensor configurations. Acoustic primary source and a single acoustic control source.

Therefore, it can be concluded that the inherent errors arising from the finite spacing do not significantly degrade the level of control achieved and the control system appears to be highly tolerant of the errors in the energy density estimate. The technique of using arbitrary nodes to estimate the energy density appears to be adequate up to a non-dimensional separation, $2kh$, of 0.73.

4.2.3 Uncoupled Acoustic System

All previous studies on energy density control have been on rigid walled enclosures with a single acoustic control source; one-dimensional ducts (Sommerfeldt & Nashif 1991, Nashif & Sommerfeldt 1992, Sommerfeldt & Nashif 1992, Sommerfeldt & Nashif 1994, Park & Sommerfeldt 1997) and a rigid walled rectangular box (Sommerfeldt et al. 1995). It was decided to use a 3D purely acoustic system for the initial investigations since: this is the basis of the simplest acoustic system; the simulations were much quicker than the fully coupled models and the results for energy density control in purely acoustic fields are well known. Having confirmed the findings from previous studies, the current work

will investigate the effects on global control of increasing the number of control sources above one per energy density sensor and it will be shown that this does not necessarily lead to a decrease in the global sound field. The use of multiple energy density sensors will be investigated along with the performance of energy density control in heavily damped enclosures. Finally, the control system will be extended to a structurally excited, fully-coupled vibro-acoustic system.

The cavity shown in Figure 4.1 was uncoupled from the structure in order to investigate the effectiveness of energy density control in a purely acoustic system and reduce the computation times. A single primary acoustic source was applied to the corner of the cavity [0.000, -0.209, 0.985] and a control source located at [0.250, 0.209, 0.985] was used. For all the simulations the systems were lightly damped (unless otherwise noted) with modal loss factors for both the cavity modes and the structural modes set at 2%, ie $\eta_a = 2\%$ and $\eta_s = 2\%$.

The performance of various cost functions are compared in Figure 4.7: Potential energy, energy density at a point, sum of the squared pressures at the 4 sensor microphones and the acoustic pressure at one of the sensor microphones. Figure 4.8 compares the level of control offered by 4 microphones placed in the box corners against energy density control and potential energy control.

The following observations can be made in reference to Figures 4.7 and 4.8. As expected, the single microphone offers the least control. The sum of the squared sensor microphone pressures performs well but still suffer from spillover. Control of the sum of the squared pressures of the 4 (corner) microphones performs as well as energy density control (Figure 4.8). Therefore, with a single control source it is clear that in general energy density control out performs all other cost functions with the exception of the 4 corner microphones, where the level of control is similar. Although not shown here, if the 4 microphones were located at random, then energy density control certainly outperforms the minimisation of the squared pressures of 4 microphones. This is the same conclusion

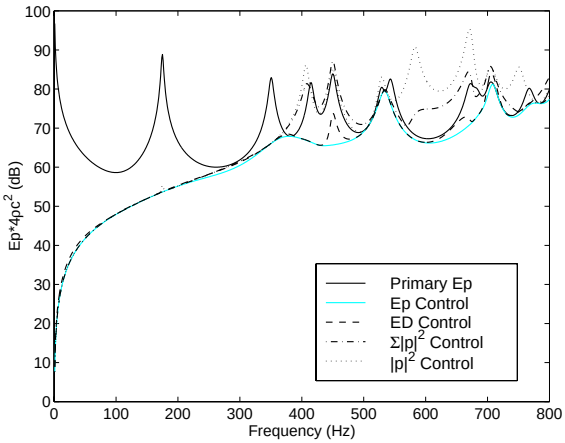

Figure 4.7: Potential energy reduction using several control strategies: potential energy, energy density, the squared pressures at the 4 energy density sensor microphones and the pressure at a single energy density sensor microphone. Acoustic primary source and a single acoustic control source.

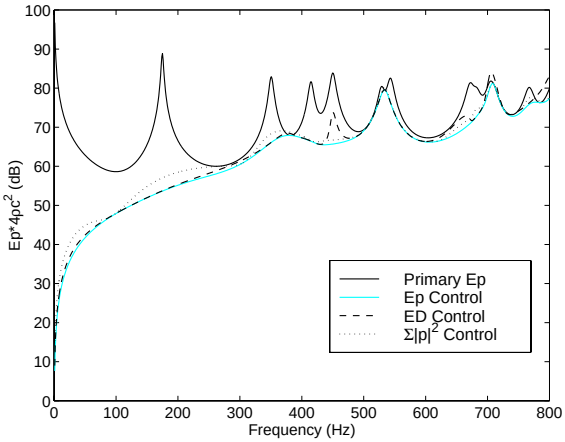

Figure 4.8: Potential energy reduction using several control strategies: potential energy, energy density and the squared pressures at 4 microphones placed in the corners of the enclosure. Acoustic primary source and a single acoustic control source.

that all other researchers have found. It will be shown in the following section that this does not necessarily hold for different control system configurations.

Sommerfeldt & Parkins (1994) found that control using energy density was relatively insensitive to sensor placement within the cavity. This finding should be clarified further; by adding the statement “provided that the sensor is not adjacent to the wall”. In Figure 4.9 the reduction in potential energy is compared for two sensor locations: the original location used in the previous figures and another at the centre of the cavity in the middle of the two short axes and a quarter of the way along the long axis at [0.117, -0.011, 0.726]. It can be seen that indeed the effect of the sensor position on the global control is small.

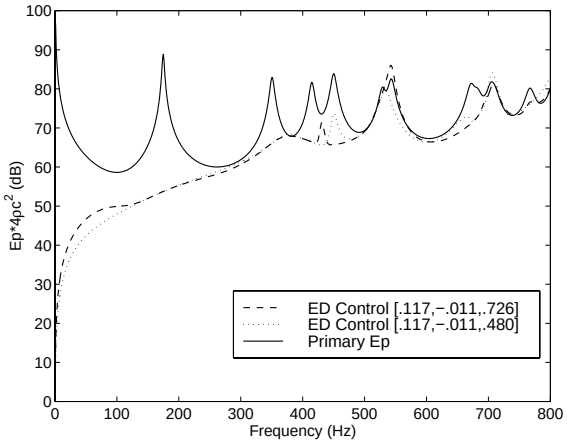

Figure 4.9: The effect of sensor location on global for a single acoustic control source. Acoustic primary source and a single acoustic control source.

4.2.3.1 Multiple energy density sensors

Theoretically, the estimate of the acoustic potential energy and therefore global control throughout the cavity should improve as more energy density sensors are used. Figure 4.10 shows the effect of adding another sensor. The two sensor positions were the same as for the example above. As can be seen, the level of control improves as the potential energy estimate is improved. The single energy density sensor suffers from observability problems around 450 and 650 Hz and therefore control is poor. The additional sensor has

overcome this problem.

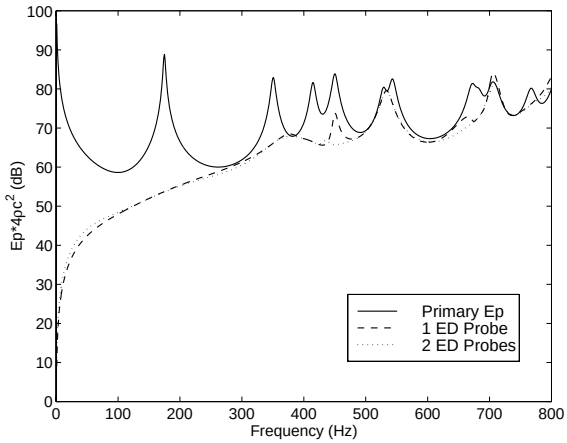

Figure 4.10: The effect on global control when the number of energy density sensors is increased from 1 to 2 with a single control source. Acoustic primary source and a single acoustic control source.

4.2.4 Energy Density Control for Several Control Sources and Several Sensors

As mentioned previously, all the previous studies of energy density control in enclosures have only considered a single control source[1]. The effect the number of control sources has on the control performance has been investigated with some surprising results and may explain the lack of published data on multiple control sources.

The acoustic potential energy achieved when minimising the sum of the squared pressures at the 4 sensor microphones is compared against minimising the energy density using 1, 2, 3 and 4 control sources in Figures 4.11, 4.12, 4.13 and 4.14 respectively. These control sources were located in the cavity corners at [0.250, 0.209, 0.985], [0.000, 0.209, 0.985], [0.000, 0.209, 0.000] [0.250, -0.209, 0.985] and respectively. The number of control sources relative to the number of error sensors determines the level

[1]This statement was true at the time the material presented here was written. However, some work on multiple control sources has also been investigated by John Parkins, “Active minimization of energy density in a three-dimensional enclosure”, Ph.D. Dissertation, Pennsylvania State University (August, 1998).

of constraint for the control system. An increase in the ratio of control sources to error sensors reduces the level of constraint. Therefore, the control systems in Figures 4.11, 4.12, 4.13 and 4.14 relate to a heavily constrained, moderately constrained, lightly constrained and an optimum system respectively. The control system with only a single control source Figure 4.11 shows that minimisation of energy density provides very good control of the potential energy with a single control source. However, minimisation of the sum of the squared pressures leads to poor control at higher frequencies as the modal density increases. This is because the sensor is located in a poor position to measure the odd ordered modes and hence the biasing of the even order modes over the odd order modes leads to significant modal spill over.

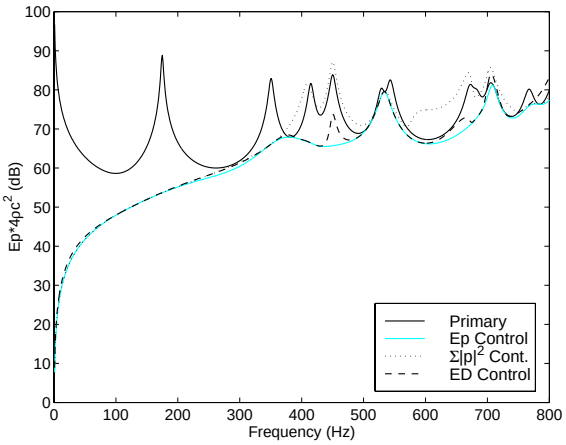

Figure 4.11: Control of energy density or squared pressures of the 4 sensor microphones for a heavily constrained control system - A single acoustic control source.

Figures 4.12 and 4.13 show that both control strategies suffer from control spillover, although the squared pressure control is generally worse than the energy density control. The spillover is not helped by the placement of the control sources: the control system with 2 control sources is unable to provide independent control to the modes with components along the y and z axis, and the control system with 3 control sources is unable to provide independent control along the y axis. This is discussed in more detail below.

In Figure 4.14 it can be seen the level of control achieved by the two techniques is

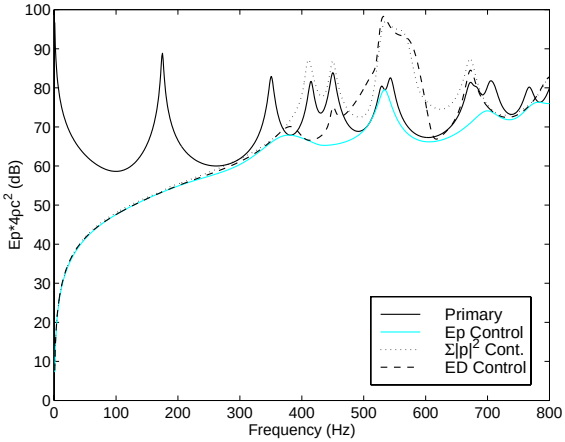

Figure 4.12: Control of energy density or squared pressures of the 4 sensor microphones for a moderately constrained control system - 2 acoustic control sources.

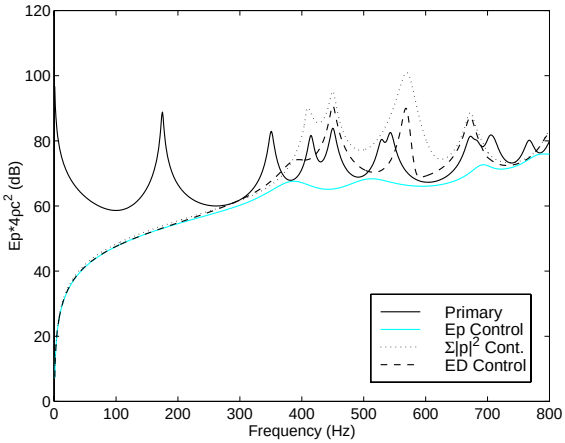

Figure 4.13: Control of energy density or squared pressures of the 4 sensor microphones for a lightly constrained control system - 3 acoustic control sources.

identical when the system is optimum or under-constrained, ie there are as many or more control sources as there are error channels (4 in this case) respectively. This is obvious since if the pressure amplitudes at the microphones are zero then the gradient must also be zero. This also holds true for multiple energy density sensors. By setting the pressure and particle velocity to zero the four control sources have effectively created an energy density node[2]. Another thing to note is the maximum permissible reduction in the potential energy is significantly larger than in Figure 4.13. This is because the control system has sufficient control sources to independently control modes along all the three orthogonal axis.

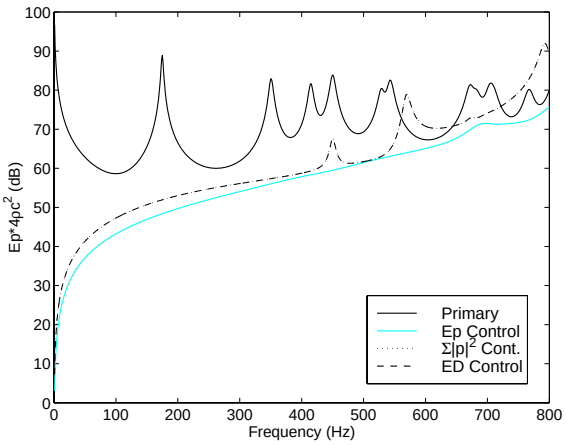

Figure 4.14: Control of energy density or squared pressures of the 4 sensor microphones for an optimum constrained control system - 4 acoustic control sources.

Initially it was expected that additional control sources would lead to a further reduction of the potential energy in the cavity. Figures 4.11, 4.12, 4.13 and 4.14 show that in fact increasing the number of control sources from 1 to 2 has lead to an increase in the internal potential energy in the cavity. With 3 control sources, the modal spillover is reduced somewhat and the control system shows an improvement against the control with 2 control sources. Only with 4 control sources did the control system show an improvement over the single control source. In conclusion, by comparing Figures 4.11 and 4.14, additional control sources lead to a slight improvement in global control at low frequencies

[2]The expression energy density node was suggested by S.D. Sommerfeldt.

to the expense of the high frequency region. To the authors knowledge this has not been explicitly reported previously.

Furthermore, if the number of control sources is equal to the number of independent control channels, it is debatable as to whether energy density control provides any improvement to the control system over simply minimising the sum of the squared pressures at the sensor microphones.

The disappointing level of global control seen when increasing the number of control sources cannot be completely attributed to lack of independent control of each axis, since the control system with 4 control sources still shows modal spillover at the higher frequencies even though there are an adequate number of control sources. It is believed that the other factor contributing to the poor performance is the control process moves from modal control to modal re-arrangement as the number of control sources is increased. Modal reduction will always lead to global control provided that the modes are orthogonal. However, in the case of an equal number of error channels and control sources, modal rearrangement is the only mechanism by which all channels can be driven to zero. Hence, this often leads to modal spill-over and subsequently an increase in the overall energy of the system. A similar effect is seen when minimising the sum of the squared pressures of the four corner microphones shown in Figure 4.15. In fact, the effect of modal rearrangement on the internal potential energy when using discrete microphones is significantly worse than when using energy density control. This phenomenon can be summarised by Figure 4.16. As the ratio of the number of control sources to the number of error sensors approaches unity, the control process moves from modal control to modal rearrangement. In doing so, the control becomes more local to the error sensors.

In Figure 4.17 the effect on the internal potential energy when minimising the energy density at two points, namely [0.117, -0.011, 0.480] and [0.117, -0.011, 0.726], using two acoustic control sources located in the cavity corners at [0.250, 0.209, 0.985] and [0.000, 0.209, 0.985] is shown. Similarly, the number of sensors and control sources

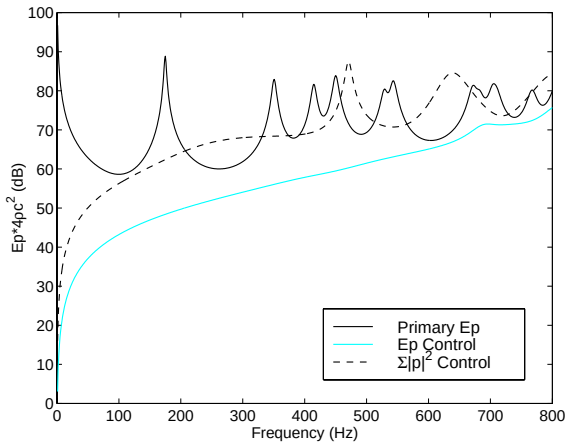

Figure 4.15: Control of the sum of the squared pressures at 4 corner microphones for 4 acoustic control sources.

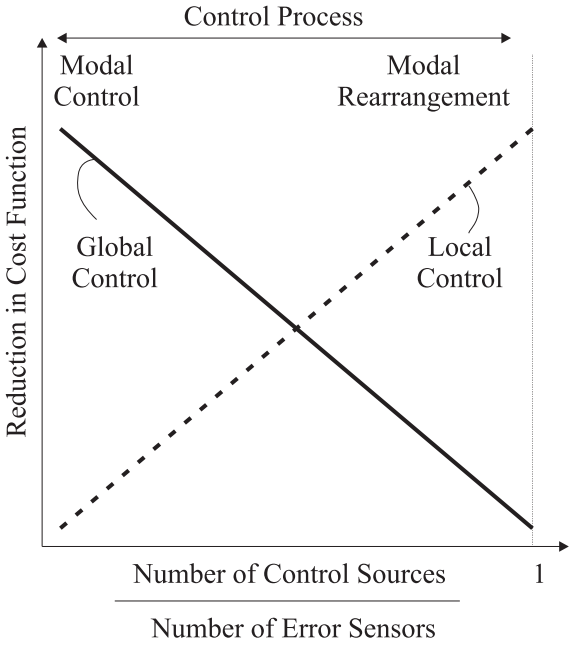

Figure 4.16: Schematic showing the effect of the number of control sources on the control process.

were increased to 4 each and the results are shown in Figure 4.18. The energy density sensors have their geometric centres at [0.117, -0.011, 0.480], [0.117, -0.011, 0.726], [0.217, 0.090, 0.380] and [0.217, 0.090, 0.626], and acoustic control sources were located in the cavity corners at [0.250, 0.209, 0.985], [0.000, 0.209, 0.985], [0.000, 0.209, 0.000] [0.250, -0.209, 0.985]. It can be seen that the modal spill-over for both cases, is generally small and that the schematic of Figure 4.16 is still relevant for multiple sensors. The energy density control when using 2 control sources shows some spillover between 500 Hz and 600 Hz. This is to be expected since the control source configuration is unable to independently control the y or z components of the acoustic modes. A more intelligent placement of the control sources (in opposite corners from each other) would have overcome this problem. This issue does not arise when the 4 control sources are used and subsequently spillover is very small.

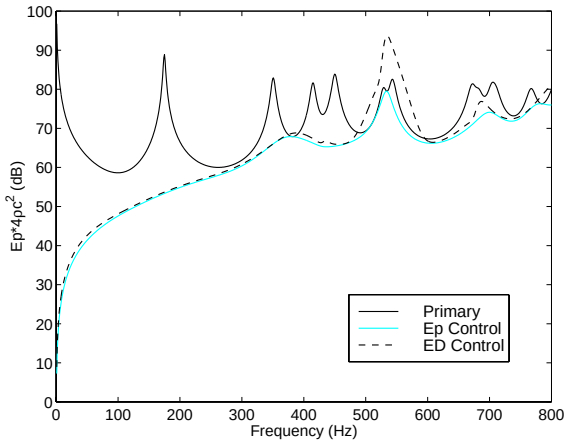

Figure 4.17: The effect on global control when the number of energy density sensors is increased from 1 to 2 with two acoustic control sources.

4.2.5 Moderately Damped Acoustic System

The modal loss factor of the cavity modes was increased from $\eta_a = 2\%$ to $\eta_a = 10\%$ to emulate the conditions that occur in many transport vehicle cavities. In practice the damping may be even higher than the value chosen here. However, the assumptions used

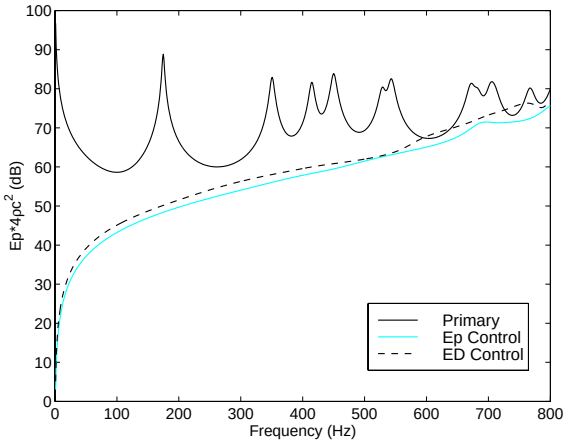

Figure 4.18: The effect on global control when the number of energy density sensors is increased to four with four acoustic control sources.

for the theoretical modal model become invalid if the damping becomes too high. The damping level at which the assumptions break down depends heavily on the particular system. Damping has the effect of increasing the modal overlap of the system.

Two control systems configurations were investigated: single channel control and 4 channel control. A single acoustic control source was used to minimise the energy density and pressure at a microphone. The level of global control at the resonances is reduced as seen by comparing Figure 4.19 with Figure 4.7. However, off-resonance the level of control for the lightly damped and moderately damped system is similar. Above 300 Hz the modal overlap becomes too high for effective global control, resulting in modal spillover for the single microphone and poor control for energy density and potential energy control.

In the second configuration, four acoustic control sources were used to minimise the energy density and pressure at a microphone (with the additional constraint of minimising the control effort). The level of global control is once again reduced as seen by comparing Figure 4.20 with Figure 4.14. By also minimising the control effort when controlling the pressure at the single point, modal spillover tends to be reduced.

Above 400 Hz the modal overlap is too high for a single control channel to provide

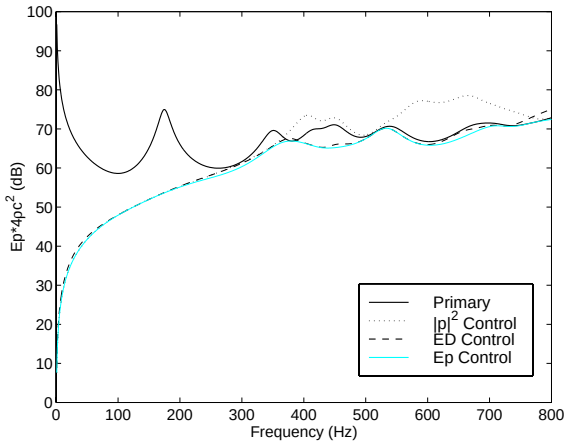

Figure 4.19: Potential energy : Comparison of energy density control versus single pressure squared control at a point in a heavily damped acoustic system with a single acoustic control source.

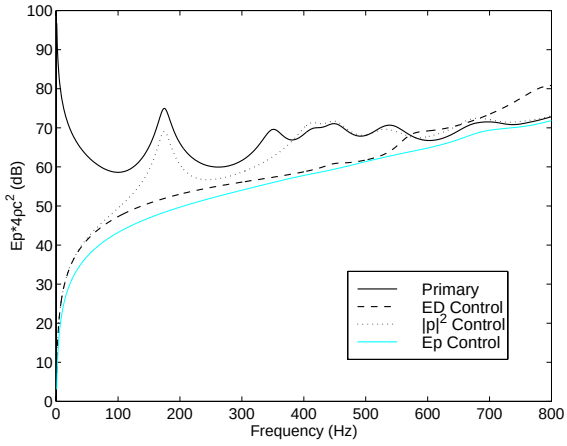

Figure 4.20: Potential energy : Comparison of energy density control versus single pressure squared control at a point in a heavily damped acoustic system with 4 acoustic control sources.

a good estimate of the potential energy and likewise, above 550 Hz the modal overlap is too high for the 4 channel energy density control to be effective at reducing the potential energy. And above 600 Hz even minimising the acoustic potential energy leads to very little reduction in the global sound field. This situation is very common with active noise control systems within heavily damped enclosures when the modal overlap is high. Therefore in these situations, rather than looking at the global potential energy, it is more beneficial to look at the reduction in sound pressure level versus distance from the error sensor. The reduction of the sum of the squared pressures was calculated at various distances away from the source. This was done by finding all the nodes which lay within a volume defined by two spheres of differing radii as shown in Figure 4.21. The radius step size Δr was set equal to h, ie half the separation distance used for the energy density sensor. Both the primary and controlled sum of the squared pressures for all these nodes was calculated for all frequencies. These values were then averaged over the frequency range 600 to 700 Hz and plotted in Figure 4.22. This narrow frequency range was chosen for two reasons: the modal density was high enough to show no reduction in the potential energy but the frequency was low enough so as not to cause too large an error in the energy density estimate; and, in order to plot the attenuation versus separation distance normalised to the wavelength, it was necessary to use a narrow frequency range.

The microphone squared pressure control shows very localised control, for both 1 and 4 control sources. The modal spillover when using a single control source with the microphone is very evident in Figure 4.22. The attenuation versus distance for energy density control using a single control source shows very poor local control in the pressure field. This is because between 600 Hz and 700 Hz the acoustic field is dominated by the 8th, 9th and 10th acoustic modes which all have pressure nodes in the centre of the cavity (where the sensor is located) and subsequently most of the control effort is spent reducing the particle velocity rather than pressure. This results in a reduction in the pressure field away from the error sensor but not adjacent to the sensor where the pressure nodes exit.

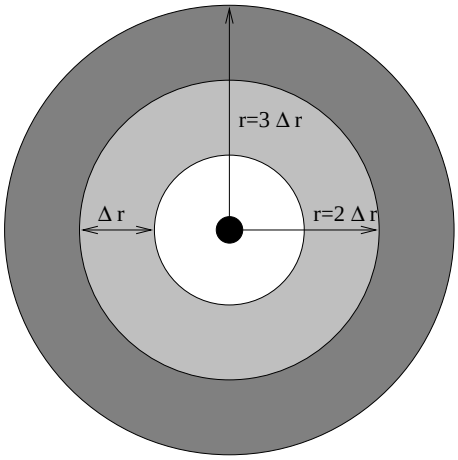

Figure 4.21: Diagram showing the process of calculating the attenuation in pressure versus distance from the error sensor using successive concentric spheres.

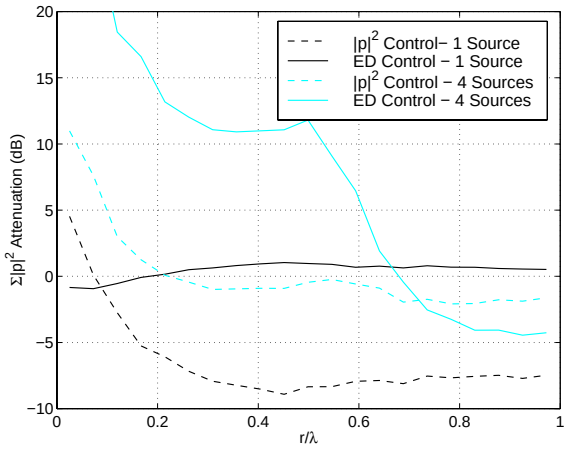

Figure 4.22: Attenuation in the sum of the FE nodal squared pressures as a function of the distance from the error sensor. The frequency range is from 600 to 700 Hz, with the separation distance normalised to the wavelength at 650 Hz.

However, despite the poor local control, the technique does not result in increases in the potential energy far from the sensor as do the optimal control system arrangements when all the error signals can be driven to zero, ie minimisation of the energy density with 4 control sources or minimisation of the pressure at a single microphone (with either one or four control sources).

The following discussion is only concerned with the optimal control cases when modal spillover is low, namely microphone pressure squared control and energy density control with 4 control sources. It is clear that energy density control produces a much larger zone of quite around the error sensor compared to a single microphone. If 10 dB is set as the limit of the zone of quiet then the zone of quiet offered by a single microphone is approximately a sphere with a radius of just over $\lambda/20$, where λ is the acoustic wavelength. The radius of the 10 dB zone of quiet when minimising energy density is approximately $\lambda/2$.

The results are very similar to that reported by Garcia-Bonito & Elliott (1995*b*) and Elliott & Garcia-Bonito (1995) when minimising the pressure and pressure gradient in a diffuse sound field. This is not surprising since the Schroeder frequency of the current system is 784 Hz, which defines the frequency above which the system is approximately diffuse (Sum & Pan 1998). Elliott et al. (1987) showed that when controlling the pressure at a point in an enclosure with a high acoustic modal densities (above the Schroeder frequency), the controlled sound field around the microphone was very similar to that around a microphone in a diffuse sound field. The authors found that when controlling pressure at a point in a diffuse sound field with a remote acoustic source the extent of the 10 dB zone of quite was a sphere with a radius of $\lambda/20$. They also found that when minimising the pressure and the pressure gradient in a single direction the result was a 10 dB ellipsoid with a shortest radius of approximately $\lambda/20$ and a longest radius of approximately $\lambda/4$.

It is interesting to note that the size of the zones of quiet in both the diffuse sound field and the damped reactive field are very similar, although the zones of quiet are slightly

larger for the damped reactive system discussed in this thesis. There are a number of reasons why this may be the case: the number of nodes used in the first sphere of the pressure squared control case were few and subsequently the standard deviation of the reduction is large; the response of the cavity is still modal and hence the effect of control extends well beyond the adjacent area of the sensors; and the previous studies of pressure and pressure gradient control in a diffuse sound field were for a single axis, if the control were to be extended for three dimensions, then it is possible that the radius of the zone of quiet in the diffuse field would increase from $\lambda/4$ to $\lambda/2$.

Therefore one may conclude that in high modal overlap acoustic systems where it is not possible to achieve global control, energy density control still offers significant advantages over pressure squared control by greatly extending the zone of quiet achieved.

4.2.6 Coupled System - Primary Acoustic Source

The simulations for the uncoupled acoustic system showed that using minimisation of energy density as a control strategy is very successful in minimising the acoustic potential energy provided that the number of error channels per control source was high. The acoustic model has been extended to include a coupled curved panel. The coupled structure has the obvious effect of modifying the eigenvalues of the cavity and coupling all acoustic modes so that they are no longer truly orthogonal. This also has the effect of increasing the modal density of the acoustic system.

Figure 4.23 shows the reduction in potential energy using a single acoustic source for several control strategies, namely minimising the following: acoustic potential energy, energy density at a point and the squared pressures from the 4 sensor microphones. The results are very similar to those of the uncoupled acoustic system as seen in Figure 4.11.

From Figure 4.23 it appears that the cross-coupling between acoustic modes from the structure does not significantly influence the global control performance with energy

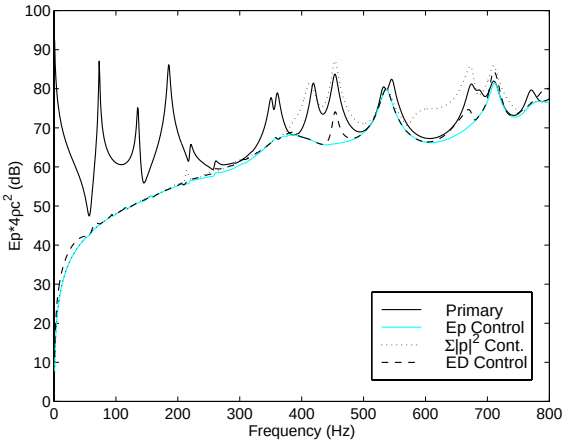

Figure 4.23: Potential energy reduction using ED control vs control of squared pressures from the 4 sensor microphones in a coupled acoustic system with an acoustic primary source and a single acoustic control source.

density control.

4.2.7 Coupled System - Primary Structural Source

A coupled vibro-acoustic system driven by the structure is probably the most common system used as a target of active control of noise in enclosures. It is typically the most difficult to treat since the structure tends to excite many more acoustic modes than do an equivalent number of monopole acoustic sources, due to interface modal filtering between the structure and the cavity. With more acoustic modes excited, more control sources are required to achieve the same level of control. Also, since the structural modes typically have a shorter wavelength compared to the acoustic modes, acoustic fields excited by the structure tend to exhibit much greater spatial variance which creates observability problems, as will be seen.

Two types of control system minimising the sound transmitted will be investigated: interior acoustic control sources; and surface mounted structural control sources. A single primary structural source with unit driving force was used, placed in a non-symmetrical position, $[0.250, 0.105, 0.328]$ so that all structural modes were excited directly. The direct

application of the force was chosen in preference to an external acoustic excitation such as a traveling wave because it is spatially white making sensing and control much more difficult. If the excitation was from an external acoustic field then the interior sound field would not contain significant contributions from the higher order acoustic modes and the results would be much like that for an interior acoustic source.

4.2.7.1 Primary structural excitation with acoustic control sources

Figure 4.24 shows the reduction in potential energy using a single acoustic control source when minimising either the energy density or the pressure at a single sensor microphone. As would be expected, the energy density control is generally a much better control strategy than simply minimising the pressure at a single sensor microphone.

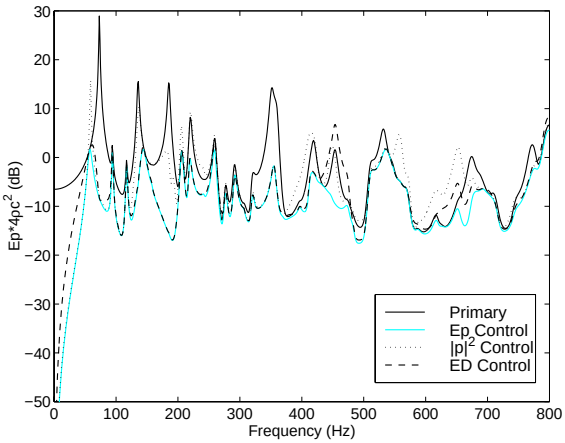

Figure 4.24: Potential energy reduction using ED control vs control of the squared pressure at a single sensor microphone in a coupled acoustic system with a single structural primary source and a single acoustic control source.

The same system was also investigated using 4 acoustic control sources, minimising the energy density and minimising the pressure at a single position (with the additional constraint of also minimising the control effort). The results are shown in Figure 4.25. It can be seen that energy density control does suffer significant control spillover, even more than single pressure squared control.

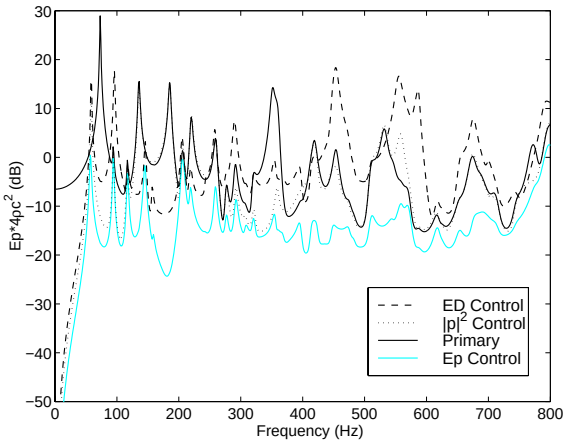

Figure 4.25: Potential energy reduction using ED control vs control of pressure at a single point in a coupled acoustic system with a single structural primary and 4 acoustic control sources.

Because of the poor performance of optimum energy density control in reducing the acoustic potential energy a second energy density sensor was added to increase fidelity of the collective error sensors. As can be seen in Figure 4.26 the controlled acoustic potential energy is substantially reduced. Therefore, the results show that if global control is the objective for any cost function derived from discrete sensors, broadly speaking there must be a greater number of error sensors than control sources. The system above, with a primary structural source and acoustic control sources, is particularly prone to modal spill-over since the primary source does not necessarily efficiently excite the same modes as the acoustic control sources. In the following section it will be seen that this is indeed the case, and when structural control sources are used the level of spillover is reduced.

With reference to the results shown in Figure 4.25, the attenuation versus distance resulting from minimisation of the pressure at a single microphone and the energy density using four control sources is plotted in Figure 4.27. As was done in Section 4.2.5, the attenuation vs distance has been calculated over the small frequency range of 600 Hz to 700 Hz to allow the separation distance to be normalised to the wavelength. Although energy density control suffers from spillover, the local zone of control is still larger than that achieved when minimising the pressure at a single location. However, both the 10 dB

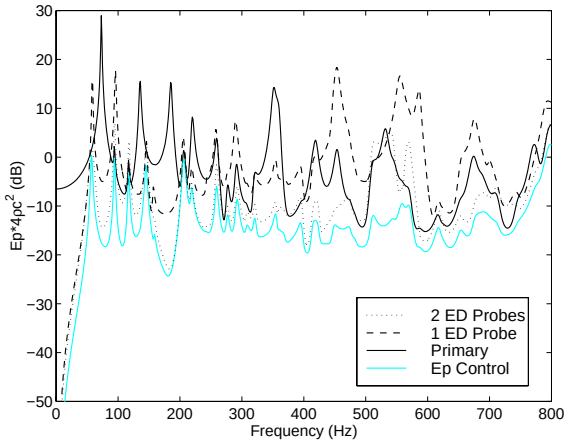

Figure 4.26: Potential energy reduction using 1 or 2 ED sensors for control in a coupled acoustic system with a single structural primary and 4 acoustic control sources.

zones of quiet are significantly smaller than previously, particularly the zone of quiet for energy density control. The reason for the decrease in the size is because the sound field is driven by the high wavenumber structural modes rather than the lower wavenumber acoustic modes. As a result, the pressure field varies much more rapidly with a change in position and therefore the zone of quiet is reduced. If the pressure attenuation vs distance shown in Figure 4.27 were normalised to the wavelength of the dominant structural modes then the figure would more closely resemble Figure 4.22.

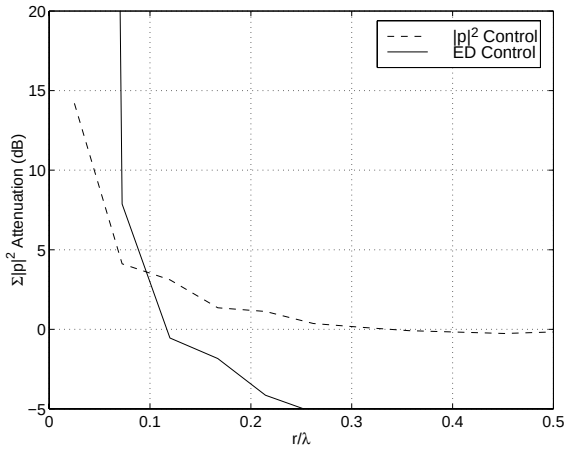

Figure 4.27: Attenuation of the sum of the FE nodal squared pressures as a function of the distance from the error sensor for a lightly damped acoustic system with a single primary structural source. The frequency range is from 600 to 700 Hz, with the separation distance normalised to the wavelength at 650 Hz.

4.2.7.2 Moderately damped vibro-acoustic system using acoustic control sources

It was shown in Section 4.2.5, when the cavity was excited directly with a primary acoustic source and the damping was increased from $\eta_a = 2\%$ to $\eta_a = 10\%$, that global control was reduced for both pressure and energy density control. However, it was found that although global control was poor, the zone of local control for energy density control was large.

In Section 4.2.7.1, with the cavity driven by structural source via the structure (as opposed to acoustic sources), it was found that the zone of local control was much smaller than reported in Section 4.2.5. In order to determine the mechanisms responsible for this significant reduction in the zone of local control the modal loss factors for both cavity and the structure were increased to 10%, ie $\eta_a = 10\%$ and $\eta_s = 10\%$ and then reanalysed.

The potential energy is plotted against frequency for energy density control and pressure squared control at a single location in Figure 4.28 using four acoustic control sources. Comparing this against Figure 4.25 it can be seen that the increase in damping acts to reduce global control, especially for energy density control.

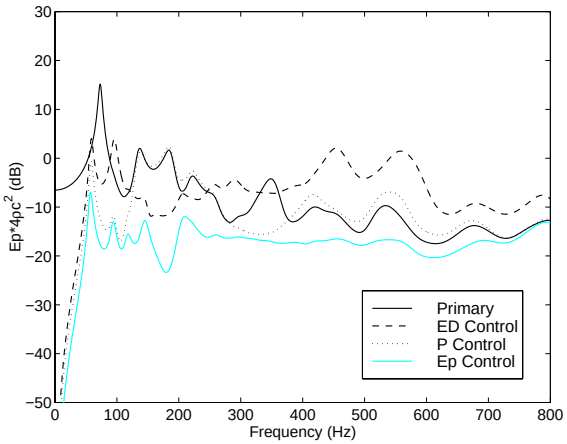

Figure 4.28: Potential energy reduction using ED control vs control of pressure at a single point in a coupled acoustic system with a single structural primary source and 4 acoustic control sources for a heavily damped coupled system.

The attenuation vs distance from the control location was calculated using the procedure described in Section 4.2.5 and is plotted in Figure 4.29. In Figure 4.30 these same results have been plotted against the attenuation versus distance for the lightly damped system shown in Figure 4.27. Comparing the heavily damped results for the zone of local control against the results for the zone of local control for the lightly damped case (see Figure 4.27) it can be seen that the size of the zone of local control achieved by minimising the energy density has increased substantially. It is interesting to note that the lines depicting the attenuation versus distance achieved using energy density control in Figures 4.27 and 4.29 are almost identical in shape, except that the heavily damped curve sits 5dB higher. The zone of local control achieved using pressure squared control shows very little change with damping.

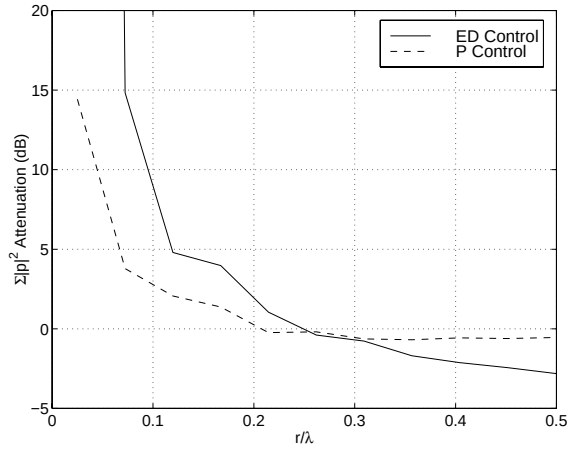

Figure 4.29: Attenuation of the sum of the FE nodal squared pressures as a function of the distance from the error sensor for a heavily damped coupled system with a single primary structural source. The frequency range is from 600 to 700 Hz, with the separation distance normalised to the wavelength at 650 Hz.

It can therefore be concluded that it is not only the excitation process which determines the size of the zone of local control but also the damping. The effect of damping is to increase the zone of local control at the expense of global control. This is consistent with the increase in the modal overlap which comes from increasing the damping of the system.

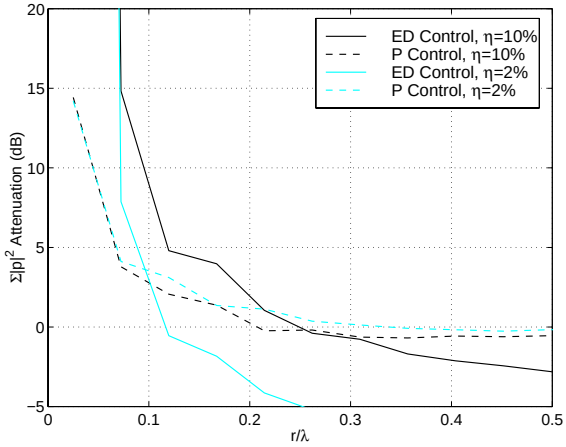

Figure 4.30: Attenuation of the sum of the FE nodal squared pressures as a function of the distance from the error sensor for both a lightly damped and heavily damped coupled system with a single primary structural source. The frequency range is from 600 to 700 Hz, with the separation distance normalised to the wavelength at 650 Hz.

4.2.7.3 Structural control sources

It has been shown that when the primary source is structural vibration, in general, structural control sources offer better control than acoustic control sources (Jones & Fuller 1989). This is because the secondary structural sources are more likely to produce a sound field which matches the primary sound field.

Figure 4.31 shows the reduction in potential energy obtained when minimising the energy density and the squared pressures at the 4 sensor microphones using a single structural control source. The control source position was chosen at random and was located at [0.250, 0.167, 0.493]. This happened to be a node for the even ordered modes along the y-axis (long axis) and subsequently the maximum achievable control was very poor for most of the bandwidth except when the response was dominated by the even ordered longitudinal modes.

Not a great deal can be said about the result except that energy density control yields results almost as good as potential energy control and minimising the squared pressures fares only slightly worse.

The effect of an additional 3 structural control sources on global control is shown in

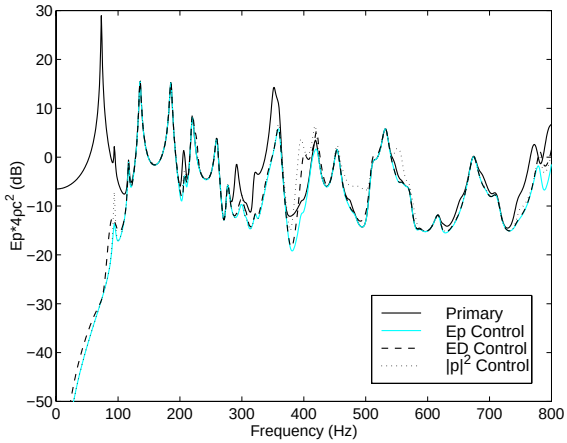

Figure 4.31: Potential energy reduction using ED control vs control of the pressure at a single microphone location in a coupled acoustic system with a single structural primary and a single structural control source.

Figure 4.32. With only a single sensor global control is very poor with the controlled levels only slightly better than the uncontrolled case. Because of the poor control that was achieved in the case above, another energy density sensor was introduced to show that if sufficient sensors are used then the global control is greatly improved. Figure 4.32 shows the effect of an additional sensor. As can be seen the global control offered by two energy density sensors is significantly better than achieved with only one because the modal spillover is substantially reduced.

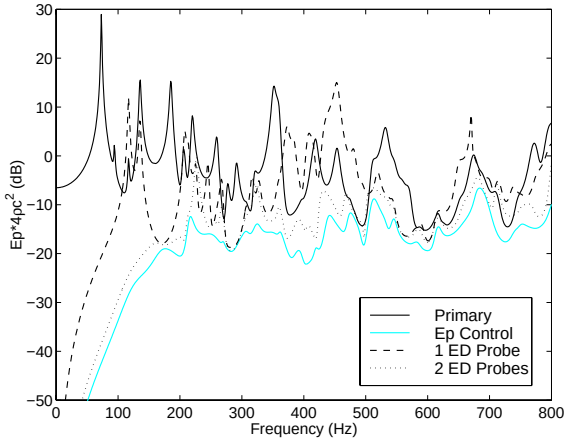

Figure 4.32: Potential energy reduction minimising the outputs from 1 or 2 ED sensors in a coupled acoustic system with a single structural primary and 4 structural control sources.

4.2.8 The Effects of Controller Error on Energy Density Control

The control results obtained using some sensing systems can exhibit dramatic sensitivity to errors in the amplitude and phase of the control system. It was necessary to determine if control using energy density was sensitive to such errors. Figure 4.33(a) shows the effect that a 1% magnitude and a 1° error has on the potential energy reduction. The error has also been applied to the control signal when controlling the potential energy so as to compare all three control strategies. The cavity was uncoupled from the structure with the same control arrangement as per Section 4.2.3. It can be seen that none of the control strategies show significant degradation in the global control from the case without the controller error shown in Figure 4.11. The decrease in the performance of the control system resulting from the controller error (given by the difference between the data shown in Figures 4.33(a) and 4.11) is plotted in Figure 4.33(b). Both the control of internal potential energy and energy density at a point suffer approximately the same decrease in global control. The effect of the controller error has been to simply limit the maximum level of control to approximately 35 dB, hence the peak at approximately 180 Hz and the rapid increase in potential energy below 25 Hz.

4.2.9 Energy Density Control with Phase Errors

The energy density estimate suffers from phase inaccuracies at low frequencies (shown in the previous chapter). It was therefore important to see if these bias errors also resulted in a reduction of the controlled cost function (energy density) and the desired cost function (acoustic potential energy). The phase error was simulated by pre-multiplying the pressure estimate at the error sensor locations by a phase error matrix, ie,

$$\hat{\mathbf{p}}_e = \mathbf{\Pi}_p \mathbf{p}_e \tag{4.20}$$

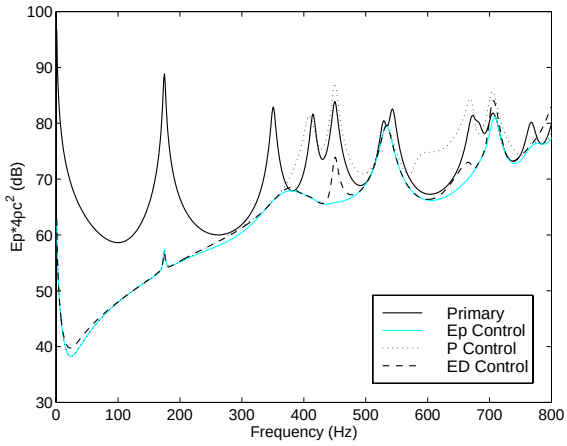

(a) Global acoustic potential energy

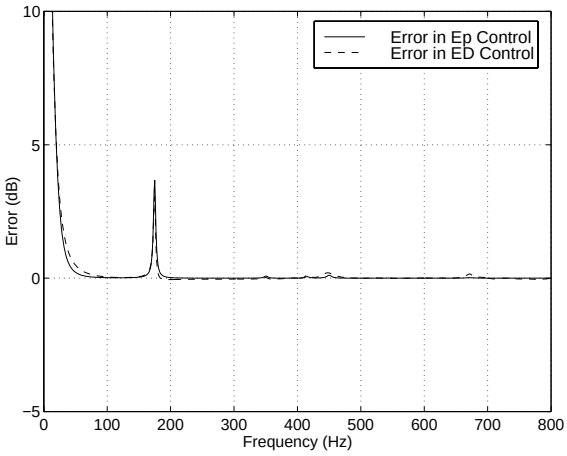

(b) Difference in performance between controlled levels with and without controller error

Figure 4.33: The effect of a 1% magnitude and a 1° phase error in the control signal has on the reduction in potential energy when minimising energy density and pressure at a single point. A single primary acoustic source and a single acoustic control source.

where $\mathbf{\Pi}_p$ is the (n_e x n_e) diagonal phase mismatch matrix defined by,

$$\mathbf{\Pi}_p = \begin{bmatrix} e^{j\pi_1} & 0 & \cdots & 0 \\ 0 & e^{j\pi_2} & \cdots & 0 \\ \vdots & \vdots & \ddots & 0 \\ 0 & 0 & 0 & e^{j\pi_{n_e}} \end{bmatrix} \tag{4.21}$$

where π_i is the phase error about some arbitrary reference. This can be incorporated into the ($4l$ x $n_d l$) band diagonal energy density transfer function matrix, ie

$$\hat{\mathbf{D}} = \mathbf{D}\mathbf{\Pi}_p \tag{4.22}$$

For the four microphone configuration used in the simulations the following phase mismatch matrix was used,

$$\mathbf{\Pi}_p = \begin{bmatrix} 1 & 0 & 0 & 0 \\ 0 & e^{j\frac{\pi}{180}} & 0 & 0 \\ 0 & 0 & e^{-j\frac{\pi}{180}} & 0 \\ 0 & 0 & 0 & 1 \end{bmatrix} \tag{4.23}$$

Figure 4.34 shows the effect that the phase mismatch has on energy density control. As would be expected from the earlier work, the error in both the energy density estimate and control increase with a decrease in the frequency.

4.2.10 Energy Density Control with Sensitivity Errors

The energy density estimate also suffers from sensitivity inaccuracies at low frequencies. The sensitivity error was simulated by pre-multiplying the pressure estimate at the error

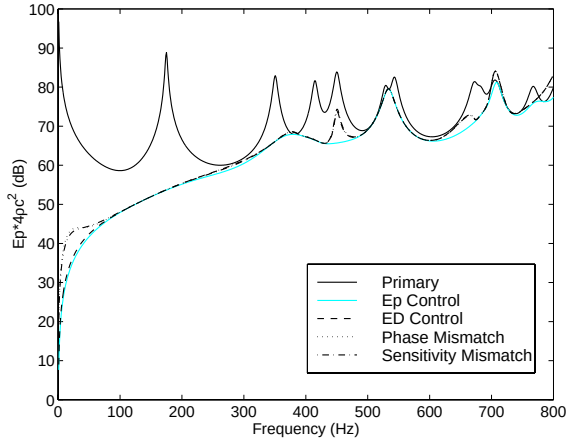

(a) 0-800 Hz

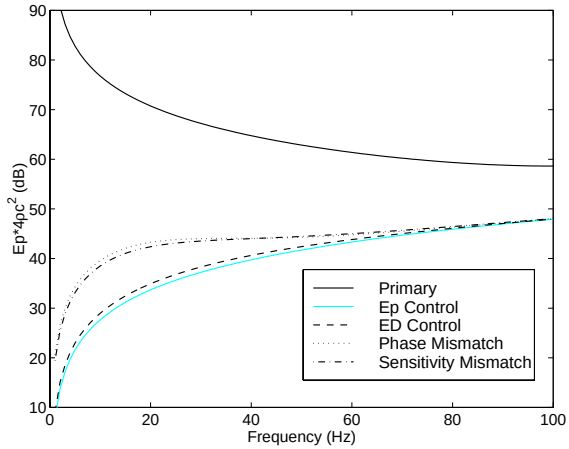

(b) 0-100 Hz

Figure 4.34: The effect of a 1° phase mismatch or a 1% sensitivity mismatch between sensors has on the reduction in potential energy when minimising energy density: (a) 0-800 Hz; (b) 0-100 Hz. A single primary acoustic source and a single acoustic control source.

sensor locations by a sensitivity error matrix, ie,

$$\hat{\mathbf{p}}_e = \mathbf{\Pi}_s \mathbf{p}_e \tag{4.24}$$

where $\mathbf{\Pi}_s$ is the (n_e x n_e) diagonal sensitivity mismatch matrix defined by,

$$\mathbf{\Pi}_s = \begin{bmatrix} 1+\pi_1 & 0 & \cdots & 0 \\ 0 & 1+\pi_2 & \cdots & 0 \\ \vdots & \vdots & \ddots & 0 \\ 0 & 0 & 0 & 1+\pi_{n_e} \end{bmatrix} \tag{4.25}$$

where π_i is the sensitivity error. This can be incorporated into the ($4l$ x $n_d l$) band diagonal energy density transfer function matrix, ie

$$\hat{\mathbf{D}} = \mathbf{D}\mathbf{\Pi}_s \tag{4.26}$$

For the four microphone configuration used in the simulations the following sensitivity mismatch matrix was used,

$$\mathbf{\Pi}_s = \begin{bmatrix} 1 & 0 & 0 & 0 \\ 0 & 1.01 & 0 & 0 \\ 0 & 0 & 0.99 & 0 \\ 0 & 0 & 0 & 1.005 \end{bmatrix} \tag{4.27}$$

Figure 4.34 shows the effect the sensitivity mismatch has on energy density control. As was seen with the phase error, the control error increases with a decrease in the frequency. It has been shown that a phase or sensitivity error in the microphone response not only leads to an error in the energy density estimate but the bias error results in sub-optimal control performance. The effect of the energy density bias error is seen in the

control performance below 100 Hz.

4.2.11 Energy Density Control with Position Errors

It was shown previously that an error in the positions of the sensor microphones results in a bias error in the velocity estimate which subsequently biases the energy density estimate. Therefore, because the sensor is located in the centre of the cavity for the simulations, there will be no significant effect of the energy density when the even order acoustic modes dominate the response.

Due to the discrete nature of the finite element model it is not directly possible to perturb the the locations of the microphones so as to have them measuring the pressures at the perturbed locations. However, it is possible to emulate this effect by making the appropriate adjustments to the position matrix when calculating the ($4l$ x $n_d l$) band diagonal energy density transfer function matrix, $\mathbf{D}_a$, given by Equation (4.19).

$$\hat{\mathbf{D}}_a = \left(\begin{bmatrix} 1 & -jk\Delta x_1 & -jk\Delta y_1 & -jk\Delta z_1 \\ 1 & -jk\Delta x_2 & -jk\Delta y_2 & -jk\Delta z_2 \\ 1 & -jk\Delta x_3 & -jk\Delta y_3 & -jk\Delta z_3 \\ 1 & -jk\Delta x_4 & -jk\Delta y_4 & -jk\Delta z_4 \end{bmatrix} + \boldsymbol{\epsilon} \right)^{-1} \tag{4.28}$$

where $\boldsymbol{\epsilon}$ is the positional error matrix used in the simulations and is given by

$$\boldsymbol{\epsilon} = -jk \begin{bmatrix} 0 & \epsilon_{x_1} & \epsilon_{y_1} & \epsilon_{z_1} \\ 0 & \epsilon_{x_2} & \epsilon_{y_2} & \epsilon_{z_2} \\ 0 & \epsilon_{x_3} & \epsilon_{y_3} & \epsilon_{z_3} \\ 0 & \epsilon_{x_4} & \epsilon_{y_4} & \epsilon_{z_4} \end{bmatrix} = -jk \begin{bmatrix} 0 & 0 & 0 & 0 \\ 0 & 1 & 1 & 1 \\ 0 & -1 & -1 & -1 \\ 0 & -\frac{1}{2} & -\frac{1}{2} & -\frac{1}{2} \end{bmatrix} \left(10^{-3}\right) \tag{4.29}$$

where ϵ_x, ϵ_y and ϵ_z are displacements from the original microphone positions in the x, y

and z axis respectively. The displacements were in the order of ± 1mm, and the relative displacements between the origin microphone and the axes-microphones were also in the order of ± 1mm as shown by the latter expression in Equation (4.29).

Figure 4.35 shows the effect that an error in the locations of microphones has on the level of control. Two error matrices were used, one as given by Equation (4.29) and one 5 times larger.

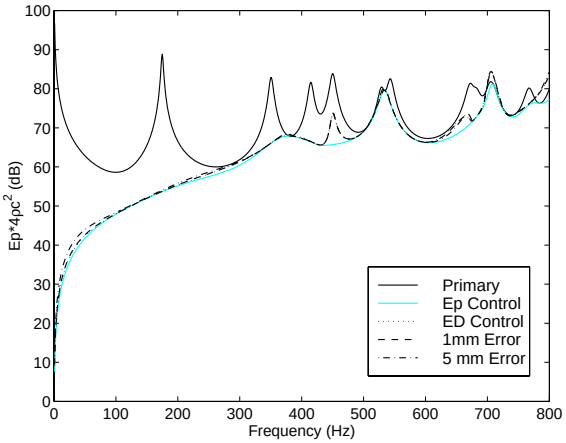

Figure 4.35: The effect of a 1 mm and a 5 mm error in the position of the microphones has on the reduction in potential energy: no spatial error, 1mm spatial error and 5 mm spatial error. A single primary acoustic source and a single acoustic control source.

As can be seen the error in the positions of the microphones have little effect on the levels of control achieved.

4.2.12 Comments

Several broad comments can be made regarding energy density control in enclosures. For purely acoustic systems in a rigid wall enclosure with a low modal density, when a single control source per sensor is used, energy density control provides a very good means of minimising the global sound field. As the modal density increases, control becomes more local to the sensor, which generates a zone of quiet significantly larger than minimising only the pressure at the point. And provided that modal spillover is not significant, these

results are very similar to those predicted for a diffuse sound field.

If the acoustic system is coupled to the enclosing structure, then the above observations still hold provided that the primary and control sources are acoustic. When the structure is the primary source (or is controlled by a structural control source) the situation is considerably different and acts to reduce the amount of global control and local control that can be achieved. This is because of the effects of modal filtering between acoustic and structural modes and the difference in wave-numbers between the cavity modes and the structural modes. The modal filtering process that occurs when the structure drives the cavity tends to excite many more acoustic modes, and in particular high order acoustic modes, than does driving the cavity directly through acoustic sources. This makes modal control (global control) very difficult except at very low frequencies.

The second process which acts to reduce the control achieved when using structural actuators is the spatial variance of pressure in the cavity field is increased greatly. Since the wavenumber of the structural modes is much larger than the acoustic modes (with a similar resonance frequency) the acoustic field is no longer dominated by acoustic modes with wave-numbers similar to the wavenumber of a free-field wave at the driving frequency but rather the field is dominated by high wavenumber structural modes. Therefore, the zone of local control is reduced. Control of sound transmission using energy density sensing will likely be more effective with air-borne sources such as propellers than structure-borne sources like engine mounts.

Care needs to be taken when increasing the number of control sources above one per energy density sensor as global control is sacrificed for local control. This is because the control process moves from modal control to modal rearrangement leading to spillover into the higher order acoustic modes. This phenomenon is not unique to energy density control and is seen when minimising the sum of squared pressures at several microphones.

The insensitivity of energy density sensor placement for low modal density acoustic systems and large zones of local control for high modal density systems justifies its use

in favor of microphones.

From the numerical simulations, it was seen that control using energy density is relatively robust to errors. With regards to the simulations involving the induced errors it would be easy to dismiss the effects these errors have on the control as being insignificant. However, there are other issues which arise in practice that are not accounted for in the simulations. In particular, the energy density estimate errors effectively reduce the dynamic range of both the acoustic sensor and the control system. This is not an issue in the simulations since the double precision calculations have a dynamic range of 320 dB whereas typical instrumentation may only have a dynamic range of 60-100 dB.

4.3 Physical Experiments

To validate the results from the numerical simulations, experiments were conducted on a physical curved panel - cavity system. The experimental setup for structural excitation is shown schematically in Figure 4.36. A photograph of the experimental apparatus is shown in Figure 4.37.

Loudspeakers with small backing enclosures were used as the acoustic sources. The volume velocity produced by the loudspeakers was measured using the internal microphone technique described in Chapter 2. Due to the size of the cavity it was not possible to use any more than a single primary acoustic source and a single acoustic control source without significantly altering the dynamics of the cavity. Although it was possible to move the sources around to obtain more transfer functions (which would have allowed more acoustic control sources to be used in the experiments), the process of removing the rear cavity wall to gain access was extremely time consuming and risked disturbing the free microphones used to measure the cavity response. Therefore only single channel control was conducted when using acoustic control sources. There was no such limitation for the number of structural force inputs and so it was possible to conduct the multichannel

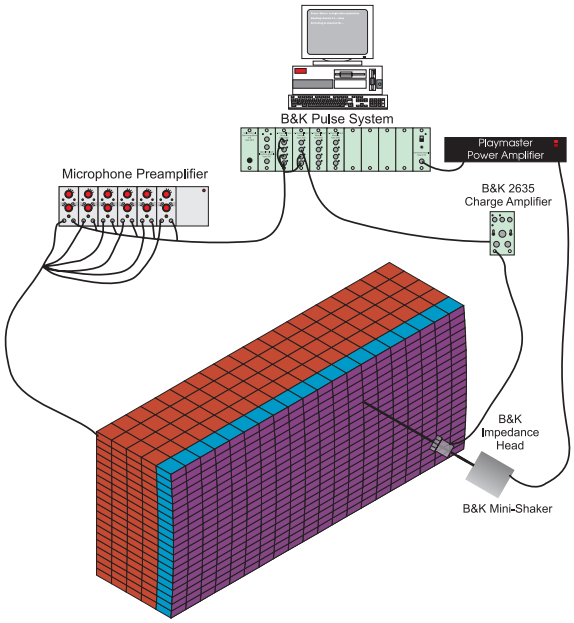

Figure 4.36: Schematic of the experimental apparatus used to predict the performance of the energy density sensor as an error sensor.

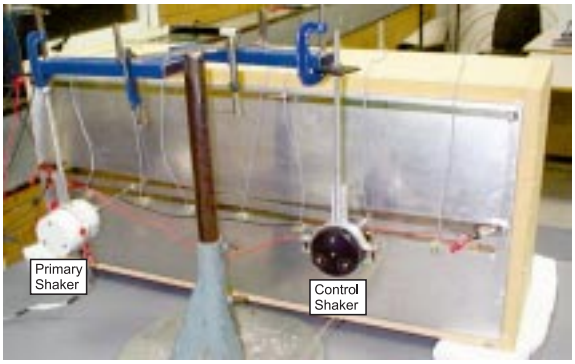

Figure 4.37: Photograph of the experimental apparatus used to predict the performance of the energy density sensor as an error sensor.

control experiments using structural control.

Six 6 mm electret microphones were used to measure the pressures at several points in the cavity. Individual microphones were also used to estimate the volume velocity of the acoustic primary and control sources. The microphones were connected to a pre-amp with a bias voltage, with the output from the pre-amp connected to a B&K Pulse system.

A B&K Type 4810 mini-shaker was used as the structural source. The driving point force was measured with B&K Type 8001 Impedance head via B&K Type 2635 charge amplifier. All transfer functions were measured on a B&K Pulse system. The transfer functions were measured against the volume velocity of the acoustic sources and the driving point forces of the structural forces. The transfer functions were exported to a text file as an ASCII matrix for each source and then imported into MATLAB for analysis.

The process of using measured transfer function data to predict the amount of control that can be achieved is outlined in Chapter 2.

Only the 4 microphone sensor, with and without the summer, was available for testing. It was shown in Section 4.2 that control using the sensor with the pressure summer showed almost no difference to the control achieved without the pressure summer. Therefore, all measurements were conducted only using the energy density sensor with the pressure summer.

4.3.1 Primary Acoustic Source

Figure 4.38 shows the reduction in potential energy obtained using a single acoustic source for the following control strategies: minimising the sum of the squared pressures from the six roving microphones; minimising the pressure at a single microphone; minimising the energy density from the sensor; and minimising the pressure at 4 of the 6 free microphones.

As was expected the control of the pressure at a single microphone provides good

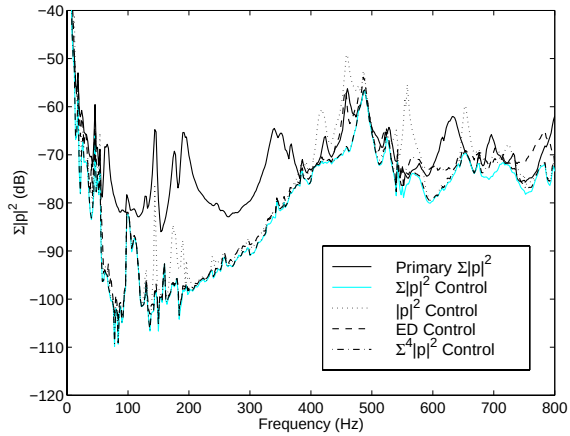

Figure 4.38: Reduction in the sum of the squared pressures for 6 microphones using various control strategies: minimising all 6 free microphones ($\Sigma|\mathrm{p}|^2$ Control), minimising the pressure of a single sensor microphone ($|\mathrm{p}|^2$Control), minimising the energy density of the sensor (ED Control) and minimising the pressure at 4 of the 6 free microphones ($\Sigma^4|\mathrm{p}|^2$ Control). A single primary acoustic source and a single acoustic control source.

global control at low frequencies but leads to large increases in the global sound field when the frequency increases. The other two strategies, both of which have 4 error channels, do not appear to suffer from modal spillover. It can be seen that both strategies provide good global control, apart from in the frequency range between 400 Hz and 500 Hz where energy density control leads to no change in the potential energy and from 650 Hz to 700 Hz where there is a small degree of modal spillover. Minimising the pressure at 4 of the 6 free microphones suffers between 550 Hz and 650 Hz where the global control is sub-optimal.

In the previous section it was shown that when the number of control sources was less than the number of error channels (4 in this case), minimising energy density generally produced better global control compared to minimising the squared pressures at the sensor microphone locations, apart from when the modal density was low when the two strategies resulted in a similar level of control. This was tested in the cavity and the results are shown in Figure 4.39. As was seen in the numerical simulations, the two control strategies generally offer the same global control at low modal densities; however, when the

modal density increases and control becomes difficult, control of the sum of the squared pressures of the sensor microphones suffers from modal spillover whereas energy density control does not. This can be seen in the frequency range between 400 Hz and 500 Hz and from 650 Hz to 700 Hz. This result therefore justifies the calculation of the particle velocity in the three orthogonal directions for the control system as opposed to simply minimising the pressures at four closely spaced microphones.

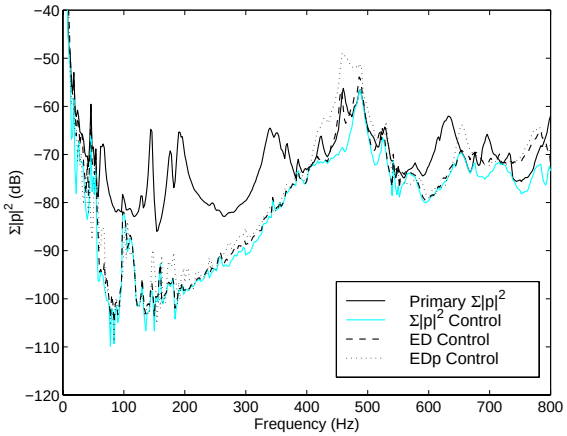

Figure 4.39: Reduction in the sum of the squared pressures for 6 microphones using various control strategies: minimising all 6 free microphones ($\Sigma|\mathrm{p}|^2$ Control), minimising the energy density of the sensor (ED Control) and minimising the pressure of the 4 sensor microphones (EDp Control). A single primary acoustic source and a single acoustic control source.

4.3.2 Primary Structural Source

A single primary shaker was attached to a non-symmetric location on the panel, namely $[0.250, 0.105, 0.328]$. This was the same position that was used for the numerical simulations. Both acoustic and structural control sources were evaluated and the results are detailed below.

4.3.2.1 Acoustic control sources

A single acoustic control source was located in a corner at [0.000, -0.209, 0.985]. Figure 4.40 shows the reduction in the sum of the squared pressures at the six microphone locations using a single acoustic source when minimising: the sum of the squared pressures of the six microphones, the energy density in the centre of the cavity, and the pressure at the centre of the cavity. Although a little difficult to see, the energy density control results in almost optimal control and much less modal spillover than does minimisation of the pressure at the same location as the sensor. This is the same result as was seen in the numerical simulations.

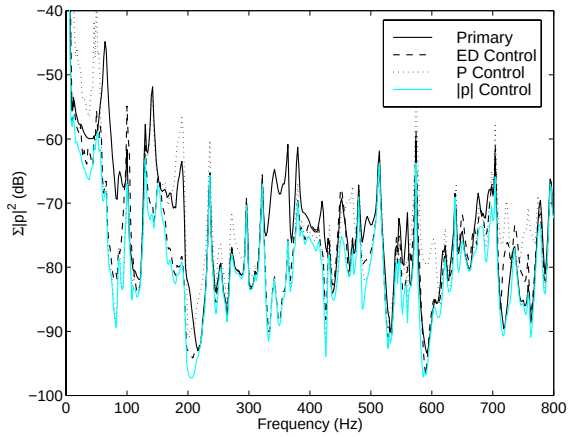

Figure 4.40: Reduction in the sum of the squared pressures for 6 microphones using various control strategies: minimising all 6 free microphones (|p| Control), minimising the pressure of a single sensor microphone (P Control) and minimising the energy density of the sensor (ED Control) using a single acoustic control source.

Figure 4.41 shows the effect on control of adding another acoustic control source to the sum of the squared pressures of the 6 microphones when using energy density control. The second acoustic control source was placed at [0.250, 0.209, 0.985]. It can be seen that when using energy density control the additional control source does not offer much improvement in global control. This result was also found in the numerical simulations.

Therefore, it may be concluded that apart from systems with very low modal densities, there is little gained in global terms by adding control sources without also increasing the

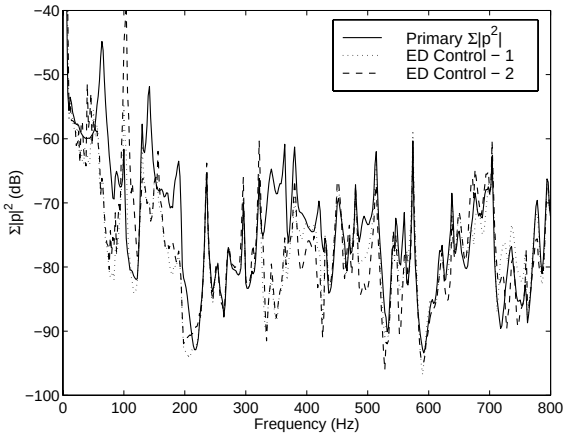

Figure 4.41: Reduction in the sum of the squared pressures for 6 microphones when minimising the energy density measured by the sensor with one (ED Control - 1) or two acoustic control sources (ED Control - 2).

number of energy density sensors. The majority of the control effort from the additional control sources is spent achieving local control and in fact, additional control sources may result in an increase in the global sound levels.

4.3.2.2 Structural control sources

It was important to see if the energy density sensor worked as well with structural control as it did with acoustic control. The shaker was moved to four structural control source locations where the panel was excited and the transfer functions measured. These positions were the same as used in the numerical simulations, namely [0.250, 0.167, 0.493], [0.250, 0.167, 0.049], [0.250, -0.084, 0.296] and [0.250, 0.146, 0.493].

Figure 4.42 shows the reduction in the sum of the squared pressures at the six microphone locations using a single structural control source when minimising: the sum of the squared pressures of the six microphones, the energy density in the centre of the cavity, and the pressure at the centre of the cavity.

Apart from the first 100 Hz where energy density control is sub-optimal, the sensor provides very good global control and certainly out-performs a single microphone. The poor performance below 100 Hz was not seen in the numerical simulations except when

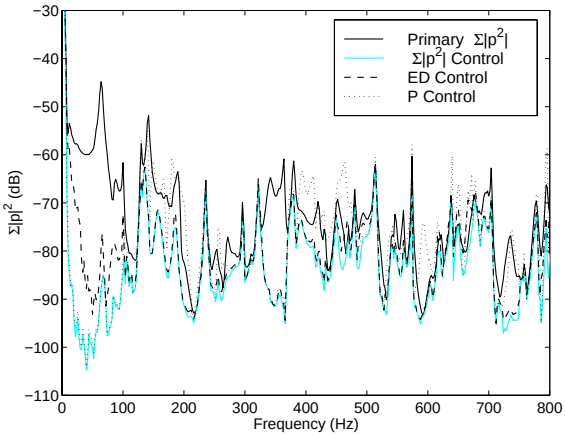

Figure 4.42: Reduction in the sum of the squared pressures for 6 microphones using various control strategies: minimising all 6 free microphones ($\Sigma|\mathrm{p}|^2$ Control), minimising the energy density of the sensor (ED Control) and minimising the pressure of the 4 sensor microphones (P Control) using a single structural control source.

a phase and magnitude error was added to the sensor microphones. Therefore, it can be concluded that the most likely source of the sub-optimal performance is due to the transducer phase and magnitude mismatch errors. This was not experienced when using acoustic control sources because the level of global control was too small for the effect to be observable.

Figure 4.43 represents the same configuration as the previous figure except that 4 structural control sources have been used instead of 1. Just as was seen in the numerical simulations, the additional control sources have improved global control when using multiple microphones but have not resulted in any significant improvement in the global energy when using energy density as a cost function.

It is believed that the additional control effort has been local to the sensor. It was intended to attempt to measure the attenuation versus distance to confirm this, but due to the difficulties in doing so and time constraints this was not completed.

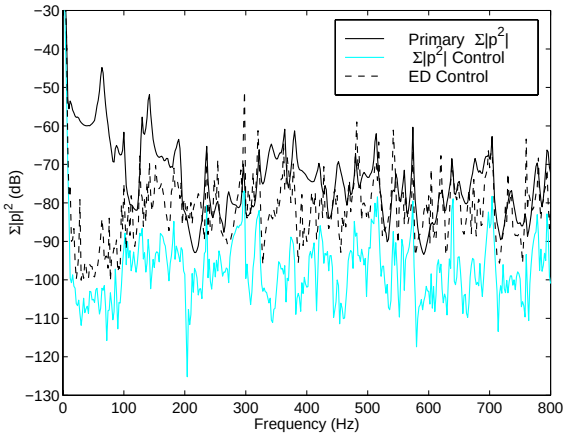

Figure 4.43: Reduction in the sum of the squared pressures for 6 microphones using various control strategies: minimising all 6 free microphones, minimising the energy density of the sensor and minimising the pressure of the 4 sensor microphones using a 4 structural control sources.

4.4 Summary

It has been shown that the energy density of a reactive sound field can be adequately measured for active noise control applications using only four microphones rather than the 6 which have been used previously. The numerical modeling and testing of the physical unit has shown a remarkable robustness to both instrumentation and finite microphone separation errors. Energy density control offers significant advantages over the equivalent number of discrete microphones, for both low and high modal density systems. The placement of the energy density sensors is not as critical as it is for microphones. At low modal densities the global control obtained by minimising energy density is generally better than minimising the sum of squared pressures at an equivalent number of microphones. At high modal densities or with an increased number of control sources the zone of local control around a point when minimising energy density is significantly larger than the local zone of control when controlling the pressure at a single location.

If the number of control sources is the same (or greater) than the number of independent channels per sensor (4), then minimising the energy density sensed by the sensor is equivalent to minimising the sum of the squared pressures at the sensor microphones.

However, if the number of control sources is less than the number of independent channels per sensor, then minimising the three orthogonal particle velocities and pressure generally provides better global control than simply minimising the sum of the squared pressures at the sensor microphones.

Energy density control under primary acoustic excitation performs significantly better than when the acoustic field is driven by the structure. This is because the structure excites many higher order modes which have wavelengths of the same order as the microphone separation distance, and this has been shown to lead to significant errors in the energy density estimate.

As with any control system, care needs to be taken when defining the objective and determining the physical layout of the system. If the objective is global control, then many more sensors are needed per control source, particularly when using structural sources. If local control is the objective then a one-to-one ratio between the number of control and error channels is quite acceptable.

Chapter 5

Radiation Modes and ASAC

5.1 Introduction

Structural sensing of radiation modes has shown great promise as an effective technique for sensing and controlling power radiated from vibrating structures into the free field. The primary objective of the work described here was to apply the technique of active control of sound transmission into enclosures using radiation modal control, and then extend the theory base to the point where it may be used in a real active control system.

A second objective was to investigate the mechanisms of sound transmission into a stiffened enclosure and the subsequent implications on the design and performance of active systems for controlling sound transmission through the boundaries. It is shown that the interior radiation mode shapes are frequency dependent. This makes the application of modal control very difficult for real systems. A new technique for overcoming this application problem is derived which allows the use of fixed shape modal sensors.

A third objective was to determine the most suitable means of sensing radiation modes using structural vibration measurements. Both discrete and continuous shaped sensors have been investigated for use as modal sensors with the latter being more practical for large, modally dense (structural) systems.

The active control of sound transmission into a rectangular cavity from a coupled curved panel, excited by an external vibration source, is investigated numerically to illustrate the implementation of the extended technique and to gain some understanding of the associated physical processes. The structure and the acoustic space were modelled numerically using the commercially available finite element package ANSYS and coupled using the modal coupling theory of Pope (1971). Alternative "radiation mode" formulations have been derived in which the surface velocity distributions are orthogonal with: power radiated into the cavity; acoustic potential energy over a subspace; and acoustic energy density at a point. Experiments using both discrete acceleration and continuous strain radiation modal sensors have been conducted with some success.

The analysis for the curved panel backed by a rectangular cavity is extended to the case of a longitudinally stiffened cylinder with an integral floor and this work has been reported in a paper (Cazzolato & Hansen 1998) which is duplicated in Appendix D.

5.2 General Theory

In this section the theory of sound transmission through a structure into a contiguous cavity is reviewed. For a more detailed discussion on the theory used to simulate the vibro-acoustic response and control system performance see Chapter 2. The transmitted sound field is derived in terms of radiation modes and the implications for structural vibration sensing of the radiation modes is also discussed. Using the modal-interaction approach to the solution of coupled problems, the response of the structure is modelled in terms of its *in vacuo* mode shape functions and the response of the enclosed acoustic space is described in terms of the rigid-wall mode shape functions (Fahy 1985). The response of the coupled system is then determined by solving the modal formulation of the Kirchhoff-Helmholtz integral equation.

5.2.1 Global Error Criteria

An appropriate global error criterion for controlling the sound transmission into a coupled enclosure is the total time-averaged frequency dependent acoustic potential energy, $E_p(\omega)$, in the enclosure (Nelson et al. 1987*a*)

$$E_p(\omega) = \frac{1}{4\rho_0 c_0^2} \int_V |p(\vec{\mathbf{r}}, \omega)|^2 d\vec{\mathbf{r}} \tag{5.1}$$

where $p(\vec{\mathbf{r}}, \omega)$ is the acoustic pressure amplitude at some location $\vec{\mathbf{r}}$ in the enclosure, ρ_0 is the density of the acoustic fluid (air), c_0 is the speed of sound in the fluid and V is the volume over which the integral is evaluated. The frequency dependence, ω, is assumed in the following analysis but this factor will be omitted from the equations for the sake of brevity. Using the modal interaction approach to the problem (Fahy 1985), the acoustic pressure at any location within the cavity is expressed as an infinite summation of the product of rigid-wall acoustic mode shape functions, ϕ_i, and the modal pressure amplitudes, p_i, of the cavity

$$p(\vec{\mathbf{r}}) = \sum_{i=1}^{\infty} p_i \phi_i(\vec{\mathbf{r}}) \tag{5.2}$$

The modal expansion for the acoustic potential energy evaluated over n_a acoustic modes is then given by

$$E_p = \mathbf{p}^{\mathrm{H}} \mathbf{\Lambda} \mathbf{p} \tag{5.3}$$

where $\mathbf{p}$ is the (n_a x 1) vector of acoustic modal amplitudes and $\mathbf{\Lambda}$ is a (n_a x n_a) diagonal weighting matrix, the diagonal terms of which are

$$\Lambda_{ii} = \frac{\Lambda_i}{4\rho_0 c_0} \tag{5.4}$$

where Λ_i is the modal volume of the i^{th} cavity mode, defined as the volume integration of the square of the mode shape function,

$$\Lambda_i = \int_V \phi_i^2(\vec{\mathbf{r}}) dV(\vec{\mathbf{r}}) \tag{5.5}$$

The pressure modal amplitudes, $\mathbf{p}$, within the cavity, arising from the vibration of the structure are given by the product of the (n_s x 1) structural modal velocity vector, $\mathbf{v}$, and the (n_a x n_s) modal structural-acoustic radiation transfer function matrix, $\mathbf{Z}_a$,

$$\mathbf{p} = \mathbf{Z}_a \mathbf{v} \tag{5.6}$$

The l, i^{th} element of the radiation transfer function matrix $\mathbf{Z}_a$ is the pressure amplitude of the acoustic mode l generated as a result of structural mode i vibrating with unit velocity amplitude and is given by Equation (2.32). Substituting Equation (5.6) into Equation (5.3) gives an expression for the acoustic potential energy with respect to the normal structural vibration,

$$E_p = \mathbf{v}^{\mathrm{H}} \mathbf{\Pi} \mathbf{v} \tag{5.7}$$

where the error weighting matrix $\mathbf{\Pi}$ is given by

$$\mathbf{\Pi} = \mathbf{Z}_a^{\mathrm{H}} \mathbf{\Lambda} \mathbf{Z}_a \tag{5.8}$$

It should be noted that the error weighting matrix $\mathbf{\Pi}$ is not necessarily diagonal which implies that the normal structural modes are not orthogonal contributors to the interior acoustic pressure field. It is for this reason that minimisation of the modal amplitudes of the individual structural modes (or kinetic energy) will not necessarily reduce the total sound power transmission.

5.2.2 Diagonalisation of the Error Criteria

Since $\mathbf{\Pi}$ is real symmetric it may be diagonalised by the orthonormal transformation;

$$\mathbf{\Pi} = \mathbf{U}\mathbf{S}\mathbf{U}^{\mathrm{T}} \tag{5.9}$$

where the unitary matrix $\mathbf{U}$ is the (real) orthonormal transformation matrix representing the eigenvector matrix of $\mathbf{\Pi}$ and the (real) diagonal matrix $\mathbf{S}$ contains the eigenvalues (singular values) of $\mathbf{\Pi}$. The physical significance of the eigenvectors and eigenvalues is interesting. The eigenvalue can be considered a radiation efficiency (or coupling strength Bessac, Gagliardini & Guyader (1996)) and the associated eigenvector gives the level of participation of each normal structural mode to the radiation mode; thus it indicates the modal transmission path (Bessac et al. 1996).

Substituting the orthonormal expansion of Equation (5.9) into Equation (5.7) results in an expression for the potential energy of the cavity as a function of an orthogonal radiation mode set,

$$E_p = \mathbf{v}^{\mathrm{H}}\mathbf{U}\mathbf{S}\mathbf{U}^{\mathrm{T}}\mathbf{v} = \mathbf{w}^{\mathrm{H}}\mathbf{S}\mathbf{w} \tag{5.10}$$

where the elements of $\mathbf{w}$ are the velocity amplitudes of the radiation modes defined by

$$\mathbf{w} = \mathbf{U}^{\mathrm{T}}\mathbf{v} \tag{5.11}$$

Equation (5.11) demonstrates that each radiation mode is made up of a linear combination of the normal structural modes, the ratio of which is defined by the eigenvector matrix $\mathbf{U}$. Since the eigenvalue matrix, $\mathbf{S}$, is diagonal, Equation (5.10) may be written as follows,

$$E_p = \sum_{i=1}^{n} s_i |w_i|^2 \tag{5.12}$$

where s_i are the diagonal elements of the eigenvalue matrix $\mathbf{S}$ and w_i are the modal amplitudes of the individual radiation modes given by Equation (5.11).

The potential energy from any radiation mode is equal to the square of its amplitude multiplied by the corresponding eigenvalue. The radiation modes are therefore independent (orthogonal) contributors to the potential energy and the potential energy is directly reduced by reducing the amplitude of any of the radiation modes. As mentioned previously, the normal structural modes are not orthogonal radiators since the potential energy arising from one structural mode depends on the amplitudes of the other structural modes. The orthogonality of the radiation modes is important for active control purposes as it guarantees that the potential energy will be reduced if the amplitude of any radiation mode is reduced (Johnson & Elliott 1995).

5.2.3 Advantages of Diagonalisation

For shells radiating into free space (Burgemeister 1996, Elliott & Johnson 1993, Borgiotti 1990, Borgiotti & Jones 1993), the eigenvalues of the radiation modes rapidly decrease in magnitude with respect to the largest eigenvalue. Therefore, in practice it is necessary to only include the first few (efficient) radiation modes with the largest radiation efficiencies to account for the majority of the sound power radiated from the structure into the free field. The same principle applies for interior radiation modes. When calculating the transmission of sound from the structure into a cavity only the few most efficient radiation modes need to be used in the transmission loss calculations. It is therefore possible to neglect the non-efficient radiation modes with no appreciable loss in accuracy of the transmission loss estimates.

With the acoustic potential energy in the form of Equation (5.12) the above property can be exploited. Therefore, if only the first n_r terms in the eigenvalue matrix are of significance (say greater than 1% of the maximum), then the error weighting matrix may

be approximated by (Otte & Van der Auweraer 1993, Naghshineh & Koopmann 1993)

$$\mathbf{\Pi} \approx \sum_{i=1}^{n_r} s_i \mathbf{u}_i \mathbf{u}_i^{\mathrm{H}} \tag{5.13}$$

which in matrix form yields

$$\mathbf{\Pi} \approx \mathbf{U}\mathbf{S}\mathbf{U}^{\mathrm{T}} \tag{5.14}$$

where $\mathbf{S} \approx diag(s_1, s_2, ..., s_{n_r})$ is a (n_r x n_r) matrix and $\mathbf{U} \approx [\mathbf{u}_1, \mathbf{u}_2, ..., \mathbf{u}_{n_r}]$ is a (n_s x n_r) matrix.

It is in this truncation of the system equations where the benefits of using radiation modes to provide error signals in active control systems become apparent. For example, "real" systems tend to be modally dense structures with several hundred normal structural modes contributing to the overall response of the structure. It will be shown that it is possible to truncate the radiation matrix used in the simulations from a (100 x 100) matrix to a (5 x 5) matrix with almost no loss in accuracy. This greatly reduces both the computation times for the simulation and the complexity of the physical control system.

5.2.4 Structural Sensing of Radiation Modes

To evaluate the potential energy using Equation (5.12) it is necessary to know the amplitudes of the radiation modes. The process of extracting the amplitudes of radiation modes from measurements of the structural vibration, known as *modal filtering*, is discussed in detail by Tanaka et al. (1996) and relies on the principle of orthogonality, ie

$$\int_S \theta_m(\vec{\mathbf{r}})\theta_n(\vec{\mathbf{r}})dS = \begin{cases} 0, & m \neq n, \\ 1, & m = n, \end{cases} \tag{5.15}$$

where θ_m is the *m*th mode of some orthogonal set of natural modes. Post multiplying Equation (5.15) by the *m*th modal velocity, w_m, and summing over all modes gives

$$\int_S v(\vec{\mathbf{r}})\theta_m(\vec{\mathbf{r}})dS = w_m \tag{5.16}$$

where $v(\vec{\mathbf{r}}) = \sum_{i=1}^{\infty} w_i\theta_i(\vec{\mathbf{r}})$ is the velocity of the structure at some location $\vec{\mathbf{r}}$. The modal filters can be constructed by implementing Equation (5.16) in its discrete form using weighted measurements of the structural vibration at discrete locations, or in a continuous form using shaped sensors such as piezo-electric film.

An alternative approach to modal filtering described above uses a least squares formulation rather than numerical integration and is derived below in matrix form for discrete sensors which are a subset of continuous sensors. The structural velocity levels at the (n_e) discrete error sensor locations are given by the following finite matrix modal expansion,

$$\mathbf{v}_e = \mathbf{\Psi}_e\mathbf{v} \tag{5.17}$$

where, $\mathbf{v}_e$ is the (n_e x 1) vector of velocity levels for the sensors and $\mathbf{\Psi}_e$ is the (n_e x n_s) mode shape matrix at the sensor locations. The velocity amplitudes of the normal structural modes are then given by,

$$\mathbf{v} = \mathbf{\Psi}_e^{-1}\mathbf{v}_e \tag{5.18}$$

Inserting Equation (5.18) into (5.11) an expression is obtained for the velocity amplitudes of the radiation modes as a function of the velocity levels at the error sensor locations

$$\mathbf{w} = \mathbf{Z}_t\mathbf{v}_e \tag{5.19}$$

where $\mathbf{Z}_t$ is the (n_r x n_e) radiation mode structural transfer function matrix (or modal filter

matrix) which relates the vibration velocity levels at the discrete error sensor locations to the modal velocity amplitudes of the radiation modes and is given by

$$\mathbf{Z}_t = \mathbf{U}^{\mathrm{T}} \mathbf{\Psi}_e^{-1} \tag{5.20}$$

The elements of each row of this modal filter matrix represent a weighting value, which when applied to the signal from the vibration sensors and summed for all sensors, will provide a measure of the amplitudes of the radiation modes.

The expression for the velocity at any point on the surface of the structure given by Equation (5.17) can be expanded, using the properties of a unitary matrix and Equation (5.11), to give the following

$$\mathbf{v}_e = \mathbf{\Psi}_e \mathbf{U} \mathbf{U}^{-1} \mathbf{v} = \mathbf{\Psi}_e \mathbf{U} \mathbf{U}^{\mathrm{T}} \mathbf{v} = [\mathbf{\Psi}_e \mathbf{U}] \mathbf{w} \tag{5.21}$$

It follows that the term $\mathbf{\Psi}_e \mathbf{U}$ in Equation (5.21) is the mode shape matrix of the radiation modes evaluated at the n_e error sensor locations, $\mathbf{\Theta}_e$. Therefore, the radiation mode shape is obtained by post multiplying the mode shape matrix of the normal structural modes by the eigenvector matrix, ie

$$\mathbf{\Theta} = \mathbf{\Psi} \mathbf{U} \tag{5.22}$$

In most practical systems the number of discrete error sensors (n_e) will be much less than the number of significant normal structural modes (n_s); therefore, the error sensor mode shape matrix, $\mathbf{\Psi}_e$, will be under-determined. It is therefore necessary to evaluate the inverse via a pseudo (least squares) inverse (Meirovitch & Bennighof 1986). Note that this technique is an approximation and will reduce the fidelity of the sensing system much like evaluating Equation (5.16) over some subspace of the surface rather than the

complete surface. It is shown in the following section that the reduction in sensor fidelity will lead to a reduction in controller performance. Morgan (1991) quantifies the effect that observation spillover arising from a finite number of sensors has on the control performance. The error is simply given by the ratio of the controlled potential energy level when the amplitudes of the radiation modes are known to the controlled potential energy level when the modal amplitudes are estimated using Equation (5.20). He shows that whenever the number of error sensors is less than the number of significant modes then some decrease in performance is to be expected. He also makes qualitative generalities to guide sensor placement, such as avoiding sensor locations near nodes of significant modes in order to preserve observability.

The practical implementation of the control system may look something like that shown in Figure 5.1, where an accelerometer array would be used to measure the velocity levels on the surface of the shell. The modal filters, $\mathbf{Z}_t$, given by Equation (5.20) would be used to decompose the velocity signal to modal amplitudes of the radiation modes. The frequency weighting (eigenvalue) filters, $\mathbf{S}$, would then be used to weight the modal amplitudes to provide inputs to the controller.

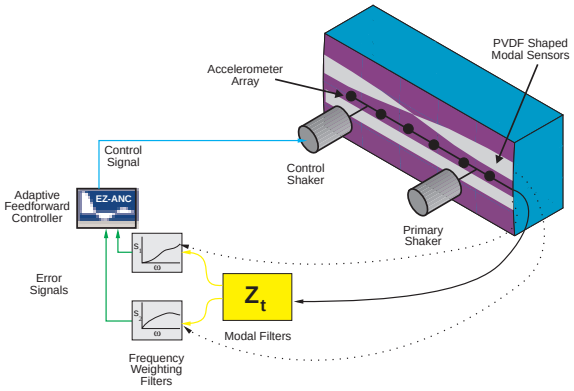

Figure 5.1: Schematic of modal and eigen-filter for an ASAC system.

5.3 Sound Transmission through a Curved Panel into a Cavity

The active control of sound transmission through the curved panel / cavity system shown in Figure 5.1 has been investigated, with the locations of the structural sources and sensors shown. This is the same system used in the previous study of energy density control, and is discussed in more detail in Section 4.2.1.

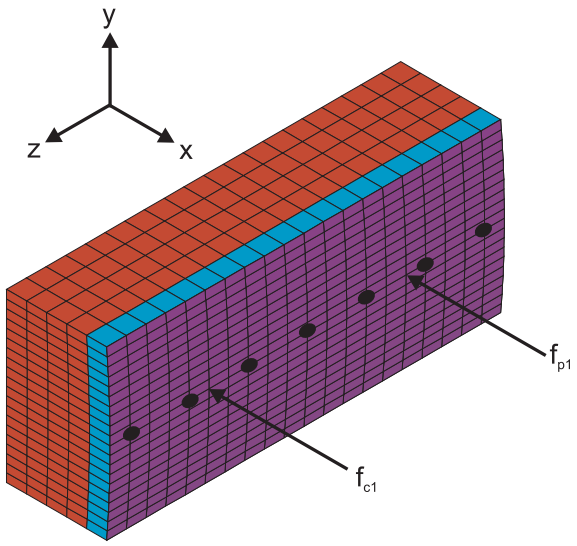

Figure 5.2: Finite element model of the structure and cavity used for the numerical simulations also showing locations of structural sources and sensors. Purple - Structural shell elements, Cyan - Acoustic brick elements with structural dofs and Red - Acoustic brick elements without structural dofs.

Cunefare & Currey (1994) found that the low order (free-space) radiation modes of rectangular panels converge quickly to their true shape after considering only a limited number of structural modes. It was found in the work discussed in the paper that this is not the case for interior radiation modes of a complex three-dimensional structure and many hundreds of modes (200) were required to achieve partial convergence to the "true" shape of the radiation mode.

When calculating the sound transmission from the structure into the enclosed space it was only necessary to consider the structural modes that were resonant or close to

resonance within the frequency bandwidth of interest, namely 0 Hz to 800 Hz. Therefore, for the sake of computational efficiency, only 100 structural modes were used during the simulation to calculate the system response.

5.3.1 Radiation Modes - Mode Shapes and Radiation Efficiencies

The eigenvalues and eigenvectors of the radiation matrix were calculated within MATLAB using the method and model outlined above. A Singular Value Decomposition (SVD) was used to calculate the orthonormal transformation of the radiation matrix rather than other eigen-extraction routines because of the singular nature of the problem. As the radiation efficiencies of the radiation modes rapidly approach zero as the radiation mode order is increased, the condition number of the matrices becomes infinite and thus the matrices become ill-conditioned. This being the case, many of the other techniques which use simple eigen-routines to construct the orthonormal radiation mode set, such as Gram-Schmidt orthogonalisation, suffer severely from round-off problems.

The eigenvalues for the first 8 (most efficient) radiation modes are shown as a function of frequency in Figure 5.3. As can be seen, the eigenvalues are very frequency dependent with the peaks in the radiation efficiency corresponding to the natural frequencies of the cavity. Figure 5.3 shows qualitatively that in general (at least at low frequencies) a single radiation mode will dominate the sound transmission from the structure into the acoustic space. It is this property that enables significant control within a limited frequency range to be achieved by controlling a single radiation mode. It should be noted that at the "cross-over" frequencies where two radiation modes have the same eigenvalue, there will be at least two radiation modes contributing to the sound transmission into the cavity. It is not critical that the active control system perform optimally in the cross-over regions as these regions are likely to occur at frequencies where the radiation efficiencies are low

and therefore the sound transmission is also low.

When the eigenvalues corresponding to a particular excitation frequency are returned by the eigen solver they are always sorted in either ascending or descending order with respect to the magnitudes. This "ranking" of the eigenvalues and eigenvectors has the benefit of arranging the modes from the biggest contributors to the sound transmission to the smallest. Therefore, only the important modes are sensed and controlled, which leads to a reduction in the number of error and control signals required by the control system.

It can be seen that the ranking of the eigenvalues creates a discontinuity in the slope of the eigenvalues at the cross-over frequencies. This manifests itself as a step change in the mode shapes of the radiation modes, so the mode shape of the most efficient mode at 100 Hz does not resemble the mode shape of the most efficient mode at 200 Hz. It should be noted that because of the discontinuities in the slope of the eigenvalues at the cross-over frequencies, this increases the number of taps in the digital filters needed to shape the error signal input to the controller (see Figure 5.1).

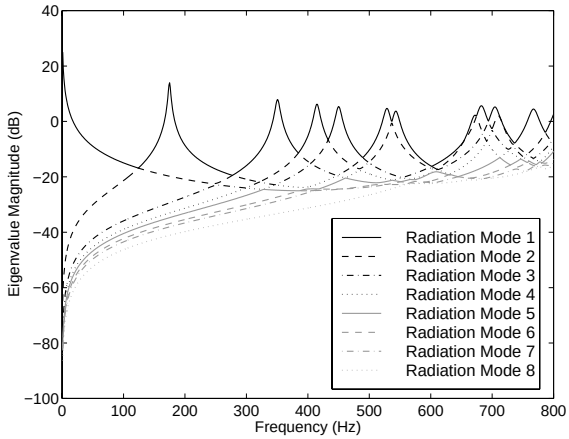

Figure 5.3: Calculated (ranked) eigenvalue magnitudes (radiation efficiencies) of the first 8 most efficient radiation modes.

The frequency dependence is also reflected in the eigenvectors, with particularly high variation at the "cross-over" frequencies where there is a change in the ranking of eigenvalues. Physically, this means that the shape of the modal sensors used to measure the

radiation modal amplitude is frequency dependent. This is illustrated in Figure 5.4 which shows the participation factors, calculated directly from $\mathbf{U}$, of the first 2 normal structural modes to the most efficient radiation mode. This weighting is typical for all the radiation modes and demonstrates how the importance of each normal structural mode alters with respect to frequency as the response of the acoustic space is dominated by different acoustic modes. The frequency dependence of the eigenvector weighting is also illustrated in Figure 5.5 where the relative contribution of the first normal structural mode to the first 2 radiation modes is shown.

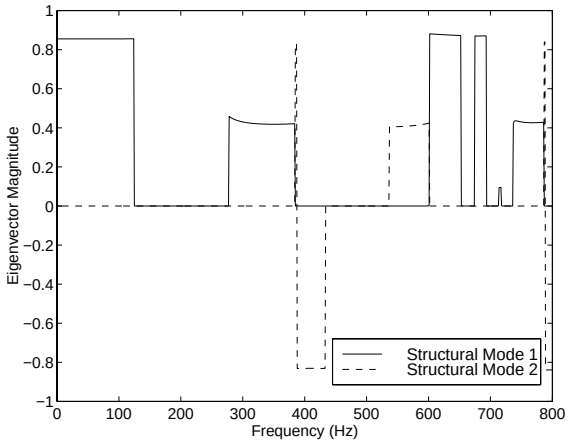

Figure 5.4: Calculated (ranked) eigenvector magnitudes of the most efficient radiation mode for the first 2 structural modes.

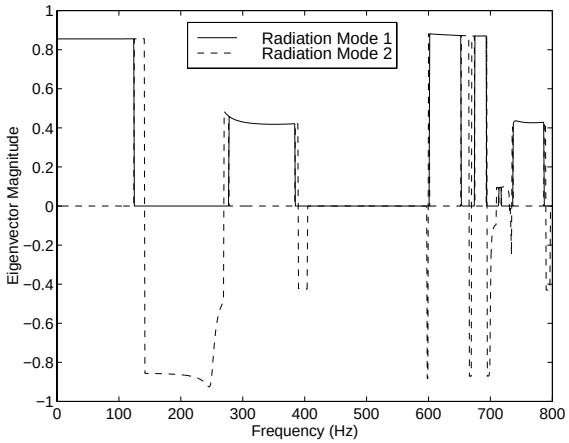

Figure 5.5: Calculated eigenvector magnitudes of the first 2 most efficient radiation modes for the first structural mode.

Since very few radiation modes contribute to the sound transmission only a few low order IIR filters are needed to implement the frequency dependent eigenvalues. However, due to the large number of structural modes needed to derive the radiation modes, the frequency dependence of the eigenvectors (mode shapes) presents a significant burden for practical implementation of the control system shown in Figure 5.1. Obviously, because of the frequency dependence of the radiation mode shapes, the modal amplitudes of these modes can only be calculated through discrete sensors weighted with digital filters rather than using fixed shape sensors. For example, the modal weightings of the 2 most efficient radiation modes for a sensor located at node 100 are shown in Figure 5.6. This effectively prohibits the calculation of the modal amplitudes using Equation (5.20) for all but the simplest physical systems. Consider for example the particular case, where 5 radiation modes are to be controlled using 16 tap IIR filters, upwards of 8000 (5 radiation modes x 16 taps x 100 sensors) multiplications may be required, presenting a significant burden even for high speed DSP's. A technique for overcoming this limitation is detailed in Section 5.4.

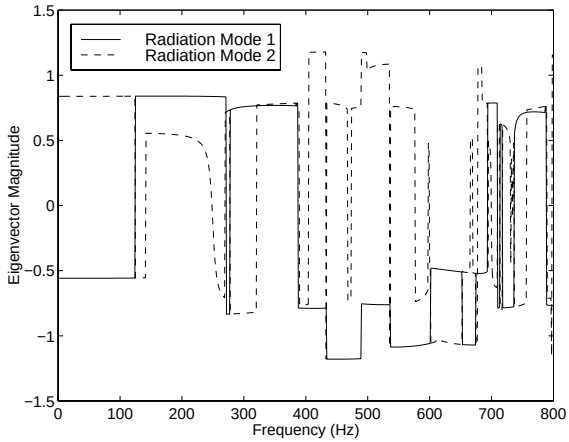

Figure 5.6: Calculated eigenvector magnitudes of the first 2 most efficient radiation modes for the 100th node.

The mode shape functions of the most efficient radiation modes calculated for the curved panel/cavity model, at 5 Hz and 175 Hz (corresponding to the natural frequencies

of the first 2 uncoupled acoustic modes) were derived using Equation (5.22) and are shown in Figs. 5.7 and 5.8. It should be noted that although the natural frequency of the bulk compression or breathing mode for a rigid walled cavity is 0 Hz, when coupled to the structure, the natural frequency of this particular mode increases. For this reason 5 Hz rather than 0 Hz was used as the frequency at which to calculate the fundamental radiation mode shape. It becomes apparent that the radiation modes reflect the dominant acoustic modes at the driving frequency as shown in Figs 5.9 and 5.10. This was also observed by Johnson (1996).

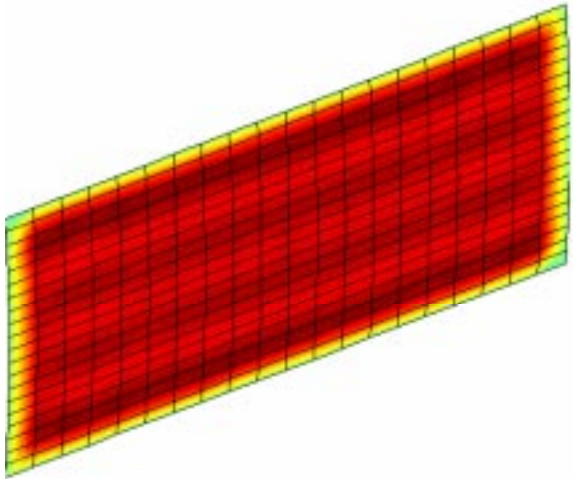

Figure 5.7: Mode shape of the most efficient radiation mode at 5 Hz.

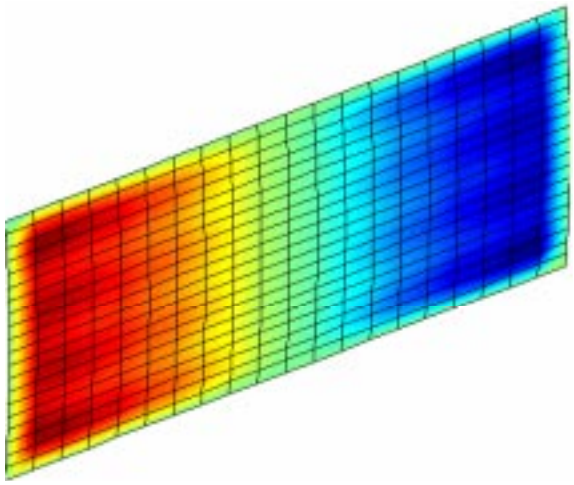

Figure 5.8: Mode shape of the most efficient radiation mode at 175 Hz.

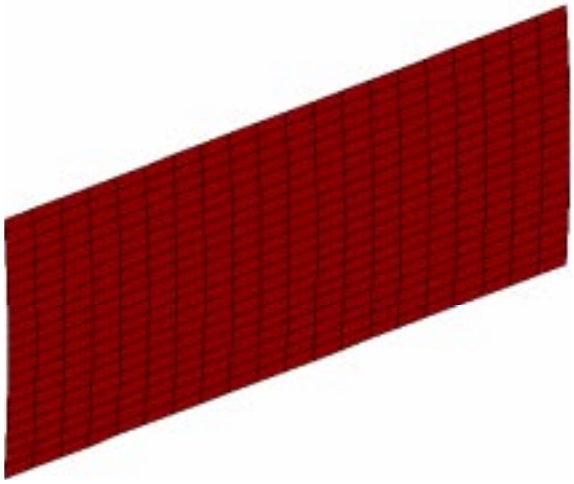

Figure 5.9: Mode shape of the first acoustic mode on the surface of the structure (0 Hz).

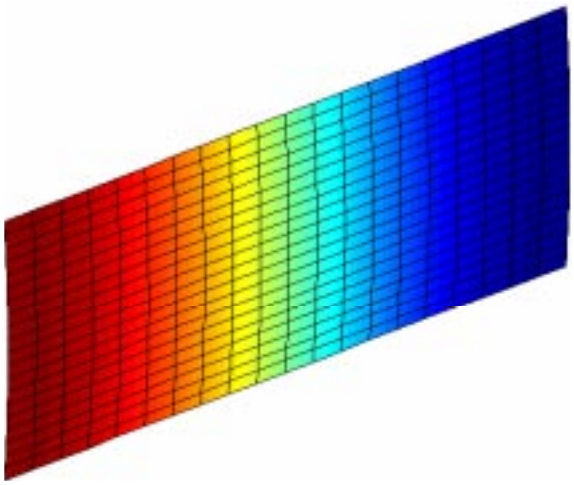

Figure 5.10: Mode shape of the second acoustic mode on the surface of the structure (175 Hz).

If a greater number of structural modes were used to estimate the radiation mode shapes then the shell motion would more closely resemble that of the dominant acoustic mode shape at the shell surface.

When compared to the normal structural modes of similar frequency (see Figure 5.11) the radiation modes have a much lower wavenumber. This property is beneficial when implementing modal sensing for the control system, as modes with lower wavenumbers are easier to measure with distributed modal sensors.

It is not surprising that the structural radiation mode shape functions are similar to the mode shapes of the dominant acoustic modes at the structure boundary, for it is well known that the coupling efficiency between acoustic and structural modes is high when the acoustic and structural mode shape functions are similar. This has important implications when it comes to designing the control system. Instead of calculating the radiation modes as was done in Section 5.2, it will be shown in Section 5.5.1 that it is adequate to assume the radiation mode shape function is the same as the acoustic mode shape function.

It is also interesting to note that the calculation of the radiation mode shapes allows identification of regions of high power transmission (which are not necessarily co-located with the areas of maximum structural vibration). It may be possible to use this information prudently to optimise the location of structural control sources.

5.3.2 Active Control of Sound Transmission - Traditional Error Criteria vs Radiation Modes

A numerical simulation was conducted where a single point force was placed a quarter of the way along the centre line of the rectangular panel at [0.250, 0.000, 0.246] to provide the primary excitation source. A single secondary source was symmetrically located at [0.250, 0.000, 0.739] to provide the control force. It should be noted that the location of the control force was not optimised in any way as this was not the aim of the study. The

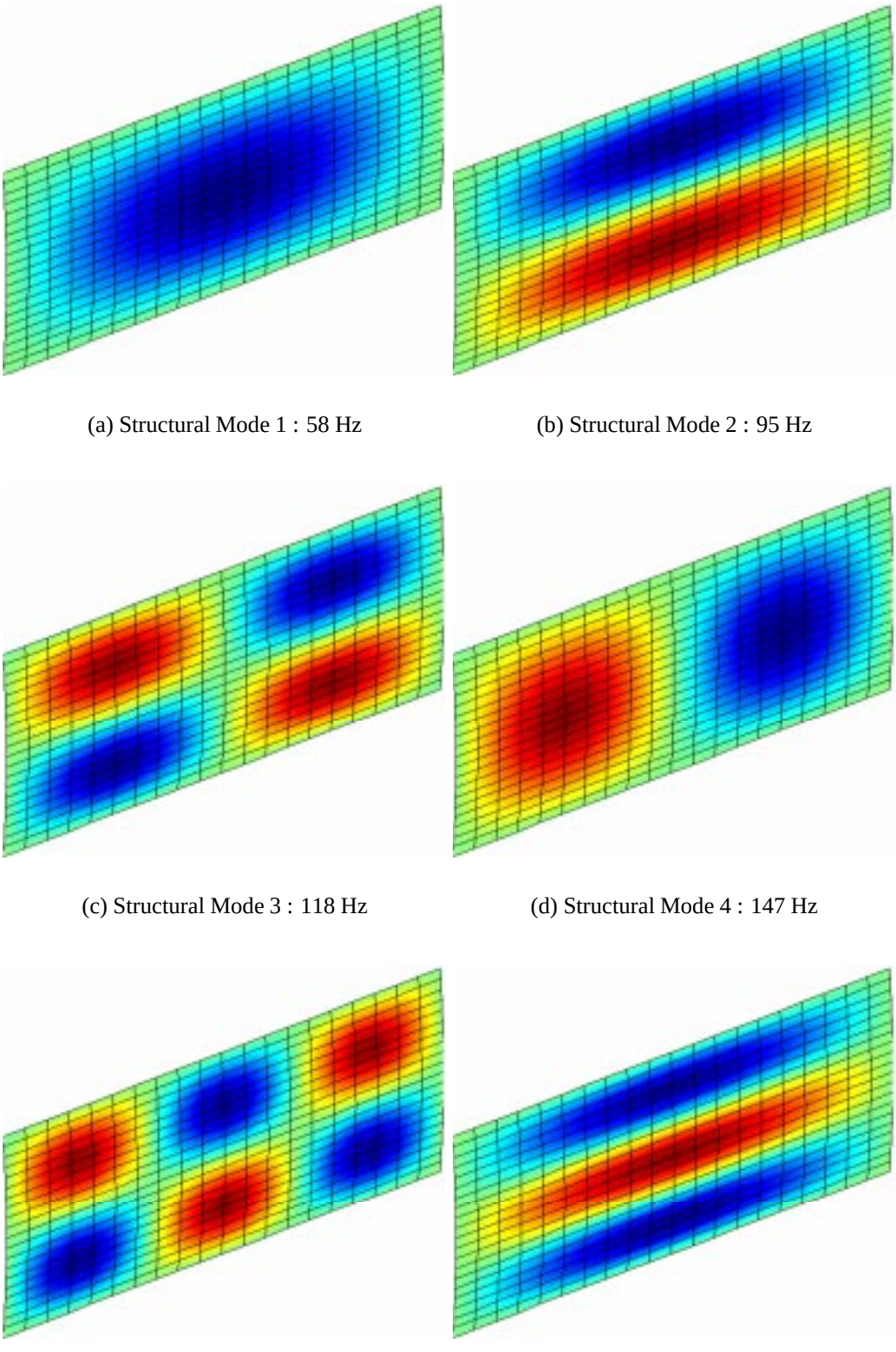

(a) Structural Mode 1 : 58 Hz

(b) Structural Mode 2 : 95 Hz

(c) Structural Mode 3 : 118 Hz

(d) Structural Mode 4 : 147 Hz

(e) Structural Mode 5 : 159 Hz

(f) Structural Mode 6 : 206 Hz

Figure 5.11: Mode shape of the first 6 normal structural modes.

research objective was to show that it is possible to use a structural error sensor to provide an error signal which would result in a similar reduction in enclosure potential energy as obtained by using the enclosure potential energy as the error signal.

Figure 5.12 compares the reduction in the acoustic potential energy obtained when minimising the two most efficient radiation modes against that obtained using conventional error criteria; namely, the acoustic potential energy (which provides an upper limit of control performance) and the structural kinetic energy. The data for all the control simulations are presented as (a) absolute acoustic potential energy, and (b) as a difference between the acoustic potential energy when minimising the cost function and minimising the acoustic potential energy. Minimised potential energy was used as the reference, rather than the more conventional approach of using the primary potential energy levels, in order to highlight the errors associated with the sensing technique. The cost function of Equation (5.12) was optimised using conventional quadratic optimisation to determine the optimum control force magnitude and phase. The velocity amplitudes of the radiation modes were estimated using the modal filter matrix given by Equation (5.19). There were as many error sensors (100) as normal structural modes used to calculate the modal filter matrix (of the radiation modes) so as to provide an upper bound on the performance offered by the technique. A lesser number would have required the use of a pseudo-inverse to evaluate Equation (5.20) which would have resulted in a decrease in the control performance. At the frequencies where the eigenvalues cross (in Figure 5.3) there is an increase in the potential energy as a result of minimising the amplitudes of the two radiation modes. This occurs for two reasons:

1. Since several radiation modes contribute to the power transmission at these cross over frequencies, a single control force (used in the simulation) is unable to provide enough independent control channels to achieve control. Subsequently, the amount of control is low for all cost functions. The corollary is that the reduction in sound

transmission is greatest where the radiation efficiencies peak.

2. Insufficient radiation modes were used to measure the power transmission, and this is particularly apparent in the frequency bands 405-475 Hz and 550-650 Hz. If more modes were used then the controlled levels would approach that of the potential energy controlled case.

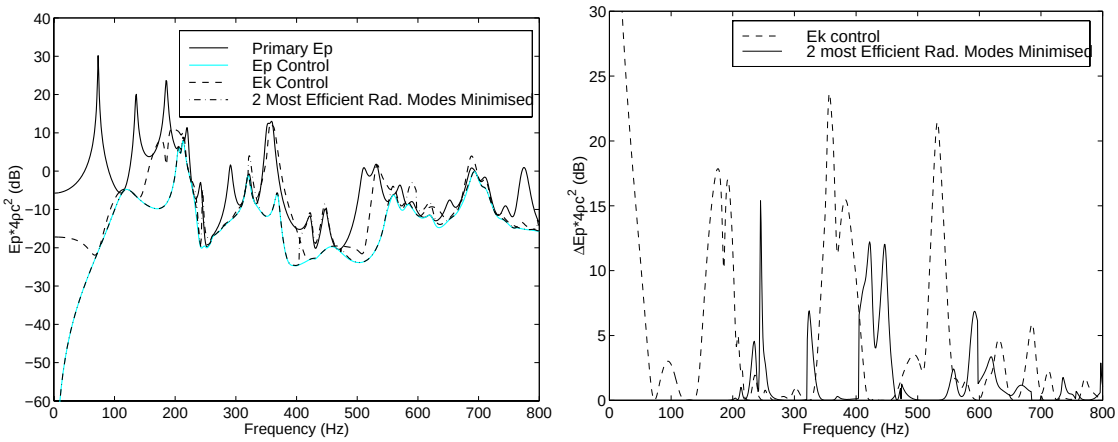

(a) Reduction in potential energy

(b) Difference in controlled levels

Figure 5.12: Reduction in acoustic potential energy - Conventional error criteria vs radiation modal sensing.

It will be shown in the following section, for the frequency range of interest (0-800 Hz), that it is sufficient to consider only the first 5 dominant radiation modes (see Figure 5.3) to achieve attenuation levels equal to those achieved by using the potential energy as a cost function.

Figure 5.13 shows the effect of having significantly fewer error sensors than the number of dominant structural modes. A practical number of 10 error sensors were randomly located over the rectangular panel. As can be seen in this example, 10 error sensors were insufficient to accurately resolve the modal amplitudes of the normal structural modes, resulting in observation spill-over. In fact, it was found that when randomly selecting the

structural sensor locations it was necessary to have at least half the number of error sensors (50) as normal structural modes before an acceptable estimate of the structural modal amplitudes using Equation (5.18) was obtained. This limitation associated with discrete error sensing has also been reported by others (Tanaka et al. 1996, Morgan 1991).

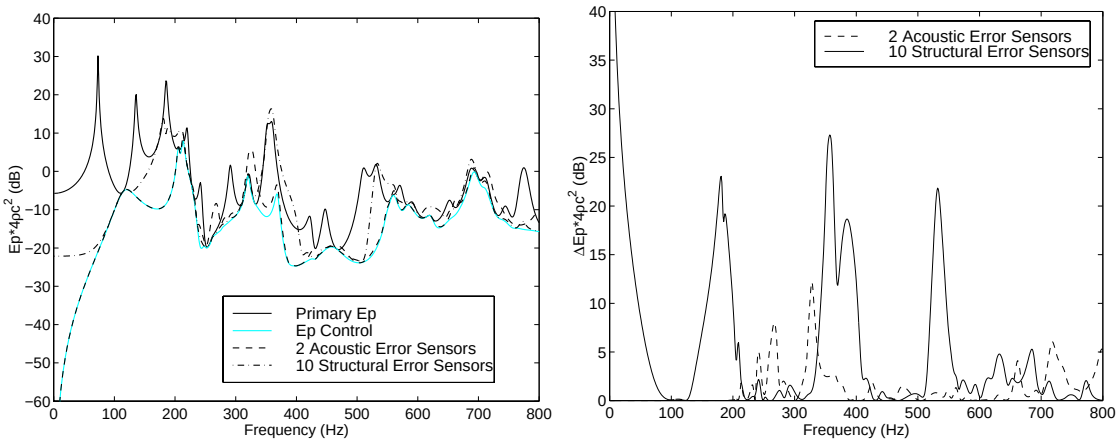

(a) Reduction in acoustic potential energy

(b) Difference in controlled levels

Figure 5.13: Effect on performance of insufficient structural sensors to measure the radiation modes and Control using 2 acoustic error sensors.

Also shown in Figure 5.13 is the acoustic potential energy when the squared sum of 2 acoustic error sensors (at $[0.000, -0.209, 0.000]$ and $[0.250, 0.209, 0.985]$) is used as the error criterion. When comparing Figure 5.13 against modal control in Figure 5.12, it becomes clear that 2 radiation modal sensors out-perform 2 traditional pressure field sensors (provided a sufficient number of structural sensors are used to properly measure the radiation modes). One may argue that it is not valid to draw comparisons between a structural system with 50-100 point sensors and an acoustic system with only 2 sensors. However, it should be noted that for active control applications it is the number of error signals, be they composite or point sensors, which define the system dimensionality.

It was shown by Snyder et al. (1995) that if the sensors were placed judiciously using information about the structural mode shapes then sensor performance could be improved by screening out undesired modes. For example, if a line of sensors is run along the centre

of the panel then the performance can be improved compared to selecting the positions at random. Seven (7) discrete structural sensors were placed along the centre-line to see if it were possible to use judicious placement to advantage and the control results are shown in Figure 5.14. The number of sensors was then increased to 21 so that every node along the line was selected. This ensured that no spatial aliasing occurred along the sensor in the x-direction. The results obtained using this "continuous" sensor are also shown in Figure 5.14. It can be seen that when the error sensor locations are well chosen, the control performance can be greatly increased. The meta-sensor containing 21 discrete sensors performs slightly better than the one with only seven sensors due to less aliasing of the higher order structural modes.

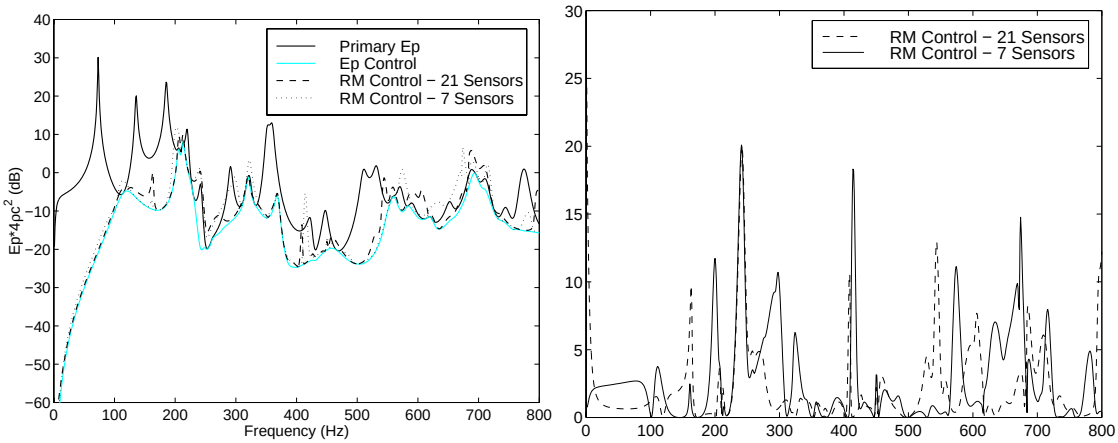

(a) Reduction in acoustic potential energy

(b) Difference in controlled levels

Figure 5.14: Control of the first 2 radiation modes when using 7 and 21 judiciously located structural sensors.

The conclusion is that error signals derived from the radiation modes outperform conventional structural and acoustic error sensing and that excellent control is achievable with very few error signals. Although the radiation mode formulation as it is described above using many discrete error sensors is unworkable for a practical control system because of the frequency dependence of the eigen-system and the large number of point sensors required, it can be used as a benchmark against which the performance of simplifications

can be compared. The limitation arising from the frequency dependence will be addressed and techniques for overcoming it will be presented in the following section.

5.4 Practical Implementation and Approximations

5.4.1 Background Theory

As already shown in the preceding section, the eigenvalue and eigenvector matrices are highly frequency dependent and it is possible in a practical control system to generate an eigenvalue filter set using a low order digital filter for each radiation mode. However, the same cannot be said about the eigenvector matrix. In the case described here, for each radiation mode of interest, the eigenvector filter would consist of several hundred individual frequency dependent digital filters, one filter for every structural sensor used to measure each radiation mode. It is difficult to store the necessary filter coefficients to model the eigenvector matrix over a large bandwidth and definitely beyond the ability of current DSP systems to implement such filters in real time. It is also impractical in most cases to implement the required number of physical error sensors.

Studies of the power flow from cylinders (Borgiotti & Jones 1994) and rectangular panels using either vibration error sensors (Snyder et al. 1993) or acoustic error sensors (Burgemeister 1996) have found that by exploiting the property that the radiation mode shapes (eigenvectors) varied slowly with respect to frequency, it is possible to select a frequency such that the radiation mode shapes at that frequency are representative of the mode shapes over a frequency range with little loss in accuracy. This was achieved by fixing the radiation transfer function matrix to that at some desired frequency (known as the *normalisation frequency*), f, resulting in a set of eigenvectors independent of frequency which can be implemented by a fixed gain. This greatly reduces the number of digital filters required for the control system.

Applying this approach to the current set of equations yields (Burgemeister 1996),

$$\mathbf{U} = \mathbf{K}\mathbf{U}_f \tag{5.23}$$

where $\mathbf{U}_f$ is the eigenvector matrix corresponding to the chosen frequency, f, and $\mathbf{K}$ is a (n_r x n_r) correction matrix and is given by

$$\mathbf{K} = \mathbf{U}\mathbf{U}_f^{-1} \tag{5.24}$$

The correction matrix is highly diagonal and by neglecting the off-diagonal terms there is little loss in accuracy; that is,

$$\mathbf{K} = \text{DIAG}[\mathbf{U}\mathbf{U}_f^{-1}] \tag{5.25}$$

Substituting Equation (5.23) into Equation (5.10) and using the property that both $\mathbf{U}$ and $\mathbf{K}$ are real, an expression for the potential energy is obtained,

$$E_p \approx \mathbf{v}^{\mathrm{H}}\mathbf{U}_f^{\mathrm{T}}\mathbf{S}_f\mathbf{U}_f\mathbf{v} \tag{5.26}$$

where $\mathbf{S}_f$ is the frequency normalised eigenvalue matrix,

$$\mathbf{S}_f = \mathbf{K}^{\mathrm{T}}\mathbf{S}\mathbf{K} \tag{5.27}$$

Although the radiation modes for internal acoustic spaces exhibit a significantly greater frequency dependence than free field radiation modes (at frequencies below the critical frequency) it is possible to apply the same technique here with surprisingly little degradation in performance.

A more elegant and accurate way of obtaining an "orthonormal" set of equations

than just described is to diagonalise the eigenvalue matrix after it has been pre and post-multiplied by the correction matrix. Thus the following expansion may be made

$$\mathbf{U}\mathbf{S}\mathbf{U}^{\mathrm{T}} = \mathbf{U}_f[\mathbf{U}_f^{-1}\mathbf{U}\mathbf{S}\mathbf{U}^{\mathrm{T}}\mathbf{U}_f]\mathbf{U}_f^{-1} \tag{5.28}$$

By using the property of the unitary matrix ($\mathbf{U}^{-1} = \mathbf{U}^{\mathrm{T}}$) it is possible to rearrange Equation (5.28) to derive a orthonormal basis independent of frequency

$$\mathbf{U}\mathbf{S}\mathbf{U}^{\mathrm{T}} = \mathbf{U}_f[\mathbf{S}_f]\mathbf{U}_f^{\mathrm{T}} \tag{5.29}$$

where $\mathbf{S}_f$ is the fixed frequency eigenvalue matrix given by

$$\mathbf{S}_f = \mathbf{U}_f^{\mathrm{T}}\mathbf{U}\mathbf{S}\mathbf{U}^{\mathrm{T}}\mathbf{U}_f \tag{5.30}$$

In this format the eigenvalue matrix is not diagonal (except at the normalisation frequency) but fully populated. It is therefore necessary to diagonalise the fixed frequency eigenvalue matrix to retain the benefits associated with the orthonormal transformation.

$$\hat{\mathbf{S}}_f = \mathrm{DIAG}[\mathbf{U}_f^{\mathrm{T}}\mathbf{U}\mathbf{S}\mathbf{U}^{\mathrm{T}}\mathbf{U}_f] \tag{5.31}$$

As with the diagonalisation of Equation (5.24), very little loss in mass (accuracy) occurs when diagonalising the already highly diagonal frequency normalised eigenvalue matrix $\mathbf{S}_f$, particularly adjacent to the normalisation frequency. The acoustic potential energy given by Equation (5.10) can now be approximated as

$$E_p \approx \mathbf{v}^{\mathrm{T}}\mathbf{U}_f\hat{\mathbf{S}}_f\mathbf{U}_f^{\mathrm{T}}\mathbf{v} \tag{5.32}$$

Likewise the fixed shape modal filter, Equation (5.20), can be written as

$$\mathbf{Z}_{t|_f} = \mathbf{U}_f^{\mathrm{T}} \Psi_e^{-1} \tag{5.33}$$

The modal amplitudes of the fixed shape radiation modes are given by

$$\mathbf{w} = \mathbf{Z}_{t|_f} \mathbf{v}_e \tag{5.34}$$

With the modal filter in a form independent of frequency, continuous shaped sensors may be used to decompose the surface velocity into modal amplitudes, thereby doing away with the many point sensors and associated eigenvector digital filters required in Section 5.3. Therefore, unlike the discrete system in Section 5.3, only the eigenvalues need be implemented with digital filters (see Figure 5.1). It should be noted that because of the discrete nature of the finite element simulations, “continuous meta sensors” were approximated from the summed output of a line of discrete point sensors.

The use of shaped error sensors made from piezo film and means for relating the charge output to the flexural motion of the surface to which they are fixed, is discussed in detail by Hansen & Snyder (1997) and will be discussed in more detail in Section 6.1.2.

5.4.2 Results

As discussed previously, a decrease in accuracy is expected as a result of neglecting the off-diagonal terms in the fixed frequency eigenvalue matrix (see Equation 5.31). The error manifests itself as an increase in the number of efficient radiation modes away from the normalisation frequency. This physically means that more "orthogonal" modes are necessary to account for the power transmission. Figure 5.15 illustrates the effect that fixing the eigenvectors to the values at a particular frequency (175 Hz) has on the eigenvalues (as compared to Figure 5.3).

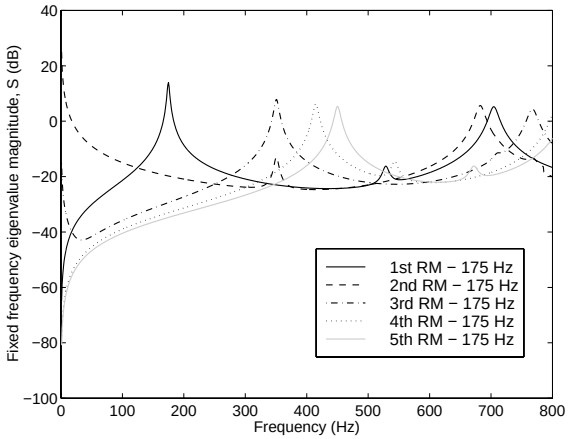

Figure 5.15: Fixed frequency eigenvalues normalised to 175 Hz.

As can be seen from Figure 5.15, the eigenvalues around the frequency at which the system of equations is fixed (175 Hz) resembles the original frequency dependent data (Figure 5.3). However, away from 175 Hz more radiation modes contribute significantly to the power transmission and as a result more modes will need to be measured to keep the control system performance equal to that of the frequency dependent case. A higher order digital filter is required to model the eigenvalues than was previously necessary for the case depicted in in Figure 5.3. However, this is still very easy to implement in a practical system.

As a benchmark, the performance achieved using the 5 most efficient radiation modes has been compared against that achieved using the first 5 fixed-shape radiation modes normalised at 175 Hz (see Figure 5.16). This figure clearly shows that the two techniques yield almost identical levels of control around the normalisation frequency demonstrating that frequency normalisation of the mode shape is an excellent and highly efficient means of simplifying the control system when using radiation modal sensors if control is required over a limited bandwidth. The reason for the poor performance around the third acoustic resonance (526 Hz) is due to high number of almost orthogonal radiation modes in this frequency region as seen in Figure 5.15. Inspection of these almost orthonormal mode shapes showed that none of them emulated the mode shape of the third acoustic mode,

hence the poor control. Were another radiation mode to be sensed, this would have picked up the particular mode shape and control would have been significantly improved over this region.

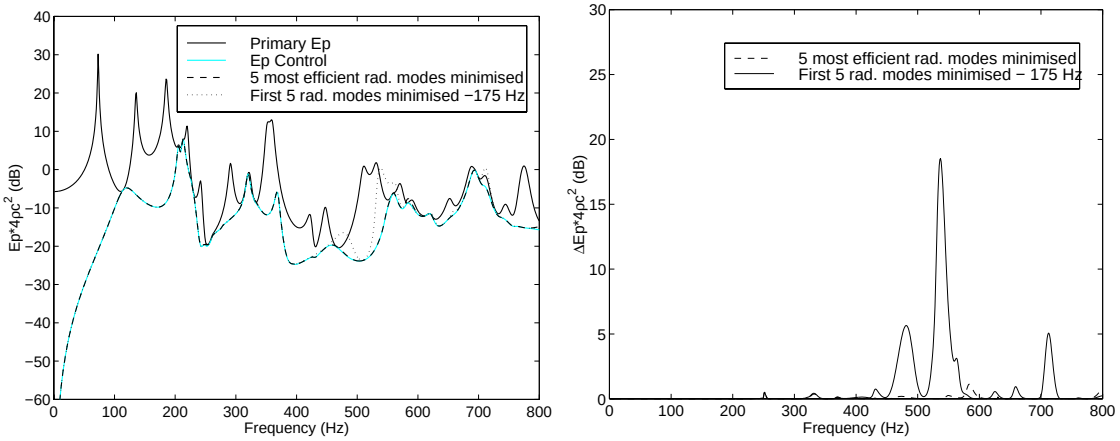

(a) Reduction in acoustic potential energy

(b) Difference in controlled levels

Figure 5.16: Cost function comparison between frequency normalised radiation modes (175 Hz) and unmodified (frequency dependent) radiation modes.

Obviously, if fewer fixed-shape radiation modes are used, then the level of control will be subsequently reduced, particularly away from the normalisation frequency (see Figure 5.18 below).

5.4.3 Control without Eigenvalue Filters

In a real system, the eigenvalue (radiation efficiency) filter may be inconvenient to implement as most commercial active control systems do not have the facility to apply a frequency dependent filter to each individual channel. By not weighting the modal amplitudes by the square root of the radiation efficiencies (eigenvalue filter), neither the modal volume nor the acoustic impedance is accounted for in the cost function. As a result, the level of control afforded by the system is reduced.

The two most efficient radiation modes were identified and their shape calculated

at the natural frequencies of the first two acoustic modes respectively (Figures 5.7 and 5.8). The modal amplitudes of these two fixed-shape radiation modes were then used as error signals for the control system over the entire frequency range of control. Figure 5.17 shows the acoustic potential energy levels obtained when minimising the two most efficient fixed-shape radiation modes normalised to the natural frequencies of the first two acoustic modes without using an eigenvalue filter in the control system.

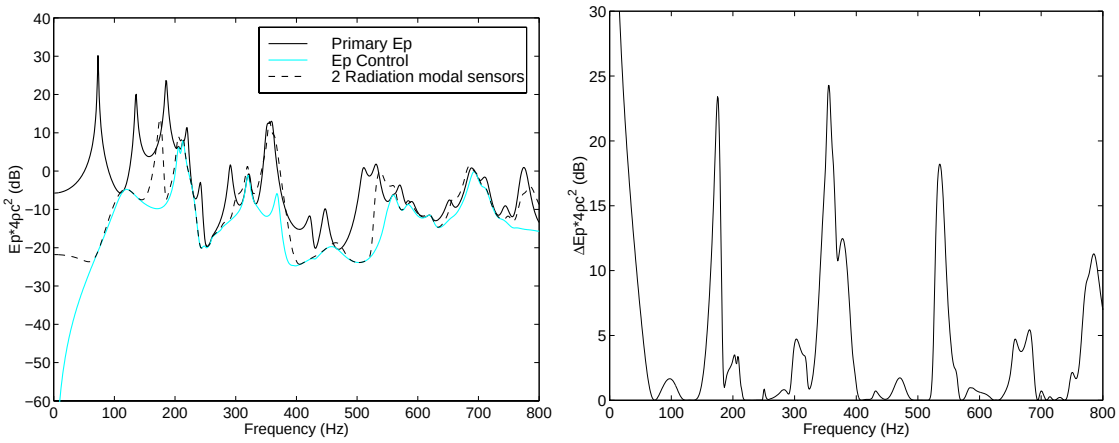

(a) Reduction in acoustic potential energy

(b) Difference in controlled levels

Figure 5.17: Multi-channel frequency normalised (at 5 Hz and 175 Hz) radiation modal sensors without radiation efficiency weighting filter.

As can be seen, the reduction in the potential energy is less than that shown in Figure 5.12. The poor performance comes from not accounting for the frequency dependent radiation efficiency of the individual radiation modes. As a result, much of the control effort is spent in reducing the amplitudes of the less-efficient modes, which do not significantly contribute to the sound transmission.

If only a single fixed-shape radiation mode is sensed, then 100% of the control effort is used in controlling that mode. Such an approach gives good results over a limited bandwidth around the frequency at which the mode shape is fixed. Figure 5.18 shows the level of control achieved by using the "raw" (unweighted) signal derived from a single radiation mode sensor whose shape was normalised at either 5 Hz or 175 Hz. If a single

channel control system were to use these two modal sensors with a cross-over at the appropriate places, then this would provide almost optimal control with an error of less than 4 dB over the entire frequency band. It should be noted that although such an approach is suitable for a system with a single control source, it is unlikely that it will work as well for systems using multiple control sources.

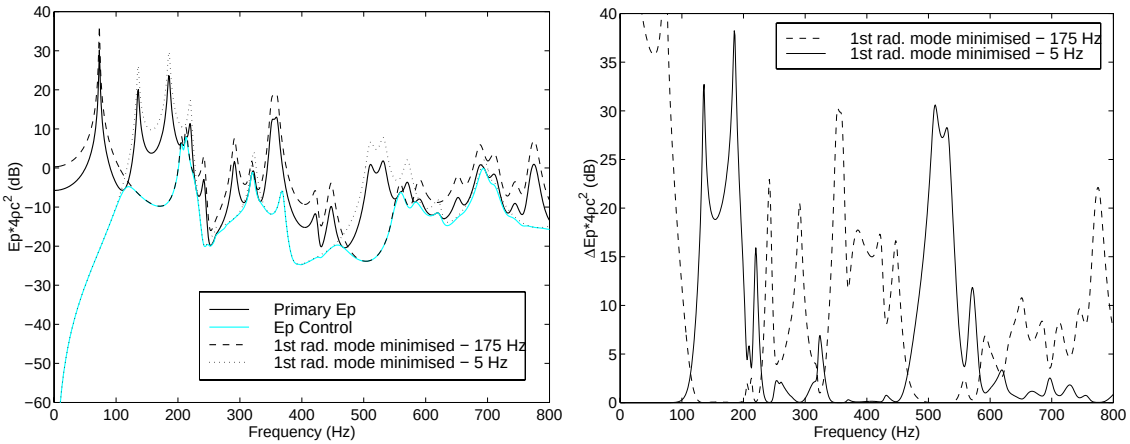

(a) Reduction in global acoustic potential energy

(b) Difference in controlled levels

Figure 5.18: Single channel frequency normalised radiation modal sensors without radiation efficiency weighting filter.

5.5 Radiation Modes derived from Alternative Cost Functions

In the previous section, it was shown that it is possible to derive a set of surface velocity patterns which are orthogonal in terms of their contributions to the interior acoustic potential energy of the cavity. It is possible to derive such patterns for a myriad of alternative objective functions. In the following sections, the radiation modes orthogonal in terms of their contribution to the cost functions listed below will be derived:

- Potential Energy : An alternative formulation

- Sum of the squared pressures over a subspace
- Radiated power into the cavity
- Energy Density at a point

5.5.1 Potential Energy : An Alternative Formulation

It will be shown in the following analysis that there exists an alternative approach to diagonalise the error weighting matrix $\mathbf{\Pi}$ used in Section 5.2. It should be noted however, that this only holds true if the cost function is global (internal acoustic potential energy), the modal density is low and the flexible structure forms a large part of the bounding surface of the cavity. If the later two conditions do not hold, then at high frequencies the internal radiation mode shapes degenerate to approximately the free field radiation mode shapes (Johnson 1996). In Section 5.5.2 where the control objective is not global, the following approach cannot be used and it is necessary to use the approach described in Section 5.2.

The reformulation of the radiation modes orthogonal to the internal potential energy will now be presented. The interior acoustic potential energy is given by

$$E_p = \mathbf{v}^{\mathrm{H}} \mathbf{Z}_a^{\mathrm{H}} \mathbf{\Lambda} \mathbf{Z}_a \mathbf{v} \tag{5.35}$$

where

$$Z_a(l,i) = \frac{j\rho_0 S\omega}{\Lambda_l(\kappa_l^2 + j\eta_{a_l}\kappa_l k - k^2)} B_{l,i} \tag{5.36}$$

Now $\mathbf{Z}_a$ can be written in matrix form,

$$\mathbf{Z}_a = \mathbf{\Upsilon B} \tag{5.37}$$

where $\mathbf{B}$ is the (n_a x n_s) non-dimensional coupling coefficient matrix and, $\mathbf{\Upsilon}$, is the (n_ax n_a) diagonal acoustic resonance matrix whose elements are given by

$$\mathbf{\Upsilon}_{l,l} = \frac{j\rho_0 S\omega}{\Lambda_l(\kappa_l^2 + j\eta_{a_l}\kappa_l k - k^2)} \tag{5.38}$$

Therefore, the potential energy may be expressed as

$$E_p = \mathbf{v}^{\mathrm{H}}\mathbf{B}^{\mathrm{H}}\mathbf{\Upsilon}^*\mathbf{\Lambda}\mathbf{\Upsilon}\mathbf{B}\mathbf{v} \tag{5.39}$$

or

$$E_p = \mathbf{y}^{\mathrm{H}}\mathbf{\Omega}\mathbf{y} \tag{5.40}$$

where $\mathbf{y}$ is the (n_a x 1) modal amplitude column vector of the radiation modes given by

$$\mathbf{y} = \mathbf{B}\mathbf{v} \tag{5.41}$$

and the (n_a x n_a) diagonal matrix, $\mathbf{\Omega}$, is given by

$$\mathbf{\Omega} = \mathbf{\Upsilon}^*\mathbf{\Lambda}\mathbf{\Upsilon} \tag{5.42}$$

Evaluating the diagonal weighting matrix, the elements are given by

$$\Omega_{ll} = \frac{(\rho_0 S\omega)\frac{Sk}{4}}{\Lambda_l\left((\kappa_l^2 - k^2)^2 + (\eta_{a_l}\kappa_l k)^2\right)} \tag{5.43}$$

It is clear that Equation (5.40) is the same format as Equation (5.10) with a fully populated participation matrix and a diagonal weighting matrix. By induction it is possible to

define an corresponding mode shape matrix

$$\mathbf{\Xi} = \mathbf{\Psi}\mathbf{B}^{\mathrm{T}} \tag{5.44}$$

Pre-multiplying Equation (5.44) by $\mathbf{\Psi}^{\mathrm{T}}$ and integrating over the surface of the structure gives

$$\frac{1}{S}\int_s \mathbf{\Psi}^{\mathrm{T}}(\vec{\mathbf{x}})\mathbf{\Xi}(\vec{\mathbf{x}})dS(\vec{\mathbf{x}}) = \frac{1}{S}\int_s \mathbf{\Psi}^{\mathrm{T}}(\vec{\mathbf{x}})\mathbf{\Psi}(\vec{\mathbf{x}})\mathbf{B}^{\mathrm{T}}dS(\vec{\mathbf{x}}) \tag{5.45}$$

and using the principle of modal orthogonality, the following expression is obtained

$$\frac{1}{S}\int_s \mathbf{\Psi}^{\mathrm{T}}(\vec{\mathbf{x}})\mathbf{\Xi}(\vec{\mathbf{x}})dS(\vec{\mathbf{x}}) = \mathbf{M}\mathbf{B}^{\mathrm{T}} \tag{5.46}$$

where $\mathbf{M}$ is the (n_s x n_s) diagonal matrix with diagonal elements given by

$$M_i = \frac{1}{S}\int_s \Psi_i^2(\vec{\mathbf{x}})dS(\vec{\mathbf{x}}) \tag{5.47}$$

The left hand term of Equation (5.46) is the same as the expression for the non-dimensional coupling coefficient matrix $\mathbf{B}$ with the exception that the mode shape matrix of the radiation mode has been used in place of the acoustic mode shape matrix. Therefore it follows that the radiation mode shape matrix is identical to the acoustic mode shape matrix in which row i is scaled by some scalar term M_i, ie

$$\mathbf{\Xi}(\vec{\mathbf{x}}) = \mathbf{M}\mathbf{\Phi}(\vec{\mathbf{x}}) \tag{5.48}$$

Since no new assumptions have been presented in the previous derivation it holds that results of the previous simulations, shown in Sections 5.3 and 5.4 still hold. The advantage of the current approach is that there is no need to use a SVD to derive the

mode shape matrices of the radiation modes. It should be noted that it is only fair to compare this current formulation with that of the "fixed-shape" radiation modes presented in Section 5.4 since the mode shapes for the current formulation obviously do not vary with frequency.

The approach just described is only suited to low frequencies where the modal density of the acoustic system is low since this ensures that the rows of the $\mathbf{B}$ matrix are unique. As the number of the acoustic modes is increased the likelihood of the acoustic mode shapes across the vibrating surface being orthogonal decreases. When non-orthogonality occurs, the advantage of this current approach begins to break down. To ensure uniqueness it is possible to collect all the acoustic modes which have the same surface pressure pattern into a "single" radiation mode. This results in removal of the redundant line in the $\mathbf{B}$ matrix and adds the corresponding terms in the diagonal weighting matrix $\mathbf{\Omega}$. The SVD approach has the advantage that this occurs automatically.

A single radiation mode has been used to demonstrate the current approach. If all the radiation modes were used the results obtained would be equivalent to minimising the acoustic potential energy.

Figure 5.19 below presents the potential energy reduction when controlling the radiation mode corresponding to the first longitudinal acoustic mode ([1,0,0]) and when minimising the most efficient radiation mode normalised to 175 Hz (using the approach of Section 5.4). As can be seen, the approaches are identical. If a realistic sensor were to be employed to estimate the modal velocities, then the control performance of both sensors would deteriorate equally.

5.5.1.1 Implications for Passive Control

The above formulation is not only applicable to active noise control but has important implications for passive control of sound transmission into cavities. This shows that when attempting to minimise the sound transmission into cavities it is just as important to have

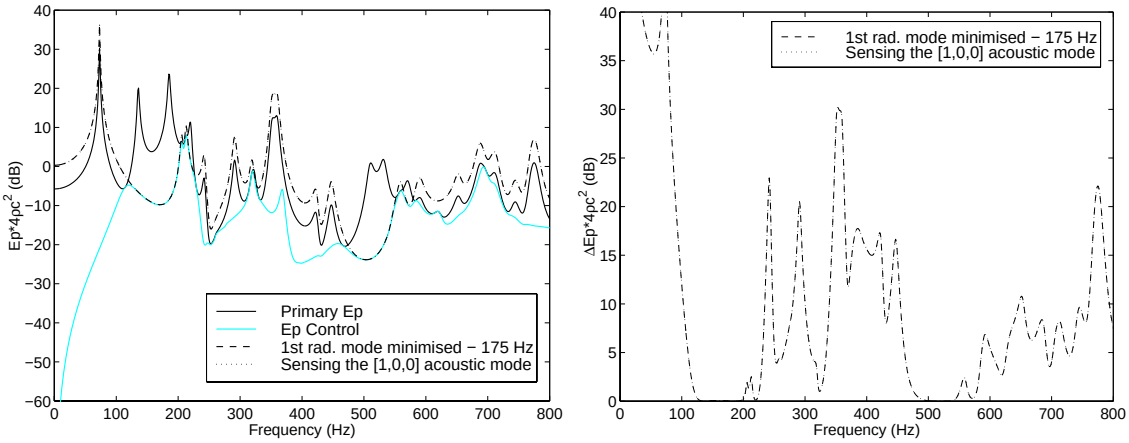

(a) Reduction in acoustic potential energy

(b) Difference in controlled levels

Figure 5.19: Comparison between minimising acoustic potential energy, minimising the most efficient radiation mode normalised to 175 Hz and minimising the radiation mode corresponding to the first longitudinal acoustic mode.

an understanding of the dynamics of the receiving space as an understanding of the dynamics of the exciting structure. Dynamic absorbers and co-located sensor/actuator pairs act to increase the impedance the structure "sees" at the mount point. Therefore, using the acoustic mode shapes to guide placement of such devices would likely achieve good results very quickly without having to analyse the dynamics of the structure. Obviously further refinement and optimisation would have to take into consideration the dynamics of both the structure and the cavity.

5.5.2 Radiation Modes using a Subspace

Borgiotti & Jones (1993) suggested that rather than minimise the total power radiated from a cylinder into free space it might be desired to minimise power radiated into a sector. Likewise Clark, Burdisso & Fuller (1993) implemented a PVDF film sensor (referred to as a PVDF microphone) to estimate the pressure at a point in the far-field of a beam. The same principle can also be applied to the sound transmitted into a cavity. Sometimes it may be that global control is not required but it is sufficient to control the acoustic

energy over some zone in the cavity, such as a passengers head for example. In this case control effort is wasted attempting to achieve global control. Therefore, using the procedure in Section 5.2 it is possible to derive radiation modes orthogonal in terms of their contribution to the sum of squared pressures over some subspace. If the subspace is a single point, then the technique produces a *virtual structural microphone* which can be "steered" to any point in the cavity.

The sum of the squared pressures at l locations is given by

$$\sum_{i=1}^{l} |p(\vec{\mathbf{r}}_i)|^2 = \mathbf{p}_e^{\mathrm{H}} \mathbf{p}_e \tag{5.49}$$

For an acoustic system driven by a bounding structure, the sum of squared pressure in terms of the velocity amplitudes is given by

$$\sum_{i=1}^{l} |p(\vec{\mathbf{r}}_i)|^2 = \mathbf{v}_p^{\mathrm{H}} \mathbf{Z}_a^{\mathrm{H}} \mathbf{Z}_w \mathbf{Z}_a \mathbf{v}_p \tag{5.50}$$

where the Hermitian weighting matrix $\mathbf{Z}_w$ is given by

$$\mathbf{Z}_w = \mathbf{\Phi}_e^* \mathbf{\Phi}_e^{\mathrm{T}} \tag{5.51}$$

Equation (5.50) is now in the same format as Equation (5.7), ie

$$\sum_{i=1}^{l} |p(\vec{\mathbf{r}}_i)|^2 = \mathbf{v}^{\mathrm{H}} \mathbf{\Pi}_s \mathbf{v} \tag{5.52}$$

where the subspace error weighting matrix $\mathbf{\Pi}_s$ is given by

$$\mathbf{\Pi}_s = \mathbf{Z}_a^{\mathrm{H}} \mathbf{Z}_w \mathbf{Z}_a \tag{5.53}$$

The subspace error matrix can now be diagonalised using the same technique as per

Section 5.2. The rectangular panel/cavity system analysed in the previous section has been reanalysed using subspace squared pressure control. The subspace chosen was the 4 nodes in the centre of the cavity used for the energy density simulations in Section 4.2.2. It was shown in Section 5.3 that when 2 ideal modal sensors are used, the control system behaves almost as if the cost function were measured directly (in this case the pressure over the subspace) as can be seen in Figure 5.20. The acoustic potential energy levels before and after control are shown in Figure 5.21. Therefore, it is more sensible to use a sensor with compromised performance for the simulations, since this always occurs in physical systems. The "continuous" strip sensor comprising 21 discrete sensors was used for this purpose. Figure 5.22 compares the reduction in the cost function obtained when minimising the sum of the squared pressures through some subspace when sensing the first 2 radiation modes with a single strip sensor. As can be seen the system performance is compromised a little when a strip sensor is used. Figure 5.23 represents the reduction in acoustic potential energy when using subspace control.

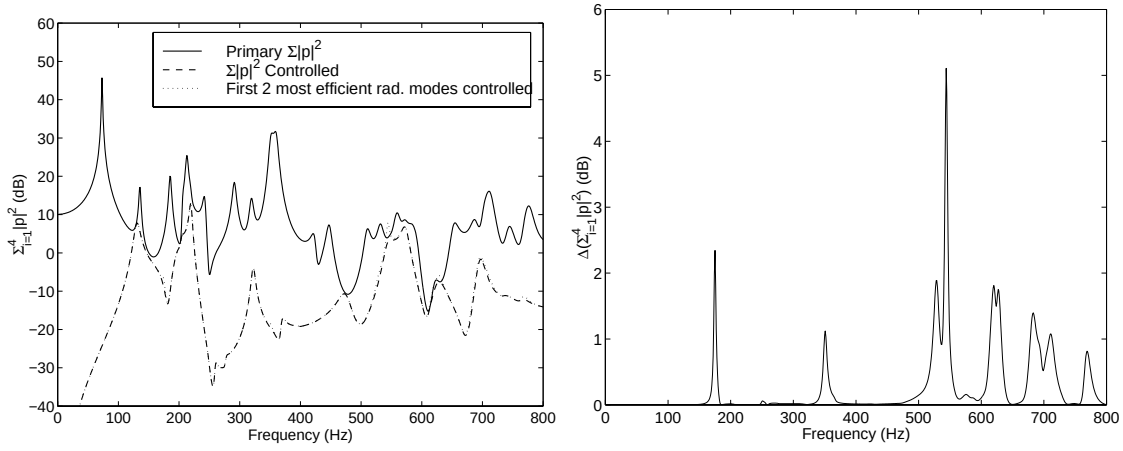

(a) Reduction in subspace cost function

(b) Difference in controlled levels

Figure 5.20: Comparison between minimisation of subspace $\Sigma|p|^2$ and first two most efficient radiation modes when using subspace control.

For the sake of completeness, the control offered by a radiation mode orthogonal to the

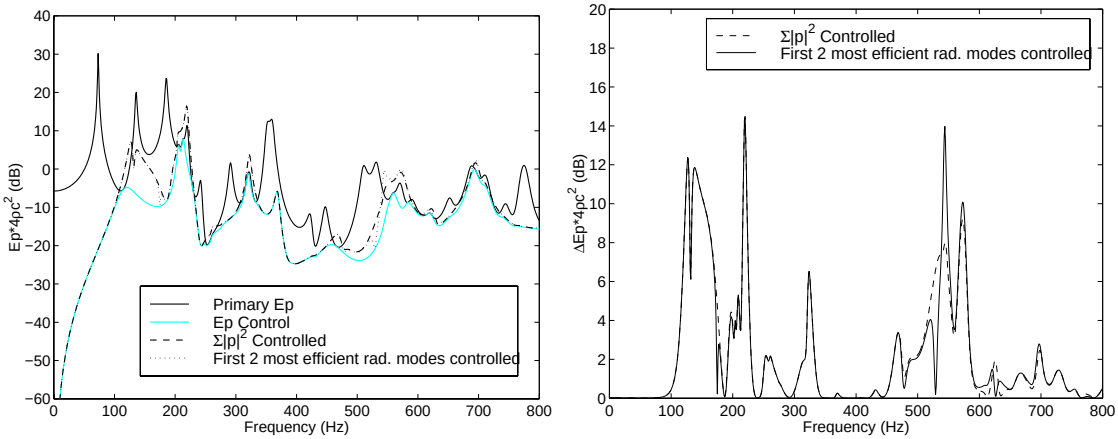

(a) Reduction global acoustic potential energy (b) Difference in controlled levels

Figure 5.21: Comparison between minimisation of acoustic potential energy, subspace $\Sigma|p|^2$ and first two most efficient radiation modes when using subspace control.

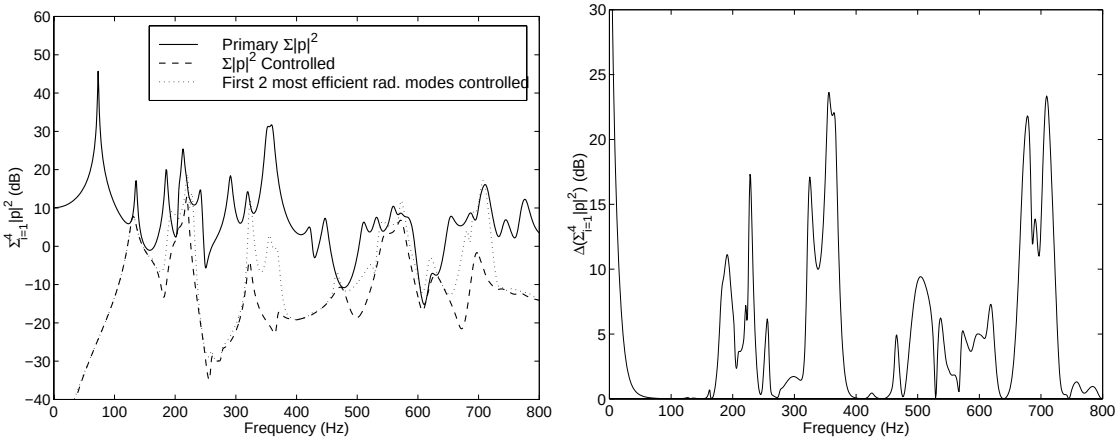

(a) Reduction in subspace cost function (b) Difference in controlled levels

Figure 5.22: Comparison between minimisation of subspace $\Sigma|p|^2$ and first two most efficient radiation modes when using subspace control with a strip sensor.

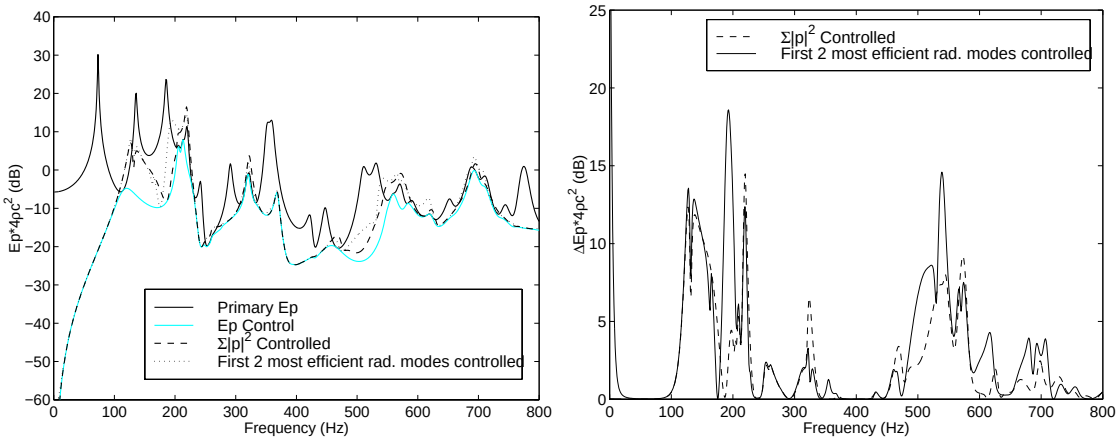

(a) Reduction in global acoustic potential energy

(b) Difference in controlled levels

Figure 5.23: Comparison between minimisation of acoustic potential energy, subspace $\Sigma|p|^2$ and first two most efficient radiation modes when using subspace control with a strip sensor.

pressure at a single location was analysed. The reduction in the acoustic potential energy is shown in Figure 5.24 for a microphone located in the centre of the cavity. As can be seen, the effect on the acoustic potential energy when controlling the two radiation mode sensors is almost equivalent to minimising the actual microphone placed in the centre.

The attenuation versus distance from the “structural microphone” and the “structural microphones” for the frequency range from 600 Hz to 700 Hz is plotted in Figure 5.25 and shows that indeed the attenuation is a maximum at the virtual microphone(s) and decreases with increasing distance. It can also be seen in Figures 5.22(a), Figures 5.24(a) and 5.25 that there is some performance loss when using only a single strip to sense the first two radiation modes, but despite this the objective of localised control is still achieved.

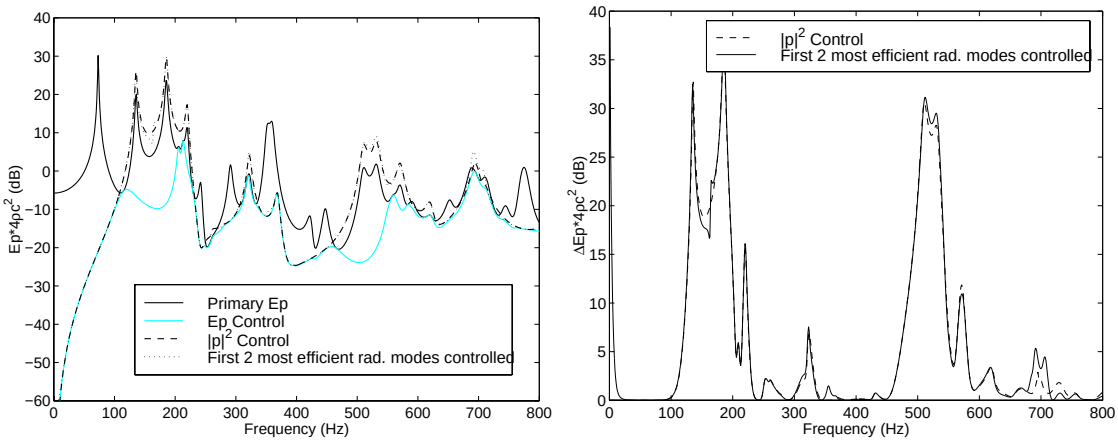

(a) Reduction in global acoustic potential energy

(b) Difference in controlled levels

Figure 5.24: Comparison between minimisation of acoustic potential energy, subspace $|p|^2$ and first two most efficient radiation modes when using point control with a strip sensor.

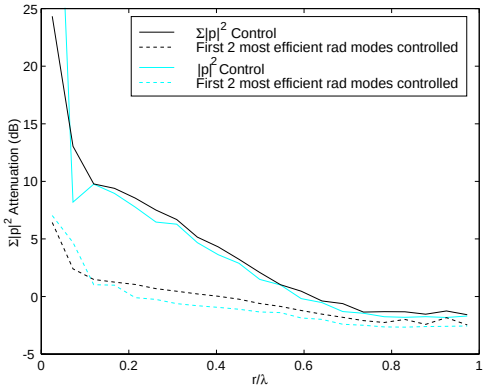

Figure 5.25: Comparison of attenuation versus distance from the structural microphone(s) made from a single strip of structural sensors and direct sensing.

5.5.3 Radiation Modes using Radiated Power

An alternative cost function for global control of the interior sound field is the total acoustic power radiated into the cavity (equivalent to the absorbed acoustic power) from the structure. It can be shown that the acoustic power input into the system is related to the potential energy in the cavity and is a function of the modal damping in the cavity and the natural frequencies of the dominant acoustic modes. Johnson (1996) derived an expression for the radiation modes of a structure radiating into a cavity based on the power radiated from the structure into the cavity using elemental radiators. He also found that the radiation mode shapes reflected the acoustic mode shapes. However, he failed to realise that the system matrices for radiation into a cavity are inherently diagonalised at low frequencies when the flexible structure forms a large part of the bounding surface (as was shown in Section 5.5.1). The following derivation shows that this is also the case for power radiated into the cavity. It also shows that minimisation of the power transmission will not necessarily minimise the interior acoustic potential energy.

The power radiated into the cavity is given by

$$W = \frac{1}{2}\int_S \Re\{v(\vec{\mathbf{x}})^* p(\vec{\mathbf{x}})\} dS(\vec{\mathbf{x}}) \tag{5.54}$$

The pressure at some point on the surface of the structure arising from the vibration of the structure is given by $p(\vec{\mathbf{x}}) = \phi(\vec{\mathbf{x}})\mathbf{Z}_a\mathbf{v}$; therefore

$$W = \frac{1}{2}\int_S \Re\{v(\vec{\mathbf{x}})^* \phi(\vec{\mathbf{x}})\mathbf{Z}_a\mathbf{v}\} dS(\vec{\mathbf{x}}) \tag{5.55}$$

Expanding the surface velocity in terms of the modal velocities, gives

$$W = \frac{1}{2}\int_S \Re\{[\psi(\vec{\mathbf{x}})\mathbf{v}]^* \phi(\vec{\mathbf{x}})\mathbf{Z}_a\mathbf{v}\} dS(\vec{\mathbf{x}}) \tag{5.56}$$

Since the mode shape matrices are real, the complex conjugate of the mode shape matrix is equal to the mode shape matrix. Thus

$$W = \frac{1}{2}\int_S \Re\{\mathbf{v}^* \psi(\vec{\mathbf{x}})\phi(\vec{\mathbf{x}})\mathbf{Z}_a\mathbf{v}\}dS(\vec{\mathbf{x}}) \tag{5.57}$$

Evaluating the integral and using the equation for the non-dimensional coupling coefficient, $B_{l,i}$ as per Equation (2.24) gives

$$W = \frac{S}{2}\Re\{\mathbf{v}^{\mathrm{H}}\mathbf{B}^{\mathrm{T}}\mathbf{Z}_a\mathbf{v}\} \tag{5.58}$$

Using the expansion for $\mathbf{Z}_a$ in terms of the non-dimensional coupling coefficient, the radiated power is given by

$$W = \frac{S}{2}\Re\{\mathbf{v}^{\mathrm{H}}\mathbf{B}^{\mathrm{T}}\boldsymbol{\Upsilon}\mathbf{B}\mathbf{v}\} \tag{5.59}$$

and since the matrix $\mathbf{B}$ is real, then

$$W = \frac{S}{2}\mathbf{v}^{\mathrm{H}}\mathbf{B}^{\mathrm{T}}\Re\{\boldsymbol{\Upsilon}\}\mathbf{B}\mathbf{v} \tag{5.60}$$

Taking the real component of the diagonal weighting matrix

$$\frac{S}{2}\Re\{\boldsymbol{\Upsilon}_{l,l}\} = \frac{\frac{S}{2}\rho_0 S\omega\eta_{a_l}\kappa_l k}{\Lambda_l\left((\kappa_l^2 - k^2)^2 + (\eta_{a_l}\kappa_l k)^2\right)} \tag{5.61}$$

It should be noted that Equation 5.61 in its current form cannot be used to calculate the weighting element for the first acoustic mode since the term κ_l is zero. Therefore, the first acoustic mode will not be accounted for when calculating the power radiated into the cavity. One technique for overcoming this is to add damping to the bulk compression mode, which may come about in practice from leakage through small holes in the cavity

walls. An alternative expression for the first acoustic resonance term including losses is (Nelson & Elliott 1992, Section 10.4)

$$\boldsymbol{\Upsilon}_{1,1} = \frac{\rho_0 S}{\Lambda_l(\frac{1}{T_a} + \frac{j}{c_0}k)} \tag{5.62}$$

where T_a is some time constant for the first acoustic mode. For the use in the numerical simulation under the limit of $\omega \to 0$ and $\eta_{a_1}\kappa_1 = \frac{c_0}{T_a}$ Equation (5.61) can be approximated by

$$\boldsymbol{\Upsilon}_{1,1} = \frac{j\rho_0 S\omega}{\Lambda_l(\frac{j\omega}{T_a} - k^2)} \tag{5.63}$$

Johnson (1996) overcame this issue in a similar manner by setting the damping term of the bulk compression mode equal to half that of the first longitudinal acoustic mode, ie

$$\eta_{a_1}\kappa_1 = \frac{\eta_{a_2}\kappa_2}{2} \tag{5.64}$$

Equation (5.60) is the same as the expression for the radiation mode shapes derived from the acoustic potential energy given by Equation (5.40) with the exception of the radiation term. The radiated power formulation has a diagonal weighting matrix (equation 5.61) which takes the real part of the acoustic mobility matrix whereas the the potential energy formulation uses the square of the magnitude of the acoustic mobility matrix (equation 5.43). Taking the ratio of the two diagonal weighting matrices gives

$$\frac{\Omega_{ll}}{\frac{S}{2}\Re\{\boldsymbol{\Upsilon}_{l,l}\}} = \frac{1}{2\eta_{a_l}\kappa_l} \tag{5.65}$$

Therefore, minimising transmitted acoustic power and minimising acoustic potential energy are subtly different and minimising radiated power will not necessarily guarantee

minimisation of the potential energy. This was acknowledged by Johnson (1996), who states that minimisation of acoustic potential energy places more emphasis on controlling the acoustic modes which have low damping. Clearly, if a single mode dominates the cavity response then the two techniques will give similar results. However, if several modes are excited and the natural frequencies and/or the modal loss factors of the modes differ significantly then the results arising from the two techniques may differ.

As has been shown previously, the weighting matrix can have a significant effect on the performance of the control system. The system analysed in the previous section has been reanalysed for minimisation of sound power radiated into the cavity. Figure 5.26 compares the reduction in the acoustic potential energy when minimising acoustic potential energy and minimising sound power radiation. The effect of including damping in the bulk compression mode (Equation 5.62) can be seen clearly below 5 Hz with the primary potential energy rolling off steeply. It can be seen there is very little difference in minimising the internal acoustic potential energy and minimising the power radiated into the cavity. This agrees with the findings of Johnson (1996). The two control strategies only differ when the system is driven off-resonance, particularly when the modal damping coefficients are significantly different.

To emulate the response found in a typical vehicle cabin the modal loss factors of both the structural modes and acoustic modes were both increased from 0.02 to 0.10 with the results shown in Figure 5.27(a). Again, even in systems with moderate damping the two techniques exhibit almost negligible difference as can be seen when the two controlled levels are compared in Figure 5.27(b).

Because the mode shapes of the radiation modes derived to sense the potential energy and radiated power are the same, then all the conclusions that have been made for the potential energy radiation modes will also be valid for radiation modes orthogonal in terms of their contributions to the radiated power. The only difference is the frequency dependent term which has been shown to have a very small effect in certain situations.

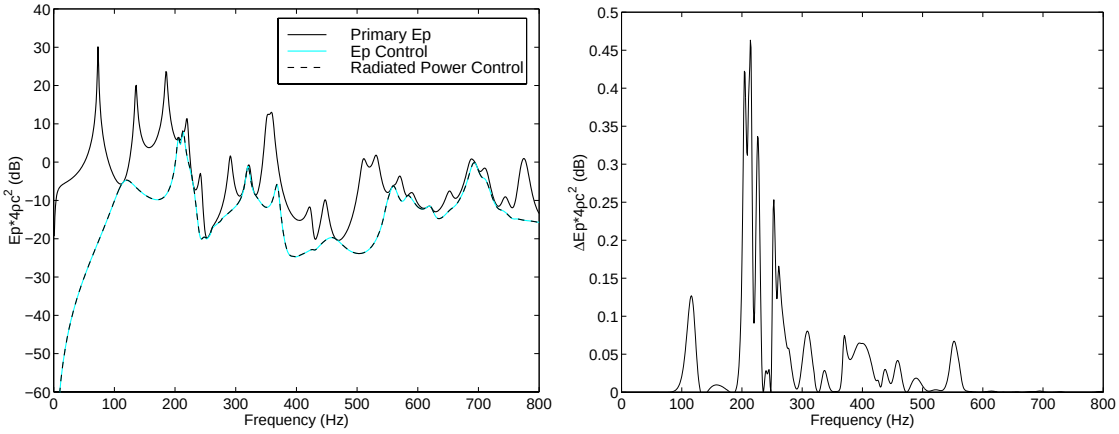

(a) Reduction in acoustic potential energy (b) Difference in controlled levels

Figure 5.26: Comparison between minimisation of acoustic potential energy and power transmission. Modal loss factor, $\eta = 0.02$.

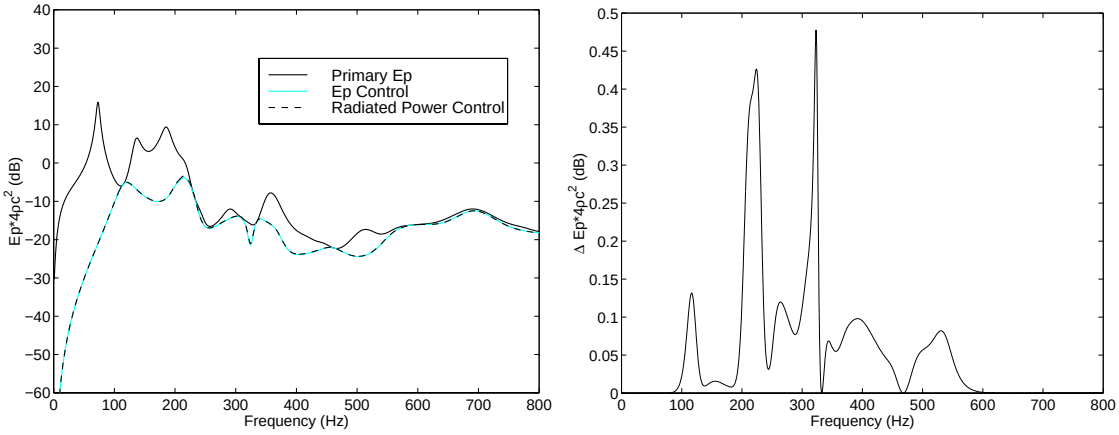

(a) Reduction in potential energy (b) Difference in controlled levels

Figure 5.27: Comparison between minimisation of acoustic potential energy and power transmission. Modal loss factor, $\eta = 0.10$.

5.5.4 Radiation Modes using Energy Density

It was shown in Chapter 4 that the energy density at a point or several points provided an effective cost function. There is no reason for attempting to minimise the energy density throughout the cavity since this is equivalent to minimising the total internal acoustic potential energy (at least in a lossless system). This is because the total instantaneous acoustic potential energy and the total instantaneous acoustic kinetic energy are equal in magnitude (and are 90° out of phase) to each other. Therefore, minimising the acoustic potential energy throughout the cavity will also minimise the acoustic kinetic energy throughout the cavity. The corollary is that the spatial integral of the energy density throughout the volume is also minimised.

There are, however, advantages to energy density control at a point such as effective local control. From Chapter 4 is was shown that for control systems with l energy density sensors, the total energy density at the l points arising from the vibration of the structure is given by

$$E_D = \sum_{i=1}^{l} \frac{1}{4\rho c^2} \left[|p(\vec{\mathbf{r}}_i)|^2 + |\rho c v(\vec{\mathbf{r}}_i)|^2 \right] = \mathbf{v}_p^{\mathrm{H}} \mathbf{Z}_a^{\mathrm{H}} \mathbf{Z}_w \mathbf{Z}_a \mathbf{v}_p \tag{5.66}$$

where

$$\mathbf{Z}_w = \frac{1}{4\rho c^2} \mathbf{\Phi}_e^* \mathbf{D}^{\mathrm{H}} \mathbf{D} \mathbf{\Phi}_e^{\mathrm{T}} \tag{5.67}$$

Equation (5.66) is now in the same format as Equation (5.7), ie

$$E_D = \mathbf{v}^{\mathrm{H}} \mathbf{\Pi}_{ED} \mathbf{v} \tag{5.68}$$

where the energy density error weighting matrix $\mathbf{\Pi}_{ED}$ is given by

$$\mathbf{\Pi}_{ED} = \mathbf{Z}_a^{\mathrm{H}} \mathbf{Z}_w \mathbf{Z}_a \tag{5.69}$$

The energy density error matrix can now be diagonalised using the same technique as per Section 5.2. The system analysed in Chapter 4 has been reanalysed for a cost function consisting of minimisation of acoustic energy density at a point located approximately in the centre of the cavity, $\begin{bmatrix} 0.117 & -0.011 & 0.480 \end{bmatrix}$.

Figure 5.28 compares the reduction in the cost function (energy density in the centre of the cavity) and Figure 5.29 compares the reduction in the acoustic potential energy when minimising energy density at a point, sensing the first 2 radiation modes using a structural error sensor comprised of 21 discrete sensors located in the centre of the panel. The "structural energy density sensor" exhibits control degradation from the strip sensor much like what was seen when using a strip sensor virtual microphone (Section 5.5.2).

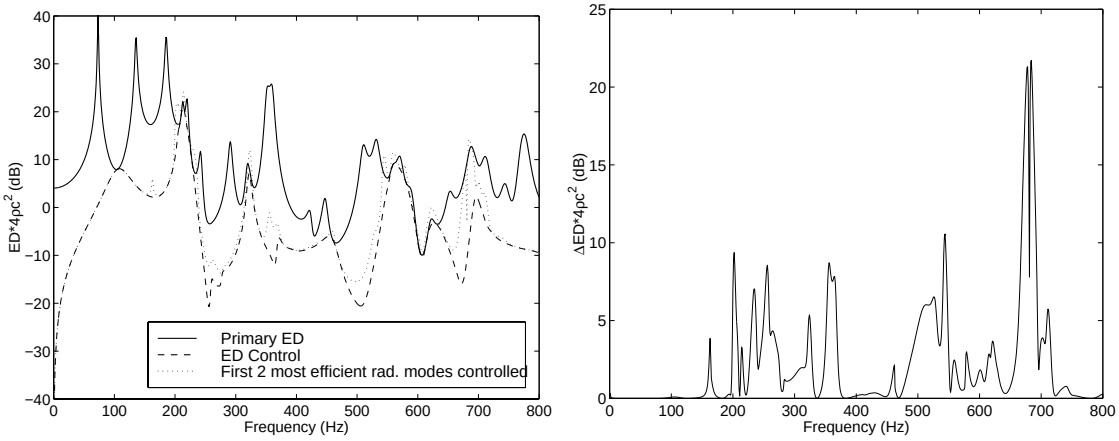

(a) Reduction in energy density cost function

(b) Difference in controlled levels

Figure 5.28: Reduction in energy density in the centre of the cavity when minimising acoustic energy density and the virtual energy density sensor.

In Figure 5.30 the attenuation of the pressure versus non-dimensional distance from the "structural energy density sensor" is plotted for the frequency range 600 Hz to 700

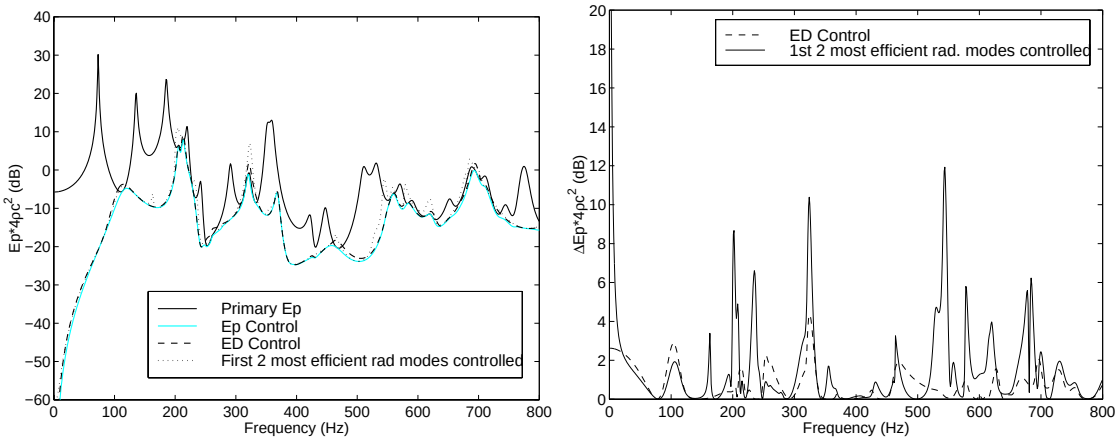

(a) Reduction in global acoustic potential energy

(b) Difference in controlled levels

Figure 5.29: Reduction in global acoustic potential energy when minimising acoustic energy density and the virtual energy density sensor.

Hz. The control using the virtual energy density sensor technique achieves good local control around the focus region of the sensor (centre of the cavity) but the global control is poor. The local control is significantly worse than when directly sensing energy density because of the poor control between 650 Hz and 700 Hz when sensing with the virtual sensor (Figure 5.28(a)). The performance could certainly be increased by improving the radiation mode sensor fidelity, such as including additional strips. The attenuation of the pressure versus distance when controlling a single microphone located in the centre of the cavity and a virtual structural microphone is also plotted in Figure 5.30. The zone of local control when controlling the virtual structural energy density sensor is slightly larger than that obtained when controlling the virtual structural microphone.

5.6 Summary

It has been shown that it is possible to decompose a large number of discrete surface vibration measurements into a small number of high quality error signals for an active noise

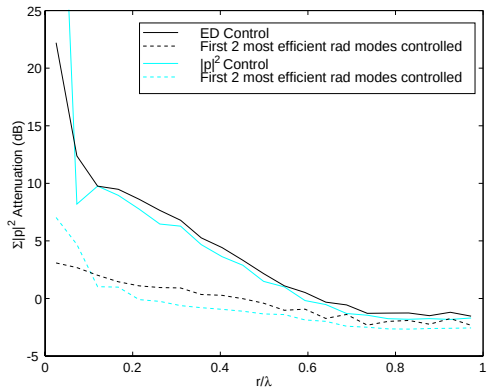

Figure 5.30: Attenuation vs distance from the cavity centre for direct energy density and pressure sensing, a virtual microphone sensor and the virtual energy density sensor made from a single strip.

control system and obtain similar or improved results to conventional acoustic and structural error sensing. The decomposed structural vibration signals are formed so that they represent amplitudes of "radiation modes" which are orthogonal in terms of their contribution to the desired cost function. The result of using such error signals is an increase in stability of the active noise control system and reduced dimensionality achieved through the reduction of the condition number of the control system transfer function matrix. Modal sensing of radiation modes provides the highest level of control with non-invasive sensors. Frequency normalisation permits the use of shaped modal sensors rather than numerous discrete sensors to provide the required error signals to minimise the enclosure acoustic potential energy.

It is possible to constrain the cost function in such a way as to control only specific regions in the cavity. This constrained global approach has the advantage that controller effort is not expended in controlling non-essential regions. The numerical simulations using the "structural microphone" and the “structural energy density sensor” have shown that local control of sound pressure squared or energy density using structural sensors is indeed possible.

At low frequencies when the flexible structure encloses a large part of the cavity, it

is possible to use the acoustic mode shapes as modal filters to sense the radiation modes. The spatial integration arising from the modal sensors shaped to the acoustic modes is similar to the interface modal filtering which happens between the structural and acoustic modes in the physical system. By employing a frequency dependent filter based on the radiation efficiency of the acoustic modes, the modal control system attempts to emulate the coupled vibro-acoustic system.

It was shown that the radiation modes orthogonal in terms of their contribution to the potential energy of the cavity are identical to the radiation modes orthogonal in terms of their contribution to the radiated power into the cavity. The eigenvalue matrix of the two radiation modes differ slightly by $2\eta_{a_l}\kappa_l$. This additional terms does not have a significant effect on the controlled levels for the cases considered here.

Chapter 6

ASAC Experiments

An experimental investigation of the curved panel-cavity system was undertaken to confirm the radiation mode theory derived in Chapter 5. Both distributed and discrete vibration transducers were used in an attempt to measure the velocity amplitudes of the radiation modes (orthogonal in terms of their contribution to the acoustic potential energy), with the pros and cons of each method discussed. The theory for using shaped PVDF sensors is reviewed here and then applied to the curved-panel system discussed in Chapter 5. The results from this experimental study have also been reported in Cazzolato & Hansen (1997). The control achieved with the discrete sensors and PVDF film sensors for the "volume velocity" radiation mode and the first longitudinal acoustic mode is compared against the control predicted from the numerical simulations.

6.1 Distributed Transducers

6.1.1 Discrete Transducers

Creating meta sensors by summing the weighted output from several discrete transducers is the simplest method of creating a distributed sensor. The sensor equations can be derived directly by using the least squares expression for the modal filter given by Equation

(5.20) (Meirovitch & Baruh 1982). Maillard & Fuller (1998) successfully used a set of discrete accelerometers to measure and control the volume acceleration (the most efficient free-field radiation mode) of a plate radiating into free space. Such discrete sensing systems are not without their problems, the biggest being aliasing of higher order modes and modal spillover as seen in Section 5.4.

Morgan (1991) and Snyder et al. (1995) discuss the issues of discrete modal sensing for real systems. As was shown in the previous chapter a non-trivial number of sensors may need to be employed. Judicious placement of the discrete sensors can improve the performance of the meta sensors. For example, when the physical system is of regular geometry, it is often possible to use symmetry to eliminate the measurement of unwanted modes (Snyder et al. 1995). This was suggested by Elliott & Johnson (1993) to aide in the sensing of particular clusters of structural modes of a rectangular panel. Symmetry has been used in the experiments described in detail below. Since the first two radiation modes do not contain any of the y-axis even order modes, the discrete sensors were placed along the centre line of the panel on the (long) x-axis (see Figures 5.1 and 6.5).

6.1.2 Piezoelectric Transducers

It has been shown that distributed sensorsactuators have many advantages over discrete sensors, the most important being the enhancement in observability and reduction in spillover (Balas 1978). The following section considers distributed parameter modal filtering using PVDF film. PVDF film is an extremely flexible piezo-electric polymer which develops a charge between the two electrodes when subjected to an applied strain. The film has been successfully used as a distributed sensor by many researchers (Lee 1990, Lee & Moon 1990, Lee et al. 1991).

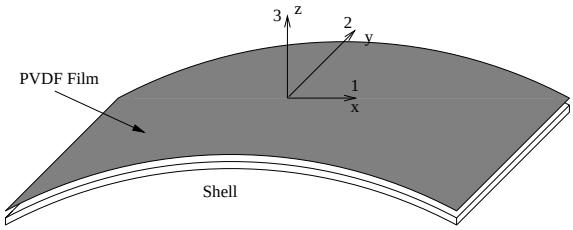

Figure 6.1: Shell and PVDF film orientation where the z-axis is the poling direction of the film.

6.1.2.1 Sensor equations

Lee (1990) showed that the total charge generated by a piezoelectric lamina is a function of the integral of strain over the surface of the lamina and is expressed as

$$q(t) = \int_S \Gamma(\vec{\mathbf{x}}) \left[e_{31} \frac{\partial u(\vec{\mathbf{x}},t)}{\partial x} + e_{32} \frac{\partial v(\vec{\mathbf{x}},t)}{\partial y} + e_{31} \left(\frac{\partial u(\vec{\mathbf{x}},t)}{\partial y} + \frac{\partial v(\vec{\mathbf{x}},t)}{\partial x} \right) - \frac{t_s + t_f}{2} \left(e_{31} \frac{\partial^2 w(\vec{\mathbf{x}},t)}{\partial x^2} + e_{32} \frac{\partial^2 w(\vec{\mathbf{x}},t)}{\partial y^2} + 2e_{36} \frac{\partial^2 w(\vec{\mathbf{x}},t)}{\partial x \partial y} \right) \right] dS(\vec{\mathbf{x}}) \tag{6.1}$$

where $u(\vec{\mathbf{x}},t)$, $v(\vec{\mathbf{x}},t)$ and $w(\vec{\mathbf{x}},t)$ are the displacements in the local coordinates x, y and z at a location $\vec{\mathbf{x}}$ at time t; $\Gamma(\vec{\mathbf{x}})$ is the shape function of the PVDF sensor, t_s and t_f are the thickness of the shell and film respectively, and e_{31}, e_{32} and e_{36} are the directional piezoelectric [(charge/area)/strain] field intensity constants given by

$$\begin{bmatrix} e_{31} \\ e_{32} \\ e_{36} \end{bmatrix} = \begin{bmatrix} E/(1-\nu^2) & E\nu/(1-\nu^2) & 0 \\ E\nu/(1-\nu^2) & E/(1-\nu^2) & 0 \\ 0 & 0 & E/2(1+\nu) \end{bmatrix} \begin{bmatrix} d_{31} \\ d_{32} \\ d_{36} \end{bmatrix} \tag{6.2}$$

where E and ν are the Young's Modulus and Poisson's Ratio of the PVDF respectively, and d_{31}, d_{32} and d_{36} are the piezoelectric strain constants given by Table 6.1. The first four terms in Equation (6.1) represent the strain arising from in plane motion ($\frac{\partial u(\vec{\mathbf{x}},t)}{\partial x}$, $\frac{\partial v(\vec{\mathbf{x}},t)}{\partial y}$, $\frac{\partial u(\vec{\mathbf{x}},t)}{\partial y}$ and $\frac{\partial v(\vec{\mathbf{x}},t)}{\partial x}$), the second three terms $\frac{\partial^2 w(\vec{\mathbf{x}},t)}{\partial x^2}$, $\frac{\partial^2 w(\vec{\mathbf{x}},t)}{\partial y^2}$ and $\frac{\partial^2 w(\vec{\mathbf{x}},t)}{\partial x \partial y}$ are the out-of-plane terms arising from bending in the shell. In general, for thin shells excited by

out-of-plane forces, the in-plane terms are negligible compared to the out-of-plane terms, and therefore may be neglected, ie

$$q(t) = \int_S -\frac{t_s + t_f}{2}\Gamma(\vec{\mathbf{x}}) \left[e_{31}\frac{\partial^2 w}{\partial x^2} + e_{32}\frac{\partial^2 w}{\partial y^2} + 2e_{36}\frac{\partial^2 w(\vec{\mathbf{x}},t)}{\partial x \partial y} \right] dS(\vec{\mathbf{x}}) \tag{6.3}$$

The subscript 6 takes into account the possibility that the principle axes of the PVDF film is not coincident with the principle axes of the structure to which it is bonded (Hansen & Snyder 1997). Subsequently, when the lamina is placed on the surface of the shell with no skew angle as shown in Figure 6.1, then the piezoelectric constant e_{36} is zero. Therefore

$$q(t) = \int_S -\frac{t_s + t_f}{2}\Gamma(\vec{\mathbf{x}}) \left[e_{31}\frac{\partial^2 w}{\partial x^2} + e_{32}\frac{\partial^2 w}{\partial y^2} \right] dS(\vec{\mathbf{x}}) \tag{6.4}$$

For the PVDF film detailed in Table 6.1 the thickness is negligible when compared to the thickness of a typical shell and is thus neglected here,

$$q(t) = \int_S -\frac{t_s}{2}\Gamma(\vec{\mathbf{x}}) \left[e_{31}\frac{\partial^2 w}{\partial x^2} + e_{32}\frac{\partial^2 w}{\partial y^2} \right] dS(\vec{\mathbf{x}}) \tag{6.5}$$

The specifications of the PVDF film supplied by AMP are given in Table 6.1.

6.1.2.2 Sensor shapes for modal sensing of radiation modes

Lee & Moon (1990) showed that for a simply supported plate with length a, width b and mode shape functions of the form

$$\psi_{i,j}(\vec{\mathbf{x}}) = \sin\left(\frac{i\pi x}{a}\right)\sin\left(\frac{j\pi y}{b}\right) \tag{6.6}$$

Electrode Type	Cu/Ni
Thickness	28 μm
Young's Modulus	2-4x10^9 N/m^2
Density	1780 kg/m^3
Poisson's Ratio	0.29
Relative Permitivity (ϵ/ϵ_0)	12-13
Maximum Operating Voltage	280 Vdc, 840 Vac
Piezo electric strain constant, d_{31}	23x10^{-12}(m/m)/(V/m)
Piezo electric strain constant, d_{33}	-33x10^{-12}(m/m)/(V/m)

Table 6.1: Typical AMP PVDF film material properties.

with the velocity normal to the surface of the structure given by

$$v(\vec{\mathbf{x}}) = \sum_{i=1}^{\infty}\sum_{j=1}^{\infty} A_{i,j}\psi_{i,j}(\vec{\mathbf{x}}) \tag{6.7}$$

and using the condition of orthogonality, Equation (6.5) can be written as

$$q(t) = -\frac{t_s}{2}\int_S \Gamma(\vec{\mathbf{x}}) \sum_{i=1}^{\infty}\sum_{j=1}^{\infty} A_{i,j}\left[e_{31}\left(-\frac{i^2\pi^2}{a^2}\sin\left(\frac{i\pi x}{a}\right)\sin\left(\frac{j\pi y}{b}\right)\right)\right.$$
$$\left. + e_{32}\left(-\frac{j^2\pi^2}{b^2}\sin\left(\frac{i\pi x}{a}\right)\sin\left(\frac{j\pi y}{b}\right)\right)\right] dS(\vec{\mathbf{x}}) \tag{6.8}$$

It should be noted that the Equation (6.8) was given incorrectly by Lee & Moon (1990). Setting the sensor shape function to

$$\Gamma(\vec{\mathbf{x}}) = \sin\left(\frac{l\pi x}{a}\right)\sin\left(\frac{m\pi y}{b}\right) \tag{6.9}$$

and evaluating the integral over the surface gives

$$q(t) = -\frac{t_s}{2}\int_S \sin\left(\frac{l\pi x}{a}\right)\sin\left(\frac{m\pi y}{b}\right)\sum_{i=1}^{\infty}\sum_{j=1}^{\infty} A_{i,j}\left[e_{31}\left(-\frac{i^2\pi^2}{a^2}\sin\left(\frac{i\pi x}{a}\right)\sin\left(\frac{j\pi y}{b}\right)\right) + e_{32}\left(-\frac{j^2\pi^2}{b^2}\sin\left(\frac{i\pi x}{a}\right)\sin\left(\frac{j\pi y}{b}\right)\right)\right] dS(\vec{\mathbf{x}}) \tag{6.10}$$

This can be correctly reduced to

$$q(t) = \delta_{il}\delta_{jm}A_{i,j}\frac{t_s}{2}\frac{1}{4}\left[e_{31}\frac{ib}{ja} + e_{32}\frac{ja}{ib}\right] \tag{6.11}$$

where δ_{il} and δ_{jm} are the Kronecker delta functions corresponding to the x and y directions. Therefore, this implies that for a simply supported panel, the sensor shape function to measure the structural modes is proportional to the normal structural mode shape displacement functions. This does not hold true for all structural mode shapes but only for systems with mode shapes proportional to the double spatial derivative of the mode shape function, ie $\frac{\partial^2 \sin(n\pi x)}{\partial x^2} = n^2\pi^2\sin(n\pi x) = k\sin(n\pi x)$.

Sensing the bulk compression acoustic mode / volume velocity radiation mode Rex & Elliott (1992) showed that if a sensor had a sensitivity which varied quadratically over the surface of a beam, then the output from the sensor was proportional to the total transverse displacement over the length of the beam. The theory of a Quadratically-Weighted Strain-Integrating Sensor (QWSIS) was extended to rectangular plates by Johnson & Elliott (1993) and Johnson (1996). The authors show that for a clamped plate the appropriate sensor shape function to measure the volume velocity from the plate is given by

$$\Gamma(x, y) = \alpha(ax - x^2) \tag{6.12}$$

where α is a constant. The total charge output from such a sensor was given by

$$q = t_s e_{31} \alpha \frac{U}{j\omega} \tag{6.13}$$

where U is the volume velocity of the plate. However, Johnson (1996) showed that for a simply supported plate the situation is a little more complicated and the solution requires two layers of PVDF on top of one another as shown in Figure 6.2. Here the piezoelectric axis of the second film is rotated by 90° and in doing so Johnson (1996) found a novel way to remove the sensitivity of the sensor to bending in the y direction. Alternatively, rather than stacking the two sensors on top of each other a sensor could be placed on either side of the panel (Carey & Stulen 1993).

Assuming the ratio of the two piezoelectric constants e_{31} and e_{32} are known, using the quadratic sensor Equation 6.12 and combining the outputs from the two layers using the appropriate weighting, the volume velocity of a simply supported panel is given by (Johnson 1996)

$$q_0 = q_1 - \frac{e_{32}}{e_{31}} q_2 = \left(1 - \left(\frac{e_{32}}{e_{31}}\right)^2\right) t_s e_{31} \alpha \frac{U}{j\omega} \tag{6.14}$$

where q_0 is the combined sensor output, and q_1 and q_2 are the charge outputs from the first and second sensor.

Johnson (1996) points out that for such an approach to work the piezoelectric constants must be accurately known and the sensor must be fixed in a manner such that they are equally sensitive to any strain across the surface of the plate. In practice this is very difficult to achieve.

Several other authors have derived the sensor shape function to measure the volume velocity radiated from a panel into free space from measured experimental modal analysis data with some success (Charette et al. 1995, Charette et al. 1998). This approach could

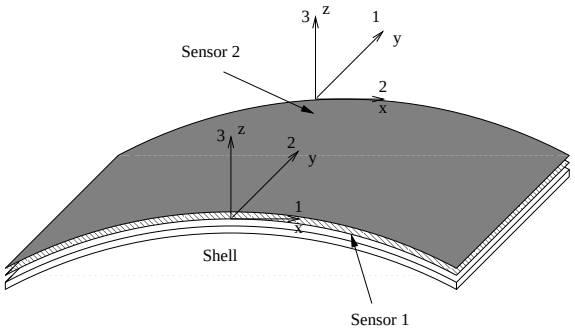

Figure 6.2: The orientation and axes for the sensor configuration used by Johnson (1996) to eliminate the q_x component of the induced charge and hence measure the volume velocity of a plate.

also be used numerically. However, both techniques are time consuming and require considerable measurement effort.

An alternative approach is to use the fact that it is the odd-odd structural modes which form the bulk compression radiation mode, just like it is the odd sine terms in the Fourier series which form a square wave. It can also be shown that a layer with unit sensitivity only responds to the the odd-odd modes. Therefore, although not entirely accurate it is possible to get a measure of the volume velocity from uniform sensors.

If the sensor shape function is set equal to unity across the shell surface, ie

$$\Gamma(\vec{\mathbf{x}}) = 1 \tag{6.15}$$

it can be shown that the charge developed by a single layer sensor is given by (Appendix B)

$$q = \frac{t_s}{2} e_{31} \frac{4}{ab} \sum_{i=1}^{\infty} \sum_{j=1}^{\infty} \frac{A_{i,j}}{ij} \left(i^2 b^2 + \frac{e_{32}}{e_{31}} a^2 j^2 \right) (1-(-1)^i)(1-(-1)^j) \tag{6.16}$$

and the charge developed by a double layer sensor is given by (Appendix B)

$$q = \frac{t_s}{2} e_{31} \left(1 - \left(\frac{e_{32}}{e_{31}} \right)^2 \right) \frac{4b}{a} \sum_{i=1}^{\infty} \sum_{j=1}^{\infty} \frac{A_{i,j}}{ij} i^2 (1-(-1)^i)(1-(-1)^j) \tag{6.17}$$

Comparing this to the charge developed by using a double layer quadratic sensor shape on a simply supported panel which accurately senses the volume velocity of the panel (Johnson 1996),

$$q = \frac{t_s}{2} e_{31} \left(1 - \left(\frac{e_{32}}{e_{31}}\right)^2\right) \frac{4\alpha}{\pi^2} \sum_{i=1}^{\infty} \sum_{j=1}^{\infty} \frac{A_{i,j}}{ij} (1 - (-1)^i)(1 - (-1)^j) \tag{6.18}$$

shows that both of the double layer techniques are identical apart from the additional i^2 term in Equation (6.17). This means that the structural modes with larger indices along the x-axis are biased when using a uniform sensor. For systems which are long and narrow, ie the j index increases much more quickly than the i index, the uniform sensor is certainly a suitable approximation at low frequencies.

Clark & Fuller (1992*b*) experienced exactly this problem when using strip sensors on a rectangular simply supported plate to control the efficiently radiating modes from the panel. They noted that as the excitation frequency increases the sensor becomes increasingly responsive to higher order modes. In concluding, they note that almost optimal levels of control were achieved on resonance (when a single mode dominates the response and the control mechanism is modal control). However, the control achieved off-resonance using the strip sensors was slightly less than that offered by several microphones (when several structural modes contribute to the response and the control mechanism is modal rearrangement). The effect of modal biasing from uniform strip sensors is simulated in Section 6.1.3.

Sensing the higher order radiation modes For higher order modes an alternative sensor shape is required. It can also be shown that the Fourier series (for $0 \leq \theta \leq 1$) of a cosine in terms of sines is given by

$$\cos(n\theta) = \sum_{k=1}^{\infty} a_{k,n} \sin(k\theta) \tag{6.19}$$

where,

$$a_{k,n} = \frac{2}{\pi}\left(1-(-1)^{k+n}\right)\frac{k}{(k-n)(k+n)} \tag{6.20}$$

Therefore, using the Fourier Series defined by Equation (6.19), it can be shown that if the sensor is to measure the higher order radiation modes (which at low frequencies resemble Equation 6.22), the charge developed should be (Appendix B)

$$\begin{aligned} q(t) &= \frac{t_s}{2}\beta\sum_{i=1}^{\infty}\sum_{j=1}^{\infty}A_{i,j}\left[(1-(-1)^{i+l})(1-(-1)^{j+m})\right. \\ &\quad \left.\times\left(\frac{i}{(i-l)(i+l)}\right)\left(\frac{j}{(j-m)(j+m)}\right)\right] \end{aligned} \tag{6.21}$$

where β is some constant. One possible solution to the sensor shape function is to use the mode shape of the desired radiation mode (which at low frequencies resemble the acoustic mode shapes), ie

$$\Gamma(\vec{\mathbf{x}}) = \cos\left(\frac{l\pi x}{a}\right)\cos\left(\frac{m\pi y}{b}\right) \tag{6.22}$$

It can be shown that the charge developed by a single layer sensor is given by (Appendix B)

$$\begin{aligned} q(t) &= \frac{t_s}{2}\frac{e_{31}}{ab}\sum_{i=1}^{\infty}\sum_{j=1}^{\infty}A_{i,j}\left[\left(i^2b^2+\frac{e_{32}}{e_{31}}j^2a^2\right)(1-(-1)^{i+l})(1-(-1)^{j+m})\right. \\ &\quad \left.\times\left(\frac{i}{(i-l)(i+l)}\right)\left(\frac{j}{(j-m)(j+m)}\right)\right] \end{aligned} \tag{6.23}$$

and the charge developed by a two layer sensor sensitive to bending in the x-direction is

given by (Appendix B)

$$q(t) = \frac{t_s}{2} e_{31} \left(1 - \frac{e_{32}^2}{e_{31}^2}\right) \frac{1}{ab} \sum_{i=1}^{\infty} \sum_{j=1}^{\infty} \left[A_{i,j} i^2 (1-(-1)^i)(1-(-1)^j) \times \left(\frac{i}{(i-l)(i+l)}\right)\left(\frac{j}{(j-m)(j+m)}\right)\right] \tag{6.24}$$

Although Equations (6.23) and (6.24) will always guarantee that the appropriate modes are sensed, they suffer from the same problem that was experienced in Equations (6.16) and (6.17), where the sensors are over sensitive to the higher order modes in two or one direction respectively. However, as a first order approximation it can be quite useful since no effort is required to calculate the sensor shape and does not require prior knowledge of the structural modes shapes.

If an accurate estimate of the higher order radiation modes is required the following formulation of the shape function is necessary. Intuitively, a sensor equation with a $\frac{1}{i^2}$ bias will remove the bias in the charge sensitivity given by Equation (6.24). It can be shown that for a simply supported rectangular panel with a sensor shape function given by (Appendix B)

$$\Gamma(\vec{\mathbf{x}}) = \sum_{k=1}^{\infty} \bar{A}_{k,l} \sin(\frac{k\pi x}{a}) \sum_{k'=1}^{\infty} \bar{A}_{k',m} \sin(\frac{k'\pi y}{b}) \tag{6.25}$$

where

$$\bar{A}_{k,l} = \frac{2}{\pi} \left(1 - (-1)^{k+l}\right) \frac{k}{(k-l)(k+l)} \frac{1}{k^2} \tag{6.26}$$

and

$$\bar{A}_{k',m} = \frac{2}{\pi} \left(1 - (-1)^{k'+m}\right) \frac{k'}{(k'-m)(k'+m)} \tag{6.27}$$

and l and m are the modal indices of the desired radiation mode, it can be shown that the

charge developed by a single sensor is given by (Appendix B)

$$\begin{aligned} q &= -\frac{t_s}{2}\frac{e_{31}}{a^2}\sum_{i=1}^{\infty}\sum_{j=1}^{\infty}A_{i,j}\left(1+\frac{e_{32}}{e_{31}}\frac{j^2a^2}{i^2b^2}\right) \\ &\quad\times\left[\left(1-(-1)^{i+l}\right)\frac{i}{(i-l)(i+l)}\left(1-(-1)^{j+m}\right)\frac{j}{(j-m)(j+m)}\right] \end{aligned} \quad (6.28)$$

and the charge developed by a two layer sensor sensitive to bending in the x-direction is given by (Appendix B)

$$\begin{aligned} q &= -\frac{t_s}{2}e_{31}\left(1-\frac{e_{32}^2}{e_{31}^2}\right)\frac{1}{a^2}\sum_{i=1}^{\infty}\sum_{j=1}^{\infty}A_{i,j} \\ &\quad\times\left[\left(1-(-1)^{i+l}\right)\frac{i}{(i-l)(i+l)}\left(1-(-1)^{j+m}\right)\frac{j}{(j-m)(j+m)}\right] \end{aligned} \quad (6.29)$$

It can be seen that Equation (6.29) is of the same form as 6.21. Therefore using Equation (6.25) for the sensor shape it is possible to measure accurately the modal amplitudes of the radiation modes. In fact if $l = 0$ and $m = 0$, then Equation (6.29) collapses to form the equation for a square wave (uniform amplitude across the surface of the panel) which is the mode shape of the volume velocity radiation mode. It can also be shown that if $l = 0$ and $m = 0$, Equation (6.25) successfully collapses to the quadratic shape function (Equation 6.12) proposed by Johnson (1996), and the charge output of the dual layer sensor given by Equation (6.29) collapses to the charge output for the dual layer volume velocity sensor (Equation 6.18) calculated by Johnson (1996). Therefore the sensor shape function given by Equation (6.25) is a universal sensor shape function for simply supported panel since it is capable of sensing all radiation modes including the volume velocity radiation mode. The sensor shapes for sensing the first four radiation modes derived from Equation (6.29) with respect to the x-axis are shown in Figure 6.3. These curves have been normalised so that the maximum absolute value is unity.

A low order polynomial was fitted to each of the sensor shapes calculated using Equa-

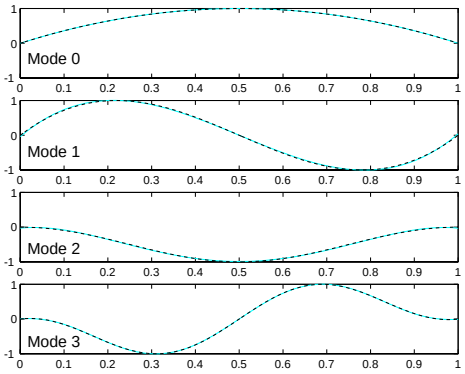

Figure 6.3: Normalised sensor shapes to measure the first four radiation modes on a simply supported panel. Sensor shape (solid) and low order polynomial (dashed).

tion (6.29) and have been plotted in Figure 6.3 with the polynomial coefficients shown in Table 6.2. It is interesting to note that the second radiation mode shape ($l = 1$) is very similar to the second order structural mode shape ($\sin(2\pi x)$), which indicates that shaped sensors designed to measure the radiation modes could be very sensitive to leak through of undesired modes.

Radiation Mode Index, l	Coefficient							
	1	x	x^2	x^3	x^4	x^5	x^6	x^7
0	0	4	-4	-	-	-	-	-
1	0	$\frac{10\pi}{3}$	-10π	$\frac{20\pi}{3}$	-	-	-	-
2	0	0	-5π	10π	-5π	-	-	-
3	0	0	0	$-\frac{600\pi}{7}$	$\frac{3000\pi}{7}$	$-\frac{5400\pi}{7}$	$\frac{4200\pi}{7}$	$-\frac{1200\pi}{7}$

Table 6.2: Sensor equation polynomial coefficients for the first 4 radiation modes bounded by $0 \leq x \leq 1$.

The expressions for the sensor shape derived above have assumed that the sensor covers the entire surface of the plate. An alternative approach is to use narrow strips shaped in the same manner as the sensors covering the entire surface. Strip sensors are known to suffer from aliasing much as the discrete sensors do; however, spatially uniform sensors covering a subspace of the surface such as strips (Clark & Fuller 1992*b*) and

patches (Callahan & Baruh 1995, Burke & Hubbard Jr. 1991) have been used successfully by several authors in cases where such an approach is suitable. Judicious placement of the strip sensors can improve the performance by avoiding sensing of undesired modes and spatial aliasing. For the curved panel system under investigation, the ideal location to avoid aliasing is along the centre-line of the panel. This location ensures that all the modes that contribute to the zeroth and first radiation mode will all be sensed equally.

It should be noted that although the radiation mode shapes are independent of boundary conditions, the sensor equations derived above are only applicable to a simply supported rectangular panel. This is because the surface strain is a function of the boundary conditions. Therefore, the surface strain mode shape of a radiation mode for a simply supported rectangular panel will be quite different than for a clamped-clamped rectangular panel.

6.1.3 Sources of Errors in Distributed Sensors

It is inevitable that physical errors in the shaped sensor will arise during the shaping and mounting of the film and it is therefore important to be aware of the magnitude of the errors. Johnson (1996) provides a very detailed investigation into the potential sources of errors arising in shaped PVDF film sensors. He quantifies the effects of: the errors due to digitisation, errors due to etching, errors inherent in the design such as using a finite number of strips, and errors due to ill-positioning of the sensor on the plate. The errors arising from modal sensors are very sensitive to the physical system to which the sensors are applied, which includes both the structure and the placement of the excitation sources.

Using the same error metric as Johnson (1996) and Morgan (1991), the performance of a discrete sensor arrangement with sensing errors was evaluated. Because of the random nature of the errors arising from shape errors it was necessary to provide a statistical estimate of the error. This was done by applying a $\pm 10\%$ error in sensitivity to each sen-

sor and then calculating the performance. This was repeated 10 times to give an estimate of the mean performance (Mean 10% Error) and worst performance (Max 10% Error). Figure 6.4 (a) and (b) shows the reduction in potential energy when using 7 equi-spaced discrete sensors mounted along the centreline of the panel as shown in Figure 5.2 with sensor weights aimed at sensing the first 2 acoustic mode shapes respectively. These results have also been compared against an ideal 7 point sensor without any error in sensitivity. The value of $\pm 10\%$ was chosen because the error in the sensor shapes used for the experiments was $\pm$2mm and the width was 20mm. The frequency range of 40 Hz to 300 Hz was selected so that the results could be compared against the experimental results shown following in Section 6.3.

It can be seen that it is sufficient to use a set of 7 co-linear discrete sensors running down the centre of the panel to sense the first 2 radiation modes up to 300 Hz if there are no errors. A single strip located in the centre of the panel will out perform the case presented here.

The decrease in control is only of interest when the sensors are operating in the optimum bandwidth for control. For the volume velocity mode this is 0 Hz to 110 Hz, and for the first longitudinal radiation mode it is approximately from 110 Hz to 220 Hz. It can be seen that the volume velocity sensor tends to suffer below 50 Hz and the first radiation mode sensor shows performance loss between 160 Hz and 170 Hz and also around 205 Hz. The performance will obviously decrease as the sensor shape error increases. Figure 6.4 shows that it is important to attempt to keep the shape error below $\pm 10\%$.

In all real physical systems there is some damping present. When damping is present the modes are no longer truly orthogonal and subsequently there will always be some leakage of undesired modes (Callahan & Baruh 1995). The same occurs when sub-systems are coupled together. Therefore, the structural modes and the acoustic modes will no longer be truly orthogonal. However, when the damping and coupling are low then it can be assumed that the mode shapes are orthogonal for the purposes of the modal decompo-

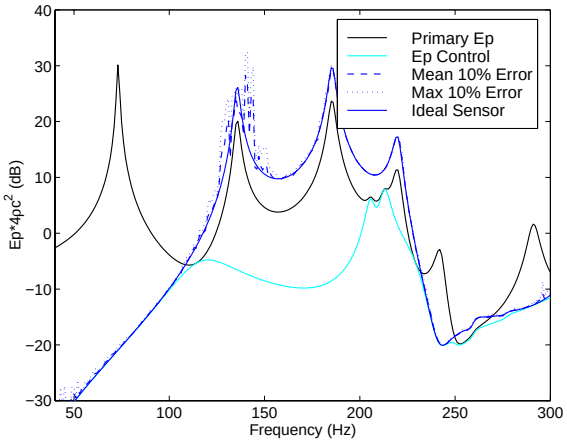

(a) Volume velocity radiation mode

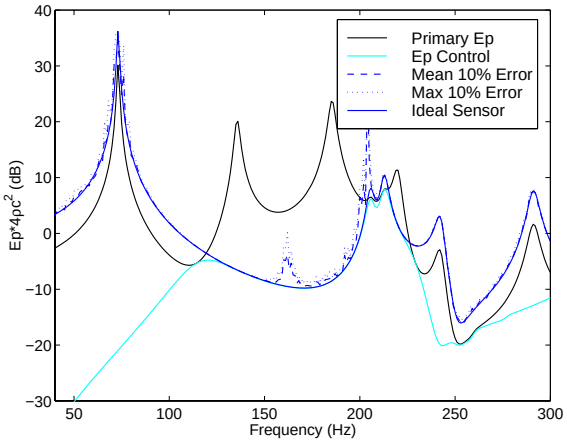

(b) First longitudinal radiation mode

Figure 6.4: Effects of error in the sensor shape when sensing radiation modes.

sition.

Other sources of error in the sensor which can act to degrade the performance of the control system include inaccuracies in the PVDF sensor capacitance and imperfect bonding between the sensor and the plate (Carey & Stulen 1993).

The effect of the biasing of higher order structural modes which occurs when using a piezoelectric shaped sensor was emulated by adjusting the magnitude of the modal amplitudes of the structural modes. The appropriate bias was achieved by post-multiplying the (l x n_s) structural model shape matrix at the l error sensor locations, $\mathbf{\Psi}_e$, by a (n_s x n_s) diagonal weighting matrix $\mathbf{W}$, ie

$$\mathbf{\Psi}_e' = \mathbf{\Psi}_e \mathbf{W} \tag{6.30}$$

where the diagonal elements of $\mathbf{W}$ are determined by the structure modal order as per Equation (6.17), ie

$$\mathbf{W} = \begin{bmatrix} 1 & 0 & 0 & 0 & 0 & 0 & 0 & 0 & 0 & 0 \\ 0 & 1 & 0 & 0 & 0 & 0 & 0 & 0 & 0 & 0 \\ 0 & 0 & 4 & 0 & 0 & 0 & 0 & 0 & 0 & 0 \\ 0 & 0 & 0 & 4 & 0 & 0 & 0 & 0 & 0 & 0 \\ 0 & 0 & 0 & 0 & 9 & 0 & 0 & 0 & 0 & 0 \\ 0 & 0 & 0 & 0 & 0 & 1 & 0 & 0 & 0 & 0 \\ 0 & 0 & 0 & 0 & 0 & 0 & 16 & 0 & 0 & 0 \\ 0 & 0 & 0 & 0 & 0 & 0 & 0 & 9 & 0 & 0 \\ 0 & 0 & 0 & 0 & 0 & 0 & 0 & 0 & 4 & 0 \\ 0 & 0 & 0 & 0 & 0 & 0 & 0 & 0 & 0 & \ddots \end{bmatrix} \tag{6.31}$$

It was found that for the current physical arrangement there was no measurable dif-

ference between the controlled levels with a uniform strip sensor (with the higher order modes biased) given by Equation (6.15) and the quadratic sensor shape given by Equation (6.22). This is only true because a single control source in a symmetrical location to the primary source has been used, and the main mechanism available for control of the radiated sound is modal control of the structural modes. This was facilitated by the fact that when controlling the sound field from 0 Hz to 100 Hz only, the first structural mode significantly contributed to the excitation of the bulk compression acoustic mode. The next two structural modes to contribute were the 6th and 8th mode, which had participation factors 30 dB less than that of the first mode at 100 Hz. Likewise, in the frequency range from 110 Hz to 230 Hz the only two structural modes to contribute to the first longitudinal acoustic mode were the 4th and 9th mode, both of which had weighting elements $w_4 = 4$ and $w_9 = 4$ respectively. Therefore, both significant modes were biased equally and the impact on the control was negligible.

Although not shown here, it was found that when the control source was moved to a non-symmetrical location, the modal spillover became significant and the control was affected by the biasing of higher order structural modes.

6.2 Experimental Setup

There were two objectives of the current set of experiments. The first was to validate the radiation mode theory derived in the previous chapter and demonstrate that radiation mode control is a feasible method of reducing the sound transmission from a structure into a coupled enclosure. The second reason was to show that there are additional benefits in performance when using radiation modal control that are not available when controlling using the physical coordinate system. Specifically these benefits are modal sensors reduce convergence time for controllers, provide robustness (to system parameter uncertainty), and minimise the number of sensors and actuators, and corresponding system dimension-

ality (Clark 1995, Morgan 1991). For this reason, a Causal Systems EZ-ANC real time control system was used for the experiments in preference to simply estimating the potential performance from measured transfer function data. A filtered-x feedforward control algorithm and an FIR filter were used.

The experimental configuration and apparatus are shown in Figures 6.5 and 6.6. A Ling V203 shaker was used to provide the primary driving force and a B&K Type 8001 impedance head was used to measure the input force. A B&K Type 4810 mini-shaker was used as the control source.

Because many discrete error sensors are required for the modal decomposition in a practical system it was necessary to use a very low cost accelerometer. The Analog Devices ADXL05 accelerometer was selected for use as it is very inexpensive at $30 each and has a high sensitivity, contains internal amplification and has the necessary bandwidth for active noise and vibration control applications. The accelerometers were attached to a patch board (see Figure 6.6) which provided the 5V DC supply voltage for the ADXL05 internal op amps and allowed calibration of the individual accelerometers. The buffered output from the patch board was fed into the modal summing board where the accelerometer signals were weighted according to the desired mode shape using trim pots and then fed into a 32 channel summer. The system was built with 32 channels for use on larger physical systems such as the stiffened cylinder studied by Cazzolato & Hansen (1998). Based on the numerical simulations in Section 5.4, 7 accelerometers were used for the discrete modal sensor.

Only a single modal summing board was used and was found to be adequate for the current study. However, in most applications it would be necessary to monitor several radiation modes which would require additional summing boards. With the present layout these can be simply daisy chained to the single patch board.

The continuous sensors were made from shaped strips of 28 micron thick Cu-Ni electrode Polyvinylidene Fluoride (PVDF) film supplied by AMP. The profile used to shape

the PVDF was, for ease of construction, set equal to the acoustic mode shapes at the surface of the panel. Although it was shown earlier to result in a sensor that was overly sensitive to the higher order modes, it was also shown that due to the symmetrical location of the control source used for the experiments, the biasing did not affect the control performance. Initially it was planned to use an electrode which covered the entire radiating surface but was later rejected in favour of a single strip sensor since it was prohibitively expensive to cover the entire shell but more importantly, it was shown that a single strip sensor was adequate for the current configuration.

There are a variety of methods for varying the film sensitivity shape function Γ: Cutting the the film to form strips, etching the film to form strips, etching the film to remove small portions of the electrode (this reduces the electrode density and subsequently the charge density), and varying the thickness of the PVDF film. Each process has its advantages. The most popular techniques are the first three, the later being impractical. For strip sensors the first technique of cutting the strip with a sharp blade has proved to be effective and quick (Snyder et al. 1995) and subsequently was used here. The film sensors were then attached to the curved panel using 25 mm wide double sided tape. This limited the maximum width of each strip to 20mm with a clearance of 2.5mm either side. The sensor profiles were generated on a computer and printed to a scale of 1:1 on a 600 dpi laser printer. Copper tape backed with a conductive adhesive was used to provide an adequate connection from the film electrodes to a charge amplifier. It was necessary to buffer the output from the PVDF film via a high impedance charge amplifier to ensure that the cut-off frequency of the high-pass filter circuit formed by the PVDF was well below the frequency range of interest. To help eliminate noise, the outer electrode of the sensor was grounded to the panel and the charge amplifier.

The potential energy of the cavity was estimated using 5 microphones randomly located throughout the interior. Numerical simulations and experience showed that this was an adequate number of microphones to estimate the potential energy of a small cavity

using a single structural control source. The single microphone used during the tests was optimally located in one of the rear corners of the backing cavity.

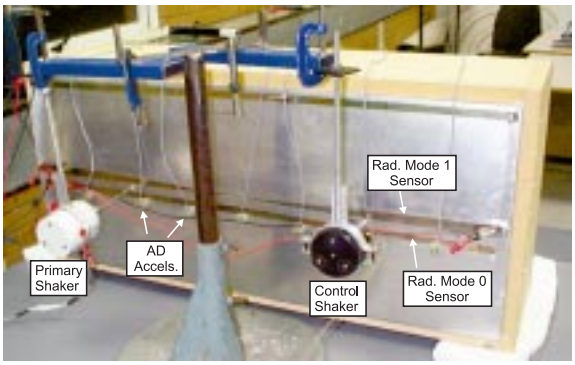

Figure 6.5: Experimental setup for active control of sound transmission.

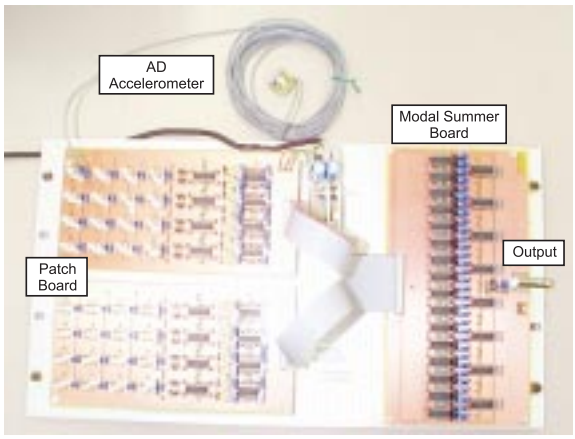

Figure 6.6: Patch board and modal summing board.

6.3 Experimental Results

The transfer functions between the driving force and the microphones, the zeroth (volume velocity) radiation mode and the first radiation mode sensors are shown in Figures 6.7, 6.8 and 6.9 respectively. The frequency range was set from 40 Hz to 300 Hz as this is the limit of dominance by the first two radiation modes. The lower limit defined by the limit of sensitivity of the microphones.

The measured acoustic response matches the predicted response quite well apart from the significant peak at 150 Hz in the measured data. This is from the [2,3] structural mode. This mode was not directly excited in the numerical simulations because the excitation point was at a node of this mode. Although this was desired for the experiments it is clear that the mount point of the primary shaker was not exactly at the node of the [2,3] mode.

The zeroth radiation mode sensor was designed to sense the bulk compression acoustic mode and should only respond to the odd-order structural modes shown in Table 6.3. Likewise, the first radiation mode sensor, shaped to sense the primary longitudinal acoustic mode, should only respond to the even-order structural modes. The measured transfer functions have also been compared against the predicted transfer functions. Because of the restrictions of the FE model it was not possible to create a “continuous strain sensor”, hence a “continuous integrating displacement sensor” formed by summing the displacement along a line of nodes was used.

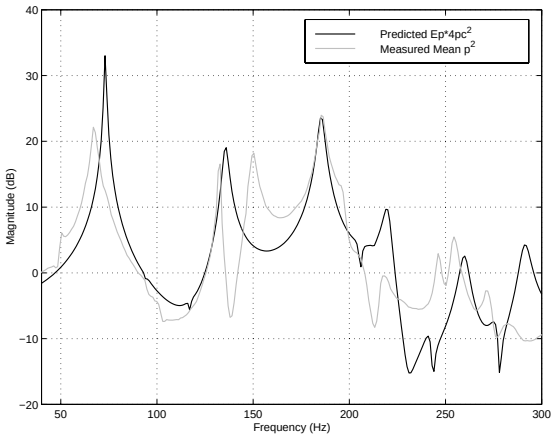

Figure 6.7: Measured and predicted transfer function between the 5 microphones and driving force.

As can be seen in Figures 6.8 and 6.9, both the PVDF and discrete radiation mode sensors respond strongly to the desired structural modes; however, it can also be seen that there is some "leak-through" of undesired structural modes due to imperfections in the film pattern and errors associated with discrete spatial sampling. It is worth noting

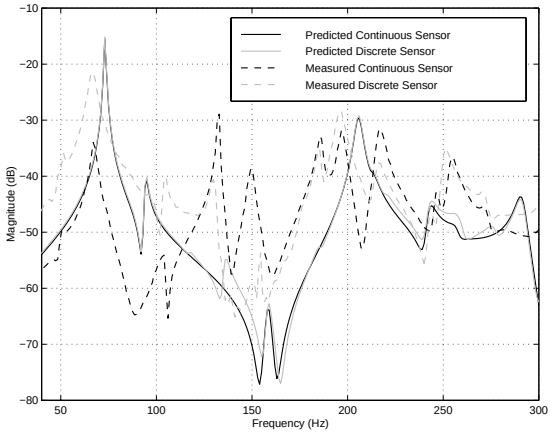

Figure 6.8: Measured and predicted transfer function between the zeroth radiation mode sensors and driving force.

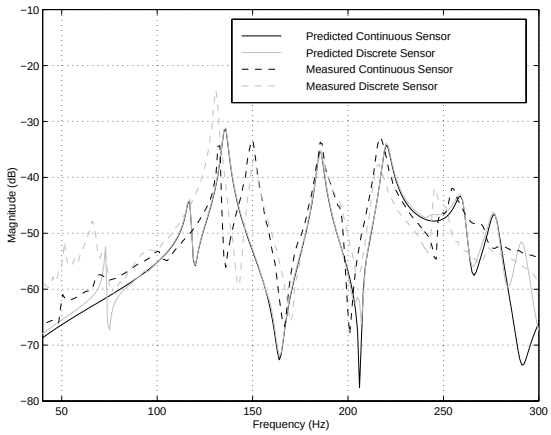

Figure 6.9: Measured and predicted transfer function between the first radiation mode sensors and driving force.

that the (uniform) zeroth radiation mode sensors are more sensitive to the even-order structural modes than the (half sine) first radiation mode sensors are to the odd-order structural modes. This phenomenon was also experienced by Lee and Moon (Lee & Moon 1990) when applying shaped sensors to measure normal structural modes on a beam, although no explanation was given as to the cause. It can also be seen that in Figure 6.8 the shaped PVDF sensor does indeed respond more strongly to the higher order modes than the discrete sensor.

Structural Mode	Resonance Frequency (Hz)	Structural Mode Participation Factor	
		Radiation Mode 0	Radiation Mode 1
[1,1]	77	-0.859	0
[2,1]	96	0	0
[2,2]	129	0	0
[1,2]	144	0	0.818
[2,3]	150	0	0
$[0,1,0]_a$	180	-	-
[3,1]	199	-0.284	0
[2,4]	204	0	0
[1,3]	204	0.272	0
[3,2]	220	0	0.273
[3,3]	234	-0.092	0

Table 6.3: Measured natural frequencies and theoretical modal participation factors of the structural modes.

As to be expected, the fidelity (ability to discriminate undesired modes) of the real sensors is not as high as the numerical simulation predicted. However, even with only seven accelerometers and a single strip, the frequency response curve shows that radiation modal sensing should still work in systems with a low modal density.

6.3.1 Active Structural-Acoustic Control

The mean square pressure level of the five microphones with and without active sound transmission control is shown as a function of frequency in Figures 6.10, 6.11 and 6.12 for both the numerical simulations and the experiments. The numerical simulations with radiation modal control (Figures 6.11(b) and 6.12(b)) have used ideal co-linear sensors to provide an estimate of the maximum achievable performance. The active noise control measurements were conducted with a sinusoidal input to the primary shaker over the frequency range 40 Hz to 300 Hz in steps of 5 Hz. Control using the 5 microphones as error sensors provides the maximum attenuation threshold that can possibly be achieved. Figure 6.10 shows that using a single microphone provides good control at most frequencies. This is only because the acoustic modal density is very low in the frequency range of interest, particularly below 250 Hz. The large increase in the controlled potential energy seen in the numerical simulations at approximately 120 Hz was not observed in the experimental results. It is not known why the experimental results do not exhibit the modal spillover but it may be because the microphone could not be placed exactly in the corner but rather approximately 15mm from it.

Because only a single radiation mode was used for the error signal at any one time, the frequency weighting filter shown in Figure 5.1 was not required. In practice, for single channel control a band pass filter for each radiation mode signal is adequate. As was shown earlier in Section 5.4.3, for multiple channel control it is often possible to neglect the filter altogether.

Control using the continuous zeroth radiation mode sensor shown in Figure 6.11(a) within the design bandwidth (0-120 Hz) was somewhat disappointing. This is believed to be due to the "leak-through" of undesired modes noted earlier. Contrary to the numerical simulation (Figure 6.11(b)), the controlled pressure level when using the discrete zeroth radiation mode sensor as an error sensor was lower than that obtained when using the

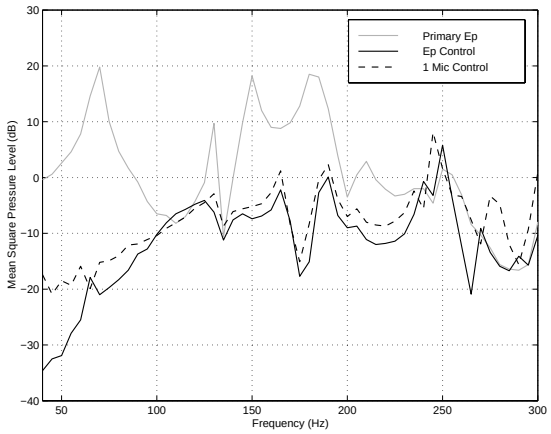

(a) Experiment

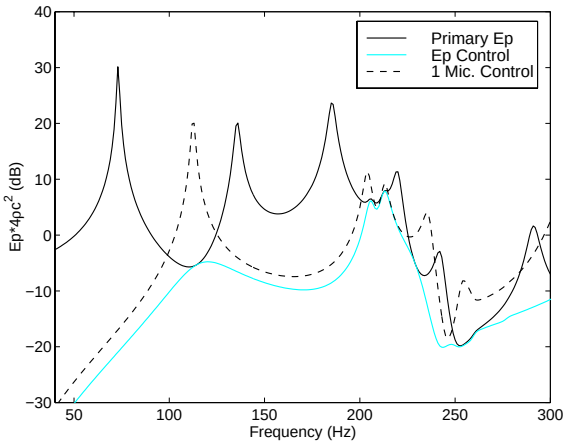

(b) Numerical Simulation

Figure 6.10: Experimentally measured and predicted mean square pressure level (Ep control) using all five microphones and a single microphone as error sensors.

equivalent continuous sensor and is likely due to higher sensitivity of the sensor to higher order structural modes. As expected, at frequencies above 120 Hz control leads to an increase in the mean square sound pressure level within the cavity.

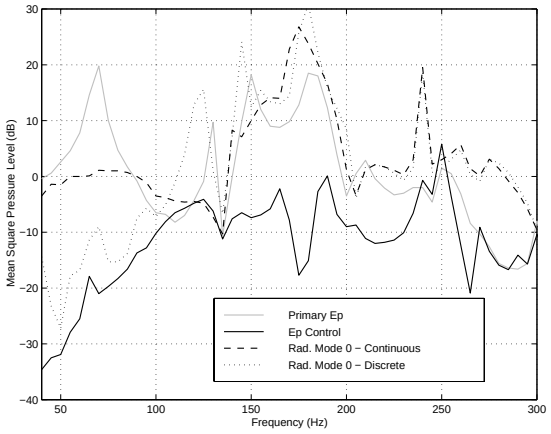

(a) Experiment

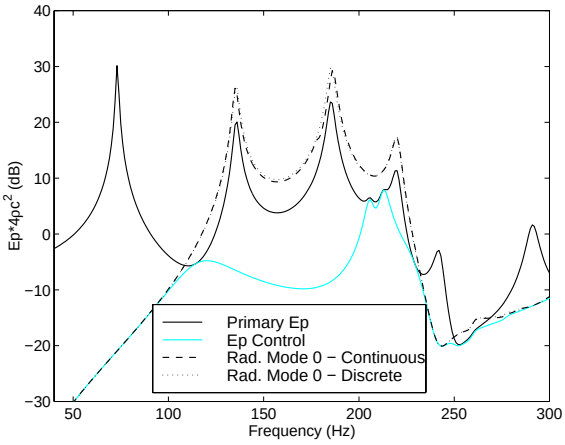

(b) Numerical simulation with ideal colinear sensors

Figure 6.11: Experimentally measured and predicted mean square pressure level using the zeroth radiation mode sensors.

Control using the continuous first radiation mode sensor within its operational bandwidth (120-270 Hz) is high, with almost optimum control achieved between 120 Hz and 200 Hz. However, control above 200 Hz is poor. This is because the second longitudinal

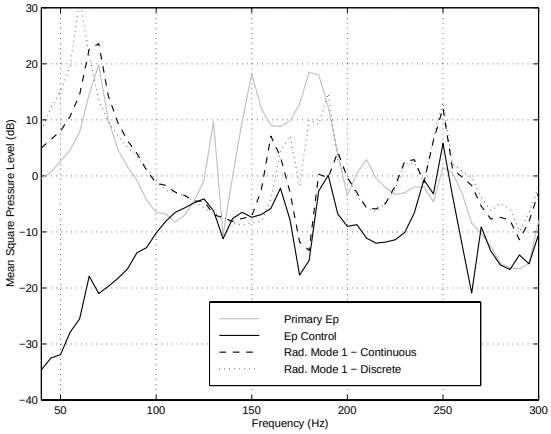

(a) Experiment

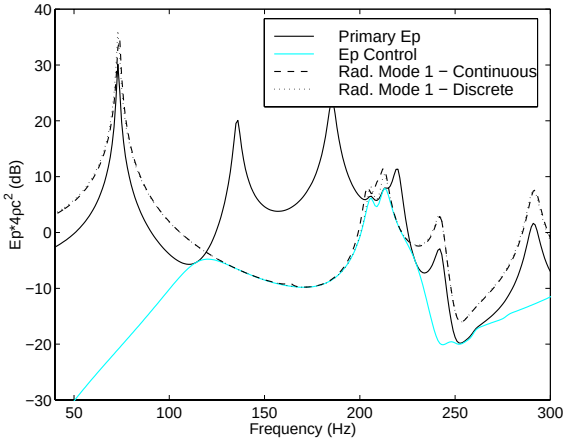

(b) Numerical simulation with ideal colinear sensors

Figure 6.12: Experimentally measured and predicted mean square pressure level using the first radiation mode sensors.

mode begins to contribute to the acoustic potential energy and this was also experienced in the numerical simulation. As before, control outside the design frequency band leads to an increase in the mean square sound pressure within the cavity. The discrete first radiation mode sensor behaves as expected and provides less control than the equivalent continuous sensor. Control around 160 Hz to 170 Hz using both sensors was less than predicted with an ideal continuous strip sensor. However, when an error was applied to the sensor shape, a decrease in performance in this frequency range was also observed (see Figure 6.4(b)). It may be concluded that the decrease in performance between 160 Hz to 170 Hz seen in Figure 6.4(a) can be attributed to the physical errors in the sensors.

Although the level of control achieved when using the modal sensors rather than using the discrete microphones as error sensors was less, the expected benefits of modal sensing, namely rapid controller convergence and high stability were definitely observed.

6.4 Summary

An expression was derived for the shape to sense the radiation modes on a simply supported panel using a piezoelectric sensor. Simplifications to the sensor shape were made and shown to provide adequate fidelity in some applications.

The experimental results indicate that although the technique of radiation mode control is feasible, the sensors appear to be very sensitive to "leak through" of undesired modes. The continuous sensors are more accurate modal sensors than discrete sensors due to spatial sampling errors associated with the discrete sensors for all but the zeroth (bulk compression) radiation mode. The modal sensors were shown to reduce the convergence time of the controller and increase the controller stability when compared to that obtained using discrete microphones. However, more work is needed in understanding the sensitivity of the control system to shape and fidelity errors before acceptable potential energy reductions will be achieved with large vibro-acoustic systems. Should the

funding become available in the future then the experiment should be repeated using the the dual layer quadratic sensor derived in Section 6.1.2 to improve the control offered by continuous sensors.

Chapter 7

Conclusions

7.1 Conclusions

A model was developed for the structural and acoustic response within an arbitrarily shaped coupled vibro-acoustic system. The rigid-walled cavity mode shapes and *in-vacuo* structure mode shapes were calculated using FEA within ANSYS and the two sub-systems were subsequently coupled using modal coupling theory. Forced harmonic response analysis of the theoretical model showed excellent agreement with the results from a fully coupled FEA.

Using the coupled vibro-acoustic model, the application of active structural acoustic control has been examined for two sensing systems; energy density at one or more points and vibration sensing of radiation modes.

7.1.1 Energy Density

The first sensing system investigated was energy density control at a point (or several points). An expression was derived for the energy density estimate in ideal one-dimensional sound fields using two or three microphones. The errors in the energy density estimate arising from several sources were considered; inherent errors (finite-difference

and finite-sum), phase errors, sensitivity errors, length errors, diffraction and interference effects, and other error sources such as temperature and humidity. The inherent errors were found to limit the upper frequency range of the energy density sensor, and the instrumentation (phase and sensitivity) errors where found to define the low frequency limit.

The error analysis was extended to 4 different three dimensional sensors where it was shown that the energy density in both a reactive sound field and a plane wave can be adequately measured for active noise control applications using only four microphones rather than the 6 used conventionally.

The normalised errors in the energy density for all the 3D sensors converged to approximately the same value for the low frequency limit in the idealised sound field since the errors at the low frequency limit are due to the finite difference approximation of the velocity. It was also found that for the low frequency limit, the errors for the three-dimensional sensors were typically 3 times larger than calculated for the one-dimensional case and this result was due to the errors arising from each axis adding to the total error. For the high frequency limit, on the other hand, the error analysis showed that for both the reactive sound field and a plane wave, the errors for the three dimensional sensors were less than those for the equivalent one-dimensional sensors. This is simply due to the three-dimensional sensors providing a better estimate of both the pressure and velocities, but particularly the pressure, through having more microphones to spatially interpolate the pressure and pressure gradient.

When investigating the inherent errors in plane wave conditions, it was shown that at the high frequency limit a 4 microphone sensor without a pressure summer performed significantly better than either a 4 microphone sensor with a pressure summer or the “standard” 6 microphone sensor. This was due to the large errors associated with the finite sum used by the latter two sensor arrangements. The gain in performance was slightly offset by the reduction in performance at the low frequency limit. Therefore, it may be concluded that the band-width of the 4 microphone sensor without a summer and

the six microphone sensor in free field conditions is approximately equal. One may argue that since the 4 microphone sensor without the summer is the simplest of the three sensor designs, then it is the better arrangement for free field control. The band-width of the 4 microphone sensor with the summer is actually less than that of the 4 microphone sensor without the summer in free field conditions, and the opposite holds in reactive conditions. Since the experiments were conducted in a reactive sound field, the 4-microphone energy density sensor with a pressure summer was used.

The numerical modeling and testing of the energy density sensor has shown a remarkable robustness to both instrumentation and finite microphone separation errors. Energy density control was shown to offer significant advantages over the equivalent number of discrete microphones, for both low and high modal density systems. The placement of the energy density sensors is not as critical as it is for microphones. At low modal densities global control obtained by minimising energy density was generally better than that obtained by minimising the sum of squared pressures at an equivalent number of microphones. At high modal densities or with an increased number of control sources, the dimensions of the zone of local control around a point obtained when minimising energy density are significantly larger (3-5 times) than the local zone of control obtained when controlling the pressure at a single location.

It was shown theoretically that if the number of control sources is the same (or greater) than the number of independent channels per sensor (4), then minimising the energy density sensed by the sensor is equivalent to minimising the sum of the squared pressures at the sensor microphones. This has important implications for multichannel control systems, as it means that it is not necessary to calculate the particle velocities and thus reduces the cost of the control system. However, if the number of control sources is less than the number of independent channels per sensor, then minimising the three orthogonal particle velocities and pressure generally provides better global control than simply minimising

the sum of the squared pressures at the sensor microphones. More than one control source per energy density sensor was found to improve local control but led to modal spillover resulting in sub-optimal global control.

The source of the acoustic excitation was shown to significantly influence the level of global and local control that could be achieved with energy density sensors. Structural sources tend to excite many higher order (short wavelength) acoustic modes which subsequently acts to reduce the control performance with energy density sensors.

A practical 3-axis energy density sensor was built and tested and showed good performance from 100 Hz to 800 Hz. The sensor was built with an optional signal conditioning unit which housed the analog electronics to calculate the mean pressure from the sensor and the 3 orthogonal velocity vectors. Experiments using the energy density sensor verified the findings of the numerical simulations.

7.1.2 Radiation Modes

It has been shown that it is possible to decompose a large number of discrete surface vibration measurements into a small number of high quality error signals for an active noise control system and obtain similar or improved results to conventional acoustic and structural error sensing. The decomposed structural vibration signals were formed so that they represent amplitudes of "radiation modes" which are orthogonal in terms of their contribution to the desired cost function. The result of using such error signals is an increase in stability of the active noise control system and reduced dimensionality achieved through the reduction of the condition number of the control system transfer function matrix. Modal sensing of radiation modes provides the highest level of control with non-invasive sensors. A technique to overcome the frequency dependence of the radiation modes was suggested which permitted the use of shaped modal sensors rather than numerous discrete sensors to provide the required error signals to minimise the enclosure acoustic potential

energy.

It is possible to constrain the cost function in such a way as to control only specific regions in the cavity in order to reduce controller effort expended in controlling non-essential regions. The numerical simulations using the "structural microphone" and the “structural energy density sensor” have shown that local control using structural sensors is indeed possible.

At low frequencies when the flexible structure encloses a large part of the cavity, it is possible to use the acoustic mode shapes as modal filters to sense the radiation modes. The spatial integration arising from the modal sensors shaped to the acoustic modes is similar to the interface modal filtering which happens between the structural and acoustic modes in the physical system. By employing a frequency dependent filter based on the radiation efficiency of the acoustic modes, the modal control system attempts to emulate the coupled vibro-acoustic system.

It was shown that the radiation modes orthogonal in terms of their contribution to the potential energy of the cavity are identical to the radiation modes orthogonal in terms of their contribution to the power radiated into the cavity. The eigenvalue matrices of the two radiation modes differ slightly by a frequency dependent term proportional to the product of the acoustic modal loss factor and the wavenumber of the acoustic mode. However, for the rectangular panel - cavity system investigated, control of the potential energy and radiated power produced identical results.

An expression was derived for the optimum shape to sense the radiation modes of a simply supported rectangular panel using a piezoelectric sensor. Simplifications to the sensor shape were made and shown to provide adequate fidelity, in terms of producing a signal proportional to the amplitude of the radiation mode, in some applications.

The experimental results indicated that although technique of using PVDF shaped sensors is feasible, the sensors appear to be very sensitive to "leak through" of undesired

modes. The continuous sensors provide more accurate modal sensing than discrete sensors due to spatial sampling errors for all but the zeroth (bulk compression) radiation mode. The modal sensors were found to reduce the convergence time of the controller and increase the controller stability when compared to that using discrete microphones.

In concluding, the two sensing techniques discussed in this thesis have been shown to offer improvement in the performance of active noise / structural-acoustic control systems for minimising sound transmission, compared to using conventional acoustic and structural error sensors. The improvements associated with enhanced observability not only lead to greater levels of control, but also provide greater system robustness and controllability.

7.2 Recommendations for Future Work

7.2.1 Energy Density

7.2.1.1 Physical energy density sensor

The current signal conditioning unit design suffers from unacceptable phase and magnitude errors. A new unit needs to be made with care taken in selecting the components to reduce the magnitude and phase errors between the microphone channels. An effort should be made to miniaturise the unit using surface mount components. A multi-pole high pass filter needs to be incorporated into the signal conditioning unit to avoid clipping of the velocity channels when the sensor is subjected to intense very low frequency noise and vibration.

The current sensor is not suitable for real environments due to its sensitivity to temperature. Therefore, a new sensor needs to be made using temperature insensitive low cost condenser microphones manufactured by LECTRET.

For low frequency applications where space is not an issue, a larger sensor with a microphone separation of $2h = 100$mm should be built. This will also help overcome the limitations of the phase mismatch between channels at low frequencies.

7.2.1.2 Numerical and experimental energy density control in a free field

Although the errors arising from the measurement of energy density in a free field have been derived, the performance of energy density control in a free field has not yet been investigated, either numerically or experimentally. More specifically, the size of the zone of quiet could be compared against that offered by a single microphone. This would most likely be similar to that found in a diffuse sound field (Garcia-Bonito & Elliott 1995*b*, Elliott & Garcia-Bonito 1995).

7.2.1.3 Error analysis for energy density in a diffuse sound field

Use the material in (Garcia-Bonito & Elliott 1995*b*, Elliott & Garcia-Bonito 1995) to derive expressions for the error in the pressure and velocity estimates using two closely spaced points in a diffuse sound field.

7.2.1.4 Experimental energy density control of a single tone in a diffuse field

It has been shown theoretically (Garcia-Bonito & Elliott 1995*b*, Elliott & Garcia-Bonito 1995) that when minimising the pressure and pressure gradient for a single tone in a diffuse sound field, the region of control is increased from $\lambda/10$ for the minimisation of pressure to $\lambda/2$. This approach has not been experimentally verified.

7.2.1.5 Virtual error sensors

Virtual microphone It has been shown that it is possible to minimise the pressure at a point located away from the sensing microphones by projecting the pressure estimate

from a physical microphone to some “virtual microphone” (Garcia-Bonito et al. 1997). The technique used a modified transfer function from the secondary source to the error sensor to achieve the “virtual microphone”. It was assumed that the spatial rate of change of the primary sound field was small and therefore the pressure at the physical microphone was used as the pressure at the virtual microphone. This was shown to lead to errors at high frequencies. Carme & De Man (1998) also uses a virtual microphone to improve the performance of an ANC headset but do not elaborate on the prediction technique.

A virtual microphone sensor was developed as just described for a diffuse sound field and the technique could be extended to investigate different types of sound field. An alternative approach could be to use a forward difference prediction of the pressure at the virtual microphone and would do away with the need for the modified secondary source to virtual microphone pressure transfer function. This approach would have the advantage that the “virtual microphone” would not need *a priori* information of the secondary source to pressure transfer functions (see Figure 7.1); however, this technique suffers from significant inaccuracies when the pressure gradient is close to zero.

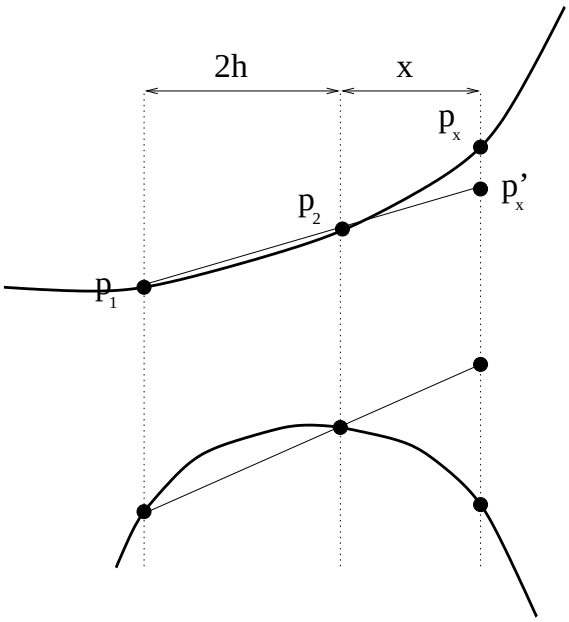

Figure 7.1: Two-microphone forward prediction technique.

The pressure at point p'_x can be approximated by the first order finite difference estimate

$$p'_x = p_2 + \frac{x}{2h}(p_2 - p_1) \tag{7.1}$$

Using a three-microphone approach it can be seen in Figure 7.2 that the forward estimate in pressure improves compared to the estimate from the two-microphone approach.

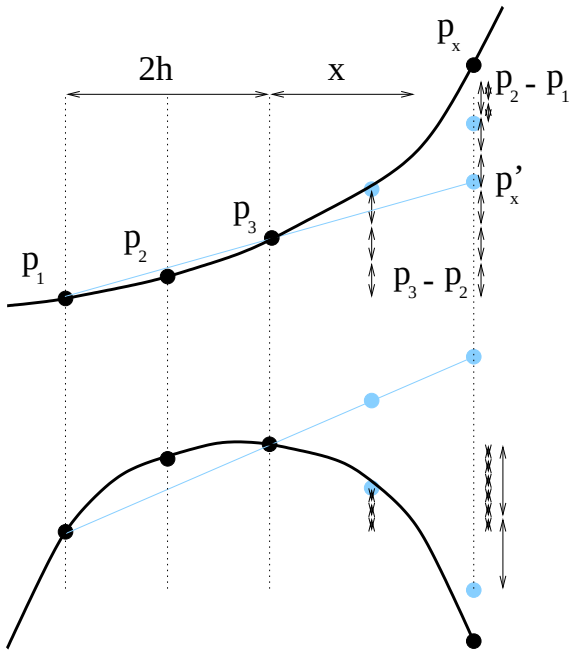

Figure 7.2: Three-microphone forward prediction technique.

The pressure at point p'_x can be approximated by the second order finite difference estimate using Lagrange's interpolation formula for unequal intervals, ie

$$p(x) = \frac{(x-x_2)(x-x_3)}{(x_1-x_2)(x_1-x_3)}y_1 + \frac{(x-x_1)(x-x_3)}{(x_2-x_1)(x_2-x_3)}y_2 + \frac{(x-x_1)(x-x_2)}{(x_3-x_1)(x_3-x_2)}y_3 \tag{7.2}$$

Therefore for the system shown in Figure 7.2, Equation (7.2) reduces to

$$p'_x = \frac{(x+h)(x)}{(h)(2h)}p_1 + \frac{(x+2h)(x)}{(h)(-h)}p_2 + \frac{(x+2h)(x+h)}{(2h)(h)}p_3 \tag{7.3}$$

collecting like terms gives

$$p'_x = \frac{x(x+h)}{2h^2}p_1 + \frac{x(x+2h)}{-h^2}p_2 + \frac{(x+2h)(x+h)}{2h^2}p_3 \tag{7.4}$$

If $x = h$ then Equation (7.4) reduces to

$$p'_x = p_1 - 3p_2 + 3p_3 = p_1 + 3(p_3 - p_2) \tag{7.5}$$

If $x = 2h$ then Equation (7.4) reduces to

$$p'_x = 3p_1 - 8p_2 + 6p_3 = p_1 - 2(p_2 - p_1) + 6(p_3 - p_2) \tag{7.6}$$

It is possible to have two closely spaced "virtual microphones" which when controlled would create a larger zone of quiet than would be achieved with a single "virtual microphone". It could be possible to define a virtual microphone array to extend the control region even further.

Virtual energy density sensor Using a forward difference approach, the pressure gradient at some point located away from the sensing microphones should also be able to be predicted. If this technique were used in conjunction with the virtual microphone then a "virtual energy density sensor" could be made. It has been shown that in general, energy density control outperforms control using the pressures at the sensor microphones and therefore this would have the advantage that it should be possible to achieve a large zone of local control away from the physical sensor. An example of such an application could be widespread local control around a passenger's head in a vehicle cabin.

For the 2 microphone sensor shown in Figure 7.1, the best estimate of pressure at a distance x from the second microphone is given by Equation (7.1), ie $p'_x = p_2 + \frac{x}{2h}(p_2 - p_1)$ and the particle velocity is obtained from the best estimate of the pressure gradient given

by

$$\frac{\partial p_{x'}}{\partial x} \approx \frac{p_2 - p_1}{2h} \tag{7.7}$$

Therefore the particle velocity estimate for a two microphone sensor is obtained by multiplying the pressure gradient in Equation (7.7) by $1/j\rho\omega$, ie

$$v_{x'} \approx \frac{p_2 - p_1}{j2h\rho\omega} \tag{7.8}$$

For the three-microphone sensor shown in in Figure 7.2, the pressure gradient estimate comes from differentiating Equation (7.4), ie

$$\frac{\partial p_{x'}}{\partial x} \approx \frac{1}{h^2}\left[\frac{2x+h}{2}p_1 - (2x+2h)\,p_2 + \frac{2x+3h}{2}p_3\right] \tag{7.9}$$

If $x = 0$ then Equation (7.9) reduces to

$$\frac{\partial p_{x'}}{\partial x} \approx \frac{1}{2h}\left[p_1 - 4p_2 + 3p_3\right] = \frac{1}{2h}\left[3\left(p_3 - p_2\right) - \left(p_2 - p_1\right)\right] \tag{7.10}$$

If $x = h$ then Equation (7.9) reduces to

$$\frac{\partial p_{x'}}{\partial x} \approx \frac{1}{2h}\left[3p_1 - 8p_2 + 5p_3\right] = \frac{1}{2h}\left[5\left(p_3 - p_2\right) - 3\left(p_2 - p_1\right)\right] \tag{7.11}$$

If $x = 2h$ then Equation (7.9) reduces to

$$\frac{\partial p_{x'}}{\partial x} \approx \frac{1}{2h}\left[5p_1 - 12p_2 + 7p_3\right] = \frac{1}{2h}\left[7\left(p_3 - p_2\right) - 5\left(p_2 - p_1\right)\right] \tag{7.12}$$

7.2.2 Radiation Modes and Modal Sensors

7.2.2.1 Sensing radiation modes with improved sensor shapes

From the experimental results in Chapter 6 it appears that radiation mode sensors are highly sensitive to leak-through of undesired modes. This was exacerbated by the use of non-optimal sensor shapes. It would be desirable to repeat the experiments using PVDF sensors with quadratic shape functions for the first 2 radiation modes. Both a single layer and a double layer strip could be used to see if this results in an improvement in control of the potential energy.

7.2.2.2 Shaped modal actuators

Using the reciprocal relationship that exists for any piezoelectric transducer it is possible to create modal actuators. These produce the same benefits that the modal sensors exhibit, namely a reduction in modal spillover and improved controllability due to un-coupling of the modal response. The application of piezo-rubber as a modal actuator could be used in conjunction with the PVDF modal sensors to improve the performance of the ASAC system.

7.2.2.3 Orthonormal basis functions for double walled systems

The work developed in the earlier chapters for forming an orthonormal basis set for single walled structural sound transmission problems can be applied to doubled walled systems as shown in Figure 7.3. In fact, the theory could be extended for multiple walled cavity systems for which there exists an infinite number of combinations of sub-system modal coupling problems.

However, the most commonly encountered vibro-acoustic systems are single and doubled walled cavities, the former being covered in this thesis and current literature. For the doubled skinned system shown above the following combinations are the most relevant to

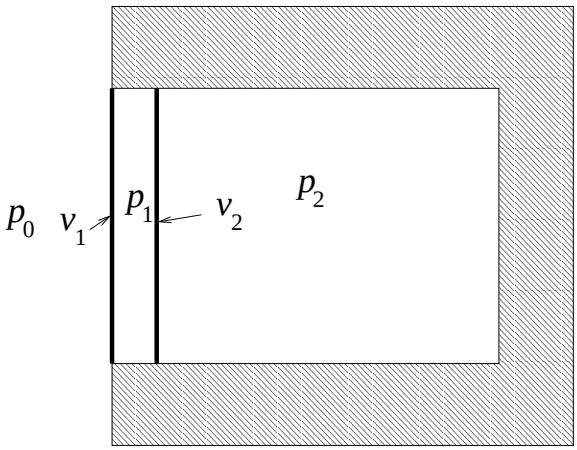

Figure 7.3: Sound transmission through a double walled enclosure.

noise control problems.

1. External to internal basis functions

   - Wall partition pressure to interior pressure, $\mathbf{p}_1 = \mathbf{Z}_{p_1 p_2}\mathbf{p}_2$
   - External shell velocity to interior pressure, $\mathbf{v}_1 = \mathbf{Z}_{v_1 p_2}\mathbf{p}_2$
   - Free-field pressure to interior pressure, $\mathbf{p}_0 = \mathbf{Z}_{p_0 p_2}\mathbf{p}_2$

2. Internal to external basis functions

   - Wall partition pressure to free-field pressure, $\mathbf{p}_1 = \mathbf{Z}_{p_1 p_0}\mathbf{p}_0$
   - Interior pressure to free-field pressure, $\mathbf{p}_2 = \mathbf{Z}_{p_2 p_0}\mathbf{p}_0$
   - Interior shell velocity to free-field pressure, $\mathbf{v}_2 = \mathbf{Z}_{v_2 p_0}\mathbf{p}_0$

The transfer functions could be derived using an extended formulation found in Chapter 2. The basis functions would then be formed from the most appropriate cost function which would most likely be radiated sound power for the free field problems and acoustic potential energy for the sound transmission into cavities.

Pan et al. (1998) has used the free-field pressure to interior pressure basis functions to study the sound transmission through a double wall cavity into a room. The authors measured the volume velocity of each panel and found that control of the second (radiating) panel provides better control of sound transmission than controlling the receiving panel.

Using the appropriate orthonormal basis functions will guarantee that minimisation of the error signals will lead to a reduction in the cost function. Although in theory such an approach will produce effective control, it will be necessary to conduct either numerical or experimental tests to see if in a practical system the benefits are realised.

For control systems with control actuators and error sensors in several sub-systems it could be possible to use sub-system control, ie error sensors, control sources and controller specific to each subsystem. This will then reduce the number of independent control channels of each controller which will rapidly speed up controller convergence.

7.2.2.4 Spatial filtering for discrete sensors

The problem with using discrete sensors for modal decomposition of radiation modes is that they are very susceptible to spatial aliasing, ie sensing short wavelength structural modes which do not contribute significantly to the long wavelength radiation modes. The continuous sensors do not suffer from this phenomenon as they have inherent wavenumber filtering.

Relating the in-plane strain (using continuous sensors) to out of plane displacements is often very difficult except for systems with the most simple boundary conditions. Therefore continuous sensors may be very difficult to implement in practice. If it were possible to have a discrete sensor which measured out of plane displacements with low pass spatial filtering such as is found with continuous sensors, then the performance of discrete sensors may be improved. This could be achieved in several ways.

- Using several closely spaced accelerometers to provide a meta accelerometer, the

mean of which defines the sensor output. This is almost the same as increasing the number of discrete sensors used for the decomposition.

- An alternative technique would be to modify the structure locally around the accelerometer using “stiff patches” to filter out the short wavelength modes. This could be achieved by attaching an additional patch or layup onto the original shell, thereby increasing the local stiffness (and mass). The dynamics of the original system would be changed a little with the addition of the patches but it is unlikely the overall energy transmission from an external source into the cavity would be significantly affected.

- Alternatively, a “soft patch” could be used. This would have insufficient mass and stiffness to significantly alter the behaviour of the structure, but rather would filter out structural modes with higher wavenumbers by “riding” above them.

Physical wavenumber filter A physical wavenumber filter could be built using a patch which physically modifies the structure locally to remove short wavelength structural modes. Alternatively, a soft foam with a light rigid backing could form the patch as seen in Figure 7.4. If the stiffness of the foam were much less than the local stiffness of the shell and the mass of the backing were light compared to the local shell mass then the patch would not modify the system response. The sensor would work most effectively in its stiffness or mass controlled region.

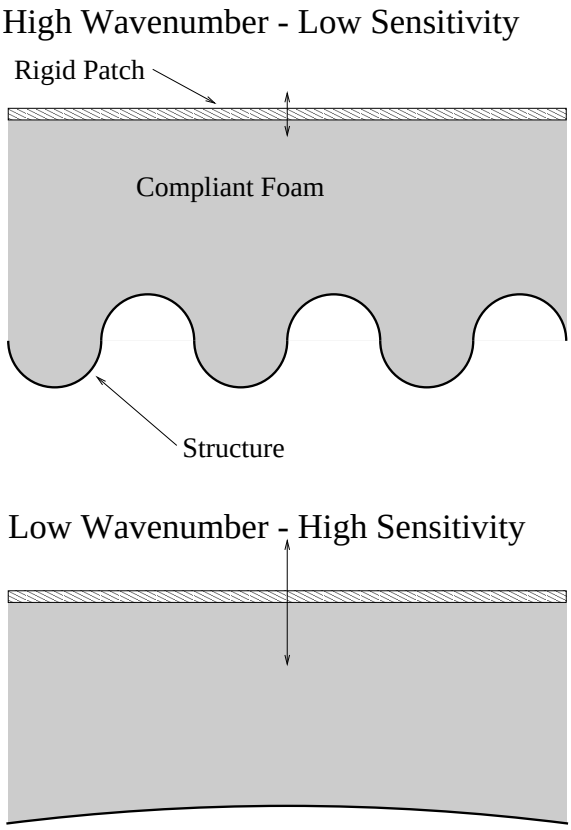

Figure 7.4: Passive structural wavenumber filter.

References

Abler, S. & Silcox, R. (1987), Experimental evaluation of active noise control in a thin cylindrical shell, *in* 'Proceedings of Noise-Con 87', pp. 341–346.

Alvelid, M. (1993), Optimisation of secondary sources for active noise control in a FE-model of an aircraft cabin, *in* 'Proceedings of Inter Noise 93', pp. 65–70.

ANSYS Structural Analysis Guide (1998), *Ansys 5.4*, 3 edn, Ansys Inc, Canonsburg, PA.

ANSYS Theory Manual (1998), *Ansys 5.4*, 8 edn, Ansys Inc, Canonsburg, PA.

Anthony, D. & Elliott, S. (1991), 'A comparison of three methods of measuring the volume velocity of an acoustic source', *Journal of the Audio Engineering Society* **39**, 355–366.

Bailey, T. & Hubbard, J. (1985), 'Distributed piezoelectric-polymer active vibration control of a cantilever beam', *AIAA Journal of Guidance, Control and Dynamics* **8**(5), 605–611.

Balas, M. (1978), 'Active control of flexible systems', *Journal of Optimization Theory and Applications* **25**(3), 415–436.

Baumann, W., Saunders, W. & Robertshaw, H. (1991), 'Active suppression of acoustic radiation from impulsively excited structures', *Journal of the Acoustical Society of America* **90**(6), 3202–3208.

Bendat, J. & Piersol, A. (1986), *Random Data - Analysis and Measurement Procedures*, 2nd edn, John Wiley & Sons, New York.

Beranek, L. (1988), *Noise and Vibration Control*, Institute of Noise Control Engineering, Washington, DC.

Bessac, F., Gagliardini, L. & Guyader, J.-L. (1996), 'Coupling eigenvalues and eigenvectors: A tool for investigating the vibroacoustic behaviour of coupled vibrating systems', *Journal of Sound and Vibration* **191**, 881–899.

Boden, H. & Abom, M. (1986), 'Influence of errors on the two-microphone method for measuring acoustic properties in ducts', *Journal of the Acoustical Society of America* **79**(2), 541–549.

Borgiotti, G. (1990), 'The power radiated by a vibrating body in an acoustic fluid and its determination from boundary measurements', *Journal of the Acoustical Society of America* **88**(4), 1884–1893.

Borgiotti, G. & Jones, K. (1993), 'The determination of the acoustic far field of a radiating body in an acoustic field from boundary measurements', *Journal of the Acoustical Society of America* **93**(5), 2788–2797.

Borgiotti, G. & Jones, K. (1994), 'Frequency independence property of radiation spatial filters', *Journal of the Acoustical Society of America* **96**(6), 3516–3524.

Bullmore, A., Nelson, P. & Elliott, S. (1986), 'Active minimisation of acoustic potential energy in harmonically excited cylindrical enclosed sound fields', *AIAAP*.

Bullmore, A., Nelson, P. & Elliott, S. (1990), 'Theoretical studies of the active control of propeller-induced cabin noise', *Journal of Sound and Vibration* **140**(2), 191–217.

Bullmore, A., Nelson, P., Curtis, A. & Elliott, S. (1987), 'The active minimisation of harmonic enclosed sound fields, part II: A computer simulation', *Journal of Sound and Vibration* **117**(1), 15–33.

Burdisso, R. & Fuller, C. (1994), 'Design of active structural acoustic control systems by eigenproperty assignment', *Journal of the Acoustical Society of America* **96**(3), 1582–1591.

Burgemeister, K. (1996), Novel methods of transduction for active control of harmonic sound radiated by vibrating surfaces, Ph.D. Dissertation, The University of Adelaide.

Burgemeister, K. & Snyder, S. (1997), 'Active minimisation of radiated acoustic power using acoustic sensors', *Submitted for Publication in the Journal of the Acoustical Society of America*.

Burke, S. & Hubbard Jr., J. (1987), 'Active vibration control of a simply supported beam using a spatially distributed actuator', *IEEE Control Systems Magazine* **7**(4), 25–30.

Burke, S. & Hubbard Jr., J. (1988), 'Distributed actuator control design for flexible beams', *Automatica* **24**(5), 619–627.

Burke, S. & Hubbard Jr., J. (1991), 'Distributed transducer vibration control of thin plates', *Journal of the Acoustical Society of America* **90**(2), 937–944.

Burke, S., Hubbard Jr., J. & Meyer, J. (1993), 'Distributed transducers and collocation', *Mechanical Systems and Signal Processing* **7**(4), 349–361.

Callahan, J. & Baruh, H. (1995), 'Modal analysis using segmented piezoelectric sensors', *AIAA Journal* **33**(12), 2371–2378.

Carey, D. & Stulen, F. (1993), Experiments with a two-dimensional multi-modal sensor, *in* 'Second Conference on Recent Advances in Active Control of Sound and Vibration', pp. S41–S52.

Carletti, E., Miccoli, G. & Vecchi, I. (1996), Earth-moving machine cab enclosed sound field active control simulation, *in* 'Proceedings of Inter Noise 96', pp. 1183–1186.

Carme, C. & De Man, P. (1998), How to improve an anc headset by using a virtual microphone, *in* 'Proceedings of the InterNoise 98', Christchurch.

Cazzolato, B. & Hansen, C. (1997), Structural sensing of sound transmission into a cavity for active structural-acoustic control, *in* 'Proceedings of the Fifth International Congress on Sound and Vibration', Adelaide, pp. 2391–2401.

Cazzolato, B. & Hansen, C. (1998), 'Active control of sound transmission using structural error sensing', *Journal of the Acoustical Society of America* **104**(5), 2878–2889.

Chaplin, G. (1983), 'Anti-noise - the essex breakthrough', *Chartered Mechanical Engineer* **30**, 41–47.

Charette, F., Berry, A. & Guigou, C. (1998), 'Active control of sound radiation from a plate using a polyvinylidene flouride volume displacement sensor', *Journal of the Acoustical Society of America* **103**(3), 1493–1503.

Charette, F., Guigou, C. & Berry, A. (1995), Development of volume velocity sensors for plates using PVDF film, *in* 'Proceedings of Active 95', pp. 241–252.

Charette, F., Guigou, C., Berry, A. & Plantier, G. (1994), 'Asymmetric actuation and sensing of a beam using piezoelectric materials', *Journal of the Acoustical Society of America* **96**(4), 2272–2283.

Chen, P.-T. (1997), 'Vibrations of submerged structures in a heavy acoustic medium using radiation modes', *Journal of Sound and Vibration* **208**(1), 55–71.

Chen, P.-T. & Ginsberg, J. (1995), 'Complex power, reciprocity, and radiation modes for submerged bodies', *Journal of the Acoustical Society of America* **98**(6), 3343–3351.

Choi, S. (1995), 'Alleviation of chattering in flexible beam control via piezofilm actuator and sensor', *AIAA Journal* **33**(3), 564–567.

Clark, R. (1995), 'Adaptive feedforward modal space control', *Journal of the Acoustical Society of America* **98**, 2639–2650.

Clark, R. & Fuller, C. (1992*a*), 'Active structural acoustic control with adaptive structures including wavenumber considerations', *Journal of Intelligent Materials Systems and Structures* **3**, 296–315.

Clark, R. & Fuller, C. (1992*b*), 'Modal sensing of efficient acoustic radiators with polyvinylidene fluoride distributed sensors in active structural acoustic control approaches', *Journal of the Acoustical Society of America* **91**(6), 3321–3329.

Clark, R. & Fuller, C. (1992*c*), 'A model reference approach for implementing active structural acoustic control', *Journal of the Acoustical Society of America* **92**(3), 1534–1544.

Clark, R. & Fuller, C. (1992*d*), 'Optimal placement of piezoelectric actuators and polyvinylidene fluoride error sensors in active structural acoustic control approaches', *Journal of the Acoustical Society of America* **92**(3), 1521–1533.

Clark, R. & Fuller, C. (1994), 'Active control of strucurally radiated sound from an enclosed finite cylinder', *Journal of Intelligent Materials Systems and Structures* **5**, 379–391.

Clark, R., Burdisso, R. & Fuller, C. (1993), 'Design approaches for shaping polyvinylidene fluoride sensors in active structural acoustic control (ASAC)', *Journal of Intelligent Materials Systems and Structures* **4**, 354–365.

Clark, R., Fuller, C. & Wicks, A. (1991), 'Characterisation of multiple piezoelectric actuators for structural excitation', *Journal of the Acoustical Society of America* **90**(1), 346–357.

Constans, E., Koopmann, G. & Belegundu, A. (1998), 'The use of material tailoring to minimise the radiated sound power of vibrating shells: Theory and experiment', *Journal of Sound and Vibration* **217**(2), 225–350.

Cook, R. & Schade, P. (1974), New method for the measurement of the total energy density of sound waves, *in* 'Proceedings of Inter-Noise 74', pp. 101–106.

Cox, D. & Lindner, D. (1991), 'Active control for vibration suppression in a flexible beam using a modal domain optical fiber sensor', *Journal of Vibration and Acoustics (ASME)* **113**, 369–382.

Coyette, J., Dubois-Pelerin, Y. & Migeot, J. (1994), Finite element treatment of large size coupled problems using unequal meshes, *in* 'Proceedings of Inter Noise 94', pp. 2003–2006.

Craggs, A. (1971), 'The transient response of a coupled plate-acoustic system using plate and acoustic finite elements', *Journal of Sound and Vibration* **15**(4), 509–528.

Cunefare, K. (1991), 'The minimum radiation efficiency of baffled finite beams', *Journal of the Acoustical Society of America* **90**(5), 2521–2529.

Cunefare, K. & Currey, M. (1994), 'On the exterior acoustic radiation modes of structures', *Journal of the Acoustical Society of America* **96**(4), 2302–2312.

Currey, M. & Cunefare, K. (1995), 'The radiation modes of baffled finite plates', *Journal of the Acoustical Society of America* **98**(3), 1570–1580.

Curtis, A., Nelson, P.A. nad Elliott, S. & Bullmore, A. (1987), 'Active suppression of acoustic resonance', *Journal of the Acoustical Society of America* **81**(3), 624–631.

Dai, Y. & Fuller, C. (1995), Numerical simulation of active control of interior noise in a business jet with point force actuators - optimization of transducers, *in* 'Proceedings of Inter Noise 95', pp. 533–536.

De Rosa, S., Pezzullo, G., Lecce, L. & Marulo, F. (1994), 'Structural acoustic calculations in the low frequency range', *Journal of Aircraft* **31**(6), 1387–1394.

Dimitriadis, E. & Fuller, C. (1991), 'Active control of sound transmission through elastic plates using piezoelectric actuators', *AIAA Journal* **29**(11), 1771–1777.

Dorling, C., Eatwell, B., Hutchins, S., Ross, C. & Sutcliffe, S. (1989), 'A demonstraton of active noise reduction in an aircraft cabin', *Journal of Sound and Vibration* **128**(2), 358–360.

Dowell, E., Gorman III, G. & Smith, D. (1977), 'Acoustoelasticity : General theory, acoustic natural modes and forced response to sinusoidal excitation, including comparisons with experiment', *Journal of Sound and Vibration* **52**(4), 519–542.

Elko, G. (1991*a*), An acoustic vector-field probe with calculable obstacle bias, *in* 'Proceedings of Noise-Con 91', pp. 525–532.

Elko, G. (1991*b*), Biased against finite-difference bias, *in* 'Proceedings of Noise-Con 91', pp. 541–546.

Elliott, S. (1981), 'Errors in acoustic intensity measurements', *Journal of Sound and Vibration* **78**(3), 439–445.

Elliott, S. & Garcia-Bonito, J. (1995), 'Active cancellation of pressure and pressure gradient in a diffuse sound field', *Journal of Sound and Vibration* **186**(4), 696–704.

Elliott, S. & Johnson, M. (1993), 'Radiation modes and the active control of sound power', *Journal of the Acoustical Society of America* **94**(4), 2194–2204.

Elliott, S. & Nelson, P. (1987), The active control of enclosed sound fields, *in* 'Proceedings of Noise-Con 87', pp. 359–364.

Elliott, S., Curtis, A., Bullmore, A. & Nelson, P. (1987), 'The active minimisation of harmonic enclosed sound fields, Part III: Experimental verification', *Journal of Sound and Vibration* **117**(1), 35–58.

Elliott, S., Joseph, P., Nelson, P. & Johnson, M. (1991), 'Power output minimisation and power absorption in the active control of sound', *Journal of the Acoustical Society of America* **90**(5), 2501–2512.

Everstine, G. (1981), 'A symmetric potential formulation for fluid-structure interaction', *Journal of Sound and Vibration* **79**(1), 157–160.

Ewins, D. (1995), *Modal Testing: Theory and Practice*, Research Studies Press, Taunton, Somerset, England.

Fahy, F. (1968), Vibration of containing structures by sound in the contained fluid, ISVR Technical Report No. 11, University of Southampton.

Fahy, F. (1969), 'Vibration of containing structures by sound in the contained fluid', *Journal of Sound and Vibration* **10**(3), 490–512.

Fahy, F. (1970), 'Response of a cylinder to random sound in the contained fluid', *Journal of Sound and Vibration* **13**(2), 171–194.

Fahy, F. (1985), *Sound and Structural Vibration: Radiation, Transmission, and Response*, Academic Press, London.

Fahy, F. (1995), *Sound Intensity*, 2nd edn, E&FN Spon, London.

Fanzoni, L. & Bliss, D. (1998), 'A discussion of modal uncoupling and an approximate closed-form solution for weakly coupled systems with application to acoustics', *Journal of the Acoustical Society of America* **103**(4), 1923–1932.

Fanzoni, L. & Dowell, E. (1995), 'On the accuracy of modal analysis in reverberant acoustic systems with damping', *Journal of the Acoustical Society of America* **97**(1), 687–690.

Fuller, C. & Jones, J. (1987), 'Experiments on reduction of propeller induced interior noise by active control of cylinder vibration', *Journal of Sound and Vibration* **112**(2), 389–395.

Fuller, C., Hansen, C. & Snyder, S. (1991), 'Active control of sound radiation from a vibrating rectangular panel by sound sources and vibration inputs: An experimental comparison', *Journal of Sound and Vibration* **145**(2), 195–215.

Fuller, C., Silcox, R., Metcalf, V. & Brown, D. (1989), Experiments on structural control of sound transmitted through an elastic plate, *in* 'Proceedings of the American Control Conference', Pittsburgh, pp. 2079–2084.

Fuller, C., Snyder, S., Hansen, C. & Silcox, R. (1992), 'Active control of interior noise in model aircraft fuselages using piezoceramic actuators', *AIAA Journal* **30**(11), 2613–2617.

Garcia-Bonito, J. & Elliott, S. (1995*a*), 'Local active control of diffracted diffuse sound fields', *Journal of the Acoustical Society of America* **98**(2), 1017–1024.

Garcia-Bonito, J. & Elliott, S. (1995*b*), Strategies for local active control in diffuse sound fields, *in* 'Proceedings of Active 95', pp. 561–572.

Garcia-Bonito, J., Elliott, S. & Boucher, C. (1997), 'Generation of zones of quiet using a virtual microphone arrangement', *Journal of the Acoustical Society of America* **101**(6), 3498–3516.

Guicking, D., Karcher, K. & Rollwage, M. (1983), Active control of the acoustic reflection coefficient at low frequencies, *in* 'Proceedings of Inter-Noise 83', pp. 419–422.

Hansen, C. & Snyder, S. (1997), *Active control of noise and vibration*, E&FN Spon, London.

Hirsch, S. & Sun, J. (1998), 'Numerical studies of acoustic boundary control for interior sound suppression', *Journal of the Acoustical Society of America* **104**(4), 2227–2235.

Howard, C. & Hansen, C. (1996), Active vibration isolation using vibrational power as a cost function, *in* 'The Third Joint Meeting Acoustical Society of America and Acoustical Society of Japan', p. 2782.

Huang, M. & Carlson, W. (1993), Prediction of sound levels in an isolated locomotive cab by the finite element method, *in* 'Proceedings of Noise-Con 93', pp. 547–552.

Humi, M. & Miller, W. (1992), *Boundary Value Problems and Partial Differential Equations*, PWS-Kent, Boston.

Jayachandran, V., Hirsch, S. & Sun, J. (1998), 'On the numerical modelling of interior sound fields by the modal expansion approach', *Journal of Sound and Vibration* **210**(2), 243–254.

Johnson, M. (1996), Active control of sound transmission, Ph.D. Dissertation, The University of Southampton.

Johnson, M. & Elliott, S. (1993), 'Volume velocity sensors for active control', *Proceedings of the Institute of Acoustics* **15**(3), 411–420.

Johnson, M. & Elliott, S. (1995), 'Active control of sound radiation using volume velocity cancellation', *Journal of the Acoustical Society of America* **98**(4), 2174–2186.

Jones, J. & Fuller, C. (1987), 'Active control of sound fields in elastic cylinders by vibrational inputs', *Proceedings of Noise-Con 87* pp. 413–418.

Jones, J. & Fuller, C. (1989), 'Active control of sound fields in elastic cylinders by multicontrol forces', *AIAA Journal* **27**(7), 845–852.

Kang, S. & Kim, Y.-H. (1997), 'Causally constrained active sound power control in an enclosed space', *Journal of Sound and Vibration* **204**(5), 807–822.

Kim, S. & Jones, J. (1991), A study of actuators for active control of distributed elastic systems, *in* 'Proceedings of Noise-Con 91', pp. 283–290.

Kitech, P. & Tichy, J. (1982), 'Intensity probe obstacle effects and error of the transfer function technique to calibrate acoustic intensity measurements', *Proceedings of Inter Noise* pp. 695–698.

Krishnappa, G. (1983), 'Interfence effects in the two microphone technique of acoustic intensity measurements', *Noise Control Engineering Journal* **21**(3), 126–135.

Kuijpers, A., Verbeek, G. & Verheij, J. (1998), Efficient low noise design of finite duct-like systems applying radiation modes, *in* 'Proceedings of Inter-Noise 98', Christchurch, New Zealand.

Lafleur, L., Shields, F. & Hendrix, J. (1991), 'Acoustically active surfaces using piezorubber', *Journal of the Acoustical Society of America* **90**(3), 1230–1237.

Lee, C. & Moon, F. (1990), 'Modal sensors/actuators', *Journal of Applied Mechanics* **57**, 434–441.

Lee, C.-K. (1990), ‘Theory of laminated piezoelectric plates for the design of distributed sensors / actuators. part I: Governing equations and reciprocal relationships’, *Journal of the Acoustical Society of America* **87**(3), 1144–1158.

Lee, C.-K., Chiang, W.-W. & O’Sullivan, T. (1991), ‘Piezoelectric modal sensor / actuator pairs for critical active damping vibration control’, *Journal of the Acoustical Society of America* **90**(1), 374–384.

Lester, H. & Fuller, C. (1987), Mechanisms of active control for noise inside a vibrating cylinder, *in* ‘Proceedings of Noise-Con 87’, pp. 371–376.

Lyon, R. (1963), ‘Noise reduction of rectangular enclosures with one flexible wall’, *Journal of the Acoustical Society of America* **35**(11), 1791–1797.

Lyon, R. & Maidanik, G. (1962), ‘Power flow between linearly coupled oscillators’, *Journal of the Acoustical Society of America* **34**, 623.

Maillard, J. & Fuller, C. (1998), ‘Comparison of two structural sensing approaches for active structural acoustic control’, *Journal of the Acoustical Society of America* **103**(1), 396–400.

Martin, V. (1993), Small-scale vibroacoustic modelling for active noise control in aircraft, *in* ‘Noise-93’, pp. 195–200.

Martin, V., Vignassa, P. & Peseux, B. (1994), ‘Numerical vibro-acoustic modelling of aircraft for the active acoustic control of interior noise’, *Journal of Sound and Vibration* **176**(3), 307–332.

Matlab 5.4 (1998), *Matlab User Guide*, 5.4 edn, Mathworks.

Meirovitch, L. & Baruh, H. (1982), ‘Control of self-adjoint distributed-parameter systems’, *AIAA Journal* **5**(1), 60–66.

Meirovitch, L. & Baruh, H. (1985), 'The implementation of modal filters for control of structures', *AIAA Journal of Guidance, Control and Dynamics* **8**(6), 707–719.

Meirovitch, L. & Bennighof, J. (1986), 'Modal control of traveling waves in flexible structures', *Journal of Sound and Vibration* **111**(1), 131–144.

Meirovitch, L. & Thangjitham, S. (1990), 'Active control of sound radiation pressure', *Journal of Vibration and Acoustics (ASME)* **112**, 237–224.

Miller, D., Collins, S. & Peltzman, S. (1990), 'Development of spatially convolving sensors for structural control applications', *AIAAP* pp. 2283–2297.

Morgan, D. (1991), 'An adaptive modal-based active control system', *Journal of the Acoustical Society of America* **89**(1), 248–256.

Naghshineh, K. & Koopmann, G. (1993), 'Active control of sound power using acoustic basis functions as surface velocity filters', *Journal of the Acoustical Society of America* **93**(5), 2740–2752.

Naghshineh, K., Chen, W. & Koopmann, G. (1995), 'Active control of sound power from a cylindrical shell', *Proceedings of Active 95* pp. 323–334.

Naghshineh, K., Chen, W. & Koopmann, G. (1998), 'Use of acoustical basis functions for active control of sound power radiated from a cylinder', *Journal of the Acoustical Society of America* **103**(4), 1897–1903.

Naghshineh, K., Koopmann, G. & Belegundu, A. (1992), 'Material tailoring of structures to achieve a minimum radiation condition', *Journal of the Acoustical Society of America* **92**(2), 841–855.

Nashif, P. & Sommerfeldt, S. (1992), An active control strategy for minimising the energy density in enclosures, *in* 'Proceedings of Inter Noise 92', pp. 357–361.

Nefske, D., Wolf, J.A., J. & Howell, L. (1982), 'Strutural-acoustic finite element analysis of the automotive passenger compartment: A review of current practice', *Journal of Sound and Vibration* **80**(2), 247–266.

Nelson, P. & Elliott, S. (1992), *Active Control of Sound*, Academic Press, London.

Nelson, P., Curtis, A., Elliott, S. & Bullmore, A. (1987*a*), 'The active minimization of harmonic enclosed sound fields, part I: Theory', *Journal of Sound and Vibration* **117**(1), 1–13.

Nelson, P., Curtis, A., Elliott, S. & Bullmore, A. (1987*b*), 'The minimum power output of free field point sources and the active control of sound', *Journal of Sound and Vibration* **116**(3), 397–414.

Otte, D. & Van der Auweraer, H. (1993), Experimental vibro-acoustic system modelling in the medium frequency area: An impedance modelling approach, *in* 'Proceedings of Inter Noise 93', pp. 885–888.

Pan, J. (1992), 'The forced response of an acoustic-structural coupled system', *Journal of the Acoustical Society of America* **91**(2), 949–956.

Pan, J. & Bies, D. (1990), 'The effect of fluid-structural coupling on sound waves in an enclosure - Theoretical part', *Journal of the Acoustical Society of America* **87**(2), 691–707.

Pan, J. & Hansen, C. (1991), 'Active control of noise transmission through a panel cavity: II. Experimental study', *Journal of the Acoustical Society of America* **90**(3), 1488–1492.

Pan, J., Hansen, C. & Bies, D. (1990), 'Active control of noise transmission through a panel into a cavity: I. Analytical study', *Journal of the Acoustical Society of America* **87**(5), 2098–2108.

Pan, J., Hansen, C. & Bies, D. (1991), ‘Active control of noise transmission through a panel cavity: III. Effect of actuator location’, *Journal of the Acoustical Society of America* **90**(3), 1493–1501.

Pan, X., Sutton, T. & Elliott, S. (1998), ‘Active control of sound transmission through a double-leaf partition by volume velocity cancellation’, *Journal of the Acoustical Society of America* **104**(5), 2828–2835.

Park, Y. & Sommerfeldt, S. (1997), ‘Global attenuation of broadband noise fields using energy density control’, *Journal of the Acoustical Society of America* **101**(1), 350–359.

Pascal, J. & Carles, C. (1982), ‘Systematic measurement errors with two microphone sound intensity meters’, *Journal of Sound and Vibration* **83**(1), 53–65.

Pavic, G. (1977), ‘Measurement of sound intensity’, *Journal of Sound and Vibration* **51**(4), 533–545.

Photiadis, D. (1990), ‘The relationship of singular value decomposition to wave-vector filtering in sound radiation problems’, *Journal of the Acoustical Society of America* **88**(2), 1152–1159.

Pines, D. (1996), Hybrid distributed modal/wave sensors for structural control, *in* ‘Smart Structures and Materials 1996 : Smart Structures and Integrated Systems’, The International Society for Optical Engieering, San Diego, Calfornia, pp. 462–471.

Pope, L. (1971), ‘On the transmission of sound through finite closed shells: Statistical energy analysis, modal coupling, and non-resonant transmission’, *Journal of the Acoustical Society of America* **50**(3), 1004–1018.

Pretlove, A. (1966), ‘Forced vibrations of a rectangular panel backed by a closed rectangular cavity’, *Journal of Sound and Vibration* **3**(3), 252–261.

Rajakumar, C., Ali, A. & Yanus, S. (1992), ‘Lanczos algorithm for acoustic boundary element eigenvalue problems’, *Journal of the Acoustical Society of America* **91**(2), 939–948.

Rex, J. & Elliott, S. (1992), The QWSIS - A new sensor for structural radition control, *in* ‘1st International Confererence on Motion and Vibration Control’, pp. 339–343.

Rossetti, D. & Norris, M. (1996), ‘A comparison of actuation and sensing techniques for aircraft cabin noise control’, *Noise Control Engineering Journal* **44**(1), 53–58.

Rossetti, D., Norris, M., Southward, S. & Sun, J. (1993), A comparison of speakers and structural based actuators for aircraft cabin noise control, *in* ‘Recent Advances in Active Control of Sound and Vibration’, pp. S1–S10.

Royston, T. (1994), Shaped PVDF sensors for intelligent measurement of acoustic pressure in liquid filled pipes, *in* ‘Proceedings of Noise-Con 94’, pp. 875–880.

Royston, T. (1995), ‘Shaped polyvinylidene fluoride (PVDF) sensors for intelligent measurement of plane-wave acoustic pressure in liquid-filled pipes’, *Noise Control Engineering Journal* **43**(1), 15–20.

Salava, T. (1988), ‘Acoustic load and transfer functions in rooms at low frequencies’, *Journal of the Audio Engineering Society* **36**, 763–775.

Sarkissian, A. (1991), ‘Acoustic radiation from finite structures’, *Journal of the Acoustical Society of America* **90**(1), 574–578.

Sas, P., Bao, C., Augusztinovicz, F. & Desmet, W. (1995), ‘Active control of sound transmission through a double panel partition’, *Journal of Sound and Vibration* **180**(4), 609–625.

Schumacher, M. & Hixson, E. (1983), 'A transducer and processing system to measure total acoustic energy density', *Journal of the Acoustical Society of America* **74**(S1), S62.

Scott, B. & Sommerfeldt, S. (1997), 'Estimating acoustic radiation from a Bernoulli-Euler beam using shaped polyvinylidene fluoride film', *Journal of the Acoustical Society of America* **101**(6), 3475–3485.

Shen, W. & Sun, J. (1997), 'A study of shell interior noise control', *SPIE* **3041**, 812–818.

Shields, F. & Lafleur, L. (1997), 'Smart acoustically active surfaces', *Journal of the Acoustical Society of America* **102**(3), 1559–1566.

Silcox, R., Fuller, C. & Lester, H. (1990), 'Mechanisms of active control in cylindrical fuselage structures', *AIAA* **28**(8), 1397–1404.

Silcox, R., Lester, H. & Abler, S. (1989), 'An evaluation of active noise control in a cylindrical shell', *Transactions of the ASME - Journal of Vibration, Acoustics, Stress, and Reliability in Design* **111**, 337–342.

Snyder, S. & Burgemeister, K. (1996), Performance enhancement of structural/acoustic active control systems via acoustic error signal decomposition, *in* 'Proceedings of Inter Noise 96', Liverpool, pp. 1141–1146.

Snyder, S. & Hansen, C. (1989), 'Active noise control in ducts; Some physical insights', *Journal of the Acoustical Society of America* **86**, 184–194.

Snyder, S. & Hansen, C. (1991), 'Mechanisms of active noise control by vibration sources', *Journal of Sound and Vibration* **147**(3), 519–525.

Snyder, S. & Hansen, C. (1994*a*), 'The design of systems to actively control periodic sound transmission into enclosed spaces, Part 1: Analytical models', *Journal of Sound and Vibration* **170**(4), 433–449.

Snyder, S. & Hansen, C. (1994*b*), 'The design of systems to actively control periodic sound transmission into enclosed spaces, Part 2: Mechanisms and trends', *Journal of Sound and Vibration* **170**(4), 451–472.

Snyder, S. & Tanaka, N. (1993*a*), 'On feedforward active control of sound and vibration using error signals', *Journal of the Acoustical Society of America* **94**(4), 2181–2193.

Snyder, S. & Tanaka, N. (1993*b*), 'To absorb or not to absorb: Control source power output in active noise control systems', *Journal of the Acoustical Society of America* **94**(1), 185–195.

Snyder, S. & Tanaka, N. (1995), 'Calculating total acoustic power output using modal radiation efficiencies', *Journal of the Acoustical Society of America* **97**(3), 1702–1709.

Snyder, S., Hansen, C. & Tanaka, N. (1993), Shaped vibration sensors for feedforward control of structural radiation, *in* 'The Second Conference on Recent Advances in Active Control of Sound and Vibration', Virginia Tech, Blacksburg, VA.

Snyder, S., Tanaka, N., Burgemeister, K. & Hansen, C. (1995), Direct-sensing of global error criteria for active noise control, *in* 'Proceedings of Active 95', pp. 849–860.

Sommerfeldt, S. (1993), Active wavenumber control of acoustic radiation from a plate, *in* 'Proceedings of Conference on Recent Advances in Active Control of Sound and Vibration', Vol. 2nd, pp. 929–940.

Sommerfeldt, S. & Nashif, P. (1991), A comparision of control strategies for minimising the sound field in enclosures, *in* 'Proceedings of Noise-Con 91', pp. 299–306.

Sommerfeldt, S. & Nashif, P. (1992), Energy based control of the sound field in enclosures, *in* 'The Second International Congress on Recent Developments is Air- and Structure-Borne Sound and Vibration', pp. 361–368.

Sommerfeldt, S. & Nashif, P. (1994), 'An adaptive filtered-x algorithm for energy based active control', *Journal of the Acoustical Society of America* **96**(1), 300–306.

Sommerfeldt, S. & Parkins, J. (1994), 'Active control of energy density in three dimensional enclosures', *Journal of the Acoustical Society of America* **95**(5), 2989.

Sommerfeldt, S. & Scott, B. (1994), 'Estimating acoustic radiation using wavenumber sensors', *Proceedings of Noise-Con 94* pp. 279–284.

Sommerfeldt, S., Parkins, J. & Park, Y. (1995), Global active noise control in rectangular enclosures, *in* 'Proceedings of Active 95', pp. 477–488.

Sullivan, J., Hubbard, J. & Burke, S. (1996), 'Modelling approach for two-dimensional distributed transducers of arbitrary spatial distribution', *Journal of the Acoustical Society of America* **99**(5), 2965–2974.

Sum, K. & Pan, J. (1998), 'A study of the medium frequency response of sound field in a panel-cavity system', *Journal of the Acoustical Society of America* **103**(3), 1510–1519.

Sun, J., Norris, M., Rossetti, D. & Highfill, J. (1994), 'Distributed piezoelectric actuators for shell interior noise control', *Journal of Vibration and Acoustics*.

Sung, S. & Nefske, D. (1984), 'A coupled structural-acoustic finite element model for vehicle interior noise', *Journal of Vibration, Acoustics, Stress and Reliability in Design* **106**, 314–318.

Tanaka, N., Kikushima, Y. & Fergusson, N. (1998), 'One-dimensional distributed modal sensors and the active modal control for planar structures', *Journal of the Acoustical Society of America* **104**(1), 217–225.

Tanaka, N., Snyder, S. & Hansen, C. (1996), 'Distributed parameter modal filtering using smart sensors', *Trans. ASME - Journal of Vibration and Acoustics* **118**, 630–640.

Taylor, D. & Everstine, G. (1986), ‘A symmetric potential formulation for fluid-structure interaction’, *Journal of Sound and Vibration* **79**(1), 327–337.

Thomas, D., Nelson, P. & Elliott, S. (1988), Active control of the acoustic field in a vibrating cylindrical shell by the application of secondary force inputs, *in* ‘Proceedings of Inter Noise 88’, pp. 1013–1016.

Thomas, D., Nelson, P. & Elliott, S. (1993*a*), ‘Active control of the transmission of sound through a thin cylindrical shell, Part I: The minimisation of vibrational energy’, *Journal of Sound and Vibration* **167**(1), 91–111.

Thomas, D., Nelson, P. & Elliott, S. (1993*b*), ‘Active control of the transmission of sound through a thin cylindrical shell, Part II: The minimisation of acoustic potential energy’, *Journal of Sound and Vibration* **167**(1), 113–128.

Thompson, J. (1982*a*), Acoustic intensity measurement error, *in* ‘Proceedings of Inter Noise 82’, pp. 723–726.

Thompson, J. (1982*b*), ‘Comments on "Finite difference approximation errors in acoustic intensity measurements"’, *Journal Sound and Vibration* **82**(3), 459–464.

Thompson, J. & Tree, D. (1981), ‘Finite difference approximation errors in acoustic intensity measurements’, *Journal Sound and Vibration* **75**(2), 229–238.

Tohyama, M. & Suzuki, A. (1987), ‘Active power minimization of a sound source in an enclosed closed space’, *Journal of Sound and Vibration* **119**(3), 562–564.

Tzou, H., Zhong, J. & Natori, M. (1991), Modal filtering of distributed shell sensors using orthogonal function, *in* ‘Proceedings of the Second Joint Japan/U.S. Conference on Adaptive Structures’, Nagoya, Japan, pp. 755–766.

Unruh, J. & Dobosz, S. (1988), ‘Fuselage structural-acoustic modelling for structure-borne interior noise transmission’, *Transactions of the ASME - Journal of Vibration, Acoustics, Stress, and Reliability in Design* **110**, 226–233.

Van Niekerk, J., Tongue, B. & Packard, A. (1995), ‘Active control of a circular plate to reduce transient noise transmission’, *Journal of Sound and Vibration* **183**(4), 643–662.

Verbeek, G., Kuijpers, A. & Verheij, J. (1998), Radiation modes and axisymmetric duct acoustics, *in* ‘Proceedings of Inter-Noise 98’, Christchurch, New Zealand.

Wang, B.-T. (1998), ‘The pvdf-based wave number domain sensing techniques for active sound radiation control from a simply supported beam’, *Journal of the Acoustical Society of America* **103**(4), 1904–1915.

Watkinson, P. (1986), ‘The practical assessment of errors in sound intensity measurement’, *Journal of Sound and Vibration* **105**(2), 255–263.

Zalas, J. & Tichy, J. (1984), Active attenuation of propeller blade passage noise, Technical Report 172386, NASA Contract Report.

Appendix A

Verification of Software Code

In order to have any confidence in the numerical simulations it was necessary to validate the modal coupling (derived in Chapter 2) software written in MATLAB. The contiguous curved panel/cavity system shown in Figure A.1 was chosen as a suitable system for testing the modal coupling code because of its simplicity and small size. The curved panel, with a radius of 2.4 m, was made of 1.6 mm thick aluminium with simply supported end conditions. The other 5 walls of the cavity, measuring 0.985m x 0.420m x 0.250m, were made from 19mm medium density fibre-board (MDF) and were considered to be rigid. The material properties used for the simulation are shown in Table A.1.

Medium	Material Property	Value
Air	Density	1.21 $\mathrm{kg/m^3}$
	Speed of Sound	343 $\mathrm{m/s}$
Aluminium	Thickness	1.6 mm
	Young's Modulus	70.3 GPa
	Density	2700 $\mathrm{kg/m^3}$
	Poisson's Ratio	0.35

Table A.1: Material properties used for the finite element models

The four points identified in Figure A.1 are the excitation and response points for both

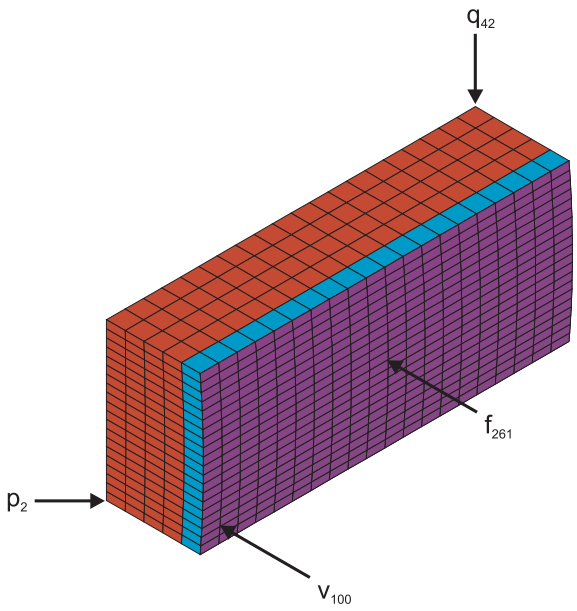

Figure A.1: Finite element model of the coupled curved panel/cavity system showing the excitation and response points used to validate the modal coupling code in MATLAB.

the structure and the cavity used during the forced response simulations. The shading of the elements represents the element type. The purple elements are structural shell elements, the cyan elements are acoustic brick elements with pressure and displacement dofs to enable structural/acoustic coupling and the red elements are pure acoustic brick elements with only pressure dofs. The displacement dofs not associated with the nodes of the structure were set to 0 to reduce the bandwidth of the frontal solver (solution effort). By default, boundary conditions for the external nodes of the fluid elements have zero pressure gradient normal to the surface, ie $\partial p/\partial \hat{n} = 0$.

The MATLAB code was verified in two stages

- Uncoupled - Structure only and Cavity only
- Fully Coupled vibro-acoustic system using modal coupling theory.

The panel and the cavity were modelled individually using the FEA package ANSYS. A modal analysis was performed on both of the models and the modal data were then exported in a form that could be read into MATLAB. It has been assumed that the modal

analysis results from ANSYS were valid (the objective was to test the modal coupling not the accuracy of the modal solver).

A forced response simulation was performed using a modal superposition technique on the uncoupled modal models using both ANSYS and Matlab and the results were compared.

Once the uncoupled models were validated including the *ad hoc* damping terms, a fully coupled forced response analysis was performed using ANSYS. This was then compared against the coupled acoustic and structural models via modal coupling theory (Snyder & Hansen 1994*a*) within MATLAB.

There was no attempt to verify that the results from either ANSYS or MATLAB reflected that physical system upon which the models were based. The sole purpose was to verify that the assumptions to the system of equations and the software code were accurate.

As shown in Chapter 2, many of the expressions used finite sum approximations, rather than integrals, because of the discrete nature of the model. The radiating surface area given by the finite sum in Equation (2.104) was calculated to be $\mathrm{S}_{Ansys} \approx 0.4121\mathrm{m}^2$. Comparing this finite approximation against the exact surface area $\mathrm{S}_{exact} = 0.4137\mathrm{m}^2$ gives a negligible error of 0.4%. It is to be expected that structures with complicated geometries, ie surfaces with high curvature and discontinuities, will have a greater error in the surface area estimate. The cylinder shown in Appendix D has an error in the calculated surface area of 0.67%, which is still negligible. Concluding that the error in Equation (2.104) is negligible.

If the curvature of the panel shown in Figure A.1 is assumed to be negligible, then the modal mass of the panel is given by the modal mass of a uniform thickness rectangular panel with simply supported boundary conditions, ie

$$M_i = \frac{\rho h S}{4} \tag{A.1}$$

where ρ is the density of the material, h is the thickness of the panel and S is the surface area of the panel. The modal volume of the cavity is given by that for a rectangular cavity

$$\Lambda_{i,j,k} = \frac{V}{2^{u(i)u(j)u(k)}} \tag{A.2}$$

where u indicates the unit step function for integers defined as

$$u(i) = \begin{cases} 0 & i = 0 \\ 1 & i \neq 0 \end{cases} \tag{A.3}$$

The calculated modal masses and modal volumes for the first 10 structural and acoustic modes are shown in Table A.2.

Structural Mode	Ansys (kg)	Exact (kg)	% Error	Cavity Mode	Ansys (m^3)	Exact (m^3)	% Error
1 (1,1)	0.4454	0.4468	-0.3	1 (0,0,0)	0.1048	0.1034	1.3
2 (1,2)	0.4452	0.4468	-0.4	2 (1,0,0)	0.0522	0.0517	0.9
3 (2,2)	0.4451	0.4468	-0.4	3 (2,0,0)	0.0516	0.0517	-0.3
4 (2,1)	0.4441	0.4468	-0.6	4 (0,1,0)	0.0509	0.0517	-1.6
5 (3,2)	0.4448	0.4468	-0.4	5 (1,1,0)	0.0253	0.0259	-2.0
6 (1,3)	0.4468	0.4468	0.0	6 (3,0,0)	0.0505	0.0517	-2.4
7 (4,2)	0.4914	0.4468	10.0	7 (2,1,0)	0.0250	0.0259	-3.3
8 (3,1)	0.4409	0.4468	-1.3	8 (3,1,0)	0.0245	0.0259	-5.2
9 (2,3)	0.4474	0.4468	0.1	9 (0,0,1)	0.0434	0.0517	-16.1
10 (3,3)	0.4496	0.4468	0.6	10 (1,0,1)	0.0216	0.0259	-16.5

Table A.2: Calculated vs exact modal masses and modal volumes for the system shown in Figure A.1.

It can be seen that as the modal order increases so does the error in both the modal mass and the modal volume. This is because with increasing nodal index the number of nodes per wavelength decreases and thus the accuracy of the surface and volume integra-

tion.

A.1 Uncoupled Response Analysis

The structure and the cavity models were analysed separately. A finite number of modes were extracted in ANSYS and these were used as the basis for a modal superposition analysis within both ANSYS and MATLAB.

A.1.1 Forced Response of Structure Only

The first 100 structural modes were extracted from the FE model, of which, the first 24 natural frequencies (below 400Hz) are shown in Table A.3. The forced response simulation of the panel used a unit force applied to the centre of the panel at node 261 as shown in Figure A.1. This symmetric location was chosen to ensure that only the odd order structural modes were driven. Should any of the even modes be driven then this would indicate that either the model or the modelling procedure was at fault. It also clearly shows the effect that modal coupling has on the excitation of additional modes (see Section A.2).

Figure A.2 shows the structural impedance of the panel when driven normal to the surface at the geometric centre (node 261) as shown in Figure A.1. The response point was located at node 100, an unsymmetric position near a corner of the panel. The system was undamped.

As can be seen the forced response results from ANSYS and MATLAB are identical. Figure A.3 shows the results of the forced response simulations using the same system and conditions as before with the exception that structural damping with a modal loss factor, η, of 2%, has been applied. Again, both the ANSYS and MATLAB results are identical. Thus it can be concluded that the modal response for the structure is calculated correctly within MATLAB.

Mode	Natural Frequency
1	58
2	95
3	118
4	147
5	160
6	206
7	209
8	216
9	219
10	243
11	258
12	261
13	277
14	293
15	308
16	320
17	323
18	356
19	359
20	361
21	369
22	373
23	394
24	397

Table A.3: Natural frequencies of the first 24 structural modes.

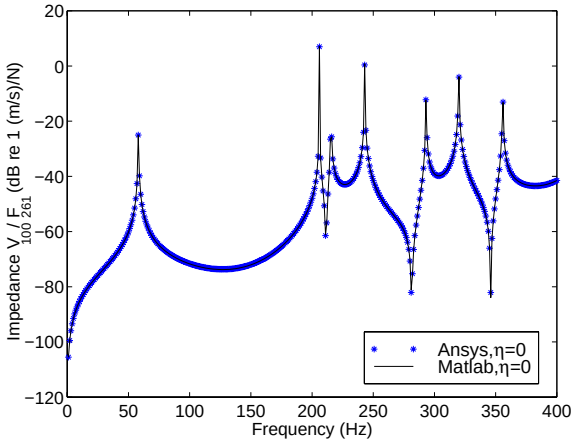

Figure A.2: Structural impedance of the panel when driven in the centre, $\eta = 0$

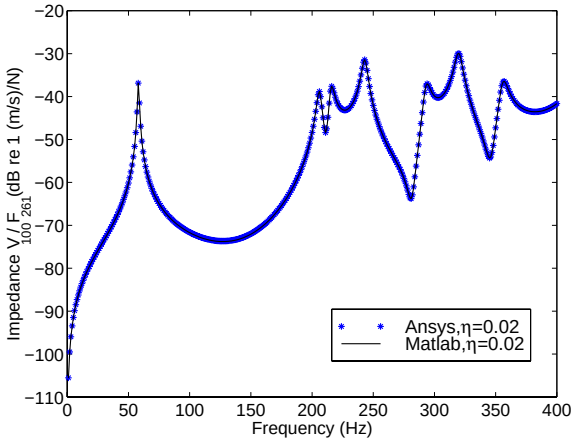

Figure A.3: Structural impedance of the panel when driven in the centre, $\eta = 2\%$

A.1.2 Forced Response of Cavity Only

The first 30 acoustic modes were extracted from the FE model, of which, the first 10 are shown in Table A.4. The forced response simulation of the cavity used a unit volume velocity applied to one of the corners of the cavity (node 42). The response point was located at the opposite position in the cavity (node 2) as shown in Figure A.1.

Mode	Natural Frequency
1	0
2	175
3	351
4	415
5	450
6	529
7	543
8	672
9	682
10	710

Table A.4: Natural frequencies of the first 10 cavity modes.

Figure A.4 shows the acoustic impedance of the cavity when driven as shown in Figure A.1. As can be seen the cavity forced response results from ANSYS and MATLAB are identical.

Figure A.5 shows the results of the forced response simulations using the same system and conditions as before with the exception that viscous damping has been applied, with a modal loss factor, η, of 2%. Again, both the ANSYS and MATLAB results are identical. Thus it can be concluded that the modal response for the cavity alone is calculated correctly within MATLAB.

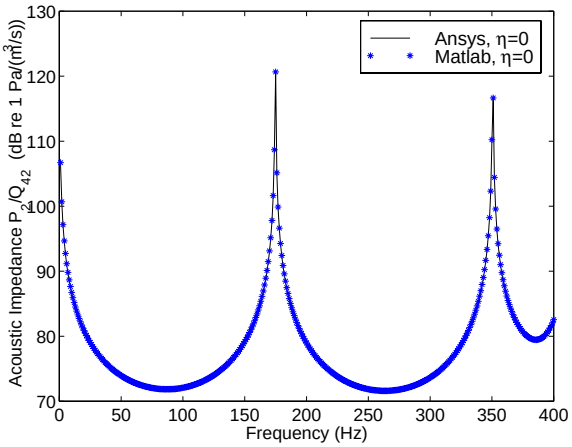

Figure A.4: Acoustic impedance of the cavity when driven in the corner, $\eta = 0$

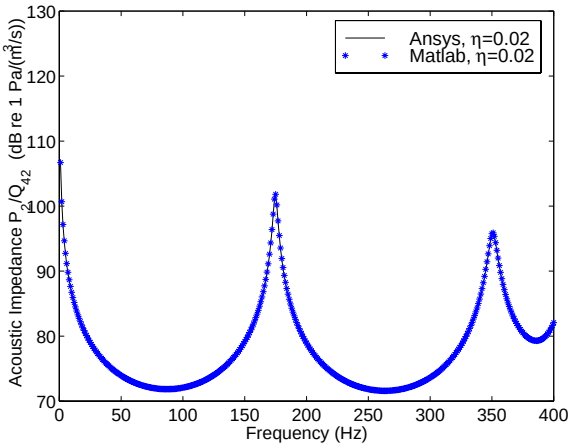

Figure A.5: Acoustic impedance of the cavity when driven in the corner, $\eta = 2\%$

A.2 Coupled Response Analysis

The FE models of the cavity and structure were coupled within ANSYS, resulting in the following homogeneous equation

$$\left[\begin{bmatrix} \mathbf{K}_s & \mathbf{K}_{fs} \\ 0 & \mathbf{K}_p \end{bmatrix} - \omega^2 \begin{bmatrix} \mathbf{M}_s & 0 \\ \mathbf{M}_{fs} & \mathbf{M}_p \end{bmatrix} + j\omega \begin{bmatrix} \mathbf{C}_s & 0 \\ 0 & \mathbf{C}_p \end{bmatrix}\right] \begin{bmatrix} \mathbf{u} \\ \mathbf{p} \end{bmatrix} = [0] \qquad \text{(A.4)}$$

where the subscripts *s* and *p* refer to the structure and cavity respectively, $\mathbf{K}$, $\mathbf{M}$ and $\mathbf{C}$ are the stiffness, mass and damping matrices respectively, **u** is the nodal displacement vector and **p** is the nodal pressure vector. The unsymmetric sub matrices $\mathbf{K}_{fs}$ and $\mathbf{M}_{fs}$ are the coupling stiffness and mass matrices respectively. The solution of the unsymmetric system of equations leads to much larger solution time than for similar sized models which have a symmetric formulation (such as the uncoupled models).

Using Equation (A.4) the first 24 modes were extracted. The natural frequencies of these coupled modes are shown in Table A.5. By comparing the natural frequencies of the coupled system against the natural frequencies of the uncoupled system (see Tables A.4 and A.3), it can be seen that the coupling significantly affects the natural frequencies of both the structure and the cavity.

In particular, the fundamental panel mode has shifted from 58 Hz to 73 Hz due to the increased stiffness arising from the bulk compression mode of the cavity. The natural frequency of the fundamental (non-zero) cavity mode has increased from 175 Hz to 185 Hz primarily due to the interaction of the [2,1] (4th) structural mode, the natural frequency of which has decreased from 147 Hz to 135 Hz. The third column in the table was obtained by looking at the forced response simulation in MATLAB and extracting the frequencies at which the peaks in the response curves occurred. Even though the panel was driven in the centre, it can be seen that all the structural modes were excited to some extent due to the modal coupling.

Mode	ANSYS	MATLAB
1	73	73
2	94	94
3	117	117
4	135	136
5	157	158
6	**185**	**185**
7	205	205
8	207	208
9	212	213
10	219	220
11	241	242
12	256	257
13	259	260
14	276	277
15	290	291
16	306	307
17	318	319
18	321	322
19	**350**	**351**
20	358	358
21	359	360
22	369	369
23	371	372
24	392	393

Table A.5: Coupled natural frequencies for both ANSYS and MATLAB. Cavity dominated modes are shown in bold type face.

The release of ANSYS (version 5.4) used for the verification process did not have the facility to evaluate the forced response of a coupled system using a the modal superposition technique outlined in Chapter 2. Rather the harmonic response solver directly solves the following system of equations

$$\left[\begin{bmatrix} \mathbf{K}_s & \mathbf{K}_{fs} \\ 0 & \mathbf{K}_p \end{bmatrix} - \omega^2 \begin{bmatrix} \mathbf{M}_s & 0 \\ \mathbf{M}_{fs} & \mathbf{M}_p \end{bmatrix} + j\omega \begin{bmatrix} \mathbf{C}_s & 0 \\ 0 & \mathbf{C}_p \end{bmatrix}\right] \begin{bmatrix} \mathbf{u} \\ \mathbf{p} \end{bmatrix} = \begin{bmatrix} \mathbf{F}_s \\ \mathbf{F}_p \end{bmatrix} \quad \text{(A.5)}$$

This unsymmetric formulation requires the use of an unsymmetric solver which greatly increases the solution times and makes the use of a fully coupled analysis extremely unattractive. When drawing comparisons between the modal superposition and fully coupled solutions it must be remembered that the modal superposition technique is evaluated for a limited set of modes, whereas the fully coupled technique is effectively evaluated over an "infinite" set of modes. Therefore, at resonance when only a single mode dominates the response the solutions should be equal. However, off resonance the solutions may differ, particularly at the anti-resonances where the residues of the higher order modes may contribute to the stiffness of the fully coupled system. As the stiffness residue term is increased (by accounting for more modes) the frequencies at which the anti-resonances occur is reduced.

A.2.1 Forced Response of the Structure with Coupled Cavity

As with the uncoupled case, the curved panel was driven with a unit force in the centre of the panel (node 261). The drive point structural impedance was calculated within ANSYS by solving the fully coupled expression given by Equation (A.5) and also by using the modal coupling technique in Matlab. The results from the two techniques are shown as a drive point structural impedance and force to pressure transfer function in Figures A.6 and A.7 respectively.

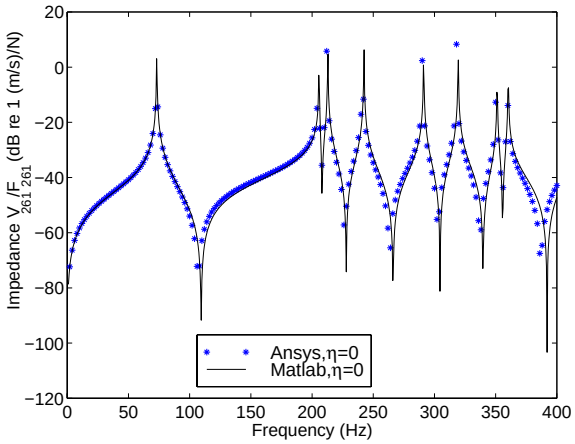

Figure A.6: Drive point structural impedance of the coupled system

Looking at Figure A.6 it is clear that the modal coupling theory is accurately predicting the behaviour of the coupled system. The resonances from the two simulations are well aligned. The slight discrepancies seen at the anti-resonances are to be expected, particularly at the high frequency end, and they are due to an inadequate number of structural and/or acoustic modes used for the simulation within MATLAB. It should also be noted that due to the long time taken for the simulations within ANSYS, the frequency spacing is course (4 Hz) and subsequently the magnitudes at the resonances are not necessarily accurate.

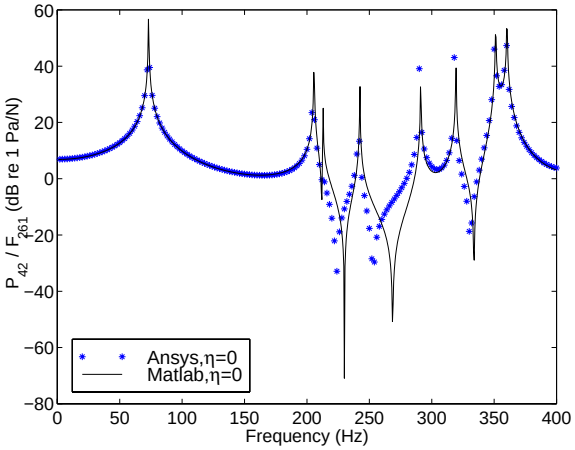

Figure A.7: Pressure / Force transfer function of the coupled system

Figure A.7 also shows that the MATLAB simulation did not have sufficient modes to

model the residues from the higher order modes. This is not such an issue for active noise control simulations as the regions around the anti-resonances contribute very little to the overall energy transmission from one subsystem to another.

A.2.2 Forced Response of the Cavity with Coupled Structure

As with the uncoupled case, the cavity was driven in a corner of the cavity (at node 42) with a unit volume velocity. The system response was calculated within ANSYS by solving the fully coupled expression given by Equation A.5 and also by using the modal coupling technique in MATLAB. The results from the two techniques are shown as an acoustic impedance between node 42 and node 2 and a volume velocity to structural velocity transfer function from node 42 to node 261 in Figures A.8 and A.9 respectively.

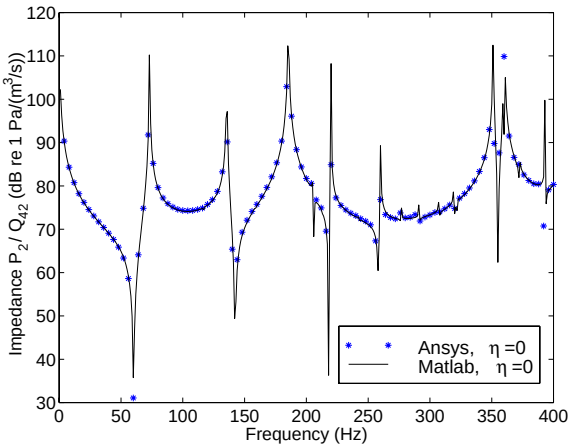

Figure A.8: Acoustic impedance of the coupled system.

Comparing Figures A.7 and A.9 it can be seen that the transfer function between the pressure, *p*, at node 42 and the driving force, *f*, at node 261 is almost identical to the transfer function between the velocity, *v*, at node 261 and the volume velocity, *q*, at node 42. This reciprocity is to be expected as it can be shown that (Fahy 1985)

$$\frac{p(\vec{\mathbf{r}}_p)}{f(\vec{\mathbf{r}}_s)} = -\frac{v(\vec{\mathbf{r}}_s)}{q(\vec{\mathbf{r}}_p)} \tag{A.6}$$

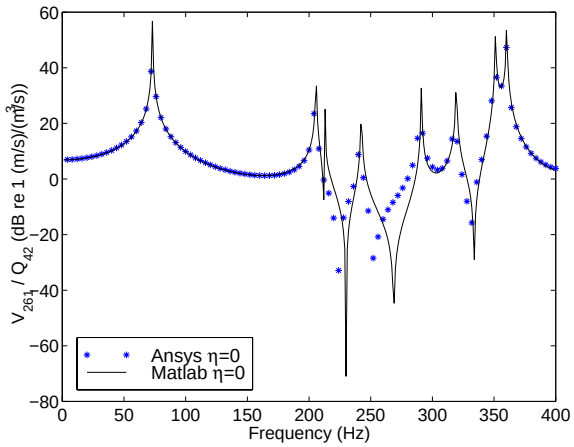

Figure A.9: Structural velocity / volume velocity transfer function of the coupled system.

where $\vec{\mathbf{r}}_p$ and $\vec{\mathbf{r}}_s$ are the position vectors in the cavity and structure respectively.

A.3 Comments

From the results of the simulations for the coupled and uncoupled models it can be concluded that the modal coupling software within MATLAB is producing valid results within the limits of the theory. It shows clearly that for a coupled analysis many more modes are required for accurate prediction of the forced response off resonance, than is typical for an uncoupled model. In addition, it has been shown that for a typical coupled structural-acoustic system the modal coupling approach provides an accurate method for analysing the system response.

Appendix B

Derivation of Mathematical Expressions

B.1 Minimisation of Acoustic Pressures at Discrete Locations

The sum of squared pressures at l error sensing locations is given by the following quadratic matrix expression

$$\sum_{i=1}^{l} |p(\vec{\mathbf{r}}_i)|^2 = \mathbf{p}_e^{\mathrm{H}} \mathbf{p}_e \tag{B.1}$$

where $\mathbf{p}_e$ is the (l x 1) column vector of complex pressures at the l error sensing locations. Using the following expressions for the pressure amplitudes arising from structural sources, $\mathbf{p} = \mathbf{Z}_a \mathbf{Z}_I^{-1} \mathbf{F}$, and acoustic sources, $\mathbf{p} = \mathbf{Z}_q^{-1} \mathbf{Q}$, Equation (B.1) can be expanded

in terms of the primary and control sources

$$\sum_{i=1}^{l} |p(\vec{\mathbf{r}}_i)|^2 = \begin{bmatrix} \mathbf{f}_p \\ \mathbf{f}_c \\ \mathbf{q}_c \end{bmatrix}^{\mathrm{H}} \begin{bmatrix} \boldsymbol{\Phi}_e^{\mathrm{T}} \mathbf{Z}_a \mathbf{Z}_I^{-1} \boldsymbol{\Psi}_p & \boldsymbol{\Phi}_e^{\mathrm{T}} \mathbf{Z}_a \mathbf{Z}_I^{-1} \boldsymbol{\Psi}_c & \boldsymbol{\Phi}_e^{\mathrm{T}} \mathbf{Z}_q^{-1} \boldsymbol{\Phi}_c \end{bmatrix}^{\mathrm{H}}$$

$$\begin{bmatrix} \boldsymbol{\Phi}_e^{\mathrm{T}} \mathbf{Z}_a \mathbf{Z}_I^{-1} \boldsymbol{\Psi}_p & \boldsymbol{\Phi}_e^{\mathrm{T}} \mathbf{Z}_a \mathbf{Z}_I^{-1} \boldsymbol{\Psi}_c & \boldsymbol{\Phi}_e^{\mathrm{T}} \mathbf{Z}_q^{-1} \boldsymbol{\Phi}_c \end{bmatrix} \begin{bmatrix} \mathbf{f}_p \\ \mathbf{f}_c \\ \mathbf{q}_c \end{bmatrix} \tag{B.2}$$

where Φ_e and Φ_c are the acoustic mode shape vectors evaluated at the sensor and actuator locations respectively. The equation above can be rewritten in the standard quadratic form as follows

$$\sum_{i=1}^{l} |p(\vec{\mathbf{r}}_i)|^2 = \begin{bmatrix} \mathbf{f}_c \\ \mathbf{q}_c \end{bmatrix}^{\mathrm{H}} \mathbf{A} \begin{bmatrix} \mathbf{f}_c \\ \mathbf{q}_c \end{bmatrix} + \begin{bmatrix} \mathbf{f}_c \\ \mathbf{q}_c \end{bmatrix}^{\mathrm{H}} \mathbf{b} + \mathbf{b}^{\mathrm{H}} \begin{bmatrix} \mathbf{f}_c \\ \mathbf{q}_c \end{bmatrix} + c \tag{B.3}$$

where

$$\mathbf{A} = \begin{bmatrix} \mathbf{Z}_a \mathbf{Z}_I^{-1} \boldsymbol{\Psi}_c & \mathbf{Z}_q^{-1} \boldsymbol{\Phi}_c \end{bmatrix}^{\mathrm{H}} \mathbf{Z}_w \begin{bmatrix} \mathbf{Z}_a \mathbf{Z}_I^{-1} \boldsymbol{\Psi}_c & \mathbf{Z}_q^{-1} \boldsymbol{\Phi}_c \end{bmatrix} \tag{B.4}$$

$$\mathbf{b} = \begin{bmatrix} \mathbf{Z}_a \mathbf{Z}_I^{-1} \boldsymbol{\Psi}_c & \mathbf{Z}_q^{-1} \boldsymbol{\Phi}_c \end{bmatrix}^{\mathrm{H}} \mathbf{Z}_w \mathbf{Z}_a \mathbf{v}_p \tag{B.5}$$

$$c = \mathbf{v}_p^{\mathrm{H}} \mathbf{Z}_a^{\mathrm{H}} \mathbf{Z}_w \mathbf{Z}_a \mathbf{v}_p \tag{B.6}$$

where

$$\mathbf{Z}_w = \boldsymbol{\Phi}_e^{*} \boldsymbol{\Phi}_e^{\mathrm{T}} \tag{B.7}$$

This can be rewritten in terms of the structural and acoustic sources operating inde-

pendently plus a cross coupling term

$$\mathbf{A} = \begin{bmatrix} \mathbf{A}_v & \mathbf{A}_{vq}^{\mathrm{H}} \\ \mathbf{A}_{vq} & \mathbf{A}_q \end{bmatrix} \tag{B.8}$$

$$\mathbf{b} = \left[\mathbf{Z}_a \mathbf{Z}_I^{-1} \boldsymbol{\Psi}_c \;\; \mathbf{Z}_q^{-1} \boldsymbol{\Phi}_c\right]^{\mathrm{H}} \mathbf{Z}_w \mathbf{Z}_a \mathbf{v}_p \tag{B.9}$$

$$c = \mathbf{v}_p^{\mathrm{H}} \mathbf{Z}_a^{\mathrm{H}} \mathbf{Z}_w \mathbf{Z}_a \mathbf{v}_p \tag{B.10}$$

Here $\mathbf{A}_v$ is the matrix $\mathbf{A}$ for vibration control sources operating alone and is given by

$$\mathbf{A}_v = \boldsymbol{\Psi}_c^{\mathrm{H}} (\mathbf{Z}_I^{-1})^{\mathrm{H}} \mathbf{Z}_a^{\mathrm{H}} \mathbf{Z}_w \mathbf{Z}_a \mathbf{Z}_I^{-1} \boldsymbol{\Psi}_c \tag{B.11}$$

$\mathbf{A}_q$ is the matrix $\mathbf{A}$ for the acoustic control source operating alone, with elements given by

$$\mathbf{A}_q = \boldsymbol{\Phi}_c^{\mathrm{H}} (\mathbf{Z}_q^{-1})^{\mathrm{H}} \mathbf{Z}_w \mathbf{Z}_q^{-1} \boldsymbol{\Phi}_c \tag{B.12}$$

and the cross-coupling matrix $\mathbf{A}_{vq}$ is given by,

$$\mathbf{A}_{vq} = \boldsymbol{\Phi}_c^{\mathrm{H}} (\mathbf{Z}_q^{-1})^{\mathrm{H}} \mathbf{Z}_w \mathbf{Z}_a \mathbf{Z}_I^{-1} \boldsymbol{\Psi}_c \tag{B.13}$$

The optimum set of control forces and volume velocities which produce the unique global minimum value of the quadratic function in Equation (B.3) are defined by the relationship

$$\begin{bmatrix} \mathbf{f}_c \\ \mathbf{q}_c \end{bmatrix}_{opt} = -\mathbf{A}^{-1} \mathbf{b} \tag{B.14}$$

producing the minimum of the squared pressure levels at the error locations

$$\sum_{i=1}^{l} |p(\vec{\mathbf{r}}_i)|^2 = c - \mathbf{b}^{\mathrm{H}}\mathbf{A}^{-1}\mathbf{b} \tag{B.15}$$

B.2 Minimisation of the Internal Acoustic Potential Energy

The acoustic potential energy, E_p in the enclosed space is given by

$$E_p = \frac{1}{4\rho_0 c_0^2} \int_V |p(\vec{\mathbf{r}})|^2 dV(\vec{\mathbf{r}}) \tag{B.16}$$

The acoustic potential energy arising from the primary and control sources can be expressed as

$$E_p = \frac{1}{4\rho_0 c_0^2} \int_V \begin{bmatrix} \mathbf{f}_p \\ \mathbf{f}_c \\ \mathbf{q}_c \end{bmatrix}^{\mathrm{H}} \begin{bmatrix} \phi(\vec{\mathbf{r}})^{\mathrm{T}}\mathbf{Z}_a\mathbf{Z}_I^{-1}\boldsymbol{\Psi}_p & \phi(\vec{\mathbf{r}})^{\mathrm{T}}\mathbf{Z}_a\mathbf{Z}_I^{-1}\boldsymbol{\Psi}_c & \phi(\vec{\mathbf{r}})^{\mathrm{T}}\mathbf{Z}_q^{-1}\boldsymbol{\Phi}_c \end{bmatrix}^{\mathrm{H}}$$
$$\begin{bmatrix} \phi(\vec{\mathbf{r}})^{\mathrm{T}}\mathbf{Z}_a\mathbf{Z}_I^{-1}\boldsymbol{\Psi}_p & \phi(\vec{\mathbf{r}})^{\mathrm{T}}\mathbf{Z}_a\mathbf{Z}_I^{-1}\boldsymbol{\Psi}_c & \phi(\vec{\mathbf{r}})^{\mathrm{T}}\mathbf{Z}_q^{-1}\boldsymbol{\Phi}_c \end{bmatrix} \begin{bmatrix} \mathbf{f}_p \\ \mathbf{f}_c \\ \mathbf{q}_c \end{bmatrix} dV(\vec{\mathbf{r}}) \tag{B.17}$$

Evaluating the integral and using modal orthogonality

$$E_p = \begin{bmatrix} \mathbf{f}_p \\ \mathbf{f}_c \\ \mathbf{q}_c \end{bmatrix}^{\mathrm{H}} \begin{bmatrix} \mathbf{Z}_a\mathbf{Z}_I^{-1}\boldsymbol{\Psi}_p & \mathbf{Z}_a\mathbf{Z}_I^{-1}\boldsymbol{\Psi}_c & \mathbf{Z}_q^{-1}\boldsymbol{\Phi}_c \end{bmatrix}^{\mathrm{H}} \boldsymbol{\Lambda} \begin{bmatrix} \mathbf{Z}_a\mathbf{Z}_I^{-1}\boldsymbol{\Psi}_p & \mathbf{Z}_a\mathbf{Z}_I^{-1}\boldsymbol{\Psi}_c & \mathbf{Z}_q^{-1}\boldsymbol{\Phi}_c \end{bmatrix} \begin{bmatrix} \mathbf{f}_p \\ \mathbf{f}_c \\ \mathbf{q}_c \end{bmatrix} \tag{B.18}$$

where $\boldsymbol{\Lambda}$ is a (n_a x n_a) diagonal matrix, the diagonal terms of which are

$$\Lambda(i,i) = \frac{\Lambda_i}{4\rho_0 c_0^2} \tag{B.19}$$

where Λ_i is the modal volume of the ith cavity mode. Equation (B.18) above can be rewritten in the standard quadratic form as follows

$$E_p = \begin{bmatrix} \mathbf{f}_c \\ \mathbf{q}_c \end{bmatrix}^{\mathrm{H}} \mathbf{A} \begin{bmatrix} \mathbf{f}_c \\ \mathbf{q}_c \end{bmatrix} + \begin{bmatrix} \mathbf{f}_c \\ \mathbf{q}_c \end{bmatrix}^{\mathrm{H}} \mathbf{b} + \mathbf{b}^{\mathrm{H}} \begin{bmatrix} \mathbf{f}_c \\ \mathbf{q}_c \end{bmatrix} + c \tag{B.20}$$

where $\mathbf{A}$, $\mathbf{b}$ and c are given by Equations (B.8), (B.9) and (B.10) respectively, with the matrix $\mathbf{Z}_w$ given by

$$\mathbf{Z}_w = \boldsymbol{\Lambda} \tag{B.21}$$

The optimum control source strengths to minimise Equation (B.20) are given by Equation (B.14) resulting in a minimum given by Equation (B.15).

B.3 Minimisation of the Squared Velocities at Discrete Points

The surface velocity level at any point $\vec{\mathbf{x}}$ is given by

$$v(\vec{\mathbf{x}}) = v_p(\vec{\mathbf{x}}) + v_c(\vec{\mathbf{x}}) \tag{B.22}$$

where the subscripts p and c refer to the primary and control levels respectively. The primary and control velocity levels at any point on the structure are given by

$$v_p(\vec{\mathbf{x}}) = \psi^T(\vec{\mathbf{x}})\mathbf{v}_p \tag{B.23}$$

$$v_c(\vec{\mathbf{x}}) = \psi^T(\vec{\mathbf{x}}) \left[\mathbf{Z}_I^{-1}\mathbf{\Psi}_c\mathbf{f}_c + \mathbf{Z}_b\mathbf{Z}_q^{-1}\Phi_c\mathbf{q}_c\right] \tag{B.24}$$

where $\psi(\vec{\mathbf{x}})$ is the (n_s x 1) vector of structural mode shape functions evaluated at a location $\vec{\mathbf{x}}$. Therefore the sum of the squared velocity levels at l structural error locations is given by the following quadratic matrix expression

$$\sum_{i=1}^{l} |v(\vec{\mathbf{x}}_i)|^2 = \mathbf{v}_e^{\mathrm{H}}\mathbf{v}_e \tag{B.25}$$

where $\mathbf{v}_e$ is the (l x 1) column vector of complex velocities at the l error sensing locations. Expanding the above equation with respect to the primary and control source strengths

$$\sum_{i=1}^{l} |v(\vec{\mathbf{x}}_i)|^2 = \begin{bmatrix} \mathbf{f}_p \\ \mathbf{f}_c \\ \mathbf{q}_c \end{bmatrix}^{\mathrm{H}} \left[\mathbf{\Psi}_e^{\mathrm{T}}\mathbf{Z}_I^{-1}\mathbf{\Psi}_p \;\; \mathbf{\Psi}_e^{\mathrm{T}}\mathbf{Z}_I^{-1}\mathbf{\Psi}_c \;\; \mathbf{\Psi}_e^{\mathrm{T}}\mathbf{Z}_b\mathbf{Z}_q^{-1}\mathbf{\Phi}_c\right]^{\mathrm{H}}$$

$$\left[\mathbf{\Psi}_e^{\mathrm{T}}\mathbf{Z}_I^{-1}\mathbf{\Psi}_p \;\; \mathbf{\Psi}_e^{\mathrm{T}}\mathbf{Z}_I^{-1}\mathbf{\Psi}_c \;\; \mathbf{\Psi}_e^{\mathrm{T}}\mathbf{Z}_b\mathbf{Z}_q^{-1}\mathbf{\Phi}_c\right] \begin{bmatrix} \mathbf{f}_p \\ \mathbf{f}_c \\ \mathbf{q}_c \end{bmatrix} \tag{B.26}$$

where $\mathbf{\Psi}_e$ is the (n_s x l) matrix of (n_s x 1) structural mode shape function vectors $\psi(\vec{\mathbf{x}})$ evaluated at the l error sensing locations. By using the above expression, the sum of the squared velocity levels at a set of error sensing points can be expressed in standard quadratic form as

$$\sum_{i=1}^{l} |v(\vec{\mathbf{x}}_i)|^2 = \begin{bmatrix} \mathbf{f}_c \\ \mathbf{q}_c \end{bmatrix}^{\mathrm{H}} \mathbf{A} \begin{bmatrix} \mathbf{f}_c \\ \mathbf{q}_c \end{bmatrix} + \begin{bmatrix} \mathbf{f}_c \\ \mathbf{q}_c \end{bmatrix}^{\mathrm{H}} \mathbf{b} + \mathbf{b}^{\mathrm{H}} \begin{bmatrix} \mathbf{f}_c \\ \mathbf{q}_c \end{bmatrix} + c \tag{B.27}$$

where

$$\mathbf{A} = \left[\mathbf{Z}_I^{-1}\mathbf{\Psi}_c \;\; \mathbf{Z}_b\mathbf{Z}_q^{-1}\mathbf{\Phi}_c\right]^{\mathrm{H}} \mathbf{Z}_w \left[\mathbf{Z}_I^{-1}\mathbf{\Psi}_c \;\; \mathbf{Z}_b\mathbf{Z}_q^{-1}\mathbf{\Phi}_c\right] \tag{B.28}$$

$$\mathbf{b} = \left[\mathbf{Z}_I^{-1}\mathbf{\Psi}_c \;\; \mathbf{Z}_b\mathbf{Z}_q^{-1}\mathbf{\Phi}_c\right]^{\mathrm{H}} \mathbf{Z}_w\mathbf{v}_p \tag{B.29}$$

$$c = \mathbf{v}_p^{\mathrm{H}}\mathbf{Z}_w\mathbf{v}_p \tag{B.30}$$

and

$$\mathbf{Z}_w = \mathbf{\Psi}_e^*\mathbf{\Psi}_e^{\mathrm{T}} \tag{B.31}$$

where $\mathbf{\Psi}_e$ is the (n_s x l) matrix of (n_s x 1) structural mode shape function vectors $\psi(\vec{\mathbf{x}})$ evaluated at the l error sensing locations.

This can be rewritten in terms of the structural and acoustic sources operating independently plus a cross coupling term

$$\mathbf{A} = \begin{bmatrix} \mathbf{A}_v & \mathbf{A}_{vq}^{\mathrm{H}} \\ \mathbf{A}_{vq} & \mathbf{A}_q \end{bmatrix} \tag{B.32}$$

$$\mathbf{b} = \left[\mathbf{Z}_I^{-1}\mathbf{\Psi}_c \;\; \mathbf{Z}_b\mathbf{Z}_q^{-1}\mathbf{\Phi}_c\right]^{\mathrm{H}} \mathbf{Z}_w\mathbf{v}_p \tag{B.33}$$

$$c = \mathbf{v}_p^{\mathrm{H}}\mathbf{Z}_w\mathbf{v}_p \tag{B.34}$$

Here $\mathbf{A}_v$ is the matrix $\mathbf{A}$ for vibration control sources operating alone and is given by

$$\mathbf{A}_v = \mathbf{\Psi}_c^{\mathrm{H}} (\mathbf{Z}_I^{-1})^{\mathrm{H}} \mathbf{Z}_w \mathbf{Z}_I^{-1} \mathbf{\Psi}_c \tag{B.35}$$

$\mathbf{A}_q$ is the matrix $\mathbf{A}$ for the acoustic control source operating alone, with elements given by

$$\mathbf{A}_q = \mathbf{\Phi}_c^{\mathrm{H}} (\mathbf{Z}_q^{-1})^{\mathrm{H}} \mathbf{Z}_b^{\mathrm{H}} \mathbf{Z}_w \mathbf{Z}_b \mathbf{Z}_q^{-1} \mathbf{\Phi}_c \tag{B.36}$$

and the cross-coupling matrix $\mathbf{A}_{vq}$ is given by,

$$\mathbf{A}_{vq} = \mathbf{\Phi}_c^{\mathrm{H}} (\mathbf{Z}_q^{-1})^{\mathrm{H}} \mathbf{Z}_b^{\mathrm{H}} \mathbf{Z}_w \mathbf{Z}_I^{-1} \mathbf{\Psi}_c \tag{B.37}$$

The optimum control source strengths to minimise Equation (B.27) are given by Equation (B.14) resulting in a minimum given by Equation (B.15).

B.4 Minimisation of the Structural Kinetic Energy

The instantaneous kinetic energy of the structure is given by the following surface integral equation

$$E_k = \frac{1}{2} \int_S \rho_s(\vec{\mathbf{x}}) h(\vec{\mathbf{x}}) |v(\vec{\mathbf{x}})|^2 dA \tag{B.38}$$

where ρ_s is the density of the structure and h is the thickness. The structural kinetic energy arising from the primary and control sources can be expressed as

$$E_k = \frac{1}{2}\int_S \rho_s(\vec{\mathbf{x}})h(\vec{\mathbf{x}}) \begin{bmatrix} \mathbf{f}_p \\ \mathbf{f}_c \\ \mathbf{q}_c \end{bmatrix}^{\mathrm{H}} \begin{bmatrix} \psi(\vec{\mathbf{x}})^{\mathrm{T}}\mathbf{Z}_I^{-1}\mathbf{\Psi}_p & \psi(\vec{\mathbf{x}})^{\mathrm{T}}\mathbf{Z}_I^{-1}\mathbf{\Psi}_c & \psi(\vec{\mathbf{x}})^{\mathrm{T}}\mathbf{Z}_b\mathbf{Z}_q^{-1}\mathbf{\Phi}_c \end{bmatrix}^{\mathrm{H}}$$
$$\begin{bmatrix} \psi(\vec{\mathbf{x}})^{\mathrm{T}}\mathbf{Z}_I^{-1}\mathbf{\Psi}_p & \psi(\vec{\mathbf{x}})^{\mathrm{T}}\mathbf{Z}_I^{-1}\mathbf{\Psi}_c & \psi(\vec{\mathbf{x}})^{\mathrm{T}}\mathbf{Z}_b\mathbf{Z}_q^{-1}\mathbf{\Phi}_c \end{bmatrix} \begin{bmatrix} \mathbf{f}_p \\ \mathbf{f}_c \\ \mathbf{q}_c \end{bmatrix} dA(\vec{\mathbf{x}}) \tag{B.39}$$

Evaluating the integral and using modal orthogonality,

$$E_k = \begin{bmatrix} \mathbf{f}_p \\ \mathbf{f}_c \\ \mathbf{q}_c \end{bmatrix}^{\mathrm{H}} \begin{bmatrix} \mathbf{Z}_I^{-1}\mathbf{\Psi}_p & \mathbf{Z}_I^{-1}\mathbf{\Psi}_c & \mathbf{Z}_b\mathbf{Z}_q^{-1}\mathbf{\Phi}_c \end{bmatrix}^{\mathrm{H}} \mathbf{M}$$
$$\begin{bmatrix} \mathbf{Z}_I^{-1}\mathbf{\Psi}_p & \mathbf{Z}_I^{-1}\mathbf{\Psi}_c & \mathbf{Z}_b\mathbf{Z}_q^{-1}\mathbf{\Phi}_c \end{bmatrix} \begin{bmatrix} \mathbf{f}_p \\ \mathbf{f}_c \\ \mathbf{q}_c \end{bmatrix} \tag{B.40}$$

where $\mathbf{M}$ is the diagonal modal mass matrix. The above equation can be rewritten in the standard quadratic form as follows

$$E_k = \begin{bmatrix} \mathbf{f}_c \\ \mathbf{q}_c \end{bmatrix}^{\mathrm{H}} \mathbf{A} \begin{bmatrix} \mathbf{f}_c \\ \mathbf{q}_c \end{bmatrix} + \begin{bmatrix} \mathbf{f}_c \\ \mathbf{q}_c \end{bmatrix}^{\mathrm{H}} \mathbf{b} + \mathbf{b}^{\mathrm{H}} \begin{bmatrix} \mathbf{f}_c \\ \mathbf{q}_c \end{bmatrix} + c \tag{B.41}$$

where $\mathbf{A}$, $\mathbf{b}$ and c are given by Equations (B.32), (B.33) and (B.34) respectively, with the

matrix $\mathbf{Z}_w$ given by

$$\mathbf{Z}_w = \frac{\mathbf{M}}{4} \tag{B.42}$$

The optimum control source strengths to minimise Equation (B.41) are given by Equation (B.14) resulting in a minimum given by Equation (B.15).

B.5 Calculation of Energy Density for Ideal Sound Fields

The following analysis applies to a one dimensional sound field with spatial variation in the direction of the sensor, which for convenience will be denoted x. According to the Taylor series expansion (Fahy 1995)

$$\begin{aligned} p(x+h,t) &= p(x,t) + hp^{i}(x,t) + (h^2/2)p^{ii}(x,t) + (h^3/6)p^{iii}(x,t) + ... \\ &\quad +(h^n/n!)p^{n}(x,t) + ... \end{aligned} \tag{B.43}$$

For a harmonic sound field the estimated acoustic energy density is given by

$$E_{D_e} \approx \frac{[P_1+P_2]\,[P_1+P_2]^*}{16\rho c^2} + \frac{[P_2-P_1]\,[P_2-P_1]^*}{16\rho\omega^2 h^2} \tag{B.44}$$

Taylor series expansion of the energy density estimate gives

$$\begin{aligned} E_{D_e} &= \frac{1}{4\rho c^2}\left[P + (h^2/2)P^{ii} + (h^4/24)P^{iv} + ... + (h^{2n}/2n!)P^{2n}\right] \\ &\quad \left[P + (h^2/2)P^{ii} + (h^4/24)P^{iv} + ... + (h^{2n}/2n!)P^{2n}\right]^* \\ &\quad +\frac{4}{4\rho\omega^2(2h)^2}\left[hP + (h^3/6)P^{iii} + (h^5/120)P^{iv} + ... + (h^{2n+1}/(2n+1)!)P^{2n+1}\right] \\ &\quad \left[hP + (h^3/6)P^{iii} + (h^5/120)P^{v} + ... + (h^{2n+1}/(2n+1)!)P^{2n+1}\right]^* \end{aligned} \tag{B.45}$$

Rearranging and neglecting the higher order terms,

$$\begin{aligned} E_{D_e} &\approx \frac{1}{4\rho c^2}\left[PP^* + \frac{h^2}{2}\left(P^*P^{ii} + PP^{ii*}\right) + \frac{h^4}{4}\left(P^{ii*}P^{ii} + \frac{PP^{iv*}}{6} + \frac{P^*P^{iv}}{6}\right)\right] \\ &+ \frac{1}{4\rho\omega^2}\left[P^iP^{i*} + \frac{h^2}{6}\left(P^{i*}P^{iii} + P^iP^{iii*}\right)\right. \\ &\left. + \frac{h^4}{12}\left(\frac{P^{iii*}P^{iii}}{3} + \frac{P^iP^{v*}}{10} + \frac{P^{i*}P^v}{10}\right)\right] \end{aligned} \tag{B.46}$$

The exact energy density is given by

$$E_D = \frac{PP^*}{4\rho c^2} + \frac{\rho VV^*}{4} \tag{B.47}$$

Given that $V = (j/\omega\rho)P^i$, then the above equation can be rewritten as

$$E_D = \frac{PP^*}{4\rho c^2} + \frac{P^iP^{i*}}{4\rho\omega^2} = \frac{1}{4\rho c^2}\left(PP^* + \frac{P^iP^{i*}}{k^2}\right) \tag{B.48}$$

The normalised error in the energy density is given by

$$e(E_D) = (E_{D_e} - E_D)/E_D \tag{B.49}$$

The Taylor series expansion of the normalised error

$$\begin{aligned} e(E_D) &\approx \left[\frac{h^2}{2}\left(P^*P^{ii} + PP^{ii*}\right) + \frac{h^4}{4}\left(P^{ii*}P^{ii} + \frac{PP^{iv*}}{6} + \frac{P^*P^{iv}}{6}\right)\right] / \left(PP^* + \frac{P^iP^{i*}}{k^2}\right) \\ &+ \frac{1}{k^2\left(PP^* + \frac{P^iP^{i*}}{k^2}\right)} \\ &\times \left[\frac{h^2}{6}\left(P^{i*}P^{iii} + P^iP^{iii*}\right) + \frac{h^4}{12}\left(\frac{P^{iii*}P^{iii}}{3} + \frac{P^iP^{v*}}{10} + \frac{P^{i*}P^v}{10}\right)\right] \end{aligned} \tag{B.50}$$

Although not clear from the above expression it will be shown that in general the majority of the inherent error comes from the finite sum rather than the finite difference approximation. It therefore interesting to consider the case of a 3 microphone energy den-

sity sensor where the centre microphone measures the pressure at the centre of the sensor as in Figure 3.2. Consequently, all the inherent error is due to the velocity approximation.

The inherent energy density error for a 3 microphone sensor in a reactive one-dimensional sound field is given by the second term in the above expression, ie

$$\begin{aligned} e(E_D) &\approx \frac{1}{k^2\left(PP^* + \frac{P^iP^{i*}}{k^2}\right)} \\ &\quad \times \left[\frac{h^2}{6}\left(P^{i*}P^{iii} + P^iP^{iii*}\right) + \frac{h^4}{12}\left(\frac{P^{iii*}P^{iii}}{3} + \frac{P^iP^{v*}}{10} + \frac{P^{i*}P^v}{10}\right)\right] \end{aligned} \tag{B.51}$$

B.5.1 One-Dimensional Reactive Sound Field

Given a stationary reactive sound field defined by the following

$$p(x,t) = P_0\cos(k_l x)\Re\{e^{i\omega t}\} = P_0\cos(k_l x)\cos(\omega t) \tag{B.52}$$

where ω and k are the frequency and wavenumber of the sound respectively. The velocity corresponding to a point x_0 is given by

$$v(x_0,t) = -\frac{1}{\rho}\int\frac{\partial p(x_0)}{\partial x}dt = \frac{P_0k_l}{\rho\omega}\sin(k_lx_0)\sin(\omega t) \tag{B.53}$$

The pressure and gradients are given by differentiating Equation (B.52)

$$P = P_0\cos(k_lx) \tag{B.54}$$

$$P^i = -k_lP_0\sin(k_lx) \tag{B.55}$$

$$P^{ii} = -k_l^2P_0\cos(k_lx) = -k_l^2P \tag{B.56}$$

$$P^{iii} = k_l^3P_0\sin(k_lx) = -k_l^2P^i \tag{B.57}$$

Using Equation (B.50) and the spatial derivatives, the normalised error for the energy

density is given by

$$e(E_D) \approx \left[\frac{h^2}{2}\left(-2k_l^2 PP\right) + \frac{h^4}{4}\left(k_l^4 PP + \frac{k_l^4 PP}{6} + \frac{k_l^4 PP}{6}\right)\right] / \left(P_0^2\right) + \frac{1}{k^2\left(P_0^2\right)}\left[\frac{h^2}{6}\left(-2k_l^2 P^i P^i\right) + \frac{h^4}{12}\left(\frac{k_l^4 P^i P^i}{3} + \frac{k_l^4 P^i P^i}{10} + \frac{k_l^4 P^i P^i}{10}\right)\right] \quad \text{(B.58)}$$

Evaluating the spatial partial derivatives and collecting the squared trig functions,

$$\begin{aligned} e(E_D) &\approx \cos^2(k_l x)\left[-\left(k_l h\right)^2 + \frac{\left(k_l h\right)^4}{3}\right] \\ &\quad + \frac{\sin^2(k_l x)}{k^2}\left[-\frac{\left(k_l h\right)^2 k_l^2}{3} + \frac{2\left(k_l h\right)^4 k_l^2}{45}\right] - \ldots \end{aligned} \quad \text{(B.59)}$$

Rearranging

$$\begin{aligned} e(E_D) &\approx -\left(k_l h\right)^2\left[\frac{3\cos^2(k_l x) + \sin^2(k_l x)\frac{k_l^2}{k^2}}{3}\right] \\ &\quad + (kh)^4\left[\frac{15\cos^2(kx) + 2\sin^2(kx)\frac{k_l^2}{k^2}}{45}\right] - \ldots \end{aligned} \quad \text{(B.60)}$$

For the three-microphone sensor the normalised inherent error is

$$e(E_{D_3}) \approx \sin^2(k_l x)\frac{k_l^2}{k^2}\left[-\frac{\left(k_l h\right)^2}{3} + \frac{2\left(k_l h\right)^4}{45} - \ldots\right] \quad \text{(B.61)}$$

For the special case of $k_l = k$ then by using the trig relationship, $\cos^2(kx) + \sin^2(kx) = 1$, it can be shown the following holds,

$$e(E_D) \approx -\left(kh\right)^2\left[\frac{2\cos^2(kx) + 1}{3}\right] + (kh)^4\left[\frac{13\cos^2(kx) + 2}{45}\right] - \ldots \quad \text{(B.62)}$$

For the three-microphone sensor the normalised inherent error in the energy density is

$$e(E_{D_3}) \approx \sin^2(kx)\left[-\frac{(kh)^2}{3} + \frac{2(kh)^4}{45} - \ldots\right] \quad \text{(B.63)}$$

B.5.2 Plane Progressive Wave

Consider a plane wave defined by the following

$$p(x,t) = \Re\{P_0 e^{j\omega t - jkx}\} \tag{B.64}$$

The pressure and gradients are given by differentiating Equation (B.64)

$$P = P_0 e^{-jkx} \tag{B.65}$$

$$P^i = -jkP \tag{B.66}$$

$$P^{ii} = -k^2 P \tag{B.67}$$

$$P^{iii} = jk^3 P = -k^2 P^i \tag{B.68}$$

Assuming P_0 is a real scalar, ie $P^* P = P_0^2$, then the normalised error for the energy density is given by

$$\begin{aligned} e(E_D) \approx & \left[\frac{h^2}{2}\left(-2k^2P_0^2\right) + \frac{h^4}{4}\left(k^4P_0^2 + \frac{k^4P_0^2}{6} + \frac{k^4P_0^2}{6}\right)\right] / \left(P_0^2 + \frac{k^2P_0^2}{k^2}\right) \\ & + \frac{1}{k^2\left(P_0^2 + \frac{k^2P_0^2}{k^2}\right)}\left[\frac{h^2}{6}\left(-2k^4P_0^2\right) + \frac{h^4}{12}\left(\frac{k^6P_0^2}{3} + \frac{k^6P_0^2}{10} + \frac{k^6P_0^2}{10}\right)\right] \end{aligned} \tag{B.69}$$

Dividing through by the square of the pressure magnitude, P_0, and collecting like terms

$$\begin{aligned} e(E_D) \approx & \frac{1}{2}\left[-(kh)^2 + \frac{1}{3}(kh)^4\right] \\ & + \frac{1}{2}\left[-\frac{1}{3}(kh)^2 + \frac{2}{45}(kh)^4\right] \end{aligned} \tag{B.70}$$

Rearranging,

$$e(E_D) \approx -\frac{2}{3}(kh)^2 + \frac{17}{90}(kh)^4 - ... \tag{B.71}$$

Therefore the error in the energy density measurement for a progressive sound field is independent of position as one would expect. It is interesting to note that the first term in the error is the same as that for the error in intensity for the two-microphone technique.

For the three-microphone sensor the normalised inherent error for a plane progressive wave is

$$e(E_{D_3}) \approx -\frac{1}{6}(kh)^2 + \frac{1}{45}(kh)^4 - ... \tag{B.72}$$

B.5.3 Effects of Phase Mismatch on Energy Density Estimates

If the actual phase difference between the transducers is ϕ_f, the transducer mismatch is $\pm\phi_s$ and the reference (plane wave and also single mode reactive sound field) value is $\phi_0 = 2kh$ where $2h$ is the sensor separation distance. Therefore, in the case of simple harmonic fields the pressure response of the two microphones are shifted by $\pm\phi_s$, ie

$$\hat{p}_1(x,t) = p_1(x,t)e^{j\phi_s} \tag{B.73}$$

$$\hat{p}_2(x,t) = p_2(x,t)e^{-j\phi_s} \tag{B.74}$$

The effects of phase mismatch will now be analysed for two types of idealised sound fields.

B.5.3.1 One-dimensional reactive sound field

Given a stationary reactive sound field defined by the following

$$p(x,t) = P_0 \cos(kx)\Re\{e^{i\omega t}\} = P_0 \cos(kx)\cos(\omega t) \tag{B.75}$$

where ω and k are the frequency and wavenumber of the sound respectively. The velocity corresponding to a point x_0 is given by

$$v(x_0,t) = -\frac{1}{\rho}\int \frac{\partial p(x_0)}{\partial x}dt = \frac{P_0 k}{\rho\omega}\sin(kx_0)\sin(\omega t) \tag{B.76}$$

The mean of the two pressures is now given by

$$\hat{p}_e = \frac{\hat{p}_1 + \hat{p}_2}{2} = \frac{P_0}{2}[\cos(kx+kh)\cos(\omega t+\phi_s) + \cos(kx-kh)\cos(\omega t-\phi_s)] \tag{B.77}$$

Expanding the time dependent term gives

$$\begin{aligned} \hat{p}_e &= \frac{P_0}{2}\cos(kx+kh)[\cos(\omega t)\cos(\phi_s) - \sin(\omega t)\sin(\phi_s)] \\ &+ \frac{P_0}{2}\cos(kx-kh)[\cos(\omega t)\cos(\phi_s) + \sin(\omega t)\sin(\phi_s)] \end{aligned} \tag{B.78}$$

Now for small ϕ_s then $\cos(\phi_s) = 1 - \frac{\phi_s^2}{2} + ... \approx 1$ and $\sin(\phi_s) \approx \phi_s$, the pressure estimate is

$$\begin{aligned} \hat{p}_e &= \frac{P_0}{2}\cos(kx+kh)[\cos(\omega t) - \sin(\omega t)\phi_s] \\ &+ \frac{P_0}{2}\cos(kx-kh)[\cos(\omega t) + \sin(\omega t)\phi_s] \end{aligned} \tag{B.79}$$

Rearranging,

$$\begin{aligned}\hat{p}_e &= \frac{P_0}{2}[\cos(kx+kh)+\cos(kx-kh)]\cos(\omega t) \\ &- \frac{P_0\phi_s}{2}[\cos(kx+kh)-\cos(kx-kh)]\sin(\omega t)\end{aligned} \tag{B.80}$$

The first term in the above expression is the pressure estimate without the phase error, therefore

$$\hat{p}_e = p_e + \alpha_p \tag{B.81}$$

where α_p is the additional error due to the phase mismatch, given by

$$\alpha_p = P_0\phi_s \sin(kx)\sin(kh)\sin(\omega t) \tag{B.82}$$

Therefore, the normalised pressure error is given by

$$\begin{aligned}e(\hat{p}) &= \frac{\hat{p}_e - p}{p} \\ &= \frac{p_e - p}{p} + \frac{\alpha_p}{p}\end{aligned} \tag{B.83}$$

Now, the nomalised pressure error associated with the phase mismatch is given by

$$\begin{aligned}\frac{\alpha_p}{p} &= \frac{P_0\phi_s \sin(kx)\sin(kh)e^{j(\omega t+\frac{\pi}{2})}}{P_0\cos(kx)e^{j(\omega t)}} \\ &= j\phi_s \tan(kx)\sin(kh)\end{aligned} \tag{B.84}$$

The velocity estimate is given by

$$\hat{v}_e = -\frac{1}{2\rho h}\int [p(x-h)-p(x+h)]dt \tag{B.85}$$

Substituting the expression for the pressures and evaluating the integral

$$\hat{v}_e = \frac{P_0}{2h\rho\omega}[\cos(kx+kh)\sin(\omega t+\phi_s) - \cos(kx-kh)\sin(\omega t-\phi_s)] \tag{B.86}$$

Expanding the time dependent term gives

$$\begin{aligned}\hat{v}_e &= \frac{P_0}{2h\rho\omega}\cos(kx+kh)[\sin(\omega t)\cos(\phi_s)+\sin(\phi_s)\cos(\omega t)] \\ &- \frac{P_0}{2h\rho\omega}\cos(kx-kh)[\sin(\omega t)\cos(\phi_s)-\sin(\phi_s)\cos(\omega t)]\end{aligned} \tag{B.87}$$

For small ϕ_s the velocity estimate can be approximated by

$$\begin{aligned}\hat{v}_e &= \frac{P_0}{2h\rho\omega}\cos(kx+kh)[\sin(\omega t)+\phi_s\cos(\omega t)] \\ &- \frac{P_0}{2h\rho\omega}\cos(kx-kh)[\sin(\omega t)-\phi_s\cos(\omega t)]\end{aligned} \tag{B.88}$$

Rearranging,

$$\begin{aligned}\hat{v}_e &= \frac{P_0}{2h\rho\omega}[\cos(kx+kh)-\cos(kx-kh)]\sin(\omega t) \\ &+ \frac{P_0\phi_s}{2h\rho\omega}[\cos(kx+kh)+\cos(kx-kh)]\cos(\omega t)\end{aligned} \tag{B.89}$$

Again the first term in the above expression is the velocity estimate without the phase error, ie

$$\hat{v}_e = v_e + \alpha_v \tag{B.90}$$

where α_v is the additional error due to the phase mismatch, given by

$$\alpha_v = \frac{P_0}{h\rho\omega}\phi_s\cos(kx)\cos(kh)\cos(\omega t) \tag{B.91}$$

The energy density estimate is given by

$$\hat{E}_{D_e} = \frac{\hat{p}_e^2}{2\rho c^2} + \frac{\rho \hat{v}_e^2}{2} \tag{B.92}$$

and expanding in terms of p_e, v_e and the additional phase errors gives

$$\hat{E}_{D_e} = \frac{p_e^2 + 2\alpha_p p_e + \alpha_p^2}{2\rho c^2} + \frac{\rho(v_e^2 + 2\alpha_v v_e + \alpha_v^2)}{2} \tag{B.93}$$

When considering the time averaged energy density, the centre terms can be neglected as their integral over a period is zero. Therefore

$$\hat{E}_{D_e} = E_{D_e} + \frac{\alpha_p^2}{2\rho c^2} + \frac{\rho \alpha_v^2}{2} \tag{B.94}$$

Substituting α_p and α_v and calculating the time average gives

$$\hat{E}_{D_e} = E_{D_e} + \frac{P_0^2 \phi_s^2}{4\rho c^2} \left(\sin^2(kx)\sin^2(kh) + \cos^2(kx)\frac{\cos^2(kh)}{k^2h^2} \right) \tag{B.95}$$

The normalised error is thus,

$$e(\hat{E}_D) = e(E_D) + \phi_s^2 \left(\sin^2(kx)\sin^2(kh) + \cos^2(kx)\frac{\cos^2(kh)}{k^2h^2} \right) \tag{B.96}$$

Therefore, as kh is small, then

$$e(\hat{E}_D) = e(E_D) + \phi_s^2 \left((kh)^2 \sin^2(kx) + \cos^2(kx)\frac{1}{k^2h^2} \right) \tag{B.97}$$

The first term in the expression is of the order $O\{\phi_s^2 e(E_D)\}$ and for small phase mismatches can be ignored. However, the second term is significant and becomes very large

as kh decreases. The above equation for small kh can be rewritten as

$$e(\hat{E}_D) = e(E_D) + \cos^2(kx)\left(\frac{2\phi_s}{2kh}\right)^2 \tag{B.98}$$

Therefore, the normalised error in the energy density arising from the phase mismatch is proportional to the ratio of the phase error to the free field phase difference. In the case of $kx = 0$

$$e(\hat{E}_D) = e(E_D) + \frac{\phi_s^2}{(kh)^2} \tag{B.99}$$

B.5.3.2 Plane progressive wave

In the case of a plane wave the effect of a phase mismatch is equivalent to modifying the sensor separation distance, ie $k\hat{h} = kh - \phi_s$ or $\frac{\hat{h}}{h} = 1 - \frac{\phi_s}{kh}$. The pressure estimate is thus

$$p(x,t) = \Re\{P_0 e^{j\omega t - jkx}\} \tag{B.100}$$

Thus

$$\begin{aligned}
\hat{E}_{D_e} \quad = \quad & \frac{1}{4\rho c^2}\left[P + (\hat{h}^2/2)P^{ii} + (\hat{h}^4/24)P^{iv} + ... + (\hat{h}^{2n}/2n!)P^{2n}\right] \\
& \left[P + (\hat{h}^2/2)P^{ii} + (\hat{h}^4/24)P^{iv} + ... + (\hat{h}^{2n}/2n!)P^{2n}\right]^* \\
& + \frac{4}{4\rho\omega^2(2h)^2}\left[\hat{h}P^i + (\hat{h}^3/6)P^{iii} + (\hat{h}^5/120)P^{iv} + ... + (\hat{h}^{2n+1}/(2n+1)!)P^{2n+1}\right] \\
& \left[\hat{h}P^i + (\hat{h}^3/6)P^{iii} + (\hat{h}^5/120)P^{v} + ... + (\hat{h}^{2n+1}/(2n+1)!)P^{2n+1}\right]^*
\end{aligned} \tag{B.101}$$

The pressure and gradients are given by differentiating Equation (B.64)

$$P = P_0 e^{-jkx} \tag{B.102}$$

$$P^i = -jkP \tag{B.103}$$

$$P^{ii} = -k^2 P \tag{B.104}$$

$$P^{iii} = jk^3 P = -k^2 P^i \tag{B.105}$$

Substituting for the pressure gradients, gives a normalised error

$$\begin{aligned} e(\hat{E}_D) \approx & \left[P_0^2 + \frac{\hat{h}^2}{2}\left(-2k^2P_0^2\right) + \frac{\hat{h}^4}{4}\left(k^4P_0^2 + \frac{k^4P_0^2}{6} + \frac{k^4P_0^2}{6}\right)\right] / \left(P_0^2 + \frac{k^2P_0^2}{k^2}\right) \\ & + \frac{\left(\frac{\hat{h}}{h}\right)^2}{k^2\left(P_0^2 + \frac{k^2P_0^2}{k^2}\right)} \\ & \times \left[k^2P_0^2 + \frac{\hat{h}^2}{6}\left(-2k^4P_0^2\right) + \frac{\hat{h}^4}{12}\left(\frac{k^6P_0^2}{3} + \frac{k^6P_0^2}{10} + \frac{k^6P_0^2}{10}\right)\right] - 1 \end{aligned} \tag{B.106}$$

Collecting like terms,

$$\begin{aligned} e(\hat{E}_D) \approx & \frac{1}{2}\left[1 - \left(\hat{h}k\right)^2 + \frac{1}{3}\left(\hat{h}k\right)^4\right] \\ & + \frac{\left(1 - \frac{\phi_s}{kh}\right)^2}{2}\left[1 - \frac{1}{3}\left(\hat{h}k\right)^2 + \frac{2}{45}\left(\hat{h}k\right)^4\right] - 1 \end{aligned} \tag{B.107}$$

Therefore, for either the two-microphone or three microphone sensor with $kh \ll \phi_s \ll 1$, the normalised error is

$$e(\hat{E}_D) \approx -24\frac{(2\phi_s)^4}{(2kh)^2} \tag{B.108}$$

B.5.4 Effects of Sensitivity Mismatch on Energy Density Estimates

If the sensitivity difference between the transducers is $\pm T$ such that the ratio of the sensitivities is given by $(1+T)/(1-T) \approx 1+2T$ for small T. Therefore, in the case of simple harmonic fields the pressure response of the second microphones is shifted by T, ie

$$\hat{p}_1(x,t) = p_1(x,t)(1-T) \tag{B.109}$$

$$\hat{p}_2(x,t) = p_2(x,t)(1+T) \tag{B.110}$$

The effects of sensitivity mismatch will now be analysed for two types of idealised sound fields.

B.5.4.1 One-dimensional reactive sound field

Given a stationary reactive sound field defined by the following

$$p(x,t) = P_0 \cos(kx) \Re\{e^{i\omega t}\} = P_0 \cos(kx)\cos(\omega t) \tag{B.111}$$

where ω and k are the frequency and wavenumber of the sound respectively. The velocity corresponding to a point x_0 is given by

$$v(x_0,t) = -\frac{1}{\rho}\int \frac{\partial p(x_0)}{\partial x} dt = \frac{P_0 k}{\rho\omega}\sin(kx_0)\sin(\omega t) \tag{B.112}$$

The mean of the two pressures is now

$$\hat{p}_{e=}\frac{\hat{p}_1+\hat{p}_2}{2}=\frac{P_0}{2}[(1-T)\cos(kx+kh)\cos(\omega t)+(1+T)\cos(kx-kh)\cos(\omega t)] \tag{B.113}$$

Expanding the sensitivity term gives

$$\begin{aligned}\hat{p}_e &= \frac{P_0}{2}[\cos(kx+kh)\cos(\omega t)+\cos(kx-kh)\cos(\omega t)] \\ &- \frac{P_0T}{2}[\cos(kx+kh)\cos(\omega t)-\cos(kx-kh)\cos(\omega t)]\end{aligned} \tag{B.114}$$

The first term in the above expression is the pressure estimate without the magnitude error, therefore

$$\hat{p}_e = p_e + \beta_p \tag{B.115}$$

where β_p is the additional error due to the magnitude mismatch, given by

$$\beta_p = P_0T\sin(kx)\sin(kh)\cos(\omega t) \tag{B.116}$$

Therefore, the normalised error of the pressure estimate is given by

$$e(\hat{p}) = (\hat{p}_e - p)/p = (p_e - p)/p + \beta_p/p \tag{B.117}$$

Substituting,

$$e(\hat{p}) = e(p) + T\tan(kx)\sin(kh) \tag{B.118}$$

The velocity estimate is given by

$$\hat{v}_e = -\frac{1}{2\rho h}\int [p(x-h) - p(x+h)]dt \tag{B.119}$$

Substituting the expression for the pressures and evaluating the integral

$$\hat{v}_e = \frac{P_0}{2h\rho\omega}[(1-T)\cos(kx+kh)\sin(\omega t) - (1+T)\cos(kx-kh)\sin(\omega t)] \tag{B.120}$$

Expanding the sensitivity term gives

$$\begin{aligned} \hat{v}_e &= \frac{P_0}{2h\rho\omega}[\cos(kx+kh) - \cos(kx-kh)]\sin(\omega t) \\ &- \frac{P_0 T}{2h\rho\omega}[\cos(kx+kh) + \cos(kx-kh)]\sin(\omega t) \end{aligned} \tag{B.121}$$

Again the first term in the above expression is the velocity estimate without the sensitivity error, ie

$$\hat{v}_e = v_e + \beta_v \tag{B.122}$$

where β_v is the additional error due to the magnitude mismatch, given by

$$\beta_v = -\frac{P_0 T}{\rho c k h}\cos(kx)\cos(kh)\sin(\omega t) \tag{B.123}$$

Therefore, the normalised error of the velocity estimate is given by

$$e(\hat{v}) = (\hat{v}_e - v)/v = (v_e - v)/v + \beta_v/v \tag{B.124}$$

Using previous results,

$$e(\hat{v}) = [\frac{\sin(kh)}{kh} - 1] + T\frac{\cos(kh)}{kh\tan(kx)} \tag{B.125}$$

The energy density estimate is given by

$$\hat{E}_{D_e} = \frac{\hat{p}_e^2}{2\rho c^2} + \frac{\rho\hat{v}_e^2}{2} \tag{B.126}$$

and expanding in terms of p_e, v_e and the additional sensitivity errors gives

$$\hat{E}_{D_e} = \frac{p_e^2 + 2\beta_p p_e + \beta_p^2}{2\rho c^2} + \frac{\rho(v_e^2 + 2\beta_v v_e + \beta_v^2)}{2} \tag{B.127}$$

For small magnitude errors the β_p^2 term is negligible, however, this is not the case for β_v due to the $1/kh$ term, therefore

$$\hat{E}_{D_e} = E_{D_e} + \frac{2\beta_p p_e}{2\rho c^2} + \frac{2\rho\beta_v v_e + \rho\beta_v^2}{2} \tag{B.128}$$

Substituting β_p and β_v and calculating the time average gives

$$\begin{aligned}\hat{E}_{D_e} &= E_{D_e} + \frac{P_0^2(2T)}{4\rho c^2}[\frac{1}{4}\sin(2kx)\sin(2kh) + \frac{2T}{4}\sin^2(kx)\sin^2(kh) \\ &\quad -\frac{1}{4(kh)^2}\sin(2kx)\sin(2kh) + \frac{1}{4(kh)^2}(2T)\cos^2(kx)\cos^2(kh)]\end{aligned} \tag{B.129}$$

The normalised error is thus,

$$e(\hat{E}_D) = e(E_D) + \frac{2T}{4}\sin(2kx)\sin(2kh)\left(1 - \frac{1}{(kh)^2}\right) + \left(\frac{2T}{2kh}\right)^2\cos^2(kx)\cos^2(kh) \tag{B.130}$$

Therefore, as kh is small, then

$$e(\hat{E}_D) = e(E_D) + \frac{2T}{2}\sin(2kx)\left(kh - \frac{1}{kh}\right) + \left(\frac{2T}{2kh}\right)^2 \cos^2(kx) \tag{B.131}$$

The first term in the expression is negligible for small sensitivity mismatches and can be ignored. However, the second and third terms are significant and become very large as kh decreases. The above equation for small kh can be rewritten as

$$e(\hat{E}_D) \approx e(E_D) - \left(\frac{2T}{2kh}\right)\sin(2kx) + \left(\frac{2T}{2kh}\right)^2 \cos^2(kx) \tag{B.132}$$

Therefore, in order to keep the error in the energy density the non-dimensional error in sensitivity $2T$ should be significantly less than the non-dimensional microphone separation $2kh$.

B.5.4.2 Plane progressive wave

The pressure estimate at any point x is given by

$$p(x,t) = \Re\{P_0 e^{j\omega t - jkx}\} \tag{B.133}$$

The mean of the two pressures with the sensitivity mismatch is now

$$\hat{p}_{e=}\frac{\hat{p}_1 + \hat{p}_2}{2} = \frac{(1-T)p(x+h) + (1+T)p(x-h)}{2} \tag{B.134}$$

Rearranging

$$\hat{p}_e = \frac{p(x+h) + p(x-h)}{2} - T\frac{p(x+h) - p(x-h)}{2} \tag{B.135}$$

Now the first component of the above expression is the standard expression for the

pressure estimate and the second term is the same as for the kernel of the velocity estimate, ie $\hat{v}_e = -\frac{1}{2\rho h}\int[p(x-h) - p(x+h)]dt$. Therefore,

$$\hat{p}_e = p_e + \beta_p \tag{B.136}$$

where β_p is the additional error due to the magnitude mismatch, given by

$$\beta_p = -Th[P^i + (h^2/6)P^{iii} + (h^4/120)P^v + ...] \tag{B.137}$$

Substituting the values for the derivatives

$$\beta_p = jhkPT[1 - \frac{(kh)^2}{6} + \frac{(kh)^4}{120} - ...] = jPT\sin(kh) \tag{B.138}$$

The normalised pressure error is therefore

$$e(\hat{p}) = (\hat{p}_e - p)/p = (p_e - p)/p + \beta_p/p \tag{B.139}$$

Using previous results to evaluate the expression above,

$$e(\hat{p}) = [\cos(kh) - 1] + jT\sin(kh) \tag{B.140}$$

Therefore, the sensitivity error introduces both an magnitude and phase error into the pressure estimate. The velocity estimate is given by

$$\hat{v}_e = -\frac{1}{2\rho h}\int[(1+T)p(x-h) - (1-T)p(x+h)]dt \tag{B.141}$$

Rearranging,

$$\hat{v}_e = -\frac{1}{2\rho h}\int\left([p(x-h) - p(x+h)] + T[p(x-h) + p(x+h)]\right)dt \tag{B.142}$$

The first term in the above expression is the velocity estimate without the sensitivity error, ie

$$\hat{v}_e = v_e + \beta_v \tag{B.143}$$

where β_v is the additional error due to the magnitude mismatch, given by

$$\beta_v = -\frac{T}{jh\rho\omega}P[1 - \frac{(kh)^2}{2} + \frac{(kh)^4}{24} - ...] = -\frac{T}{jh\rho\omega}P\cos(kh) \tag{B.144}$$

The normalised velocity error is therefore

$$e(\hat{v}) = (\hat{v}_e - v)/v = (v_e - v)/v + \beta_v/v \tag{B.145}$$

Using previous results,

$$e(\hat{v}) = [\frac{\sin(kh)}{kh} - 1] + jT\frac{\cos(kh)}{kh} \tag{B.146}$$

Unlike the normalised pressure error, the sensitivity error introduces both an magnitude and phase error which becomes very large as kh approaches zero.

The energy density estimate is given by

$$\hat{E}_{D_e} = \frac{\hat{p}_e\hat{p}_e^*}{2\rho c^2} + \frac{\rho\hat{v}_e\hat{v}_e^*}{2} \tag{B.147}$$

and expanding in terms of p_e, v_e and the additional sensitivity errors gives

$$\hat{E}_{D_e} = \frac{p_e^2 - \beta_p^2}{2\rho c^2} + \frac{\rho(v_e^2 - \beta_v^2)}{2} \tag{B.148}$$

Rearranging in terms of the finite spacing normalised error,

$$\hat{E}_{D_e} = E_{D_e} - \frac{\beta_p^2}{2\rho c^2} - \frac{\rho \beta_v^2}{2} \tag{B.149}$$

Substituting β_p and β_v and calculating the time average gives

$$\hat{E}_{D_e} = E_{D_e} + \frac{P^2 T^2 \sin^2(kh)}{4\rho c^2} + \frac{T^2 P^2 \cos^2(kh)}{4\rho c^2 (kh)^2} \tag{B.150}$$

The normalised error is thus,

$$e(\hat{E}_D) = e(E_D) + \frac{T^2}{2}\left(\sin^2(kh) + \frac{\cos^2(kh)}{(kh)^2}\right) \tag{B.151}$$

The Taylor series expansion for the sine and cosine terms are

$$\sin^2(kh) \approx (kh)^2 - \frac{(kh)^4}{3} + ... \tag{B.152}$$

and

$$\frac{\cos^2(kh)}{(kh)^2} \approx \frac{1}{(kh)^2}\left(1 - (kh)^2 + ...\right) \tag{B.153}$$

Therefore, the normalised error can be approximated as

$$e(\hat{E}_D) = e(E_D) + \frac{T^2}{2}\left(\frac{1}{(kh)^2} - 1 + ...\right) \tag{B.154}$$

For small kh,

$$e(\hat{E}_D) = e(E_D) + \frac{T^2}{2(kh)^2} \tag{B.155}$$

B.5.5 The Effects of Geometric Errors on the Energy Density Estimate

Because of manufacturing tolerances, the distance between acoustic centres of the microphones can vary. Typically, the accuracy may be in the order of ± 1mm. It has been shown that length errors can lead to significant errors in intensity measurements (Boden & Abom 1986, Fahy 1995). In the case of one-dimension sound fields, it is only the positional error in the direction of energy flux that will cause errors in the estimates, ie for $\frac{\partial p}{\partial y} = 0$ and an error in the y position, $\hat{y} = y + \epsilon$, pressure estimate, $p(\hat{y}) = p(y)$ is unaffected.

If the error in position is given by $\pm\epsilon$, then the non-dimensional spacing is given by $k\hat{h} = kh + k\epsilon$ or $\frac{\hat{h}}{h} = 1 + \frac{k\epsilon}{kh}$. The effects of length errors will now be analysed for two types of idealised sound fields.

B.5.5.1 One-dimensional reactive sound field

The normalised error for the pressure and velocity estimate is given by

$$e(\hat{p}) = \cos(k\hat{h}) - 1 \approx -\frac{(k\hat{h})^2}{2} + \frac{(k\hat{h})^4}{24} - \frac{(k\hat{h})^6}{720} + ... \tag{B.156}$$

$$e(\hat{v}) = \frac{\sin(k\hat{h})}{kh} - 1 \approx \left(1 + \frac{k\epsilon}{kh}\right)\left(1 - \frac{(k\hat{h})^2}{6} + \frac{(k\hat{h})^4}{120} - \frac{(k\hat{h})^6}{5040} + ...\right) - 1 \tag{B.157}$$

Evaluating the spatial partial derivatives and collecting the squared trig functions,

$$\begin{aligned} e(\hat{E}_D) \;\approx\; & \cos^2(kx)\left[1 - \left(k\hat{h}\right)^2 + \frac{(k\hat{h})^4}{3}\right] \\ & + \sin^2(kx)\left(\frac{k\hat{h}}{kh}\right)^2\left[1 - \frac{(k\hat{h})^2}{3} + \frac{2(k\hat{h})^4}{45}\right] - 1 \end{aligned} \tag{B.158}$$

Using $\frac{\hat{h}}{h} = 1 + \frac{k\epsilon}{kh}$,

$$\begin{aligned} e(\hat{E}_D) &\approx \cos^2(kx)\left[1 - \left(k\hat{h}\right)^2 + \frac{(k\hat{h})^4}{3}\right] \\ &\quad + \sin^2(kx)\left(1 + \frac{k\epsilon}{kh}\right)^2\left[1 - \frac{(k\hat{h})^2}{3} + \frac{2(k\hat{h})^4}{45}\right] - 1 \end{aligned} \tag{B.159}$$

B.5.5.2 Free progressive wave

In the case of a plane wave the effect of an error in the length is the same as a phase mismatch. For a length error of 2ϵ then $k\hat{h} = kh + k\epsilon$ or $\frac{\hat{h}}{h} = 1 + \frac{k\epsilon}{kh}$. The normalised errors for the pressure, velocity and energy density can be found by substitution of the shifted non-dimensional microphone spacing into the previously derived expressions for the normalised errors with a phase mismatch, ie

$$e(\hat{p}) = \cos(k\hat{h}) - 1 \approx -\frac{(k\hat{h})^2}{2} + \frac{(k\hat{h})^4}{24} - \frac{(k\hat{h})^6}{720} + ... \tag{B.160}$$

$$e(\hat{v}) = \frac{\sin(k\hat{h})}{kh} - 1 \approx \left(1 + \frac{k\epsilon}{kh}\right)\left(1 - \frac{(k\hat{h})^2}{6} + \frac{(k\hat{h})^4}{120} - \frac{(k\hat{h})^6}{5040} + ...\right) - 1 \tag{B.161}$$

$$\begin{aligned} e(\hat{E}_D) &\approx \frac{1}{2}\left[1 - \left(\hat{h}k\right)^2 + \frac{1}{3}\left(\hat{h}k\right)^4\right] \\ &\quad + \frac{\left(1 + \frac{k\epsilon}{kh}\right)^2}{2}\left[1 - \frac{1}{3}\left(\hat{h}k\right)^2 + \frac{2}{45}\left(\hat{h}k\right)^4\right] - 1 \end{aligned} \tag{B.162}$$

For small ϵ/h then $(1+\epsilon/h)^n \approx 1 + n\epsilon/h$. Therefore it can be shown that the effect of the spacing error is to increase the finite difference/sum error by a factor of approximately $\frac{\epsilon}{h}$.

For a 3-microphone sensor the normalised errors are identical to the errors for the phase mismatch with $\phi_s = k\epsilon$. The normalised error in the pressure is the obviously zero, the error for the velocity is the same as given above and the normalised error in the energy density is given by the second term in the above expression. Therefore, it can be concluded that the use of the additional microphone reduces the error in the energy density by approximately a factor of three and thereby reducing the lower frequency limit.

B.6 Calculation of the Charge Sensitivity for a Uniform PVDF Sensor

B.6.1 Single PVDF Layer

With the sensor shape function is set equal to unity across the shell surface, ie

$$\Gamma(\vec{\mathbf{x}}) = 1 \tag{B.163}$$

the charge developed by the sensor is given by the following

$$\begin{aligned} q(t) &= -\frac{t_s}{2}\int_S \sum_{i=1}^{\infty}\sum_{j=1}^{\infty} A_{i,j}\left[e_{31}\left(-\frac{i^2\pi^2}{a^2}\sin\left(\frac{i\pi x}{a}\right)\sin\left(\frac{j\pi y}{b}\right)\right)\right. \\ &+ \left. e_{32}\left(-\frac{j^2\pi^2}{b^2}\sin\left(\frac{i\pi x}{a}\right)\sin\left(\frac{j\pi y}{b}\right)\right)\right] dS(\vec{\mathbf{x}}) \end{aligned} \tag{B.164}$$

Evaluating the integral

$$\begin{aligned} q(t) &= -\frac{t_s}{2}\sum_{i=1}^{\infty}\sum_{j=1}^{\infty} A_{i,j}\left[\left(-e_{31}\frac{i^2\pi^2}{a^2} - e_{32}\frac{j^2\pi^2}{b^2}\right)\right. \\ &\left.\left(-\frac{a}{i\pi}\cos\left(\frac{i\pi x}{a}\right)\right)\left(-\frac{b}{j\pi}\cos\left(\frac{j\pi y}{b}\right)\right)\right]_{x=0:a,y=0:b} \end{aligned} \tag{B.165}$$

Rearranging

$$q(t) = -\frac{t_s}{2}\sum_{i=1}^{\infty}\sum_{j=1}^{\infty} A_{i,j}\left[\left(-e_{31}\frac{i^2\pi^2}{a^2} - e_{32}\frac{j^2\pi^2}{b^2}\right) \times \frac{4ab}{ij\pi^2}(1-(-1)^i)(1-(-1)^j)\right] \quad \text{(B.166)}$$

Rearranging further

$$q(t) = -\frac{t_s}{2}\sum_{i=1}^{\infty}\sum_{j=1}^{\infty} A_{i,j}\left[4\left(-e_{31}\frac{ib}{aj} - e_{32}\frac{aj}{ib}\right) \times (1-(-1)^i)(1-(-1)^j)\right] \quad \text{(B.167)}$$

Finally gives

$$q(t) = \frac{t_s}{2}e_{31}\sum_{i=1}^{\infty}\sum_{j=1}^{\infty}\frac{4A_{i,j}}{abij}\left(i^2b^2 + \frac{e_{32}}{e_{31}}a^2j^2\right)(1-(-1)^i)(1-(-1)^j) \quad \text{(B.168)}$$

B.6.2 Double PVDF Layer

Now if two PVDF layers are used with the piezoelectric axes normal to each other, and the outputs are summed and weighted as follows

$$q_0 = q_1 - \frac{e_{32}}{e_{31}}q_2 \quad \text{(B.169)}$$

then the total charge output is given by

$$\begin{aligned} q(t) &= \frac{t_s}{2} e_{31} \sum_{i=1}^{\infty}\sum_{j=1}^{\infty} \frac{4A_{i,j}}{abij}\left(i^2b^2 + \frac{e_{32}}{e_{31}}a^2j^2\right)(1-(-1)^i)(1-(-1)^j) \\ &+ -\frac{e_{32}}{e_{31}}\frac{t_s}{2}e_{32}\sum_{i=1}^{\infty}\sum_{j=1}^{\infty}\left[\frac{4A_{i,j}}{abij}\left(i^2b^2 + \frac{e_{31}}{e_{32}}a^2j^2\right)\right. \\ &\left. \times (1-(-1)^i)(1-(-1)^j)\right] \end{aligned} \tag{B.170}$$

Rearranging,

$$q(t) = \frac{t_s}{2} e_{31}\left(1 - \frac{e_{32}^2}{e_{31}^2}\right)\frac{b}{a}\sum_{i=1}^{\infty}\sum_{j=1}^{\infty}\frac{4A_{i,j}}{ij} i^2 (1-(-1)^i)(1-(-1)^j) \tag{B.171}$$

B.7 Sensing of Higher Order Radiation Modes

B.7.1 Single PVDF Layer

If the sensor shape function is set equal to the mode shapes of the acoustic modes, ie

$$\Gamma(\vec{\mathbf{x}}) = \cos\left(\frac{l\pi x}{a}\right)\cos\left(\frac{m\pi y}{b}\right) \tag{B.172}$$

the charge developed by the sensor is given by

$$\begin{aligned} q(t) &= -\frac{t_s}{2}\int_S \left[\cos\left(\frac{l\pi x}{a}\right)\cos\left(\frac{m\pi y}{b}\right)\sum_{i=1}^{\infty}\sum_{j=1}^{\infty} e_{31}\left(-\frac{i^2\pi^2}{a^2}\sin\left(\frac{i\pi x}{a}\right)\sin\left(\frac{j\pi y}{b}\right)\right)\right. \\ &\left. + e_{32}\left(-\frac{j^2\pi^2}{b^2}\sin\left(\frac{i\pi x}{a}\right)\sin\left(\frac{j\pi y}{b}\right)\right)\right] dS(\vec{\mathbf{x}}) \end{aligned} \tag{B.173}$$

Expanding and rearranging

$$q(t) = -\frac{t_s}{2}\int_S \sum_{i=1}^{\infty}\sum_{j=1}^{\infty}\left[\left(-e_{31}\frac{i^2\pi^2}{4a^2} - e_{32}\frac{j^2\pi^2}{4b^2}\right)\left(\sin\left(\frac{(i-l)\pi x}{a}\right) + \sin\left(\frac{(i+l)\pi x}{a}\right)\right)\right.$$
$$\left.\times\left(\sin\left(\frac{(j-m)\pi y}{b}\right) + \sin\left(\frac{(j+m)\pi y}{b}\right)\right)\right] dS(\vec{\mathbf{x}}) \quad \text{(B.174)}$$

Evaluating the integral

$$q(t) = -\frac{t_s}{2}\sum_{i=1}^{\infty}\sum_{j=1}^{\infty}\left[\left(-e_{31}\frac{i^2\pi^2}{4a^2} - e_{32}\frac{j^2\pi^2}{4b^2}\right)\right.$$
$$\left(-\frac{a}{(i-l)\pi}\cos\left(\frac{(i-l)\pi x}{a}\right) - \frac{a}{(i+l)\pi}\cos\left(\frac{(i+l)\pi x}{a}\right)\right)$$
$$\times\left(-\frac{b}{(j-m)\pi}\cos\left(\frac{(j-m)\pi y}{b}\right)\right.$$
$$\left.\left.-\frac{b}{(j+m)\pi}\cos\left(\frac{(j+m)\pi y}{b}\right)\right)\right] \quad \text{(B.175)}$$

Rearranging

$$q(t) = -\frac{t_s}{2}\sum_{i=1}^{\infty}\sum_{j=1}^{\infty}\left[\left(-e_{31}\frac{i^2\pi^2}{4a^2} - e_{32}\frac{j^2\pi^2}{4b^2}\right)(1-(-1)^{i+l})\left(\frac{a}{(i-l)\pi} + \frac{a}{(i+l)\pi}\right)\right.$$
$$\left.\times(1-(-1)^{j+m})\left(\frac{b}{(j-m)\pi} + \frac{b}{(j+m)\pi}\right)\right] \quad \text{(B.176)}$$

rearranging further

$$q(t) = \frac{t_s}{2}4\sum_{i=1}^{\infty}\sum_{j=1}^{\infty}\left[\left(e_{31}\frac{i^2}{4a^2} + e_{32}\frac{j^2}{4b^2}\right)(1-(-1)^{i+l})(1-(-1)^{j+m})\right.$$
$$\left.\times\left(\frac{ia}{(i-l)(i+l)}\right)\left(\frac{jb}{(j-m)(j+m)}\right)\right] \quad \text{(B.177)}$$

finally reduces to

$$q(t) = \frac{t_s}{2}\frac{e_{31}}{ab}\sum_{i=1}^{\infty}\sum_{j=1}^{\infty}A_{i,j}\left[\left(i^2b^2+\frac{e_{32}}{e_{31}}j^2a^2\right)(1-(-1)^{i+l})(1-(-1)^{j+m})\right.$$
$$\left.\times\left(\frac{i}{(i-l)(i+l)}\right)\left(\frac{j}{(j-m)(j+m)}\right)\right] \quad \text{(B.178)}$$

B.7.2 Double PVDF Layer

Now if two PVDF layers are use with the piezoelectric axes normal to each other, and the outputs are summed and weighted as follows

$$q_0 = q_1 - \frac{e_{32}}{e_{31}}q_2 \quad \text{(B.179)}$$

then the total charge output is given by

$$q(t) = \frac{t_s}{2}\frac{e_{31}}{ab}\sum_{i=1}^{\infty}\sum_{j=1}^{\infty}A_{i,j}\left[\left(i^2b^2+\frac{e_{32}}{e_{31}}j^2a^2\right)(1-(-1)^{i+l})(1-(-1)^{j+m})\right.$$
$$\left.\times\left(\frac{i}{(i-l)(i+l)}\right)\left(\frac{j}{(j-m)(j+m)}\right)\right]$$
$$-\frac{e_{32}}{e_{31}}\frac{t_s}{2}\frac{e_{32}}{ab}\sum_{i=1}^{\infty}\sum_{j=1}^{\infty}A_{i,j}\left[\left(i^2b^2+\frac{e_{31}}{e_{32}}j^2a^2\right)(1-(-1)^{i+l})(1-(-1)^{j+m})\right.$$
$$\left.\times\left(\frac{i}{(i-l)(i+l)}\right)\left(\frac{j}{(j-m)(j+m)}\right)\right] \quad \text{(B.180)}$$

Rearranging,

$$q(t) = \frac{t_s}{2} e_{31} \left(1 - \frac{e_{32}^2}{e_{31}^2}\right) \frac{1}{ab} \sum_{i=1}^{\infty} \sum_{j=1}^{\infty} \left[A_{i,j} i^2 (1-(-1)^i)(1-(-1)^j) \times \left(\frac{i}{(i-l)(i+l)}\right)\left(\frac{j}{(j-m)(j+m)}\right)\right] \quad \text{(B.181)}$$

B.8 An Improved Sensor Shape Function for a Simply Supported Plate

B.8.1 Single PVDF Layer

If an accurate estimate of the higher order radiation modes is required, then an alternative sensor shape function is necessary to remove the i^2 term from the charge sensitivity equation. Therefore if the sensor equation has a $1/i^2$ bias to start with, it will be shown following that the resulting expression for the charge sensitivity is not biased. Using

$$\Gamma(\vec{\mathbf{x}}) = \sum_{k=1}^{\infty} \bar{A}_{k,l} \sin(\frac{k\pi x}{a}) \sum_{k'=1}^{\infty} \bar{A}_{k',m} \sin(\frac{k'\pi y}{b}) \quad \text{(B.182)}$$

where

$$\bar{A}_{k,l} = \frac{2}{\pi} \left(1 - (-1)^{k+l}\right) \frac{k}{(k-l)(k+l)} \frac{1}{k^2} \quad \text{(B.183)}$$

and

$$\bar{A}_{k',m} = \frac{2}{\pi} \left(1 - (-1)^{k'+m}\right) \frac{k'}{(k'-m)(k'+m)} \quad \text{(B.184)}$$

and l and m are the modal indices of the desired radiation mode. Substituting this shape function into the sensor equation gives the following charge output,

$$\begin{aligned} q &= -\frac{t_s}{2}\int_S \sum_{k=1}^{\infty} \bar{A}_{k,l}\sin(\frac{k\pi x}{a}) \sum_{k'=1}^{\infty} \bar{A}_{k',m}\sin(\frac{k'\pi y}{b}) \\ &\quad \times \left[\sum_{i=1}^{\infty}\sum_{j=1}^{\infty} e_{31}\left(-\frac{i^2\pi^2}{a^2}\sin\left(\frac{i\pi x}{a}\right)\sin\left(\frac{j\pi y}{b}\right)\right)\right. \\ &\quad \left. + e_{32}\left(-\frac{j^2\pi^2}{b^2}\sin\left(\frac{i\pi x}{a}\right)\sin\left(\frac{j\pi y}{b}\right)\right)\right] dS(\vec{\mathbf{x}}) \end{aligned} \tag{B.185}$$

Evaluating the integral and using orthogonality,

$$\begin{aligned} q &= -\frac{t_s}{2}\sum_{i=1}^{\infty}\sum_{j=1}^{\infty} A_{i,j} \\ &\quad \times \left[e_{31}\frac{i^2\pi^2}{a^2}\frac{1}{4}\frac{2}{\pi}\left(1-(-1)^{i+l}\right)\frac{i}{(i-l)(i+l)}\frac{1}{i^2}\frac{2}{\pi}\left(1-(-1)^{j+m}\right)\frac{j}{(j-m)(j+m)}\right] \\ &\quad \times \left[e_{32}\frac{j^2\pi^2}{b^2}\frac{1}{4}\frac{2}{\pi}\left(1-(-1)^{i+l}\right)\frac{i}{(i-l)(i+l)}\frac{1}{i^2}\right. \\ &\quad \left. \times \frac{2}{\pi}\left(1-(-1)^{j+m}\right)\frac{j}{(j-m)(j+m)}\right] \end{aligned} \tag{B.186}$$

Simplifying,

$$\begin{aligned} q &= -\frac{t_s}{2}\frac{e_{31}}{a^2}\sum_{i=1}^{\infty}\sum_{j=1}^{\infty} A_{i,j}\left(1+\frac{e_{32}}{e_{31}}\frac{j^2a^2}{i^2b^2}\right) \\ &\quad \times \left[\left(1-(-1)^{i+l}\right)\frac{i}{(i-l)(i+l)}\left(1-(-1)^{j+m}\right)\frac{j}{(j-m)(j+m)}\right] \end{aligned} \tag{B.187}$$

B.8.2 Double PVDF Layer

Now if two PVDF layers are used with the piezoelectric axes normal to each other, and the outputs are summed and weighted as follows

$$q_0 = q_1 - \frac{e_{32}}{e_{31}} q_2 \tag{B.188}$$

then the total charge output is given by

$$\begin{aligned} q &= -\frac{t_s}{2} e_{31} \left(1 - \frac{e_{32}^2}{e_{31}^2}\right) \frac{1}{a^2} \sum_{i=1}^{\infty} \sum_{j=1}^{\infty} A_{i,j} \\ &\quad \left[\left(1 - (-1)^{i+l}\right) \frac{i}{(i-l)(i+l)} \left(1 - (-1)^{j+m}\right) \frac{j}{(j-m)(j+m)} \right] \end{aligned} \tag{B.189}$$

B.9 Schroeder Frequency for the Curved Panel - Cavity System

The modal overlap index is given by (Sum & Pan 1998)

$$M_a = \Delta f_{3\mathrm{dB}} n_a(f) \tag{B.190}$$

where

$$\Delta f_{3\mathrm{dB}} = \frac{2.2}{T_{60}} \tag{B.191}$$

and

$$n_a(f) = \frac{4\pi V_0 f^2}{c_o^3} + \frac{\pi S f}{2c_o^2} + \frac{L}{8c_0} \tag{B.192}$$

Here f is the excitation frequency, $\Delta f_{3\mathrm{dB}}$ is the half-power band width of the cavity mode, L is the total edge lengths of the cavity, S is the total surface area of the cavity interior, V is the volume of the cavity and T_{60} is the cavity reverberation time. By definition the modal loss factor for the modal model is related to the half-power bandwidth by,

$$\eta_a = \frac{\Delta f_{3\mathrm{dB}}}{f} \tag{B.193}$$

Therefore the modal overlap is given by

$$M_a = \eta_a \left(\frac{4\pi V_0 f^3}{c_o^3} + \frac{\pi S f^2}{2c_o^2} + \frac{L f}{8c_0} \right) \tag{B.194}$$

For the cavity of dimensions 0.985m x 0.420m x 0.250m,

$$V = 0.1034\,\mathrm{m}^3$$

$$S = 1.530\,\mathrm{m}^2$$

$$L = 6.620\,\mathrm{m}$$

Substituting these parameters into the expression for the modal overlap gives

$$M_a = \eta_a \left(1.300x^3 + 2.403x^2 + 0.8275x \right) \tag{B.195}$$

where $x = \frac{f}{c_0}$. Now the modal overlap at the Schroeder frequency is 3. Setting $\eta_a = 0.1$ and solving the above expression gives the Schroeder frequency,

$$f_{\mathrm{Sch}} = 784\,\mathrm{Hz}$$

For $\eta_a = 0.02$ and the Schroeder frequency is

$$f_{\mathrm{Sch}} = 1470\,\mathrm{Hz}$$

Appendix C

Circuit Diagrams

Circuit Diagrams for the 3-D Energy Density Sensor

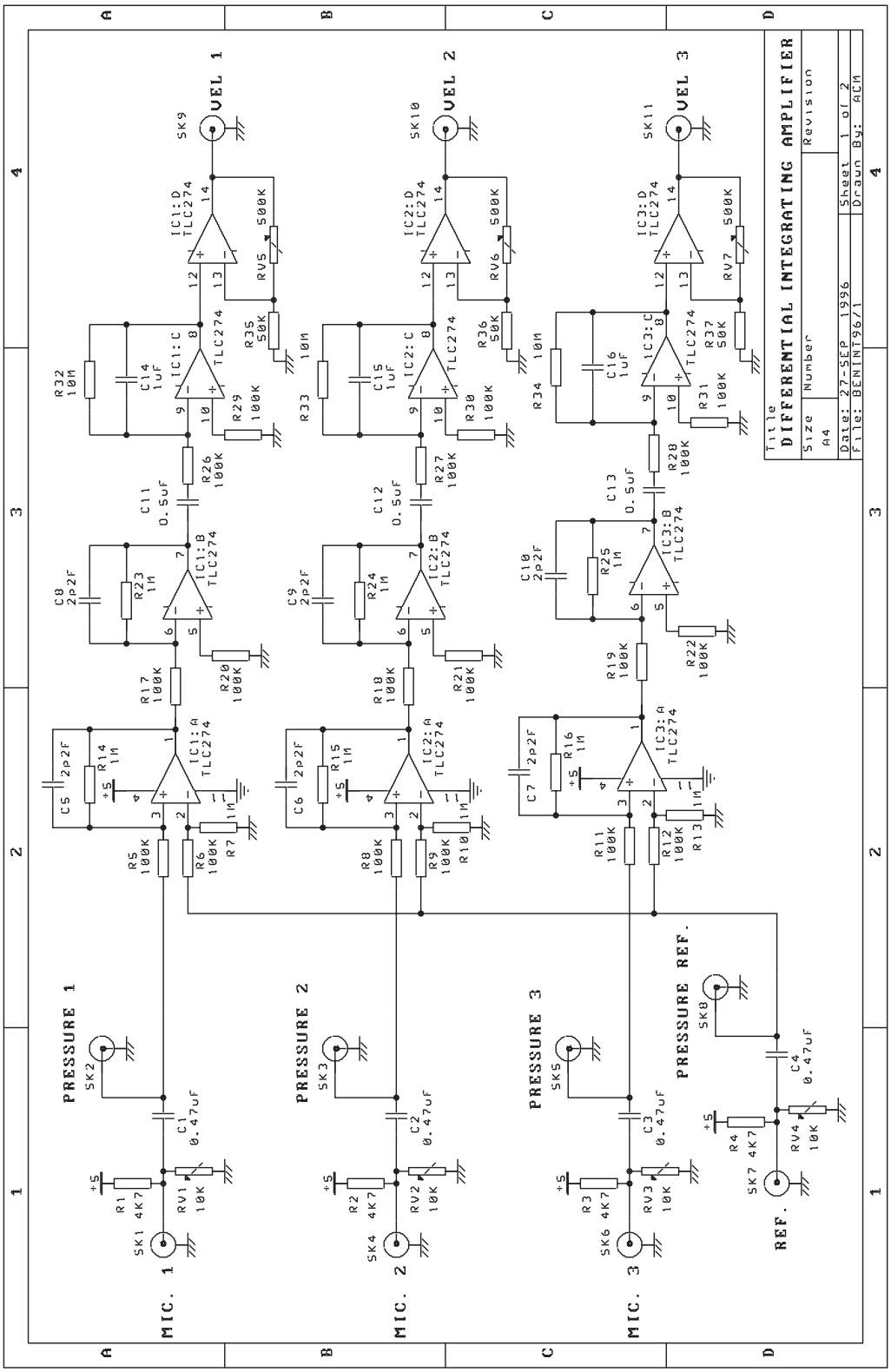

Circuit Diagram for the 3-D Energy Density Sensor

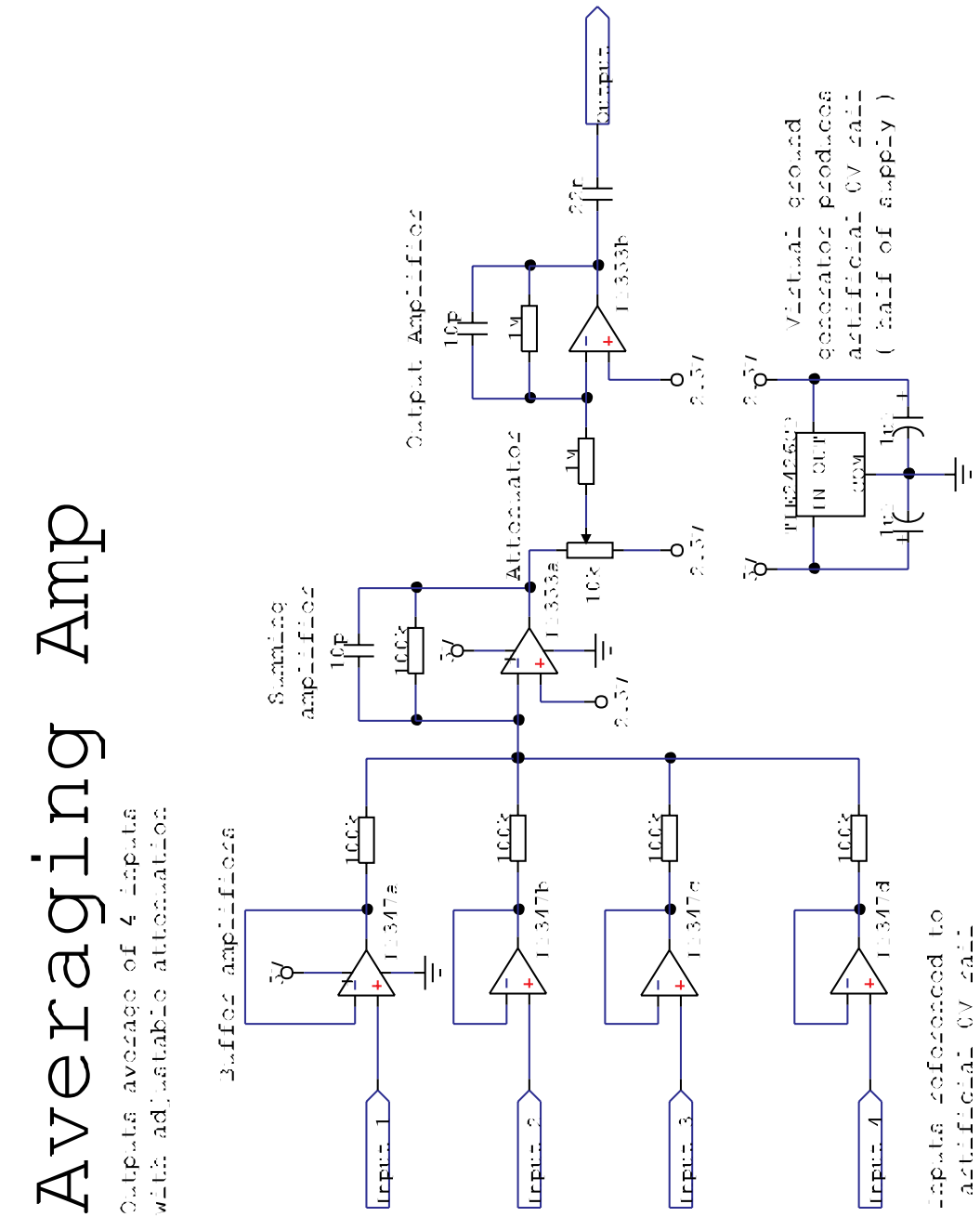

Circuit Diagram for the 4-Microphone Average

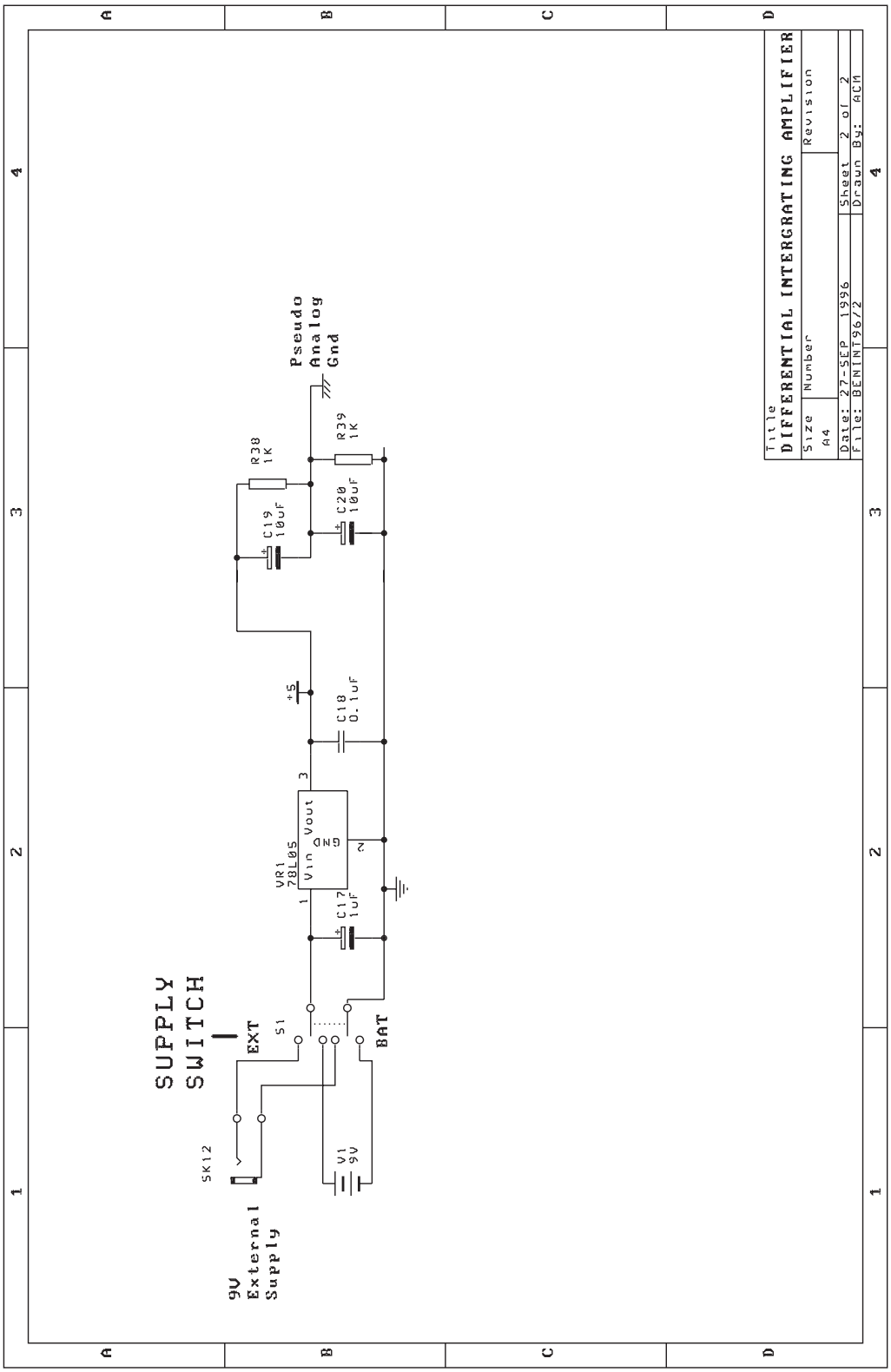

Circuit Diagram for the Power Supply

Circuit Diagrams for the Patch Board & Modal Summing Board

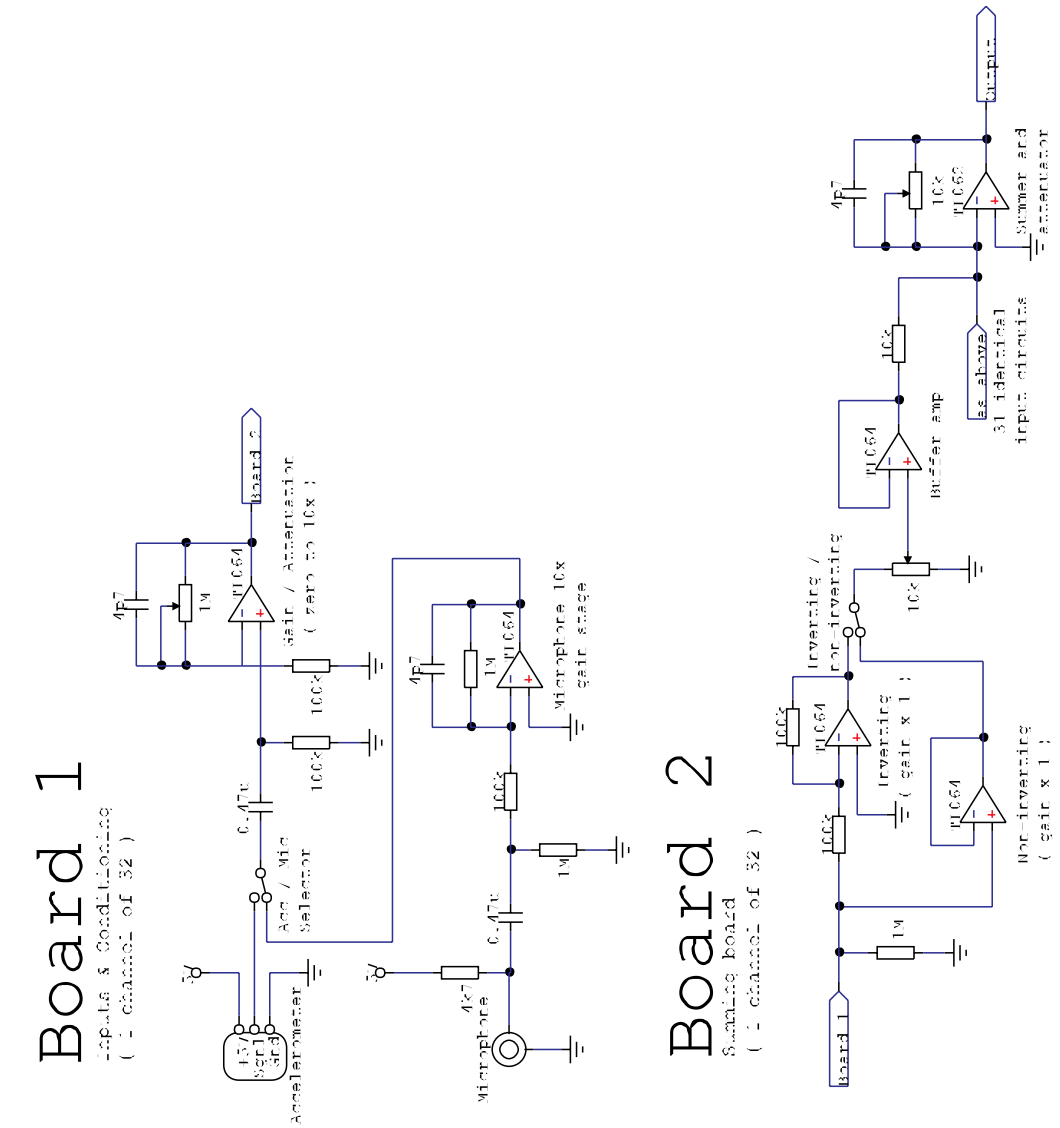

Circuit Diagram for a single channel on the Patch Board and Modal Summing Board

Appendix D

Publications Arising from this Thesis

Active control of sound transmission using structural error sensing

Ben S. Cazzolato and Colin H. Hansen
Department of Mechanical Engineering, The University of Adelaide, South Australia 5005, Australia

(Received 13 May 1997; revised 15 June 1998; accepted 28 July 1998)

The active minimization of harmonic sound transmission into an arbitrarily shaped enclosure using error signals derived from structural vibration sensors is investigated numerically. It is shown that by considering the dynamics of the coupled system, it is possible to derive a set of ''structural radiation'' modes which are orthogonal with respect to the global potential energy of the coupled acoustic space and which can be sensed by structural vibration sensors. Minimization of the amplitudes of the ''radiation modes'' is thus guaranteed to minimize the interior acoustic potential energy. The coupled vibro-acoustic system under investigation is modelled using finite element analysis which allows systems with complex geometries to be investigated rather than limiting the analysis to simple analytically tractable systems. Issues regarding the practical implementation of sensing the orthonormal sets of structural radiation modes are discussed. Specific examples relating to the minimization of the total acoustic potential energy within a longitudinally stiffened cylinder are given, comparing the performance offered using error sensing of the radiation modes on the structure against the more traditional error criteria; namely, the discrete sensing of the structural kinetic energy on the boundary and the acoustic potential energy in the enclosed space. [S0001-4966(98)02211-5]

PACS numbers: 43.50.Ki [GAD]

INTRODUCTION

The use of vibration control sources to minimize sound transmission through lightweight structures into coupled enclosures offers two advantages over the use of more conventional acoustic sources: fewer secondary sources are generally required for global control of the interior noise field;[1] and surface mounted actuators are far less intrusive than bulky speaker/cabinet arrangements. However, the gains in system compactness are not necessarily realized in practice when microphones placed throughout the cavity are used to provide the controller error signals to achieve global control.

As an alternative, surface mounted structural vibration sensors have also been used as error sensors and, although a reduction in the vibration of the structure has been achieved, a reduction in the interior sound field did not necessarily follow, particularly at low frequencies where the modal density is low.[2] Clearly a control system using structural error sensors to directly measure the surface vibration is unsuitable for the control of sound transmission. However, it has been shown recently that is possible to calculate a quantity from the vibration of the structure which is directly proportional to the sound radiated into the enclosed space.[3]

This paper develops a procedure in which the sound transmission from a structure into an enclosed space can be sensed using structural vibration error sensors. It draws from the work of previous researchers who have investigated the sound power radiated into free field from vibrating beams,[4,5] plates,[6–12] and shells[13–17] using orthogonal surface velocity patterns, commonly referred to as acoustic ''radiation modes.'' The approach involves decomposing the surface vibration, usually via a singular value decomposition, into a number of surface velocity distributions which contribute independently to the radiated sound field. Snyder and Tanaka[3] have extended the work to include a brief study of the active control of sound transmitted into a coupled rectangular enclosure. However, their work failed to address many of the practical implementation issues discussed in this paper.

It has been shown that for both free-field radiation and transmission problems only a very limited number of radiation modes contribute to the sound radiated from the vibrating structure and it is the number of efficiently radiating modes, rather than the modal response of the structure, which defines the system dimensionality[13] and subsequently, the control system order. Distributed parameter modal sensors called ''smart sensors'' may then be employed to measure the modal amplitudes of the radiation modes and to provide inputs into an active control system.[18,19]

The use of independent (orthogonal) error signals for active noise control problems has been shown to offer a number of practical advantages, as it can: reduce convergence time for controllers; provide robustness to system parameter uncertainty; and minimize the number of sensors and actuators, and corresponding system dimensionality.[20,21]

The primary objective of the work described here was to extend the technique of active control of sound transmission into enclosures using radiation modal control, to the point where it may be used in a real active control system.

A second objective was to investigate the mechanisms of sound transmission into a stiffened cylindrical enclosure and the subsequent implications on the design and performance of active systems for controlling sound transmission through the boundaries. It is shown that the interior radiation mode shapes are frequency dependent. This makes the application of modal control very difficult for real systems. A new technique for overcoming this application problem is derived which allows the use of fixed shape modal sensors.

A third objective was to determine the most suitable means of sensing radiation modes using structural vibration measurements. Both discrete and continuous shaped sensors have been investigated for use as modal sensors, with the latter being more practical for large, modally dense (structural) systems.

The active control of sound transmission into a longitudinally stiffened cylinder with an integral floor, excited by an external vibration source is investigated numerically to illustrate the implementation of the extended technique and to gain some understanding of the associated physical processes. The structure and the acoustic space enclosed by the cylinder have been modeled numerically using the commercially available finite element package ANSYS, which has enabled the investigation to be extended to geometrically complex, modally dense systems that are typically found in most real situations.

I. GENERAL THEORY

In this section the theory of sound transmission through a structure into a contiguous cavity is developed. The transmitted sound field is derived in terms of radiation modes and the implications for structural vibration sensing of the radiation modes is also discussed. Using the modal-interaction approach to the solution of coupled problems, the response of the structure is modeled in terms of its *in vacuo* mode shape functions and the response of the enclosed acoustic space is described in terms of the rigid-wall mode shape functions.[22] The response of the coupled system is then determined by solving the modal formulation of the Kirchhoff–Helmholtz integral equation.

A. Global error criteria

An appropriate global error criterion for controlling the sound transmission into a coupled enclosure is the total time-averaged frequency-dependent acoustic potential energy, $E_p(\omega)$, in the enclosure[23]

$$E_p(\omega)=\frac{1}{4\rho_0 c_0^2}\int_V |p(\mathbf{r},\omega)|^2 d\mathbf{r}, \tag{1}$$

where $p(\mathbf{r},\omega)$ is the acoustic pressure amplitude at some location $\mathbf{r}$ in the enclosure, ρ_0 is the density of the acoustic fluid (air), c_0 is the speed of sound in the fluid, and V is the volume over which the integral is evaluated. The frequency dependence, ω, is assumed in the following analysis but this factor will be omitted in the equations for the sake of brevity. Using the modal interaction approach to the problem,[22] the acoustic pressure at any location within the cavity is expressed as an infinite summation of the product of rigid-wall acoustic mode shape functions, ϕ_i, and the modal pressure amplitudes, p_i, of the cavity

$$p(\mathbf{r})=\sum_{i=1}^{\infty} p_i \phi_i(\mathbf{r}). \tag{2}$$

The modal expansion for the acoustic potential energy evaluated over n_a acoustic modes is then given by

$$E_p=\mathbf{p}^H \mathbf{\Lambda} \mathbf{p}, \tag{3}$$

where $\mathbf{p}$ is the $(n_a\times 1)$ vector of acoustic modal amplitudes and $\mathbf{\Lambda}$ is a $(n_a\times n_a)$ diagonal weighting matrix, the diagonal terms of which are

$$\Lambda_{ii}=\frac{\Lambda_i}{4\rho_0 c_0}, \tag{4}$$

where Λ_i is the modal volume of the ith cavity mode, defined as the volume integration of the square of the mode shape function,

$$\Lambda_i=\int_V \phi_i^2(\mathbf{r})\, dV(\mathbf{r}). \tag{5}$$

The pressure modal amplitudes, $\mathbf{p}$, within the cavity, arising from the vibration of the structure are given by the product of the $(n_s\times 1)$ structural modal velocity vector, $\mathbf{v}$, and the $(n_a\times n_s)$ modal structural-acoustic radiation transfer function matrix,[24] $\mathbf{Z}_a$,

$$\mathbf{p}=\mathbf{Z}_a \mathbf{v}. \tag{6}$$

The l, ith element of the radiation transfer function matrix $\mathbf{Z}_a$ is the pressure amplitude of the acoustic mode l generated as a result of structural mode i vibrating with unit velocity amplitude. Substituting Eq. (6) into Eq. (3) gives an expression for the acoustic potential energy with respect to the normal structural vibration,

$$E_p=\mathbf{v}^H \mathbf{\Pi} \mathbf{v}, \tag{7}$$

where the error weighting matrix $\mathbf{\Pi}$ is given by

$$\mathbf{\Pi}=\mathbf{Z}_a^H \mathbf{\Lambda} \mathbf{Z}_a. \tag{8}$$

It should be noted that the error weighting matrix $\mathbf{\Pi}$ is not necessarily diagonal, which implies that the normal structural modes are not orthogonal contributors to the interior acoustic pressure field. It is for this reason that minimization of the modal amplitudes of the individual structural modes (or kinetic energy) will not necessarily reduce the total sound power transmission.

B. Diagonalization of the error criteria

As $\mathbf{\Pi}$ is real symmetric, it may be diagonalized by the orthonormal transformation;

$$\mathbf{\Pi}=\mathbf{U}\mathbf{S}\mathbf{U}^T, \tag{9}$$

where the unitary matrix $\mathbf{U}$ is the (real) orthonormal transformation matrix representing the eigenvector matrix of $\mathbf{\Pi}$ and the (real) diagonal matrix $\mathbf{S}$ contains the eigenvalues (singular values) of $\mathbf{\Pi}$. The physical significance of the eigenvectors and eigenvalues is interesting. The eigenvalue can be considered a radiation efficiency (or coupling strength[25]) and the associated eigenvector gives the level of participation of each normal structural mode to the radiation mode; thus it indicates the modal transmission path.[25]

Substituting the orthonormal expansion of Eq. (9) into Eq. (7) results in an expression for the potential energy of the cavity as a function of an orthogonal radiation mode set,

$$E_p=\mathbf{v}^H \mathbf{U}\mathbf{S}\mathbf{U}^T \mathbf{v}=\mathbf{w}^H \mathbf{S} \mathbf{w}, \tag{10}$$

where the elements of **w** are the velocity amplitudes of the radiation modes defined by

$$\mathbf{w}=\mathbf{U}^T\mathbf{v}. \tag{11}$$

Equation (11) demonstrates that each radiation mode is made up of a linear combination of the normal structural modes, the ratio of which is defined by the eigenvector matrix **U**. As the eigenvalue matrix, **S**, is diagonal, Eq. (10) may be written as follows:

$$E_p=\sum_{i=1}^{n} s_i|w_i|^2, \tag{12}$$

where s_i are the diagonal elements of the eigenvalue matrix **S** and w_i are the modal amplitudes of the individual radiation modes given by Eq. (11).

The potential energy from any radiation mode is equal to the square of its amplitude multiplied by the corresponding eigenvalue. The radiation modes are therefore independent (orthogonal) contributors to the potential energy and the potential energy is directly reduced by reducing the amplitude of any of the radiation modes. As mentioned previously, the normal structural modes are not orthogonal radiators since the potential energy arising from one structural mode depends on the amplitudes of the other structural modes. The orthogonality of the radiation modes is important for active control purposes as it guarantees that the potential energy will be reduced if the amplitude of any radiation mode is reduced.[10]

C. Advantages of diagonalization

For shells radiating into free space,[6,7,13,17] the eigenvalues of the radiation modes rapidly decrease in magnitude with respect to the largest eigenvalue. Therefore, in practice it is necessary to only include the first few (efficient) radiation modes with the largest radiation efficiencies to account for majority of the sound power radiated from the structure into the free field. The same principle applies for interior radiation modes. When calculating the transmission of sound from the structure into the cavity only the few most efficient radiation modes need to be used in the transmission loss calculations. It is therefore possible to neglect the nonefficient radiation modes with no appreciable loss in accuracy of the transmission loss estimates.

With the acoustic potential energy in the form of Eq. (12) the above property can be exploited. Therefore, if only the first n_r terms in the eigenvalue matrix are of significance (say greater than 1% of the maximum), then the error weighting matrix may be approximated by[5]

$$\mathbf{\Pi}\approx\sum_{i=1}^{n_r} s_i\mathbf{u}_i\mathbf{u}_i^H, \tag{13}$$

which in matrix form yields

$$\mathbf{\Pi}\approx\mathbf{U}\mathbf{S}\mathbf{U}^T, \tag{14}$$

where $\mathbf{S}\approx\mathrm{diag}(s_1,s_2,...,s_{n_r})$ is a $(n_r\times n_r)$ matrix and $\mathbf{U}\approx[\mathbf{u}_1,\mathbf{u}_2,\ldots,\mathbf{u}_{n_r}]$ is a $(n_s\times n_r)$ matrix.

It is in this truncation of the system equations where the benefits of using radiation modes to provide error signals in active control systems become apparent. For example, ''real'' systems tend to be modally dense structures with several hundred normal structural modes contributing to the overall response of the structure. It will be shown that it is possible to truncate the radiation matrix used in the simulations from a (200×200) matrix to a (5×5) matrix with almost no loss in accuracy. This greatly reduces both the computation times for the simulation and the complexity of the physical control system.

D. Structural sensing of radiation modes

To evaluate the potential energy using Eq. (12) it is necessary to know the amplitudes of the radiation modes. The process of extracting the amplitudes of radiation modes from measurements of the structural vibration, known as modal filtering, is discussed in detail by Tanaka *et al.*[19] and relies on the principle of orthogonality, i.e.,

$$\int_S \theta_m(\mathbf{r})\,\theta_n(\mathbf{r})\,dS=\begin{cases}0, & m\neq n,\\ 1, & m=n,\end{cases} \tag{15}$$

where θ_m is the mth mode of some orthogonal set of natural modes. Post multiplying Eq. (15) by the mth modal velocity, w_m, and summing over all modes gives

$$\int_S v(\mathbf{r})\,\theta_m(\mathbf{r})\,dS=w_m, \tag{16}$$

where $v(\mathbf{r})=\Sigma_{i=1}^{\infty}w_i\theta_i(\mathbf{r})$ is the velocity of the structure at some location **r**. The modal filters can be constructed by implementing Eq. (16) in its discrete form using weighted measurements of the structural vibration at discrete locations, or in a continuous form using shaped sensors such as piezo-electric film.

An alternative approach to modal filtering described above uses a least-squares formulation rather than numerical integration and is derived below in matrix form for discrete sensors which are a subset of continuous sensors. The structural velocity levels at the (n_e) discrete error sensor locations are given by the following finite matrix modal expansion,

$$\mathbf{v}_e=\mathbf{\Psi}_e\mathbf{v}, \tag{17}$$

where $\mathbf{v}_e$ is the $(n_e\times1)$ vector of velocity levels for the sensors and $\mathbf{\Psi}_e$ is the $(n_e\times n_s)$ mode shape matrix at the sensor locations. The normal structural modal amplitudes are then given by

$$\mathbf{v}=\mathbf{\Psi}_e^{-1}\mathbf{v}_e. \tag{18}$$

Inserting Eq. (18) into (11), an expression is obtained for the velocity amplitudes of the radiation modes as a function of the velocity levels at the error sensor locations

$$\mathbf{w}=\mathbf{Z}_t\mathbf{v}_e, \tag{19}$$

where $\mathbf{Z}_t$ is the $(n_r\times n_e)$ radiation mode structural transfer function matrix (or modal filter matrix) which relates the vibration velocity levels at the discrete error sensor locations to the modal velocity amplitudes of the radiation modes and is given by

$$\mathbf{Z}_t=\mathbf{U}^T\mathbf{\Psi}_e^{-1}. \tag{20}$$

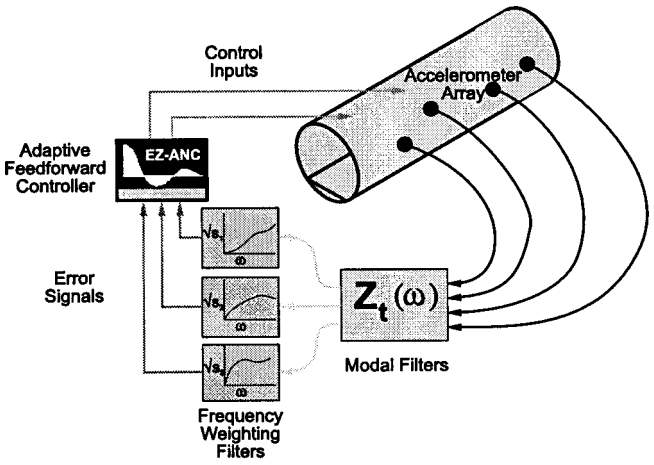

FIG. 1. Schematic of modal and eigenfilter for an ANVC system.

The elements of each row of this modal filter matrix represent a weighting value, which when applied to the signal from the vibration sensors and summed for all sensors, will provide a measure of the amplitudes of the radiation modes.

The expression for the velocity at any point on the surface of the structure given by Eq. (17) can be expanded, using the properties of a unitary matrix and Eq. (11), to give the following:

$$\mathbf{v}_e = \mathbf{\Psi}_e \mathbf{U}\mathbf{U}^{-1}\mathbf{v} = \mathbf{\Psi}_e \mathbf{U}\mathbf{U}^{T}\mathbf{v} = [\mathbf{\Psi}_e \mathbf{U}]\mathbf{w}. \tag{21}$$

It follows that the term $\mathbf{\Psi}_e\mathbf{U}$ in Eq. (21) is the mode shape matrix of the radiation modes evaluated at the n_e error sensor locations, $\mathbf{\Theta}_e$. Therefore, the radiation mode shape is obtained by post-multiplying the mode shape matrix of the normal structural modes by the eigenvector matrix, i.e.,

$$\mathbf{\Theta} = \mathbf{\Psi}\mathbf{U}. \tag{22}$$

In most practical systems the number of discrete error sensors (n_e) will be much less than the number of significant normal structural modes (n_s); therefore, the error sensor mode shape matrix, $\mathbf{\Psi}_e$, will be underdetermined. It is therefore necessary to evaluate the inverse via a pseudo (least squares) inverse. Note that this technique is an approximation and will reduce the fidelity of the sensing system much like evaluating Eq. (16) over some subspace of the surface rather than the complete surface. It is shown in the following section that the reduction in sensor fidelity will lead to a reduction in controller performance.

The practical implementation of the control system may look something like that shown in Fig. 1, where an accelerometer array would be used to measure the velocity levels on the surface of the shell. The modal filters, $\mathbf{Z}_t$, given by Eq. (20) would be used to decompose the velocity signal to modal amplitudes of the radiation modes. The frequency weighting (eigenvalue) filters, **S**, would then be used to weight the modal amplitudes to provide inputs to the controller.

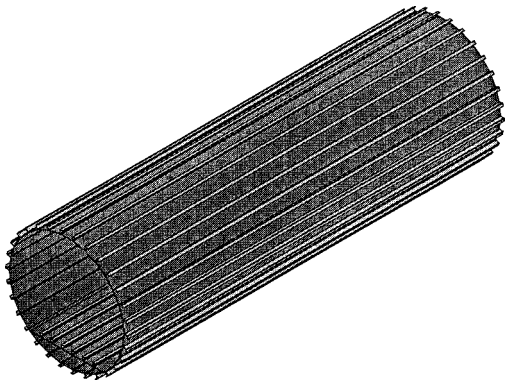

FIG. 2. Solid model of the longitudinally stiffened cylinder with an integral floor.

II. SOUND TRANSMISSION THROUGH A STIFFENED CYLINDER

The active control of sound transmission through the 3.0-m-long, 0.9-m-diam longitudinally stiffened cylinder with an integral floor shown in Fig. 2 has been investigated. The floor was rigidly fixed to the shell and subtended an angle of 80 degrees. The shell was constructed from 1-mm-thick stainless steel with 30 longerons around the circumference of the cylinder and 6 along the floor. The boundary conditions of the ends of the structure were shear diaphragm and the acoustic boundary conditions of the end caps were rigid. Damping of the system was light with the modal loss factor for both the structure and the cavity set to 2%.

Studies of the importance of representative structural models for aircraft interior acoustics have shown that it is necessary to account for the stiffness and mass provided by stiffeners attached to the skin as well as interior structures such as the floor. Omitting to account for such elements leads to poor correlation between the numerical model and experimental results.[26] Therefore the geometry of the cylinder was designed to reflect the complex, modally dense nature of a typical fuselage.

A. Finite element analysis

The cylinder and the contiguous acoustic space were modeled separately using the FEA package ANSYS, then coupled using modal coupling theory[22] within MATLAB. The FE models of the structure and the cavity are shown in Fig. 3

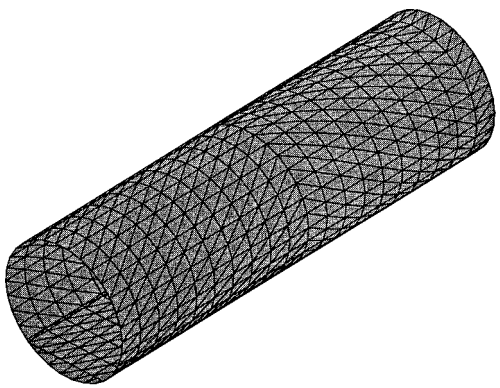

FIG. 3. Finite element model of the structure.

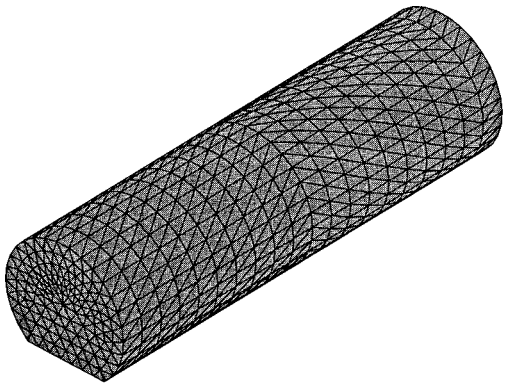

FIG. 4. Finite element model of the acoustic space.

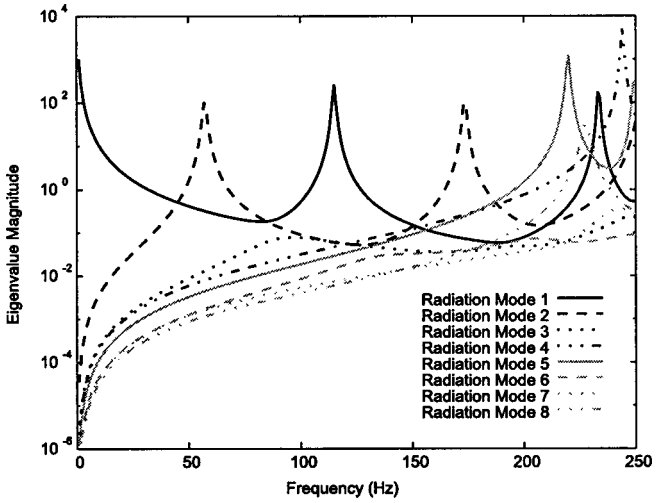

FIG. 5. Eigenvalue magnitudes (radiation efficiencies) for the first eight radiation modes.

and Fig. 4, respectively. The structural FE model consisted of 2280 triangular shell elements and 4032 degrees of freedom. The C-section longerons attached to the shell were modeled using 3-D beam elements. The acoustic model consisted of 11 242 acoustic tetrahedral elements and 2341 degrees of freedom.

ANSYS has the facilities to analyze a fully coupled vibroacoustic system. However, a fully coupled approach results in an unsymmetric system of equations, the solution of which is computationally intensive. In the interests of keeping the model size manageable and keeping track of the modal coupling mechanisms, it was decided to analyze the two subsystems individually, then post-couple the two modal models using the modal interaction approach.[22] The structural and acoustic models have been meshed with coincident nodes to facilitate coupling of the FE models in MATLAB. This resulted in an excessively fine acoustic model but did not significantly extend the time taken for the forced response analysis.

The first 50 acoustic modes and the first 400 normal structural modes were extracted using the finite element model described previously. The natural frequencies of the lowest 10 acoustic modes are shown in Table I.

Cunefare and Currey[4] found that the low order (free-space) radiation modes of rectangular panels converge quickly to their true shape after considering only a limited number of structural modes. It was found in the work discussed in the paper that this is not the case for interior radiation modes of a complex three-dimensional structure and many hundreds of modes (400) were required to achieve partial convergence to the ''true'' shape of the radiation mode.

TABLE I. Natural frequencies of the first ten acoustic modes.

Mode	Natural frequency (Hz)
0	0
1	57
2	117
3	173
4	220
5	228
6	233
7	244
8	250
9	251

When calculating the sound transmission from the structure into the enclosed space it was only necessary to consider the structural modes that were resonant or close to resonance within the frequency bandwidth of interest, namely 0 to 250 Hz. Therefore, for the sake of computational efficiency, only 100 structural modes were used during the simulation to calculate the system response.

B. Radiation modes—mode shapes and radiation efficiencies

The eigenvalues and eigenvectors of the radiation matrix were calculated within MATLAB using the method and model outlined above. A singular value decomposition (SVD) was used to calculate the orthonormal transformation of the radiation matrix rather than other eigenextraction routines because of the singular nature of the problem. As the radiation efficiencies of the radiation modes rapidly approach zero, the condition number of the matrices becomes infinite and thus ill-conditioned. This being the case, many of the other techniques which use simple eigenroutines to construct the orthonormal radiation mode set, such as Gram–Schmidt orthogonalization, suffer severely from round-off problems.

The eigenvalues for the first eight (most efficient) radiation modes are shown as a function of frequency in Fig. 5. As can be seen, the eigenvalues are very frequency dependent with the peaks in the radiation efficiency corresponding to the natural frequencies of the cavity. Figure 5 shows qualitatively that in general (at least at low frequencies) a single radiation mode will dominate the sound transmission from the structure into the acoustic space. It is this property that enables significant control within a limited frequency range to be achieved by controlling a single radiation mode. It should be noted that at the ''crossover'' frequencies where two radiation modes have the same eigenvalue, there will be at least two radiation modes contributing to the sound transmission into the cavity. It is not critical that the active control system perform optimally in the crossover regions as

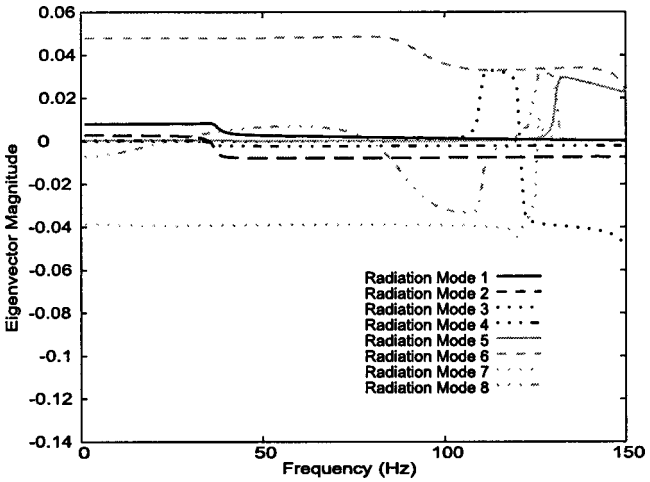

FIG. 6. First eight eigenvectors for the eleventh structural mode.

these regions are likely to occur at frequencies where the radiation efficiencies are low and therefore the sound transmission is also low.

The frequency dependence is also reflected in the eigenvectors, with particularly high variation at the ''crossover'' frequencies where there is a change in the ranking of eigenvalues. Physically, this means that the shape of the modal sensors used to measure the radiation modal amplitude is frequency dependent. As an example, the eigenvector weighting of the first eight radiation modes for the eleventh normal structural mode is shown in Fig. 6. This weighting is typical for all the normal structural modes and demonstrates how the importance of each normal structural mode alters with respect to frequency as the response of the acoustic space is dominated by different acoustic modes.

As very few radiation modes contribute to the sound transmission, only a few low order IIR filters are needed to implement the frequency dependent eigenvalues. However, due to the large number of structural modes needed to derive the radiation modes, the frequency dependence of the eigenvectors (mode shapes) presents a significant burden for practical implementation of the control system shown in Fig. 1. Obviously, because of the frequency dependence of the radiation mode shapes, the modal amplitudes of these modes can only be calculated through discrete sensors weighted with digital filters rather than using fixed shape sensors. This

FIG. 8. Mode shape of the most efficient radiation mode at 117 Hz.

effectively prohibits the calculation of the modal amplitudes using Eq. (20) for all but the simplest physical systems. Consider for example the particular case, where 5 radiation modes are to be controlled using 16 tap IIR filters, upward of 8000 (5 radiation modes$\times$16 taps$\times$100 sensors) multiplications may be required, presenting a significant burden even for high speed DSPs. A technique for overcoming this limitation is detailed in Sec. III.

The mode shape functions of the most efficient radiation modes calculated for the stiffened cylinder model, at 57 Hz and 117 Hz (corresponding to the natural frequencies of the first two acoustic modes) were derived using Eq. (22). These are shown in Figs. 7 and 8 in an exploded format to show more clearly the vibration profile of the floor. It becomes apparent that the radiation modes reflect the dominant acoustic modes at the driving frequency, as shown in Figs. 9 and 10.

As the floor of the cylinder is significantly more compliant than the shell, the modal masses of the majority of the structural modes are dominated by the floor motion. Subsequently, the calculated radiation mode shapes are more accurate for the floor than for the rest of the shell. If a greater number of structural modes were used to estimate the radiation mode shapes, then the shell motion would more closely resemble that of the dominant acoustic mode shape.

When compared to the normal structural modes of similar frequency (see Figs. 11 and 12) the radiation modes have a much lower circumferential wave number. This property is beneficial when implementing modal sensing for the control

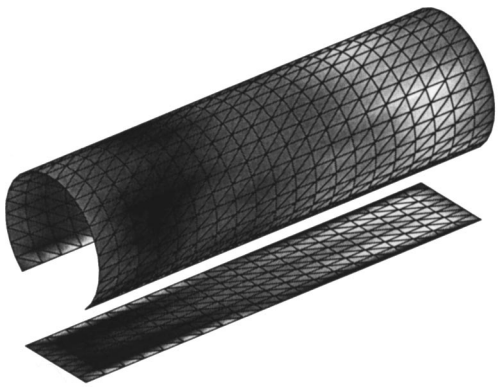

FIG. 7. Mode shape of the most efficient radiation mode at 57 Hz.

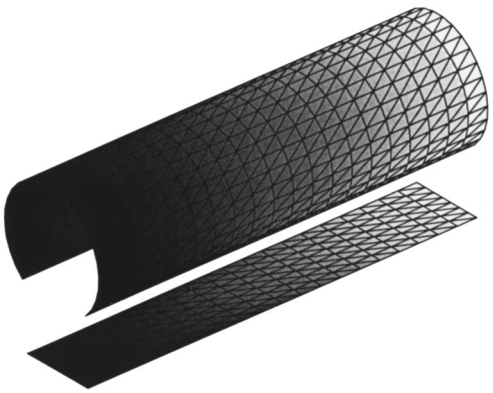

FIG. 9. Mode shape of the first acoustic mode (57 Hz).

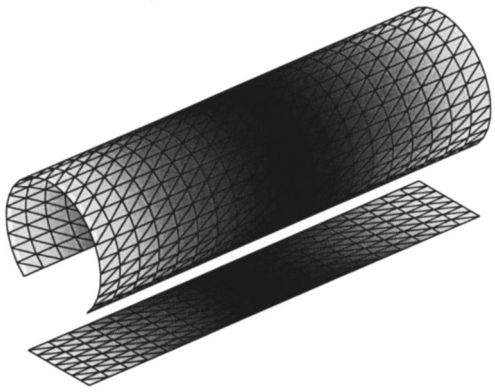

FIG. 10. Mode shape of the second acoustic mode (117 Hz).

FIG. 12. Mode shape of the fourth normal structural mode (34 Hz).

system, as modes with lower wave numbers are easier to measure with distributed modal sensors.

It is not surprising that the structural radiation mode shape functions are similar to the mode shapes of the dominant acoustic modes at the structure boundary, for it is well known that the coupling efficiency between acoustic and structural modes is high when the acoustic and structural mode shape functions are similar. This has important implications when it comes to designing the control system. Instead of calculating the radiation modes as was done in Sec. I, for structural/acoustic systems with ''regular'' geometries, it may be adequate to assume the radiation mode shape function is the same as the acoustic mode shape function as a first approximation.

It is also interesting to note that the calculation of the radiation mode shapes allows identification of regions of high power transmission (which are not necessarily colocated with the areas of maximum structural vibration). It may be possible to use this information prudently to optimize the location of structural control sources.

When the eigenvalues corresponding to a particular excitation frequency are returned by the eigensolver, they are always sorted in either ascending or descending order with respect to the magnitudes. This ''ranking'' of the eigenvalues and eigenvectors has the benefit of arranging the modes from the biggest contributors to the sound transmission to the smallest. Therefore, only the important modes are sensed and controlled which leads to a reduction in the number of error and control signals required by the control system.

FIG. 11. Mode shape of the third normal structural mode (33 Hz).

For example, the ranked eigenvalues for the first eight (most efficient) radiation modes are shown in Fig. 13. It can be seen that the ranking of the eigenvalues creates a discontinuity in the slope of the eigenvalues at the crossover frequencies. This manifests itself as step changes in the modes shapes of the radiation modes, so the mode shape of the most efficient mode at 40 Hz does not resemble the mode shape of the most efficient mode at 60 Hz.

In comparing Fig. 5 and Fig. 13, it can be seen that with the radiation modes ranked with respect to their radiation efficiencies, only two radiation modes need to be considered at each frequency up to 250 Hz to account for most of the sound transmission, otherwise six or seven ''unranked'' radiation modes would need to be considered to account for a similar level of sound transmission.

It should be noted that because of the discontinuities in the slope of the ranked eigenvalues at the crossover frequencies, a greater number of taps in the digital filters used to shape the error signal input to the controller (see Fig. 1) are required. However, the system requirements are not significantly greater than for the unranked case because fewer (ranked) radiation modes contribute to the sound transmission.

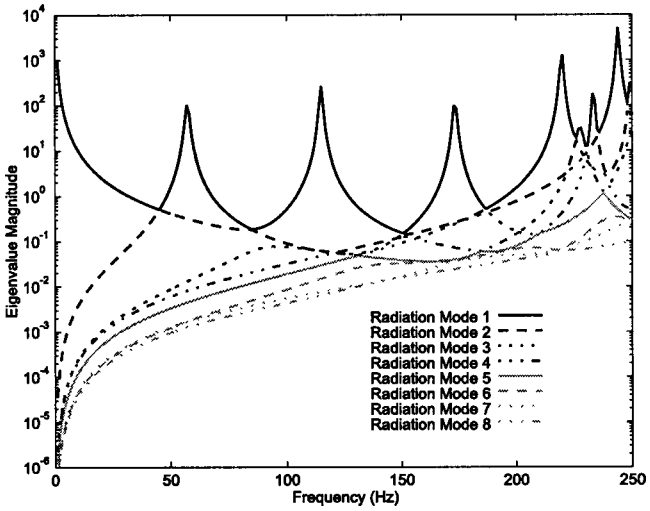

FIG. 13. Calculated (ranked) eigenvalue magnitudes of the first eight most efficient radiation modes.

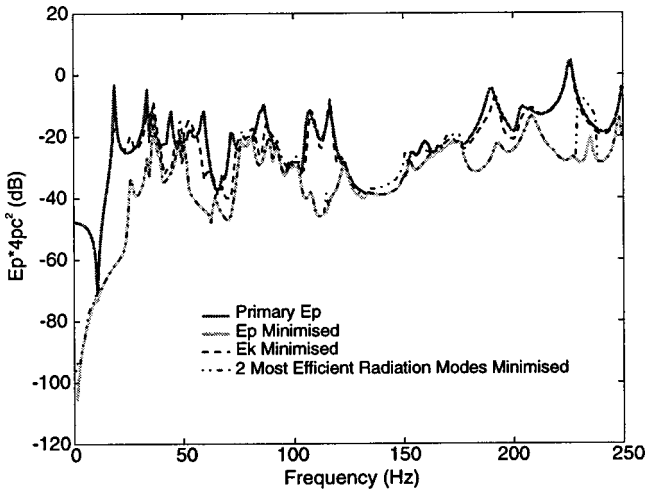

FIG. 14. Reduction in acoustic potential energy—Conventional error criteria versus radiation modal sensing.

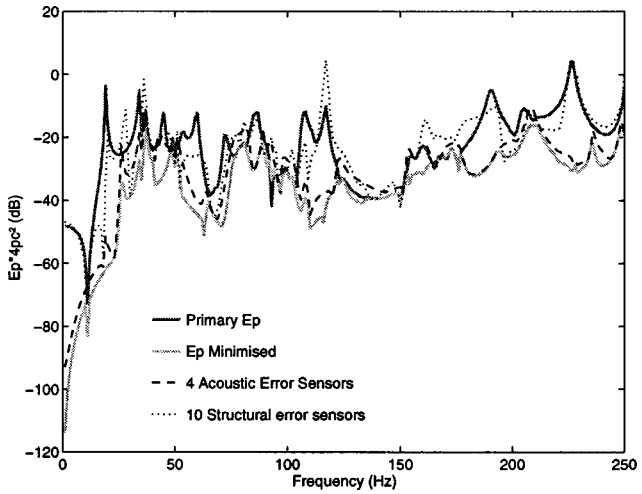

FIG. 15. Effect of insufficient structural sensors on performance and Control using four acoustic error sensors.

C. Active control of sound transmission—traditional error criteria versus radiation modes

A simulation was conducted where a single point force was placed randomly in a nonsymmetric location on the outside of the cylinder to provide the primary excitation source (78° at 1.35 m). A single secondary source was symmetrically located with respect to the floor on the shell to provide the control force (258° at 1.35 m). It should be noted that the location of the control force was not optimized in any way as this was not the aim of the study. The research objective was to show that it is possible to use a structural error sensor to provide an error signal which would result in a similar reduction in enclosure potential energy as obtained by using the enclosure potential energy as the error signal.

Figure 14 compares the reduction in the acoustic potential energy obtained when minimizing the two most efficient radiation modes against that obtained using conventional error criteria; namely, the acoustic potential energy (which provides an upper limit of control performance) and the structural kinetic energy. The cost function of Eq. (12) was optimized using conventional quadratic optimization to determine the optimum control force magnitude and phase. The velocity amplitudes of the radiation modes were estimated using the modal filter matrix given by Eq. (19). There were as many error sensors (100) as normal structural modes used to calculate the modal filter matrix (of the radiation modes) so as to provide an upper bound on the performance offered by the technique. A lesser number would have required the use of a pseudo-inverse to evaluate Eq. (20) which would have resulted in a decrease in the control performance. At the frequencies where the eigenvalues cross (in Fig. 13) there is an increase in the potential energy as a result of minimizing the amplitudes of the two radiation modes. This occurs for two reasons: (1) As several radiation modes contribute to the power transmission at these crossover frequencies, a single control force (used in the simulation) is unable to provide enough independent control channels to achieve control. Subsequently, the amount of control is low for all cost functions. The corollary is that the reduction in sound transmission is greatest where the radiation efficiencies peak. (2) Insufficient radiation modes were used to measure the power transmission, and this is particularly apparent in the frequency bands 140–160 Hz and 230–240 Hz. If more modes were used then the controlled levels would approach that of the potential energy controlled case.

It will be shown in the following section, for the frequency range of interest, that it is sufficient to consider only the first five dominant radiation modes (see Fig. 13) to achieve attenuation levels equal to those achieved by using the potential energy as a cost function.

Figure 15 shows the effect of having significantly fewer error sensors than the number of dominant structural modes. A practical number of ten error sensors were randomly located around the circumference of the cylinder and on the floor. As can be seen in this example, ten error sensors were insufficient to accurately resolve the modal amplitudes of the normal structural modes, resulting in observation spillover. In fact, it was found that it was necessary to have at least half the number of error sensors (50) as normal structural modes before an acceptable estimate of the structural modal amplitudes using Eq. (18) was obtained. This limitation associated with discrete error sensing has also been reported by others.[19,21]

Also shown in Fig. 15 is the acoustic potential energy when the squared sum of four acoustic error sensors is used as the error criterion. When comparing Fig. 15 against modal control in Fig. 14, it becomes clear that two radiation modal sensors outperform four traditional pressure field sensors (provided a sufficient number of structural sensors are used to properly measure the radiation modes). One may argue that it is not valid to draw comparisons between a structural system with 50–100 point sensors and an acoustic system with only 4 sensors. However, it should be noted that for active control applications it is the number of error signals, be they composite or point sensors, which define the system dimensionality.

The conclusion is that error signals derived from the radiation modes outperform conventional structural and acoustic error sensing and that excellent control is achieved with very few error signals. Although the radiation mode

formulation as it is described above using many discrete error sensors is unworkable for a practical control system because of the frequency dependence of the eigensystem and the large number of point sensors required, it can be used as a benchmark against which the performance of simplifications can be compared. The limitation arising from the frequency dependence will be addressed and techniques for overcoming it will be presented in the following section.

III. PRACTICAL IMPLEMENTATION AND APPROXIMATIONS

A. Background theory

As already shown in the preceding section, the eigenvalue and eigenvector matrices are highly frequency dependent and it is possible in a practical control system to generate an eigenvalue filter set using a low order digital filter for each radiation mode. However, the same cannot be said about the eigenvector matrix. In the case of the cylinder, for each radiation mode of interest, the eigenvector filter would consist of several hundred individual frequency dependent digital filters, one filter for every structural sensor used to measure each radiation mode. It is difficult to store the necessary filter coefficients to model the eigenvector matrix over a large bandwidth and definitely beyond the ability of current DSP systems to implement such filters in real time. It is also impractical in most cases to implement the required number of physical error sensors.

Studies of the power flow from cylinders[16] and rectangular panels using either vibration error sensors[18] or acoustic error sensors[6] have found that by exploiting the property that the radiation mode shapes (eigenvectors) varied slowly with respect to frequency, it was possible to select a frequency such that the radiation mode shapes at that frequency were representative of the mode shapes over a frequency range with little loss in accuracy. This was achieved by fixing the radiation transfer function matrix to that at some desired frequency (known as the *normalization* frequency), *f*, resulting in a set of eigenvectors independent of frequency which can be implemented by a fixed gain. This greatly reduces the number of digital filters required for the control system.

Applying this approach to the current set of equations yields[6]

$$\mathbf{U}=\mathbf{K}\mathbf{U}_f, \tag{23}$$

where $\mathbf{U}_f$ is the eigenvector matrix corresponding to the chosen frequency, *f*, and $\mathbf{K}$ is a $(n_r \times n_r)$ correction matrix and is given by

$$\mathbf{K}=\mathbf{U}\mathbf{U}_f^{-1}. \tag{24}$$

The correction matrix is highly diagonal and by neglecting the off-diagonal terms there is little loss in accuracy; that is,

$$\mathbf{K}=\mathrm{DIAG}[\mathbf{U}\mathbf{U}_f^{-1}]. \tag{25}$$

Substituting Eq. (23) into Eq. (10), an expression for the potential energy is obtained;

$$E_p \approx \mathbf{v}^H\mathbf{U}_f^H\mathbf{S}\mathbf{U}_f\mathbf{v}, \tag{26}$$

where $\mathbf{S}_f$ is the frequency normalized eigenvalue matrix,

$$\mathbf{S}_f=\mathbf{K}^H\mathbf{S}\mathbf{K}. \tag{27}$$

Although the radiation modes for internal acoustic spaces exhibit a significantly greater frequency dependence than free-field radiation modes (at frequencies below the critical frequency) it is possible to apply the same technique here with surprisingly little degradation in performance.

A more elegant and accurate way of obtaining an ''orthonormal'' set of equations than just described is to diagonalize the eigenvalue matrix after it has been pre- and post-multiplied by the correction matrix. Thus the following expansion may be made:

$$\mathbf{U}\mathbf{S}\mathbf{U}^T=\mathbf{U}_f[\mathbf{U}_f^{-1}\mathbf{U}\mathbf{S}\mathbf{U}^T\mathbf{U}_f]\mathbf{U}_f^{-1}. \tag{28}$$

By using the property of the unitary matrix ($\mathbf{U}^{-1}=\mathbf{U}^T$) it is possible to rearrange Eq. (28) to derive a orthonormal basis independent of frequency

$$\mathbf{U}\mathbf{S}\mathbf{U}^T=\mathbf{U}_f[\mathbf{S}_f]\mathbf{U}_f^T, \tag{29}$$

where $\mathbf{S}_f$ is the fixed frequency eigenvalue matrix given by

$$\mathbf{S}_f=\mathbf{U}_f^T\mathbf{U}\mathbf{S}\mathbf{U}^T\mathbf{U}_f. \tag{30}$$

In this format the eigenvalue matrix is not diagonal (except at the normalization frequency) but fully populated. It is therefore necessary to diagonalize the fixed frequency eigenvalue matrix to retain the benefits associated with the orthonormal transformation:

$$\hat{\mathbf{S}}_f=\mathrm{DIAG}[\mathbf{U}_f^T\mathbf{U}\mathbf{S}\mathbf{U}^T\mathbf{U}_f]. \tag{31}$$

As with the diagonalization of Eq. (24), very little loss in mass (accuracy) occurs when diagonalizing the highly diagonal frequency normalized eigenvalue matrix $\mathbf{S}_f$, particularly adjacent to the normalization frequency. The acoustic potential energy given by Eq. (10) can now be approximated as

$$E_p \approx \mathbf{v}^T\mathbf{U}_f\hat{\mathbf{S}}_f\mathbf{U}_f^T\mathbf{v}. \tag{32}$$

Likewise the fixed shape modal filter, Eq. (20), can be written as

$$\mathbf{Z}_{t|_f}=\mathbf{U}_f^T\Psi_e^{-1}. \tag{33}$$

The modal amplitudes of the fixed shape radiation modes are given by

$$\mathbf{w}=\mathbf{Z}_{t|_f}\mathbf{v}_e. \tag{34}$$

With the modal filter in a form independent of frequency, shaped sensors may be used to decompose the surface velocity into modal amplitudes (Fig. 16), thereby doing away with the many point sensors and associated eigenvector digital filters required in Fig. 1. Therefore, unlike the system in Fig. 1, only the eigenvalues need be implemented with digital filters (see Fig. 16). It should be noted that because of the discrete nature of the finite element simulations, ''continuous meta sensors'' were approximated from the summed output of a line of discrete point sensors.

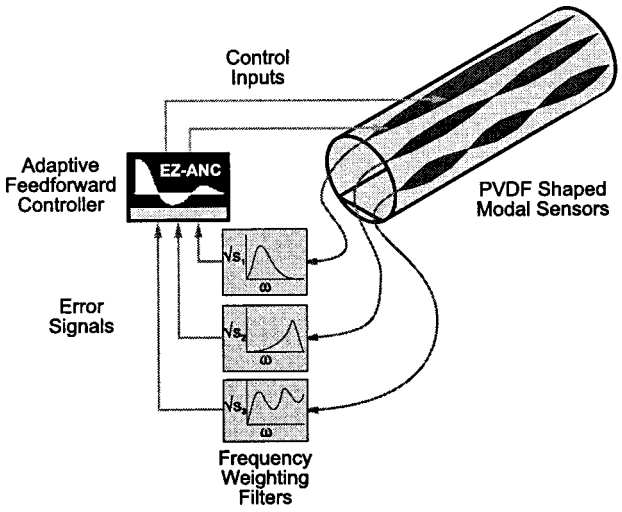

FIG. 16. Modal filter arrangement with frequency normalization of modal filter.

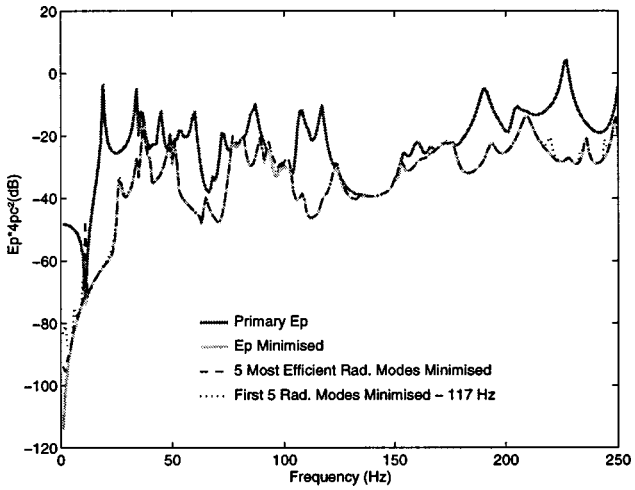

FIG. 18. Cost function comparison between frequency normalized radiation modes (117 Hz) and unmodified (frequency dependent) radiation modes.

The use of shaped error sensors made from piezo film and means for relating the charge output to the flexural motion of the surface to which they are fixed is discussed in detail by Hansen and Snyder.[27]

B. Results

As discussed previously, a decrease in accuracy is expected from neglecting the off-diagonal terms in the fixed frequency eigenvalue matrix [see Eq. (31)]. The error manifests itself as an increase in the number of efficient radiation modes away from the normalization frequency. This physically means that more ''orthogonal'' modes are necessary to account for the power transmission. Figure 17 illustrates the effect of fixing the eigenvectors to the values at a particular frequency has on the eigenvalues (as compared to Fig. 5).

As can be seen from Fig. 17, the eigenvalues around the frequency at which the system of equations is fixed (117 Hz) resembles the original frequency dependent data (Fig. 5). However, away from 117 Hz more radiation modes contribute significantly to the power transmission and as a result more modes will need to be measured to keep the control system performance equal to that of the frequency dependent case. A higher order digital filter is required to model the eigenvalues than was previously necessary in Fig. 5. However, this is still very easy to implement in a practical system.

As a benchmark, the performance achieved using the five most efficient radiation modes has been compared against that achieved using the first five fixed-shape radiation modes normalised at 117 Hz (see Fig. 18). This figure clearly shows that the two techniques yield almost identical levels of control (with the exception of 200–250 Hz where the acoustic modal density is high) demonstrating that frequency normalization of the mode shape is an excellent and highly efficient means of simplifying the control system when using radiation modal sensors.

Obviously, if fewer fixed-shape radiation modes are used, then the level of control will be subsequently reduced, particularly away from the normalization frequency. Figure 19 shows the reduction in the acoustic potential energy using

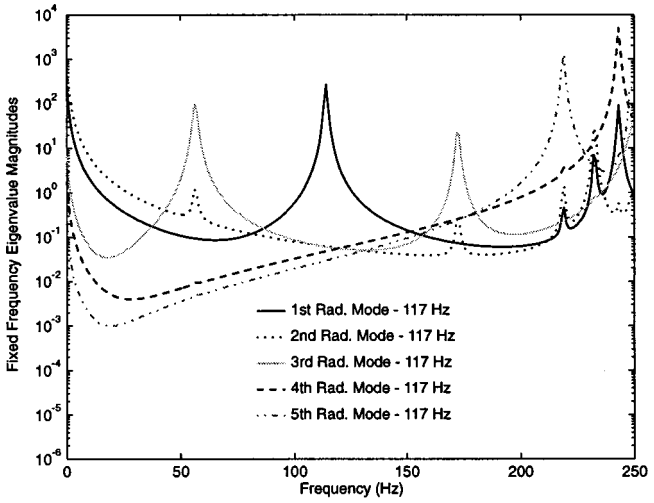

FIG. 17. Fixed frequency eigenvalues normalized to 117 Hz.

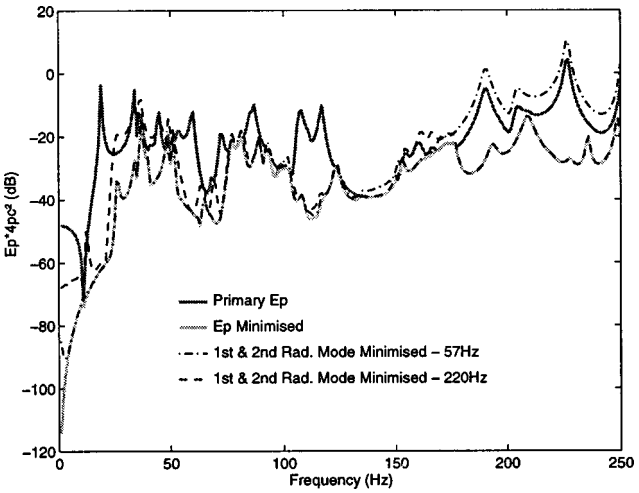

FIG. 19. Reduction in acoustic potential energy when minimizing frequency normalized mode shape functions.

the first two radiation modes when normalized to the first and fourth (nonzero) natural frequency of the cavity (57 and 220 Hz, respectively). For both cases, it can be seen that the performance drops away from the normalization frequency as the number of efficient radiation modes increases.

A close look at the results shows that control with the first two radiation modes fixed at 57 Hz is good between 10 and 140 Hz. Inspection of the mode shapes of the two most efficient fixed-shape radiation modes (fixed at 57 Hz) found that these reflected the first two acoustic modes (57 and 117 Hz). It is for this reason that control was only achieved up to 140 Hz. Likewise, when the radiation mode shapes were fixed to their shapes at 220 Hz, the first two radiation mode shapes matched the 173- and 220-Hz acoustic mode and good control was only achieved around the bandwidth bounded by these two frequencies.

C. Control without eigenvalue filters

In a real system, the eigenvalue (radiation efficiency) filter may be inconvenient to implement as most commercial active control systems do not have the facility to apply a frequency dependent filter to each individual channel. By not weighting the modal amplitudes by the square root of the radiation efficiencies (eigenvalue filter), neither the modal volume nor the acoustic impedance is accounted for in the cost function. As a result, the level of control afforded by the system will be reduced.

The five most efficient radiation modes were identified and their shape calculated at the natural frequencies of the first five acoustic modes, respectively. The modal amplitudes of these five fixed-shape radiation modes were then used as error signals for the control system over the entire frequency range of control. Figure 20 shows the acoustic potential energy levels obtained when minimizing the five most efficient fixed-shape radiation modes normalized to the natural frequencies of the first five acoustic modes without using an eigenvalue filter in the control system.

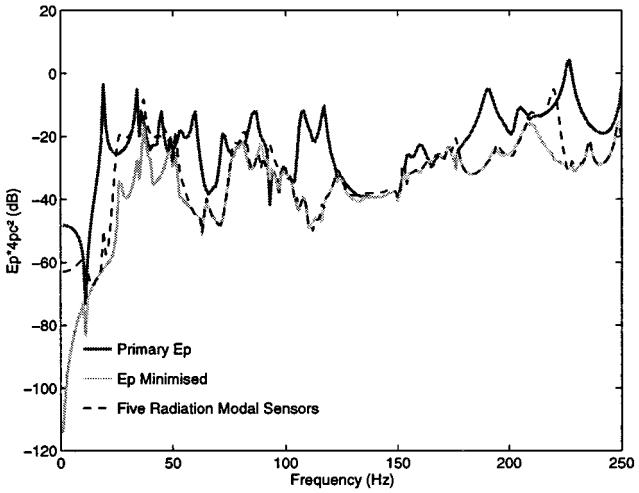

FIG. 20. Multi-channel frequency normalized radiation modal sensors without radiation efficiency weighting filter.

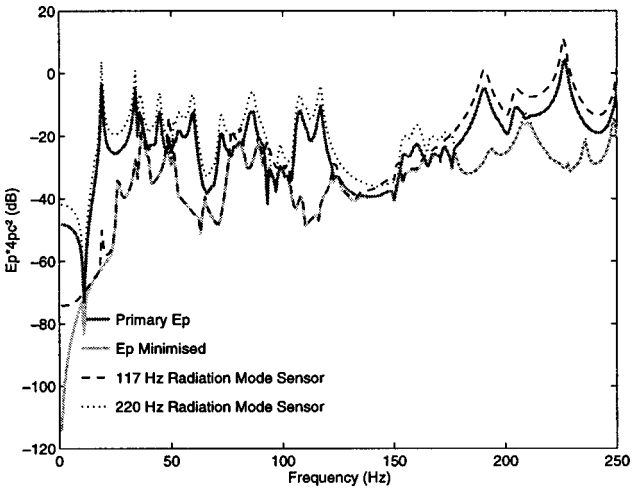

FIG. 21. Single channel frequency normalized radiation modal sensors without radiation efficiency weighting filter.

As can be seen, the reduction in the potential energy is less than that shown in Fig. 18. The poor performance is a result of not accounting for the frequency dependent radiation efficiency of the individual radiation modes. As a result, much of the control effort is spent in reducing the amplitudes of the less efficient modes, which do not significantly contribute to the sound transmission.

If only a single fixed-shape radiation mode is sensed, then 100% of the control effort is used in controlling that mode. Such an approach gives good results over a limited bandwidth around the frequency at which the mode shape is fixed. Figure 21 shows the level of control achieved by using the ''raw'' (unweighted) signal derived from a single radiation mode sensor whose shape was normalized at either 117 or 220 Hz. If a single channel control system were to use these two modal sensors with a crossover at approximately 170 Hz, this would provide almost optimal control over the 0–250 Hz frequency band. It should be noted that although such an approach is suitable for a system with a single control source, it is unlikely that it will work as well for systems using multiple control sources.

IV. CONCLUSIONS

It has been shown that it is possible to decompose a large number of discrete surface vibration measurements into a small number of high quality error signals for an active noise control system and obtain similar or improved results to conventional acoustic and structural error sensing. The decomposed structural vibration signals are formed so that they represent amplitudes of ''radiation modes'' which are orthogonal in terms of their contribution to the acoustic potential energy in the enclosure. The result of using such error signals is an increase in stability of the active noise control system and reduced dimensionality achieved through the reduction of the condition number of the control system transfer function matrix. Modal sensing of radiation modes provides the highest level of control with noninvasive sensors. Frequency normalization permits the use of shaped modal sensors rather than numerous discrete sensors to provide the

required error signals to minimize the enclosure acoustic potential energy. The work derived is not limited to stiffened cavities and may be applied to any coupled vibro-acoustic system. Preliminary experimental investigations involving the use of the technique to control the sound transmission from a small curved panel into an enclosed box have been very promising, although more work is needed in understanding the sensitivity of the control system to shape and fidelity errors before acceptable potential energy reductions will be achieved with large vibro-acoustic systems.[28]

ACKNOWLEDGMENTS

The authors gratefully acknowledge the financial support for this work provided by Australian Research Council and the Sir Ross & Keith Smith Fund. The authors would also like to thank colleagues Dr. K. A. Burgemeister and Dr. S. D. Snyder for their most enlightening discussions and contributions.

[1] F. Charette, C. Guigou, and A. Berry, ''Development of volume velocity sensors for plates using pvdf film,'' in Active 95, pp. 241–252 (1995).
[2] J. Pan, C. Hansen, and D. Bies, ''Active control of noise transmission through a panel into a cavity: I. Analytical study,'' J. Acoust. Soc. Am. **87**, 2098–2108 (1990).
[3] S. Snyder and N. Tanaka, ''On feedforward active control of sound and vibration using error signals,'' J. Acoust. Soc. Am. **94**, 2181–2193 (1993).
[4] K. Cunefare and M. Currey, ''On the exterior acoustic radiation modes of structures,'' J. Acoust. Soc. Am. **96**, 2302–2312 (1994).
[5] K. Naghshineh and G. Koopmann, ''Active control of sound power using acoustic basis functions as surface velocity filters,'' J. Acoust. Soc. Am. **93**, 2740–2752 (1993).
[6] K. Burgemeister, ''Novel methods of transduction for active control of harmonic sound radiated by vibrating surfaces,'' Ph.D. dissertation, The University of Adelaide, 1996.
[7] S. Elliott and M. Johnson, ''Radiation modes and the active control of sound power,'' J. Acoust. Soc. Am. **94**, 2194–2204 (1993).
[8] S. Snyder and K. Burgemeister, ''Performance enhancement of structural/acoustic active control systems via acoustic error signal decomposition,'' in *Inter-Noise 96* (Liverpool), pp. 1141–1146 (1996).
[9] M. Currey and K. Cunefare, ''The radiation modes of baffled finite plates,'' J. Acoust. Soc. Am. **98**, 1570–1580 (1995).
[10] M. Johnson and S. Elliott, ''Active control of sound radiation using volume velocity cancellation,'' J. Acoust. Soc. Am. **98**, 2174–2186 (1995).
[11] K. Burgemeister and S. Snyder, ''Active minimisation of radiated acoustic power using acoustic sensors,'' J. Acoust. Soc. Am. (submitted).
[12] S. Snyder, N. Tanaka, K. Burgemeister, and C. Hansen, ''Direct-sensing of global error criteria for active noise control,''in Active 95, pp. 849–860 (1995).
[13] G. Borgiotti, ''The power radiated by a vibrating body in an acoustic fluid and its determination from boundary measurements,'' J. Acoust. Soc. Am. **88**, 1884–1893 (1990).
[14] D. Photiadis, ''The relationship of singular value decomposition to wave-vector filtering in sound radiation problems,'' J. Acoust. Soc. Am. **88**, 1152–1159 (1990).
[15] P.-T. Chen and J. Ginsberg, ''Complex power, reciprocity, and radiation modes for submerged bodies,'' J. Acoust. Soc. Am. **98**, 3343–3351 (1995).
[16] G. Borgiotti and K. Jones, ''Frequency independence property of radiation spatial filters,'' J. Acoust. Soc. Am. **96**, 3516–3524 (1994).
[17] G. Borgiotti and K. Jones, ''The determination of the acoustic far field of a radiating body in an acoustic field from boundary measurements,'' J. Acoust. Soc. Am. **93**, 2788–2797 (1993).
[18] S. Snyder, C. Hansen, and N. Tanaka, ''Shaped vibration sensors for feedforward control of structural radiation,'' in *The Second Conference on Recent Advances in Active Control of Sound and Vibration* (Virginia Tech, Blacksburg, VA, 1993).
[19] N. Tanaka, S. Snyder, and C. Hansen, ''Distributed parameter modal filtering using smart sensors,'' Trans. ASME, J. Vib. Acoust. **118**, 630–640 (1996).
[20] R. Clark, ''Adaptive feedforward modal space control,'' J. Acoust. Soc. Am. **98**, 2639–2650 (1995).
[21] D. Morgan, ''An adaptive modal-based active control system,'' J. Acoust. Soc. Am. **89**, 248–256 (1991).
[22] F. Fahy, *Sound and Structural Vibration: Radiation, Transmission, and Response* (Academic, London, 1985).
[23] P. Nelson, A. Curtis, S. Elliott, and A. Bullmore, ''The active minimization of harmonic enclosed sound fields, part I: Theory,'' J. Sound Vib. **117**, 1–13 (1987).
[24] S. Snyder and C. Hansen, ''The design of systems to actively control periodic sound transmission into enclosed spaces, part 1: Analytical models,'' J. Sound Vib. **170**, 433–449 (1994).
[25] F. Bessac, L. Gagliardini, and J.-L. Guyader, ''Coupling eigenvalues and eigenvectors: A tool for investigating the vibroacoustic behaviour of coupled vibrating systems,'' J. Sound Vib. **191**, 881–899 (1996).
[26] M. Mercadal and A. Flowtow, ''On the importance of representative structural models in turboprop acoustics,'' J. Sound Vib. **188**, 753–759 (1995).
[27] C. Hansen and S. Snyder, *Active Control of Noise and Vibration* (E&FN Spon, London, 1997).
[28] B. Cazzolato and C. Hansen, ''Structural sensing of sound transmission into a cavity for active structural-acoustic control,'' in *Proceedings of the Fifth International Congress and Vibration* (The International Institute of Acoustics and Vibration, Adelaide), pp. 2391–2401 (1997).

Structural sensing of sound transmission into a cavity for active structural-acoustic control

Ben S. Cazzolato and Colin H. Hansen
Department of Mechanical Engineering, The University of Adelaide, South Australia 5005, Australia

Abstract

The problem of actively minimising the transmission of harmonic sound through a curved panel into a contiguous cavity using structural sensors is investigated both numerically and experimentally. It is well known that a control system that simply aims to minimise the structural vibration does not necessarily lead to a reduction in sound transmission. However, by considering the dynamics of the coupled system, it is possible to derive an orthonormal set of structural "radiation modes" which are orthogonal with respect to their contribution to the acoustic potential energy of the internal coupled acoustic space. Minimisation of the amplitudes of these "radiation modes" is guaranteed to result in a reduction of the interior potential energy, in contrast to minimising the normal structural modes. Sensing of the orthogonal sets of "radiation modes" is accomplished by using "smart sensors" made from either shaped PVDF film or a linear combination of accelerometers, adjusted to sense a particular radiation mode.

1 INTRODUCTION

Over the past 10 years vibration control sources have been used extensively to minimise sound transmission through light-weight structures into coupled enclosures. Vibration control sources have two distinct advantages over more conventional acoustic sources: fewer secondary sources are generally required for global control of the interior noise field (Charette *et al.*, 1995); and surface mounted actuators are far less intrusive than bulky speaker/cabinet arrangements. However, the gains in system compactness are not necessarily realised in practice as microphones placed throughout the cavity are used to provide the controller error signals to achieve global control.

Surface mounted accelerometers offer an alternative to microphones and although a reduction in the vibration of the structure may be achieved, a reduction in the interior sound field does not necessarily follow, particularly at low frequencies where the acoustic modal

density is low. However, it has been shown recently that is possible to calculate a quantity from the vibration of the structure, commonly referred to as a radiation mode, which is directly proportional to the sound radiated into the enclosed space (Snyder and Tanaka, 1993, Cazzolato and Hansen, 1997).

This paper uses the procedure developed by Cazzolato and Hansen (1997) where the sound transmission from a structure into an enclosed space can be measured directly using structural error sensors. The approach involves decomposing the surface vibration, usually via Singular Value Decomposition, into a number of velocity distributions which contribute independently to some cost function. It has been shown that for sound transmission problems only a very limited number of radiation modes contribute in most cases to the sound radiated from the vibrating structure and it is the number of efficient radiation modes, rather than the modal response of the structure, which defines the system dimensionality and subsequently, the control system order (Borgiotti, 1990).

Distributed parameter modal sensors called "smart sensors" have been employed to measure the modal amplitudes of the radiation modes and to provide inputs into an active control system. The use of independent (orthogonal) error signals for active noise control problems has been shown to offer a number of practical advantages, as it can: reduce convergence time for controllers; provide robustness to system parameter uncertainty; and minimise the number of sensors and actuators, and corresponding system dimensionality (Morgan, 1991).

The objective of the work described here was two fold: to investigate the feasibility of using structural sensors rather than microphones to control the sound transmission into cavities and in doing so, gain some understanding of the mechanisms of sound transmission into enclosures and the implications for active noise control systems; and to determine the most suitable means of sensing radiation modes using structural vibration measurements.

The active control of sound transmission into a rectangular cavity from a coupled curved panel excited by an external vibration source is investigated numerically. The structure and the acoustic space were modelled numerically using the commercially available finite element package ANSYS and coupled using modal coupling theory (Snyder and Hansen, 1994). Preliminary experiments using both discrete acceleration and continuous strain radiation modal sensors have been conducted with some success.

2 BACKGROUND THEORY

It has been assumed for the following analysis that the acoustic pressure, $p(\vec{\mathbf{r}})$, at any location, $\vec{\mathbf{r}}$ within a cavity can be expressed as an infinite summation of the product of rigid-wall acoustic mode shape functions, ϕ_i, and the modal amplitudes of the cavity, p_i.

$$p(\vec{\mathbf{r}}) = \sum_{i=1}^{\infty} p_i \phi_i(\vec{\mathbf{r}}) \tag{1}$$

The acoustic potential energy within an enclosure provides a suitable global error criterion for controlling the sound transmission from a coupled structure. This is given by the following

$$E_p = \frac{1}{4\rho_0 c_0^2} \int_V |p(\vec{\mathbf{r}})|^2 d\vec{\mathbf{r}} \tag{2}$$

where ρ_0 is the density of the acoustic fluid (air), c_0 is the speed of sound in the fluid and V is the volume over which the integral is evaluated. This volume may be the entire cavity or it may be a smaller volume within the cavity. By limiting the volume over which the integral is evaluated, controller effort is not expended in controlling non-essential regions. Subsequently, the attenuation within the zone is greater than when the total acoustic potential energy of the cavity is used as the cost function. Such an approach may be suitable when controlling the sound around the heads of passengers in automobiles or aircraft.

Substitution of the modal expansion (1) evaluated over n_a acoustic modes into (2) leads to the expression

$$E_p = \mathbf{p}^{\mathrm{H}} \Lambda \mathbf{p} \tag{3}$$

where $\mathbf{p}$ is the (n_a x 1) vector of acoustic modal amplitudes and Λ is a (n_a x n_a) diagonal weighting matrix, the diagonal terms of which are $\Lambda_{ii} = \frac{1}{4\rho_0 c_0^2} \int_V \phi_i^2(\vec{\mathbf{r}}) dV(\vec{\mathbf{r}})$.

The matrix expression for the pressure in the cavity arising from the vibration of the structure is given by (Snyder and Hansen, 1994)

$$\mathbf{p} = \mathbf{Z}_a \mathbf{v} \tag{4}$$

where $\mathbf{Z}_a$ is the (n_a x n_s) modal structural-acoustic radiation transfer function matrix and $\mathbf{v}$ is the (n_s x 1) structural modal velocity vector. Substituting equation (4) into (3), the potential energy arising from the vibration of the structure is given by

$$E_p = \mathbf{v}^{\mathrm{H}} \Pi \mathbf{v} \tag{5}$$

where the frequency dependent (n_s x n_s) error weighting matrix Π is given by $\Pi = \mathbf{Z}_a^{\mathrm{H}} \Lambda \mathbf{Z}_a$. The weighting matrix Π is real symmetric and may be diagonalised via an orthonormal transformation. This leads to an expression for the potential energy as a function of an orthogonal set of structural modes, commonly referred to as radiation modes,

$$E_p = \mathbf{v}^{\mathrm{H}} \Pi \mathbf{v} = \mathbf{v}^{\mathrm{H}} \mathbf{U} \mathbf{S} \mathbf{U}^{\mathrm{T}} \mathbf{v} = \mathbf{w}^{\mathrm{H}} \mathbf{S} \mathbf{w} \tag{6}$$

where the unitary matrix $\mathbf{U}$ is the (real) orthonormal transformation matrix representing the eigenvector matrix of Π, the (real) diagonal matrix $\mathbf{S}$ contains the eigenvalues (singular values) of Π and $\mathbf{w}$ is the (n_s x 1) radiation mode modal amplitude vector. By writing the potential energy in the form of equation (6), we have a set of structural velocity patterns (radiation mode shapes) which are orthogonal contributors to the error criterion (in this case, the potential energy in the volume). Therefore, a reduction in the amplitude of any of the radiation modes will directly result in a reduction in the potential energy.

The physical significance of the eigenvectors and eigenvalues is interesting. The eigenvalue can be considered a radiation efficiency (or coupling strength) and the associated eigenvector gives the level of participation of each normal structural mode to the radiation mode; thus it indicates the modal transmission path.

To evaluate (6) it is necessary to know the magnitude of the modal amplitudes of the radiation modes. In a physical system, these amplitudes may be estimated by decomposing the vibration at several discrete locations on the structure, ie

$$\mathbf{w} = \mathbf{Z}_t \mathbf{v}_e \tag{7}$$

where, $\mathbf{v}_e$ is the (n_e x 1) vector of velocity levels for the discrete structural sensors and $\mathbf{Z}_t$ is the (n_{rm} x n_e) radiation mode structural transfer function matrix (or modal filter matrix) which relates the vibration velocity levels at the discrete error sensor locations to the modal amplitudes of the radiation modes. Using the principle of modal orthogonality it can be shown that (Cazzolato & Hansen, 1997)

$$\mathbf{Z}_t = \Psi_e \mathbf{U} = \Theta_e \tag{8}$$

where Ψ_e is the (n_e x n_s) mode shape matrix at the sensor locations and Θ_e is the mode shape matrix of the radiation modes evaluated at the error sensor locations.

It will be shown in the following section that only a very small number of the radiation modes contribute to the sound transmission into the cavity over a narrow frequency range. This means that using radiation mode sensors rather than microphones, the number of inputs into the control system can theoretically be reduced.

It has been shown by Cazzolato and Hansen (1997) that the eigenvalues and eigenvectors can be highly frequency dependent. Subsequently the radiation mode shapes are also frequency dependent and therefore equation (6) as it stands does not easily lend itself to practical implementation. To overcome the frequency dependence of the mode shapes it is possible to select a frequency, *f*, at which to fix or "normalise" the eigenvector matrix. The acoustic potential energy given by (6) can now be approximated as

$$E_p \approx \mathbf{v}^{\mathrm{H}} \mathbf{U}_f \hat{\mathbf{S}}_f \mathbf{U}_f^{\mathrm{T}} \mathbf{v} = \mathbf{w}_f^{\mathrm{H}} \hat{\mathbf{S}}_f \mathbf{w}_f \tag{9}$$

where $\mathbf{U}_f$ is the eigenvector matrix corresponding to the chosen frequency, *f*, $\mathbf{S}_f$ is the diagonalised frequency normalised eigenvalue matrix and $\mathbf{w}_f$ is the modal amplitude vector of the frequency independent radiation modes. The mode shapes and the modal filter may still be calculated using equation (8).

This results in a non-orthogonal set of equations at all frequencies apart from the "normalisation frequency". However, at frequencies close to the normalisation frequency the resulting eigenvalue matrix is highly diagonal and can be approximated by only using the diagonal elements with little loss of mass from the matrix and accuracy in the error criterion.

With the mode shapes of the radiation modes now independent of frequency, the modal decomposition can be performed using shaped sensors, doing away with the need for a modal filter (see Figure 1). The use of shaped error sensors and means for relating the charge output to the flexural motion of the surface to which they are fixed, is discussed in detail by Lee and Moon (1990).

3 NUMERICAL SIMULATION OF SOUND TRANSMISSION THROUGH A CURVED PANEL INTO A COUPLED CAVITY

The coupled curved panel/cavity system shown in Figure 1 has been numerically investigated to determine the effectiveness of using radiation modal sensing to actively minimise the sound transmission into a cavity. The curved panel was made of 1 mm thick aluminium with simply supported end conditions. The other 5 walls of the cavity, measuring 0.985m x 0.420m x 0.250m, were rigid. The panel and the cavity were modelled individually using the FEA package ANSYS, then coupled using modal coupling theory (Snyder and Hansen, 1994) within MATLAB. The natural frequencies of the coupled system are shown in Table 1.

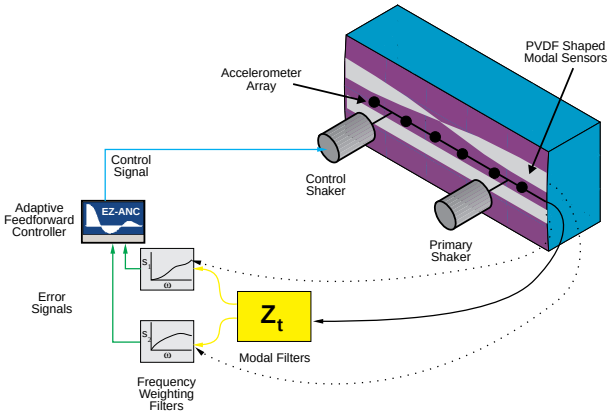

Figure 1 : Schematic showing the setup of the numerical experiment

Table 1 : Natural frequencies of the coupled vibro-acoustic system

Mode	Frequency (Hz)
$[1,1]_s$	73
$[2,1]_s$	94
$[2,2]_s$	117
$[1,2]_s$	135
$[2,3]_s$	158
$[0,1,0]_a$	185
$[3,1]_s$	205
$[2,4]_s$	207
$[1,3]_s$	212
$[3,2]_s$	219
$[3,3]_s$	241
$[2,5]_s$	256
$[1,4]_s$	259
$[3,4]_s$	276
$[1,5]_s$	290

s = structural, a = acoustic

A single primary shaker was located slightly off centre approximately a quarter of the way along the panel and a single control shaker was located symmetrically at the opposite end as shown in Figure 1.

Singular Value Decomposition was used to calculate the eigenvectors and eigenvalues of the radiation matrix. It was decided to optimise the system to control the first longitudinal acoustic mode. Using the technique given in Equation (9), the radiation mode shapes have been fixed to the shape that they have at the natural frequency of the first longitudinal mode, viz 185 Hz. The magnitude of the frequency normalised eigenvalues (radiation efficiencies) are shown in Figure 2. The mode shapes of the first 2 corresponding radiation modes are shown in Figures 3 and 4.

It is clear from Figure 2 that below 120 Hz the zeroth radiation mode dominates the sound transmission into the cavity. Between 120 Hz and 270 Hz the first mode becomes the most efficient. At the "cross over" frequencies (viz, 120 and 270 Hz) two modes contribute to the sound transmission and subsequently control will be ineffective with only a single control force.

It becomes clear when looking at Figures 3 and 4 that the mode shapes of the radiation modes looks very much like the acoustic mode shape on the surface of the panel. For systems with low acoustic modal density, this always occurs when the equations are normalised so that the mode shapes are fixed to

the shape they have at a frequency corresponding to the natural frequency of the acoustic system. In fact, when this is the case, the acoustic mode shape at the panel surface can be used instead of the mode shape of the radiation mode to decompose the modal amplitudes with little loss in accuracy.

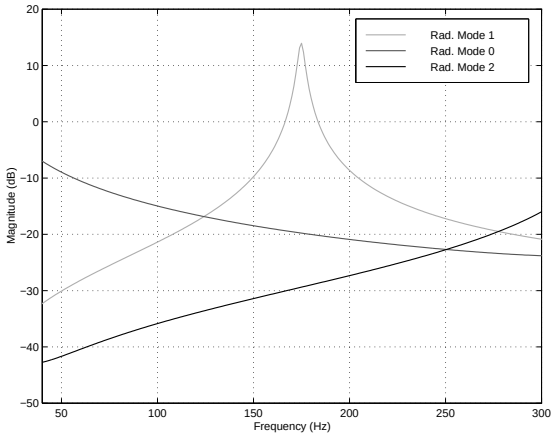

Figure 2 : Radiation efficiencies of the first 3 radiation modes fixed to 185 Hz

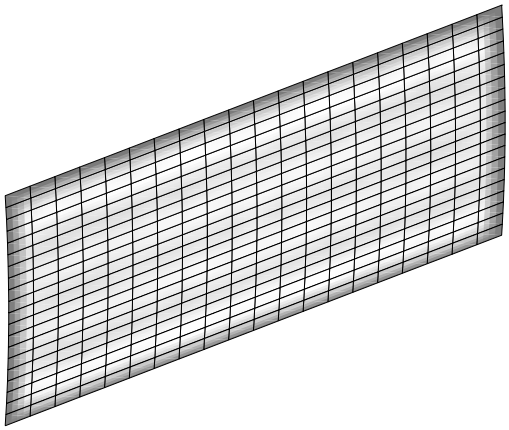

Figure 3 : Mode shape of the zeroth radiation mode at 185 Hz.

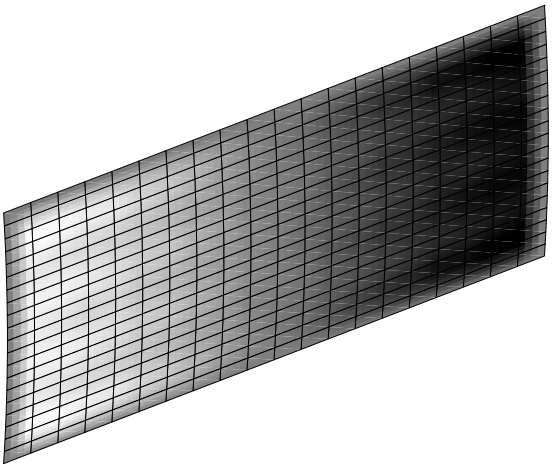

Figure 4 : Mode shape of the first radiation mode fixed to 185 Hz.

In Figure 5, the reduction in the total acoustic potential energies obtained when using conventional error criteria; namely, the acoustic potential energy (providing an upper limit of control performance), structural kinetic energy and the pressure at a single microphone are compared. As expected, minimising the structural kinetic energy does not necessarily lead to a reduction in the acoustic potential energy.

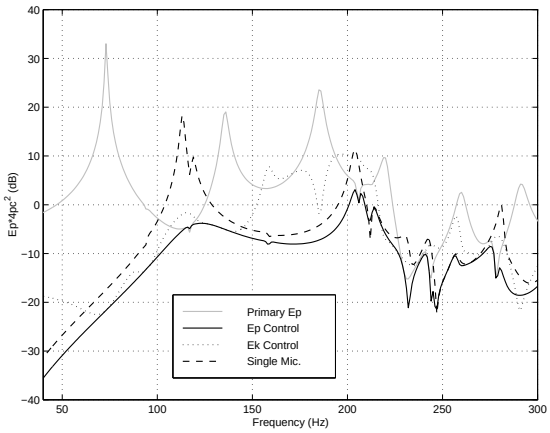

Figure 5 : Reduction in acoustic potential energy using various cost functions

In Figures 6 and 7, a comparison is made between using 11 discrete sensors and a continuous surface sensor to control the zeroth and first radiation modes respectively. The control achieved by sensing the first 2 radiation modes using continuous sensors is almost as effective as directly sensing the potential energy. As has been observed previously (Lee and Moon, 1990), the use of discrete sensors suffers from spatial sampling problems which leads to significant "leak through" of undesired modes. This contamination of the error signal results in sub-optimal performance.

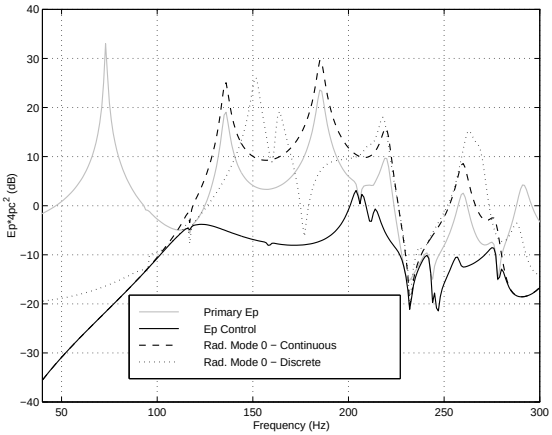

Figure 6 : Acoustic potential energy using zeroth radiation mode sensors.

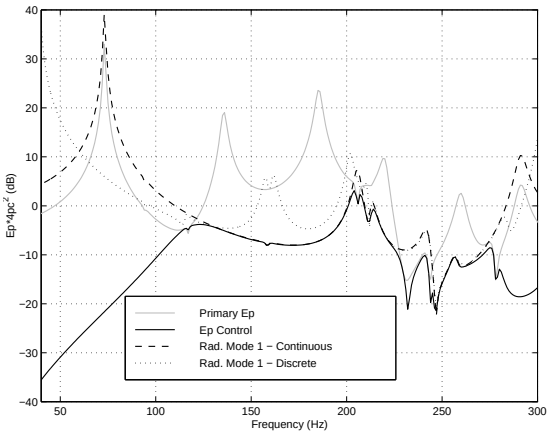

Figure 7 : Acoustic potential energy using first radiation mode sensors.

4 EXPERIMENTAL SETUP

A preliminary experimental investigation of the curved panel-cavity system was undertaken in order to confirm the theory derived by Cazzolato and Hansen (1997). The experimental configuration is shown in Figures 8 and 9.

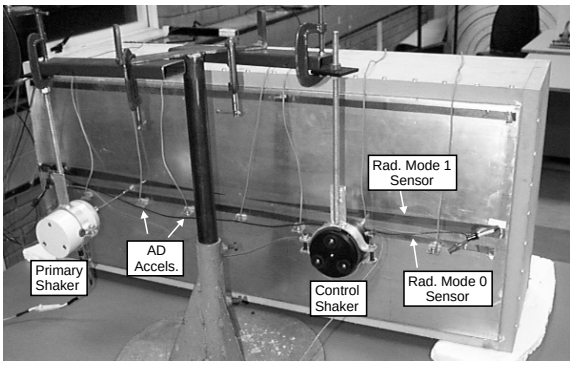

Figure 8 : Experimental setup for active control of sound transmission

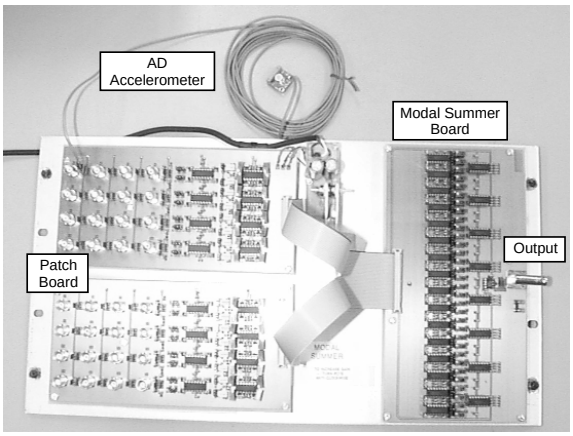

Figure 9 : Patch board and modal summing board

A Ling V203 shaker was used to provide the primary driving force and a B&K Type 8001 impedance head was used to measure the input force. A B&K Type 4810 mini-shaker was used as the control source.

Because many discrete error sensors are required for the modal decomposition in a practical system it was necessary to use a very low cost accelerometer. The Analog Devices ADXL05 accelerometer was selected for use as it is very inexpensive at $30 each and has a high sensitivity, contains internal amplification and has the necessary bandwidth for active noise and vibration applications. The accelerometers were attached to a patch board (see Figure 9) which provided the 5V dc supply voltage for the ADXL05 internal op amps and allowed calibration of the individual accelerometers. The buffered output from the patch board was fed into the modal summing board where the accelerometer signals were weighted according to the desired mode shape using trim pots and the fed into then 32 channel summer.

Only a single modal summing board was used which was found to be adequate for the current study. However, in most applications it would be necessary to monitor several radiation modes which would require additional summing boards. With the present layout these can be simply daisy chained to the single patch board.

The continuous sensors were made from shaped strips of 28 micron thick Cu-Ni electrode Polyvinylidene Fluoride (PVDF) film. The PVDF is sensitive to strain (rather than displacement as are the accelerometers) and consequently needed a profile equal to the second spatial derivative of the desired modes (Lee and Moon, 1990). These were cut to shape using a sharp blade and then attached to the curved panel using double sided tape. Copper tape backed with a conductive adhesive was used to provide an adequate connection from the film to a charge amplifier. It was necessary to buffer to output from the film via a high impedance charge amp to ensure that the cut-off frequency of the high-pass filter circuit formed by the PVDF was well below the frequency range of interest.

The potential energy of the cavity was estimated using 5 microphones randomly located throughout the interior. Numerical simulations and experience showed that this was an adequate number of microphones to estimate the potential energy of a small cavity using a single structural control source. The single microphone used during the tests was optimally located in one of the rear corners of the backing box.

5 EXPERIMENTAL RESULTS

The transfer functions between the driving force and the microphones, the zeroth radiation mode and the first radiation mode sensors are shown in Figures 10, 11 and 12 respectively. It has been shown that for simply supported structural systems that the even-order radiation modes are formed from the odd-order structural modes, and vice-versa. Therefore the zeroth radiation mode sensor, designed to sense the bulk compression acoustic mode, should only respond to the odd-order structural modes shown in Table 2. Likewise, the first radiation mode sensor, shaped to sense the primary longitudinal acoustic mode, should only respond to the even-order structural modes.

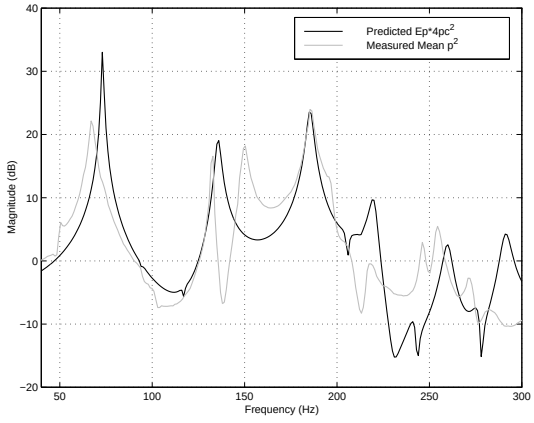

Figure 10 : Measured and predicted transfer function between the 5 microphones and driving force

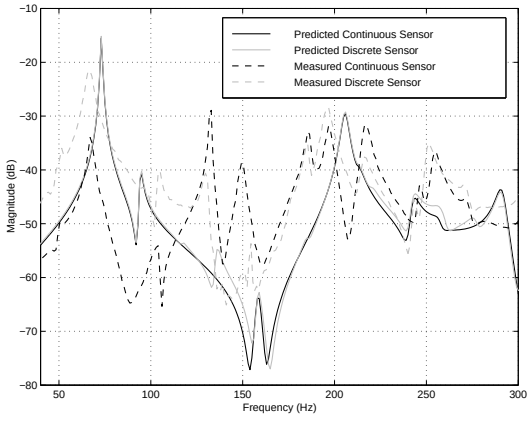

Figure 11 : Measured and predicted transfer function between the zeroth radiation mode sensor and driving force

As can be seen in Figures 11 and 12 both the PVDF and discrete radiation mode sensors respond strongly to the desired structural modes; however, it can also be seen that there is some "leak-through" of undesired structural modes due to imperfections in the film pattern and errors associated with discrete spatial sampling. It is worth noting that the (straight) zeroth radiation mode sensors are more sensitive to the even-order structural modes than the (half sine) first radiation mode sensors are to the odd-order structural modes. This phenomenon was also experienced by Lee and Moon (1990) when applying shaped sensors to measure normal structural modes on a beam, although no explanation was given as to the cause.

Table 2 : Natural frequencies and modal participation factors of the structural modes

Structural Mode	Resonance Frequency (Hz)	Structural Mode Participation Factor	
		Radiation Mode 0	Radiation Mode 1
[1,1]	77	-0.859	0
[2,1]	96	0	0
[2,2]	129	0	0
[1,2]	144	0	0.818
[2,3]	180	0	0
[3,1]	199	-0.284	0
[2,4]	204	0	0
[1,3]	204	0.272	0
[3,2]	220	0	0.273
[3,3]	234	-0.092	0

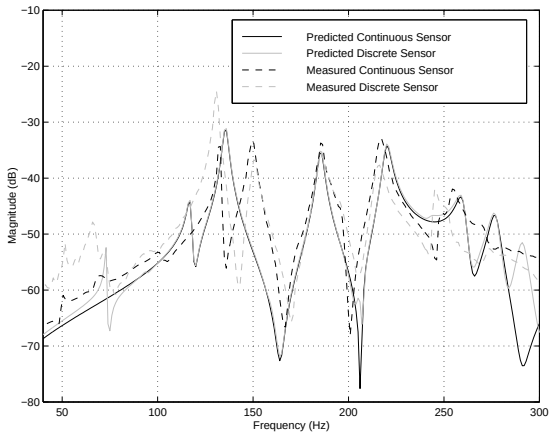

Figure 12 : Measured and predicted transfer function between the first radiation mode sensors and driving force

As to be expected, the discrimination quality of the real sensors is not as effective as the numerical simulation predicted. However, even with only seven accelerometers and a single strip, the frequency response curve shows that radiation modal sensing will still work in systems with a low modal density.

Active Structural-Acoustic Control

The mean square pressure level of the five microphones with and without active sound transmission control is shown as a function of frequency in Figures 13, 14 and 15. Control using the 5 microphones as error sensors provides the maximum attenuation threshold that can possibly be achieved. Figure 13 shows that using a single microphone provides good control at most frequencies. This is only because the acoustic modal density is very low in the frequency range of interest, particularly below 250 Hz.

Because only a single radiation mode was used for the error signal at any one time, the frequency weighting filter shown in Figure 1 was not required. In practice, for single channel control a band pass filter for each radiation mode signal is adequate. For multiple channel control it is often possible to neglect the filter altogether (Cazzolato and Hansen, 1997).

Control using the continuous zeroth radiation mode sensor within the design bandwidth (0-120 Hz) is somewhat disappointing. This is believed to be due to the "leak-through" of undesired modes noted earlier. Contrary to the numerical simulation, the controlled pressure level when using the discrete zeroth radiation mode sensor as an error sensor was lower than that obtained when using the equivalent continuous sensor. This is believed to be due to inaccuracies in the shape of the PVDF film. As expected, at frequencies above 120 Hz control leads to an increase in the mean square sound pressure level within the cavity.

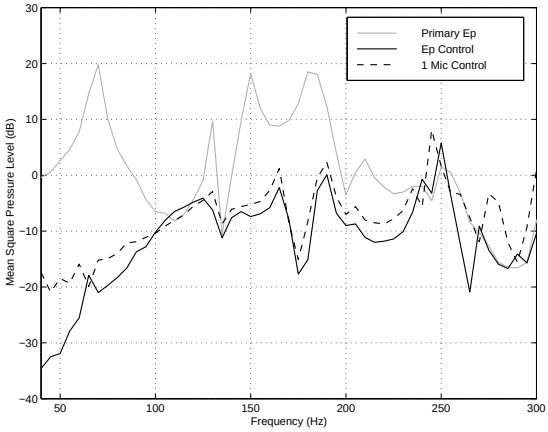

Figure 13 : Mean square pressure level using all five mics. and a single mic. as error sensors.

Control using the continuous first radiation mode sensor within its operational bandwidth (120-270 Hz) is high, with almost optimum control achieved between 120 Hz and 200 Hz. However, control above 200 Hz is poor. This is because the second longitudinal mode begins to contribute to the acoustic potential energy. This was not experienced in the numerical simulation because the shakers were placed close to the nodes of the structural modes that excite the second acoustic mode. As before, control outside the design frequency band leads to an increase in the mean square sound pressure within the cavity. The discrete first radiation mode sensor behaves as expected and provides less control than the equivalent continuous sensor.

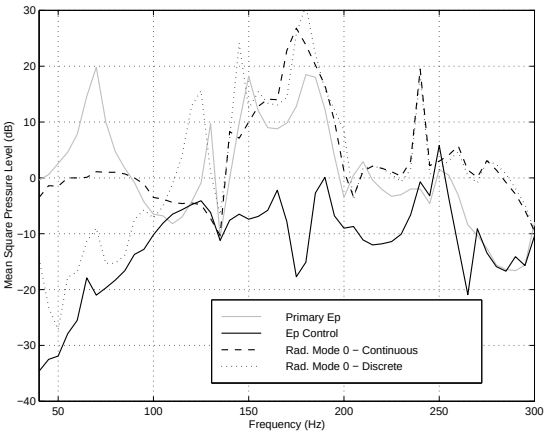

Figure 14 : Mean square pressure level using the zeroth radiation mode sensors.

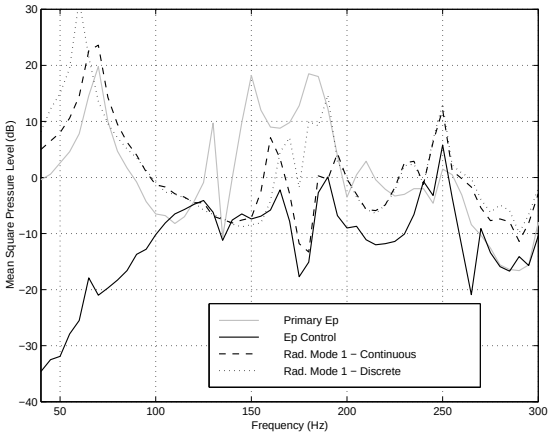

Figure 15 : Mean square pressure level using the first radiation mode sensors.

Although the level of control achieved when using the modal sensors rather than using the discrete microphones as error sensors was less, the expected benefits of modal sensing, namely rapid controller convergence and high stability were definitely observed.

6 CONCLUSIONS

It has been shown both numerically and experimentally that it is possible to use structural sensors to actively minimise the transmission of sound from a structure into a coupled enclosure. The preliminary results indicate that the although technique is feasible, the sensors appear to be very sensitive to "leak through" of undesired modes. The continuous sensors are more accurate modal sensors than discrete sensors due to spatial sampling errors for all but the zeroth (bulk compression) radiation mode. The modal sensors were shown to reduce the convergence time of the controller and increase the controller stability when compared to that using discrete microphones. Although not presented here, it is possible to constrain the cost function in such a way as to only control specific regions in the cavity. This constrained global approach has the advantage that controller effort is not expended in controlling non-essential regions. This "virtual microphone" is the subject of a future paper.

References

Borgiotti, G.V. (1990), "The power radiated by a vibrating body in an acoustic fluid and its determination from boundary measurements," *J. Acoust. Soc. Am.*, **88**, 1884-1893.

Cazzolato, B.S. and Hansen, C.H. (1997), "Active control of sound transmission using structural error sensing", *submitted for publication in the J. Acoust. Soc. Am.*

Charette, F., Guigou, C. and Berry, A. (1995), "Development of volume velocity sensors for plates using PVDF film," *Proc. Active 95*, 241-252.

Lee, C.-K. and Moon, F.C. (1990), "Modal Sensors/Actuators", *Transactions of the ASME*, **57**, 434-441.

Morgan, D.R. (1991), "An adaptive modal-based active control system," J. Acoust. Soc. Am., **89**, 248-256.

Snyder, S.D. and Hansen, C.H. (1994), "The design of systems to actively control periodic sound transmission into enclosed spaces, Part 1. analytical models," *J. Sound Vib.*, **170**, 433-449.

Snyder, S.D. and Tanaka, N. (1993), "On feedforward active control of sound and vibration using error signals," *J. Acoust. Soc. Am.*, **94**, 2181-2193.

Glossary

Note: Vectors and matrices are shown in boldface. Over-bars indicate estimates; over-arrows indicate location vectors.

$B_{l,i}$	structural acoustic coupling coefficient
$\mathbf{B}$	modal coupling matrix
c,c_0	speed of sound in air
$\mathbf{d}$	energy density column vector
$\mathbf{D}_i$	pressure to energy density transfer matrix
e_{31}, e_{32}, e_{36}	piezoelectric field intensity constants
$e(p)$	normalised pressure error
$e(p)$	normalised velocity error
$e(E_D)$	normalised energy density error
E_D	energy density
$\bar{E}_D$	energy density estimate
E_k	structural kinetic energy
E_p	acoustic potential energy

f	excitation frequency
f_c	control force
f_p	primary force
f_{Sch}	Schroeder frequency
$\mathbf{F}$	total generalised force vector
G_a	acoustic Green's function
G_s	Green's function of the structure
h	half the microphone spacing
k	acoustic wavenumber
$\mathbf{K}$	correction matrix
$\mathbf{K}_f$	fluid equivalent stiffness matrix
$m(\vec{\mathbf{x}})$	mass density of the structure at a point $\vec{\mathbf{x}}$
M	Mach number
M_i	modal mass of the i^{th} structural mode
$\mathbf{M}$	diagonal modal mass matrix
$\mathbf{M}_f$	fluid equivalent mass matrix
$\mathbf{M}_{f_e}$	fluid element mass matrix
$\mathbf{M}_{s_e}$	structural element mass matrix
n_a	number of acoustic modes

n_d	number of microphones per energy density sensor
n_s	number of structural modes
N	linear shape function of the fluid element, linear shape function of the structural element.
p_e	pressure estimate
$\hat{p}_e$	pressure estimate due to phase or magnitude mismatch
$\mathbf{p}$	column vector of pressure modal amplitudes
P	pressure magnitude
q	acoustic source strength, charge developed across a piezoelectric element
$\mathbf{q}$	row vector of acoustic source strengths
$\mathbf{Q}$	generalised volume velocity
$\mathbf{R}$	rotation matrix
$\mathbf{s}$	nodal area vector
S	surface area of the structure, surface area of the cavity.
$\mathbf{S}$	diagonal singular value matrix equivalent to the radiation efficiencies
$\mathbf{S}_f$	frequency normalised eigenvalue matrix
$\mathbf{S}_i$	microphone perturbation displacement matrix
t	time
t_f	thickness of PVDF film
t_s	thickness of shell

T	half the sensitivity mismatch
U	volume velocity of the shell
$\mathbf{U}$	real orthonormal transformation matrix representing the eigenvectors of the radiation modes
$\mathbf{U}_f$	eigenvectors matrix of the radiation modes at a particular frequency
$\hat{v}$	velocity estimate due to phase or magnitude mismatch
v_i	complex amplitude of the i^{th} structural mode
$\mathbf{v}$	column vector of structural modal velocities
V	volume of the cavity, velocity magnitude
$\mathbf{w}$	column vector of velocity amplitudes of the radiation modes
W	radiated power
$\mathbf{X}_i$	matrix defining the positions of the microphone elements in the energy density probe
$\mathbf{Z}_a$	structural to acoustic modal internal radiation transfer function
$\mathbf{Z}_b$	acoustic to structural modal internal radiation transfer function
Z_i	*in vacuo* structural input impedance of the i^{th} structural mode
$\mathbf{Z}$	diagonal *in vacuo* structural input impedance matrix
$\mathbf{Z}_I$	structural modal input impedance matrix
Z_l	rigid-walled acoustic input impedance of the l^{th} acoustic mode
$\mathbf{Z}_q$	acoustic modal input impedance matrix

$\mathbf{Z}_t$	radiation mode structural transfer function matrix (or modal filter matrix)
α_p	error in pressure estimate due to phase mismatch
α_v	error in velocity estimate due to phase mismatch
β_p	error in pressure estimate due to magnitude mismatch
β_v	error in velocity estimate due to magnitude mismatch
δ	Kronecker delta function
γ	coherence function
Γ	shape function of the PVDF sensor
$\boldsymbol{\epsilon}$	positional error matrix
η_a	modal loss factor of the acoustic modes
η_s	modal loss factor of the structural modes
θ	phase angle
$\boldsymbol{\Theta}$	mode shape matrix of the radiation modes
κ	eigenvalue of the acoustic mode (same dimensions as the wavenumber)
λ	acoustic wavelength
Λ_l	modal volume of the l^{th} acoustic mode
$\boldsymbol{\Lambda}$	diagonal modal volume matrix
ν	Poisson's ratio
$\boldsymbol{\Xi}$	mode shape matrix of the radiation modes

$\mathbf{\Pi}$	error weighting matrix
$\mathbf{\Pi}_p$	diagonal phase mismatch error
$\mathbf{\Pi}_s$	diagonal sensitivity mismatch error
ρ_0	density of air
ϕ_s	half the total phase mismatch
$\boldsymbol{\phi}$	acoustic mode shape vector
Φ	acoustic potential function
$\mathbf{\Phi}$	phase mismatch matrix
$\mathbf{\Phi}_c$	mode shape matrix evaluated at the acoustic control source locations
$\mathbf{\Phi}_e$	mode shape matrix evaluated at the acoustic error sensor locations
$\boldsymbol{\psi}$	structural mode shape vector
$\mathbf{\Psi}_c$	mode shape matrix evaluated at the structural control source locations
$\mathbf{\Psi}_e$	mode shape matrix evaluated at the structural error sensor locations
$\mathbf{\Upsilon}$	diagonal acoustic resonance matrix
ω	angular frequency
ω_i	eigenvalue of the structural mode (same dimension as angular frequency)
$\mathbf{\Omega}$	diagonal weighting matrix